830-A10 (MF)   NAS 1.55:2250

Rotordynamic Instability Problems in High-Performance Turbomachinery - 1982

ORIGINAL

NASA

Rotordynamic Instability Problems in High-Performance Turbomachinery - 1982

NASA

National Aeronautics
and Space Administration

Scientific and Technical
Information Branch

1982

I

BLANK PAGE

II

PREFACE

An appreciation of this workshop's proceedings is enhanced by a look backward at the proceedings of the first workshop, which was held at Texas A&M University on May 12-14, 1980. The initial workshop was organized in response to severe instability problems that had been encountered in the development of space shuttle main engine turbopumps and various commercial multistage compressors. The first workshop proceedings emphasized a feeling of uncertainty in predicting the stability characteristics of turbomachinery based on perplexing and, in many cases, unexplainable results obtained in field experiences with unstable turbomachinery. Further, many proposed analyses and models for forces, particularly fluid forces, developed in turbomachinery were clearly speculative and were largely unsupported by test data.

The present workshop proceedings demonstrates that many of the uncertainties that were present two years ago have been substantially reduced. To a considerable extent, papers presented herein report the results of programs that have been established to systematically resolve the problems of predicting stability characteristics of high-performance turbomachinery. The emphasis on experimental validation of the forces that influence rotordynamics is particularly encouraging.

This second workshop was organized to address the general problem of rotordynamic instability by gathering those persons with immediate interest, experience, and knowledge for a discussion and review of both past stability problems and present research and development efforts. The intent of the workshop organizers and sponsors is that the workshop and these proceedings provide a continuing impetus for an understanding and resolution of these problems.

Chairmen:

Dara W. Childs and
John M. Vance
Texas A&M University

Robert C. Hendricks
NASA Lewis Research Center

iii

BLANK PAGE

DEDICATION

The proceedings of this workshop is respectfully dedicated to the memory of Lawrence P. Ludwig, Chief of the Mechanical Components Branch, NASA Lewis Research Center. Mr. Ludwig died on September 11, 1981, after an extended illness. He is survived by his widow, two daughters, and a son.

Larry's research on seals over a period of two decades resulted in advances in sealing technology that significantly affected the design of a broad range of machines from aircraft turbine engines, rocket engine turbopumps, and rotorcraft transmissions to commercial pumps and compressors. He was an internationally recognized expert on sealing technology and the holder of numerous patents on seals. He was coinventor of the lift pad or self-acting seal, which has advanced the speed and pressure ratio capability of face seals in advanced turbine engines, turbopumps, and compressors, significantly improving their efficiency. He is the inventor of two new shaft-riding seals that extend both the speed capability and life of transmissions. One of these seals, now standard equipment on both a commercial and a military helicopter, has great reduced maintenance costs and downtime.

With the evolution of self-acting seals into the applications stage he concentrated his efforts on leading research on gas path sealing for turbine engines. The first of several promising concepts was engine tested and should significantly reduce turbine engine fuel consumption.

Without the multiplicity of improvements in seal technology for which Larry was responsible, high-speed turbomachines would be far less advanced than they are today. He was awarded the NASA Exceptional Scientific Achievement Medal.

BLANK PAGE

CONTENTS

CONTROL OF ROTOR INSTABILITIES

ROTORDYNAMIC INSTABILITY FIELD PROBLEMS

J. C. Wachel
Southwest Research Institute
San Antonio, Texas 78284

SUMMARY

Vibration data obtained during several rotor instability investigations is presented to illustrate the effect of changes in system parameters on overall rotor stability. The data includes the effects of bearing and seal changes as well as those due to variations in speed and pressure ratio. Field problems indicate that the stability of rotors is often highly sensitive to fairly minor variations in bearing and seal parameters. Measured field data is valuable in normalizing analytical computer models so that effective solutions can be obtained.

INTRODUCTION

Rotor instability vibrations in compressors and turbines have occurred more frequently in recent years and have caused severe failures and costly downtime for several large projects. Rotor instabilities can occur in flexible shaft units which operate above their first critical speed. The whirling instability frequency is usually near one of the shaft critical speeds and can be caused by many factors, including hydrodynamic cross coupling of bearings and seals, internal friction, aerodynamic cross coupling, and torsional coupling. The whirling motion can be subsynchronous or supersynchronous, and may be forward or backward precession; however, in general most problems are subsynchronous and have forward whirl.

During the past few years, vibration data has been collected on several compressors that have experienced severe shaft instabilities. These compressors differed in manufacture, shaft diameter, weight, bearing span, critical speeds, and running speed. The spectral characteristics of shaft vibrations were observed as the compressors/turbines approached the onset of instability; i.e., before the machine experienced the high level vibrations normally associated with unbounded instabilities. On most units that have instability problems, a trace of vibration at some instability frequency normally exists at all times; however, it is not possible to verify the severity of the instability from vibration measurements at one operating condition. The threshold of instability can be fully defined only from testing over the full performance range of the machine, and even this approach is not always completely adequate. Some units have run satisfactorily for several years before serious instability trip-outs occurred. After one year of satisfactory operation, one compressor failed eight times in the next three years from instabilities. Because the stability margin on some units is so delicately balanced, its characteristics can be drastically changed whenever small changes are made in factors such as pressure ratio, flow, bearing clearance, oil temperature, unbalance, alignment, etc., or upsets in the process such as liquid slugs, surge transients, or electrical trip-outs.

It follows, therefore, that the threshold of stability can likewise be improved by small changes in these same parameters, but the exact improvement required to make an unstable system stable is sometimes difficult to predict.

The most sensitive elements which influence rotor stability include the following: (1) hydrodynamic cross coupling in fluid film bearings, seals, and labyrinths, (2) aerodynamic cross coupling forces, (3) hysteretic or internal friction damping, (4) pulsations, (5) pulsating torque and axial loads, (6) asymmetric shafting, (7) fluid trapped in rotor, (8) stick-slip rubs and chatter, (9) dry friction whip.

To properly calculate the stability margin of a rotor, the mathematical model must be able to simulate all possible destabilizing components. The logarithmic decrement evaluation of rotor system damping is useful for predicting rotor stability. Field experience shows that while this technique provides proper direction in designing for stability, uncertainty still exists in quantitatively predicting the onset of instability and defining the contribution of individual influencing parameters.

When instability vibrations occur in installed machinery, better estimates of the possible effects of system changes can be made if measured field data is available for normalization of the mathematical model. The normalization procedures compensate for unknown dimensional variations which affect bearing and seal properties and adjust for actual aerodynamic loading. This paper will present measured field data gathered over the past nine years on several machines which exhibited instabilities (ref. 1). The data analysis techniques presented were used to define rotor stability thresholds and the effects of modifications to seals, bearings, shafts, and process variations.

CASE 1. INSTABILITY OF A STEAM TURBINE

On startup of a steam turbine after a complete turn-around in which new pressure pad bearings were installed, the measured shaft vibrations indicated the turbine first critical speed was at 1800 rpm as shown in figure 1 which gives the amplitude and phase angle response versus speed. When the unit speed approached 4800 rpm, a subsynchronous instability at 1800 cpm suddenly appeared (fig. 2).

A stability analysis revealed that the calculated logarithmic decrement for this rotor with tight bearing clearances was only 0.04. Investigations were made into possible field modifications to improve the stability that could be implemented in a short time. Calculations showed that if the pressure pad bearing clearance was increased and the bearing length reduced, then the logarithmic decrement increased to 0.2 with the critical frequency remaining near 1800 cpm.

The bearings were then modified and installed. Vibration data with the new bearings is shown in figure 3. The turbine speed could be increased to 5100 rpm without any instability occurring and the unit has continued to operate without instabilities. This case illustrates that some instability problems can be solved by fairly simple modifications.

CASE 2. STEAM TURBINE INSTABILITY IN A METHANOL PLANT (ref. 2)

This case deals with a 13,000 hp, 10,600 rpm, three stage steam turbine. The rotor had pressure pad bearings at a bearing span of 236 cm (60 inches). The bearings were later changed to 5 shoe tilted pad bearings in an attempt to eliminate the half speed problems which occurred at maximum speed. Data taken during the turbine startup with the new bearings (fig. 4) revealed a vibration component at one-half speed when the speed reached 7200 rpm, thus showing that the change to tilted pad bearings was not sufficient to eliminate the half speed vibrations. During subse-

quent runs, two subharmonic criticals at 4500 and 7000 cpm were excited as well as the half speed component (fig. 5).

During another run a subsynchronous frequency occurred at approximately 0.3 times the running speed. Figure 6 shows that a large amplitude component occurred at 2500 cpm when the running speed was 9000 rpm. Both oil pumps were running during this test and one tripped out for a few seconds. The turbine running speed suddenly dropped 200 rpm. The instantaneous frequency analysis shown in the upper trace of figure 6 shows that this upset moved the subsynchronous component from 2500 to 4400 cpm. Frequency analyses made later showed that the subsynchronous vibration components were also different on the horizontal and vertical probes of the turbine (fig. 7). These two instability frequencies were near calculated damped instability frequencies.

Several modifications were implemented that reduced the magnitude of the instability. These included changing the seal design, increasing the bearing clearances, and strengthening the bearing housing. This case illustrates that changing to tilted pad bearings may improve the stability characteristics of a rotor but does not necessarily eliminate instabilities. With the tilted pad bearings for this rotor, however, only slight changes were required to control the instabilities.

CASE 3. INSTABILITY OF GAS REINJECTION COMPRESSOR (ref. 3)

This case deals with a much discussed reinjection compressor which experienced excessive nonsynchronous vibrations on startup. Field vibration data will be presented which shows the influence of oil ring seals, aerodynamic cross coupling, and speed on instability frequencies and amplitudes. These areas are of major concern to rotordynamists; however, very little experimental data is available in the open technical literature. The 22,000 horsepower, eight stage compressor with back-to-back impellers (fig. 8) was rated at 8500 rpm, had a design suction pressure of 24.1 MPa (3500 psi), and discharge pressure of 63.4 MPa (9200 psi). The calculated first critical speed of the rotor was 3800 cpm for a bearing span of 206 cm (81 inches). Floating oil seals were located a few inches inboard of the bearings. The compressor originally could not be brought to design speed and pressure without tripping out on high vibrations (fig. 9). The units were monitored by shaft vibration probes which automatically shut down the unit whenever the vibrations exceeded 64 μm (2.5 mils); however, due to the monitor's finite response time and suddenness of the instability trip-outs, vibration amplitudes equaling total bearing clearance were experienced.

The frequency of the nonsynchronous instability was 4400 cpm which was higher than the calculated rigid bearing critical speed of 4200 cpm. This can occur if the floating oil seals lock up and carry some load, thereby effectively reducing the bearing span. In the computer simulation of this shaft, an effective oil seal stiffness of 286,000 N/cm (500,000 lb/in) was required to calculate an instability frequency of 4400 cpm. Using this stiffness for the oil seals the calculated log decrement reduced to 0.08 compared to 0.3 calculated for the original rotor, neglecting the effect of the seals. Therefore, the calculations indicated that the seals significantly reduced the stability of the unit.

To improve the rotor instability, two circumferential grooves were cut into the sealing surface of the seals, the pressure balance of the rings was improved, and the coefficient of friction of the sliding surfaces was reduced. The compressor was still unstable, as can be seen in figure 10. A nonsynchronous instability occurred at 4700 cpm; however, instabilities above running speed at 9500 and 10,500 cpm were also excited. As the unit speed reduced, the instability component at 10,000 cpm

3

remained. The rotor was found to be sensitive to the rate of acceleration; therefore, by slowing down the startup procedure, it was possible to operate in the normal speed range.

To more fully define the stability limits, data was obtained throughout the entire performance map. For a constant speed of 7600 rpm, figure 11 shows how the aerodynamic loading affects the amplitude of the instability component at 5160 cpm (a forward precessional mode). As the suction pressure increased, the amplitude of the instability increased but remained within bounds until a limiting pressure was reached. The frequency of the instability component moved from 4400 to 5160 cpm as pressure was increased. To show the effect of speed on the instability the suction pressure was held constant at 10.3 MPa (1500 psi) and the speed increased. The instability amplitude increased almost linearly with speed (fig. 12).

After these tests were made, several seal designs were tested (fig. 13); however, there was little improvement in the overall rotor stability. The type of seal design greatly affected the frequency of the nonsynchronous instability and the threshold speed. One seal design studied had large radial clearances and only one land, less than 5 mm (0.2 inch) long. The test was primarily to study the effect on the instability frequency since the seal oil leakage was excessive. Shortening the seal length should reduce its load-carrying effect, thus reducing the instability frequency. However, test results showed that nonsynchronous instabilities occurred at frequencies above running speed (10,000 and 11,000 cpm) similar to the data presented in figure 10.

Another test using a different seal design also showed instabilities above running speed. These instability frequencies appeared to be a function of suction pressure as shown in figure 14. During this test the compressor speed was 7523 rpm and suction pressure 8.28 MPa (1200 psi). Figure 14 gives the frequency analysis showing 13 μm (0.5 mil) at running speed and 25 μm (1.0 mil) at 10,500 cpm and a trace at 4500 cpm. As the suction pressure was reduced, the higher frequency component lowered to 8900 cpm and then separated into two components, 8900 and 9300 cpm.

Some specifications require that the first critical speed be greater than 0.6 times the running speed to help prevent instabilities. Figure 15 shows that an instability component at 0.8 times running speed occurred when the running speed was 4000 rpm or slightly above the first critical speed. In this data, the instability occurred when the ratio of running speed to first critical was 1.25, showing that a ratio of running speed to first critical of less than 2:1 does not necessarily ensure that a rotor will be stable. The majority of the instability trip-outs were at speeds where the ratio of running speed to first critical speed was less than 2:1.

The data presented shows that the stability frequency characteristics were dramatically changed by changing only the oil seals; however, no change in seal design made this system stable. This indicates that the seals were not the predominant destabilizing factor.

Major efforts were then expended to reduce other destabilizing factors. These changes included aerodynamic changes to the impellers and diffusers, seal modifications, shortening the bearing span, and changing the bearings to 5 shoe, nonpreloaded tilted pad bearings. Log decrement calculations indicated that these changes represented a significant improvement in the rotor stability.

Even after these modifications were installed, instabilities still occurred. On startup, an instability component (5200 cpm) was present with a fluctuating ampli-

tude. The instability frequency then shifted up to 5800 cpm, and the amplitude jumped to greater than 152 μm (6 mils) in approximately one second. The instability component was particularly sensitive to pressure ratio across the machine, which confirmed that the aerodynamic destabilizing effects were of major importance and overshadowed other improvements that were made.

The stability of the unit was markedly improved when a damper bearing was installed in series with the inboard bearing. Squeeze film damper bearings employ an oil film in the space between the outside of the bearing and the case, to which oil is continuously supplied. Stiffness of the damper bearing is usually supplied by a mechanical support such as a squirrel cage cylinder with ribs, welded rod support, corrugated metal ring, or o-rings. Figure 16 gives the frequency analysis of the shaft vibrations and two probes monitoring the damper bearing for 8450 rpm with a suction pressure of 23.1 MPa (3350 psi) and a discharge pressure of 56.9 MPa (8250 psi). Instability frequencies were still present, but the added damping from the damper bearing prevented the amplitudes from becoming unbounded. The improvement in the stability characteristics of this rotor illustrates the potential of damper bearings in high pressure applications.

At the time of this study, the mathematical techniques for predicting instabilities were not as developed as today's procedures and the application of a damper to an industrial compressor involved some tuning to obtain the optimum stiffness and damping for an individual rotor. This can be amply illustrated by the fact that a damper bearing installed in a second identical unit was not successful in eliminating instability trip-outs (fig. 17). After some tuning of the damper bearing, the stability was significantly improved.

In the process of evaluating the performance of the damper bearing, the oil temperature was varied to determine if it had a significant effect. At an oil temperature of 51° C (124° F), the frequency analysis of shaft vibrations showed instability components at 2800 and 4800 cpm along with the running speed component. Some surprising results were noted as the temperature was lowered. At a temperature of approximately 48.9° C (120° F), the 6 μm (0.25 mil) component at 2800 cpm disappeared (fig. 18). Again this points out that very small changes can be significant to the stability of a rotor.

This case history illustrates that many factors influence the onset, frequency and amplitude of instability vibrations, and that sophisticated mathematical models are required to simulate the instability phenomena measured in these machines.

This instability problem was controlled primarily by increasing the shaft diameter to raise the first critical speed, thus significantly increasing the ability of the shaft to withstand the large aerodynamic loading effects.

Aerodynamic loading effects are the most predominant destabilizing components in many high pressure systems. In the design stage the designer needs to estimate the level of equivalent aerodynamic loading so that the rotor will have an adequate stability margin. The author has consulted on several instability problems and has developed an empirical formula for estimating the level of aerodynamic loading (ref. 4).

$$K_{xy} = \frac{B(hp)(Mol\ Wt)}{Dhf}\ \frac{\rho_D}{\rho_S}$$

K_{xy} = aerodynamic loading, N/m (lb/in)

B = cross coupling constant, 16 (105)

hp = power, kW (hp)

Mol Wt = molecular weight

D = impeller diameter, m (in)

h = restrictive dimension in flow path, m (in)

f = speed, Hz

ρ_D = density of fluid at discharge conditions, kg/m^3 (lb/cu ft)

ρ_S = density of fluid at suction conditions, kg/m^3 (lb/cu ft)

When this formula was applied to several rotors that had instabilities, it appeared to give overall levels of aerodynamic loading near that required to cause the logarithmic decrement to be negative. This equation is presented so that it may be further evaluated.

CASE 4. INSTABILITY OF ATOMIZER SHAFT

An atomizer was driven by a 250 hp, 3600 rpm, electric motor through a variable speed transmission over a speed range between 10,000 and 13,500 rpm. A slurry was pumped by positive displacement pumps to the atomizer which was mounted on top of a large cone-shaped tank. The slurry was then sprayed into the tank and was instantly dried by hot air which was blown directly at the atomizer wheel. The heated air was forced through the heater and into the tank by a forced draft fan. The dried powder was then drawn out of the tank by an induced draft fan into a bag house where the powder was collected. Upon startup, high vibrations were experienced on the atomizer shaft, resulting in several shaft failures near a carbon bushing. A field investigation was made to determine the causes of the high vibration and failures and to develop a solution.

During the tests the atomizer shaft vibrations were measured with a proximity probe mounted inside the atomizer housing approximately 15.2 cm (6 inches) above the carbon bushing (fig. 19). Torsional vibrations were measured with a CEC torsiograph mounted on a special stub shaft attached to the motor shaft. Pulsations in the liquid feed line and the tank near the atomizer wheel were measured with pressure transducers. Vibrations on the atomizer, gearbox, and motor were measured with accelerometers.

Several tests were made, including running the unit without condensate or slurry, running with water alone, running with fans on but atomizer off, running with heater only at a low feed rate, and shock excitation runs to determine natural frequencies.

When the shaft was run dry, two instability frequencies at 12 and 26 Hz were indicated in the real time spectral analysis of the proximity probe measurements of the carbon. When the unit was run with condensate water, the amplitudes at the instabilities increased (fig. 20). The vibrations at the forward whirl mode occurred first and built up until the shaft touched the carbon bushing which caused a backward whirl mode to be excited at 12 Hz. Measured pulsations at the slurry input showed pulsations at 26 Hz which could excite the forward mode at 26 Hz. The sensitivity of

6

the instability modes can be seen in figure 21. When the vibrations were measured over the range of flow rates, the vibrations became severe as shown in figure 22.

Based upon the analysis of the data, it was determined that the excitation for the instability was the pulsative fluid flow. The atomizer was designed for a feed rate of 50 cubic meters per hour; however, the maximum flow rate was only 19 cubic meters per hour. The atomizer was creating a vacuum in the feed header line even at full flow rates. This caused the liquid to enter the atomizer in slugs rather than a smooth flow. The liquid slugs entering the atomizer wheel acted as destabilizing forces which caused the forward whirl.

Several modifications were implemented to improve the inlet flow characteristics. The distributor flow area was reduced approximately 70% by an orifice restrictor and the inlet feed tube diameters were reduced and connected together through a "Y" connection.

These modifications on the inlet flow lines and the new distributor improved the inlet flow characteristics and reduced the instability vibration amplitudes; however, the shaft continued to rub against the carbon bushing under all flow conditions. Plugs were then installed in 12 of the 24 discharge holes in the atomizer wheel to further restrict the flow rate.

After these modifications were installed, the vibrations were low (fig. 23) and the shaft no longer rubbed against the carbon bushing. The atomizers have run successfully without failures since 1977.

This case history illustrates that if the excitation source for an instability can be identified and reduced, the instability can be controlled without shaft modifications.

REFERENCES

1. Wachel, J. C., Case Histories of Rotordynamic Installations in the Field, Short Course on Rotordynamics of Turbomachinery, Texas A&M University, College Station, Texas, May 18-20, 1981.

2. Wachel, J. C., Turbine and Compressor Vibration, Ammonia Plant Safety, vol. 15, 1973, American Institute of Mechanical Engineers, pp. 69-76.

3. Wachel, J. C., Nonsynchronous Instability of Centrifugal Compressors, ASME Paper 75-Pet-22.

4. Wachel, J. C. and W. W. von Nimitz, Ensuring the Reliability of Offshore Gas Compressor Systems, Society of Petroleum Engineers of AIME, Journal of Petroleum Technology, Nov. 1981, pp. 2252-2260.
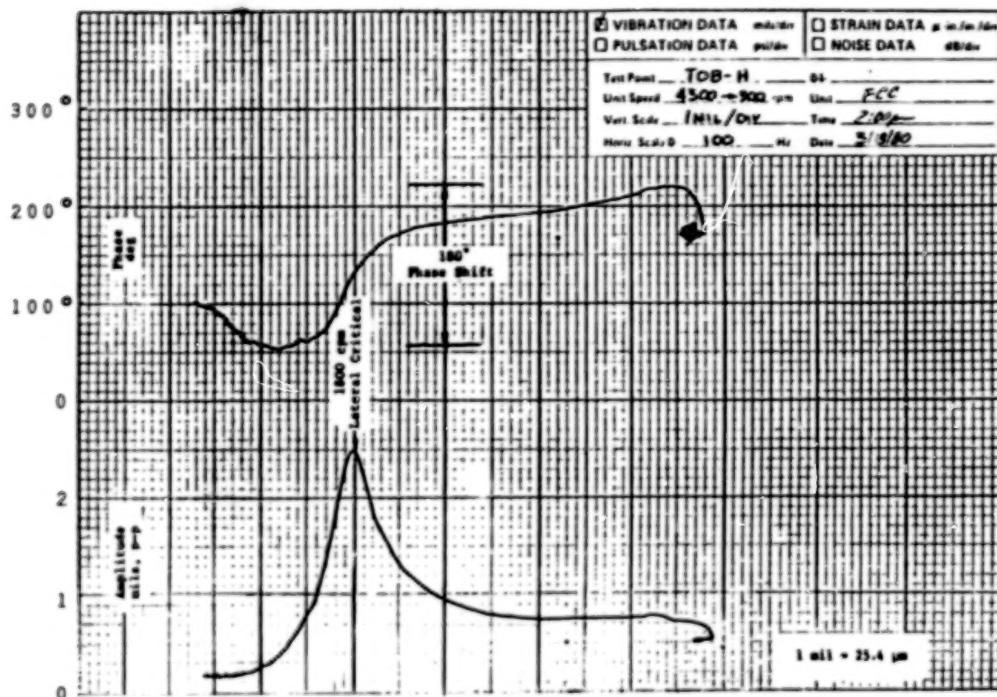
Figure 1. - Vibration and phase angle measured during shutdown.
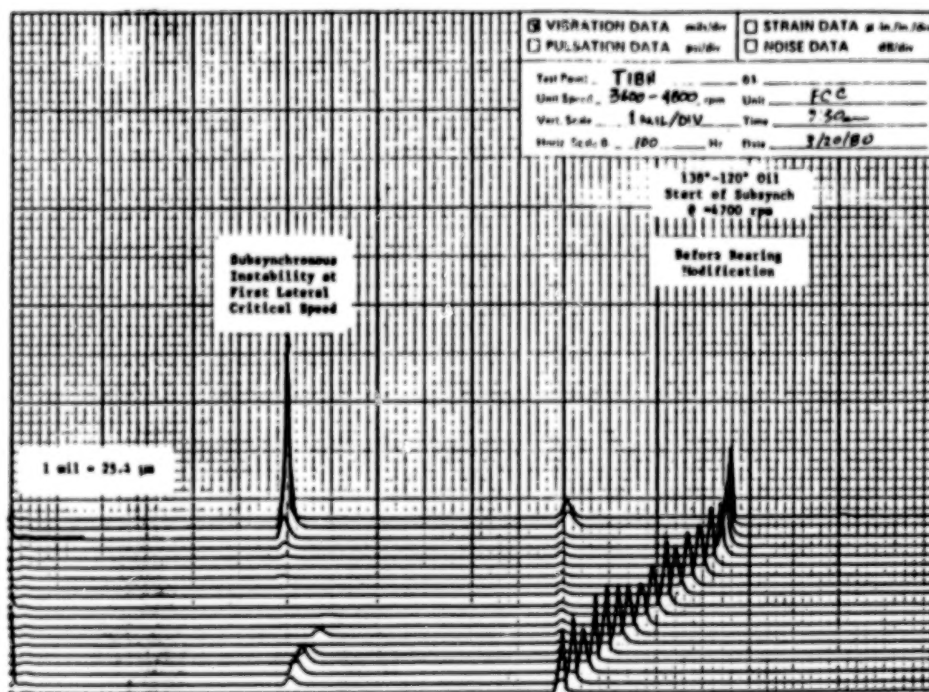
Figure 2. - Subsynchronous instability excited on turbine.
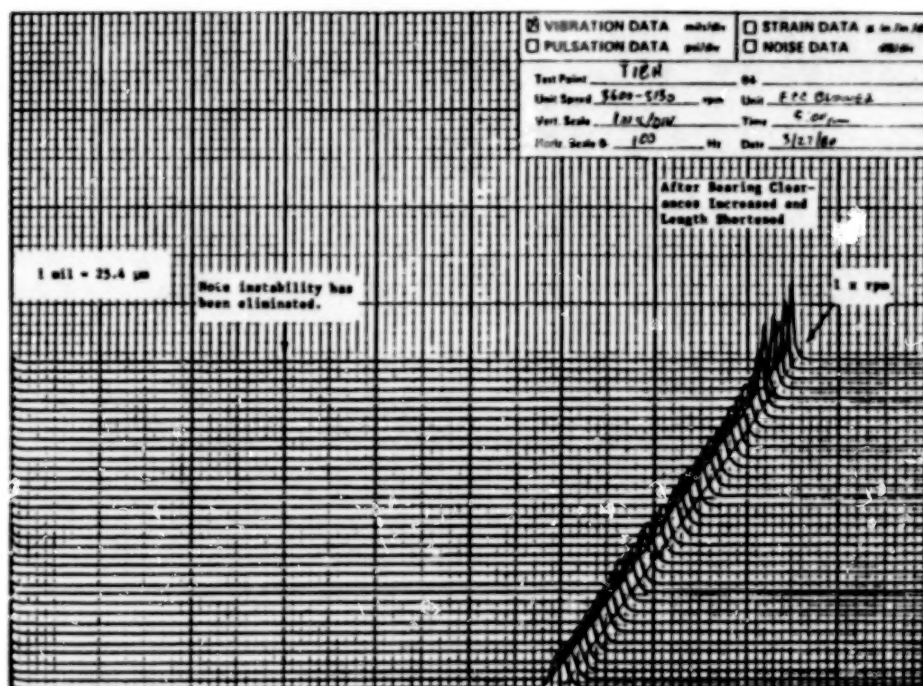
Figure 3. - Elimination of instability by bearing modification.

Time

0   3   6   9   12   15

CPM x 10^{-3}
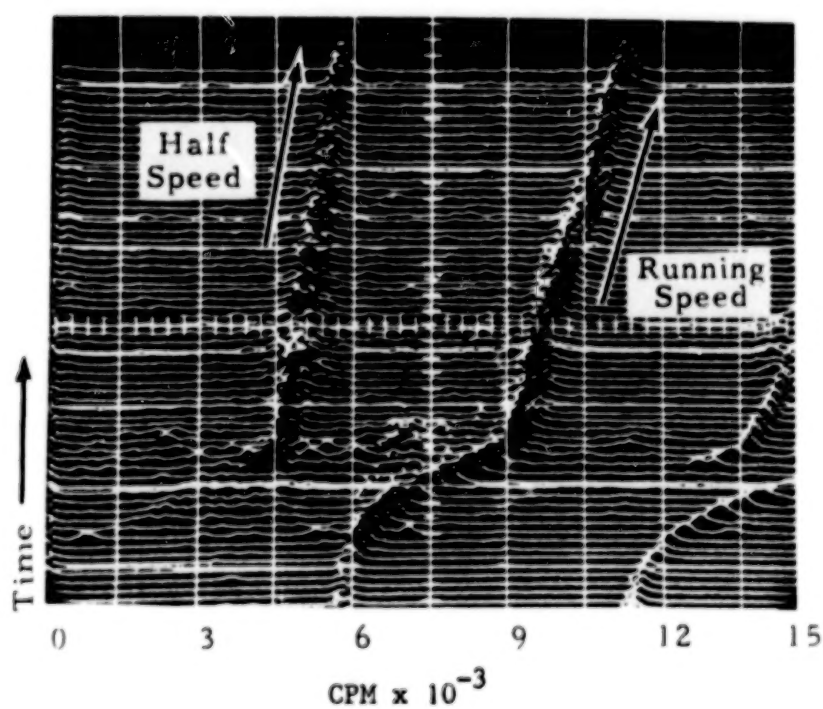
Figure 4. - Spectral time history of half speed vibrations on
turbine with tilted pad bearings.

9
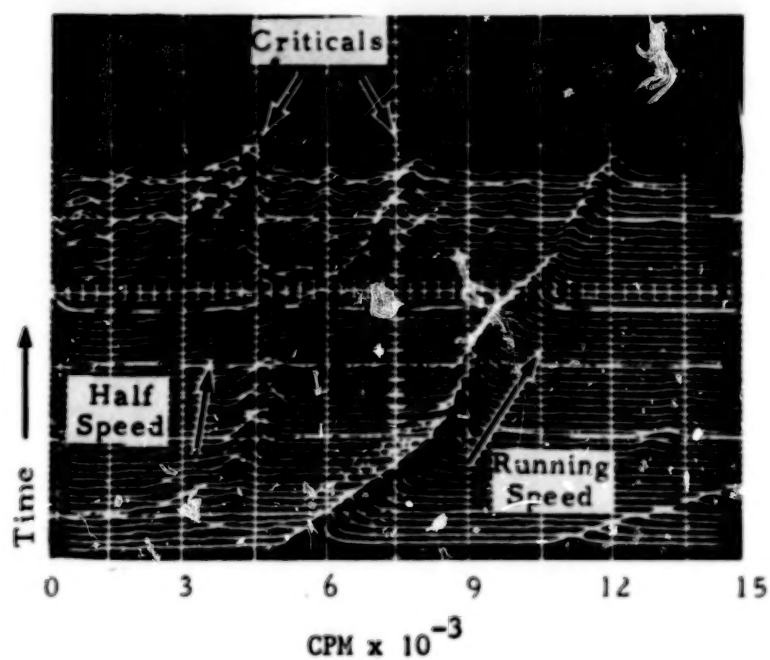
Figure 5. - Spectral time history of turbine showing
subharmonic vibrations in normal speed range.
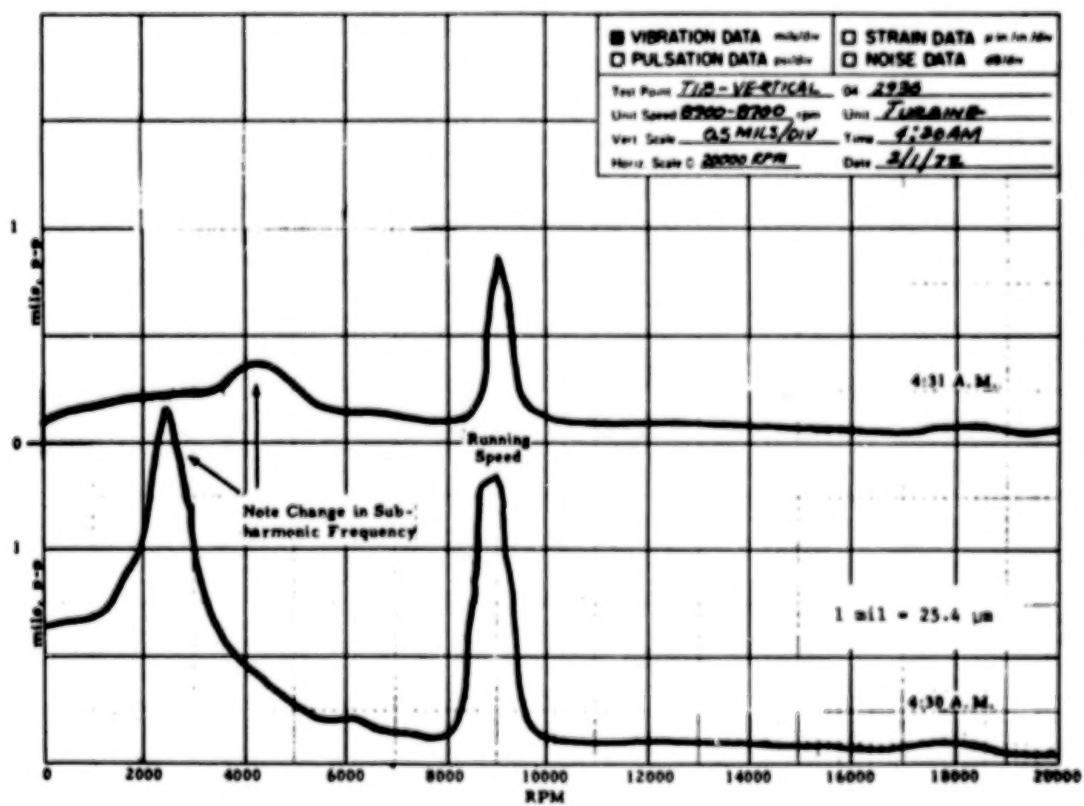
Figure 6. - Subharmonic vibrations of turbine.

10
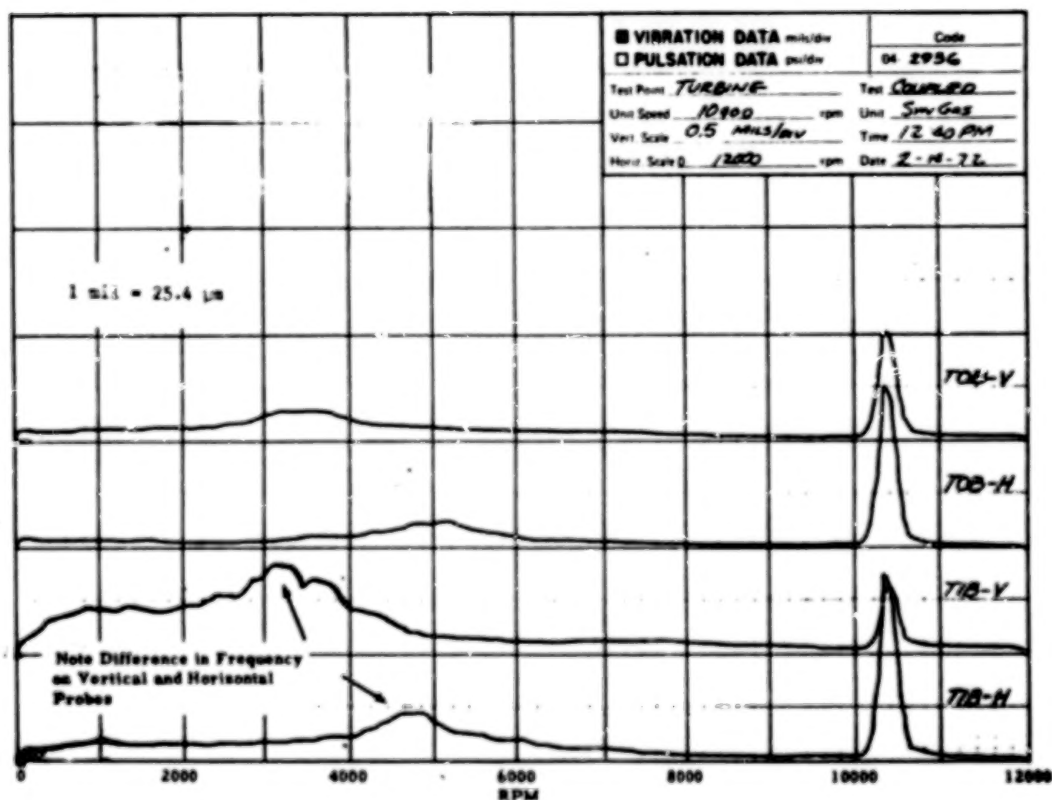
Figure 7. - Subharmonic turbine vibrations measured at 10400 RPM.
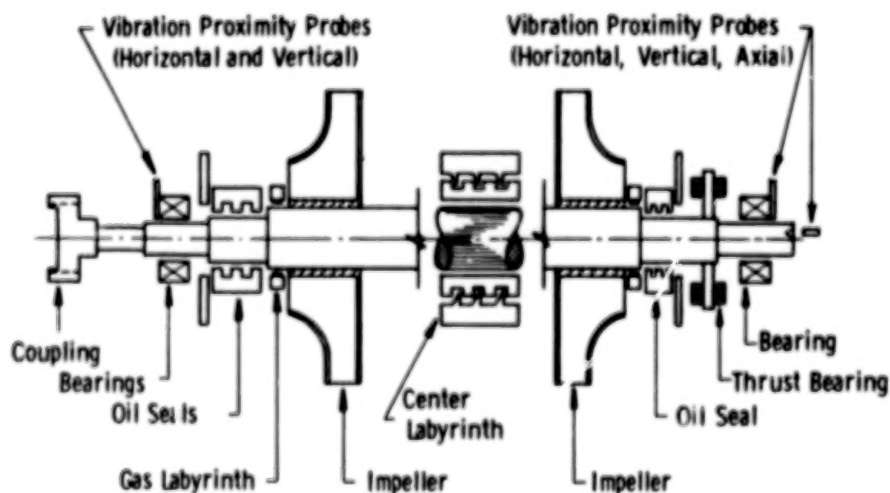
Figure 8. - Typical high pressure compressor design.

11
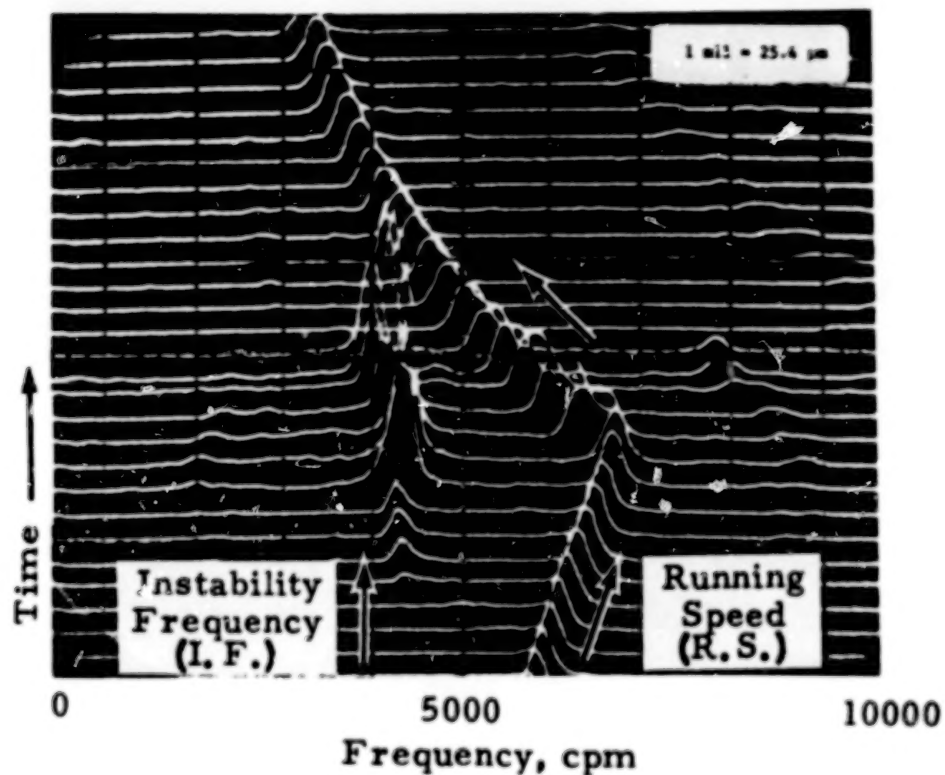
Figure 9. - Tripout of compressor as speed is increased.
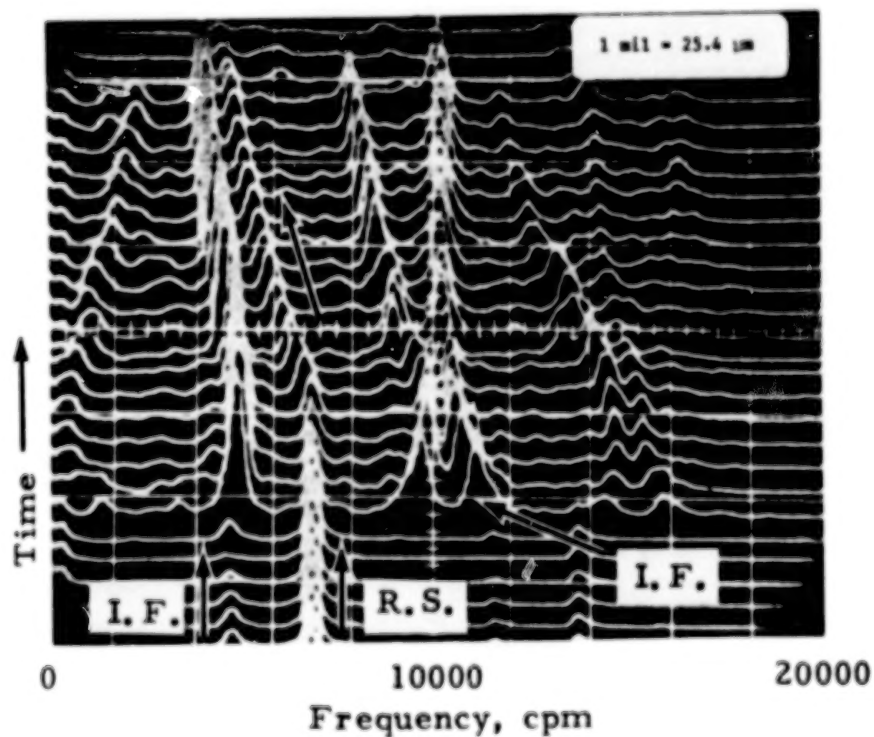
Figure 10. - Compressor instability with improved seal design.

12
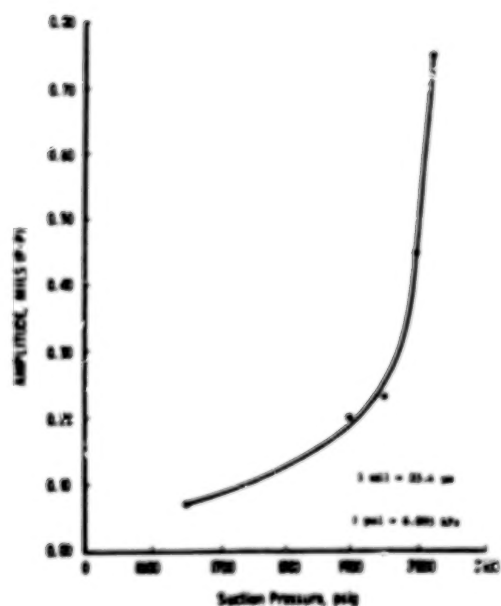
Figure 11. - Instability amplitude versus suction pressure.
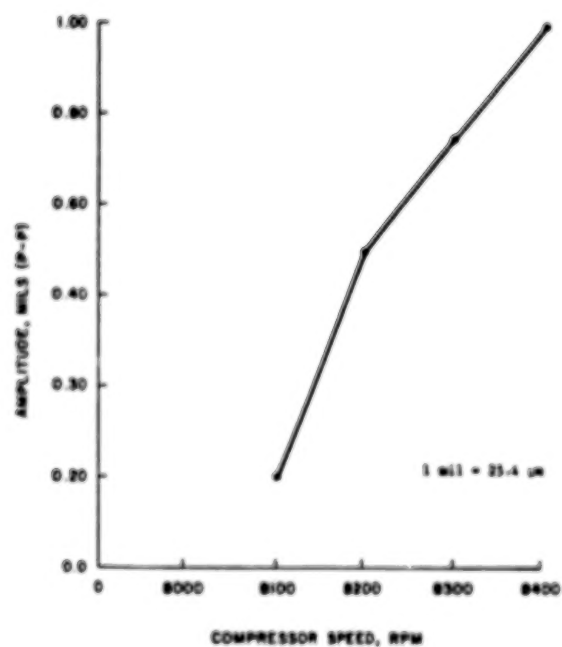
Figure 12. - Instability amplitude versus compressor speed.

13
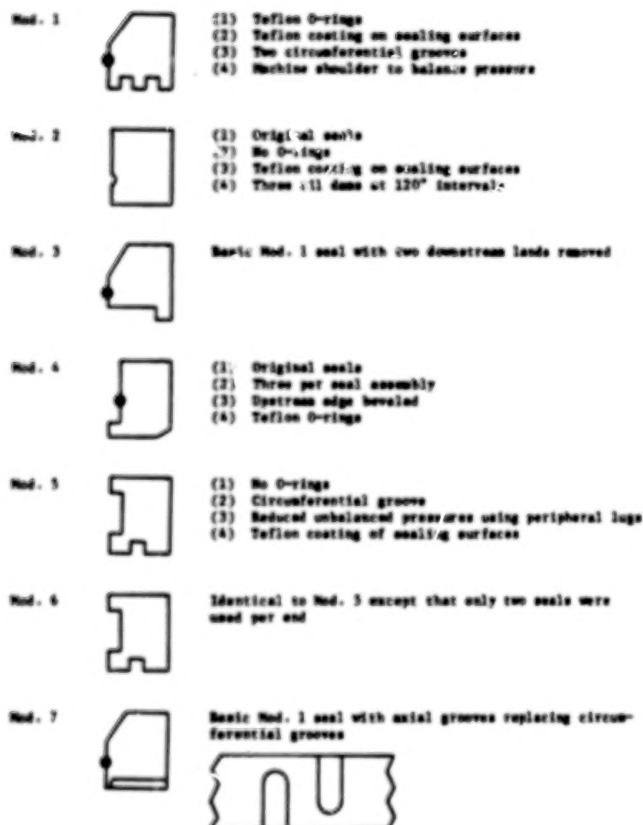
Figure 13. - Oil seal designs tested.
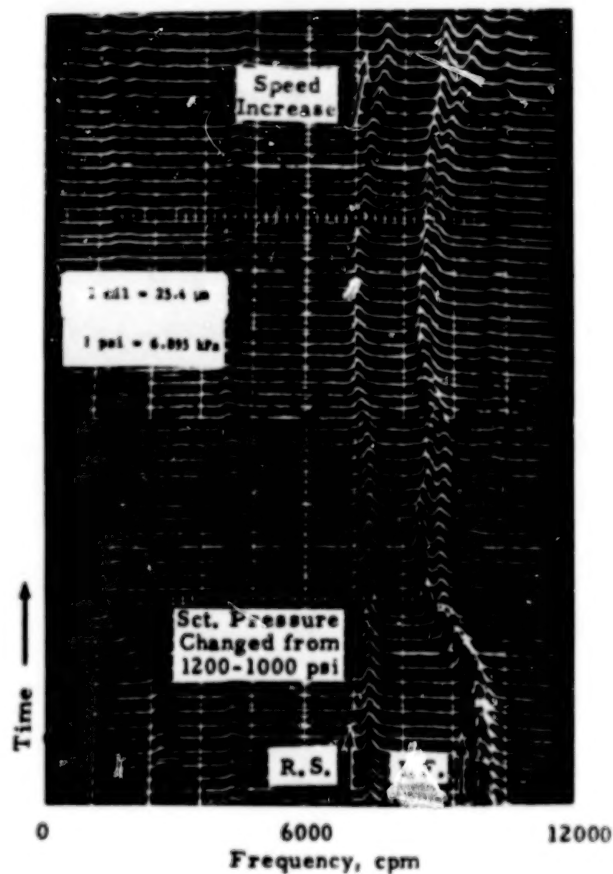
Figure 14. - Variation of instability frequency with suction pressure.

14
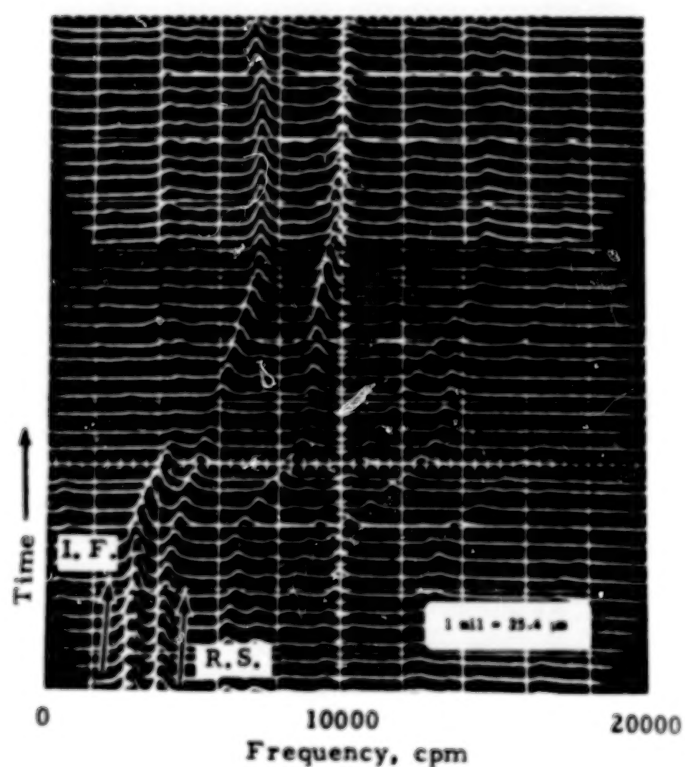
Figure 15. - Instability excited as compressor goes through first critical.
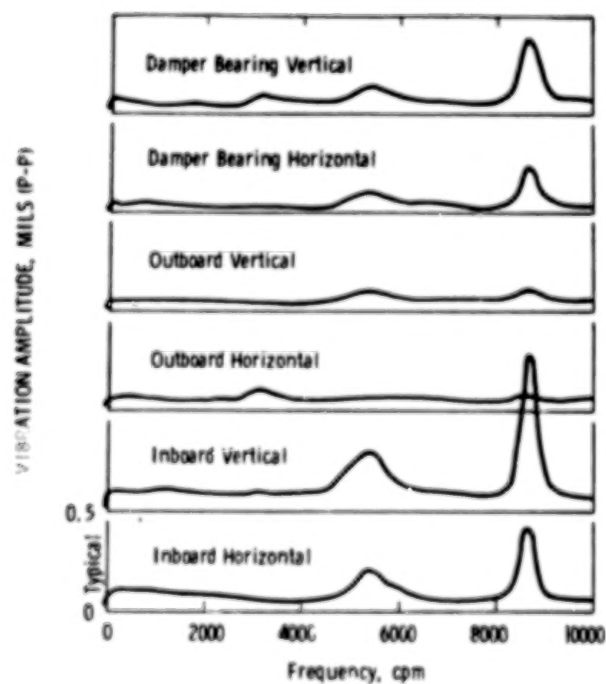
Figure 16. - Frequency analysis of shaft and damper bearing vibration
with discharge pressure of 8250 PSI (56.9 MPa).

15

BEST DOCUMENT AVAILABLE
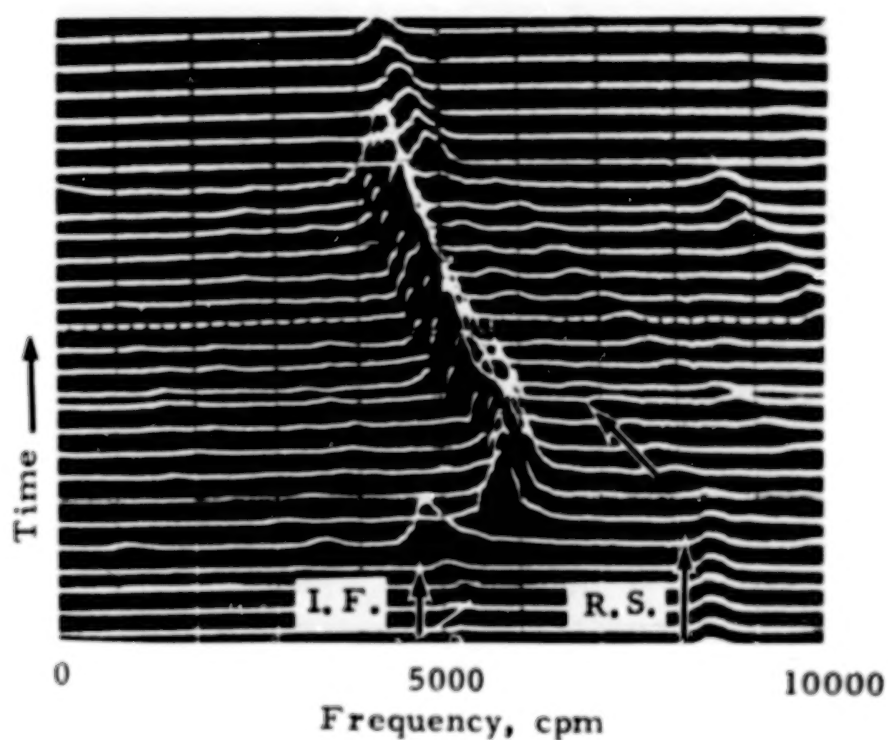
Figure 17. - Instability tripout of rotor with damper bearing installed.
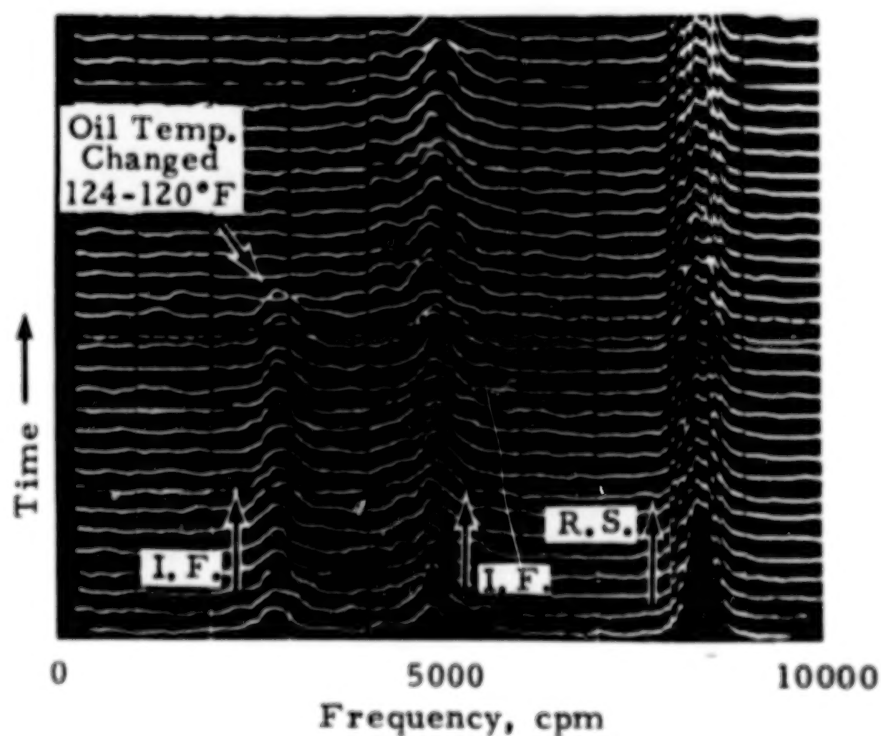
Figure 18. - Elimination of instability component as oil temperature reduced.

16
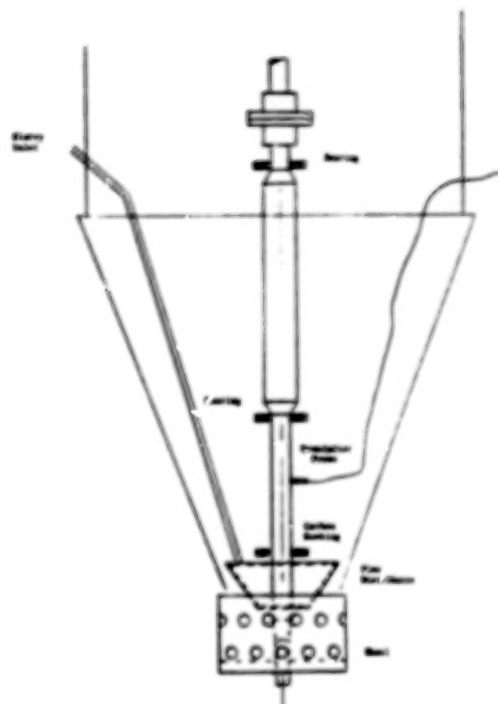
Figure 19. - Cutaway view of atomizer.
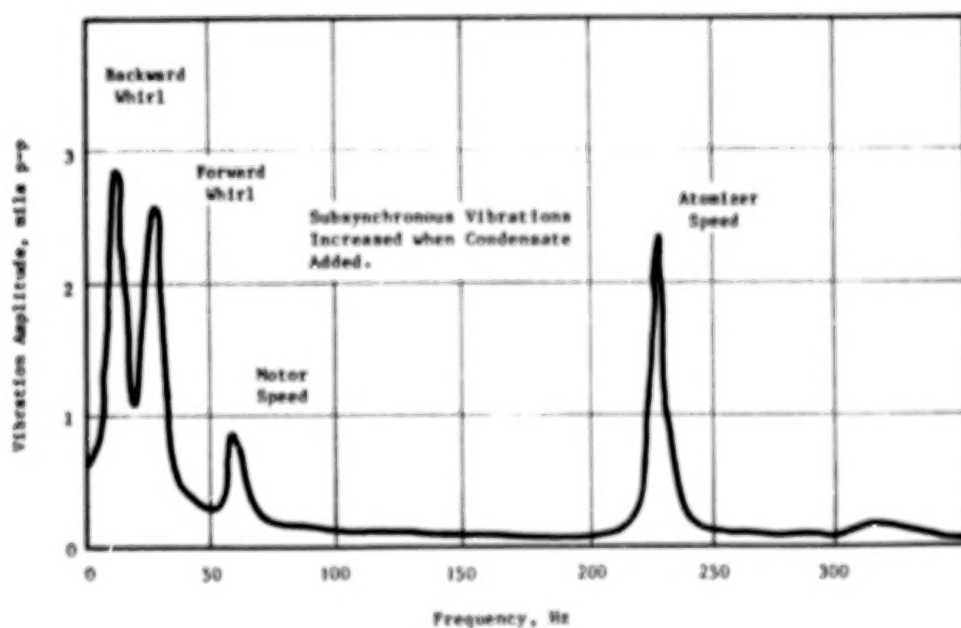
Figure 20. - Instabilities excited on atomizer.

17
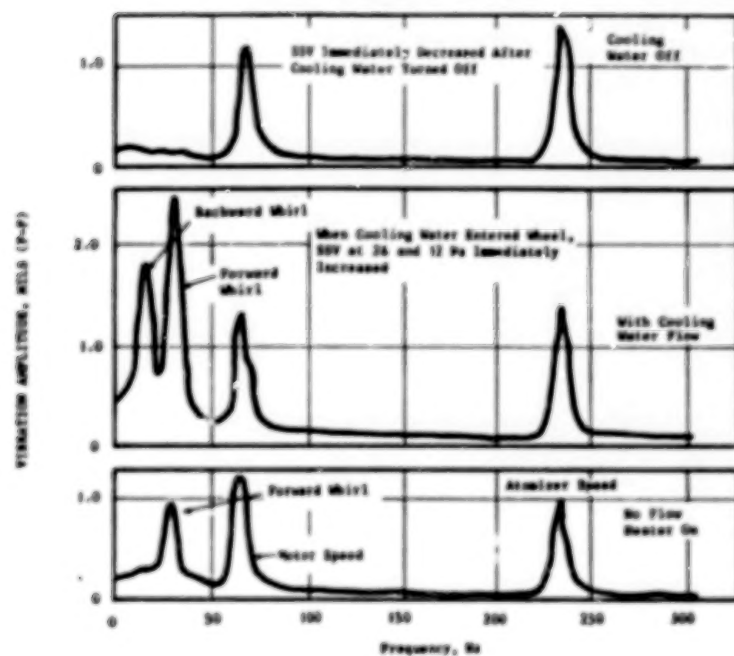
Figure 21. - Effect of fluid flow on instabilities.
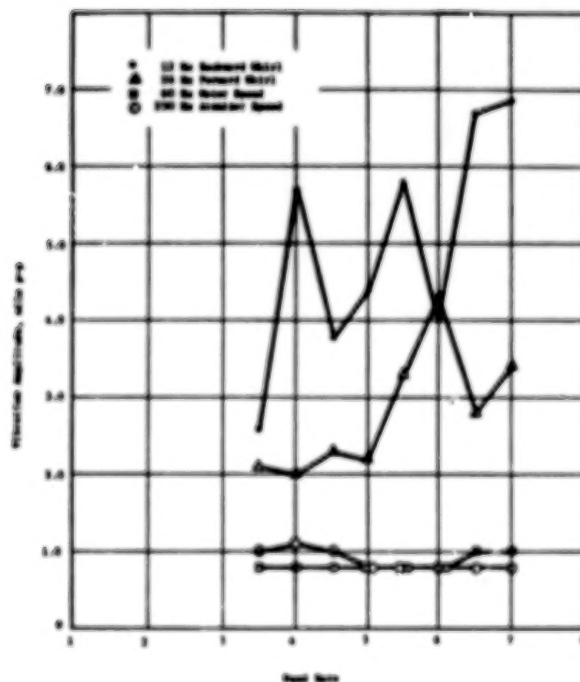
Figure 22. - Plot of atomizer shaft vibrations versus feed rate.

18
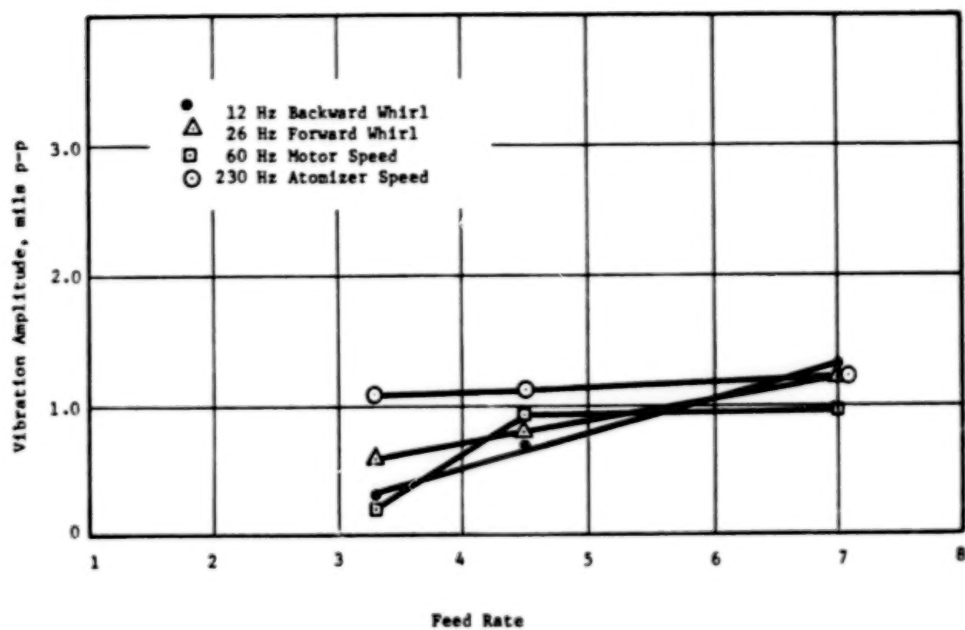
Figure 23. - Atomizer shaft vibrations after modifications.

FIELD EXPERIENCES WITH RUB INDUCED INSTABILITIES IN TURBOMACHINERY*

David G. Goggin
Radian Corporation
P.O. Box 9948
Austin, Texas   78766

SUMMARY

Rotordynamic instability problems are not uncommon in high speed industrial turbomachinery. One type of the many destabilizing forces that can occur is caused by a rub between the stationary and rotating parts.

Descriptions are given of several cases of rub induced instabilities. Included in the descriptions are the conditions at onset, the whirl frequency and direction, and the steps taken to eliminate the problem.

INTRODUCTION

Rotordynamic instability problems are not uncommon in high speed industrial turbomachinery. Actually, a large percentage of industrial machines operating at high speed will sustain some low level subharmonic vibrations even during normal operation. Some of these units have been observed to develop instability problems. One mechanism that has been responsible for some of these instabilities is a rub between the rotating and stationary parts.

The mechanics involved during a rub have been described by several authors. Den Hartog (ref. 1) describes rubs from the standpoint of dry friction whip with Coulomb friction between the rotating and stationary parts providing the destabilizing force. Ehrich (ref. 2) added stator flexibility to this model in an attempt to define the conditions necessary for a rub to be unstable since not all rubs produce instabilities. Both analyses conclude that the instability should produce a backward whirl at the rotor natural frequency.

Bentley (ref. 3) proposed and experimentally demonstrated that several mechanisms, including a partial rotor-stator rub, could produce a subsynchronous vibration due to the periodic variation it causes in the rotor's support stiffness. The subsynchronous vibration was stated to occur most often at exactly 1/2 the running speed when operating at or slightly above twice the first critical speed. The whirl direction could be forward, backward, or even in a single plane. Although less common, the whirl frequency was noted to also have occurred at 1/3 and 1/4 running speed. It was also stated that it was possible, but not likely, for the subharmonic to occur at 1/5, 1/6, . . . and 2/3, 3/4, 2/5, 3/5, . . . of running speed. This parametric excitation mechanism was further analyzed by Childs (ref. 4 and 5). The rub model used included the effects of both Coulomb friction and the

periodic variation in support stiffness. The analysis indicated that zones of instability exist around integer multiples of the first critical speed within which a rub could cause an instability to occur. The frequency of the whirl would occur at slightly more than the first critical speed causing a vibration at exactly 1/2, 1/3, . . of running speed. The possibility that the rub would be unstable was found to be primarily dependent on the amount of damping of the first mode, the magnitude of the Coulomb friction factor, and a parameter q which represents several parameters that essentially indicate the severity of the rub. An unstable rub was found to be promoted by low damping, a high friction coefficient, or a high q factor, i.e., a severe rub.

In this paper some field experiences with rub induced instabilities are reviewed. As with most industrial problems, the pressure to resume production often prevented a more detailed investigation. But most of the essential characteristics involved are presented including the conditions at onset, the whirl frequency, the direction of whirl, and the steps taken to correct the problem. Some rubs, of course, have occurred that were not unstable, such as the one shown in figure 1 from a 5000kw turbine generator. These are usually characterized by increases in the higher order harmonics as well as a general increase in the low level broad band vibration. While these types of rubs can be serious, it is usually the unstable rubs that have the most potential for damage and so are of deep concern to the industry.

BACK PRESSURE TURBINE ON SYNTHESIS GAS COMPRESSORS

Figure 2 shows a schematic of a 20,000 H.P., 11,000 rpm Synthesis Gas Compressor train composed of a condensing turbine, a back pressure turbine, a low pressure and a high pressure compressor. The back pressure turbine, or topping turbine as it is referred to, is a two stage 12,000 H.P. drive through turbine using 10.34 MPa (1500 psi) inlet and 3.79 MPa (550 psi) exhaust steam. The first and second critical speeds are 6750 rpm and 13,000 rpm respectively as determined from proximity probe data during start-ups and overspeed trip tests. The 5800 kg (913 lb) rotor is supported in a 12.7 cm (5 in) diameter bearing at the inlet end and a 7.6 cm (3 in) diameter bearing at the discharge end. Both are 5 shoe tilting pad bearings with a load on pad orientation. This machine, like many others, tends to show some low level (2.54 μm or 0.1 mil) subharmonic vibration over a broad band of about 30-150 Hz during normal operation.

During the start-up of one of the many units like this, a vibration instability problem developed at the discharge end of the topping turbine. The vibration levels, as indicated by proximity probes, increased from 25 - 38 μm (1.0-1.5 mils) to 76 - 89 μm (3.0-3.5 mils) in a few seconds. Since a real time analyzer was present to monitor the start-up, it was observed that the vibration was dominated by a large fluctuating component at 5150 rpm (85.8 Hz) or exactly 1/2 running speed. The suddenness with which the instability developed, the rapid fluctuations in the subharmonic component, and the fact that the subharmonic was at exactly 50% of running speed, led to the suspicion that a rub was involved. No explanation could be made for the fact that the whirl frequency was 5150 rpm (85.8 Hz) when the first critical was 6750 rpm (112.5 Hz). The problem was almost completely isolated to the topping turbine discharge end bearing. Some 1/2 running speed vibration was observed at the inlet end bearing, but only low levels (<5 μm or 0.2 mil) of this component were observed on other rotors in the train.

A shutdown and inspection of the bearing revealed that everything was normal including proper orientation, clearance, crush fit, alignment, etc. The bearing's inboard oil guard, however, was found to be heavily rubbed and was replaced with one that was checked to insure it had the proper clearances. This was the only change made before the machine was restarted. Since no subharmonic vibrations occurred during start-up and subsequent operation, it was concluded that the rubbing oil guard had been the source of the instability.

Another identical unit exhibited the same instability characteristics. This unit had developed a history of vibration problems during its eleven years of operation. One problem was occasional bouts of fluctuating high vibration at the topping turbine discharge end bearing. It had been found that using water on the bearing pedestals to change the alignment would sometimes reduce or eliminate the vibrations. An analysis was made during one vibration excursion to determine what effect the water was having. Figure 3 shows a spectra taken at 3:29 p.m. with water being used on one pedestal. There was a running speed vibration of 64 μm (2.5 mils) at 10,200 rpm (170 Hz) and a 1/2 running speed peak of 38 μm (1.5 mils). The 1/2 running speed peak was superimposed over the normal band of low level subharmonic noise and there was some electrical interference at 60 Hz, 120 Hz, 180 Hz, etc. The water was taken off the pedestal and figure 4, taken at 3:35 p.m., shows the resulting increase in the subharmonic. The water was then put on the other pedestal and the results are shown in figure 5, taken at 3:47 p.m. The instability had ceased suddenly and the running speed vibration slowly decreased from 64 μm (2.5 mils) to 38 μm (1.5 mils). During a subsequent outage, the bearings and seals at this point were inspected and found to be severely rubbed over a bottom quarter of their diameter. It was concluded that this was another rub which had produced both a large subsynchronous component as well as an increase in the unbalance from non-uniform heat input to the shaft. Once the rub was removed by changing the alignment, the subharmonic component ceased suddenly and the running speed vibration returned to normal slowly.

On a later occasion, this same turbine experienced high vibrations during a start-up. The machine was warmed up and brought up to minimum governor speed (9000 rpm) one evening and the load was to be progressively increased over the next 24 hours. However, at 11:00 the next morning while operating at 10,583 rpm, the vibration levels at the topping discharge end suddenly increased from about 50 μm (2 mils) to in excess of 127 μm (5 mils), the limit of the vibration monitors. By 12:00, an analysis had revealed (fig. 6) vibration levels in excess of 152 μm (6 mils) with a running speed component of approximately 91 μm (3.6 mils) and a fluctuating 1/2 running speed component of 114 μm (4.3 mils). Table 1 details the vibration levels during the excursion. A check of the gap voltages showed an increase of 0.9-1.1 volts had taken place. While some of this may have been due to the increase in the rotor orbit shifting the rotor's mean position, it still indicated that the rotor was located significantly lower in the bearing than normal. A slight increase in speed to 10,672 rpm failed to reduce the vibration level as it had with other rub induced instabilities. During the increase, the subharmonic tracked the increase in running speed so as to remain at exactly 1/2 running speed. The direction of whirl during the entire episode was forward. Water was used on the turbine casing supports in an attempt to lower the bearing relative to the shaft and hopefully clear the rub. When water was placed on one support pedestal, the vibrations increased to about 229 μm (9 mils). But when water was quickly placed on the other pedestal as well, the vibrations began to decrease. Within an hour, the gap voltages had returned to normal and, as shown in figure 7, the vibration levels were almost normal. During a subsequent inspection of the turbine, the bottom part of

the bearings and seals at the discharge end showed severe rub damage and some breakage. Again, the instability was thought to be caused by a rub brought about by a severe misalignment during a thermally transient condition. There was still no explanation for the whirl frequency to be at 5250 rpm (87.5 Hz) when the first critical speed was 6750 rpm (112.5 Hz).

TURBINE ON CO_2 COMPRESSOR

Figure 8 shows a schematic of a CO_2 compressor train driven by a 8200 H.P., 9300 rpm, single extraction, condensing turbine. The 19,240 kg (3030 lb) rotor was supported on 15.2 cm (6 in) journals with sleeve type bearings. The first and second critical speed were approximately 4900 rpm and 10,150 rpm respectively as determined from proximity probe data during start-ups and overspeed trip tests. This unit had been in operation over nine years with no reported vibration problems except for occasional temporary bows during start-ups. The machine's susceptibility to thermal bows was due to short warm-up and start-up periods that were necessitated by plant design. Due to the trouble free operation of the unit, it had only been overhauled once five years after installation. The train was located outdoors with a protective roof over it.

A problem was first noted one February when the turbine thrust position monitor showed a temporary alert condition after a sudden change in wind direction. Future changes in wind direction caused the problem to recur with enough regularity that a portable blower was used to keep a constant air flow directed at the thrust bearing housing. This worked until March, when a rainstorm occurred which resulted in all the turbine vibration alarms going off as well as a thrust alert condition. The condition lasted for about one minute and subsided as quickly as it started.

During a brief outage in the summer, the bearings were inspected and found to be acceptable. But the bearing's oil seals were replaced at the governor end due to excessive leakage. These seals were noted to be tighter than normal with 50-75 μm (2-3 mils) diametral clearance. During the start-up, another vibration excursion occurred. The turbine had reached minimum governor speed and the speed was being increased slowly as needed. At 9250 rpm, the vibration levels suddenly increased from about 25-38 μm (1.0-1.5 mils) to about 76 μm (3 mils) and fluctuated rapidly between 25-38 μm (3 and 4 mils). The thrust monitor showed an alert condition also. The condition lasted two to three minutes and it was found that a slight increase in speed caused the vibrations to return to normal.

During a rainstorm several days later, another vibration excursion occurred lasting less than a minute with symptoms very similar to the previous excursion. The problem subsided when the speed was increased from approximately 9300 rpm to 9500 rpm. Several more vibration excursions occurred during rapid changes in weather conditions over the next few weeks.

Due to the transient nature of the problem, the plant connected their tape recorder to the proximity probe monitors and the operators were instructed to turn the recorder on during any sudden changes in weather that might precipitate another vibration excursion. Local thunderstorms resulted in three vibration excursions in the next 24 hours.

Typical frequency spectra from just prior to and just after the start of a vibration excursion are shown in figures 9 and 10 respectively while operating at 9360 rpm (156 Hz). The transition time between figure 9 and figure 10 was less than 0.1 second. The overall vibration level had been 33 μm (1.3 mils) with 15.7 μm (0.62 mils) at running speed and approximately 5 μm (0.2 mils) at 62 Hz or 2/5 of running speed. During the excursion, the vibration level increased to approximately 76 μm (3 mils) with the majority of this increase due to the 62 Hz component. The amplitude of the subsynchronous component averaged about 53 μm (2.1 mils), but was fluctuating wildly over a range as wide as 13 to 89 μm (0.5 to 3.5 mils) but typically from 38 to 64 μm (1.5 to 2.5 mils). The orbit developed into a "double orbit" from a relatively circular one and the whirl direction was noted to be forward. Various other frequencies noted during the excursion were found to be sum and difference frequencies of the two dominant frequencies of 62 Hz (subsynchronous vibration) and 156 Hz (running speed). These are shown in more detail in figure 11. A very narrow band analysis verified that the subsynchronous component was 2/5 of running speed to within 0.1 Hz.

The problem was thought to be due to a transient rub condition since:

1) the condition was closely related to weather conditions,
2) the wide fluctuations in the subharmonic component,
3) that slight increases in speed caused the instability to cease.

The unit had a great deal of hot piping attached, all of which was routed through the roof and exposed to the weather. Significant piping strains associated with transients was thought to have contributed to the units sensitivity to changes in weather. The fact that the 62 Hz component was present at a very low level prior to the excursion was not thought to be very significant since a review of the vibration records showed that it was almost always present with levels between about 1 to 5 μm (0.05 to 0.2 mils). Also, as stated earlier, it is not uncommon for high speed units to display a low level subharmonic even during normal operation. The reason the whirl occurred at 62 Hz (3720 rpm) when the first critical was known to be at approximately 81.7 Hz (4900 rpm) remains unexplained.

The possibility that the instability was an oil whirl condition precipitated by a change in alignment, as has been known to occur, was considered but discarded for several reasons. First, changes in alignment would probably not cause the almost instantaneous change in subharmonic vibration level. Also, while subsynchronous components due to oil whirl instabilities can fluctuate, they have not previously been observed to fluctuate so rapidly and over so wide a range. And finally, the fact that slight increases in speed were sufficient to eliminate the instability was not at all a characteristic of oil whirl. The newly installed oil seals were obviously suspected as the source of the rub. However, due to the violence of the instability and the fact that these seals had probably rubbed at other times in the unit's nine year history, without causing an instability, it was decided that a full dismantle inspection was in order.

This dismantle inspection revealed that:

1) Standing at the turbine governor end, the governor end of the rotor was misaligned 510 μm (20 mils) low and 254 μm (10 mils) to the right and the coupling end was 101 μm (4 mils) to the right.

2) A sliding key at the turbine governor end meant to maintain axial alignment while sliding to accommodate thermal growth, had frozen preventing the case from moving axially.
3) The bearing oil seals were lightly rubbed.
4) The rotor was heavily rubbed at the center by the interstage labyrinths.

It was concluded that the frozen footing was primarily responsible for the rubs. The case was apparently bowing in the center quite severely during sharp thermal transients as it tried to accommodate the change in casing growth and pipe strain. This also was thought to be the reason for the rub during start-up since the case again could not shift to accommodate thermal growth. Although other rubs had probably occurred at some time in the machine's history, there had been none this severe as indicated by the depth of scoring on the rotor. This explained why this problem had not occurred before.

The rotor was realigned and the frozen footing was freed. The machine has since operated for a year and a half with no further problems except for the usual problem of thermal bows during startups.

CONCLUSION

Some cases of rub induced instabilities have been described. These have been noted to appear and cease very suddenly, can sometimes be controlled during operation by changing the alignment, and have sometimes been eliminated with minor increases in speed. On one occasion the whirl frequency was noted to track an increase in rotor speed so as to remain at 1/2 running speed. The whirl frequencies are usually at 50 percent of running speed and the whirl direction has often been forward. However, whirl frequencies have been observed at other fractions of running speed. Also, whirl frequencies have been observed at speeds significantly lower than their first critical speed. Some rubs have produced sum and difference frequencies based on the whirl frequency and the running speed frequency.

REFERENCES

1. Den Hartog, J. P.: Mechanical Vibrations. Fourth Edition, McGraw Hill Book Company, New York, 1956, pp. 292-293.

2. Ehrich, F. F.: The Dynamic Stability of Rotor/Stator Radial Rubs in Rotating Machinery. J. of Eng. Indus., Nov. 1969, pp. 1025-1028.

3. Bentley, D. E.: Forced Subrotative Speed Dynamic Action of Rotating Machinery, A.S.M.E. Paper No. 74-PET-16.

4. Childs, D. W.: Rub-Induced Parametric Excitation in Rotors. A.S.M.E. Paper No. 78-WA/DE-14.

5. Childs, D. W: Fractional-Frequency Rotor Motion Due to Nonsymmetric Clearance Effects. A.S.M.E. Paper No. 81-GT-145.

TABLE. I - SUMMARY OF VIBRATION LEVELS (mils$_{p-p}$)

TIME	Point #3						Point #4					
	VERTICAL			HORIZONTAL			VERTICAL			HORIZONTAL		
	½X	1X	Total	½X	1X	Total	½X	1X	Total	½X	1X	Total
10:45pm	—	0.5	0.6	—	0.35	0.4	—	0.8	0.95	—	0.6	0.75
11:43am	0.5	0.6	1.7	0.8	0.2	1.3	4.3	2.3	75	4.3	3.6	75
12:02pm							2.5	3.8	5.8	4.8	3.6	6.0
12:10pm							2.5	3.5	5.8	4.5	3.5	6.0
12:13pm							4.5		8.5	4.5		8.0
12:17pm							3.0		9.0	5.6		8.5
12:19pm									8.3			8.2
1:45pm	0.17	0.25	0.48	0.45	0.8	1.05	0.7	1.6	1.79	0.1	0.4	0.6
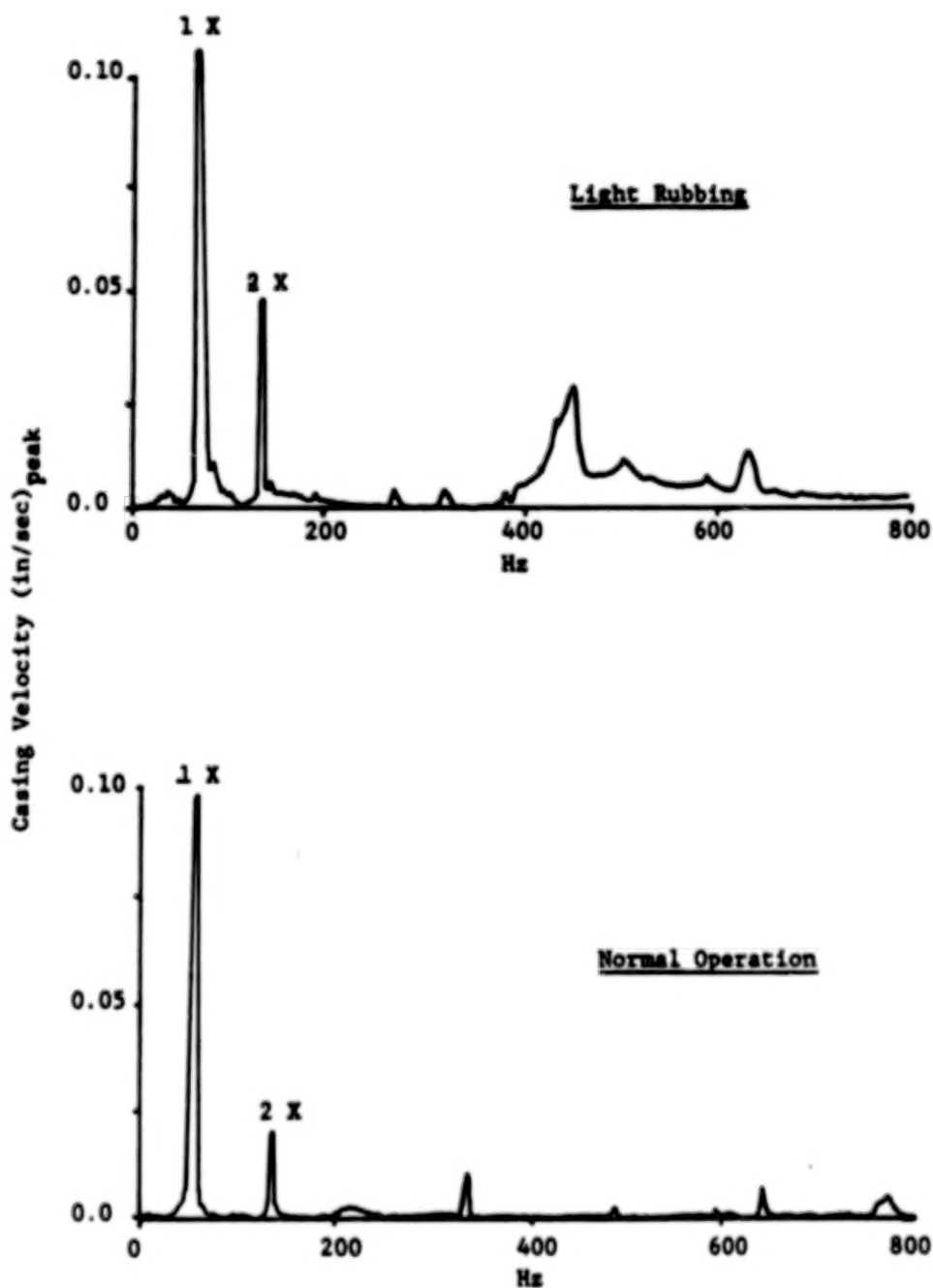
Figure 1. - Turbine case vibration on a 5000 kw turbine-generator.

DRAWING & LOCATION OF DATA POINTS
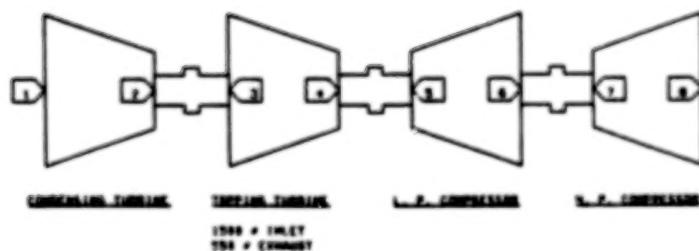
Figure 2. - Schematic of the Syn Gas Compressor.
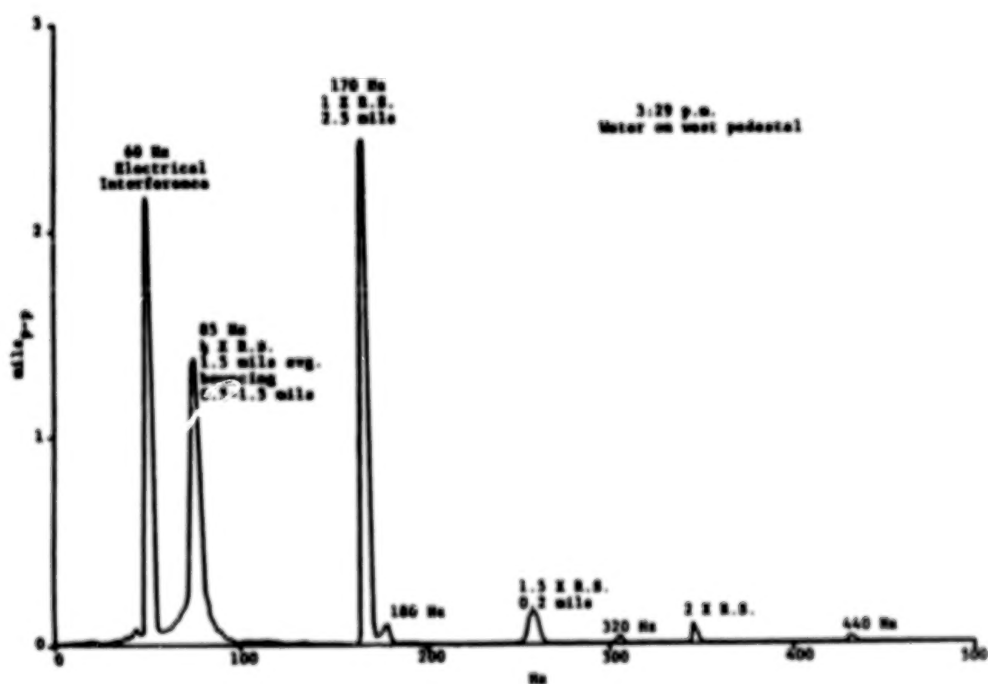
Figure 3. - Topping turbine discharge end vibration -
with water on west pedestal.

28
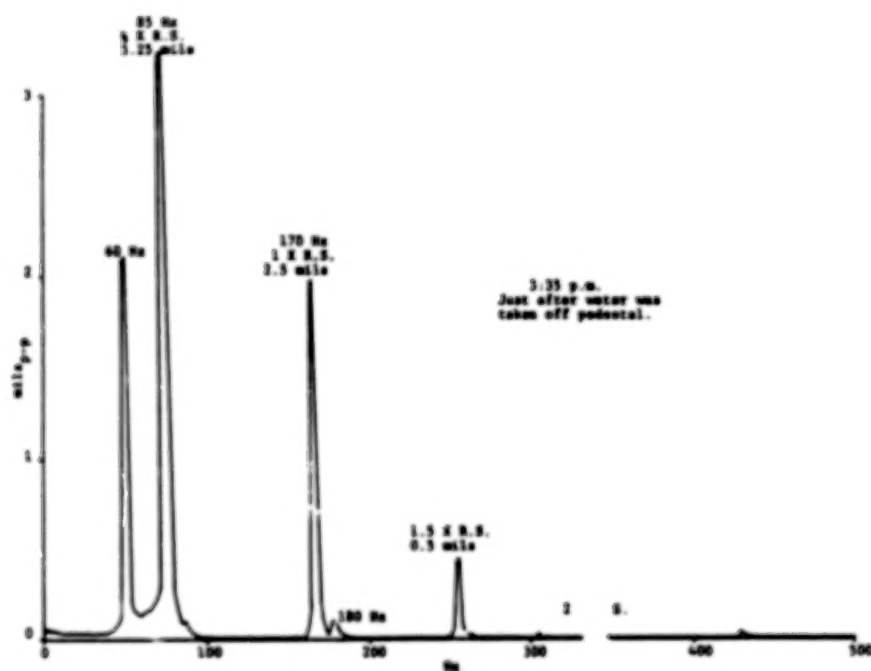
Figure 4. - Topping turbine discharge end vibration -
water taken off pedestal.
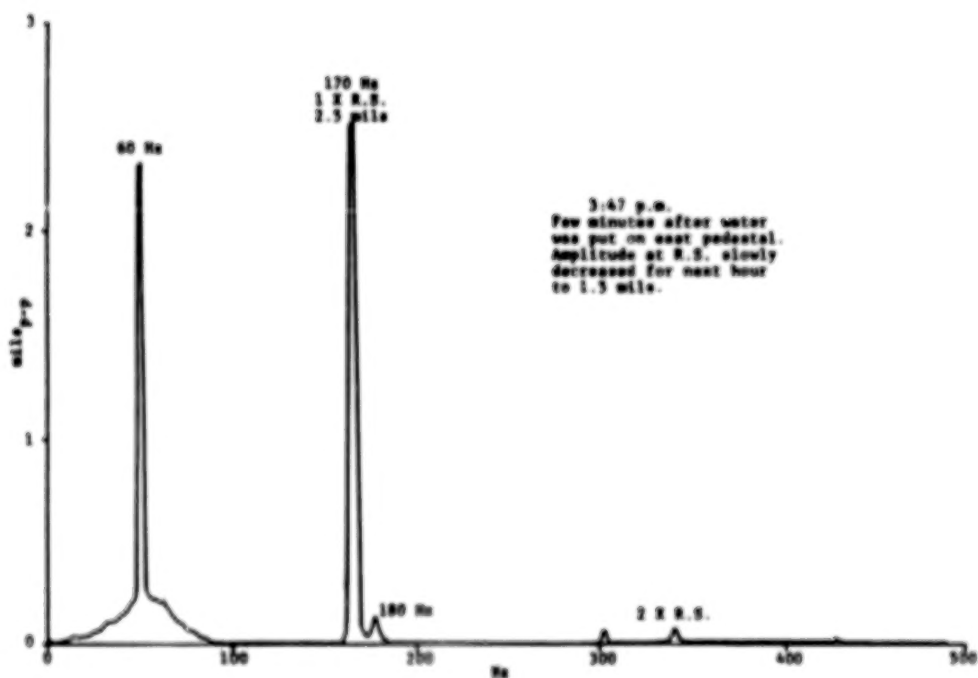
Figure 5. - Topping turbine discharge end vibration -
with water on east pedestal.

29

BEST DOCUMENT AVAILABLE
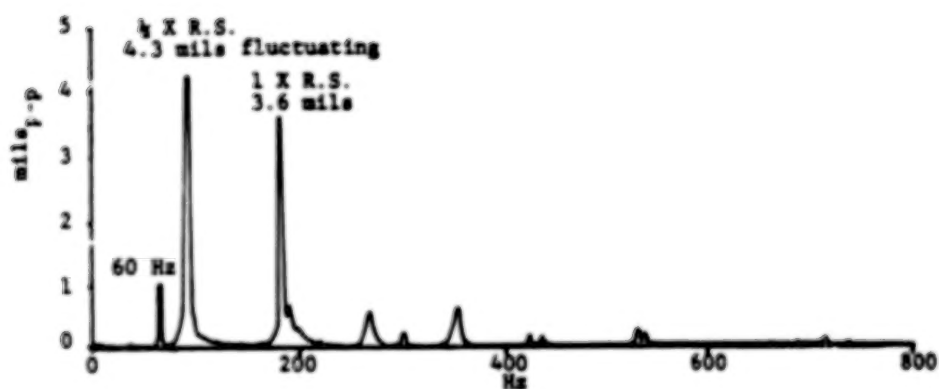
Figure 6. - During vibration excursion.
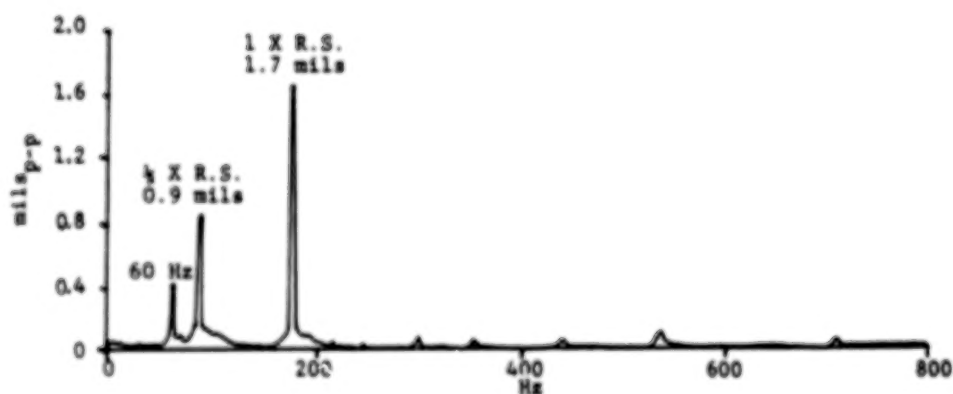
Figure 7. - At conclusion of vibration excursion.

30

Figure 8. - Schematic of the CO_2 Compressor.

Figure 9. - Turbine outboard bearing - just prior to excursion.

31
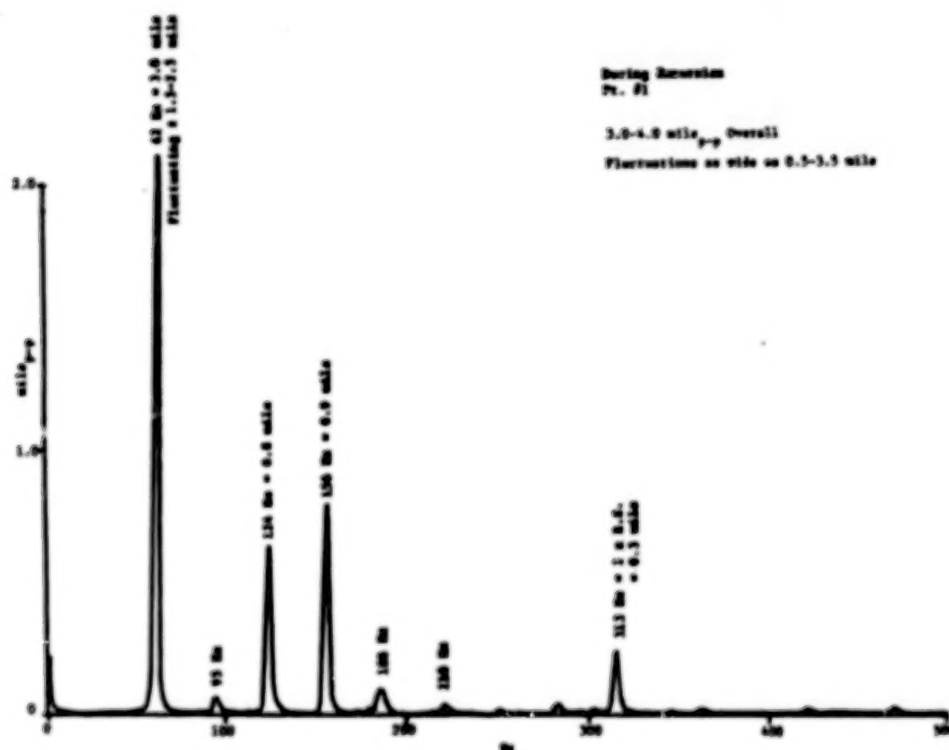
Figure 10. - Turbine outboard bearing - during vibration excursion.
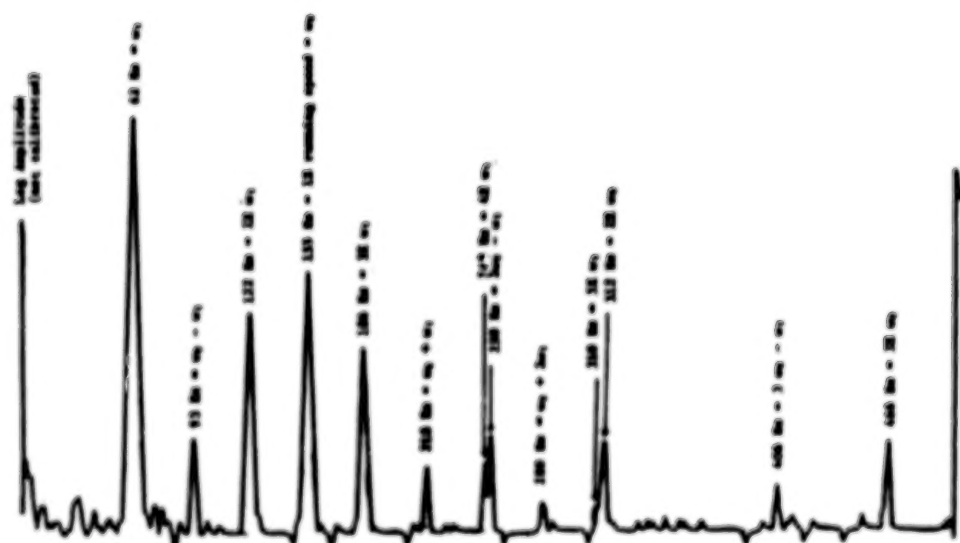
Figure 11. - Turbine vibration - during excursion: sum and difference frequencies.

BEST DOCUMENT AVAILABLE

ANALYSIS OF A TURBINE ROTOR CONTAINING A

TRANSVERSE CRACK AT OAK CREEK UNIT 17

G. W. Rogers and C. A. Rau, Jr.
Failure Analysis Associates
Palo Alto, California 94303

J. J. Kottke and R. H. Menning
Wisconsin Electric Power Company
Milwaukee, Wisconsin 53201

SUMMARY

Transient increases in one, two and three per revolution vibration characteristics of a low pressure steam turbine were observed during steam temperature reduction operations. Vibration and fracture mechanics analyses suggested the presence of a transverse shaft crack which was eventually identified by ultrasonic inspection and confirmed by destructive sectioning. Signature analyses of vibration data recorded over a two-year period prior to crack identification are correlated with fatigue crack growth, which occurred intermittently during transient temperature decreases. The apparent increased response of the rotor to vibration is due to asymmetric stiffness changes introduced by the growing transverse crack. The vibration response is predicted to increase with increasing crack depths in excess of 10% of the shaft diameter. Fracture mechanics analyses predict that fatigue crack growth occurred during periods of steam temperature decrease, when high surface tensile stresses are present. These same transient thermal stresses are shown to have retarded and prevented subsequent fatigue crack growth during steady operation.

INTRODUCTION

Failure Analysis Associates (FAA) was retained by Wisconsin Electric Power Company (WEPCO) to analyze abnormal transient vibration levels observed during boiler deslagging operations of their Oak Creek Unit 7 320 MW General Electric turbine generator. Of particular interest were the vibration levels recorded on main bearing caps of the low pressure, 1800 rpm turbine/generator set.

Boiler deslagging was performed on this unit to dislodge slag that accumulated on the outside wall of water and steam tubes. The procedure calls for reduction in furnace firing rates which causes cooling in particular tube regions. Subsequent thermal contraction effectively dislodges mineral deposits.

The subject turbine/generator utilizes four journal bearings, one pair supporting each of the turbine and generator rotors. The vibration characteristics of the bearing caps monitored when the turbine/generator was at a fully loaded condition were essentially the same as those recorded during early stages of unit operation. Horizontal, vertical, and axial vibrations were recorded for each bearing cap. In addition, shaft rider sensors monitored vibration at an angle of approximately 25° from vertical.

33

VIBRATION ANALYSIS

Figure 1a is the normal steady state vibration signature obtained with a shaft rider probe at the number 1 turbine bearing. A strong synchronous 1800 rpm signal and very slight two and three per revolution signals are present. Figure 1b, on the other hand, shows the signature at peak vibration levels subsequent to a thermal down ramp of $140^{\circ}F$ ($77^{\circ}C$). Note the increase in the one, two, and three per revolution amplitudes.

The vibration characteristics of turbine bearings number 1 and 2 were similar. Both bearings exhibited a significant increase in synchronous and twice-synchronous signals during the transient temperature decrease.

A comparison of vibration data and other parameters indicated a correlation between steam temperature and vibration amplitude. It was observed that a decrease in steam temperature resulted in a delayed vibration level increase. Increases in steam temperature, on the other hand, either did not affect the vibration or reversed a vibration increase associated with a previous temperature decrease. As expected with thermally induced phenomena, there was a definite time lag between steam temperature change and the observed change in vibration. An example of the vibrational response associated with steam temperature variation is shown in Figure 2. Reduction in steam temperature cools the surface of the shaft relative to the shaft bore. This condition produces tensile hoop stresses and tensile axial stresses of sufficient magnitude that a transverse crack in the shaft near the surface would open. Such a crack was subsequently identified near the mid span of the double-flow rotor under the inlet edge of the first shrunk-on, turbine wheel of the governor end.

FATIGUE CRACK PROPAGATION ANALYSIS

Fractography of the cracked rotor shaft after removal from service showed the presence of a fatigue crack of size and shape illustrated by Figure 3. Fracture mechanics calculations of fatigue crack growth were performed by integration of the material's crack growth rate law over the range of crack driving forces to obtain the crack progression between some initial size and the final size.

The crack driving force is conveniently characterized by the crack tip stress intensity factor ΔK, which is proportional to nominal stress range $\Delta \sigma$, the square root of the crack size a, and the specific crack and part geometry. To compute the specific magnitude of the steady (K_s) and cyclic (ΔK) crack driving force for the crack shape modelled in Figure 3, we have utilized a general purpose fracture mechanics computer program BIGIF [1]. The crack driving forces (ΔK and K_s) for shaft bending are summarized in Table I. BIGIF was used to accurately compute K_s and ΔK for the more complex stress distribution near the shaft surface. This distribution is affected by the stress concentration associated with the diameter change, fillet radius, and shrunk-on disk contact stress. However, because these localized surface stresses affect the magnitudes of K_s and ΔK only for cracks near a surface, it was not necessary to compute their magnitude in order to quantify K_s and ΔK for the deeper crack depths between four and seven inches where vibration changes were introduced.

The rate of fatigue crack growth in rotors made from Ni-Cr-Mo-V low alloy steels has been studied by various investigators. The crack growth rate per cycle, da/dN

can be represented over a wide range of growth rates by a power law of the form

$$\frac{da}{dN} = C \ \Delta K^{\eta} \tag{1}$$

where C is $5.9^n \times 10^{-10}$ for $K_{min}/K_{max} = 0$ and increases with increasing K_s; η is approximately 2.o. At low values of ΔK, the crack growth rate falls below that predicted by equation (1), and eventually a threshold value of $\Delta K = \Delta K_{th}$, is reached below which fatigue crack growth does not occur. The fatigue threshold, ΔK_{th}, is also dependent on the ratio of steady stress (σ) to cyclic stress ($\Delta \sigma$), or the ratio of K_s to ΔK. Specifically, Hopkins and Rau [2] have shown that the specific effect of the stress ratio, $R = \sigma_{min}/\sigma_{max} = K_{min}/K_{max}$, can be estimated as

$$\Delta K_{th}(R) = \frac{A-R}{B} \ \Delta K_{th} \ (R=0) \tag{2}$$

where A and B are material constants and generally $A \simeq B \simeq 1.6$.

The nominal cyclic stresses during steady state operation are estimated by the manufacturer to be ± 1.6 ksi (or $\Delta \sigma = 3.2$ ksi). With a bearing misalignment of 0.050 inch, the nominal cyclic stresses will be $\Delta \sigma = 4$ ksi. The steady stress from centrifugal force and the small steady-state axial and radial thermal gradients should be near zero and probably less than 5 ksi. However, during the deslagging operation, the the steam temperature is quickly reduced by 100-150°F, and the shaft surface is cooled relative to the bore, setting up a radial temperature gradient which introduces surface tensile stresses up to $\sigma_s = E \ \alpha \ \Delta T = (30 \times 10^3) \times (6.6 \times 10^{-6}) \times 130$°F $= 26$ ksi, where E = elastic modulus in ksi, α = coefficient of thermal expansion in inches per inch°F, and ΔT = change in temperature in °F.

Utilizing BIGIF, the crack driving force, ΔK, corresponding to $\Delta \sigma = 3.2$, was calculated for a range of crack depths. BIGIF was also used to numerically integrate equation (1) to obtain the increase in crack depth, a, caused by rotating bending during the periods of the high steady stresses produced during deslagging. The results are shown in Figure 4 for the case where C, in equation (1), is elevated by the high mean stress during the deslag cycle to 5.7 times the value at $K_{min}/K_{max} = 0$.

CRACK GROWTH THRESHOLD CONDITIONS

Because the 1800 rpm turbine speed introduces fatigue cycles very quickly (1800 x 60 min/hr x 24 hr/day = 2.6 million cycles per day), crack growth could not have been occurring continuously during normal operation. Otherwise the crack would have grown to a size where the rotor would have failed. The reason that cracking does not occur during normal operating conditions is that the ΔK produced is below the material's apparent threshold considering prior loading history. In the absence of any steady stress ($\sigma_s = 0$), the threshold of these rotor steels is typically between 6 and 10 ksi$\sqrt{in}$. Using a 6 ksi$\sqrt{in}$ threshold value, the cyclic nominal stress at which a 6.7 inch deep crack would grow is obtained from Table I and equation (2) to be $\Delta \sigma = 3.0$ ksi. Therefore, since the nominal cyclic stress of $\Delta \sigma = 3.2$ ksi with perfect bearing alignment is greater than this value, fatigue crack growth did not occur under steady-state operation in this case because the high steady stress which caused fatigue crack

35

growth during deslag also served as an overload, increasing the effective threshold above which fatigue crack growth can occur. Figure 5 shows published results of Hopkins, Rau, Leverant and Yuen [3]. These results indicate a major increase in the apparent threshold stress intensity factor, ΔK_{th}, when preceded by an overload. The larger the relative overload, the higher the apparent threshold for subsequent crack growth. In the case of the OC7 rotor, the ratio of maximum overload stress to maximum steady state stress is at least

$$\frac{26 + 1.6}{5 + 1.6} = 4.2$$

and perhaps as high as

$$\frac{26 + 1.6}{1.6} = 17.$$

The data of Figure 5 show that the corresponding apparent threshold for fatigue crack growth during turbine operation after a deslag cycle will be at least 1.6 times higher and may be more than five times higher than the threshold would have been without the deslag overload cycle. Specifically, the cyclic nominal stress above which the 6.7-inch crack can continue to grow when $\sigma_s = 0$, is between 1.6 x 3 = 4.8 ksi and 5 x 3 = 15 ksi. If steady-state operation produces some small tensile steady stress, the apparent threshold will be reduced by the factor computed by equation (2). Nevertheless, the magnitude of the overload produced by the deslag was sufficient to prevent continued propagation during subsequent steady operation.

CRACK GROWTH VS. VIBRATION INCREASE

The correlation of crack growth to changes in the vibration characteristics of the turbine rotor involves many factors. First it has been recognized [4,5,6,7,8] that a continuously open crack produces a twice per revolution rotor response due to a rotating, asymmetrical stiffness analogous to an elliptical shaft geometry. An opening and closing crack, on the other hand, may produce synchronous, two, three, four, and even higher multiples of synchronous responses due to the form of rotor orbit.

The nature of the crack and the state of stress associated with the thermal transients previously described suggest the the crack was, in fact, continuously open during the periods of high vibrational response. Grabowski, in particular, [9] has shown analytically that the change in shaft compliance and hence the dynamic response due to the asymmetry is relatively insensitive to crack size until the crack depth is approximately 10% of the shaft diameter.

As shown in Figure 2, the amplitude of the second harmonic vibration is near a maximum for a period of approximately three (3) hours. It was estimated that the crack is fully open for this period of time due to the state of transient thermal stress. The total number of deslag operations performed on the OC7 unit between installation and the time such procedures were eliminated was approximately 1100. Using the three (3) hour time estimate for each, the total number of high thermal stress state cycles can thus be calculated as

$$1100 \text{ cycles} \times 3 \text{ hours} \times \frac{1800 \text{ cycles}}{\text{min.}} \times \frac{60 \text{ min.}}{\text{Hr.}} = 356 \times 10^6 \text{ cycles} \tag{3}$$

The calendar period over which these cycles occurred was reviewed and correlated to

recorded maximum increase in vibration during selected deslag operations. The form of the recorded data is unfiltered peak to peak displacement, in mils, as sensed on the number 1 bearing cap in the vertical direction. A curve fit of these data as a function of cycles under the thermal transient conditions as calculated in equation (3) is shown in Figure 6. Figure 7 shows the correlation of the maximum change in low-pressure turbine bearing cap vibration during deslag with predicted rotor crack growth.

The graph shows that the point at which the change in vibration becomes recognizable corresponds to a crack depth between 3 and 4 inches: or between 8% and 10% of the shaft diameter. This correlates very well with the crack depth (10% of rotor diameter) predicted analytically by Grabowski [9] as necessary for significant increase in rotor vibration response.

At the time of this writing, sufficient data reduction to establish similar time history amplitude curves for individual synchronous and twice-synchronous components of the unfiltered bearing cap vibration data has not been completed. Figure 2, however, shows an example of expected differences between the first and second harmonics. Whereas the absolute magnitude of change in velocity for the two harmonics is of the same order, the percentage change in the second harmonic is much greater than in the first harmonic.

Vibration data for certain rotor coast downs were also recorded on magnetic tape. Bode plots of amplitude vs. frequency for first, second, and third harmonics of rotor speed were generated as shown in Figure 8. Note that the ordinate is a logrithmic scale of velocity. The first critical speed was observed to be approximately 1035 cpm. The second and third harmonics responded at 1050 and 1080 cpm, respectively, most probably due to the increase in stiffness in the bearing oil film with reduced rotor speed.

MODIFIED UNIT OPERATION

Acting upon an initial belief that the rotor contained a transverse crack, but prior to actual determination of that fact by inspection, WEPCO decided to continue operation with revised procedures. This decision was based primarily on the fact that steady-state, full-load operation showed no trend towards vibration increase and the conclusion that the crack was propagating only during the deslag cycles as previously discussed.

The operating procedures were therefore modified to minimize high vibrations and hence to minimize the magnitude of thermal down ramps. This was accomplished by limiting the unit to a constant 200 MW output, regardless of system demand. At the 200 MW load, the boiler slagging is minimized, thereby eliminating the need for continual deslagging cycles.

The procedure for taking the unit off line was also revised since it was believed desirable to have crack closure while coasting down through critical speeds. This was accomplished by keeping the shaft at approximately constant temperature. The method employed brought the unit to a minimum load until vibration returned to normal after which the load was dropped rapidly while maintaining high steam temperatures.

The result of these procedures was that the trend of continually increased vibration level with age or deslag cycles ceased. Also, no increase in steady-state vibration

was observed. These operating restrictions continued until the unit was shut down, ultrasonically inspected, and the rotor removed for repair.

SUMMARY AND CONCLUSIONS

Some vibrational characteristics of a large steam turbine rotor containing a transverse crack have been identified. It was determined that the measured vibration signatures during thermal transient deslag operations correspond to analytically predicted responses for a continuously open crack. The vibration signatures also showed significant increase in the twice per revolution response of the rotor and an overall vibration amplitude increase with increasing crack depth.

Fracture machanics analysis, including the effects of prior "overloads" on subsequent fatigue crack growth, was used to predict crack growth. The increase in bearing cap vibration was correlated with the predicted crack growth. This trend compared very well with the analytically predicted onset of rotor response to stiffness asymmetry caused by a growing transverse crack near the mid span of a rotor. It was shown that a crack depth corresponding to approximately ten percent of the shaft diameter is necessary to produce a significant change in the rotor vibration response.

Although there are many factors which affect rotor vibration response to cracking (such as axial position of the crack or the phase relationship of the crack to rotor eccentricity), it has been shown that vibration monitoring, rotor dynamics analysis, and fracture mechanics analysis can be used to identify, predict and understand the presence and growth of transverse cracks in large steam turbine rotors.

REFERENCES

1. Besuner, P.M., Rau, S.A., Davis, C.S., Rogers, G.W., Grover, J.L., and Peters, D.C., "BIGIF: Fracture Mechanics Code for Structures--Introduction and Theoretical Background - Manual 1," EPRI NP-1830, April 1981.

2. Hopkins, S.W., and Rau, C.A., Jr., "Prediction of Structural Growth Behavior Under Fatigue Loading," Fatigue Crack Growth Measurements and Data Analysis, ASTM STP 783, 1981.

3. Hopkins, S.W., Rau, C.A., Jr., Leverant, G.R., and Yuen, A., "Effect of Various Programmed Overloads on the Threshold for High-Frequency Fatigue Crack Growth," Fatigue Crack Growth Under Spectrum Loads, ASTM STP 595, 1976.

4. Grabowski, B., "The Vibrational Behavior of a Turbine Rotor Containing a Transverse Crack," Transactions of the ASME, Vol. 102, January 1980.

5. Mayes, I.W., Crack Propagation in Rotating Shafts, ASME 77-DET-164.

6. Mayes, I.W., and Davies, W.G.R., The Vibrational Behavior of a Rotating Shaft System Containing a Transverse Crack, I. Mech. E. C168/76.

7. Okah-Avae, B.E., Analogue Computer Simulation of a Rotor System Containing a Transverse Crack, Simulation, Dec. 1978.

8. Zrebarth, H., and Baumgartner, B.J., Early Detection of Cross-Sectional Rotor Cracks by Turbine Shaft Vibration Monitoring Techniques, 81-JPGC-Pwr-20.

9. Grabowski, B., "The Vibrational Behavior of a Rotating Shaft Containing a Transverse Crack -- Part 1 - Crack Models and the Vibration of a Rotor with Single Disk on a Massless Shaft Containing a Transverse Crack," (to be published) 1982.

TABLE 1. - NORMALIZED CRACK DRIVING FORCE FOR CHORD CRACK IN CIRCULAR SHAFT UNDER LINEAR STRESS VARIATION (BENDING)

Crack Depth (inches)	K/σ $(\Delta K/\Delta\sigma)$	ΔK (for $\Delta\sigma = 3.2$ ksi) (ksi $\sqrt{in}$)	K_s (for $\sigma_s = 25$ ksi) (ksi $\sqrt{in}$)
0.99	1.395	5.02	34.88
1.98	1.940	6.98	48.50
2.80	2.235	8.05	55.88
4.00	2.630	8.42	65.75
5.60	2.990	9.57	74.75
6.70	3.260	10.43	81.50
7.92	3.510	12.64	87.75
11.20	4.060	14.62	101.50
15.80	5.440	19.58	136.00
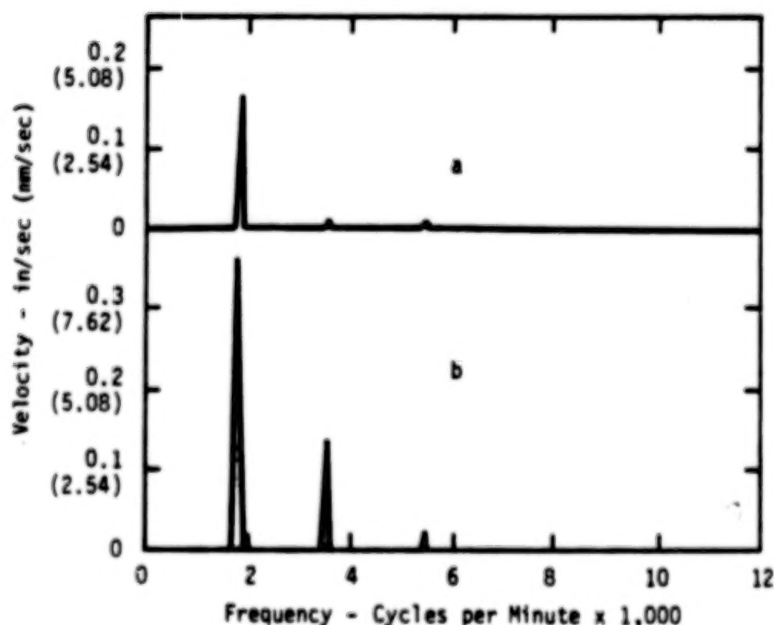
Figure 1. - Vibration signatures of amplitude vs. frequency in a radial direction, a) during normal full load operation, b) during peak vibration subsequent to a thermal down ramp.
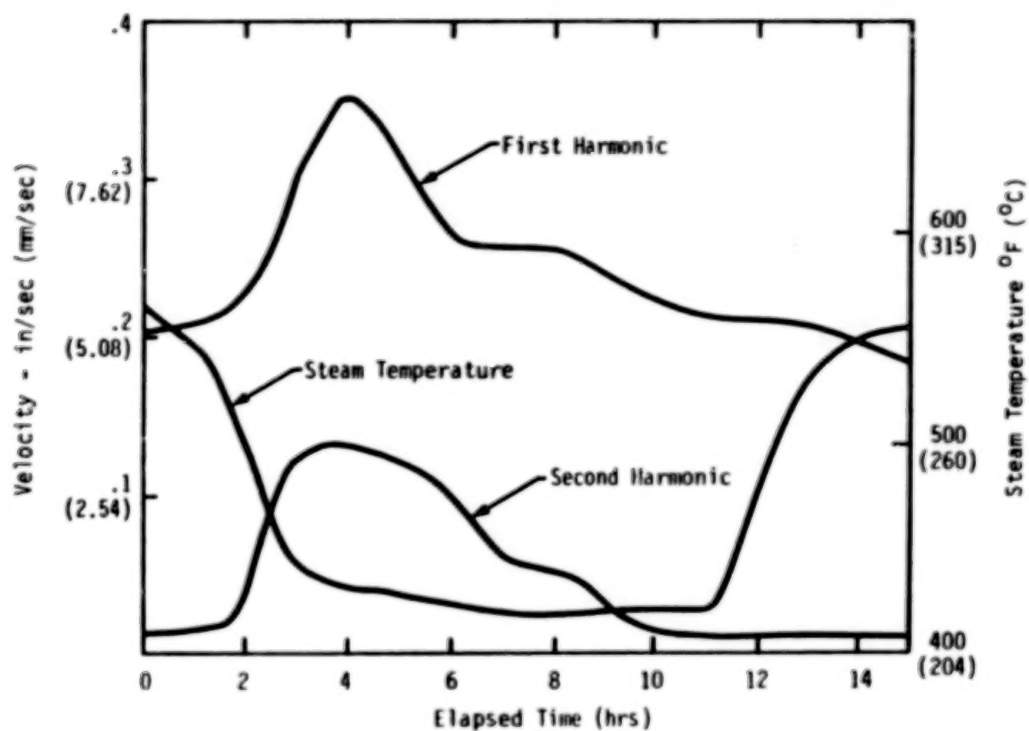
Figure 2. - Vibration amplitude of first and second harmonic and inlet steam
temperature vs. time.

Oak Creek #7 Shaft Diameter = 39.569"

--- BIGIF Model of Crack Shape
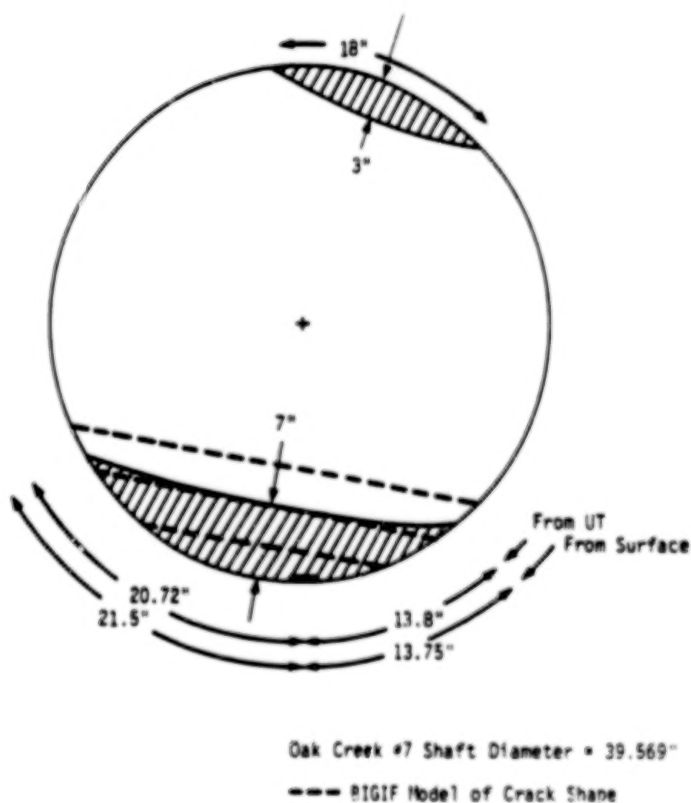
Figure 3. - Representation of Oak Creek #7 LP turbine shaft transverse cracking
including BIGIF model.

41
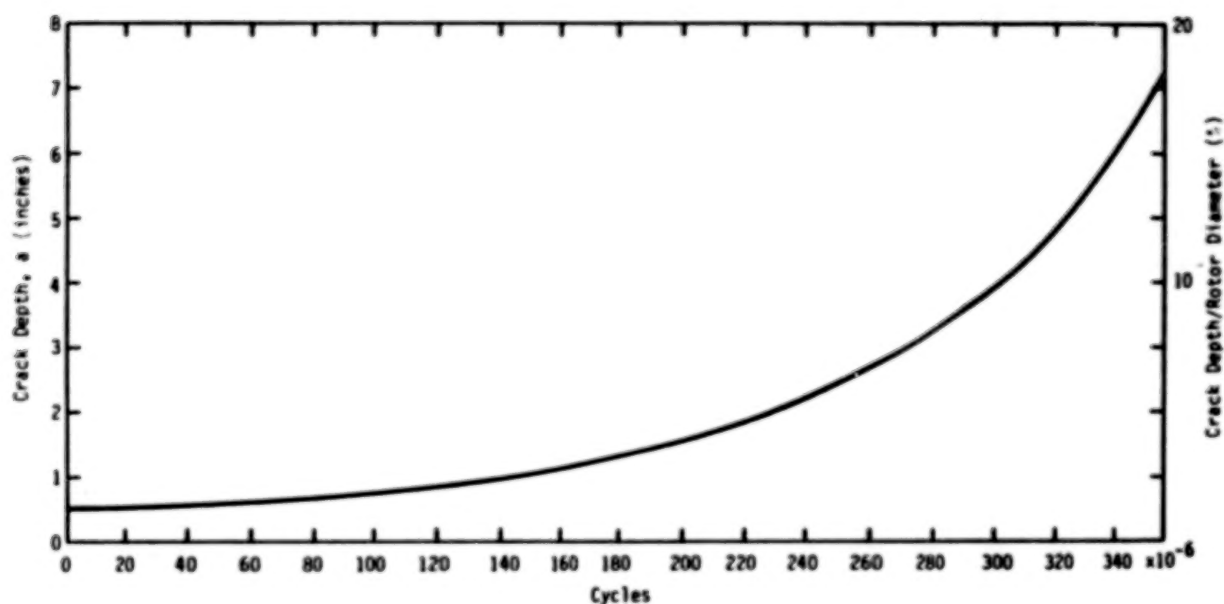
Figure 4. - Transverse crack growth rate due to deslag thermal transients predicted using BIGIF transverse crack model.
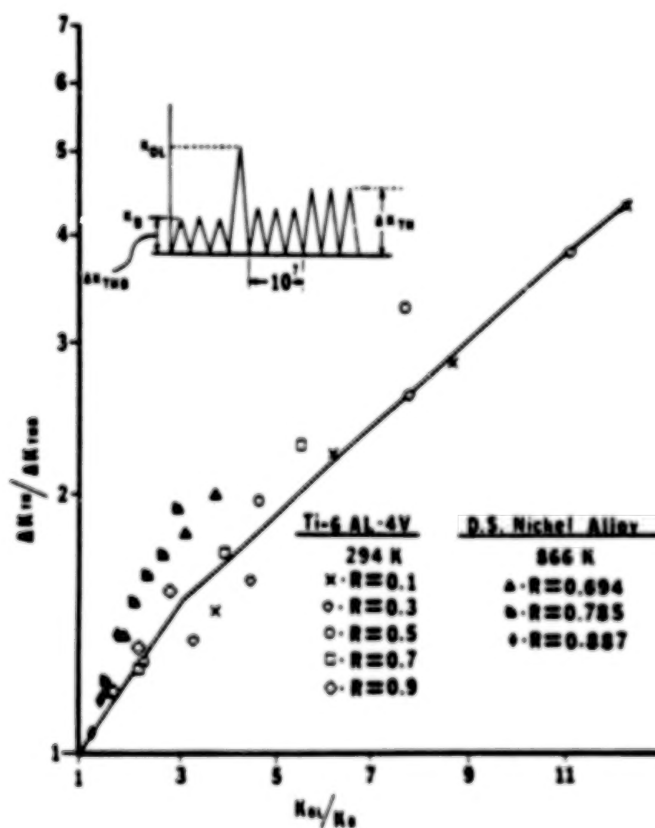
Figure 5. - Relative change in fatigue threshold after single cycle overloads as a function of the relative overload for the alloys and R ratios shown.

42
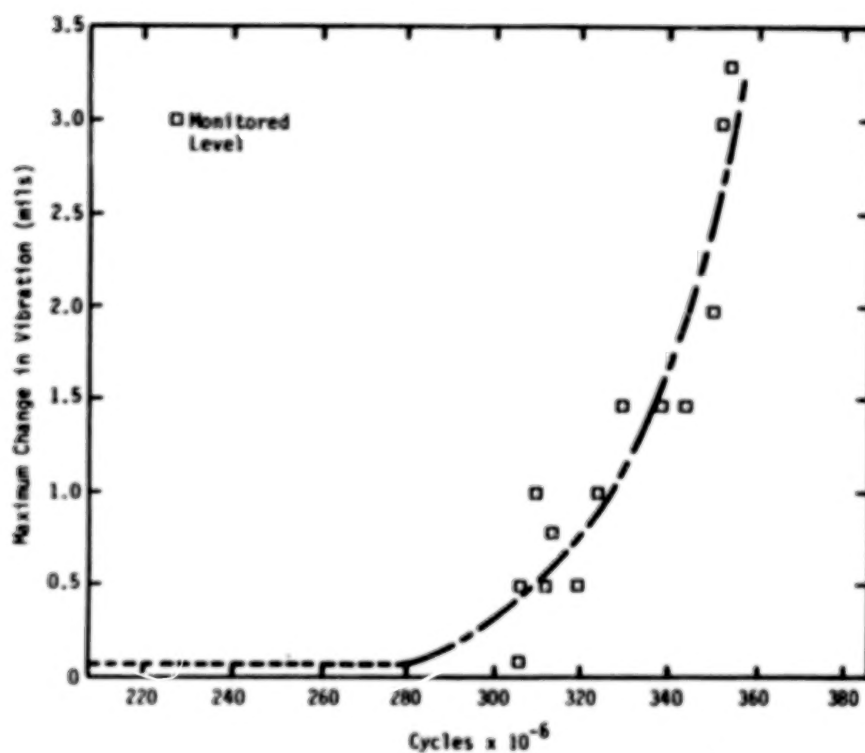
Figure 6. - Maximum changes in LP turbine bearing cap vibration during deslag as a function of total number of cycles at thermal transient stress state.
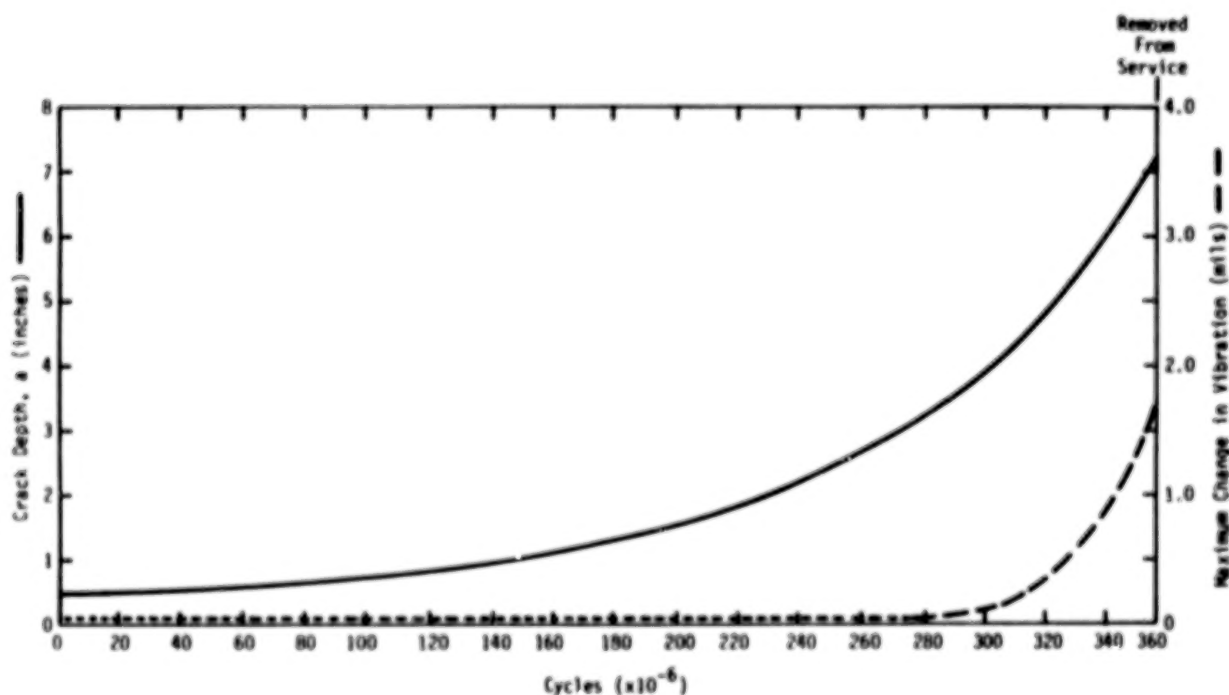
Figure 7. - Correlation of maximum change in LP turbine bearing cap vibration during deslag with predicted rotor crack growth.

43
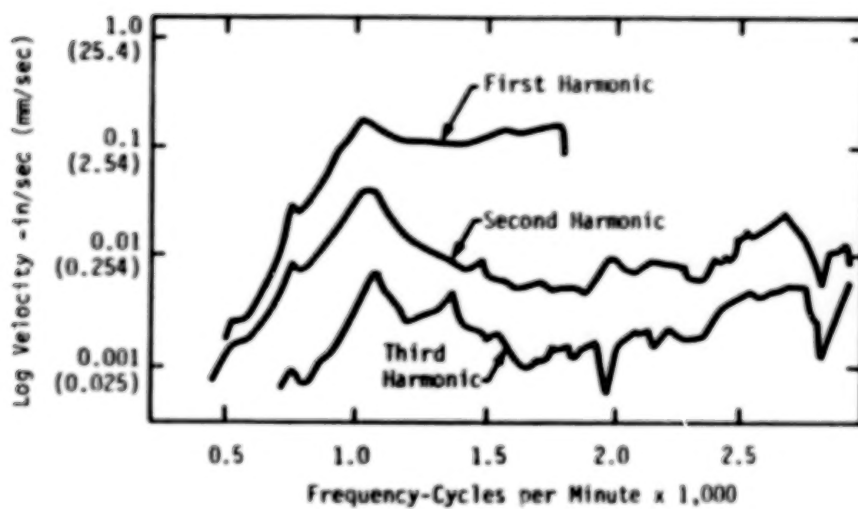
Figure 8. - Bode plot of amplitude vs. frequency for first, second, and third harmonics of running speed.

ASPECTS OF COULOMB DAMPING IN ROTORS

SUPPORTED ON HYDRODYNAMIC BEARINGS

P. G. Morton
G.E.C. Power Engineering Ltd.
Lichfield Road, Stafford,
England   ST17 4LN

ABSTRACT

The paper is concerned with the effect of friction in drive couplings on the non-sychronous whirling of a shaft. A simplified model is used to demonstrate the effect of large coupling misalignments on the stability of the system. It is concluded that provided these misalignments are large enough, the system becomes totally stable provided the shaft is supported on bearings exhibiting a viscous damping capacity.

SUMMARY

Rotating damping is well known to be a source of instability in shaft systems and many physical and mathematical explanations of the phenomenon exist. Published work seems mainly to be concentrated on a viscous or hysteretic damping model for the rotor, with simple dissipative bearings. The present paper considers non-linear damping of the Coulomb type in a simple rotor supported on 'realistic' linearized bearings, characterized by 4 stiffness and 4 damping coefficients.

The paper examines the nature of the sub-synchronous limit cycles resulting from interplay between the Coulomb damping within the rotor and viscous damping in the bearings. The rotating damping in the present model is assumed to arise from rubbing within gear type couplings at both ends of the rotor. The qualitative findings are however applicable to any mechanism producing friction forces depending on rotor flexure. It is also shown that as the couplings are misaligned in any plane, a level is reached above which the sub-synchronous oscillations collapse. A map of these limiting misalignments is compared with the shaft orbit under conditions of perfect alignment.

INTRODUCTION

Rotating damping has long been recognised as a source of instability in shaft systems. Both physical and mathematical explanations of the reasons for this instability have been advanced. A good summary has been given by Crandall (Ref. 1). Viscous and hysteretic damping is easily incorporated in a linear mathematical model. In many practical cases, however, the damping arises from relative motions within the rotating structure, the force-motion relationships obeying non-linear laws. A Coulomb damping model gives a reasonable representation of the energy exchanges resulting from slipping mechanisms, although to accurately incorporate such a model in a rotor/bearing system presents some problems in analysis.

Intuitively, one might suppose that instability due to any saturable type of rotating damping would be subject to limit cycles. This is only so if the system also contains positive damping elements with a more powerful energy-amplitude ratio. Such a system is a shaft with rotating Coulomb type damping supported on realistic, albeit linearized, hydrodynamic bearings. Very little published work exists on this very commonly occurring system and the present paper deals with a particular phenomenon of considerable practical significance.

The system dealt with is a rotor supported on two hydrodynamic bearings and driven by a gear type coupling. The rotating damping arises from movements between mating teeth of the coupling.

THE MODEL

The paper deals with an idealised model (Fig. 1). The degrees of freedom have been limited to 4, this being the minimum necessary to give a qualitatively adequate solution. The system comprises an isotropic non-damped shaft symmetric about its centre of span and characterised by a single flexural mode. The shaft is supported on two linearized hydrodynamic bearings, notionally represented as 8 stiffness and damping coefficients, each varying with running speed. Each end of the shaft moves within a coupling which has a fixed slope but is free to move in translation. The laws governing the force-velocity relationship within the couplings can be either of the viscous or Coulomb type. Provision is made for altering the coupling slope in both vertical and horizontal planes.

SYMBOLS

Axx_{11} etc.	kg	Elements of Inertia Matrix
Bxx_{11} etc.	Nsm^{-1}	Elements of Damping Matrix
Exx_{11} etc.	Nm^{-1}	Elements of Stiffness Matrix
B		Parameter concerned with viscous rotating damping (Eqn.7)
Bxx etc.		Non dimensional oil film damping
$B^{1}xx$ etc.	Nsm^{-1}	Dimensional oil film damping
b	Nsm^{-1}	Dimensional viscous damping of all coupling teeth moving axially
C	m	Radial clearance of bearings
Exx etc.		Non dimensional oil film stiffness
$E^{1}xx$ etc.		Dimensional oil film stiffness
ex, ey	rad	Angular misalignment of couplings, Planes x, y
F	N	Coulomb damping force generalised (Eqn.12)
f	N	Coulomb damping force of all coupling teeth moving axially
g	ms^{-2}	Acceleration due to gravity
L	m	Half span of shaft

Subscripts denote position in matrices.

M	kg	Half mass of shaft
m	kg/m^{-1}	Mass of increment of shaft
q_1x etc.		Generalised co-ordinate. Shaft centre x plane
r	m	Radius of coupling teeth
t	s	Time
Vx, Vy	ms^{-1}	Generalised velocity of rubbing of gear teeth
Wc	(Nm)	Work due to Coulomb damping/cycle
Wv	(Nm)	Work due to viscous damping/cycle
x, y		Horizontal and vertical planes
γ		Viscous rotating damping factor (Eqn.7)
Δ		Modal parameter (Eqn.4)
δx, δy		Misalignment parameters (Eqn.9)
ϕ		Mode shape of shaft
ϕ_0	m	Modal co-ordinate at shaft centre
ϕa^1	θ (rad)	Modal slope at shaft end
χ		Co-ordinate vector (Eqn.2)
ψ		Modal parameter (Eqn.6)
λ	rad.s^{-1}	Natural frequency of pinned-pinned shaft
ω	rad.s^{-1}	Lowest natural frequency
Ω	rad.s^{-1}	Running speed

EQUATIONS OF MOTION

The system co-ordinates (Fig. 2) relate to movements in the horizontal and vertical planes. The coefficients of the equations of motion are expressed as elements of square matrices using a subscript code where x, y determine the plane and $_1$, $_2$ relate to the shaft and bearing respectively. Thus Axy$_{12}$ would appear in a matrix as follows:-

$$
\begin{bmatrix}
- & - & | & - & + & - & |Axy_{12} \\
- & - & | & & + & & | \\
- & - & | & - & + & - & | & - & -
\end{bmatrix}
\begin{bmatrix}
\ddot{X} \\
\hline
\ddot{Y}
\end{bmatrix}
\tag{1}
$$

In the systems with viscous rotating damping the equations of motion are:-

$$A\ddot{\chi} + B\dot{\chi} + E\chi = 0 \tag{2}$$

47

Dimensional	Non Dimensional Inertia	
$Axx_{11} = Ayy_{11} = \Sigma m (\frac{\phi}{\phi_0})^2$	$\frac{\Sigma m \phi^2}{M\phi_0^2} = \Delta$	
$Axx_{22} = Ayy_{22} = M$	1	
$Axx_{12} = Ayy_{21} = Axx_{21} = Ayy_{21} = \Sigma m (\frac{\phi}{\phi_0})$	$\frac{\Sigma m \phi}{M\phi_0} = \psi$	
$Bxx_{22} = B^1 xx$	$g\, Bxx/\Omega$	
$Bxy_{22} = B^1 xy$	$g\, Bxy/\Omega C$	
$Byx_{22} = B^1 yx$	$g\, Byx/\Omega C$	
$Byy_{22} = B^1 yy$	$g\, Byy/\Omega C$	
$Bxx_{11} = Byy_{11} = \frac{br^2}{2}(\frac{\phi a^1}{\phi_0})^2$	$B = \frac{br^2}{2M}(\frac{\phi a^1}{\phi_0})^2$	(3)
$Exx_{11} = Axx_{11}\lambda^2$	$\lambda^2 \Delta$	
$Eyy_{11} = Ayy_{11}\lambda^2$	$\lambda^2 \Delta$	
$Exx_{22} = E^1 xx$	$g\, Exx/C$	
$Exy_{22} = E^1 xy$	$g\, Exy/C$	
$Eyx_{22} = E^1 yx$	$g\, Eyx/C$	
$Eyy_{22} = E^1 yy$	$g\, Eyy/C$	
$Exy_{11} = -Eyx_{11}{}^2 = \frac{br^2}{2}(\frac{\phi a^1}{\phi_0})^2 \Omega$	$\frac{br^2}{2M}(\frac{\phi a^1}{\phi_0})^2 \Omega$	

Regarding the shaft geometry, since the equations of motion are set up in terms of the pinned-pinned shaft modes ϕ, then it is convenient to assume a simple shaft geometry. The choices are a disc/weightless shaft combination or a uniform shaft. The latter model has been chosen and this results in a sinusoidal modal shape for which:-

$$\Delta = \Sigma m \phi^2 / M\phi_0^2 = 0.5 \tag{4}$$

$$\psi = \Sigma m \phi / M\phi_0 = 2/\pi \tag{5}$$

$$\frac{\phi a^1}{\phi_0} = \pi/2L \tag{6}$$

Roots of equation 2 give both system frequencies and dampings. If the system damping factor is plotted against the rotating damping (Fig. 3) it is possible to find the reserve of viscous damping possessed by the system. The viscous rotating damping factor is conveniently expressed as:-

$$\gamma = \frac{r^2}{4\Delta}(\frac{\phi a^1}{\phi_0})^2 \cdot \frac{b}{M\lambda} = \frac{B}{2\lambda\Delta} \tag{7}$$

γ being given as a proportion of critical damping of the shaft vibrating in flexure.

The damping B arises from the axial rubbing of the gear teeth in the coupling. These teeth are assumed to be continuously distributed on a pitch circle of radius r. The value b relates to the total viscous force/unit velocity obtained from sliding the coupling axially. The values of all parameters used in plotting the curve of Figure 3 are shown on that sheet and will be used for all further work in the paper. The bearing coefficients relate to a specific non-circular bearing profile of the fixed arc type.

Solutions of the linear equation of motion yield not only the system frequencies and dampings but the orbit shape, the size being, of course, arbitrary.

The coupling damping operates on the relative velocities of teeth arising from small vibrations in the system. It is possible to generalise these velocities in terms of the shaft co-ordinates as follows:-

$$V_x = \dot{q}_1 x + \Omega (q_1 y + \delta y)$$
$$V_y = \dot{q}_1 y - \Omega (q_1 x + \delta x)$$

(8)

where δx, δy relate to the angular misalignments of the coupling ex, ey thus:-

$$\delta x = ex \left(\frac{\phi_0}{\phi_a^1}\right) \qquad \delta y = ey \left(\frac{\phi_0}{\phi_a^1}\right)$$

(9)

The energy reserve/cycle in viscous damping at the coupling is given by:-

$$W_v = B \int_0^{2\pi/\omega} (V_x \dot{q}_1 x + V_y \dot{q}_1 y) dt$$

(10)

Coulomb Damping

Suppose now that the damping mechanism in the coupling is of the Coulomb type and that f is the force resisting axial movement of the teeth. The Coulomb energy/cycle is:-

$$W_c = F \int_0^{2\pi/\omega} \frac{(V_x \dot{q}_1 x + V_y \dot{q}_1 y) dt}{(V_x^2 + V_y^2)^{\frac{1}{2}}}$$

(11)

where

$$F = \frac{2r}{\pi} \left(\frac{\phi_a^1}{\phi_0}\right) \frac{f}{M} = \frac{r}{L} \cdot \frac{f}{M}$$

(12)

Note that strictly speaking Vx, Vy are not the same in the Coulomb case as in the viscous case, but for reasons which will be discussed later, the error involved in assuming both orbits to be identical ellipses is very small.

Plotting the work function (Wc − Wv) against orbit size for zero misalignment (Fig. 4) yields the magnitude of a limit cycle at the cross-over point. The fact that the cross-over slope is negative indicates that this is a stable cycle. The orbit size which refers to the length of the major axis of the ellipse at the shaft centre is proportional to f/M.

Misalignments

Having fixed the orbit size for the system under consideration, the values ex, ey are now systematically varied. Figure 5 shows that depending on the values of these parameters the character of the work function changes. Under some circumstances the function shows 2 cross-over points. The smaller orbit is unstable and the larger one is stable. Certain combinations of the misalignments give a totally stable system, there being a threshold at which a collapse from a finite orbit to zero takes place.

It is possible to plot a map of constant orbit combinations as in Figure 6. Here it will be seen that there exists a boundary in the ex/ey plane beyond which, for the model assumed, instability cannot exist. Within the boundary, limit cycles exist which are smaller than the limit cycle of the zero misaligned case.

DISCUSSION

It is first necessary to examine the validity of the model with regard to its general applicability. The semi-rigid modelling of the shaft implies certain constraints. This does not, however, affect the qualitative behaviour of the system, particularly that relating to the stabilizing effects of large misalignments. It does, however, mean that the system frequency and the orbit size will be incorrect, but to obtain a more accurate model it is only necessary to incorporate more shaft freedoms. Either a finite element or a modal representation could be used.

The present mathematical treatment of Coulomb damping also requires justification. It is reasonably easy, if tedious, to arrive at limit cycles by time marching methods or other slightly more elegant algorithms. Alternatively, a carefully constructed analogue computer circuit can solve the problem. All of these techniques have been used by the author on the particular problem presented in the present paper and for this case it can be shown that the orbits are very nearly elliptical with little harmonic content. Thus the assumptions used in deriving the energy expression (Wc - Wv) are valid. The reasons for this are fairly obvious. The energy supplied by the Coulomb damping is a small proportion of the inertial and strain energy in the system so that the orbits are largely controlled by these latter energy exchanges. This circumstance results from the fact that the shaft is very flexible, as evidenced by the small ratio of frequency: running speed (ω/Ω Figure 3).

The question arises as to what happens if the shaft is stiffer. As shaft stiffness increases, so does the stability margin. This margin is expressed in the present context as the viscous rotating damping necessary to reduce the system damping to zero. The author has found that reasonably accurate results can occur when this viscous damping margin is well over 15%.

Any rotating damping, whether viscous, hysteretic or Coulomb, reduces the stability margin of a rotating system. This means that non-sychronous whirling will start at a lower speed than that dictated solely by consideration of the oil film. Since most rotors contain some rotating damping mechanism, then extractions of the oil film coefficients from rotor/bearing systems may well be subject to inaccuracies.

More important, however, is what, in the authors' view, is the erroneous deduction from many tests and case histories, that oil film non-linearities are responsible for the small limit cycles often experienced prior to large non-sychronous orbits. The probability is that these limit cycles arise from the existance of friction in the drive mechanism. To be sure oil film non-linearities operate to limit journal orbits which are large compared with the bearing clearance, but this is a gross condition in which the oil film becomes effective around the complete bearing circumference.

In the present mathematical example, a single running speed has been considered so far. Obviously as this running speed rises and its associated oil film coefficients change, the stability margin reduces. According to our simple model the orbits should increase with running speed and at the 'resonant oil whirl' threshold, should grow without limit. Under these circumstances, however, it is obvious that constraints associated with bearing clearances etc. will take over so that the increase in orbit size may not be as dramatic as Figure 7 predicts. In any case the present theory deals with small vibrations and above a certain level the force/spatial relationships within the coupling may become much more complex than those assumed here.

The nearer the running speed approaches the 'true' oil film instability threshold, the easier it is to supply the small amount of friction damping necessary to promote limit cycles. Figure 8 shows a shaft weighing 700 kgs supported on 2, 100 mm dia hydrodynamic bearings. Figure 9 shows friction being introduced by 3 small steel 'fingers' supported on a freely rotating layshaft. The pressure between the fingers and the main shaft was introduced by elastic bands. This very small amount of damping produced from the dynamic slope of the shaft was quite sufficient to lower the instability threshold and produce stable limit cycles. The stabilizing effect of large misalignments was also demonstrated by varying the angle of the layshaft.

CONCLUDING REMARKS

The author has dealt with the subject of limit cycles in a shaft/hydrodynamic bearing system with rotating damping present in the drive coupling. The same conclusions, i.e. that limit cycles exist when saturable damping mechanisms are present, would apply whenever friction was caused by shaft flexure. The point brought out in the present paper is that the destabilizing effect of Coulomb damping can be 'biased out' by friction arising in a fixed plane and resulting from the rotation. In many practical situations such a biasing would be impossible in that very heavy fretting wear would be brought about by the gross misalignments necessary to achieve stability. Nevertheless, the mechanism is of some interest and may not only apply to couplings, but to other sources of rubbing in rotating elements.

REFERENCES

1. Crandall, S.H.: Physical Explanations of the Destabilizing Effect of Damping in Rotating Parts. NASA Conference Publication 2133, May 12-14, 1980, Pages 369-382.
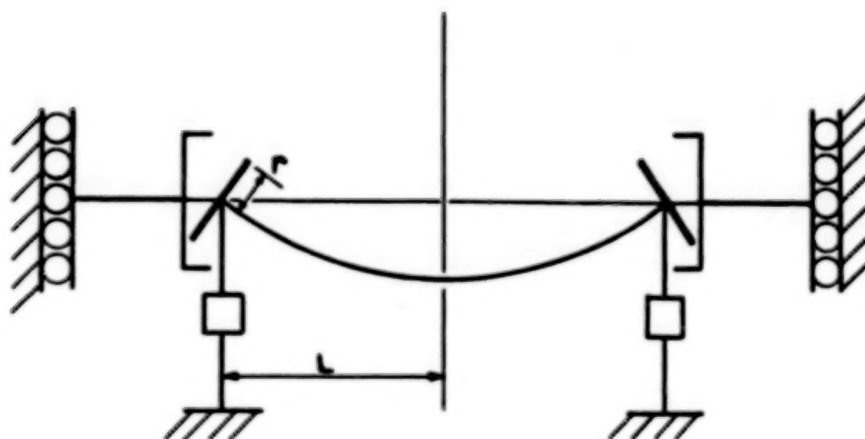
Figure 1. - Diagrammatic arrangement of shaft and couplings.
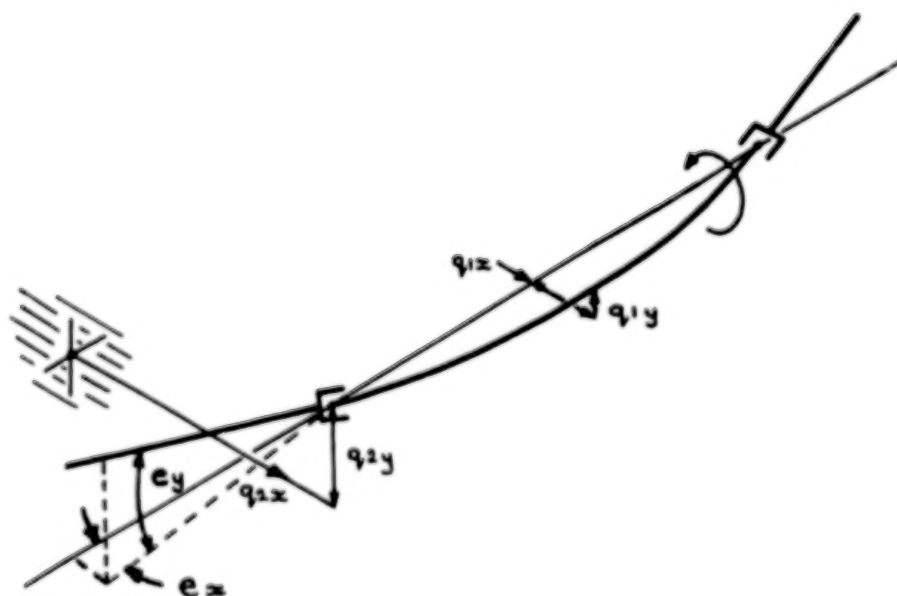
Figure 2. - Coordinate system.
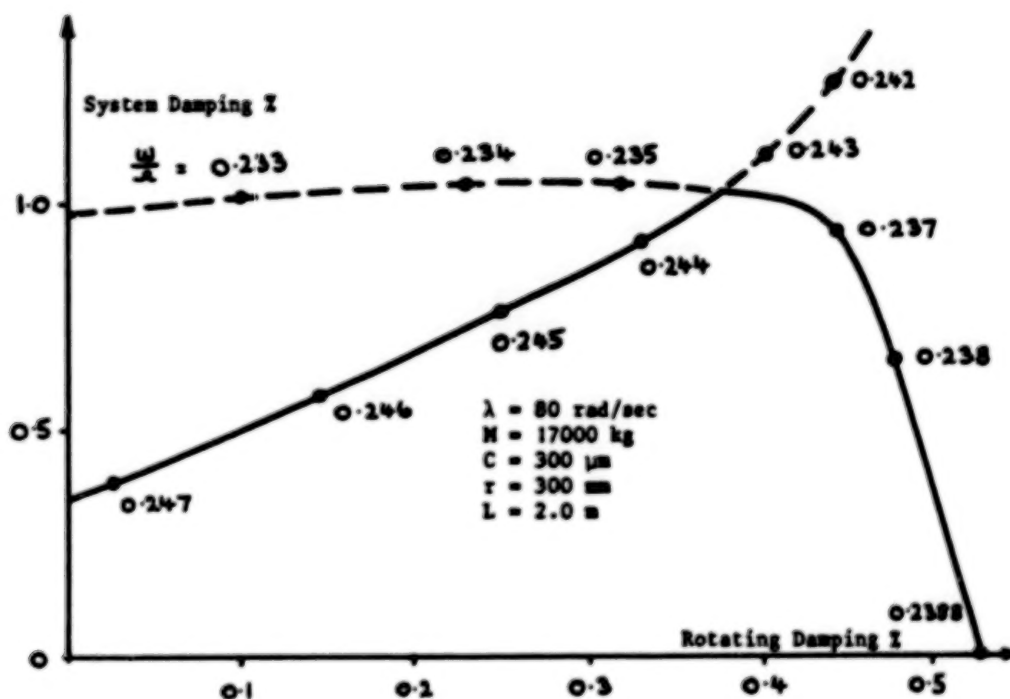
Figure 3. - Relationship between system damping and rotating viscous damping.
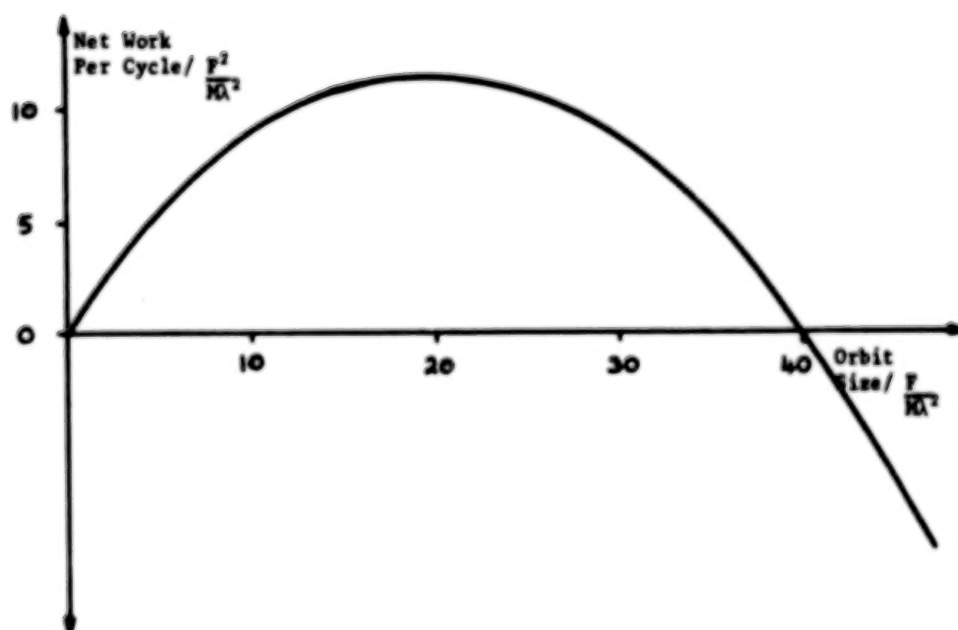
Figure 4. - Net work _ orbit size.

53
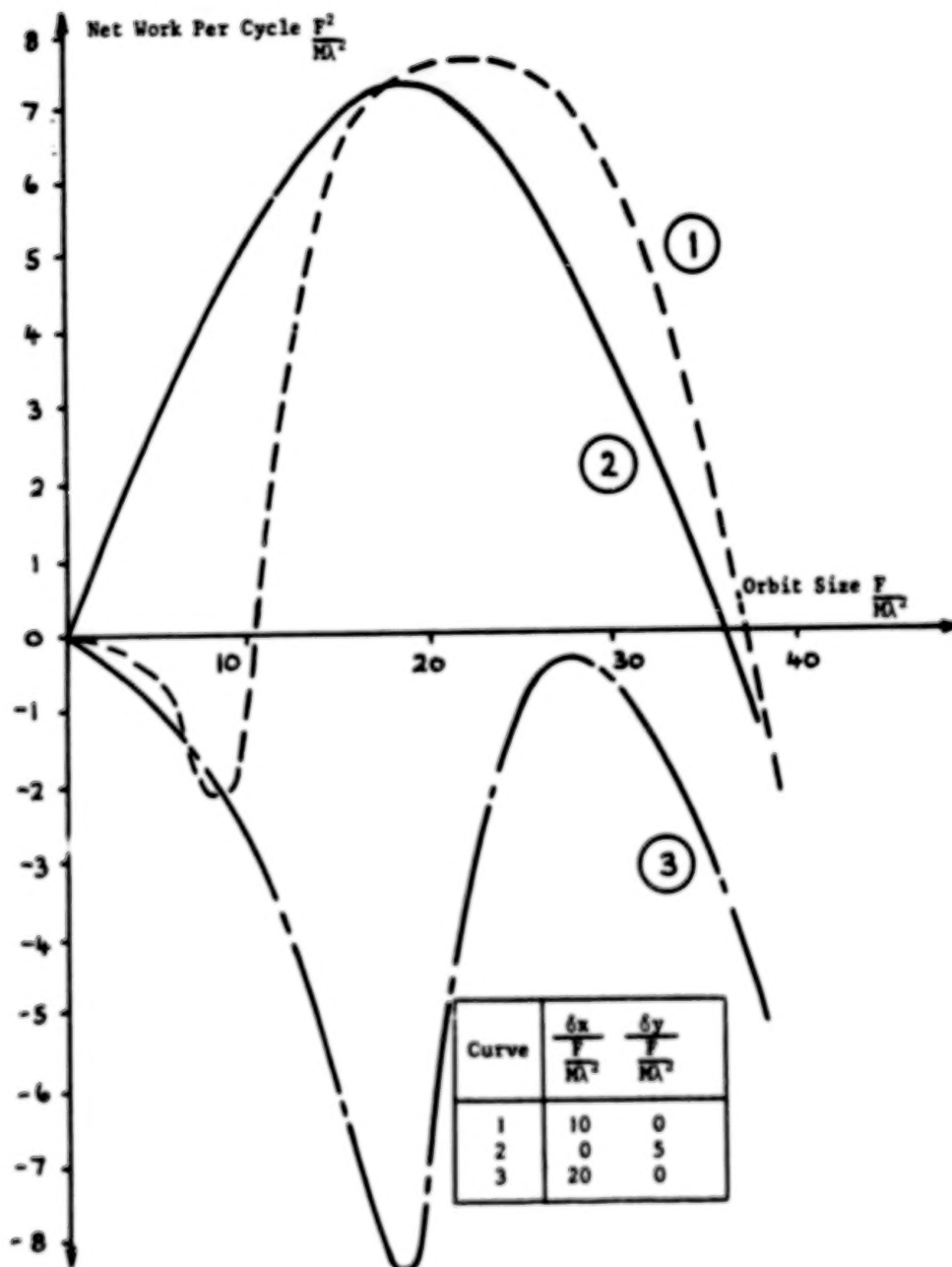
Figure 5. - Effect of misalignment on work function.

Curve	$\dfrac{\delta x}{\frac{F}{M\lambda^2}}$	$\dfrac{\delta y}{\frac{F}{M\lambda^2}}$
1	10	0
2	0	5
3	20	0

54
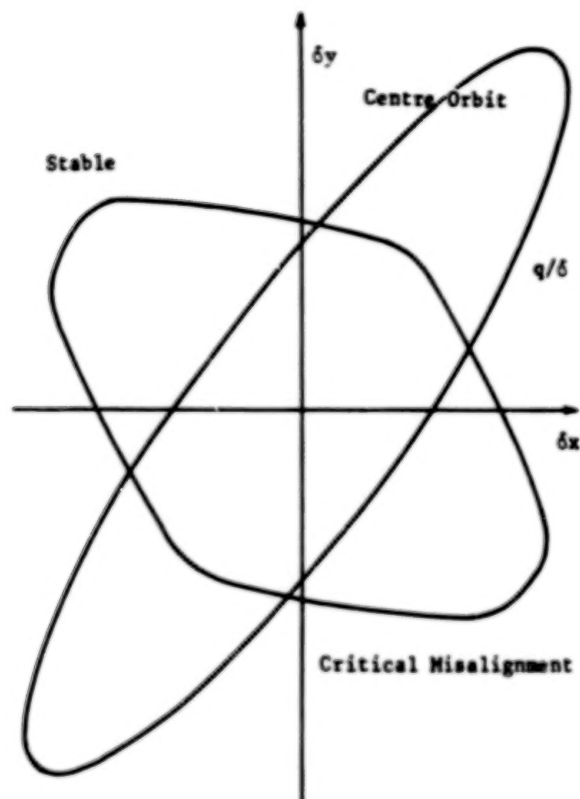
Figure 6. - Critical misalignment boundary compared with orbit of fully aligned system.
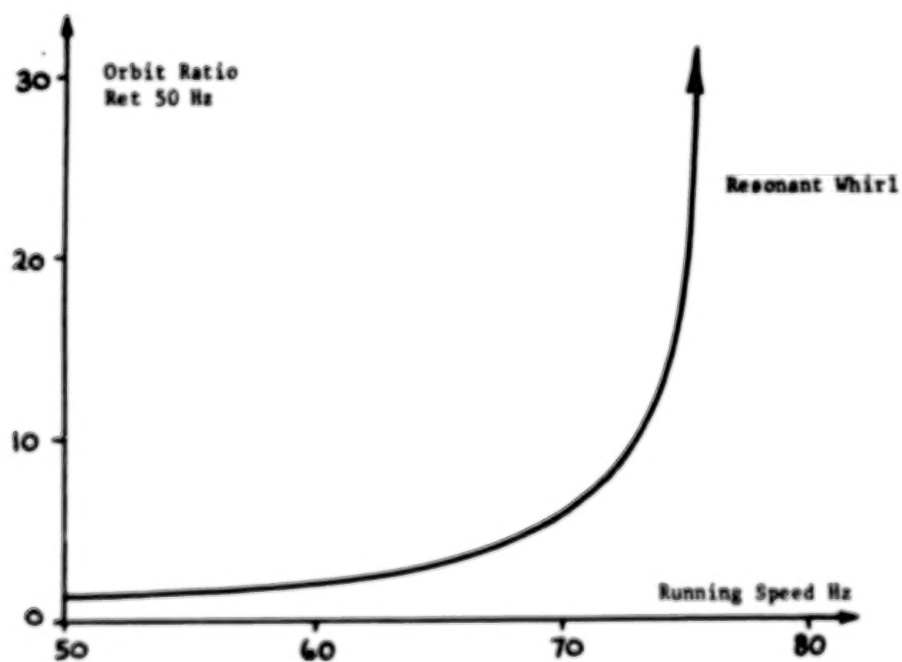
Figure 7. - Growth of orbit size with running speed.

55
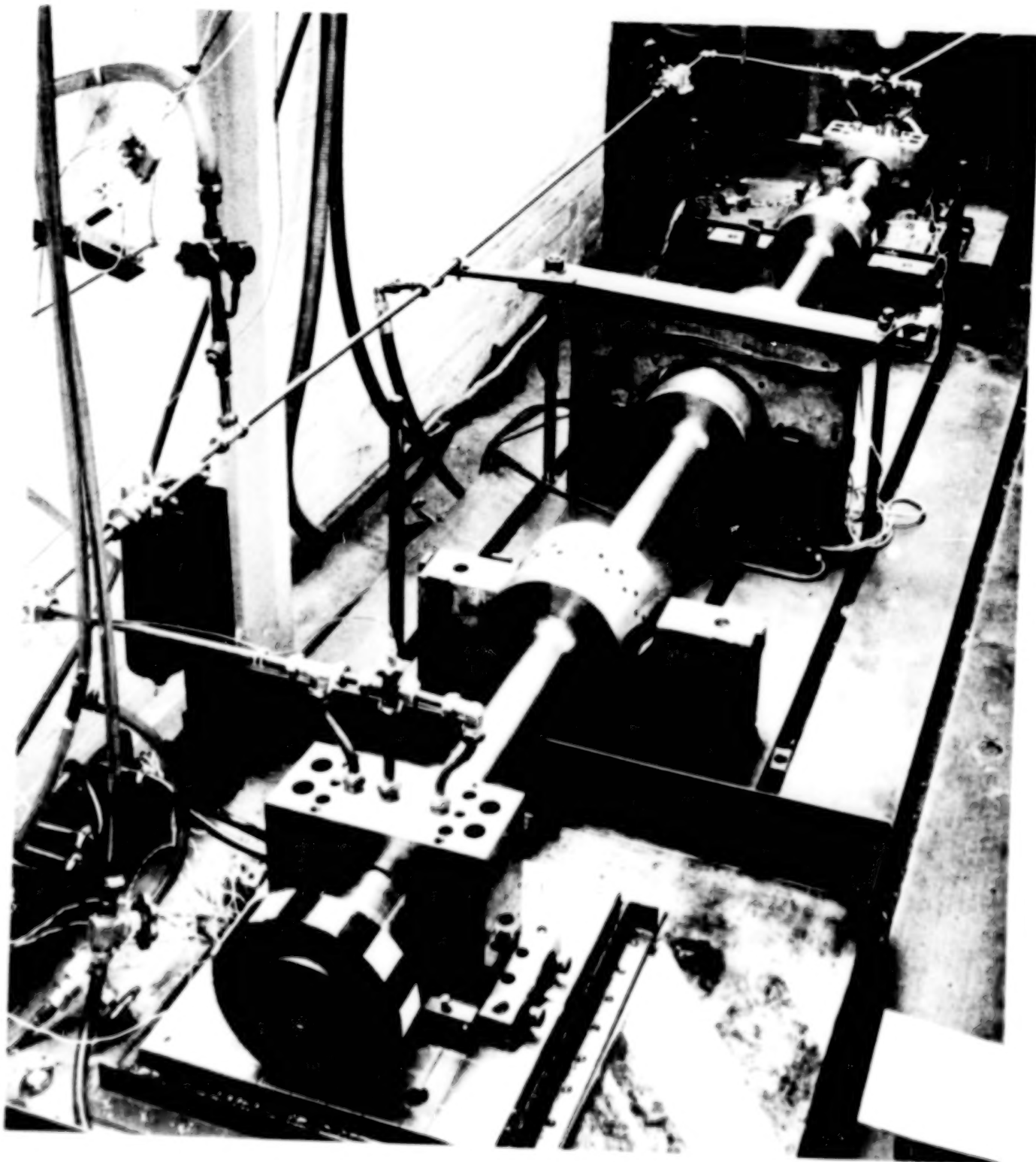
Figure 8. -Model rotor supported on 100mm dia. hydrodynamic bearings.
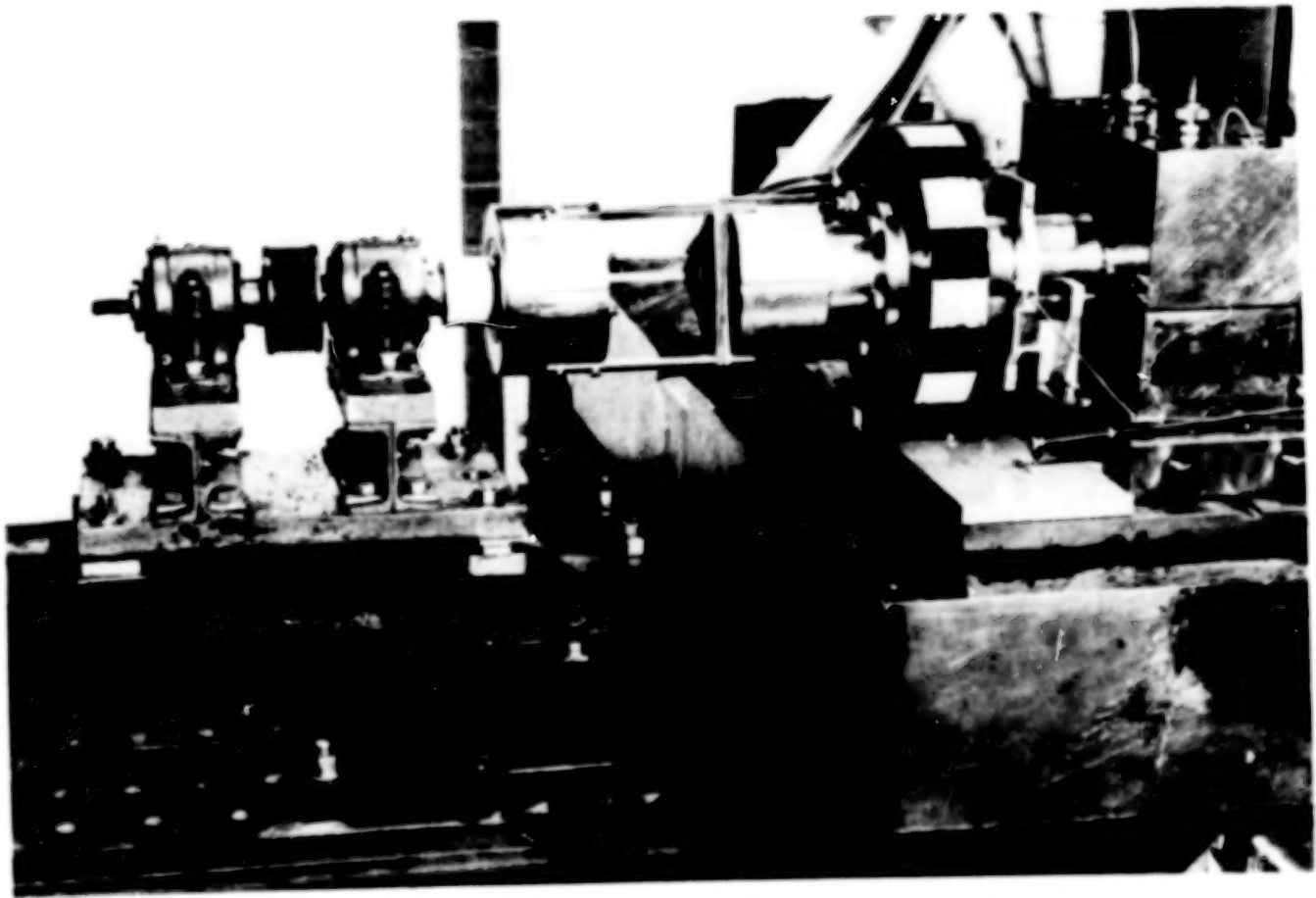
Figure 9. - Method of introducing friction damping into model rotor.

INSTABILITIES OF GEARED COUPLINGS - THEORY AND PRACTICE

R. Gordon Kirk, Roy E. Mondy, and Richard C. Murphy
Ingersoll-Rand Company
Phillipsburg, New Jersey 08865

SUMMARY

The use of couplings for high speed turbocompressors or pumps is essential to transmit power from the driver. Typical couplings are either of the lubricated gear or dry diaphragm type design. Gear couplings have been the standard design for many years and recent advances in power and speed requirements have pushed the standard design criteria to the limit. Recent test stand and field data on continuous lube gear type couplings have forced a closer examination of design tolerances and concepts to avoid operational instabilities. Two types of mechanical instabilities are reviewed in this paper: (1) entrapped fluid, and (2) gear mesh instability resulting in spacer throw-out onset.

Test stand results of these types of instabilities and other directly related problems are presented together with criteria for proper coupling design to avoid these conditions. An additional test case discussed shows the importance of proper material selection and processing and what can happen to an otherwise good design.

INTRODUCTION

In many instances of pre-order coupling selection, little consideration is given to either the dynamics of the coupling spacer as an individual body or its half weight effects on the shaft ends of the coupled units. Some efforts may be made to minimize weight but typically standard couplings are selected from a horsepower-speed aspect. This method is adequate in most cases because the spacer behaves as a rigid body with minimal influence on the connected shaft ends. It is this minimal influence on adjoining shaft ends and lack of response cross-coupling across the spacer which enables a single body analysis to accurately represent the individual unit's characteristics in the field.

The general technique for studying spacer tube dynamics is to consider it as a uniform beam with simple supports at each gear mesh as a worst case in the untorqued condition. As the torque level being transmitted through the spacer increases, the theory allows the coulombic gear mesh forces to restrain the spacer tube ends from rotating and effectively raise the spacer's critical speed. For some equipment strings the gear coupling's spacer tends toward this behavior. However, on units with flexible shaft ends, light journal loads, and large shaft end separation, the spacer cannot necessarily be considered to adhere to this proposed theory.

The amount of torque which a gear coupling is transmitting at a particular speed not only affects the amount of moment restraint which the adjoining shaft ends may induce upon the spacer but also greatly influences a mesh instability phenomena known as spacer throwout. Spacer throwout occurs when the mass unbalance

forces on the spacer become sufficiently great as to cause the spacer to move off of the gear mesh pitch line creating a step function increase in the unbalance forces being exerted on the adjoining shaft ends.

In attempts to minimize the potential for throwout problems, the tendency is to specify a coupling with the lightest spacer possible which is capable of transmitting the required torque. Employing this philosophy may result in a spacer tube calculated critical falling near design speed. If the spacer tube critical is at least 120% of design speed, then satisfactory operation should result according to Staedeli and Vance (ref. 1 and 2). On large center hung machines with short, stiff shaft ends, this criteria may be acceptable. However, on machines where the shaft ends are flexible and the coupling half weight is a substantial percentage of the total journal loading, then the 120% criteria can result in unacceptable system, lateral dynamics.

In order to alleviate this potentially problematic coupling - shaft end configuration, the tendency is to increase both inside and outside spacer tube diameters while decreasing concentricity tolerances and gear mesh clearances. The result is a special design of coupling which may be significantly more expensive than the original, standard coupling would be. Although this coupling design would eliminate the amplification effects associated with operating near the spacer tube critical and reduce the maximum displacement possible due to throwout, the increase in spacer tube weight may nearly offset the gains of the coupling design change. Therefore, if the coupling is not properly specified, one set of dynamics problems may be simply traded for another set of problems. One major problem which may exist in this increased diameter spacer design is that of entrapped coupling lubricant within the spacer tube. Although this type of phenomena is documented in the literature (ref. 3,4,5) it can be difficult to diagnose during field operation due to limited vibration data acquisition capability. Another more important fact is that the vibration characteristics may not match the reported theories in all regards as this paper will illustrate. Therefore, efforts to preclude oil from entering the spacer should be included as part of the coupling design.

The remainder of this paper documents several case histories of turbomachinery vibration problems wherein the source of the problem was concluded to be inherent in the coupling design selected for each particular application. Further discussion on the theories and methods of calculations for coupling selection and analysis follows the review of the test results. Design standards are given and recommendations are made to assure the best possible dynamic response characteristics for high speed couplings.

REVIEW OF TEST STAND DATA RELATING TO GEAR COUPLINGS

The following case histories exemplify the basic problems described above. Each case history spotlights a particular problem encountered and what actions were required to correct the problem. Since all corrective actions were made on the coupling itself and none were made on either the test driver or driven unit, all problems were considered to be initiated by the coupling's dynamic characteristics and its interaction with the adjoining units.

Case 1 - Spacer Critical Speed and Balance

The first coupling to be considered is shown in Figure 1. The shaft end separation is 1727.2 mm (68 inches) and the coupling weight is 79.1 kg (174 pounds). The spacer is 149.2 mm (5-7/8 inches) O.D., 136.5 mm (5-3/8 inches) I.D. This coupling is rated for 11.6 MW (15,500 horsepower) at 95 Hz (5700 RPM) with a maximum continuous operating speed (MCOS) of 100 Hz (6000 RPM). The calculated spacer critical speed is 131 Hz (7860 RPM) or 1.31 times MCOS. In the field this coupling transmits power from an overhung design expander to a center slung design axial flow compressor. The compressor was tested using this coupling and at 100 Hz (6000 RPM), the compressor's bearing vibration adjacent to the coupling was approximately 0.025 mm (1 mil), Figure 2. This same coupling was then used to drive the expander for its mechanical run test.

The set-up for the expander test is shown schematically in Figure 3 where the variable speed motor drives the expander through a 5:1 speed increasing gearbox. The initial results of this test are depicted in Figure 4 which represents the initial run up to speed. As can be seen, vibration levels are acceptable at 83.3 Hz (5000 RPM), approximately 0.010 mm (0.4 mil), but the amplitude rises sharply above 83.3 Hz (5000 RPM) approaching 0.051 mm (2.0 mils) at 91.7 Hz (5500 RPM). The amplitude was nearly all at synchronous frequency. This rapid increase in synchronous response amplitude is usually indicative of a critical speed. A review of the rotor dynamics analysis of the expander, including the coupling half weight, did not indicate a critical speed in this speed range. Upon running an analysis of the test system, the indication was that a system critical existed which was primarily controlled by the coupling. It was necessary to field balance this coupling placing balance weights at the spacer midspan to enable a satisfactory vibration level to be achieved. The field balance required numerous trials due to the sensitive nature of the coupling spacer critical. Figure 5 shows the final balance condition with an acceptable level of 0.038 mm (1.25 mils) being achieved at 100 Hz (6000 RPM). The existence of the critical speed is indicated by the substantial shift in phase angle above 91.7 Hz (5500 RPM).

Case 2 - Gear Tooth Damping

Several proposals were considered to resolve the vibration problems of Case 1. One proposal was to coat the coupling gear teeth with a product which the coupling manufacturer recommends for the running in of new couplings. This coating is a polyphenylene sulfide resin placed on the flanks of the teeth to help the teeth share the load. After a reasonably acceptable level of balance was achieved by field balancing, this coating was applied to the coupling teeth. Figure 6 depicts the results. With the coating on the coupling, the vibration as measured by the expander's coupling end vibration probe reached .076 mm (3.0 mils) at 91.7 Hz (5500 RPM) as seen on Curve 1. The coating was removed by a light sandblasting; the balance of the coupling was considered to be unchanged. Curve 2, showing 0.025 mm (1.0 mil) at 91.7 Hz (5500 RPM), reflects the results upon rerunning the coupling on the test stand. Since the only change between these two runs was the removal of the coating, it was concluded that the difference in response was due to an increase in the coulombic damping in the gear meshes which resulted from the removal of the slippery coating that had been applied to the teeth flanks.

Case 3 - Entrapped Oil

Since test stand field balancing of the coupling was not considered as an acceptable permanent fix, an investigation of prior experience with similar configured machinery was undertaken. One result of this investigation was the discovery that on other jobs the ratio of calculated lateral critical speed of the coupling floating member to maximum continuous operating speed was substantially greater than on this application. This ratio was found to vary from about 1.9 to 6.3. It was concluded from this data that for a permanent fix, a coupling was required wherein the spacer critical to MCOS ratio would have a minimum value of 2.0.

The coupling design resulting from this study is shown in Figure 7. The shaft end separation is still 1727.2 mm (68 inches), but the weight has been increased to 97.7 kg (215 pounds). The main spacer has an O.D. of 235 mm (9.250 inches) and an I.D. of 223.9 mm (8.813 inches). The calculated critical speed is 207.6 Hz (12,457 RPM) or 2.08 times an MCOS of 100 Hz (6000 RPM).

In order to confirm the acceptability of this coupling, it was run on the next similar unit to go on the test stand. Figures 8-a through 8-d depict the initial results. An extremely high level of vibration would suddenly occur with a very small increase in speed. As can be seen from a chronological review of the figures, the speed at which this phenomenon would occur was lower with each successive start and the source of the high amplitude was a subsynchronous component varying from .94/rev. on the first start to .83/rev. on the fourth start. Although the amplitude at synchronous frequency was never higher than 0.015 mm (0.6 mil), the subsynchronous component reached levels approximating 0.241 mm (9.5 mils) at 84.8 Hz (5090 RPM) on the first start.

The first step in disassembly of the unit was the removal of the coupling. Upon breaking the flanges, a substantial quantity of oil was observed to have been entrapped in the spacer tube. In order to permit the oil to escape from the spacer, twelve 6.35 mm (0.250 inch) holes were drilled in the spacer; four at each end and four in the middle. The spacer assembly was check balanced and found to be acceptable. The unit was reassembled. Figures 9 and 10 show the results of the retest run. Figure 9 shows that the subsynchronous component, due to the entrapped oil, has been completely eliminated and Figure 10 indicates that the critical speed, previously seen at about 96.7 Hz (5800 RPM) has been eliminated. An additional modification has since been incorporated into this coupling design to preclude oil from entering the spacer from the gear mesh area. This modification consists of interference fitting dam plates in the ends of the spacer. The oil drain holes are retained.

Case 4 - Manufacturing Tolerances

Of necessity, couplings similar to that of Figure 7 consist of a number of pieces which must be assembled. Where possible, rabbet fits are used to maintain consistency in reassembly. However, fits may have clearance and may not be concentric with each other which can result in either constant or variable unbalance being manufactured into the coupling. This same problem can also exist for the fits and pilot diameter of the gear meshes.

The coupling of Figure 7 has a floating member weight of 84.1 kg (185 pounds) which results in an unbalance of 106.7 gm-cm (1.48 ounce inches) for each 0.025 mm

61

(1 mil) of floating member eccentricity. Figures 11 and 12 graphically depict what can happen as a result of manufacturing tolerances and eccentricities. Figure 11 indicates an overall amplitude of 0.081 mm (3.2 mils) at a speed of 96.7 Hz (5800 RPM). For this test run the coupling was assembled using the manufacturer's match marks. The assembled coupling was indicated with mechanical dial indicators and depending upon axial location, ran out as much as 0.127 - 0.152 mm (5-6 mils). When ignoring the manufacturer's match marks, and rotating components relative to each other, the run out was reduced to under 0.051 mm (2 mils). The test results for this configuration are shown in Figure 12 where the overall vibration level at 96.7 Hz (5800 RPM) is approximately 0.037 mm (1.45 mils).

Case 5 - Throwout of Mesh

As discussed in the introduction, gear type couplings require a minimim torque transmission in order to center the floating member. In the absence of this minimum torque, the residual unbalance in the floating member may cause it to move eccentric until the tooth tip clearance is reduced to zero in the heavy spot's radial direction. This situation creates an additional unbalance in the coupling.

This phenomena is graphically displayed in Figure 13a, where a speed reducing gear box is being driven by a gas turbine with the load compressor uncoupled. As long as the accelerating torque is applied, the vibration amplitude gradually increases to a level of 0.013 mm (0.5 mil) at 209.2 Hz (12550 RPM). Since the accelerating torque decreases as the unit approaches idle speed, the vibration quickly increases to 0.018 mm (0.7 mil) at 211.3 Hz (12680 RPM). When torque is reapplied through the coupling during acceleration to MCOS, the vibration amplitude immediately drops to .009 mm (0.36 mil) and gradually increases again as the driving torque decreases while the unit comes up to speed.

Figure 13b shows a separate test run for the subject equipment string. Both accel and decel signatures clearly show the response step increase associated with coupling spacer throwout. The speed-amplitude drift signature is included as additional information to show the absence of a response critical of any kind in this speed range.

Case 6 - Coupling Failure

Figure 14 depicts a peak hold plot of overall vibration during the startup of a unit similar to the one just described above. As can be seen, the amplitude starts rising rapidly above 120 Hz (7200 RPM) and peaks at about 0.330 mm (13 mils) at 160 Hz (9600 RPM). The unit was tripped and after coast down, the coupling guard was disassembled. Figure 15 shows the condition of the coupling spacer. Three large cracks were evident. The darkened area above the center balancing band was caused by the coupling rubbing the guard. The driven gear box showed no distress and the coupling was not transmitting load as the load compressor was not coupled for this start nor had it been coupled. Metallurgical investigation later determined that the cracks had been formed during the heat treatment cycle of the spacer.

THEORY AND GUIDELINES TO PROPER COUPLING DESIGN FOR
ROTOR DYNAMICS CONSIDERATIONS

Entrapped Fluids

The analysis for the dynamics of a rotor partially filled with liquid was published by Wolfe (3,4) and Ehrich (5) in the mid-sixties in the U.S. Wolfe references earlier work from Europe dating to the late fifties. Other authors have more recently written on the subject of entrapped fluids (6,7) which refine the fluid dynamics and mathematics of the work by Ehrich. The published theory of entrapped fluids has been proven by experimental tests on vertical rotors wherein the system undergoes a zone of instability after passing a "reduced critical speed". This reduced critical is not a function of the fill ratio but is determined by calculating the system critical with an equivalent rotor mass. The equivalent rotor mass is found by adding the mass of the entrapped fluid required to fill the rotor full of liquid to the dry rotor mass. This theory indicates that higher and higher speeds may be reached as the rotor is filled with liquid before the instability onset occurs. The test stand data presented by Ehrich indicated the presence of a 0.87 x synchronous speed component that presented a speed zone of large response that the jet engine was able to pass through. The results of his analysis seemed to satisfy the test stand results of the jet engine for the one run he reported.

The results of the more extensive test runs with increasing volumes presented in this paper indicate that a mechanism of instability exists that produces a lowered threshold of instability as the volume of entrapped fluid increases and further that the whirl rate varies from almost synchronous for small volumes to 0.84 x synchronous as the volume increases. The difficulty in applying the simple theory to a real machinery situation is the identification of the critical of concern and the effective mass of the rotor. Additionally, the theory indicates a nonsynchronous component at 0.50 x synchronous for small volumes of entrapped fluid with whirl ratios increasing as the rotor is filled with more fluid. Wolfe noted that when his experimental rotor was unstable it whirled for the most part at frequencies below the reduced critical speed, the exact ratios not reported.

No attempt is made in this paper to apply the published criteria for instability onset since the nature of the observed instability differs from the theory as published to date. The practical solution is to prevent the admission of oil into a long spacer and further, to provide ample discharge outlets along the spacer length. The oil flow in gear couplings should not be oversimplified since the current design problem was considered by the manufacturer with the conclusion that it was impossible to get oil into the spacer. This indeed is logical if one does not consider axial pumping action or gear mesh oil ring instabilities that could increase the oil ring thickness. A minimum dam height at the spacer ends of double the normal gear mesh oil ring thickness is considered essential and preferably a solid blockage plate should be used on all coupling spacers that can entrap oil. The severity of the problem is amplified when lightly loaded coupling end bearings are present such as in the case of overhung expanders, turbines, compressors, or lightly loaded gear boxes.

When consideration is given to the potential imbalance from spacer I.D. non-uniformatives that can produce a nonuniform oil film in the spacer, the admission of oil into a spacer is quickly concluded to be highly undesirable.

Example 1

Consider the imbalance of 0.254 mm (10 mil) thickness of oil, 50.8 mm (2.0 inches) wide, along a 1524 mm (60.0 in.) spacer tube with an I.D. of 223.5 mm (8.8 in.), and an oil having a weight density of $\gamma = 0.0307$ lb/in^3.

$$U = \gamma \times V \times D/2 = .0307 \text{ lb/in}^3 \times (2.0 \times 60.0 \times .010) \times (8.8) \times 16$$

$$U = 2.59 \text{ oz-in or } 186.7 \text{ gm-cm}$$

(A typical coupling component balance is made to a level of 0.1 oz-in).

Coupling Spacer Critical Speed and Amplification

Manufacturers of high speed couplings typically calculate a spacer lateral critical by considering it as a simply supported beam as the worst case (see Eq. 1). The general opinion is that the critical is typically higher due to the frictional constraint and damping arising from the torque condition for a gear coupling. This type of constraint is not present in a dry diaphragm type coupling.

For large center hung turbomachinery this calculation is typically adequate with the bearing reactions effectively giving a restraint to validate the approximate calculation. For lightly loaded coupling end bearing machinery, however, the coupling represents a large portion of the modal mass of the coupling end critical (typically the turbomachines 2nd mode) and hence the system sensitivity to imbalance on the coupling is important not only at the spacer critical but also at the rotor system criticals. The standard practice of using coupling half weights located at their respective c.g.'s is considered totally acceptable for machinery having the spacer critical ratio of approximately 2.0 or larger.

The analysis of turbomachinery having the coupling spacer critical speeds less than 2.0 times the maximum continuous operating speed should include a response analysis of the coupling joining the two adjacent rotor bearing systems. This type analysis is commonly referred to as a train or partial train analysis. The detailed train analysis results in the identification of the actual system critical speeds and response sensitivities. The justification for this is supported by the resulting amplification or deviation from a speed-square response as the spacer critical speed ratio N_{cr}/N becomes less than 2.0. This is shown in Table I where it is noted that a 33% deviation from a speed-square curve exists when $N_{cr}/N = 2.0$. A 176% deviation is indicated for $N_{cr}/N = 1.25$. This means that any residual imbalance force has been amplified by 176%. For $N_{cr}/N = 1.1$, an amplification of 425% would occur for the residual imbalance forces to the adjoining rotor bearing systems.

The proposed design procedure for preliminary selection of couplings is as follows:

1. Size coupling for torque capacity requirements.

2. Check placement of spacer N_{cr} by the following equation (American Units)

$$N_{cr} = \frac{4.73 \times 10^6}{L^2} \sqrt{\frac{D^2 + d^2}{1 + \left[\dfrac{9 \, W_e}{L(D^2 - d^2)}\right]}} \quad \text{(RPM)} \tag{1}$$

64

where

D = spacer nominal outer diameter, in.

d = spacer nominal inner diameter, in.

W_e = effective modal mass of flanges or torque meters referred to the spacer midspan, lb_m.

L = mesh to mesh distance, in.

Spacer is assumed to be of standard steel having a Young's Modulus, E = 28.7 x 10^6 lb/in^2 and weight density, γ = 0.283 lb/in^3.

3. If the spacer is in the satisfactory region given in Figure 16 (Zones I and II, and the upper part of Zone III) for each of the adjoining machines journal reaction ratio, 1/2 Wcplg/Wjournal, the design specifications need not require a train analysis.

4. If the design falls in the marginal region of Figure 16, a train or partial train analysis should be performed for test stand and field conditions if the spacer cannot be redesigned to move into the satisfactory region.

5. If the design falls in the unacceptable region the coupling spacer should be redesigned to move the calculated critical as far as possible toward the satisfactory zone, analysis being made as noted above.

Coupling Throwout

The previous discussion on amplification is important to be able to fully appreciate the potential problems relating to the mesh throwout instability. According to the results given in reference (1), a gear coupling in perfect balance will center on the mesh pitch line when the torque transmitted is either equal to or larger than

$$T = M \times E \times \omega^2 \times D/4 \tag{2}$$

where

M = mass of floating member

E = spacer eccentricity to be centered

D = mesh pitch diameter

ω = rotor speed, rad/sec.

This torque is typically very small for standard tooth tip clearances.

Example 2 (American Units)

Assume the following conditions:

E = .001 in. = .0254 mm

N = 6000 RPM; ω = 628.3 rad/sec.

65

W = 160 lb. = 72.6 Kg

D = 9.0 in. = 228.6 mm

Applying Eq. (2) and converting to horsepower gives

$$H.P. = \frac{2 \pi T N}{33,000} = \frac{2 \pi (W E \omega^2 \frac{D}{4} \times 1/12) \times N}{33,000}$$

H.P. = 17.52 to center mesh at 6000 RPM.

Consider now the influence of the spacer imbalance on the centering action of the mesh. For a coefficient of friction of 0.15, it may be shown that the centering will not be maintained for an imbalance larger than

$$U_{T.O.} = \frac{1.07 \times 10^{10} \times H.P.}{D \times N^3 \times Q} \quad \text{(American Units)} \tag{3}$$

where

H.P. = transmitted horsepower

D = mesh pitch diameter, in.

N = rotor speed, RPM

Q = spacer amplification factor

$U_{T.O.}$ = oz-in. imbalance to cause throwout

Example 3

H.P. = 500 = 372.5 kw

D = 9 in. = 228.6 mm

N = 6000 RPM

Q = 5.0

$$U_{T.O.} = \frac{1.07 \times 10^{10} \times 500}{9 \times (6000)^3 \times 5} = 0.55 \text{ oz-in (39.6 g-cm)}$$

This imbalance represents an eccentricity of 0.43 mil TIR of a 160 lb. spacer. Hence, the likelihood of centering under unloaded or lightly loaded test stand conditions is very small for this example coupling.

A formula given by Staedeli (1) referred to as the Conti-Barbaran formula, which was developed from test stand experience, gives an estimate of goodness:

$$E = \frac{P \times 10^9}{1.36 \times M \times D^2 \times N^3} \quad \text{(Metric Units)} \tag{4}$$

where

P = power, KW

M = spacer mass, Kg

D = pitch dia., meters

N = speed, RPM

For $E \geq 10$, stable and trouble free

$E \leq 5$, problems with mesh centering

Converting to units of H.P., lb_m, in.,

$$E = \frac{1.87 \times 10^{12} \times H.P.}{W \times D^2 \times N^3} \quad \text{(American Units)} \tag{5}$$

Example 4

Consider the calculation of Eq.(5) for the conditions of Example 3:

$$E = \frac{1.87 \times 10^{12} \times 500}{160 \times 9.0^2 \times 6000^3} = .334 \text{ --- Problems}$$

For H.P. = 10,000

$E = 6.68 - - -$ Problems not likely

The above formula is similar to Equation 3 for the calculation of $U_{T.0.}$ The advantage of Equation 3 is that it gives a result that has physical meaning and gives the designer an imbalance level to achieve for best results.

The concern for mesh centering is two-fold in that gear wear would increase with the mesh off the pitch line and secondly, imbalance of the spacer is a function of the eccentric position of the floating member. The nominal tooth clearance at zero speed is increased at running speed and temperature to give typically 0.051 - 0.076 mm (.002 - .003 inch) diametral clearance. For the 72.7 Kg (160 lb.) spacer of the previous example, this would represent an additional imbalance level of 160 x 16 x .003/2 = 278.3 gm-cm (3.84 oz-in).

Typical balance standards would call for a balance of

$U = 4W/N = 7.21$ gm-cm (0.1 oz-in)

For 40 W/N; $U = 1.0$ oz-in (72.1 gm-cm)

Hence, the throwout imbalance is over 38 times the desired balance level and 3.8 times the practical balance level. This type of imbalance further amplified by proximity to a spacer critical is not desirable for turbomachinery.

Guidelines for Manufacturing Tolerances and Balance Requirements

The design and manufacture of long couplings required for machinery such as reported in this paper must be treated with due concern for the potential problems previously discussed and demonstrated by test stand experience. The design of such couplings typically necessitate a multicomponent design spacer with bolted flanges and close tolerance fits. It is therefore of utmost importance for couplings falling into Zone III of Figure 16, that the concentricities of the individual components be held below certain minimum standards. Component balance of the hubs, sleeves, and

the floating member is required. The final coupling assembly, as mounted on the turbomachinery, must have a total indicator reading on each of the ground balancing journals on the floating member of less than .051 mm (.002 in). This requirement necessitates that the coupling manufacturer achieve runout levels of less than .038 mm (.0015 in) for each balance journal relative to its mounting bore or rabbet fit. This criteria is relaxed for couplings in Zone I and Zone II as indicated on Figure 16.

When the floating member balance journal runout levels cannot be reduced to the required levels by selective component assembly, it becomes necessary to require an arbor balance of the total coupling assembly. The concentricities of the balance arbor must be controlled to preclude significant arbor induced imbalance which can result in a built-in imbalance when a correction is made and the coupling is removed from the arbor.

For couplings having a spacer critical speed ratio larger than 2.0, 2 plane correction on the floating member is adequate. For couplings having the spacer critical lower than 2.0, correction on the floating member should be made in three or more planes along the spacer length, to reduce unwanted modal amplification of the residual imbalance.

CONCLUDING REMARKS

This paper has presented test stand data that points clearly to the importance for rigorous design standards on couplings for turbomachinery, with added precautions for machines that may have lightly loaded coupling end bearings. Turbomachinery likely to experience this condition includes power turbines and compressors of an overhung design. The major conclusions that may be drawn from this paper are:

1. Coupling designs that are below the marginal zone of Figure 16 should not be accepted for Turbomachinery application.

2. Coupling spacers should be designed to have a critical speed ratio of 2.0 or larger. Smaller ratios may be acceptable if adequate analysis is conducted to assure an insensitive design as outlined in this paper.

3. Design features of gear couplings should preclude the admission of oil into the spacer tube.

4. The manufacturing tolerances for couplings should meet specific minimum standards as outlined in this paper.

5. Gear couplings should be designed to have a minimum increase in mesh tip clearance at design speed and temperature.

6. Turbomachinery conditions having low horsepower requirements and utilizing gear couplings are particularly susceptible to larger than normal imbalance levels on the coupling due to spacer throwout.

7. Long spacer couplings having a critical speed ratio less than 2.0 should have at least three planes for balance correction.

8. The balance procedures outlined in this paper could apply to all couplings but are considered essential for those applications in Zone III of Figure 16.

9. Attention to proper material processing and heat treatment is essential in addition to the above considerations.

REFERENCES

1. Staedeli, O.: Toothed Couplings. MAAG Gear Wheel Company, Ltd. 8023 Zurich, Switzerland.

2. Vance, J.: Influence of Coupling Performance on the Dynamics of High Speed Power Transmission Shafts. ASME Paper 72-PTG-36, 1972.

3. Wolf, J. A., Jr.: Whirl Dynamics of a Rotor Partially Filled with Liquid. ScD. Thesis, Massachusetts Institute of Technology, Cambridge, Massachusetts, Sept. 1966.

4. Wolf, J.A., Jr.: Whirl Dynamics of a Rotor Partially Filled with Liquid. Journal of Applied Mechanics, Trans. ASME, Dec. 1968, pp. 676-682.

5. Ehrich, F. F.: The Influence of Trapped Fluids on High Speed Rotor Vibrations. J. of E. Ind., Trans. ASME, Nov. 1967, pp. 806-812.

6. Saito, S. and Someya, T.: Self-Excited Vibration of a Rotating Hollow Shaft Partially Filled with Liquid. Journal of Mechanical Design, Trans. ASME, ASME Preprint 79-DET-62.

7. Lichtenberg, G.: Vibrations of an Elastically Mounted Spinning Rotor Partially Filled with Liquid. Journal of Mechanical Design, Trans. ASME, ASME Preprint 81-DET-54.

TABLE I. - UNDAMPED MODAL AMPLIFICATION DUE TO APPROACH TO A CRITICAL SPEED

Speed Ratio $\frac{N_{cr}}{N} = \frac{1}{\Omega}$	Dimensionless Speed $\frac{N}{N_{cr}} = \Omega$	Speed-Square Ω^2	Undamped Response $\frac{\Omega^2}{1-\Omega^2}$	Percent Deviation from Speed-Square Curve
∞	0	0	0	0.0
4	.25	.0625	.0667	6.4
3	.33	.1089	.122	13.2
2.5	.4	.16	.19	19
2.3	.434	.189	.233	23.2
2.0	.50	.25	.333	33 (33.04)*
1.81	.55	.302	.434	43
1.67	.60	.36	.5625	56 (55.5)*
1.42	.70	.49	.96	96
1.25	.80	.64	1.77	176
1.11	.90	.81	4.26	425
1.0	1.0	1.0	∞	∞ (900)*

*Denotes value for typical damping value of Q = 10
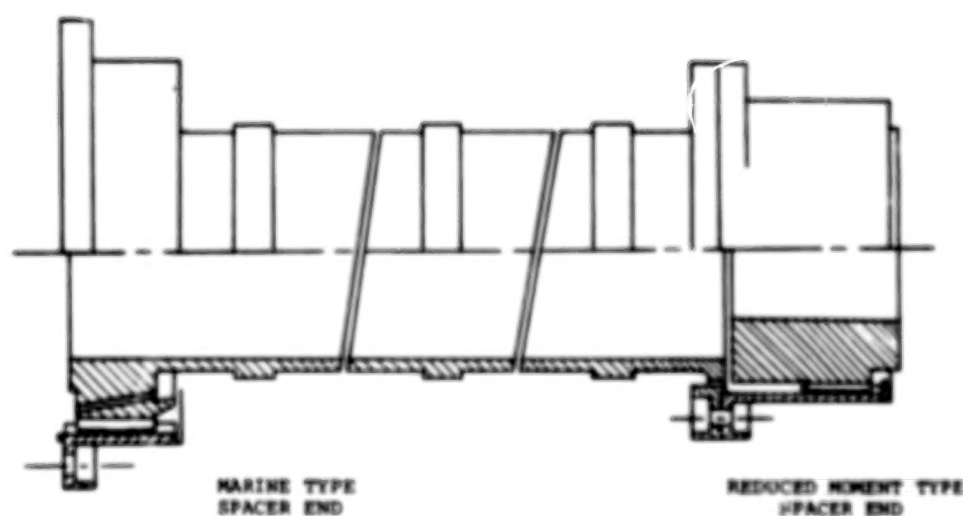
Figure 1. - Expander original coupling design employing both marine and reduced moment spacer design features.

MARINE TYPE
SPACER END
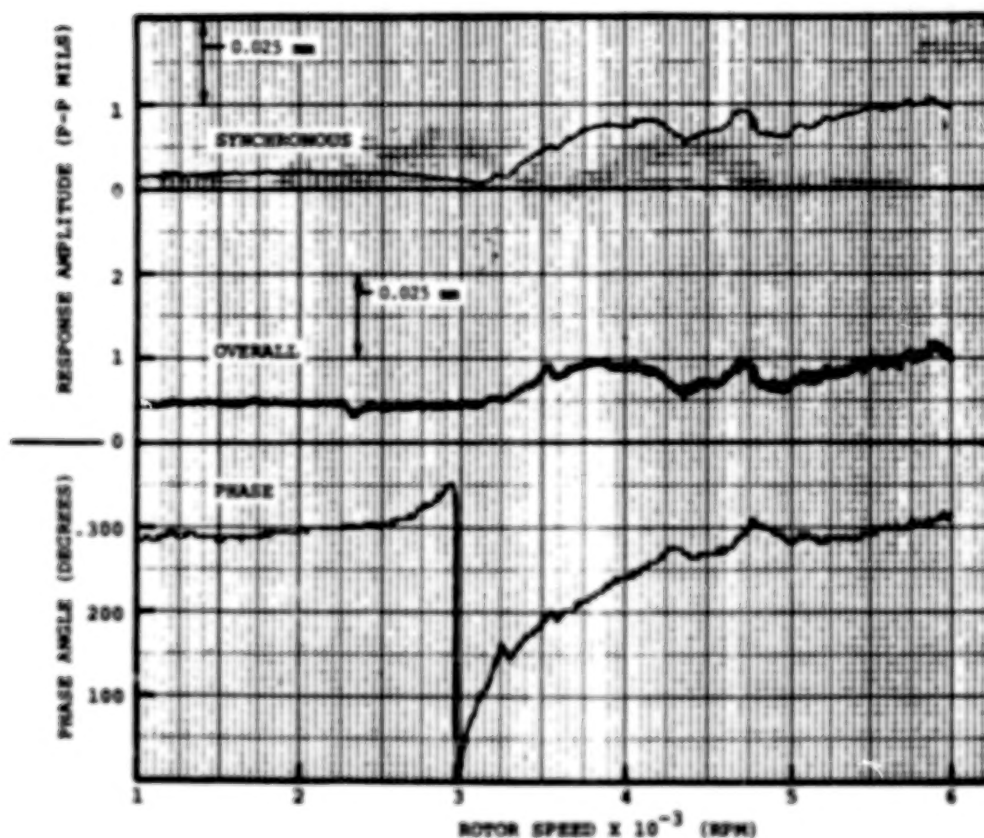
REDUCED MOMENT TYPE
SPACER END

Figure 2. - Acceptable axial compressor vibration (speed vs. amplitude) signature. Four-hour mechanical test run.

TEST SET UP

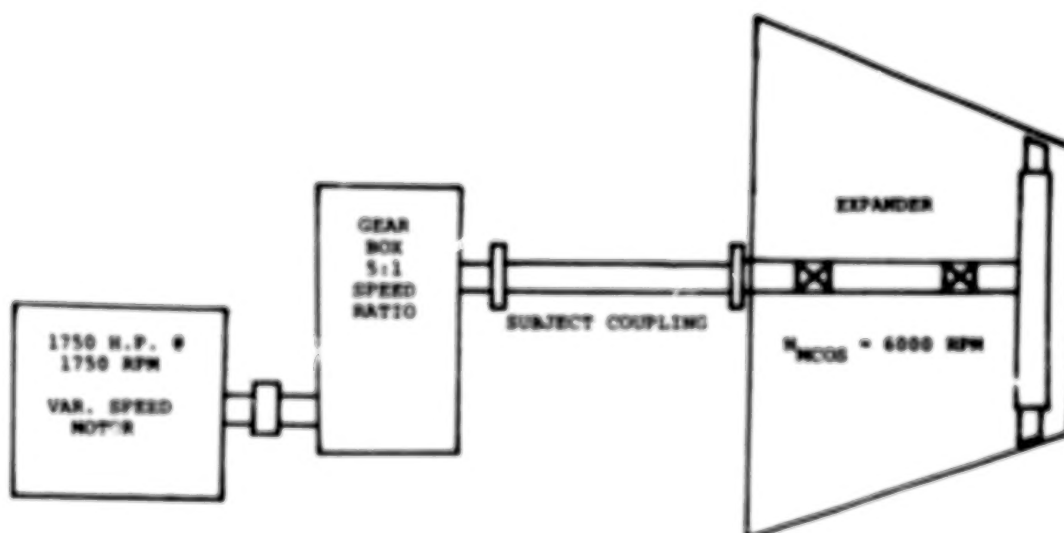Figure 3. - General configuration of expander test stand assembly.
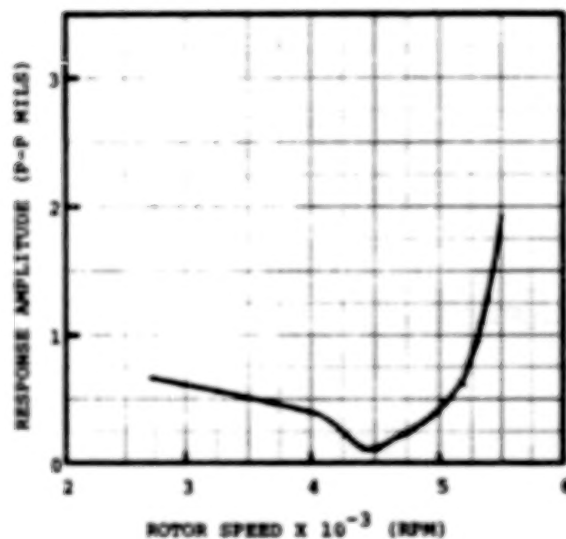
71

BEST DOCUMENT AVAILABLE

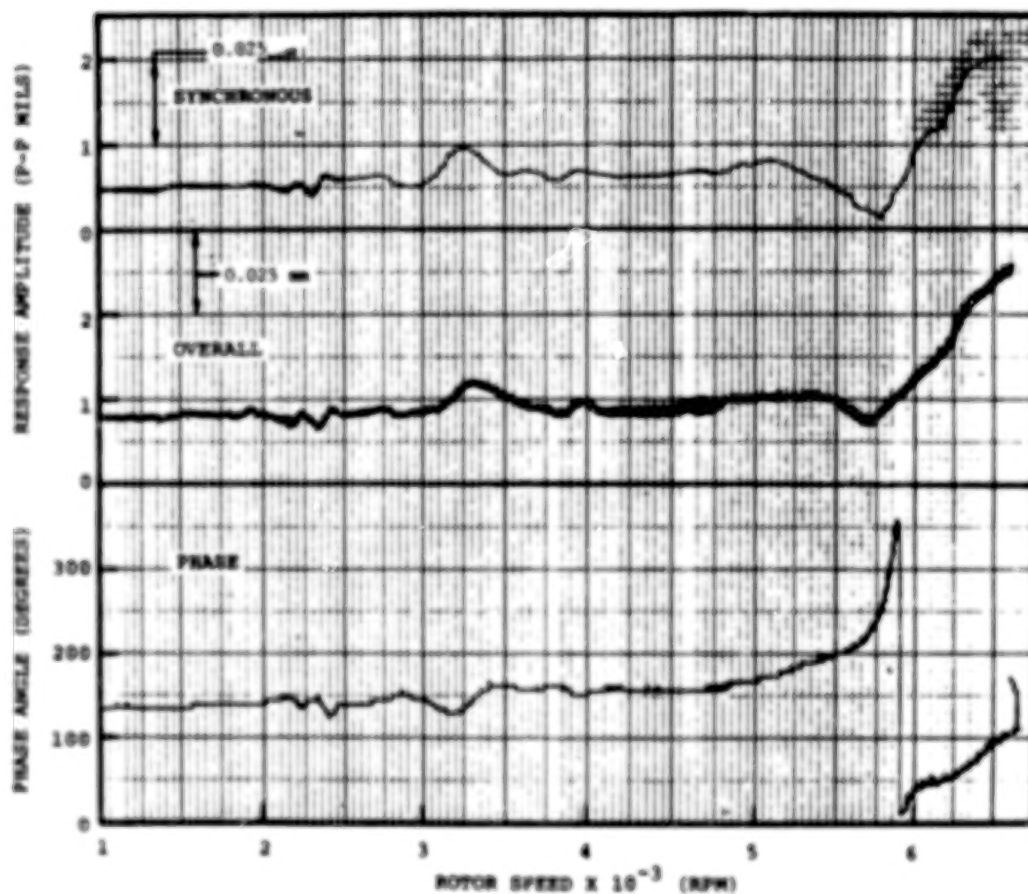Figure 4. - Expander vibration signature for initial acceleration on test stand.

Figure 5. - Expander vibration signature for final balance condition of coupling on test stand during mechanical run.
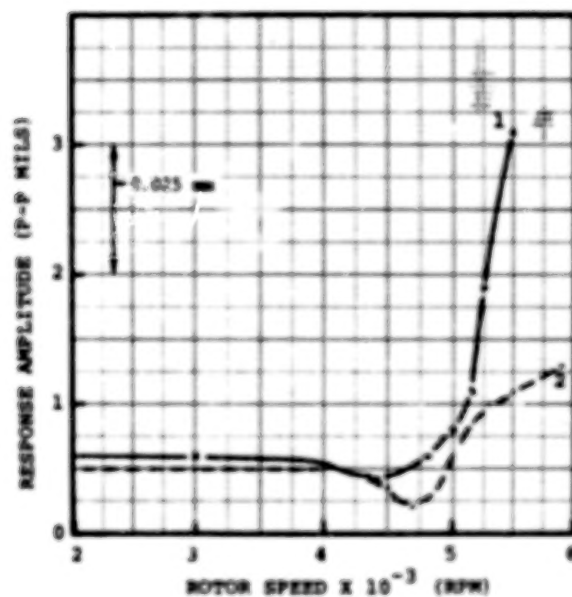
72

Figure 6. - Test stand vibration signature comparison for balanced spacer with and without polyphenylene tooth coating.
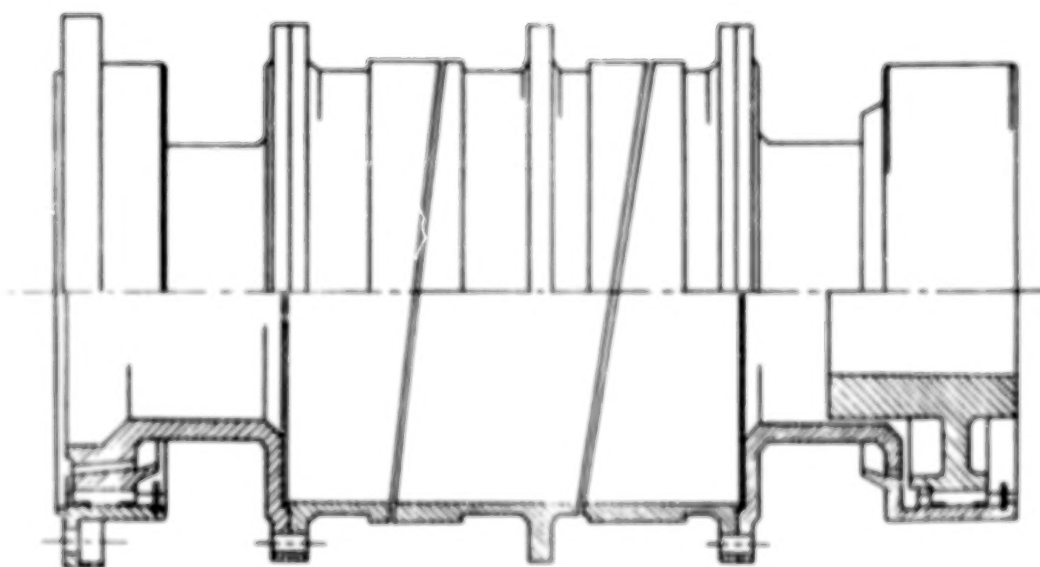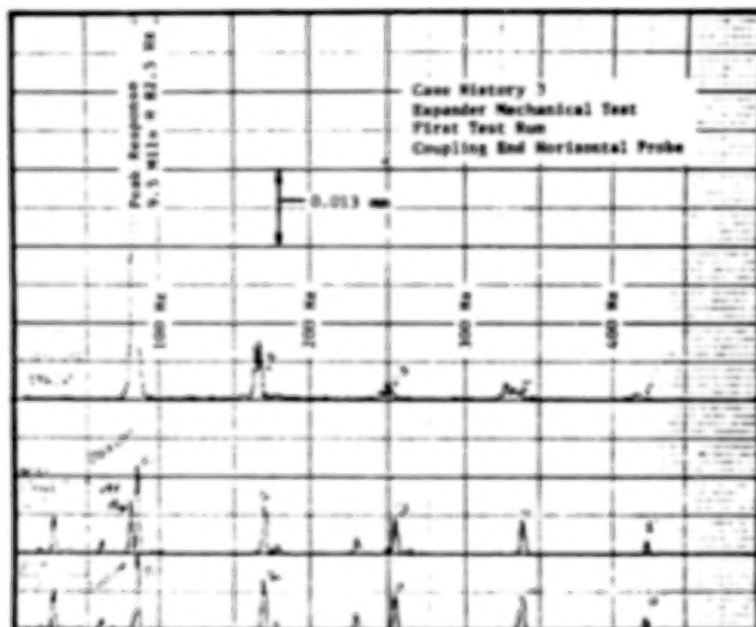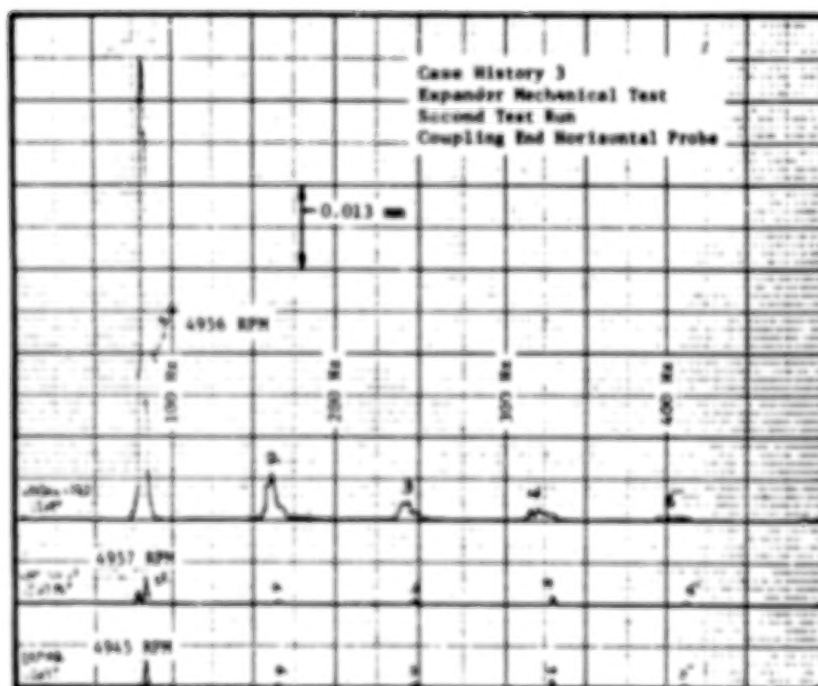

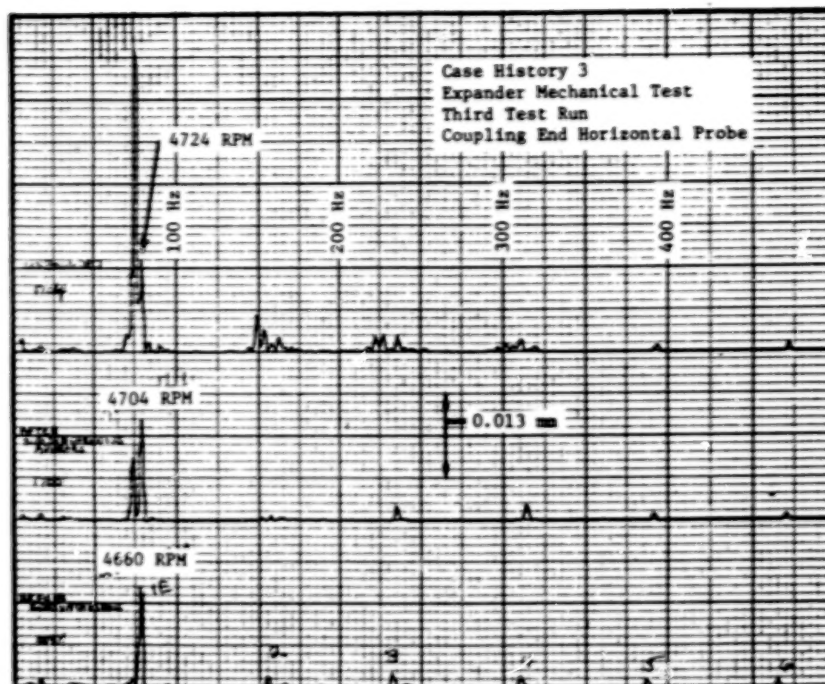Figure 7. - Expander redesigned coupling with increased spacer tube diameters.

73

(a) First acceleration with entrapped oil.

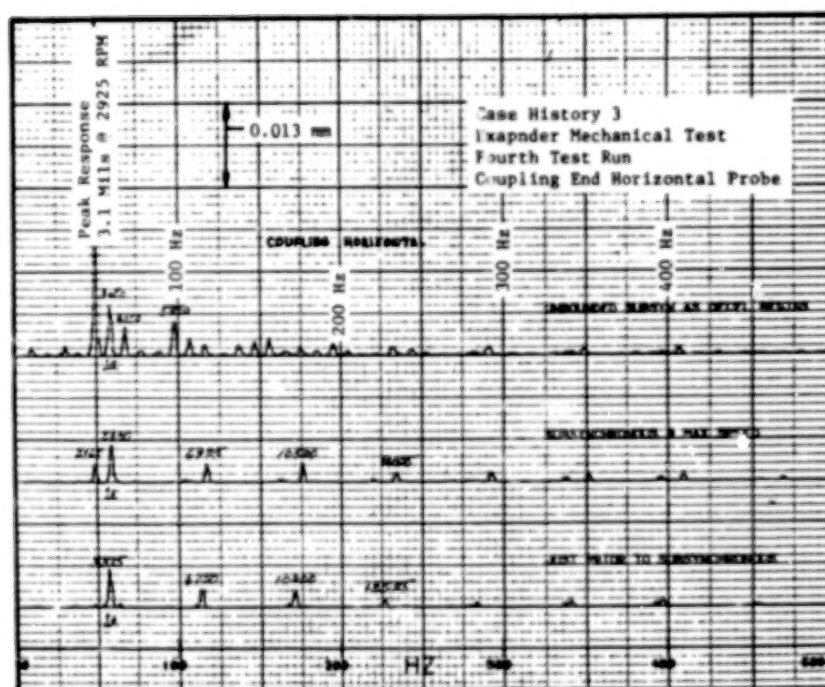(b) Second acceleration with entrapped oil.

Figure 8. - Test stand vibration spectrum signature.

(c) Third acceleration with entrapped oil.

(d) Fourth acceleration with entrapped oil.

Figure 8. - Concluded.

75
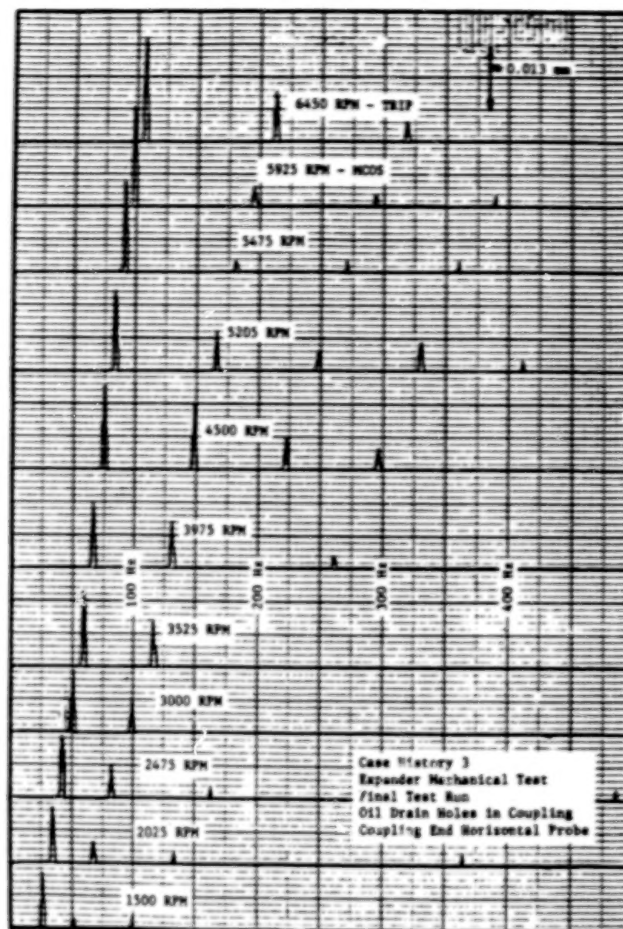
Figure 9. - Test stand vibration spectrum signature after oil drain holes were drilled in spacer.
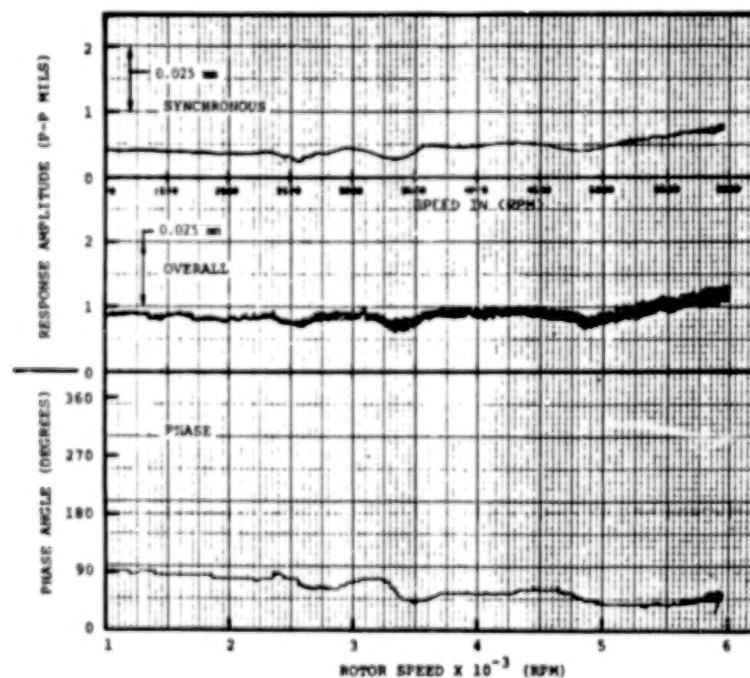
Figure 10. - Test stand vibration signature for retest run with oil drain holes in coupling spacer.
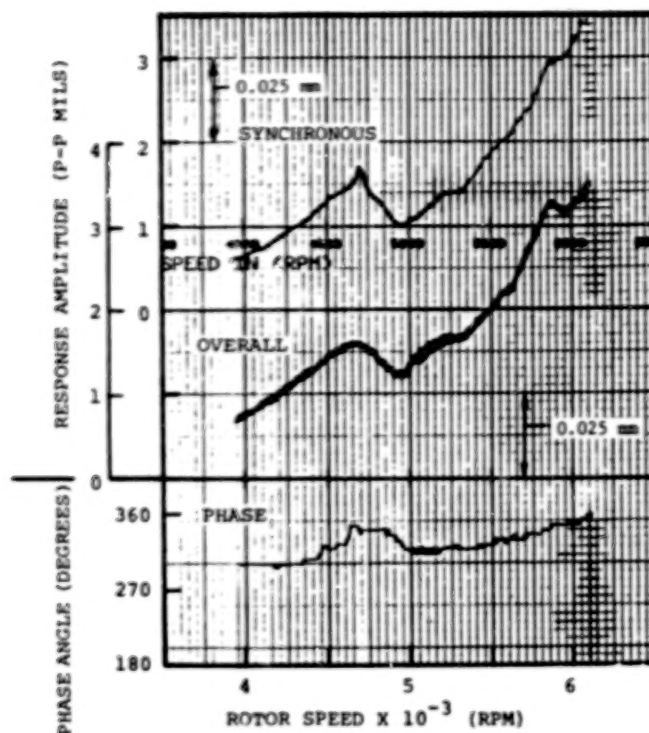
Figure 11. - Test stand vibration signature with coupling assembled using manufacturer's match marks (5-6 mils TIR).
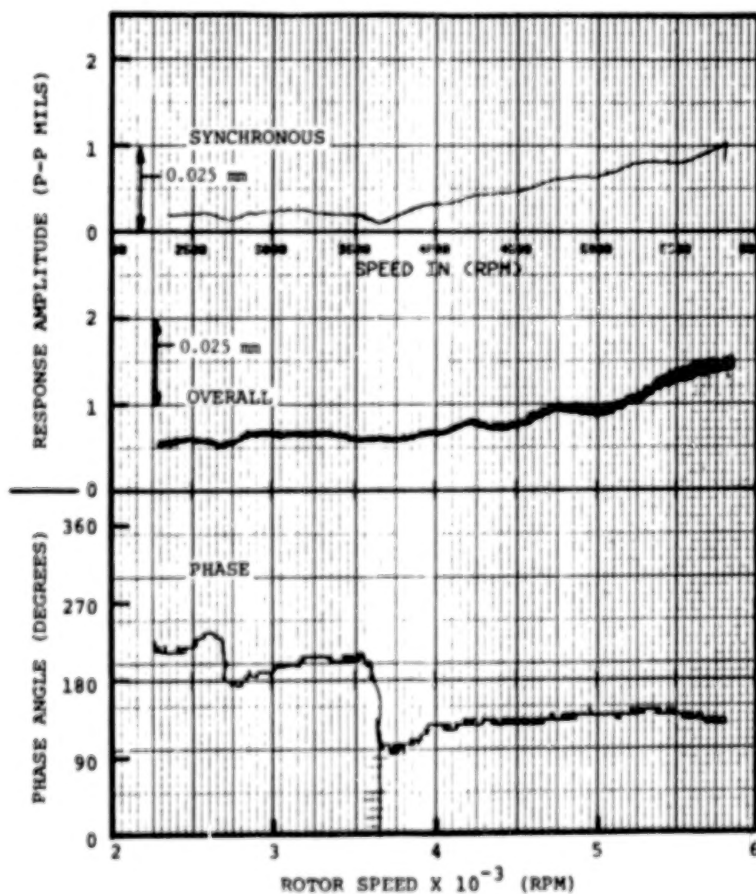
Figure 12. - Test stand vibration signature with coupling assembled to minimize coupling spacer runout imbalance.

77
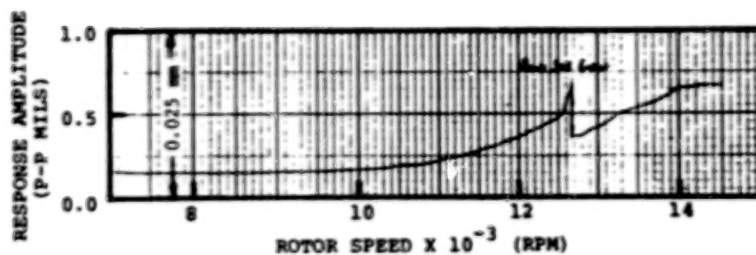
(a) Exemplifying spacer throwout.
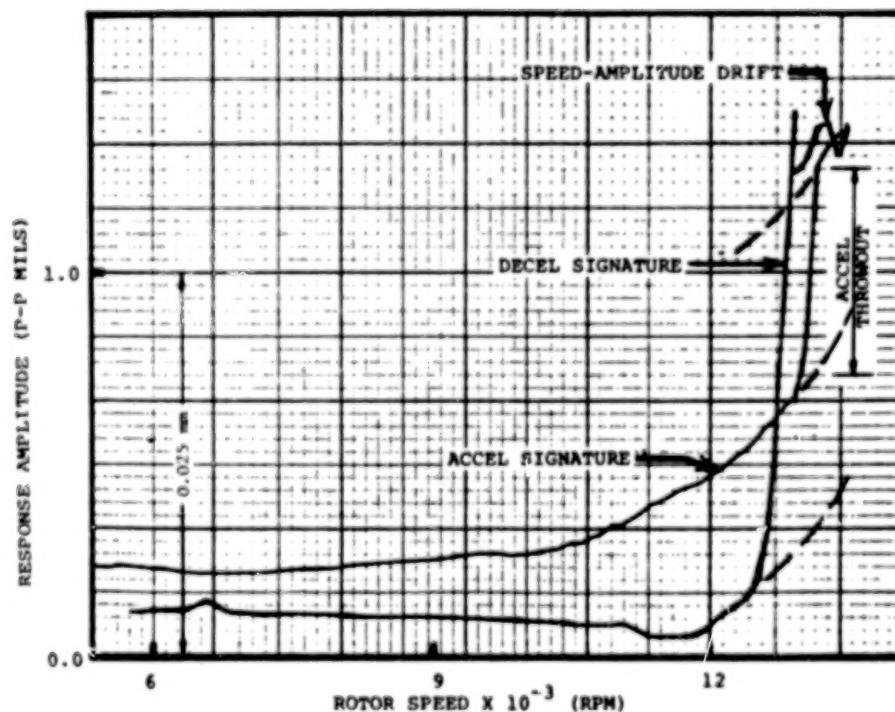
(b) For acceleration and deceleration showing spacer throwout.

Figure 13. - Gas turbine test stand vibration signatures.

78
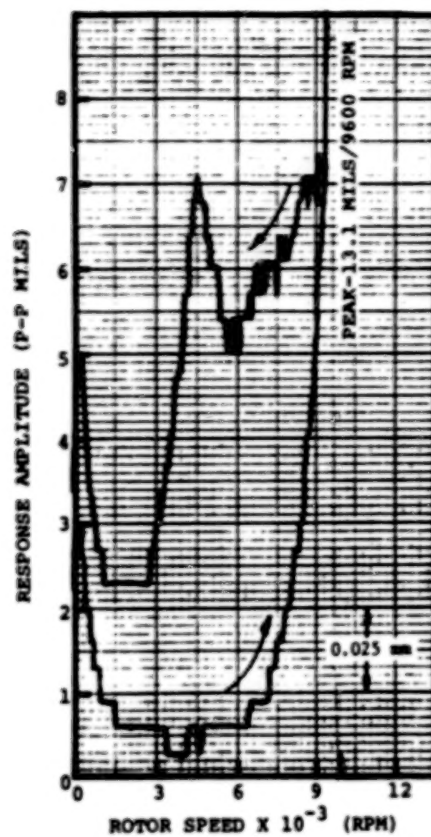
Figure 14. - Gas turbine test stand vibration signature for the condition of a cracked coupling spacer.
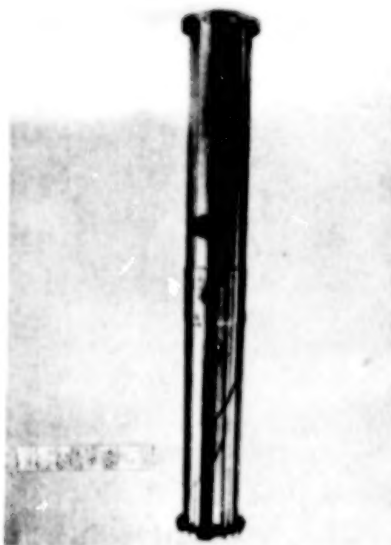
(a)
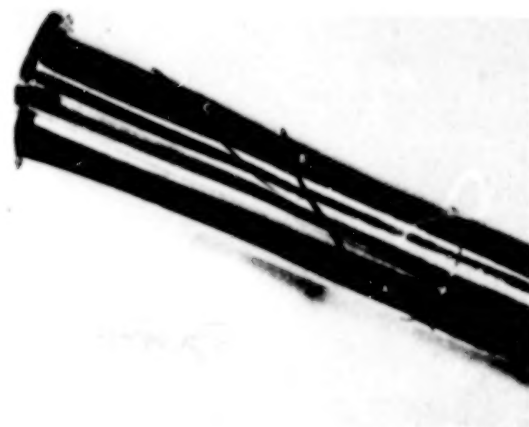
(b)

Figure 15. - Failed coupling spacer.

79
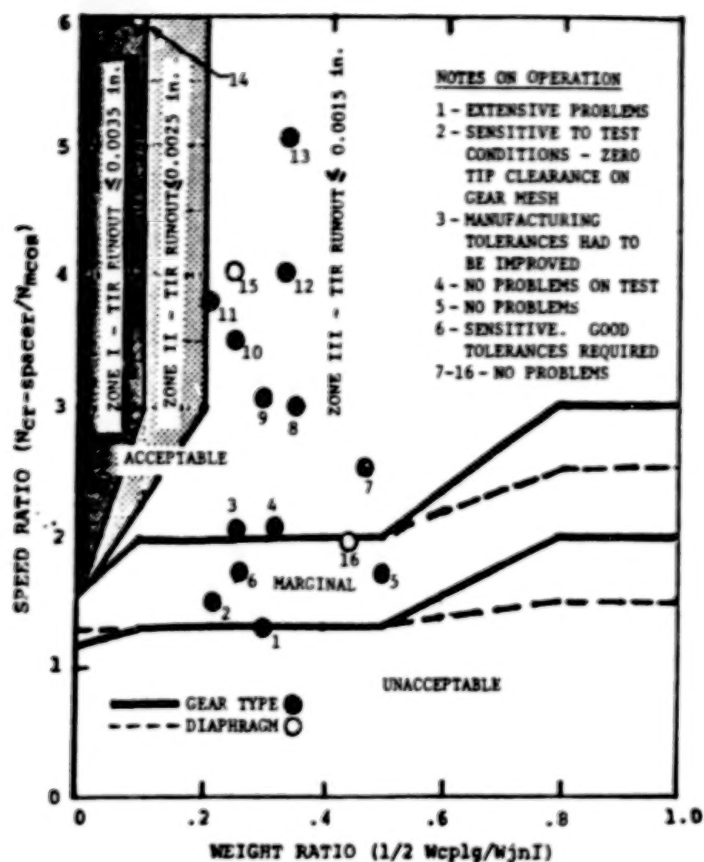
Figure 16. - Chart for coupling selection showing degree of acceptibility with overhung turbomachinery. Experience overplotted. Zones indicate runout level of balance bands relative to the mounting bore or rabbet fit.

SHAFT VIBRATIONS IN TURBOMACHINERY EXCITED BY CRACKS

Burkhard Grabowski
Institut für Mechanik
Universität Hannover
Hannover, Federal Republic of Germany

SUMMARY

During the past years the dynamic behavior of rotors with cracks has been investigated mainly theoretically. This paper deals with the comparison of analytical and experimental results of the dynamics of a rotor with an artificial crack. The experimental results verify the crack model used in the analysis. They show the general possibility to determine a crack by extended vibration control.

INTRODUCTION

Frequently cracks in turbine rotors have been found. Nevertheless, until now it is not really known, how cracks can be recognized early enough so that large ensuing damage can be prevented.

The latest greater damage in Germany occured in the nuclear power plant in Würgassen (ref. 1). For one year the plant had to be put out of operation because two new rotors had to be produced. Both of the LP-rotors had a crack in about the middle of the shaft. A higher level of vibration amplitudes at running speed was noticed and during rundown the resonance amplitudes were very large, but these vibrations were not assumed to be caused by a crack. The crack has been discovered accidentally. This demonstrates the unawareness of the influence of a crack on the vibrational behavior of a shaft. Certainly there is to take into account that cracks in practice are comparatively rare. On the other hand Stodola (ref. 2) in 1922 has already shown on principle the effect of a crack and these investigations were continued by other authors (refs. 3, 4, 5).

As far as known the first measurement results of a rotating shaft with a crack were published by Mayes and Davies (ref. 6) in September 1980 and at last by Inagaki et.al. in September, 1981 (ref. 7). Like in Würgassen an abnormal increase in shaft vibration was noticed in many other cracked rotors. But in some cases the warning signs were too small and some rotors were broken. Some turbine plants even virtually exploded and fragments of the shafts flew away upto a few hundred meters. Henry and Okah-Avae (ref. 8) also present cases in which deep cracks have been found without any influence on vibration amplitudes.

The cause for shaft vibrations due to a crack is the asymmetric cross section at the crack position in connexion with the self-weight of the shaft. Depending on the depth of the crack, on its position and on the damping of the system, the crack can excite small or large vibration amplitudes or the system can even become unstable.

For a location above the horizontal diameter, the crack is subjected to only compression and the entire cross-section is supporting. When further rotated, a part of the crack area opens. A model according to figure 1 was selected to present this gradual change. At the angle of $\varphi = 90^\circ$ the complete opening of the crack is assumed. Thus in the range between $\varphi = 90^\circ$ and $\varphi = 270^\circ$ the simple model for the complete gaping crack is taken for valid. Due to the opening and closing of the crack area we call it a breathing crack in opposite to an always gaping crack, e.g. a cut.

The main axes of the second moments of area at the crack position are not fixed to the body anymore. However, this fact will have no influence on the numerical calculation, since space-fixed coordinates will be used anyway because of the non-conservative sleeve bearings. The second moments of area along the vertical and horizontal axes and the deviation moment are needed.

When the crack opens the change in stiffness along the axis of the rotor does not jump, but the change is continuous in the neighbouring range. Buerhop (ref. 9) examined the effects of such cross-sections in more detail and has come to the conclusion that the 45° approximation (wedge angle $\alpha = 90^\circ$) which has been applied up to now, is sufficient. In order to simplify the mathematical model, the wedge-shaped cut-out in figure 2 is approximately replaced by a square cut with $L = T$.

Figure 1. - Crack model cross-sections showing rotation-angle-dependent stressed regions (shaded areas).
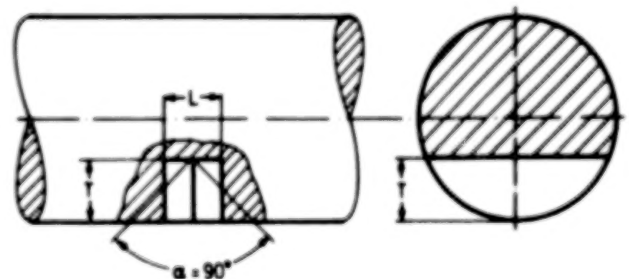
Figure 2. - Simulation of decreased cross-section open crack location.

A clear picture of the stiffness depending on the angle of rotation can be attained when observing the static deflection of the cracked shaft due to its self-weight during one revolution.

Where a constant gaping crack is concerned, the shaft would move on a circular orbit twice per revolution. Where a breathing crack is concerned, the shaft moves only once on an onion-shaped orbit. The calculated curves of deflection in figure 3 are in good agreement with measured results of Ziebarth et. al. (ref. 10). In order to compare the shapes of the two curves the level of the measured and the calculated amplitudes have been equalized.

In addition to the development of the theoretical crack model the stiffness of a cracked shaft has been investigated. In a shaft of 46 mm diameter and 300 mm length (fig. 4) the crack was simulated by a thin milled transverse cut of 0,5 mm width. This shaft was loaded in such a way that near the crack a constant bending moment existed.

Parallel to these measurements the stiffness of the shaft with a gaping crack has been calculated. At the crack position a square cut with L = T was assumed, but only for crack depths up to 50 percent. For deeper cracks L has to be reduced analogically.

In figure 5 the results of measurement and calculation are compared. The total compliance of the shaft depending on the crack depth is plotted. The difference between measurement and calculation amounts to less than 10 percent, except for crack depths of 20 and 70 percent. In consideration of the simple crack model even with these differences the agreement is remarkably good.
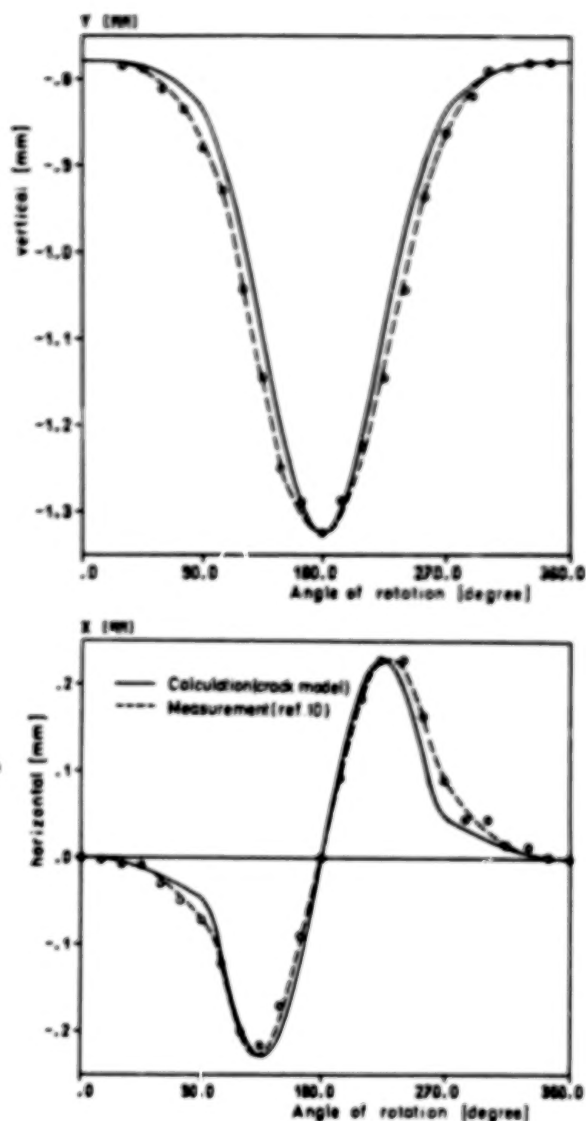
Figure 3. - Example for self-weight deflection for a breathing crack of 50 percent depth.
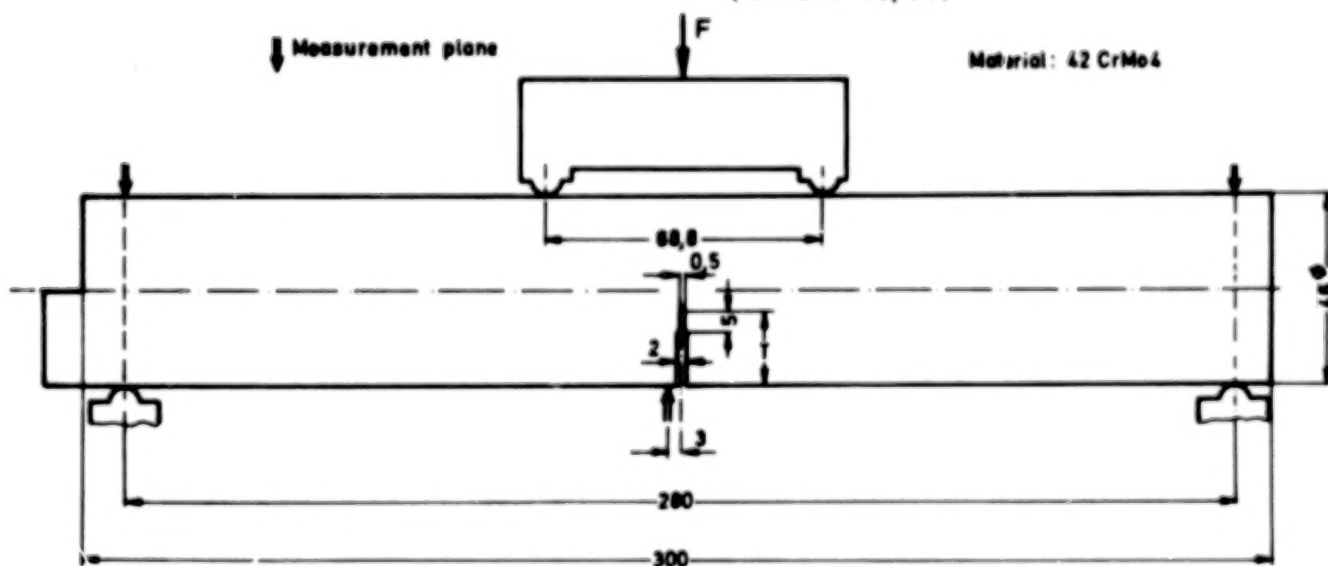
Figure 4. - Shaft with milled cut.

83
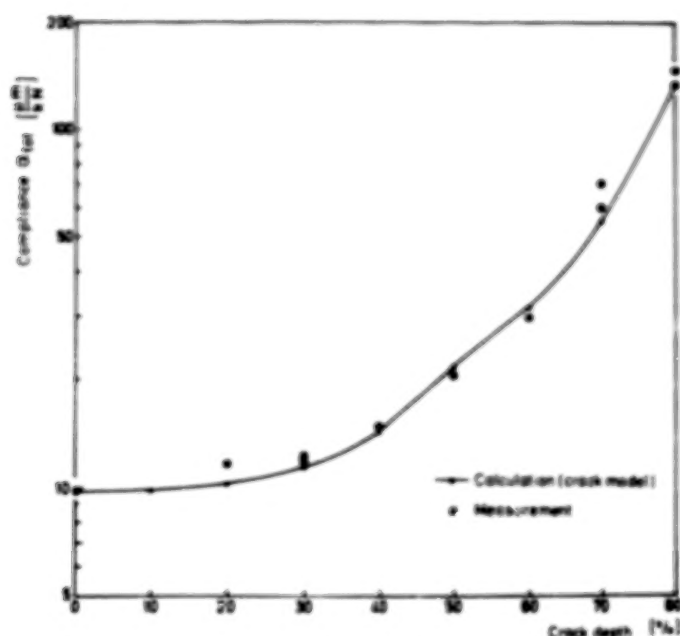
Figure 5. - Compliance α_{tot} of shaft depending on crack depth.

ANALYSIS

The mathematical model for a real rotor with cracked cross-section is a system of differential equations with time dependent coefficients. An exact solution is not possible. The vibrational behavior can, however, be calculated by means of numerical integration. For a large system, this kind of procedure with digital calculation takes a lot of time. Therefore, the behavior of the rotor can be described by its first few eigenfunctions, where the eigenfunctions $Y_o(x)$ and $Z_o(x)$ of the uncoupled conservative system for the vertical and the horizontal planes are a good approximation.

The range of the local change of stiffness due to a crack covers the length L. A mean stiffness between open and closed crack will be taken approximately for the calculation of the eigenfunctions in this region. This is necessary for the consideration of the major curvature at the crack position, compared with the uncracked shaft.

The deflections in the vertical direction $y(x,t)$ and in the horizontal direction $z(x,t)$ will be composed by the first few eigenfunctions weighted with the generalized time dependent coordinates $q(t)$, as follows

$$y(x,t) = \sum_{k=1}^{K} Y_{ok}(x)\ q_{yk}(t) \tag{1}$$

$$z(x,t) = \sum_{\ell=1}^{L} Z_{o\ell}(x)\ q_{z\ell}(t) \tag{2}$$

The transformation, which includes the complete bearing stiffness and damping coefficients, yields a system of $K + L$ coupled equations of motion for the generalized coordinates $q(t)$ which is

84

$$M\ddot{q} + C\dot{q} + K(t)q = F(t) + g \qquad . \qquad (3)$$

M, C and K can be considered as mass matrix, damping matrix and stiffness matrix. On the right-hand side the function F(t) includes the out-of-balance distribution, while g contains the self-weight load.

The time dependent elements in the stiffness matrix K(t) can be separated and we obtain

$$M\ddot{q} + C\dot{p} + [K_m + \Delta K(t)]q = F(t) + g \qquad . \qquad (4)$$

A Runge-Kutta-Fehlberg procedure of 5th order with constant step-size (ref. 11) which proved to be very exact for the necessary computing time, will be used by the numerical integration for the calculation of the instationary vibrational behavior. The necessary initial values will be taken from the stationary solution of equation (4) without the term $\Delta K(t)$. The time variable system has a stationary periodic solution.

After the retransformation according to equations (1) and (2) the deflection of the entire rotor which depends on the angle of rotation is obtained. The first few harmonics for certain positions on the rotor can be determined by means of Fourier analysis.

A detailed presentation of the mathematical method is given in references 11 and 13. Additional theoretical results are in references 13 and 14.

EXPERIMENTAL AND THEORETICAL INVESTIGATIONS

Experimental Rotor and Crack Propagation

To confirm the theoretical results of the vibrational behavior of cracked shafts experimental investigations were carried out. Figure 6 shows the experimental rotor, which is supported by journal bearings in an experimental Helium-compressor housing. At first it was intended to produce the crack by an oscillating load. However, other experiments with this kind of load have shown, that a crack surface due to such a treatment is different from a crack surface which is produced by an alternating load. Therefore, we decided to produce the crack during the rotation of the shaft in the rig itself by application by an external force.

Due to the high bearing load as a result of the external force F (fig. 6) the journal bearing at the crack side of the rotor was replaced by a ball bearing. The load was afforded by a ball bearing, too. To reduce the necessary amount of the external force the diameter of the shaft at the crack position was reduced to a diameter of 45 mm with a cut radius of 5 mm. For crack initiation a 4 mm deep cut was sawn with a thin wire of 70 μm diameter (fig. 7).

For crack propagation an external force of 5000 N and 3000 N, depending on the crack depth, was necessary during about 3 h. The crack propagation was controlled by observing the twice per revolution resonance amplitude near the crack position using a 2-channel Fast-Fourier-Analyser. The rotating speed was equal to correspon-
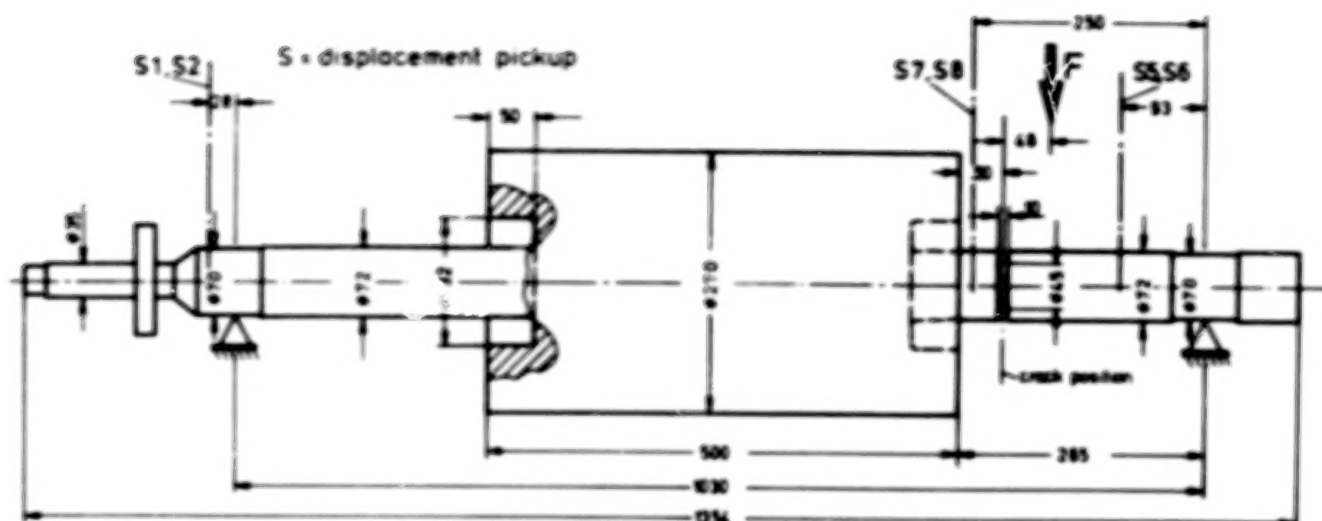
Figure 6. - Experimental rotor.

ding resonance frequency. Unfortunately, two cracks came into existence. Probably on the opposite side of the cut a small groove was the cause for the second crack. Therefore, the comparison of the theoretical and experimental results is uncertain.

For the theoretical calculations we have assumed a linear shape of the crack ground (fig. 7) and a crack depth of 45 % of the diameter. We intend to carry out additional experiments with this rotor, e.g. with different unbalances. Therefore, we did not break the shaft at the crack position.
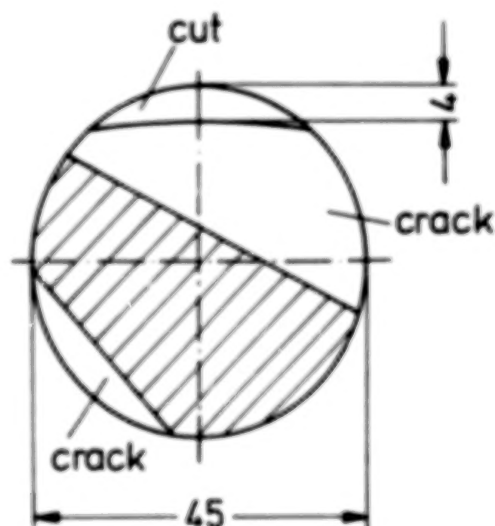
Figure 7. - Cross-section at crack position.

Theoretical Model of the Rotor

The vibrational behavior of the rotor has been caluclated with the FEM and the transfer matrix method. To make use of the crack model with $L = T$, the geometry in the neighbourhood of the crack had to be modified. We have assumed one element of a diameter of 64 mm and a length of 32 mm (fig. 8). This gives the same flexural shape as the real geometry.

The change of stiffness due to the crack is the same as in the case of the original rotor. But difficulties result from the uncertain knowledge of the stiffness and damping coefficients of the journal bearings.

Figure 8. - Rotor model for calculation.
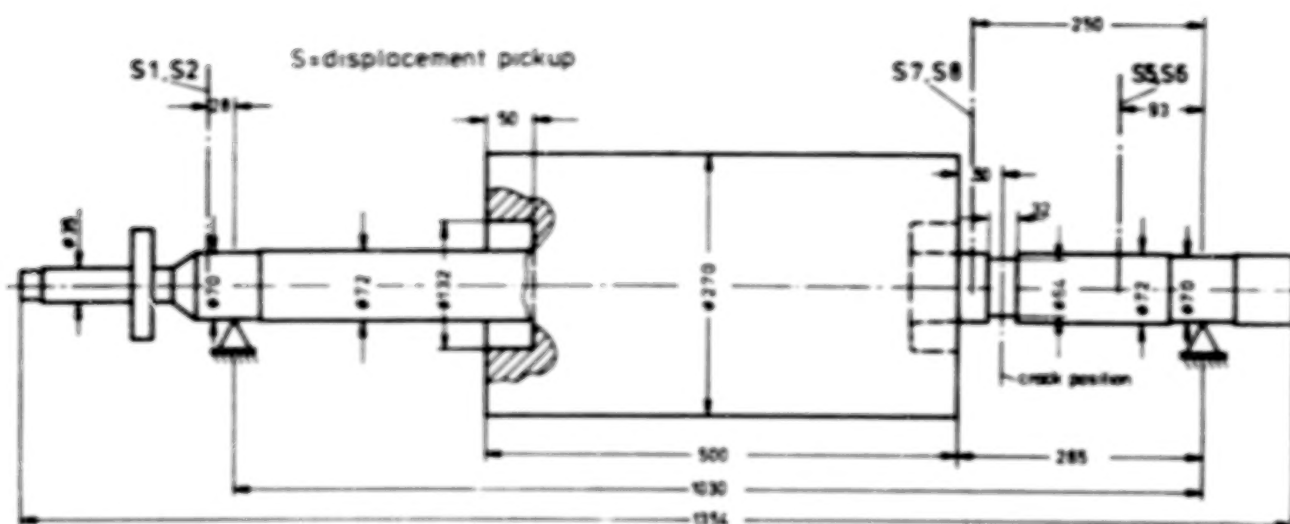
The vibrations excited by a crack depend severely on the curvature of the eigenmodes at the crack position and on the weight influence (see ref. 13). If

$$\int_{o}^{\ell} g \; \mu(x) \; Y_{ok}(x) \; dx \; = \; 0 \qquad , \qquad (5)$$

g - gravity constant,

$\mu(x)$ - shaft weight/unit length,

Y_{ok} - eigenmode,

the crack does not excite any vibration. This is approximately the case for the second eigenmodes in the horizontal and the vertical plane (figs. 9 to 12) and accordingly for the third and fourth complex eigenmode of the complete system (fig. 13), too.

So, already the eigenmodes give an idea about the speed ranges in which crack-excited vibrations can be expected.

THEORETICAL AND EXPERIMENTAL RESULTS

Eigenfrequencies and Eigenmodes

The results of the numerical investigation of the vibrational behavior of the cracked rotor are obtained by using the uncoupled eigenmodes of the conservative system (figs. 10 and 12). The modal transformation includes the complete bearing stiffness and damping coefficients.

Figures 8 and 9 and figures 10 and 11 show, that the difference between the calculated eigenfrequencies of the uncracked and the cracked rotor amounts to approximately 3 %. The measured frequencies in figure 14 (uncracked) and figure 16

87

(cracked) differ approximately 12 %. This indicates that the assumed mean stiffness reduction in the calculation of the eigenfrequencies is too small. In the case of the uncracked rotor the measured and calculated eigenfrequencies are in good agreement. For comparison only the first few eigenmodes of the complete coupled nonconservative rotor (fig. 13) are calculated with FEM.

Rotor with Cut

An interesting experimental result is depicted in the figures 14 and 15. The cut with a depth of approximately 10 % of the diameter has no influence on the once per revolution vibration amplitudes. This corresponds to the theory for a gaping crack. (The small difference may be the result of a change in the distortion due to the storage during some days.) The amplitudes at low speeds seem to be due to the runout. The rotor is neither balanced nor equipped with an additional unbalance. The twice per revolution vibration amplitudes may also contain runout, but less than 1 µm. The resonance amplitude increases up to 16 µm. One or two additional resonance frequencies can be observed at higher speeds. The small amplitudes of these resonance vibrations can be explained by the weight influence (see eq. (5)). The rotor with cut has not been theoretically investigated.

Cracked Rotor

As mentioned, the missing knowledge of the exact bearing stiffness and damping coefficients is a problem when calculating the vibrational behavior of rotating shafts. The theoretical model of this rotor does not include the measured rigid-body eigenmode at 2400 rev/min (figs. 16 and 18). The resonance frequency at 4000 rev/min is not theoretically determinable, too. But for crack detection this effects are of secondary order. The comparison of the measured (figs. 17 and 19) and calculated (figs. 16 and 18) once per revolution vibration amplitudes shows a very good agreement at both mesuring planes S 56 and S 78. We indeed expected a good agreement, but this exact agreement must be an accidental one.

On the other hand, between the measured and calculated twice per revolution resonance amplitudes exist a factor of 2. This is to be explained with the two cracks in the shaft. The stiffness changes two times per revolution and therefore we have a greater excitation of twice per revolution vibrations than the crack model delivers.

In figures 20 and 21 the complete frequency spectrum of the rotor with cut is compared with the spectrum of the cracked rotor. The scales are the same. This representation gives a good survey of the change of the vibrational behavior due to the crack.

At the rotational speed of 7000 rev/min a resonance vibration appeared with a frequency of approximately 3500 rev/min for a very short time. Until now we have no explanation for this effect.
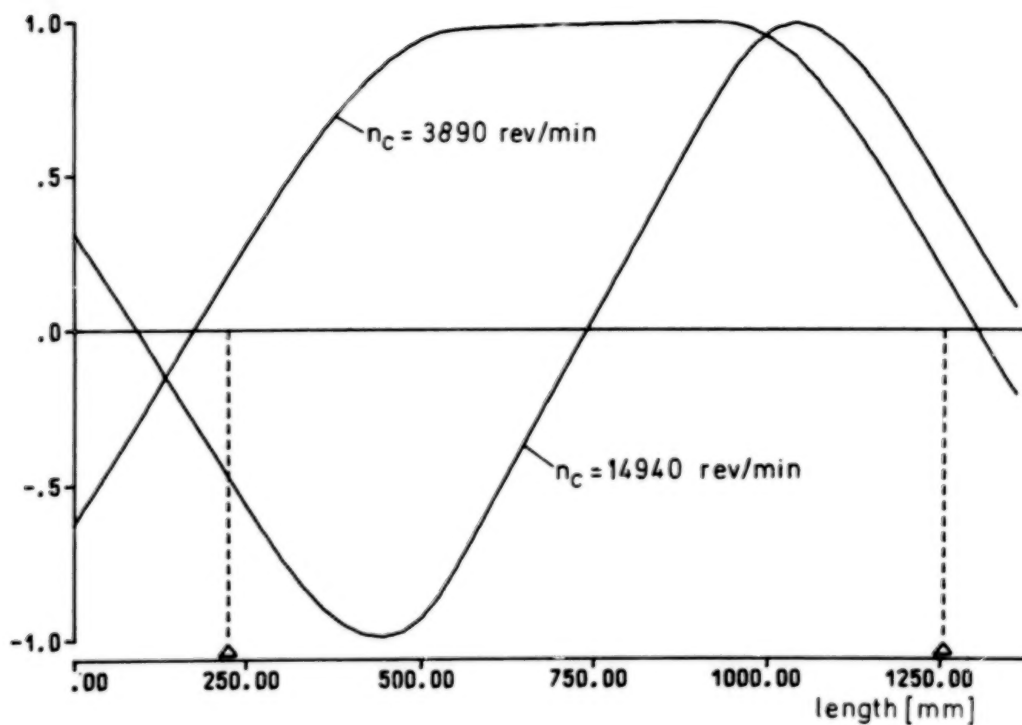
Figure 9. - Horizontal eigenmodes of undamped system (uncracked rotor).
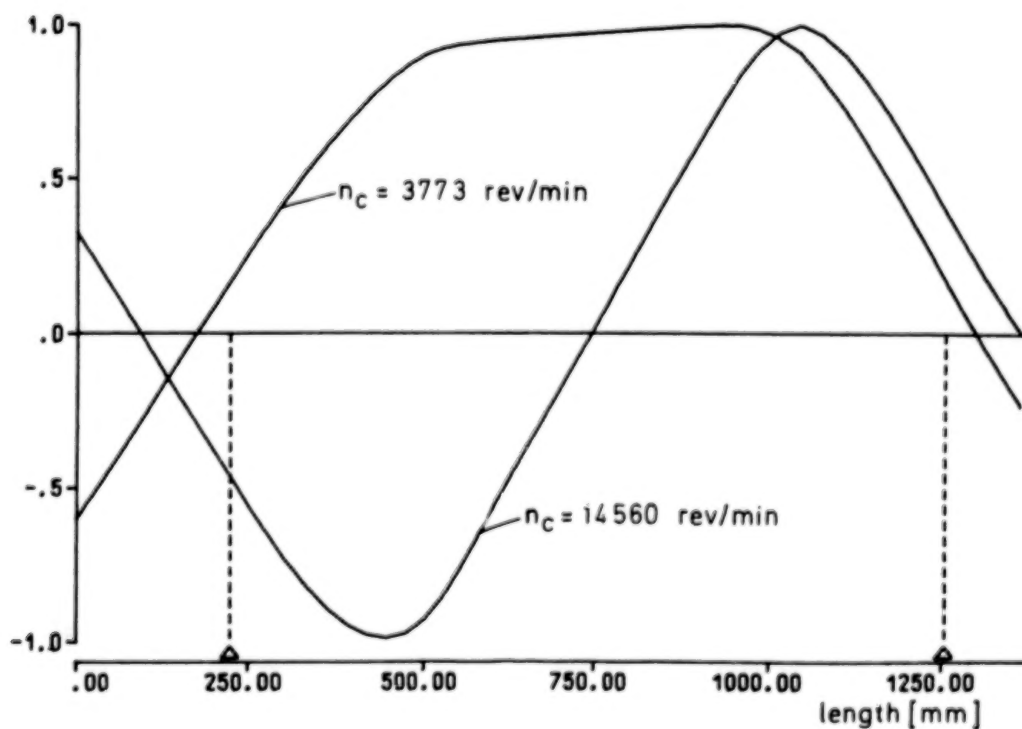
Figure 10. - Horizontal eigenmodes of undamped system (cracked rotor).

89
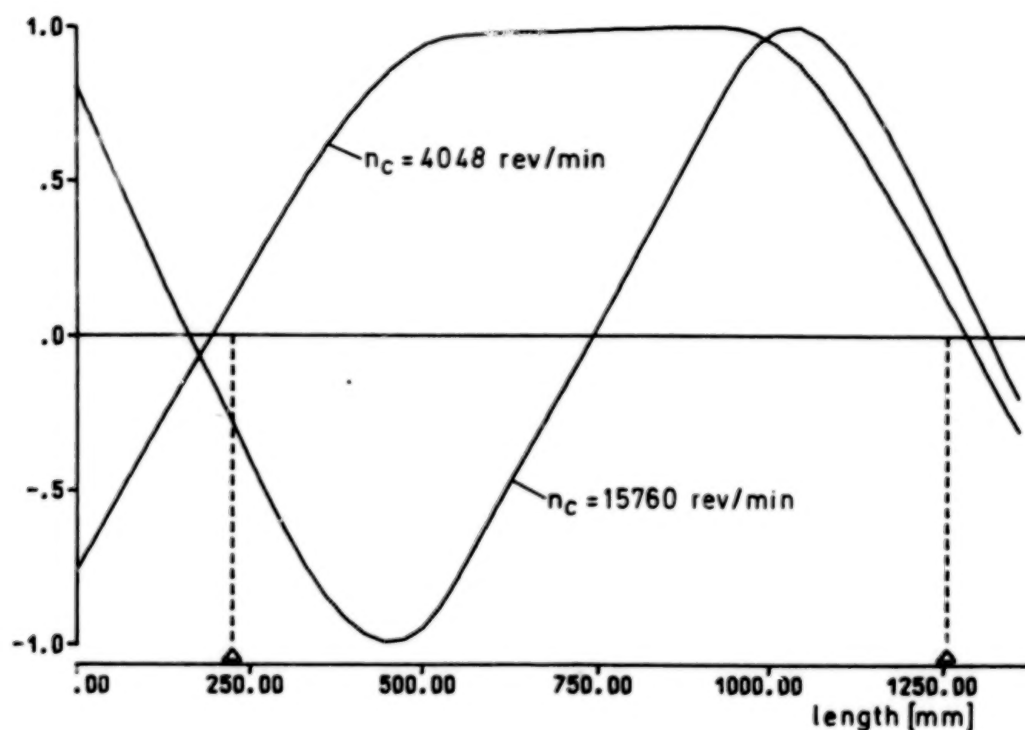
Figure 11. - Vertical eigenmodes of undamped system (uncracked rotor).
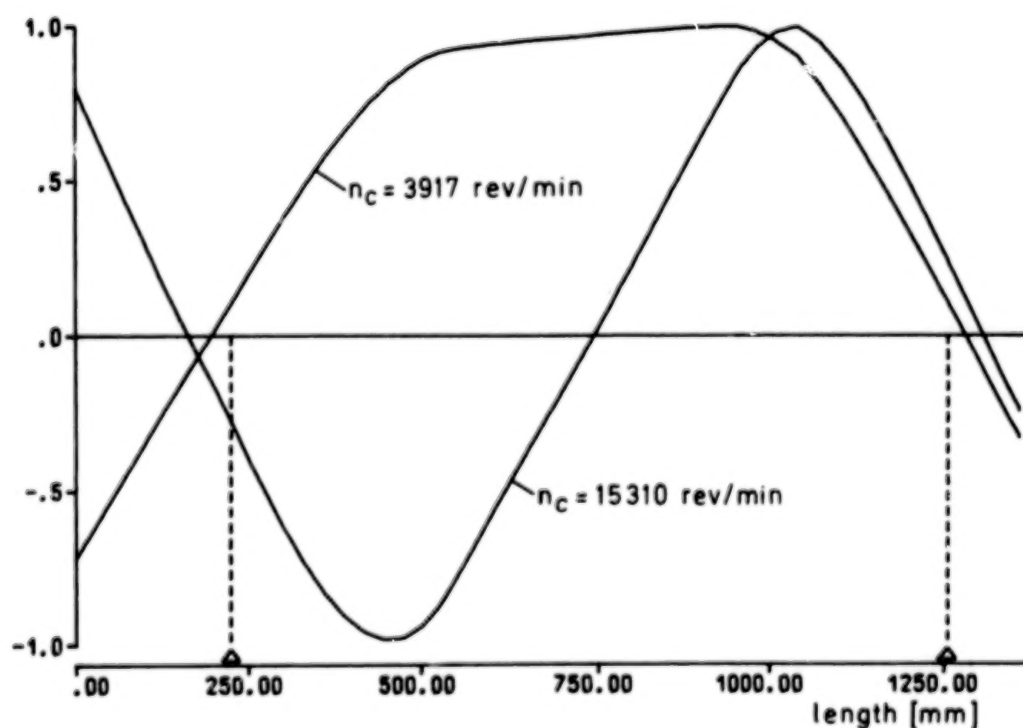
Figure 12. - Vertical eigenmodes of undamped system (cracked rotor).

90
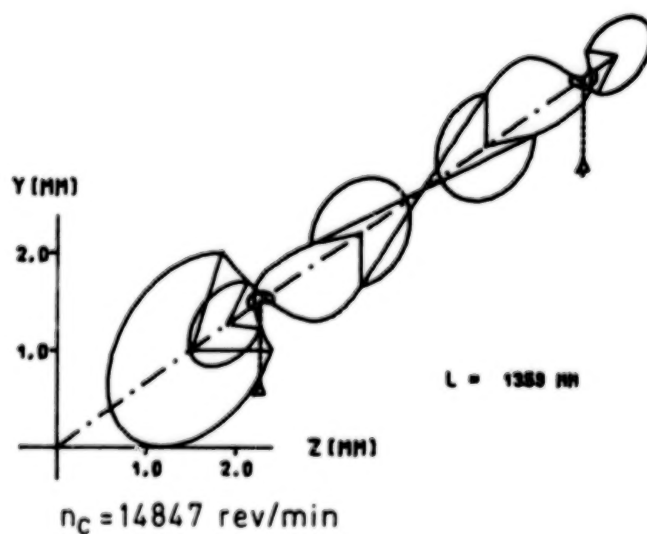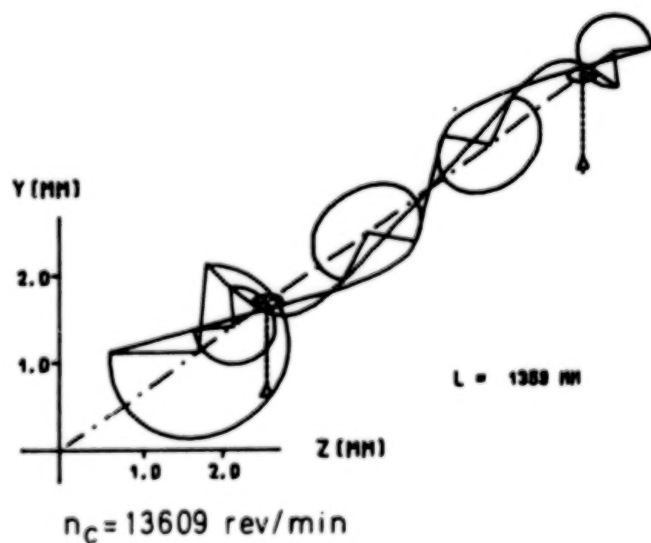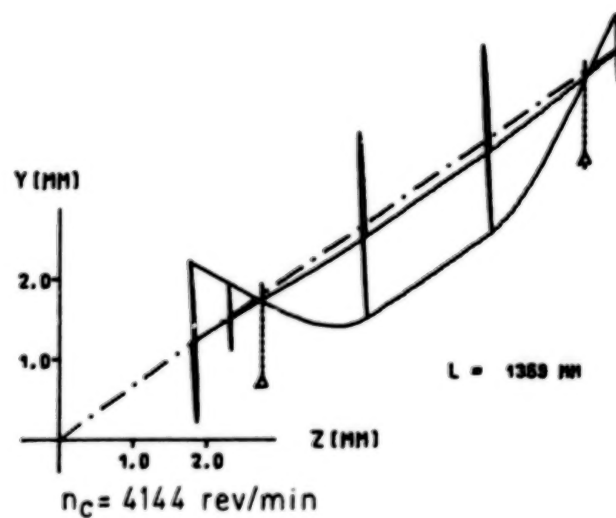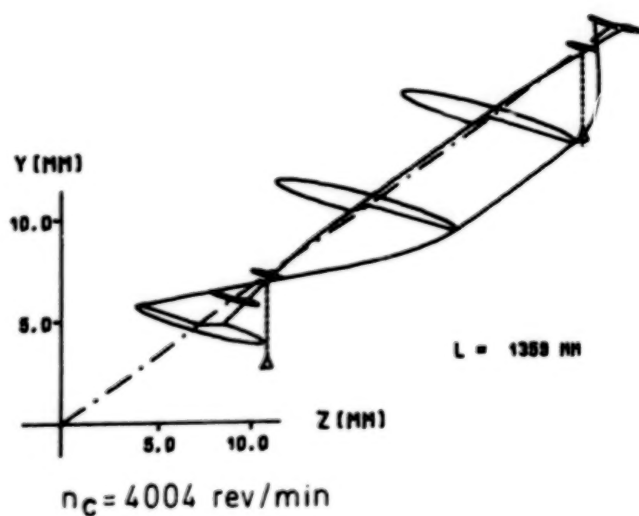
Figure 13. - First four complex eigenmodes of complete damped system
(uncracked rotor).

91
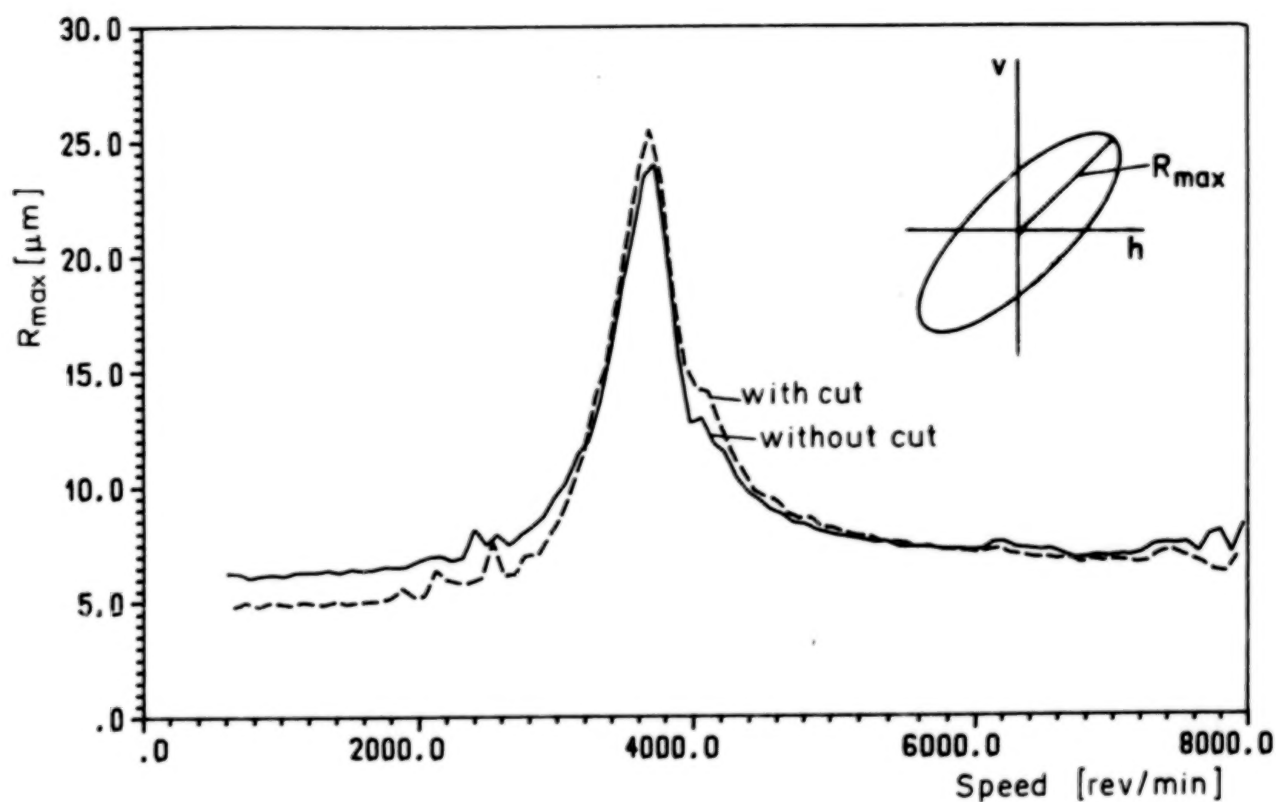
Figure 14. - Once-per-revolution vibration amplitudes of rotor without and with cut measured at position S78.
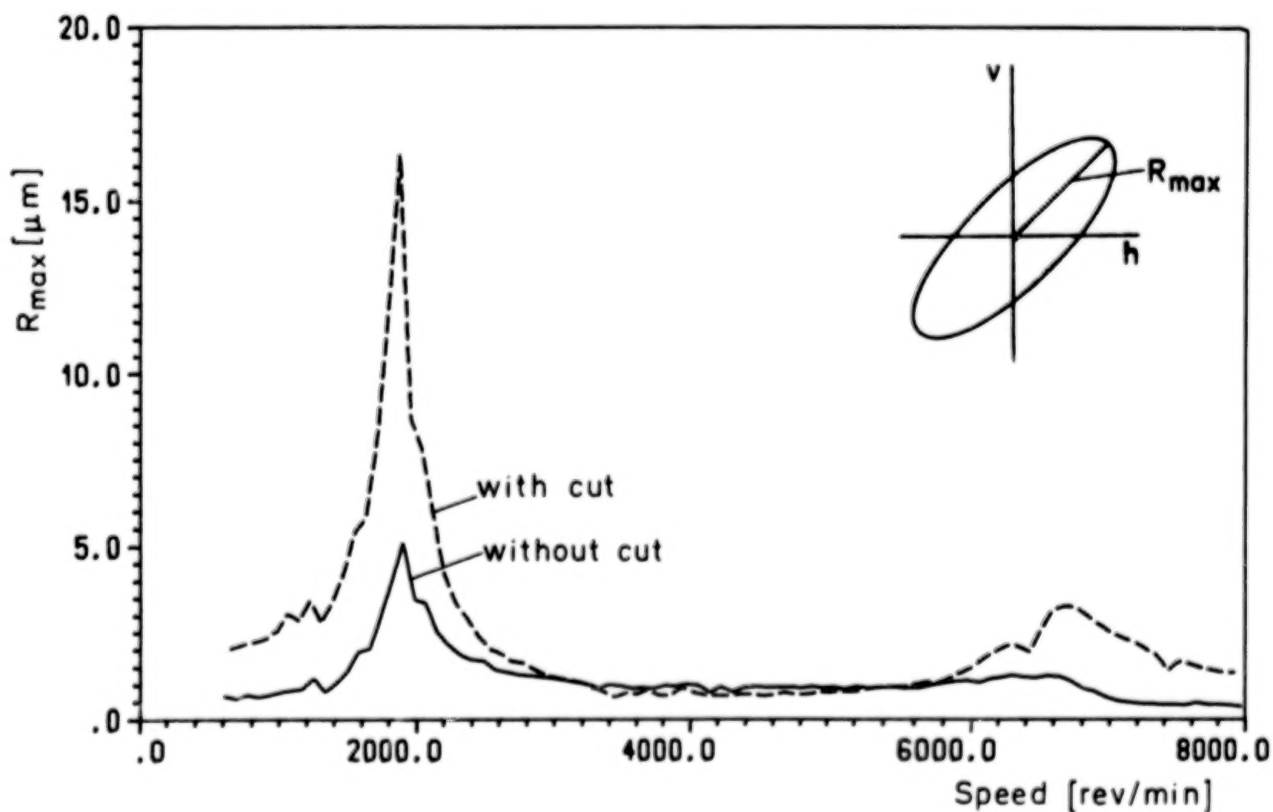
Figure 15. - Twice-per-revolution vibration amplitudes of rotor without and with cut measured at position S78.

92
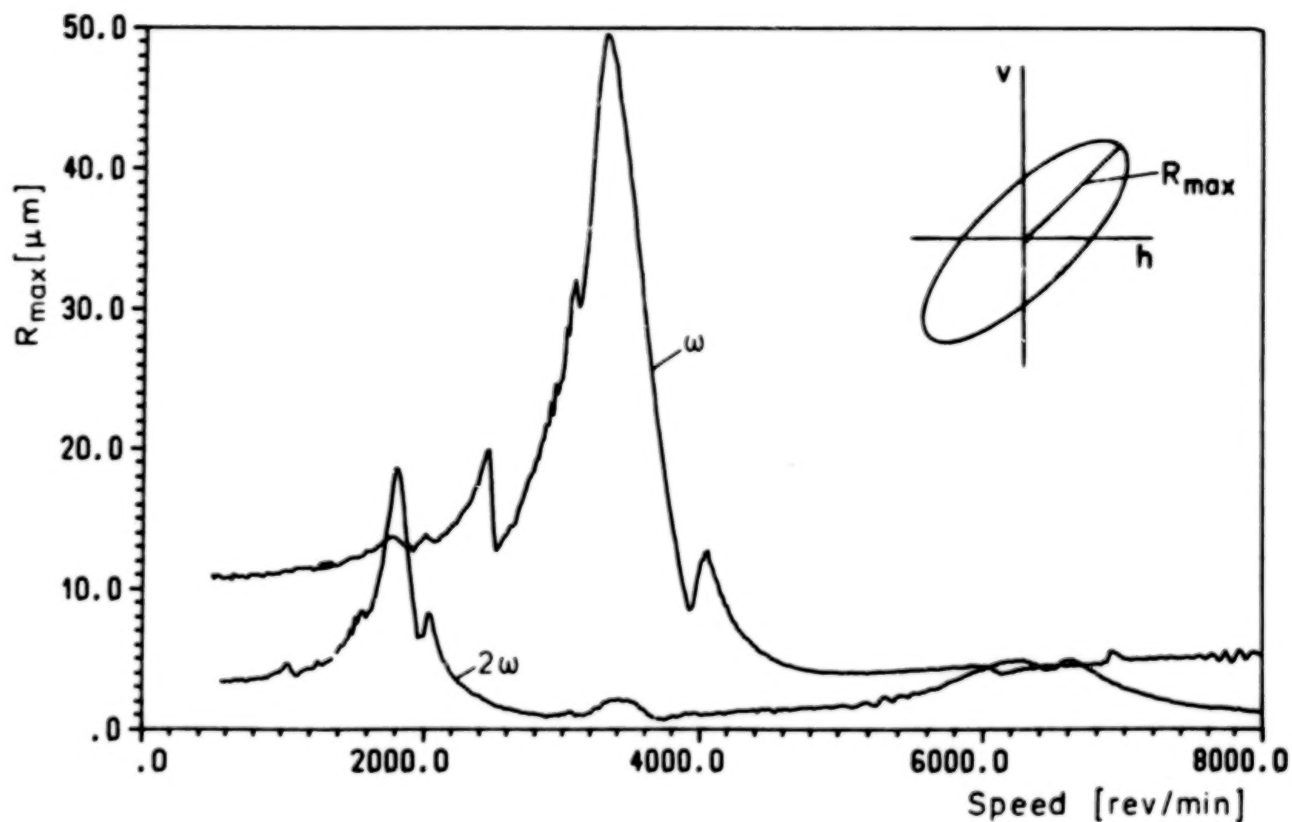
Figure 16. - Measured vibration amplitudes of cracked rotor at position S56.
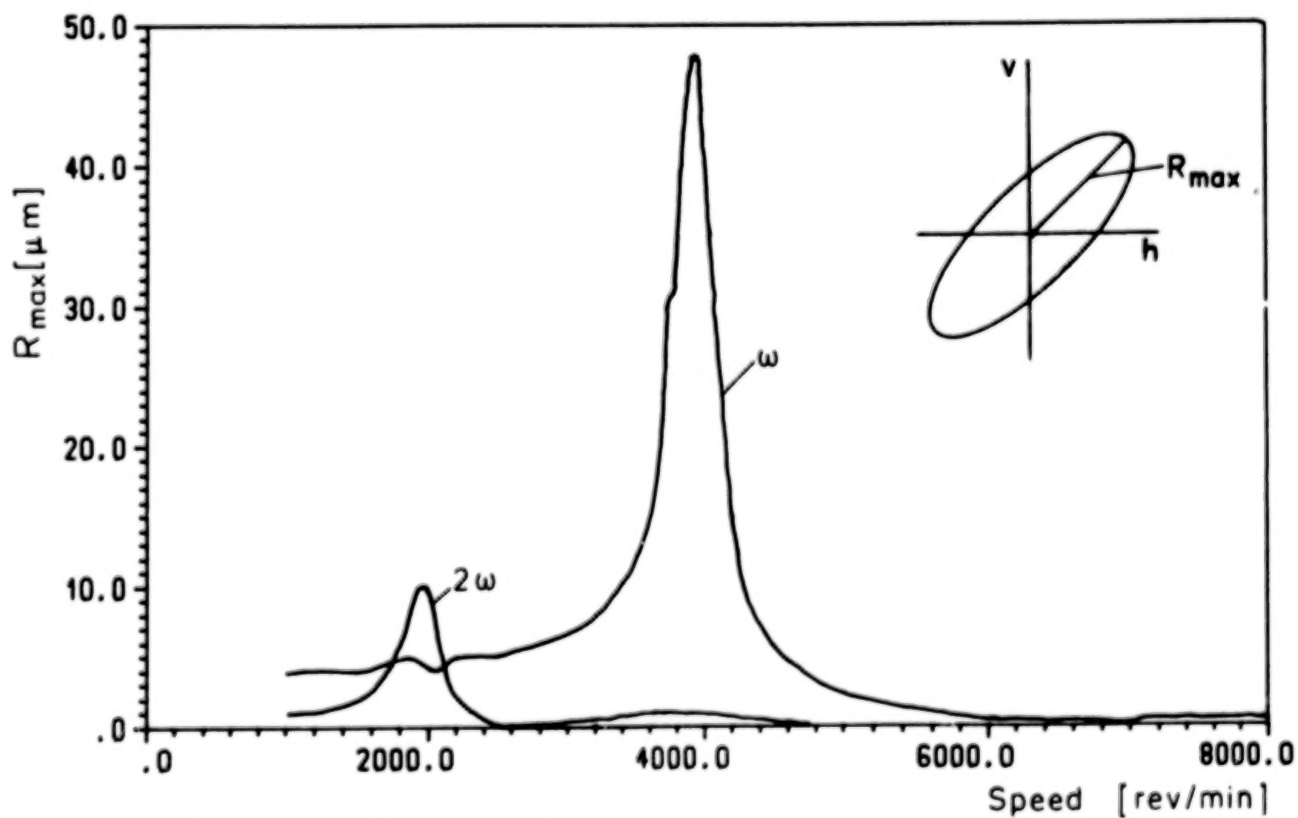
Figure 17. - Calculated vibration amplitudes of cracked rotor at position S56. (crack depth 45 % of diameter).

93

BEST DOCUMENT AVAILABLE
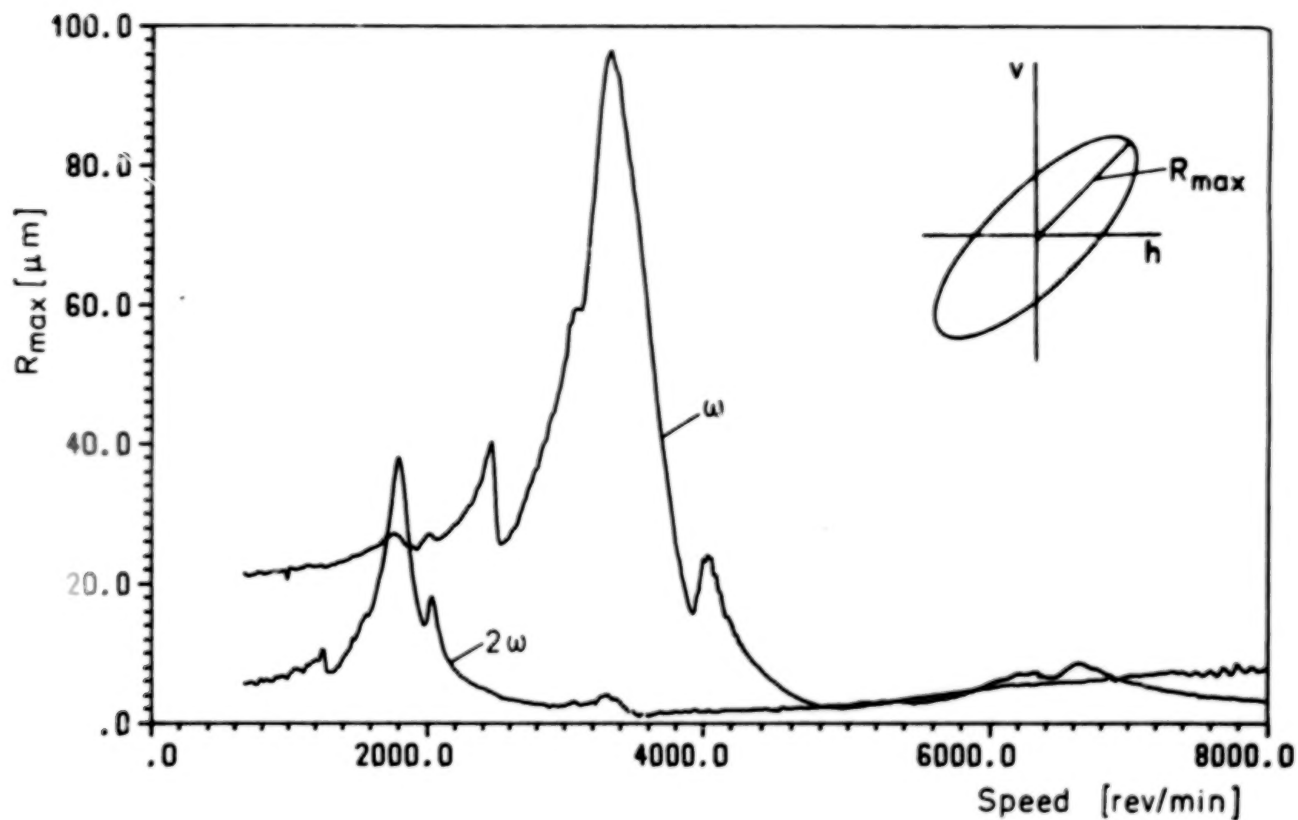
Figure 18. - Measured vibration amplitudes of cracked rotor at position S78.
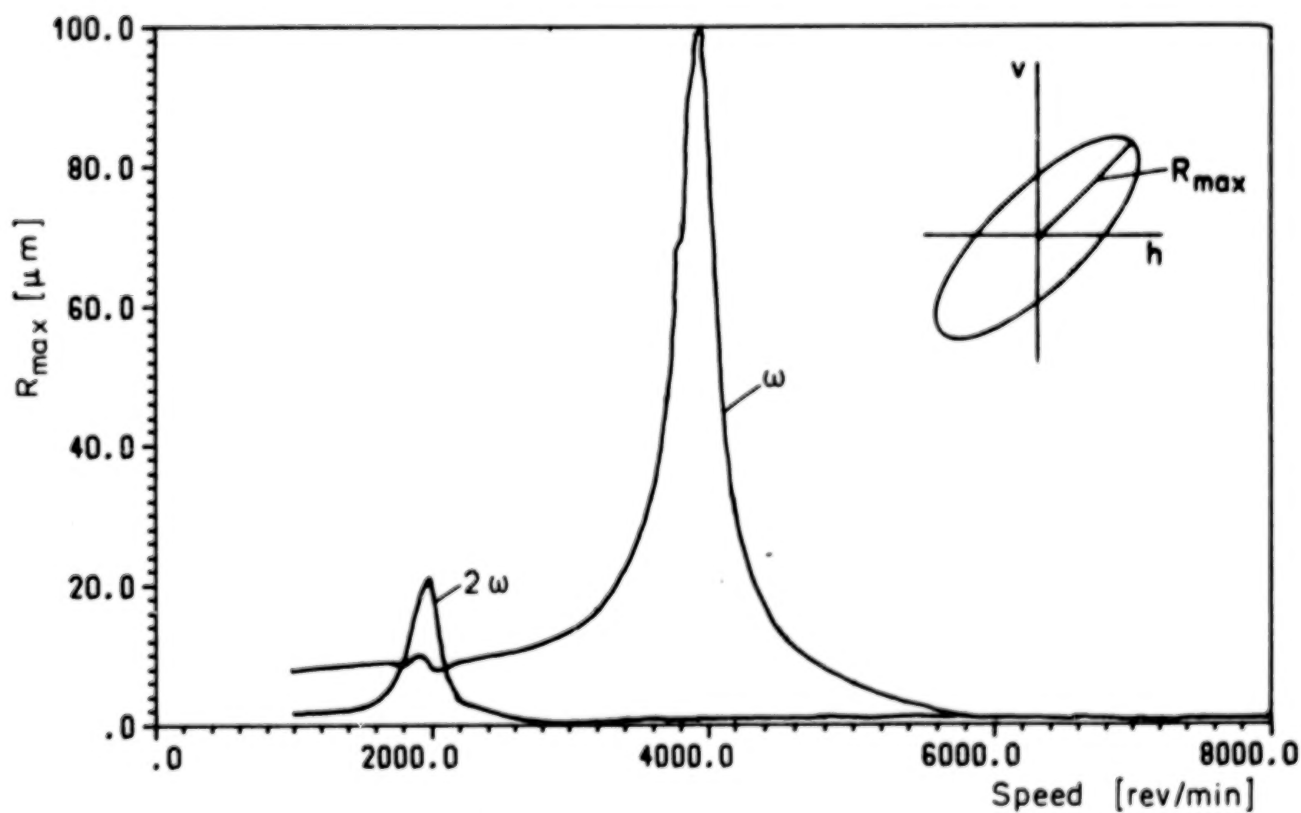
Figure 19. - Calculated vibration amplitudes of cracked rotor at position S78 (crack depth 45 % of diameter).

94
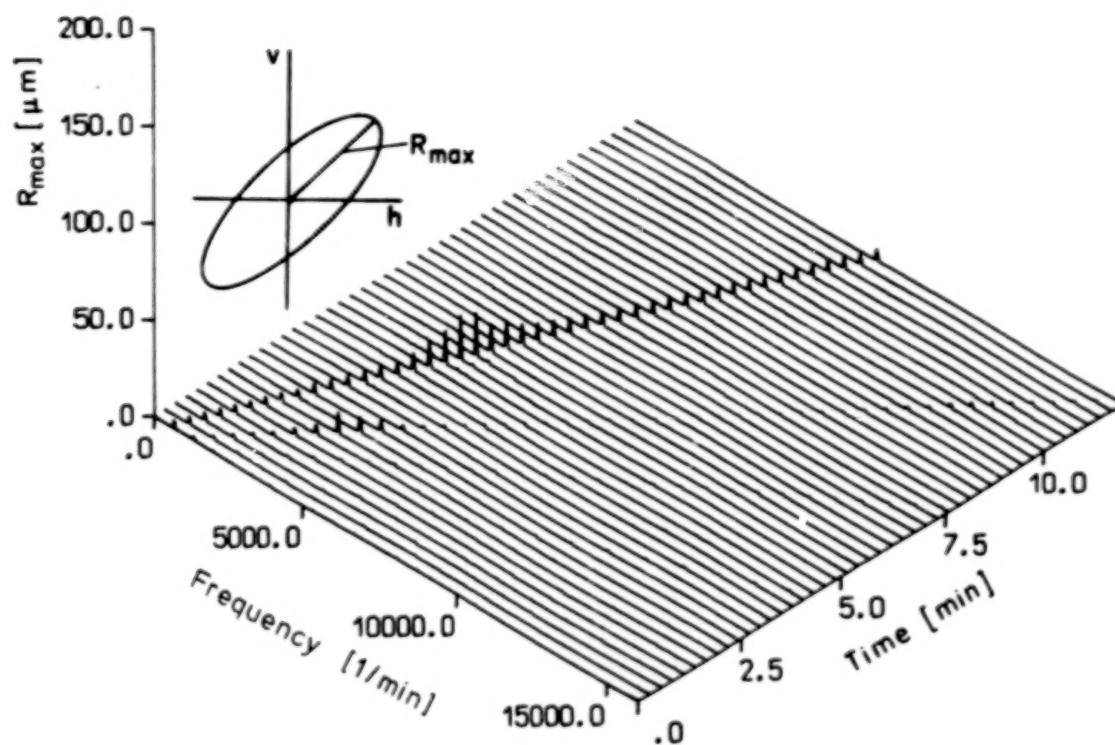
Figure 20. - Frequency spectrum of rotor with cut.
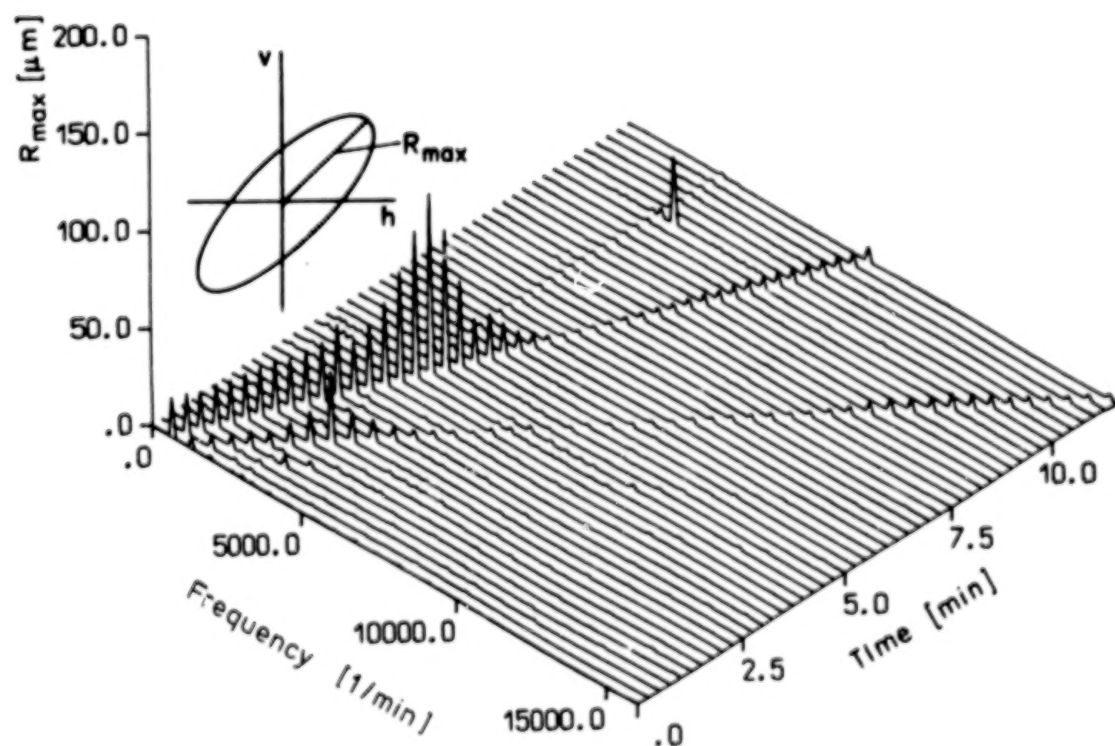
Figure 21. - Frequency spectrum of cracked rotor.

CONCLUSION

The comparison of calculation and measurement shows in principle that it is possible to predetermine the vibration amplitudes excited by a crack. But at the same time this investigation shows the problems in modelling the system. The developed crack model seems to be useful.

For crack supervision the phase should be taken into account, too, because the amplitude of the sum of the original vibration and the vibration due to crack can become smaller with crack propagation.

In the future the influence of unbalance is to be investigated. Our calculations have shown, that this influence frequently is small for greater turbine rotors because the statical deflection is greater than the vibration amplitudes. But in rotors constructed like this experimental rotor an influence can be expected. Here the vibration amplitudes at crack position have the same magnitude like the statical deflection.

REFERENCES

1. Haas, H.: Großschäden durch Turbinen- oder Generatorläufer, entstanden im Bereich bis zur Schleuderdrehzahl. Der Maschinenschaden, 50. Jahrgang, Heft 6, 1977, pp. 195-204.

2. Stodola, A.: Dampf- und Gasturbinen. Springer, Berlin, 5. Auflage, 1922, pp. 931.

3. Kellenberger, W.: Biegeschwingungen einer unrunden, rotierenden Welle in horizontaler Lage. Ingernieur-Archiv, XXVI, 1958, pp. 302-318.

4. Tondl, A.: The Effect of Unequal Moments of Intertia of the Shaft Section on the Motion and Stability of a Rotor. Some Problems of Rotor Dynamics, 1st ed., Chapman & Hall, London.

5. Bishop, R.E.D. and Parkinson, A.G.: Second Order Vibration of Flexible Shafts. Phil. Trans. of Royal Society of London, vol. 259, no. 1095, 1965.

6. Mayes, I.W. and Davies, W.G.R.: A Method of Calculating the Vibrational Behaviour of Coupled Rotating Shafts Containing a Transverse Crack. Second Int. Conference Vibrations in Rotating Machinery, University of Cambridge, 2-4 Sept., 1980.

7. Inagaki, T.; Kanki, H.; and Shiraki, K.: Transverse Vibrations of a General Cracked-Rotor Bearing System. ASME Paper No. 81-Det-45, Sept. 1981.

8. Henry, T.A. and Okah-Avae, B.E.: Vibrations in Cracked Shafts. Conf. on Vibrations in Rotating Machinery, University of Cambridge, Sept. 1976, pp. 15-19.

9. Buerhop, H.: Zur Berechnung der Biegesteifigkeit abgesetzter Stäbe und Wellen unter Anwendung von finiten Elementen. VDI-Fortschrittsberichts, Reihe 1, Nr. 36, 1975.

10. Ziebarth, H.; Schwertfeder, H. und Mühle, E.-E.: Auswirkung von Querrissen auf das Schwingungsverhalten von Rotoren. VDI-Berichte 320, 1978, pp. 37-43.

11. Fehlberg, E.: Neue genaue Runge-Kutta-Formeln für Differentialgleichungen zweiter Ordnung bzw. n-ter Ordnung. ZAMM 40, 1960, pp. 449-455.

12. Grabowski, B.: Zur modalen Simulation des instationären Schwingungsverhaltens von Turboläufern. VDI-Fortschrittberichte, Reihe 11, Nr. 25, 1976.

13. Grabowski, B.: The Vibrational Behavior of a Turbine Rotor Containing a Transverse Crack. Trans. ASME, J. Mech. Design., vol. 102, Jan. 1980, pp. 140-146.

14. Grabowski, B.: Das Schwingungsverhalten eines angerissenen Turbinenläufers. VDI-Bericht Nr. 320, 1978, pp. 31-36.

DETERMINATION OF BALL BEARING DYNAMIC STIFFNESS*

R. F. Beatty and B. F. Rowan
Rocketdyne Division
Rockwell International
Canoga Park, California 91304

ABSTRACT

The dynamic radial stiffness characteristics of rolling element bearings are currently determined by analytical methods that have not been experimentally verified. These bearing data are vital to rotating machinery design integrity because accurate critical speeds and rotor stability predictions are highly dependent on the bearing stiffness. A tester was designed capable of controlling the bearing axial preload, speed, and rotor unbalance. The rotor and support structures were constructed to permit critical speeds that are predominantly determined by a 57 mm test bearing. A curve of calculated critical speed versus stiffness was used to determine the actual bearing stiffness from the empirical data. The results of extensive testing are used to verify analytical predictions, increase confidence in existing bearing computer programs, and to serve as a data base for efforts to correct these programs.

INTRODUCTION

The radial stiffness of a ball bearing is one of the key elements in the rotordynamic analysis of rotating machinery and is strongly dependent on axial preload, the constraints of the outer race and shaft speed. Attempts to determine bearing stiffness in the past by measuring applied loads and deflections have been complicated by the large required loads and very small deflections. Also, shaft rotation is difficult to include in such conventional tests. The method used in this experiment avoids these problems by utilizing a tester designed such that the lowest rotor critical speed is primarily a function of the test bearing stiffness. The overall purpose of this test program was to advance the technology of measuring ball bearing dynamic stiffness in support of theoretical rotordynamic analysis and rotating machinery design.

DESCRIPTION OF TESTER

The tester (Fig. 1) consists of a simple rigid rotor with control over the variables that affect the bearing stiffness. The significant features of the test rotor are as follows:

1. Axial preload can be accurately controlled by a hydraulic piston. This preload can be easily varied without disassembly of the tester.

2. Setscrew holes are provided in the large rotor disk for *in situ* balance corrections and access is provided in the supporting structure for easy corrections.

3. The rotor mass can be changed by substituting a heavy or lightweight spacer disk to shift the critical speed so that the stiffness can be found at various speeds. The rotor weight differential is 9.3 kg (20.5 pounds) between configurations.

4. The mass distribution of the tester rotor is proportioned so that the critical speed is effectively independent of the slave bearing stiffness.

5. Locations are provided for two pairs of orthogonal displacement transducers to monitor rotor motion.

6. The test rotor is driven by a variable speed motor.

7. Different test bearing sizes can be accommodated by substituting bearing sleeves. The selection of a 57 mm test bearing was influenced by the radial stiffness effect of this bearing on the rotordynamic characteristics of the Space Shuttle Main Engine (SSME) High-Pressure Oxidizer Turbopump (HPOTP). Details of this turbine end bearing on the dynamic performance of this machine are documented in the literature by Rowan (ref. 1).

Figure 2 shows a schematic arrangement of the test setup, and Fig. 3 is a photograph of the actual installation. The rotor and supporting structures were designed so that their dynamic properties could be accurately predicted by analysis. Pertinent design data of the tester is presented in Table I.

ANALYTICAL APPROACH

A finite element model of the rotating assembly was generated, and a parametric computer analysis was performed to calculate the rotor critical speeds as a function of the test bearing stiffness to ground. The resulting critical speed plot is shown in Fig. 4, and the close spacing of curves A, B, and C indicate that the critical speed is nearly independent of the slave bearing stiffness. The critical speed can be easily detected by test, and by referring to Fig. 4, the test bearing stiffness can be determined. The slope of the curve in Fig. 4 indicates that the critical speed is highly dependent on the test bearing stiffness and should ensure accurate results. The lowest rotor critical speed mode shape is shown in Fig. 5.

By changing the mass of the rotor, the critical speed can be shifted so that a curve of test bearing stiffness versus speed can be plotted. Additional tests can be run with different axial preloads and/or unbalance to investigate these parameters.

TESTING

The general testing procedure consisted of determining the rotor residual unbalance, setting the hydraulic cylinder to maintain a given axial preload, and running a slow speed ramp through the critical speed while monitoring the rotor motion. The radial motion was monitored by two pairs of orthogonal displacement transducers that produced orbit plots on oscilloscopes. Photographic documentation of the orbits were taken every 1000 rpm starting at 15,000 rpm while speed was controlled manually to produce a series of step dwells to define the critical speed.

The rotor was installed with the heavyweight spacer, and the initial run indicated that no balance correction was needed because the residual was sufficient to produce a resonance, without excessively loading the bearings. All tests conducted are listed in Table II and the bearing stiffness was found by using the Fig. 4 curve, which relates the critical speed to test bearing stiffness. Table II also contains the analytically predicted stiffnesses in accordance with the procedures of ref. 2 for comparison.

Typical radial displacements from Test No. 3 are shown in Fig. 6 for 445 Newtons (100 pounds) axial preload and an estimated 6.4 gm-in. unbalance. This test indicated a critical speed at 20,000 rpm and a resulting test bearing stiffness of 9.1 x 10^7 N/m (0.52 x 10^6 lb/in.). Bearing outer race clearance in the fixture is evident

by the abrupt post-critical drop in displacement above 22,000 rpm. This agrees with the theoretical behavior of a rotor with deadband bearing installations.

It was found during testing that the facility gearbox drain was not large enough to allow free oil flow above 23,000 rpm. Since increased preload or use of the lightweight spacer would tend to raise the current critical speed in the 19,000 to 20,000 rpm range, testing was limited to that shown in Table II and further testing suspended.

CONCLUSIONS

The tester and very practical testing technique functioned as intended with the exception of the gearbox lubrication, which is not related to the tester design. The data indicate that the dynamic stiffness of this 57 mm ball bearings is on the order of 8.75×10^7 N/m (0.5×10^6 lb/in.) for 445 to 890 Newtons (100 to 200 pounds) axial preload in the vicinity of 20,000 rpm. The value may differ in the usual spring preloaded installation since the preload piston in this test may resist bearing tilting more than a conventional preload spring and this tilt resistance may be responsible for some of the difference.

The analytically calculated value with the race free to tilt is approximately 20 percent lower than the measured value for the larger rotating radial load situation. A closer lower stiffness correlation is obtained for the lower dynamic loading cases. Stiffness increases for larger loading are typical of angular contact ball bearings and a nonlinear system. The data do indicate some sensitivity to the nonlinearity of the clearance between the outer race and the fixture.

Computer program bearing stiffness such as calculated per ref. 2 are adequate approximations for rotordynamic analyses if adequate design margin is incorporated. It is recommended as a guideline that rotor systems be designed so that the operating speed is not within ±20 percent of any calculated critical speed.

FURTHER TESTING

To increase scope, the tester is designed so that tests with various clearances between the support and outer race can be conducted. This clearance is generally referred to as the bearing deadband. The effect of outer race constraint can be investigated by machining the diameter of the test bearing support so that an increased clearance is produced and installing a preload spring between the hydraulic piston and outer race. The rotor would then be ramped through its critical speed with similar axial preload and unbalance conditions for comparison with the original clearance. This nonlinear effect of the deadband produces an apparent shift in the critical speed and influences the effective bearing stiffness. As of this time, these tests are still in the planning stages, and no schedule is available. Budget and the rotordynamic community interest will be the determining factors.

REFERENCES

1. Rowan, B. F.: "Rotordynamics Analysis of the Space Shuttle Main Engine High-Pressure Oxidizer Pump," presented at the 21st Structures, Structural Dynamics, and Materials Conference, Seattle, Washington, May 1980.

2. Jones, A. B.: "A General Theory for Elastically Constrained Ball and Radial Roller Bearing Under Arbitrary Load and Speed Conditions," Journal of Basic Engineering, June 1960.

TABLE I. - TESTER DESIGN DATA

ROTOR MATERIAL	INCO 718 STEEL
TEST BEARING	57 mm
SLAVE BEARING	45 mm
BEARING SPACING	34.3 cm (13.5 INCHES)
DUMMY MASS OUTER DIAMETER	20.32 cm (8.0 INCHES)
HOLLOW SHAFT OUTER DIAMETER	10.16 cm (4.0 INCHES)
ROTOR WEIGHT:	
HEAVY DISK	33.3 kg (73.5 POUNDS)
LIGHT DISK	24.0 kg (53.0 POUNDS)
MAXIMUM SPEED	35,000 RPM

TABLE II. - 57mm BEARING DYNAMIC STIFFNESS

TEST NO.	TEST DESCRIPTION	CRITICAL SPEED, RPM	MEASURED BEARING STIFFNESS* $N/m \times 10^{-8}$ $(LB/IN. \times 10^{-6})$	ANALYTICAL BEARING STIFFNESS** (WITH TILT AT 20,000 RPM) $N/m \times 10^{-8}$ $(LB/IN. \times 10^{-6})$	% ERROR
1	445 N (100 LB) PRELOAD ESTIMATED UNBALANCE = 2.8 GM-IN.	18,000	0.70 (0.40)	0.61 (0.35)	-12.5
2	890 N (200 LB) PRELOAD ESTIMATED UNBALANCE = 2.8 GM-IN.	19,000 TO 20,000	0.857 (0.49)	0.945 (0.54)	+10.2
3	445 N (100 LB) PRELOAD ESTIMATED UNBALANCE = 6.4 GM-IN.	20,000	0.91 (0.52)	0.70 (0.40)	-23.0

*SLAVE BEARING STIFFNESS CAN PRODUCE ±5% ERROR. AVERAGE CURVE B IS USED (FIG. 4)
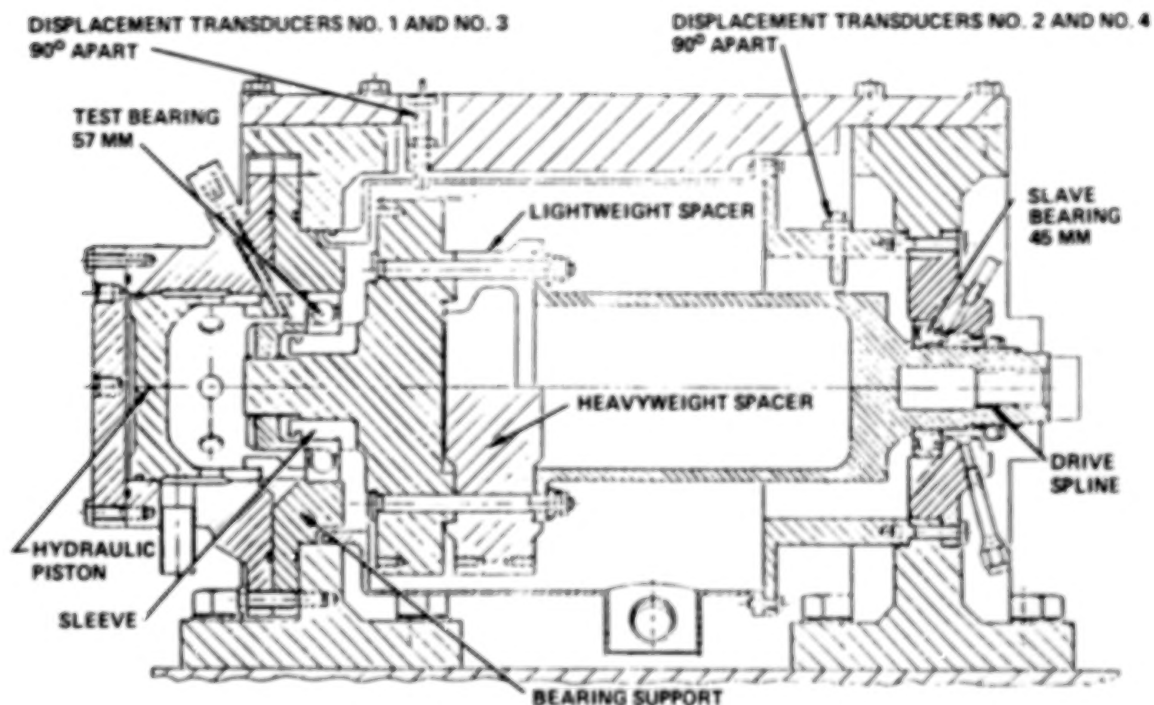**REF. 2, CALCULATED BY FRANCIS LEE, ROCKETDYNE.
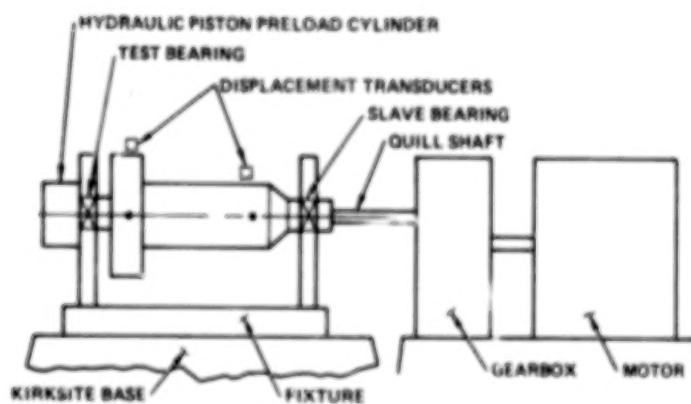
Figure 1. - Bearing tester.

Figure 2. - Test setup schematic.
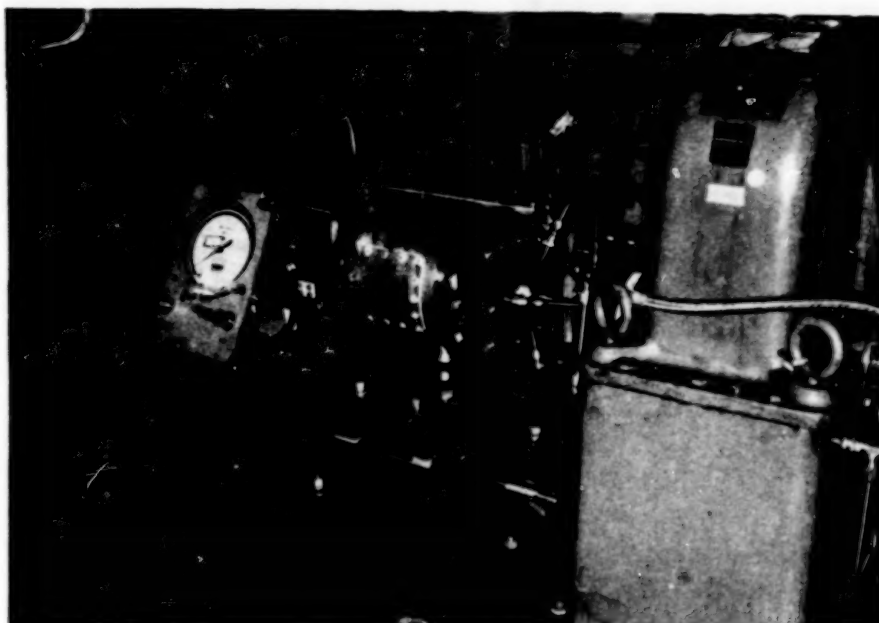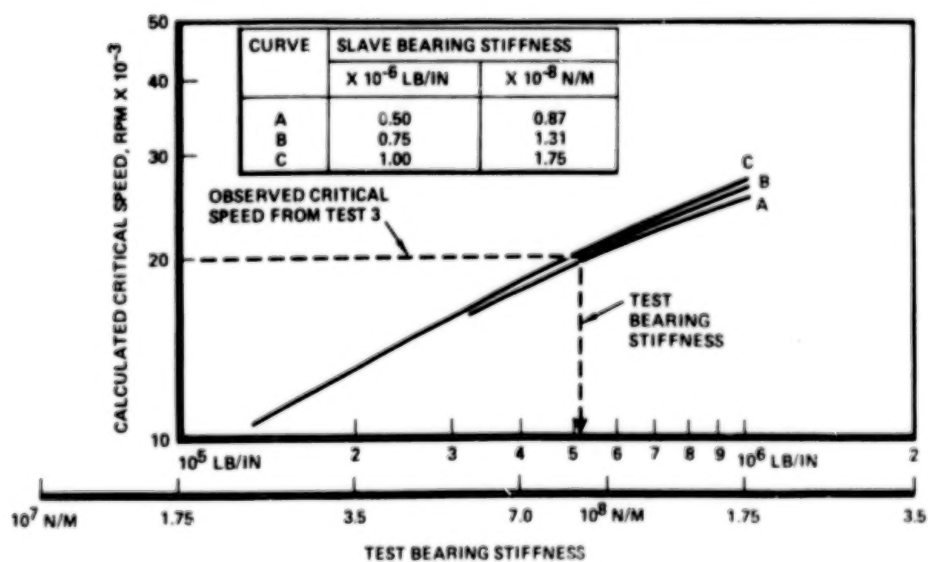
Figure 3. - Test setup.

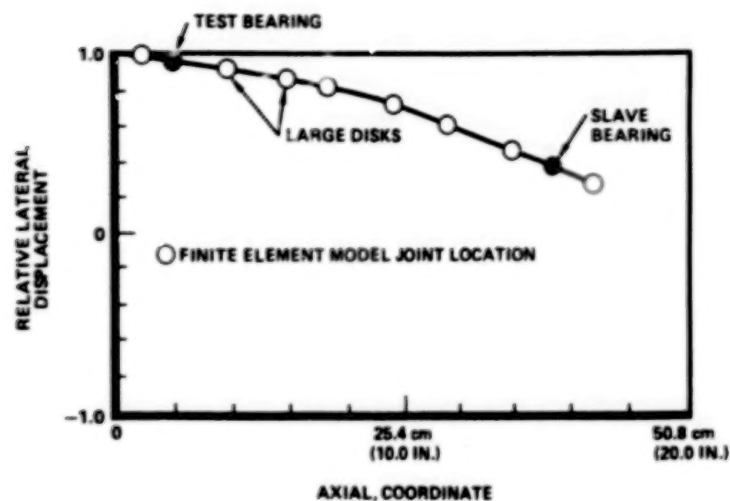Figure 4. - Heavyweight spacer critical speed plot.

103

Figure 5. - Test rotor lowest mode shape relative displacement versus axial coordinate.
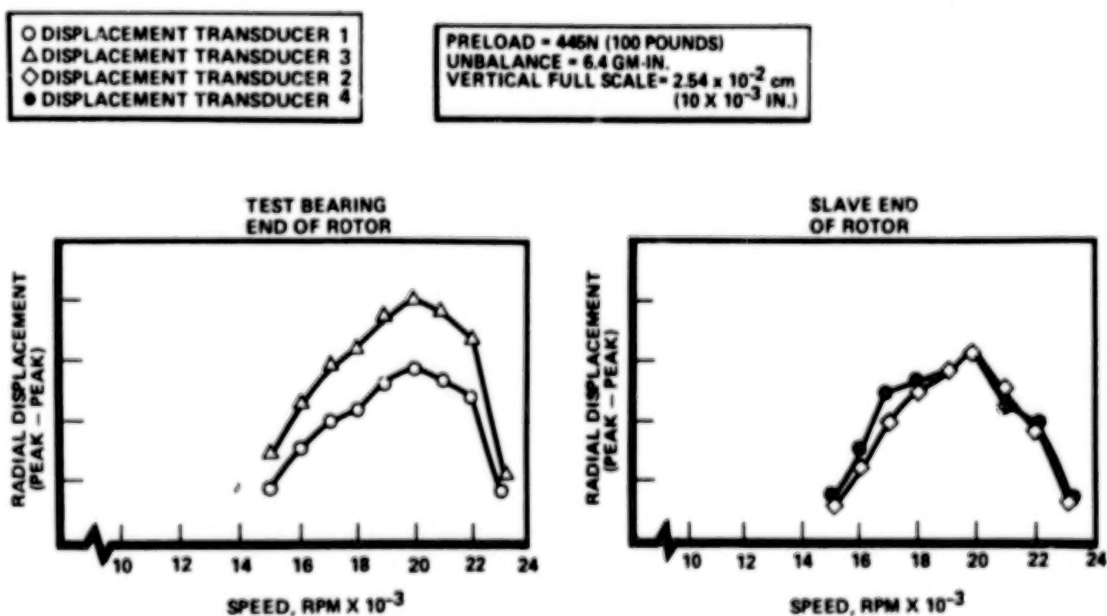
Figure 6. - Test no. 3 displacements vs. speed.

104

ROTOR VIBRATION CAUSED BY EXTERNAL EXCITATION AND RUB

Osami Matsushita, Michiyuki Takagi, Katsuaki Kikuchi, and Makio Kaga
Mechanical Engineering Research Laboratory
Hitachi, Ltd.
502, Kandatsu-Machi Tsuchiura-shi,
Ibaraki-ken 300 Japan

SUMMARY

For turbomachinery with low natural frequencies, considerations have been recently required for rotor vibrations caused by external forces except unbalance one, such as foundation motion, seismic wave, rub and so forth. Such a forced vibration is investigated analytically and experimentally in the present paper.

Vibrations in a rotor-bearing system under a harmonic excitation are analyzed by the modal techique in the case of a linear system including gyroscopic effect. For a nonlinear system a new and powerful quasi-modal technique is developed and applied to the vibration caused by rub.

From the above analyses the following results are derived.
1. In a high speed rotor, two resonances of a forward whirl motion and backward one are induced under a directional external excitation, because of large gyroscopic effect. Although rub of rotor usually causes instability, it is possible to stabilize the rotor vibration by selecting a rubbing stopper suitable to each resonance severity.
2. In a low speed rotor such as a vertical pump with small gyroscopic effect, a response is a directional vibration within limits of no rubbing. However, when a rotor begins to rub, a directional respose changes to a stable forward whirl motion due to the nonlinearity in the water bearing.

These analytical results characterized by gyroscopic effect and bearing nonlinearity are confirmed by excitation tests of a high speed spin rotor and a pump model rotor, respectively.

1. INTRODUCTION

Many studies deal with vibration responses for some kinds of excitation in structure dynamics. However, a response of rotor under external excitation shows different features of motion from that of structure, i.e. forward whirl motion and backward whirl motion at each resonance. Some papers (ref. 1, 2) describe such a response of a rigid rotor.

In this paper, a general description of a forced vibration in linear rotor-bearing system is given and a rub vibration induced by contact between a rotor and a stator is also included in the discussion on nonlinear rotor dynamics.

Two kinds of rotors are selected for the study of rub vibration. The one is a rotor with high speed rotation and large gyroscopic effect. The stopper effect for the suppression of a rotor vibration due to rub is discussed. The other is a pump model rotor with low speed rotation and water lubricated bearings. Nonlinearity of a water bearing and rub vibration of a journal are considered.

B^*, B_i^* ; modal quantum in state equation
C_g ; gyroscopic matrix
C_g^* ; modal gyro
C_f, C_b ; complex type of damping matrix
C_{ij} (i,j = x,y) ; damping matrix
F ; external force
i ; imaginary unit $\sqrt{-1}$
I_d ; transverse moment of inertia of a disk
I_p ; polar moment of inertia of a disk
K_f, K_b ; complex type of stiffness matrix
K_{ij} (i,j = x,y) ; stiffness matrix
K ; stiffness of storper with a clearance
K^* ; modal stiffness
m ; mass of a disk
M , M^*; mass matrix , modal mass
S, S_i ; normal coordinate
t ; time
$Q_z = Q_x + iQ_y$; nonlinear restoring force
$Z = X + iY$; rotor absolute displacement
$z_0 = x_0 + iy_0$; foundation absolute displacement
$z = Z - z_0$; rotor relative displacement
δ ; clearance
$\zeta = -\alpha/|\lambda|$; modal damping ratio C/Cc
λ, λ_k ; complex eigenvalue
μ; friction factor
ν; excitation frequency
ϕ, ϕ_i ; eigen vector
ω, ω_f, ω_b ; natural frequency in rotation
ω_n ; natural frequency in no rotation
Ω ; rotational speed

2. EQUATION OF MOTION AND MODE SEPARATION

2.1 Equation of Motion in Rotor-Casing System

The equation of motion on a coordinate system fixed in the space is derived for entire system including a rotor, bearings and casing, as shown in Fig.1. The system is discretized by a beam model along longitudinal axis with ξ -direction. Representing the absolute displacements at each location of a rotor with X and Y and that of a casing with x and y , the equation of motion is given as follows

$$M\ddot{X} - \Omega C_g \dot{Y} + K_{xx}(X-x_0) + K_{xy}(Y-y_0) + C_{xx}(\dot{X}-\dot{x}_0) + C_{xy}(\dot{Y}-\dot{y}_0) = Q_x$$
$$M\ddot{Y} + \Omega C_g \dot{X} + K_{yx}(X-x_0) + K_{yy}(Y-y_0) + C_{yx}(\dot{X}-\dot{x}_0) + C_{yy}(\dot{Y}-\dot{y}_0) = Q_y$$

(1)

where Q_x and Q_y are nonlinear restoring forces.

A complex numbered type of displacement is introduced here for the sake of convenience of description.

$$Z = X + iY \qquad z_0 = x_0 + iy_0 \qquad\qquad (2)$$

Since the acceleration $\ddot{z}_0$ (t) of the foundation of the casing is usually measured, the equation (1) is rearranged to obtain the acceleration excitation of foundation. Applying relative displacement $z=Z-z_0$, where the rotor motion is measured with respect to the casing motion, the following equation of motion is obtained from Eq.(1).

$$M \ddot{z} + i \Omega C_g \dot{z} + K_f z + K_b \bar{z} + C_f \dot{z} + C_b \dot{\bar{z}} = -M \ddot{z}_0 - i \Omega C_g \dot{z}_0 + Q_2 \equiv F \qquad (3)$$

This formula is fundamental for the study of vibration under seismic excitation in rotor dynamics.

In the formula, the second term with the coefficient of rotational speed Ω shows gyroscopic effect which exists only in a rotor system. The matrices M and Cg consist of inertias of each disk on a shaft in the following forms.

$$M \approx diagonal\ (\cdots m,\ I_d \cdots)$$
$$C_g \approx diagonal\ (\cdots 0,\ I_p \cdots) \qquad (4)$$

Therefore, if the casing moves in a parallel way with acceleration $\ddot{z}_0 = [\ddot{\delta}_0,\ \ddot{\theta}_0 = 0]$, excitation force, stated on the righthand side of Eq.(3), reduces to only inertia force $M\ddot{z}_0$ of mass as usual. On the other hand, if the casing is rocking in a non-parallel way with $\ddot{z}_0 = [\ddot{\delta}_0,\ \ddot{\theta}_0]$, an additional force $-\Omega C_g \dot{\theta}_0$ adds up the excitation force. That is a gyroscopic moment which is proportional to a polar moment of inertia of disks and rotational speed.

2.2 Response at Each Mode

Table 1 is utilized to derive the modal response at each mode based upon orthogonality of eigensolution. There are two columns I and II in Tab.1. One of them concerns with a rotor system suspended vertically and the other one with a horizontally suspended rotor system. The former one indicates a free motion with a circular whirl and the latter one indicates a motion with an elliptical whirl. This classification is due to symmetry or asymmetry in bearing dynamic properties.

For each case, it is assumed that eigensolution of free equation of motion indicated in the line No.3 of table 1 is given by the formula as shown in the line No.4. The corresponding eigenvalue problem is obtained, and orthogonality condition is guaranteed in the forms given by the line No.8.

Therefore, by using these eigensolutions of free vibration, it is possible to separate a general response into each mode response on normal coordinate system. From a physical system with symmetrical bearings of I in Tab.1 to a normal coordinate system, the modal transformation is defined by the relationship as follows.

$$z = [\phi_1 \cdots\cdots \phi_m]s = [\phi]s \qquad (5)$$

The state equation with normal coordinate resulted by post-transformation becomes

$$\dot{s}_i - \lambda s_i = -\frac{\lambda_i \phi_i^t F}{B_i^*} \qquad (6)$$

where

$$B_i^* = -\lambda_i^2 \phi_i^t M \phi_i + \phi_i^t K \phi_i \ \rightarrow \ B^* = -\lambda^2 M^* + K^* \approx \omega^2 M^* + K^*$$

The normal transformation for a system with asymmetrical bearing of II in tab.1 is also derived by the same manner.

3. HARMONIC FOUNDATION EXCITATION

3.1 Harmonic Excitation
The external force in the equation of motion Eq.(3) becomes

$$F = -M\ddot{z}_0 - i\Omega C_g \dot{z}_0 \qquad (7)$$

where the harmonic acceleration in a certain direction e.g., fixed at X-axis

$$\ddot{z}_0 = a \cos \nu t \qquad (8)$$

is substituted into Eq.(7). Then, the external force is defined as following exponential expression.

$$F = -(M + \frac{\Omega}{\nu} C_g)\, \frac{a}{2}\, e^{i\nu t} - (M - \frac{\Omega}{\nu}\, C_g)\, \frac{a}{2}\, e^{-i\nu t} \qquad (9)$$

Movements of the foundation in parallel and rocking motions are generally included in the amplitude a of an acceleration. As usual, in the case of no rocking motion the external force is simplified into the following formula.

$$F = -M\, \frac{a}{2}\, e^{i\nu t} - M\, \frac{a}{2}\, e^{-i\nu t} \qquad (9')$$

As the one directional force acts upon the rotor, it is equivalent to two whirling forces expressed by exponential form, with forward component $i\nu$ and backward component $-i\nu$.

Now, suppose that an eigenvalue $\lambda = -\alpha + i\omega\ (\omega > 0)$ with a rotor in rotation is obtained, a resonance occurs when excitation frequency ν comes close to a natural frequency ω i.e., $\nu \approx \omega$. On the other hand, the conjugate value $\bar{\lambda} = -\alpha - i\omega$ does not become an eigenvalue in rotor system, because of gyroscopic effect. So no resonance appears at the condition of $-\nu \approx -\omega$. Therefore, it is clear that only one of the two whirl forces contributes to a resonance.

Each whirl force, divided from one directional harmonic force, has half of the magnitude of one directional force. Then the rotor response on a resonance, while in rotation, is reduced to about half of the amplitude, compared with the one with no rotation.

3.2 Features of Response
Some features appearing in the response are summarized for a vertically suspended rotor here. A modal response corresponding to an eigenvalue and also to an eigen vector is obtained by substituting Eq.(9') into Eq.(6).

$$S(t) = \frac{\phi^t M}{\beta^*} \left\{ \frac{\lambda}{i\nu - \lambda}\, \frac{a}{2}\, e^{i\nu t} + \frac{\lambda}{-i\nu - \lambda}\, \frac{a}{2}\, e^{-i\nu t} \right\} \qquad (10)$$

[1] Forward Whirl Resonance; As the condition $\nu \to \omega_f$ with the relationship between eigenvalue $\lambda = -\alpha + i\omega_f$ and exciting frequency ν, a forward whirl resonance becomes remarkably large as described in the first part of Eq.(10).

$$S(t) \approx \frac{1}{2}\, \frac{\phi^t M}{K^*}\, \frac{2}{1 + \omega_f^2/\omega_n^2}\, \frac{a}{2S}\, e^{i(\nu t - 270°)} \qquad (11)$$

The phase relationship between rotor position and exponential exciting force is shown in Fig.3, for three instances of pre, on and post resonance when the excitation frequency is swept. The phase lag of rotor behind the force is 270 deg. when just on a resonance in the X-direction. And it is less than 270 deg. at pre-resonance and more than 270 deg. at post-resonance.

[2] Backward whirl Resonance; When the relationship between eigenvalue $\lambda = -\alpha - i\omega_b$ and excitation frequency ν approaches the range of $-\nu \approx -\omega_b$, the rotor response becomes a backward resonance, as described in the second part of Eq.(10).

$$S(t) \approx \frac{1}{2}\, \frac{\phi^t M}{K^*}\, \frac{2}{1 + \omega_b^2/\omega_n^2}\, \frac{a}{2S}\, e^{-i(\nu t - 270°)} \qquad (12)$$

The phase lag of rotor behind the force is 270 deg. when just on a resonance. And it is changing from less than 270 deg. to more than 270 deg. through the resonance as shown in Fig.4.

[3] Whirl Motion;   The rotor has two eigenvalues which correspond to a mode shape. These values are different from conjugate relation and are independent from each other.   Here the forward natural frequency is higher than the backward one.

Therefore, when rotating the rotor at a high speed, the response whirl motion is changing from left to right as shown in Fig.5, corresponding with increase of excitation frequency. At the beginning the backward resonance occurs with a circular orbit, and later on through elliptical orbits the forward resonance appears again with a circular whirl orbit. On the boundary line, between forward direction and backward direction, an elliptical whirl orbit becomes a straight line thus whirl direction can be interchanged.

[4] Low Gyroscopic Effect;   In the case of low gyroscopic effect such as low rotational speed or small disks, forward eigenvalue and backward one corresponding to an eigen mode are not independent of each other, and they approach to a conjugate relation. The typical state such as low gyroscopic effect leads to dynamics of nonrotational rotor. Eigenvalues maintain conjugate form, for example,

$$\lambda_K = \lambda \qquad \lambda_{K+1} = \bar{\lambda}$$

Resonance response is described by the following form

$$S(t) \approx \frac{1}{2} \frac{\phi^t M}{K^*} \left\{ \frac{\lambda}{i\nu - \lambda} e^{i\nu t} + \frac{\bar{\lambda}}{-i\nu - \bar{\lambda}} e^{-i\nu t} \right\} \tag{13}$$

such that rotor, vibrating only in X-direction, coincides with the direction of the acting force without a whirl motion.

3.3 Harmonic Respose Curve

Figure 8 shows the response curve under harmonic excitation. In the case of Ω =0 i.e., no rotation, a resonance peak appears. On the other hand, at high speed rotation two resonance peaks appear with backward whirl and forward whirl. The separation of a peak into two peaks is due to gyroscopic effect or rotor rotation. This figure is described by nondimensional frequency and amplitude, which are normalized by the values of the resonance frequency and amplitude at no rotation, respectively. The peak at the forward resonance is less than the half of the peak at the resonance in no rotation, because of $\omega_f/\omega_n \gtrless 1$ in Eq. (11). On the other hand, the peak at the backward is more than the half of that, because of $\omega_b^2/\omega_n^2 \leq 1$ in Eq. (12). Therefore it is clear that these two peak amplitudes reduce to about half of the amplitude at no rotation and the backward amplitude is slightly higher than the forward one.

4.   SEISMIC EXCITATION

Instead of equation of motion in physical coordinate system, the state equation in normal coordinate system is used for analysis of time history response caused by seismic excitation. In Eq.(6), an arbitrary external force

$$F = -M\ddot{z}_0 - i\Omega C_g \dot{z}_0 \tag{14}$$

is defined by insertion of the acceleration $\ddot{z}_0$ measured in the field. Substitution of Eq.(14) into Eq.(6) and integration of the resulting equation gives time history response of rotor in normal coordinate system. In order to return the normal response to the response in physical system the following relationship is used:

$$Z(t) = \sum_i \phi_i S_i(t) \tag{15}$$

5. SEISMIC EXCITATION WITH NONLINEAR SYSTEM

Here we discuss a rotor vibration induced by seismic excitation which becomes larger than the clearance between a rotor and a stopper. In such situation the rotor begins to contact the stopper fixed on the casing.

In this rub vibration, the response on normal coordinate system is given by Eq.(6) and the external force is defined as follows.

$$F = - M \ddot{z}_0 - i \Omega C_g \dot{z}_0 + Q_z \qquad (16)$$

The force Qz is a nonlinear restoring force generated by the contact of a rotor with a stopper. The two types of configuration of a cylindrical stopper are mentioned here.

(1) Type I   contact between an outer surface of a rotor and an inner surface of a stopper i.e., a rotor in a stopper

(2) Type II   contact between an inner surface of a rotor and an outer surface of a stopper i.e., a stopper in a rotor

The types I and II here are called an outer contact and an inner contact with respect to the rotor.

Representing the stiffness of a stopper, the clearance between a rotor and a stopper and the friction factor with K, δ and μ , respectively, the nonlinear restoring force is defined as follows.

$$Q_z = F_r \pm i F_\theta \qquad \begin{array}{l} \text{+ for outer contact type} \\ \text{- for inner contact type} \end{array} \qquad (17)$$

where
$$F_r = - K (|z| - \delta) z / |z|$$

and $F_\theta = \mu F_r$ sign (angular velocity of contact face on rotor)

In the simulation of a nonlinear vibration caused by rub, the second term in Eq.(17) indicates an unstable friction force which induces a whirl motion. Therefore, to suppress the rotor vibration by a cylindrical stopper, the outer type of a stopper is more effective in a rotor with higher forward resonance severity. On the other hand, the inner type of a stopper is more effective with higher backward resonance severity.

For the response history analysis in such a nonlinear system a quasi-modal technique is effective, and a hybrid integration method based upon it is developed, as described in Appendix.

6. EXCITATION TEST OF HIGH SPEED ROTOR

6.1 Harmonic Excitation

The features of a rotor response excited by a harmonic wave, stated in the previous chapters, are reconfirmed by an experiment in which the rotor shown in Fig.7 is used. The rotor rotates in very high speed, and it has large gyroscopic effect. The rotor is suspended by bearings at both sides. The vibration mode with a low natural frequency is the conical mode in which the right side of the rotor vibrates with the nodal point in the left side.

The vibration response waveform, the response curve and the Lissajous figure of rotor motion are presented in Fig.8, including a harmonic waveform with the excitation frequency ν. When the rotor does not rotate, the rotor vibration response is one directional and the resonance frequency agree with the natural frequency ω_n in a structure i.e., $\nu = \omega_n = 4.95$ Hz.

Under a rotation of the rotor, two resonance peaks in the rotor response appear in the backward and forward resonances at the excitation frequency $\nu = 0.66\omega_n$ and $\nu = 1.21\omega_n$, respectively. The peak amplitude severity Q at the backward resonance becomes about half of the peak amplitude severity $Q_n = 156$ μm/gal at the resonance of the rotor with no rotation. The other one at the forward resonance is about one fifth of Q_n. The calculated values of the resonance frequency and peak amplitude severity, as shown in Fig.5, well coincide with these experimental values.

6.2 Rub Vibration

An aseismic stopper with a fine gap is installed in the rotor system with large gyroscopic effect, as schematically shown in Fig.7. This stopper is not a usual circular type, but one directional type with a clearance of x-direction as shown in (i) of Fig.6.

Figure 9 shows vibration history response and its Lissajous figure of the rotor subjected to a seismic wave. The magnitude of excitation acceleration increases in turn by (A), (B) and (C). In the case of (A), excitation acceleration is so small that the rotor moves in the clearance with no rub and nearly circular whirl orbit.

In the case of (B) and (C) rubs occur. Comparing the case (C) with the case (B) a larger acceleration causes a stronger rub between the rotor and the stopper, close to an impact.

In the rotor system with large gyroscopic effect, the vibration of a rotor is always generated in a circular whirl motion by an external force in one direction. Then, vibration is satisfactorily suppressed by even one directional stopper at an arbitrary phase location, as demonstrated in this numerical simulation. One directional stopper is rather preferable than a circular stopper, because the duration of rub in the former is less than one in the latter and the corresponding friction force which induces unstable vibration becomes less.

The effect of the stopper upon vibration suppression is indicated in Fig.10. The horizontal axis shows the maximum value of the acceleration in the seismic wave, normalized by the value in which the rotor begins to rub with the stopper. The perpendicular axis gives the value of the displacement in the response, normalized by the clearance δ. The stable suppression of the rotor vibration is seen in the range of about five times of the acceleration at the beginning of rub in Fig. 10. This numerical result proves a good agreement with the corresponding experimental result.

7. EXCITATION TEST OF PUMP MODEL ROTOR

7.1 Outline of Experiment

Figure 11 shows the outline of the experimental equipment which is simplified into a vertically suspended pump model rotor for atomic power plant. The experimertal rotor has two disks and two bearings. A self-centering ball bearing is used at the upper part and water is filled in the cylindrical water bearing located at the lower part. Two weights are added to the lower part of the rotor. An aseismic support is located at the lowest part of the casing in order to prevent large vibration of the casing.

The pump model rotor is vertically located on a shaking table which can stand the load of 294 kN (30 tons). The excitation wave is sinusoidal one in this test. In this measurement system, the usual way is employed, except for a load cell with strain gages to measure the dynamic force in the lower water bearing.

7.2 Natural Frequency

The experimental rotor is discretized by beam element and a calculation model is obtained as shown in Fig.11. Natural frequencies and corresponding mode shapes are represented in Tab.2 and Fig.12,respectively.

From the calculation   results considering virtual mass effect (Ref.3) of water
and assuming water bearing stiffness of 9.8 MN/m (10^3 kgf/mm) natural frequencies are
13.6 Hz and 18.0 Hz. With the stiffness of 39.2 kN/m (4.0 kgf/mm), they are 14.9
Hz, 6.4 Hz and 27.6 Hz. The former stiffness is picked up to simulate the contact
of the journal with the stator of bearing under the condition of large journal
vibration, and the latter one is equivalent to the stiffness of water bearing under
the condition of small journal vibration. In the latter, the rotor vibrates
remarkably in the first and second mode and the casing in the first mode.

The comparison of calculation values of natural frequency with experimental
ones is presented in Tab.2. The first natural frequency of 6.4 Hz in calculation
agrees well with the experimental value of 7.0Hz. Concerning the casing mode, a
good agreement is also obtained by comparison between the calculation value of
$13.6 \sim 14.9$ Hz and the experimental value of 14.0 Hz.

With respec to the second natural frequency of rotor mode, the experimental
value of $18 \sim 20$ Hz is negligibly different from the calculation value of 27.6 Hz
under the assumption of no contact within small journal vibration. However, in the
case of large stiffness i.e., assuming a contact in the bearing, this experimental
value becomes close to the value obtained by the calculation.   From these compar-
isons, it is estimated that the restoring force with a hard type of nonlinearity
due to a contact is induced in a water lubricated bearing, and the large journal
vibration increases the bearing stiffness.

The first mode resonance does not appear remarkably in the excitation test
because of very high modal damping ratio.

As stated above, the good agreement of natural frequencies between the
calculation and the experiment suggests the reasonable modeling of the pump rotor
system, including dynamics in the water bearing.

7.3   Rotation Test

A rotation test is done before an excitation test. In this test the casing is
tightly fixed by the aseismic support with no clearance. The vibration of the rotor
itself is seen in the amplitude response curve in Fig.13. The first unbalance
resonance appears at the rotational speed of $7 \sim 8$ rps.

The second resonance varies greatly with the unbalance. In the case of a small
unbalance, the second resonance peaks occur at the rotational speed of $17 \sim 19$ rps.
It changes to 20 rps when a large unbalance is applied to the rotor. It is noticed
that the peak amplitude becomes very sharp in this case.

The large unbalance induces a large amplitude of vibration such that the rotor
moves in a large whirl orbit in the clearance of the bearing, and the rub often
occurs. Consequently the increase of the stiffness and the decrease of the damping
effect at the bearing are induced by a large whirl motion and they lead to a sharper
amplitude and a higher resonance frequency. In fact the scratches of rub can
be seen when opening the bearing.

The comparison between amplitude responses in the rotation test and in the
harmonic excitation test with no rotation is described in Fig.13 and 14. Both
response curves are very different from each other. In the excitation test, only one
high peak appears at the excitation frequency of about 18 Hz. Its response curve is
similar to the unbalance response curve with large unbalance.

Therefore, it can be said that this excitation acceleration of 0.1 G seems
to be small in value, but it has a large influence on the rotor vibration. From the
fact, an actual pump rotor with low load capacity in the water bearing is very
sensitive to an external excitation. This fact indicates the necessity of aseimic
design for a pump rotor suspended vertically.

7.4 Harmonic Excitation Test

Influence of some parameters on a rotor response is examined by sweeping of a harmonic excitation frequency.

(1) Influence of Clearance in Water Bearing

The displacement of the rotor vibration is shown in Fig.14 by changing the bearing clearance of 0.127 mm and 0.381 mm. Here, the casing is fixed by the aseismic stopper with no clearance. In case of 0.127 mm (normal specification), the resonance occurs at the excitation frequency of 18.5 Hz and its peak amplitude reaches up to the value of 760 μm. With the clearance of 0.381 mm, the corresponding peak amplitude is 580 μm. As shown in the response curve with the clearance of 0.381 mm, larger clearance results in high damping effect which reduces the peak amplitude, and it produces a curve which shows true nonlinear phenomena due to a hard spring.

(2) Influence of Rotor Rotation with Fixed Casing

A harmonic excitation test is done at each rotational speed with the casing being fixed. The rotor response and dynamic bearing load, including the responses in X and Y direction, are summarized in Figs.15.

When the rotor is rotating and is subjected to harmonic excitation, Y-direction vibration appears in addition to X-directional vibration. This result indicates that a rotor response is a whirl motion, in spite of the extremely small gyroscopic effect in the pump rotor against the fact as mentioned in paragraph 3.2. It is seen that the hydraulic force in a fine clearance and the rub force due to larger journal vibration cause a whirling agitation for a rotor.

From these graphs, it is clear that an increase in rotational speed decreases the response peak amplitude and the dynamic bearing load in X-direction. However, the peak amplitude and the bearing load increase in Y-direction. When a rotor is in rotation, the sum of vibration responses in both directions becomes in balance with the power of external force. Then, it is clear that a rotor with no rotation is most sensitive to an external force and the rotation reduces such sensitivity.

Although two peaks are seen in a response curve just like influence of gyroscopic effect, it is not clear why the separation of a peak appears in spite of the rotor with an extremely small gyroscopic effect.

7.5 Whirl Orbit due to Rub

The response waveforms and whirl orbits of the journal motion at a resonance in the sweeping test are given in Fig.16. The one directional orbit at the no rotation changes into a circular whirl orbit with rotation due to rub. Therefore, the waveform of the bearing load at the rotation contains the ordinary harmonic component plus the spiky peak component due to rub.

7.6 Simulation of Rub Vibration

A dynamic model of the water bearing is assumed by a nonlinear relationship between the journal of displacement and the restoring for , as described in Fig.17. The nonlinear stiffness K is extremely greater than the linear stiffness K_0, like a hard type of spring.

The numerical result given in Fig.18 simulates a onance in the harmonic sweeping test. The journal vibration is suppressed by the bearing clearance, but the Y-directional vibration occurs simultaneously near the resonance. The waveform of the bearing load is nearly harmonic. High spiky peak is superposed on the harmonic one at the instance of rub, like projections on the waveform of bearing load.

The whirl orbits obtained in the calculation of history response are shown in Fig.19. At no rotation of 0 rps, one directional vibration is generated, coinciding with the excitation direction. A whirl motion is induced by rub at the rotation of 24 rps.

Comparing Fig.19 with Fig.16, the calculated whirl orbit at no rotation agrees with the experimental one. With respect to results at 24 rps, they are different from each other. The experimental whirl orbit is nearly circular and the calculation one closes to be rectangular. The disagreement may be attributed to the fact that a whirling force, generated in a fine gap when the journal rubs with the stator in the water bearing, and an unbalance force which actually exists are neglected in the calculation.

The comparison of the bearing load between the experiment and calculation is given in Fig.20. The horizontal axis shows the value assumed by a nonlinear stiffness K. Generally speaking, good agreement is seen with respect to the harmonic component and the spiky peak component in the bearing load waveform.

8. CONCLUSIONS

Conclusions summarized in this study are as follows.

(1) The modal technique is acceptable for the vibration analysis in a linear system with rotor, casing and bearings under an external excitation, and the division of the vibration response at harmonic excitation into each component of eigen modes is achieved. On the other hand, for the nonlinear vibration analysis, a new technique called quasi-modal is developed, and a hybrid integration method based on it is presented. The effectiveness of the new method is proved by numerical simulations of vibration due to such rub and nonlinearity in a water bearing.

(2) The peak amplitudes at a backward resonance and a forward resonance under a harmonic excitation when rotating a rotor in high speed are reduced to about half of the peak amplitude at no rotation. It is also proved that the backward resonance severity is slightly greater than the forward one. These general features of rotor response at a harmonic excitation are made clear in relation to gyroscopic effect.

(3) The selection of a stopper for the suppression of rotor vibration i.e., inner or outer type, depends upon which response severity is greater between a backward resonance and a forward one. It is verified by calculation and experiment that one directional stopper is rather stable and effective for the suppression of rotor vibration in the system with large gyroscopic effect, compared with a cylindrical type of stopper as usually used.

(4) Very high response sensitivity of vertically suspended rotor such as a pump to external excitation and rub becomes experimentally clear, including the dependence on bearing clearance and rotational speed.

(5) In spite of very small gyroscopic effect in a pump rotor, the rotor response indicates a whirl motion due to rub and nonlinearity in a water bearing. The response of bearing dynamic load contains a ordinary harmonic component and a spiky component in waveforms. It is demonstrated that these experimental values of bearing load can be estimated by the calculation assuming a dynamic model of a water bearing with clearance.

REFERENCES

(1) Kawamoto, I and Urushidani, H ; Trans. JSME, vol.45-400 (1979-12), P 1451
(2) Kanai, S. and Tamura, A. ; Preprint, JSME No 784-5 (1978-3), P 77
(3) Fritz, R.J. ; Trans. ASME Ser. B, 94-2 (1972-2), P 167

TABLE 1. - DAMPED EIGENVALUE ANALYSIS OF ROTOR-BEARING SYSTEM

No.	ITEM	I	II
1	SYSTEM	Circular Whirl Orbit with Symmetric Support Vertically Suspended Rotor	Elliptical Whirl Orbit with Asymmetric Support Horizontally Suspended Rotor
2	DYNAMIC PROPERTIES OF BEARING	$k_{xx}=k_{yy}$ $k_{xy}=-k_{yx}$ $c_{xx}=c_{yy}$ $c_{xy}=-c_{yx}$	—
3	EQUATION OF MOTION	$M\ddot{z}+i\Omega C_g \dot{z}+(C_d-iC_c)\dot{z}+(K_d-iK_c)z=F$ where $K_d=K_d-iK_c=\left[\frac{k_{xx}+k_{yy}}{2}\right]+i\left[\frac{k_{yx}-k_{xy}}{2}\right]$ $C_d=C_d-iC_c=\left[\frac{c_{xx}+c_{yy}}{2}\right]+i\left[\frac{c_{yx}-c_{xy}}{2}\right]$	$M\ddot{z}+i\Omega C_g\dot{z}+C\dot{z}+C_d\dot{z}+Kz+K_d\bar{z}=F$ where $K_d=\left[\frac{k_{xx}-k_{yy}}{2}\right]+i\left[\frac{k_{yx}+k_{xy}}{2}\right]$ $C_d=\left[\frac{c_{xx}-c_{yy}}{2}\right]+i\left[\frac{c_{yx}+c_{xy}}{2}\right]$
4	EIGEN SOLUTION	$z=\phi e^{\lambda t}$	$z=\phi_1 e^{\lambda t}+\bar{\phi}_2 e^{\lambda t}$ $|\phi_1|>|\phi_2|$
5	EIGENVALUE PROBLEM $\lambda B\phi=A\phi$ cf. $\lambda B^t \Psi = A^t \Psi$	$B=\begin{bmatrix}-M & 0 \\ 0 & K_d-iK_c\end{bmatrix}$ $\phi=\begin{bmatrix}\phi\lambda \\ \phi\end{bmatrix}$ $A=\begin{bmatrix}i\Omega C_g+C_d-iC_c & K_d-iK_c \\ K_d-iK_c & 0\end{bmatrix}$	$B=\begin{bmatrix}B_1 & B_2 \\ B_2 & B_1\end{bmatrix}$ $B_1=\begin{bmatrix}-M & 0 \\ 0 & K_1\end{bmatrix}$ $B_2=\begin{bmatrix}0 & 0 \\ 0 & K_d\end{bmatrix}$ $\phi=\begin{bmatrix}\phi_1\lambda \\ \phi_1 \\ \phi_2\lambda \\ \phi_2\end{bmatrix}$ $A=\begin{bmatrix}A_1 & A_2 \\ A_2 & A_1\end{bmatrix}$ $A_1=\begin{bmatrix}i\Omega C_g+C_1 & K_1 \\ K_1 & 0\end{bmatrix}$ $A_2=\begin{bmatrix}C_d & K_d \\ K_d & 0\end{bmatrix}$
6	MATRIX B,A	symmetric	—
7	EIGENVALUE	$\lambda=a+iq$ Damped Frequency $=q$ Modal Damping $=-a/\sqrt{a^2+q^2}$	
8	ORTHOGONALITY CONDITION	$\phi_i^t B \phi_j \begin{cases}=0 \\ \neq 0\end{cases}$ $\phi_i^t A \phi_j \begin{cases}=0 & \text{for } i\neq j \\ \neq 0 & \text{for } i=j\end{cases}$	$\Psi_i^t B \phi_j \begin{cases}=0 \\ \neq 0\end{cases}$ $\Psi_i^t A \phi_j \begin{cases}=0 & \text{for } i\neq j \\ \neq 0 & \text{for } i=j\end{cases}$
9	FORCED VIBRATION	$B^t[z-(\lambda)z]=(\lambda)Mod(\phi)\cdot F$ where $z=\Sigma \phi_i z_i$ for $i=-\infty n$ $=Mod(\phi)\cdot s$	$B^t[z-(\lambda)z]=(\lambda)(Mod(\phi)\cdot F+Mod(\bar{\phi})_2\cdot \bar{F})$ where $z=\Sigma(\phi_1 z_1+\bar{\phi}_2 \bar{z}_2)$ for $i=-\infty n$ $=Mod(\phi_1)\cdot s+Mod(\bar{\phi}_2)\cdot \bar{s}$

TABLE 2. - COMPARISON OF NATURAL FREQUENCIES

| Item	Vibration Mode			Comment
	CASING	ROTOR		
	1-ST	1-ST	2-ND	
	Natural Frequency, Hz			
EXPERIMENT				
Impulse response	14.0			Hit casing
Unbalance response	14.0	7	17-19	
Harmonic excitation	14.0	No peak	18-20	Rotation N = 20 rps
CALCULATION				
Water bearing (linear)	14.9	6.4	27.6	Bearing stiffness = 4.0 kgf/mm = 39 kN/m (no rub)
Water bearing (nonlinear)	13.6		18.0	Bearing stiffness = 10³ kgf/mm = 9.8 MN/m (with rub)

115
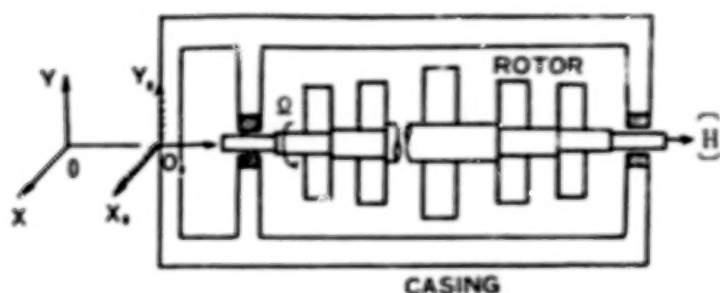
Figure 1. - Rotor-bearing-casing system.

Figure 2. - Coordinate system.

1   PRE-RESONANCE
2   ON-RESONANCE
3   POST-RESONANCE
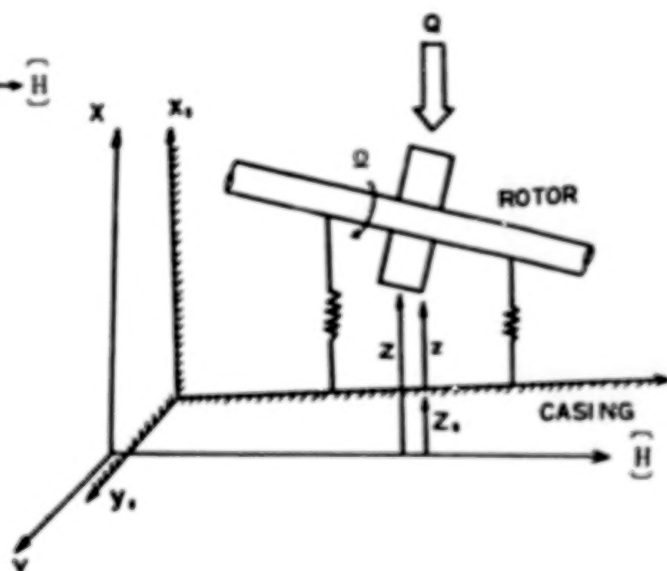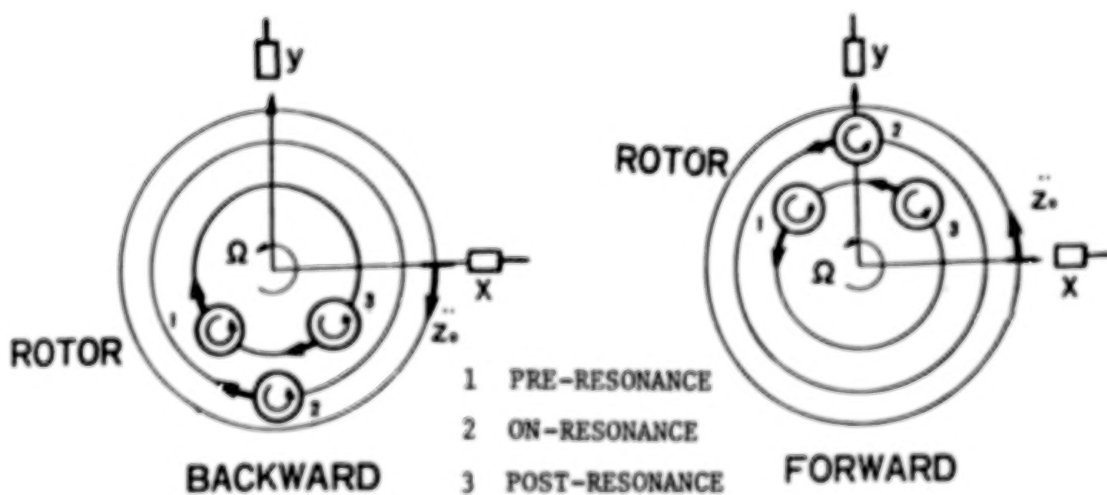
Figure 3. - Phase relationship between rotor and excitation acceleration.
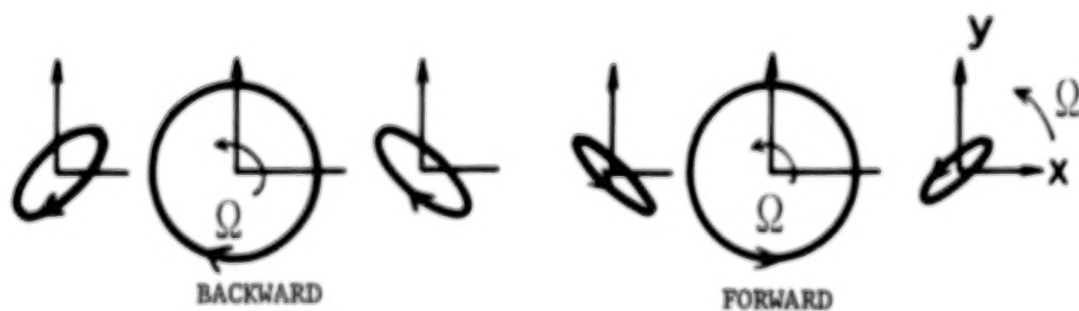
Figure 4. - Whirl orbit.

116
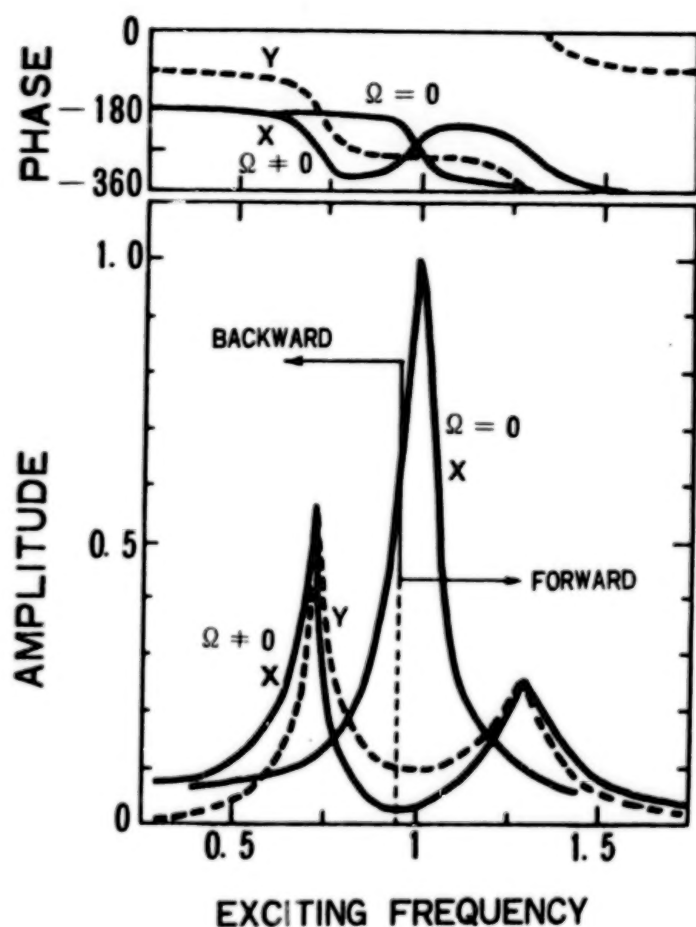
Figure 5. - Response curve in
harmonic excitation.
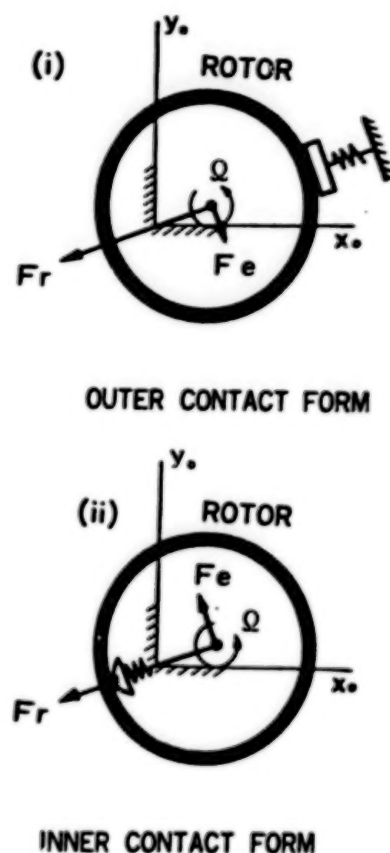
Figure 6. - Stopper with clearance.
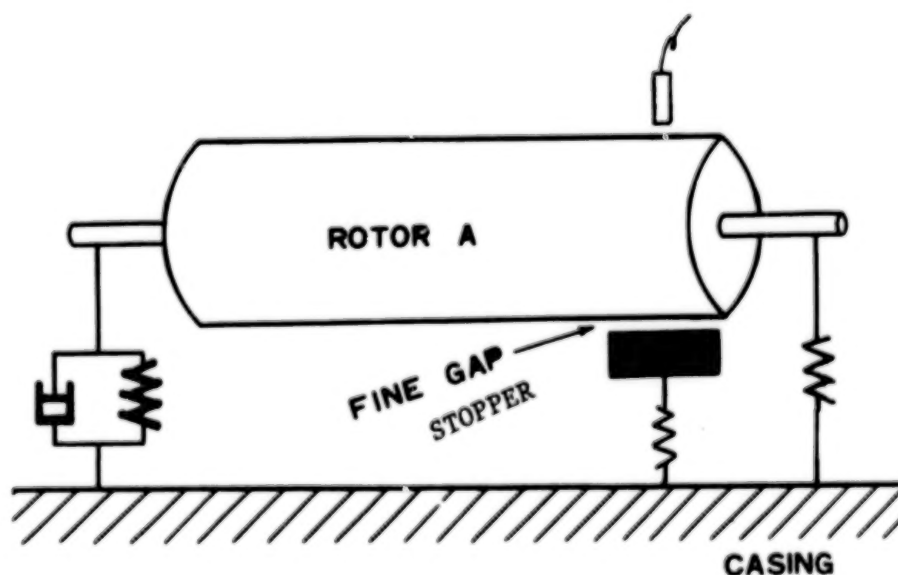
Figure 7. - A high speed rotor.

117
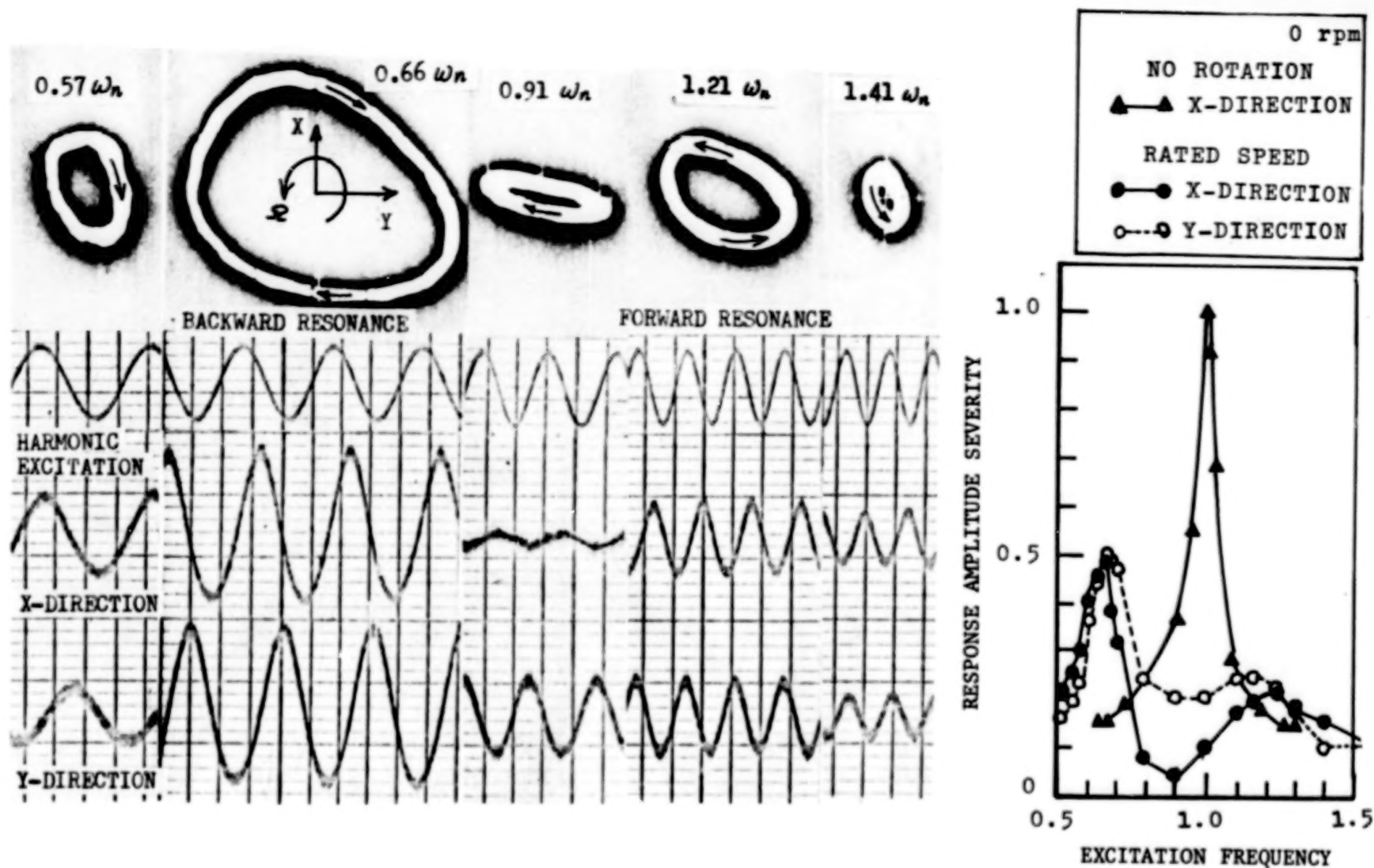
Figure 8. - Response of high speed rotor in harmonic excitation.
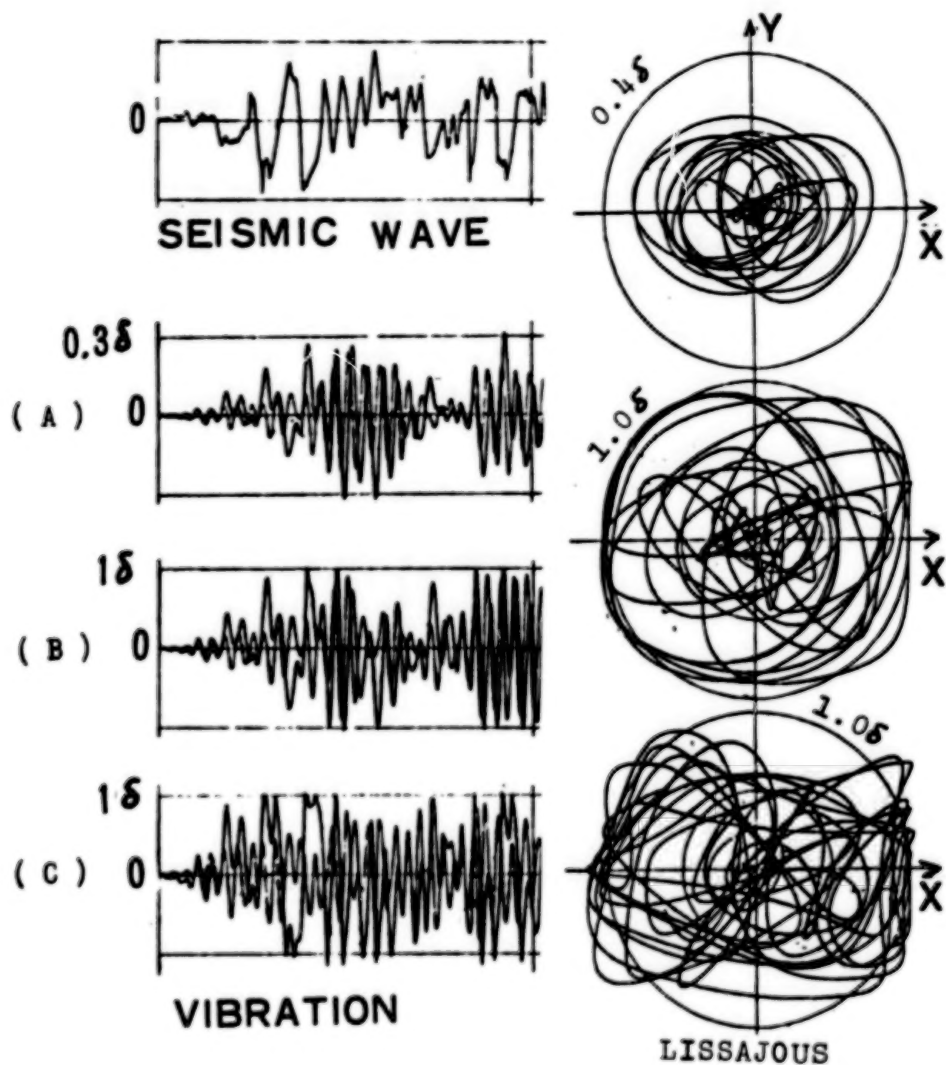
Figure 9. - History response analysis (one directional stopper).
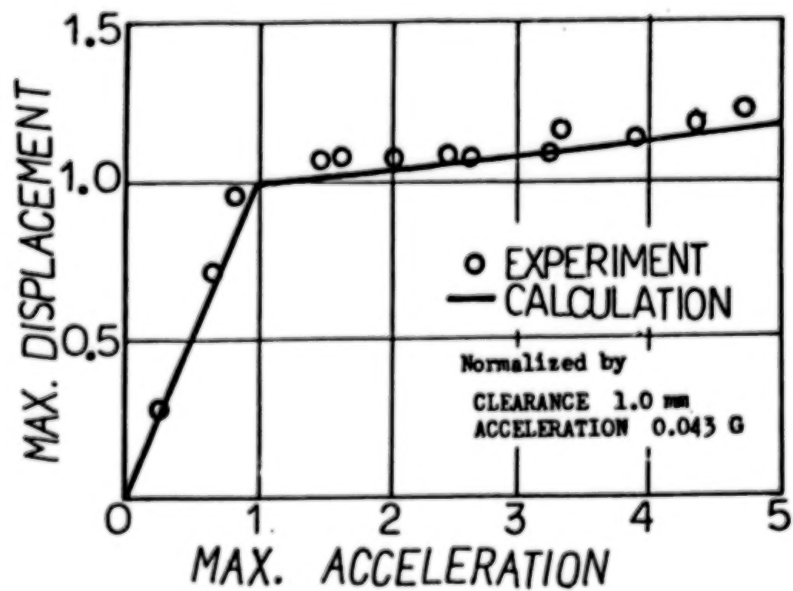
Figure 10. - Suppression of rotor vibration by stopper.

BEST DOCUMENT AVAILABLE
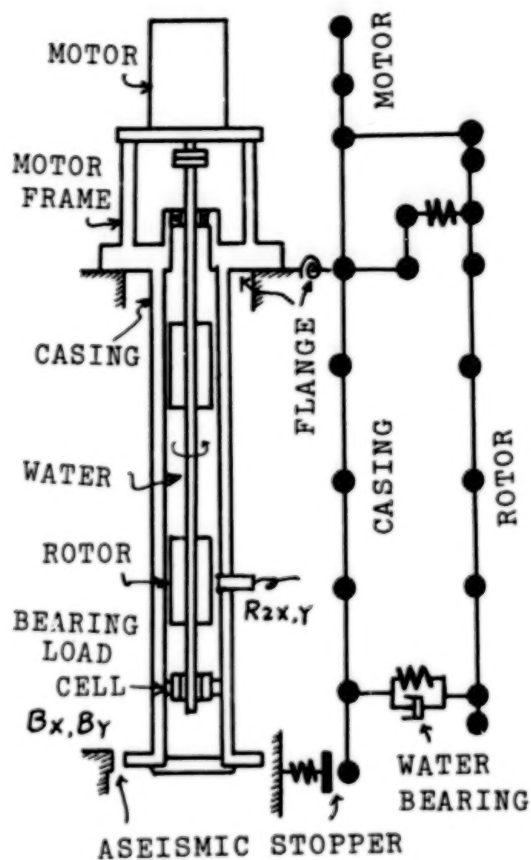
Figure 11. - A pump model rotor and its beam model.
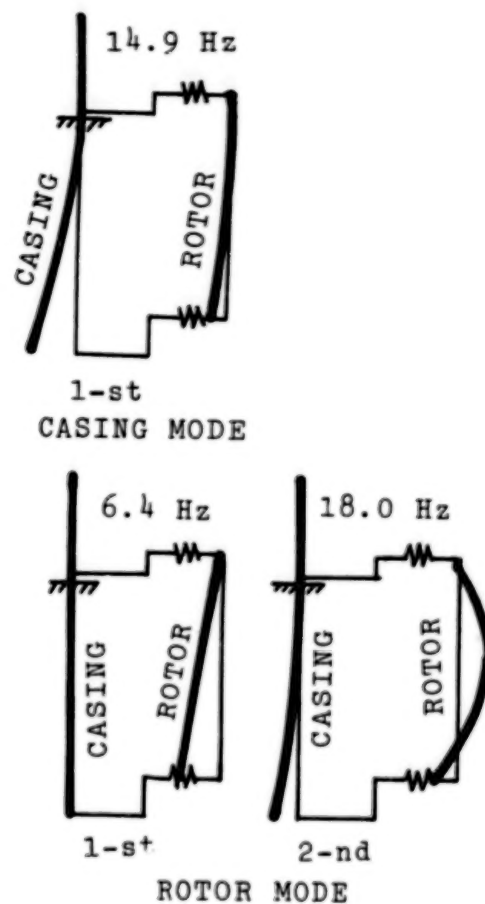
Figure 12. - Free eigen modes.
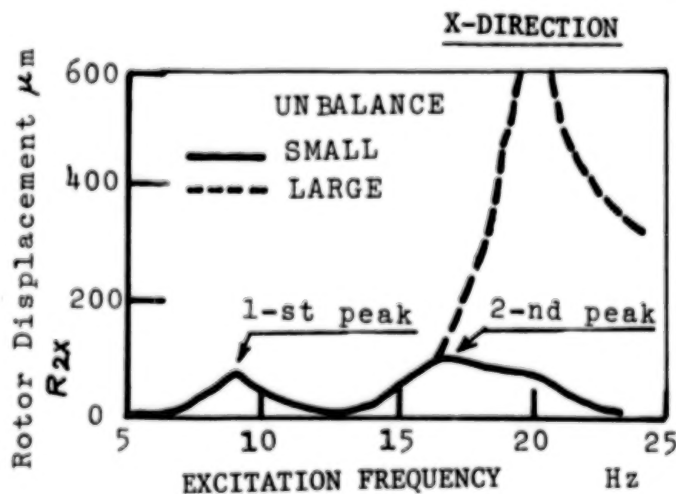
Figure 13. - Influence of unbalance.
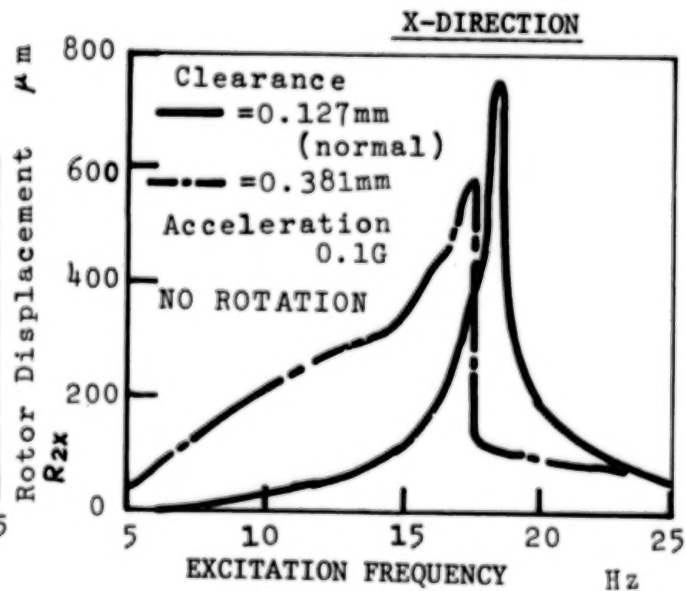
Figure 14. - Influence of clearance in water bearing.

120
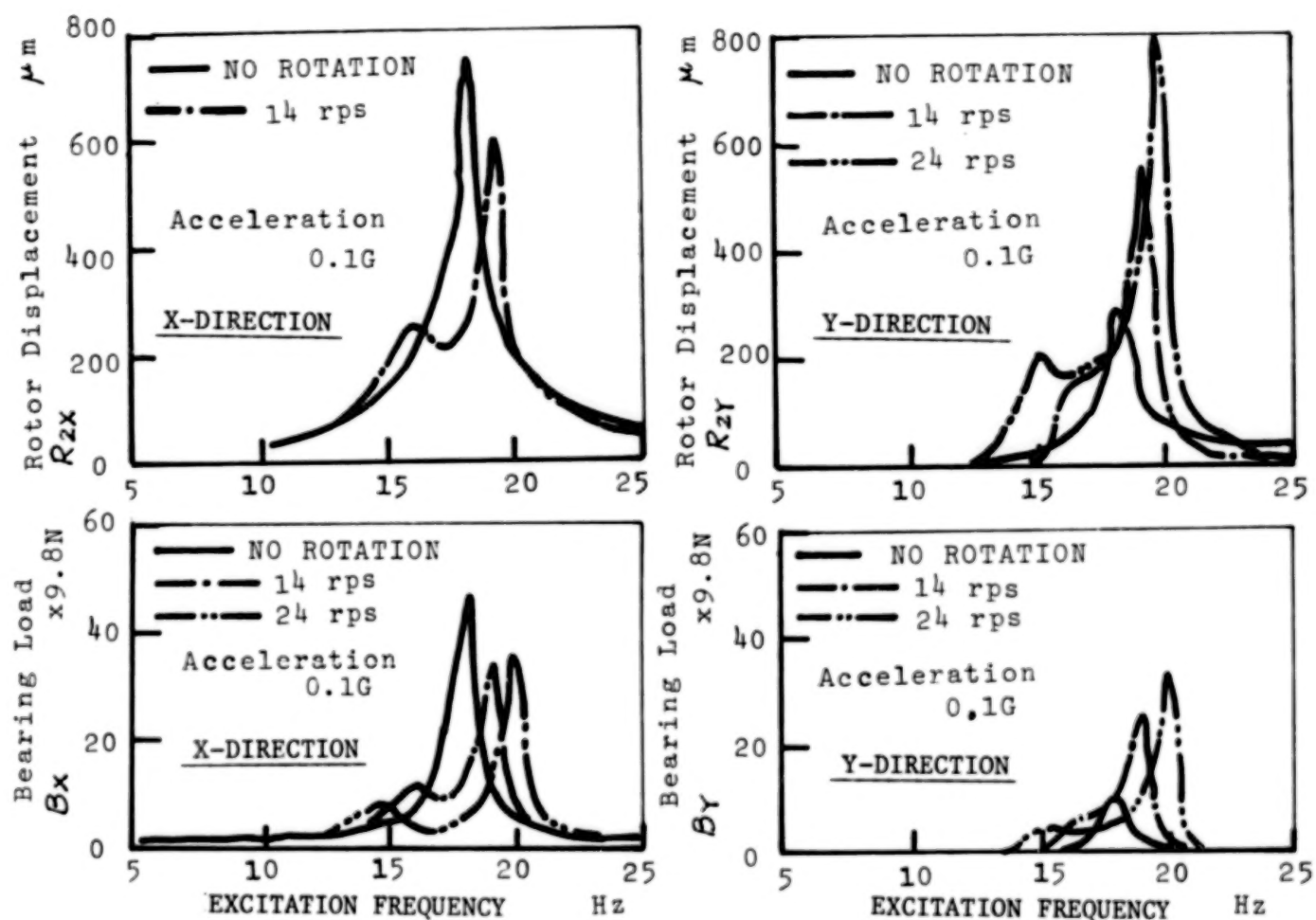
Figure 15. - Influence of rotational speed.
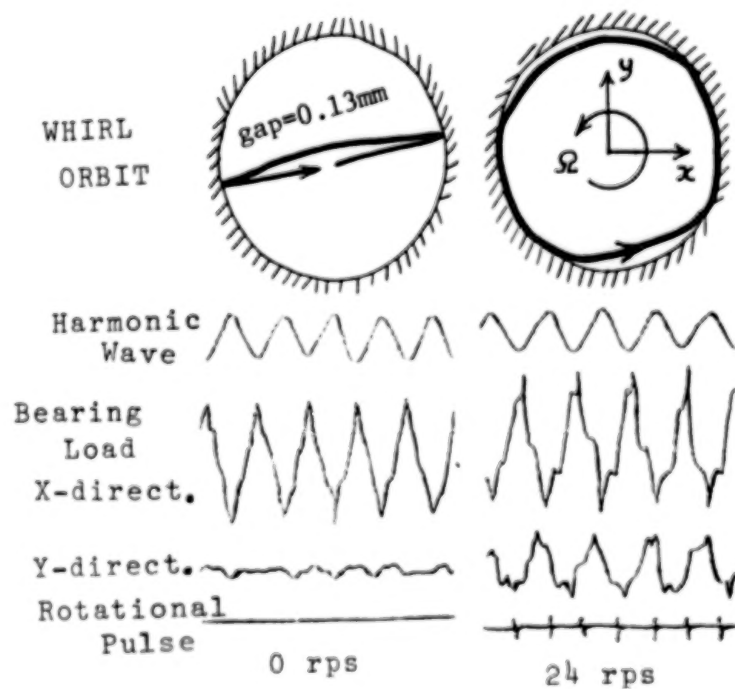
Figure 16. - Waveforms and whirl orbits.
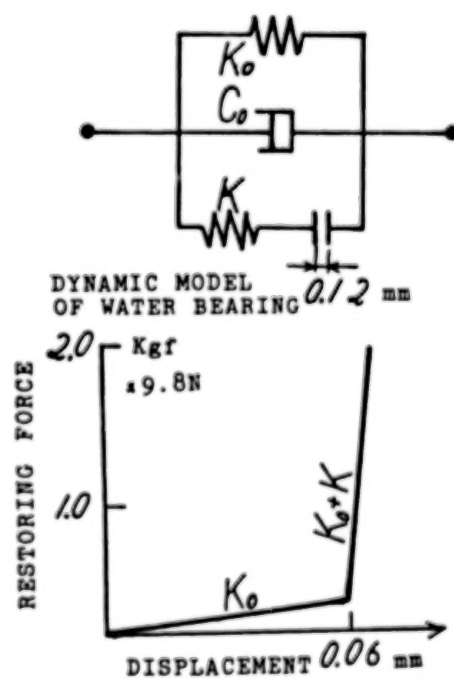
Figure 17. - Restoring force in water bearing.

121
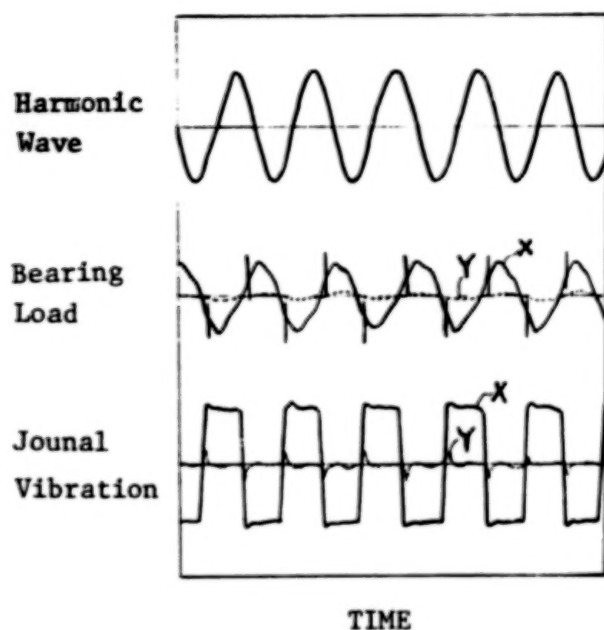
Figure 18. - Response waveforms near a resonance.
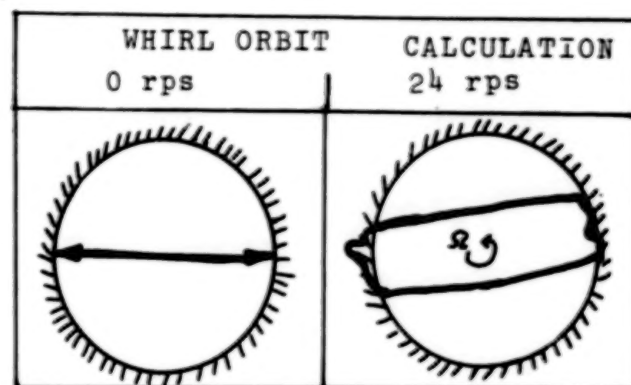
Figure 19. - Whirl orbit in resonances.
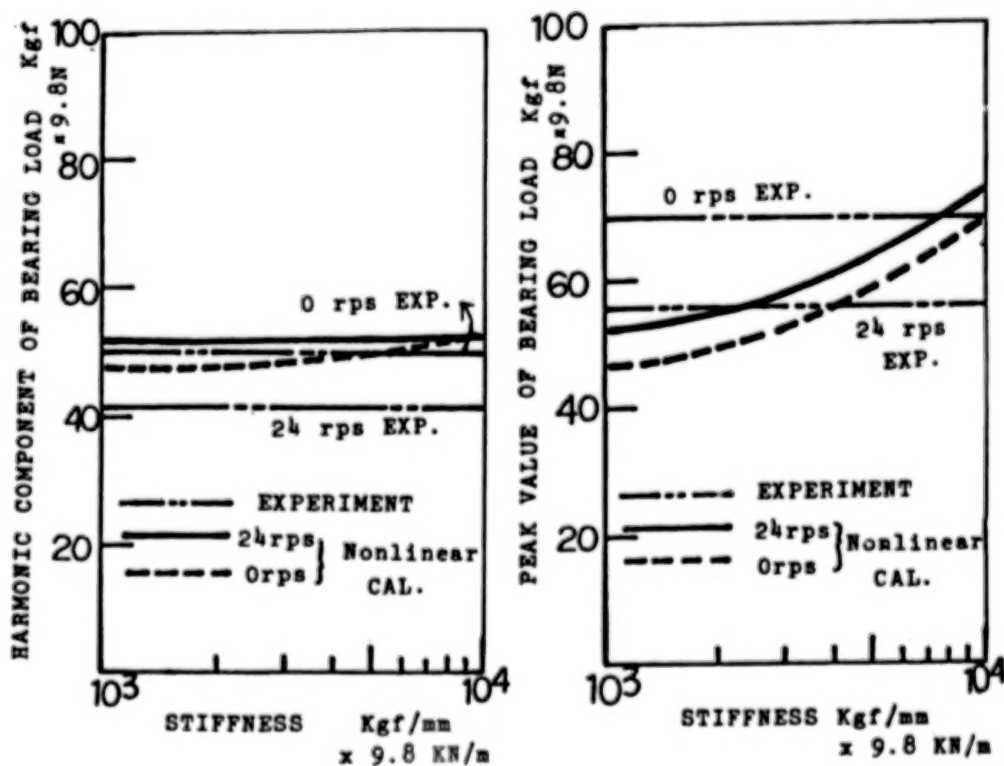
Figure 20. - Comparison of bearing dynamic load.

122

APPENDIX

Time History Response Analysis of Nonlinear Rotor-Bearing System
by Quasi-Modal Technique

1.   INTRODUCTION

In structure dynamics with many degrees of freedom of motion, time history response analysis involves two integration methods. One of them is direct integration and the other is modal. Generally speaking, the former is accurate, but not convenient for large structure systems because too much computational time is required. The latter is effective due to the great reduction of freedom of motion by the normal transformation, but its accuracy depends how many eigen vectors are introduced in the modal matrix. Each integration method inevitably contains its own advantages and disadvantages.

These methods are also applied for non stationary rotor vibration analysis in rotor dynamics as well as in analyzing the gyroscopic effect and large damping force in bearings. The authors have already presented the special form of the orthogonality condition in rotor dynamics and the modal integration technique for analyzing non-stationary vibration of a rotor in a system with linearity or somewhat weak non-linearity.

In many cases, the modal technique is more convenient and powerful than the direct one. However, even the modal technique is not perfect and is inconvenient for time history response analysis in a rotor-bearing system with strong nonlinear boundary conditions.

However, in our experience it is very difficult to numerically simulate such a vibration mode -changing due to rubbing- by the modal integration technique, which guarantees only a linear system, and not a nonlinear one. The modal technique is limited to linear analysis and its forcible application to a nonlinear system is essentially unreasonable.

In this study a new method, which is exclusively applied for nonlinear analysis is developed on the basis of modal synthesis and the substructure method. A quasi-modal transformation is defined considering gyroscopic force and damping force for a general rotor system. The integration method is then introduced by the quasi-modal technique.

NOMENCLATURE

A, B : matrices after the quasi modal transformation
C : damping matrix
c^* : equivalent damping coefficient for the inner system
C_{g_*} : gyroscopic matrix
c_g^* : equivalent gyroscopic effect for the inner system
$F = [F_1, Q_2]^t$: external force
$F_1(t)$: external force acting upon the inner system
F_s : force on the quasi modal coordinate system
$i = \sqrt{-1}$: imaginary unit
K : stiffness matrix
k^* : equivalent stiffness for the inner system
M : mass matrix

$Q(z_2, \dot{z}_2, t)$: resistance force acting upon the boundary point
$S=[s_1, s_{2v}, s_{2d}]^t$: state vector on the quasi-modal coordinate system
s_1 : weighting value corresponding to ϕ mode
$s_{2d}=z_2$: weighting value corresponding to δ mode, i.e. rotor displacement of the boundary point
$s_{2v}=\dot{z}_2$: weighting value corresponding to ξ mode, i.e. rotor velocity of the boundary point
t : time
$z=[z_1, z_2]^t$: rotor displacement vector in a complex form ($z=x+iy$)
z_1 : rotor displacement vector of the inner system
z_2 : rotor displacement of the boundary point
δ : deflection mode generated by the forced displacement
$\lambda=\alpha+iq$: complex eigenvalue
ξ : deflection mode generated by the forced velocity
Φ : matrix of the quasi-modal transformation
ϕ : eigen mode of the inner system
ψ : eigen mode of the entire system including the inner system and the boundary point
Ω : rotational speed
δ_{ij} : Dirac's function

2. QUASI-MODAL TRANSFORMATION

Equation of motion

This study deals with the rotor vibration in an entire system, including bearings and disks, as shown in Fig.1. The rotor displacement is measured on the coodinate system of O-XYH which is fixed in the space. The complex form of the rotor displacement is denoted here by $z=x+iy$ for the displacements in the X-direction and Y-direction of x and y, respectively. The equation of motion of a rotor is written as:

$$M\ddot{z}+i\,\Omega C_g\dot{z}+K_f z+K_b\bar{z}+C_f\dot{z}+C_b\dot{\bar{z}}=F \qquad (1)$$

This equation represents the elliptical whirl motion of a rotor supported by general bearings with asymmetrical dynamic properties. In the case of the circular whirl motion due to symmetrical dynamic properties,
where

$$k_{xx}=k_{yy} \quad k_{xy}=-k_{yx} \quad C_{xx}=C_{yy} \quad C_{xy}=-C_{yx} \quad ,$$

the equation of motion becomes little simpler, and can be written as:

$$M\ddot{z}+i\Omega\,C_g\dot{z}+Kz+C\dot{z}=F \qquad (2)$$

To simplify the description, the vibration of a vertically suspended rotor with symmetrical bearing dynamics is studied first and a new quasi-modal technique is presented. This technique is also extended to general rotor vibration including asymmetrical bearing dynamics, but the explanation is omitted in this paper.

Discrimination of boundary point and inner system

The cantilever type of rotor, as shown in Fig.2, is selected in order to clearly explain the concept of this new technique. In this rotor system, the left side is a fixed point which is clearly a boundary location. A bearing with non-

linearity is located on the right side of the rotor. It is assumed that the bearing dynamic properties are not constant.

This rotor system is a typical example of a system having one changing boundary condition. The right side is thus designated as a nonlinear boundary point, denoted by z_2. The rest of the rotor system is designated as a linear inner system, and its displacement vector is denoted by z_1.

A resistance force of Q_2 acts upon the boundary point, and an external force of F_1 is distributed on the inner system of the rotor.

The equation of motion (2) is rewritten, inserting displacements z_1 and z_2, as :

$$\begin{bmatrix} M_1 & 0 \\ 0 & M_2 \end{bmatrix}\begin{bmatrix} \ddot{z}_1 \\ \ddot{z}_2 \end{bmatrix} + i\Omega \begin{bmatrix} C_{g1} & 0 \\ 0 & C_{g2} \end{bmatrix}\begin{bmatrix} \dot{z}_1 \\ \dot{z}_2 \end{bmatrix} + \begin{bmatrix} K_{11} & K_{12} \\ K_{21} & K_{22} \end{bmatrix}\begin{bmatrix} z_1 \\ z_2 \end{bmatrix} + \begin{bmatrix} C_1 & 0 \\ 0 & C_2 \end{bmatrix}\begin{bmatrix} \dot{z}_1 \\ \dot{z}_2 \end{bmatrix} = \begin{bmatrix} F_1(t) \\ Q_2(z_2,\dot{z}_2,t) \end{bmatrix} \equiv F \qquad (3)$$

Where, subscripts 1 and 2 mean the inner system and the boundary point, respectively.

Transformation modes

An arbitrary vibration mode shape in the system with a changing boundary condition can be arranged by the synthesis of three kinds of special mode shapes, as shown in Fig.3. The quasi-modal transformation matrix thus consists of the three modes: ϕ , δ and ξ . The first two modes, ϕ and δ , are used in the conventional methods, called the substructure technique or modal synthesis. The third mode, ξ ,is introduced in this study for the first time and its necessity is emphasized.

ϕ mode

This is the complex eigen mode of the restricted system on the boundary point, as shown Fig.3(a). It is obtained by damped eigenvalue solving with respect to the M_1-C_{g1}-K_{11}-C_1 system.
The equation of motion of the inner system becomes

$$M_1\ddot{z}_1 + i\Omega\, C_{g1}\dot{z}_1 + K_{11}z_1 + C_1\dot{z}_1 = 0 \qquad (4)$$

and the free vibration solution is assumed to be given by the following formula with the ϕ mode,

$$z = \phi\, e^{\lambda t} \qquad (5)$$

The orthogonality condition with respect to these eigen vectors is derived as:

$$\begin{bmatrix} \lambda_j \phi_j \\ \phi_j \end{bmatrix}^t \begin{bmatrix} -M_1 & 0 \\ 0 & K_{11} \end{bmatrix}\begin{bmatrix} \phi_k \lambda_k \\ \phi_k \end{bmatrix} = \delta_{jk}$$

$$\begin{bmatrix} \lambda_j \phi_j \\ \phi_j \end{bmatrix}^t \begin{bmatrix} i\Omega\, C_{g1}+C_1 & K_{11} \\ K_{11} & 0 \end{bmatrix}\begin{bmatrix} \phi_k \lambda_k \\ \phi_k \end{bmatrix} = \delta_{jk}$$

(6)

δ mode

This is the deflection mode when the rotating shaft is subject to forced displacement on the boundary point,as shown in Fig.3(b). Under a load Q_2^{*}, the

relationship between the shaft stiffness and the displacement is expressed as:

$$\begin{bmatrix} K_{11} & K_{12} \\ K_{21} & K_{22} \end{bmatrix} \begin{bmatrix} z_1 \\ z_2 \end{bmatrix} = \begin{bmatrix} 0 \\ Q_2^\bullet \end{bmatrix} \tag{7}$$

where $Z_1 = \delta$ is the deflection mode
and $Z_2 = 1$ is the forced displacement on the boundary point. This load is equivalent to the shaft stiffness, when the inner system is viewed from the nonlinear boundary point, and is determined by the following relationship,

$$k^\bullet = Q_2^\bullet = K_{12}\delta + K_{22} \tag{8}$$

ξ mode

This is the deflection mode when the rotating shaft is subject to forced velocity on the nonlinear boundary point, as shown in Fig.3(c). This mode shape has not been used heretofore.

Under a load $Q_2^\bullet$, which generates the forced velocity, the relationship including the gyroscopic force and the damping force up to the first-order differential equation of Eq.(3) becomes

$$\begin{bmatrix} i\Omega C_{g1} + C_1 & 0 \\ 0 & i\Omega C_{g2} + C_2 \end{bmatrix} \begin{bmatrix} \dot{z}_1 \\ \dot{z}_2 \end{bmatrix} + \begin{bmatrix} K_{11} & K_{12} \\ K_{21} & K_{22} \end{bmatrix} \begin{bmatrix} z_1 \\ z_2 \end{bmatrix} = \begin{bmatrix} 0 \\ Q_2^\bullet \end{bmatrix} \tag{9}$$

Assuming the deflection of a nonlinear boundary point with

$$\dot{Z}_2 = 1 \qquad Z_2 = t, \tag{10}$$

the deflection mode shapes of the inner system with the form

$$\dot{Z}_1 = \delta \quad , \quad Z_1 = \delta t + \xi \tag{11}$$

are determined by the following relationship

$$\xi = i\Omega \xi_g + \xi_c \tag{12}$$

where,

$$\xi_g = -K_{11}^{-1} C_g ; \quad \delta = K_{11}^{-1} C_{g1} K_{11}^{-1} K_{12}$$

$$\xi_c = -K_{11}^{-1} C_1 \quad \delta = K_{11}^{-1} C_1 K_{11}^{-1} K_{12}$$

Furthermore, this load $Q_2^\bullet$ is equal to the sum of equivalent gyroscopic effect $c_g^\bullet$ and equivalent damping coefficient $c^\bullet$, when the inner system is viewed from the boundary point. The latter values are determined by the following formulas :

$$c_g^\bullet = C_{g2} + \delta^t C_{g1} \, \delta \tag{13}$$

$$c^\bullet = C_2 + \delta^t C_1 \, \delta \tag{14}$$

Where,

$$Q_2^\bullet = k^\bullet t + i\Omega c_g^\bullet + c^\bullet$$

It is obvious in Eq.(12) that the ξ mode is generated by the gyroscopic force, reflecting the spin effect of the rotor, and by strong damping forces in the bearings. Thus these three modes must be considered in analyzing rotor dynamics. For ordinary structure dynamics, however, the third mode is not needed for the vibration analysis of nonrotating structures with negligible damping forces. This is why the conventional modal synthesis techniques applied to structure dynamics employ only the eigen mode ϕ of a restricted system and the deflection mode δ at a forced displacement. The new technique presented here for analyzing rotor dynamics is thus based upon a more general concept, and includes the usual substructure and modal synthesis techniques as well as the ξ mode.

Transformation of coordinate system

The quasi-normal transformation matrix is defined by analogy with the modal transformation, as follows :

$$\begin{bmatrix} \dot{z} \\ z \end{bmatrix} = \begin{bmatrix} \dot{z}_1 \\ \dot{z}_2 \\ z_1 \\ z_2 \end{bmatrix} = \begin{bmatrix} \phi\lambda & \delta & 0 \\ 0 & 1 & 0 \\ \phi & \xi & \delta \\ 0 & 0 & 1 \end{bmatrix} \begin{bmatrix} s_1 \\ s_{2v} \\ s_{2d} \end{bmatrix} \equiv \phi s \tag{15}$$

The equation of motion of Eq.(2) is rewritten using a state equation :

$$\begin{bmatrix} -M & 0 \\ 0 & K \end{bmatrix} \begin{bmatrix} \ddot{z} \\ \dot{z} \end{bmatrix} = \begin{bmatrix} i\,\Omega\,C_g + C & K \\ K & 0 \end{bmatrix} \begin{bmatrix} \dot{z} \\ z \end{bmatrix} + \begin{bmatrix} -F \\ 0 \end{bmatrix} \tag{16}$$

Putting the transformation relationship of Eq.(15) into the state equation of Eq. (16), and premultiplying the transposed matrix of the transformation matrix ϕ , a simple differential equation with respect to the quasi-modal coordinate of s vector is obtained as :

$$B\dot{s}=As-F_s \tag{17}$$

where,

$$s=[s_1,s_{2v},s_{2d}]^t$$

$$B=\begin{bmatrix} B_{11} B_{12} & 0 \\ B_{21} B_{22} & 0 \\ 0 \quad 0 & k^{\bullet} \end{bmatrix} \quad A=\begin{bmatrix} A_{11} & 0 & 0 \\ 0 & i\,\Omega\,c_g^{\bullet}+c^{\bullet} & k^{\bullet} \\ 0 & k^{\bullet} & 0 \end{bmatrix} \quad F_s=\begin{bmatrix} (\phi\lambda)^t F_1 \\ \delta^t F_1 + Q_2 \\ 0 \end{bmatrix}$$

The structures of the transformed matrices B and A of Eq.(17) are shown in Fig.4. The matrices B_{11} and A_{11} contain zero elements in the off-diagonal part, because the eigen vectors of the linear inner system are orthogonal with each other, and these matrices become diagonal. The rest of B matrix, $B_{12}=B_{21}^t$ is equal to the nonzero elements because there is no orthogonality in the relationship between eigen vector ϕ and deflection modes δ and ξ . All off-diagonal elements of the coefficient matrices B and A are not zero, but many parts of them are. Consequently, this transformation can not give a theoretically perfect diagonalization of the transformed matrices, it does facilitate almost perfect diagonalization with non-zero elements at the edge of matrix B. This transformation technique is much closer to the modal one ; hence we call it the quasi-modal technique.

It should be noted that the almost perfect diagonalization with the non-zero

edge can not be accomplished without the ξ mode. That is why we introduce the ξ mode for this new quasi-modal technique.

In state equation (17) obtained by a quasi-modal transformation, the state vector s contains physical coordinates of $\dot{z}_2=s_{2v}$ and $z_2=s_{2d}$, corresponding to the velocity and displacement on the boundary point, respectively. And the resistance force Q_2 on the boundary point is also included in the force vector F_S without being reformed. These quantities related to the boundary point are maintained by the same description in the physical coordinate system. Therefore, the superposing operation is guaranteed after the quasi-normal transformation, as in the same manner as the FEM operation.

The degree of state equation (17) is equal to the degree of the modal transformation for the linear inner system plus twice the number of boundary points. Consequently the scale of the problem is greatly reduced, as compared with Eq.(3) or Eq.(17).

3.   TIME HISTORY RESPONSE ANALYSIS

Hybrid Integration

The integration of the state equation (17) on the quasi-modal coordinate system gives the time history response under an external excitation $F_1(t)$.

The vector s_1 of the quasi-modal vector s indicates the weighted values corresponding to the eigen modes of the inner coordinate system. Thus, it can be said that the inner system is processed by the well known modal integration method.

On the other hand, the remaining elements of s_{2v} and s_{2d} in the quasi-modal vector s equal the physical coordinates with the relationship

$$z_2=s_{2d} \qquad \dot{z}_2=s_{2v} \qquad\qquad\qquad\qquad (18)$$

Thus, the boundary points are handle by physical quantities even in post-transformation, and are easily processed by the direct integration method.

Therefore, integration with respect to the quasi-modal coordinate s is equivalent to hybrid integration where modal and direction methods are mixed, as shown in Fig.5. The two conventinal methods have their own advantages and disadvantages, but the advantages of both methods are guaranteed in this new method. Thus the new technique is highly applicable to nonlinear vibration response analysis.
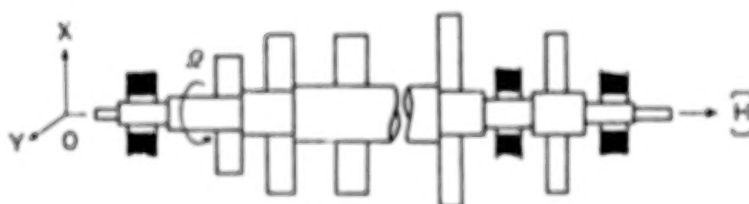
Figure 1. - Rotor-bearing system.

128
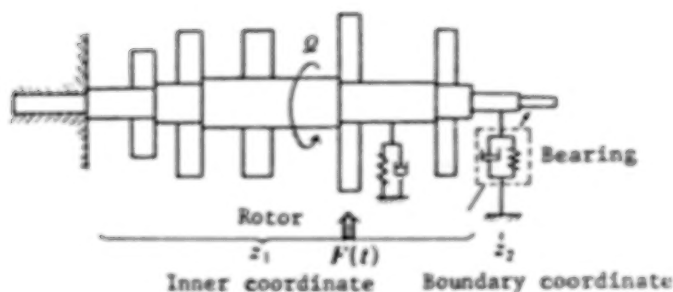
Figure 2. - Boundary point and inner system.

Physical system

Constrained system free vibration Modes ϕ_j (a)

Unit displacement Mode δ (b)

Unit velocity Mode ξ (c)

$$\begin{bmatrix} M_1 & \\ & M_2 \end{bmatrix}\begin{bmatrix} \ddot{z}_1 \\ \ddot{z}_2 \end{bmatrix} + i\Omega\begin{bmatrix} C_{11} & \\ & C_{22} \end{bmatrix}\begin{bmatrix} \dot{z}_1 \\ \dot{z}_2 \end{bmatrix} + \begin{bmatrix} K_{11} & K_{12} \\ K_{21} & K_{22} \end{bmatrix}\begin{bmatrix} z_1 \\ z_2 \end{bmatrix} + \begin{bmatrix} C_1 & \\ & C_2 \end{bmatrix}\begin{bmatrix} \dot{z}_1 \\ \dot{z}_2 \end{bmatrix} = \begin{bmatrix} F(t) \\ Q_2(z_2,\dot{z}_2,t) \end{bmatrix}$$

mass   gyro   stiffness   damping   force

Quasi normal system

Figure 3. - Transformation modes.

Figure 4. - Quasi normal coordinate system.

Direct Intergration
$z(t) = \int \ddot{z}(t)dt$
Accurate
  Large computational time and cost
Inconvenient
Non-linearity is OK

Model Intergration
$a(t) = \int \dot{a}(t)dt$
$z = [\phi]\,a(t)$
Convenient Economical
Non-linearity is NG.

Hybrid Intergration

$\dot{z}_d = z_r$

Q_2 : non-linear
Convenient Economical
Non-linearity is OK
Difficult Programming

Figure 5. - Hybrid intergration.

129

LINEAR FORCE AND MOMENT EQUATIONS FOR AN ANNULAR SMOOTH

SHAFT SEAL PERTURBED BOTH ANGULARLY AND LATERALLY*

J. Fenwick
Rocketdyne Division
Rockwell International
Canoga Park, California 91304

R. DiJulio, M. C. Ek, R. Ehrgott,
H. Green, and S. Shaolian
California State University at Northridge
Northridge, California 91330

SUMMARY

Coefficients are derived for equations expressing the lateral force and pitching moments associated with both planar translation and angular perturbations from a nominally centered rotating shaft with respect to a stationary seal.

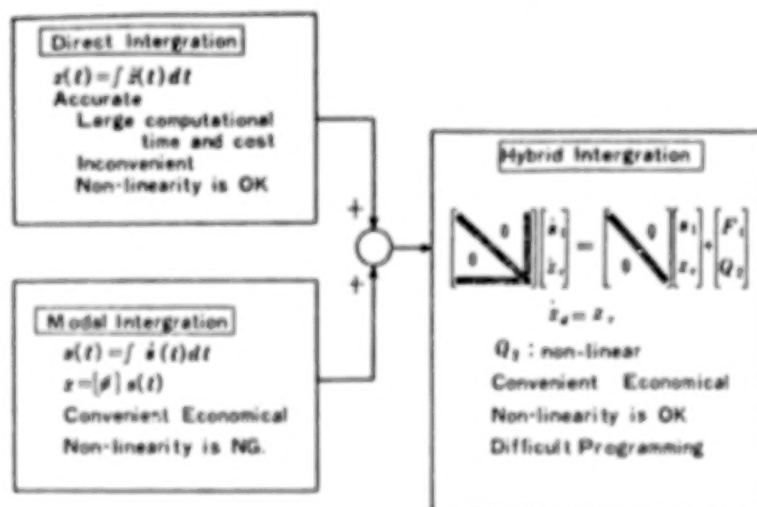The coefficients for the lowest order and first derivative terms emerge as being significant and are of approximately the same order of magnitude as the fundamental coefficients derived by means of Black's equations. Second derivative, shear perturbation, and entrance coefficient variation effects are adjudged to be small.

The outcome of the investigation delineated in this report defines the coefficients of the equations:

$$\tau = A\varepsilon + B\dot{\varepsilon} + C\ddot{\varepsilon} + D\alpha + E\dot{\alpha} + F\ddot{\alpha}$$
$$\bar{F} = a\varepsilon + b\dot{\varepsilon} + c\ddot{\varepsilon} + d\alpha + e\dot{\alpha} + f\ddot{\alpha}$$

(1)

The assumptions utilized, mathematical means employed, and conclusions derived thereby will be the objective of this report.

The effects of the additional terms upon a typical rotordynamic system are presented.

INTRODUCTION

The factors leading to increasing pressures, speeds, and temperatures in jet engines, high performance pumps, and turbomachinery for rocket engine applications have been widely noted in the literature, e.g., Rothe (ref. 1).

The increased incidence of stability problems as a function of increased power density, particularly the phenomenon of "subsynchronous whirl," has been noted by many authors.

Among the design features strongly contributing to this phenomenon in a wide variety of high-powered turbomachinery are annular shaft seals. These seals are in general utilized to separate regions of high and low gas or liquid pressure. In addition to their strong effects as pseudo bearings and destabilizing devices, they offer, when

---

*All work performed under NASA Marshall Space Flight Center Contract NAS8-27980

properly configured, in many designs the only real possibility for the introduction of damping in rotating systems. Various authors have delineated the extent of both the problems and remedies surrounding these possibilities; for example, Alford (ref. 2), Ek (ref. 3), Childs (ref. 4), and Gunter (ref. 5).

A very significant part of the understanding of the dynamic behavior of annular smooth shaft seals has come from the pioneering work of Henry Black of Heriott Watt University, Edinburgh, United Kingdom, who in a series of papers (refs. 6-12) defined the effect of shaft displacements with both long and short seal assumptions up to and including the second derivative of the displacement. A number of workers have extended his work significantly, these being Jensen (refs. 7 and 8), Hirs (ref. 13), Childs (ref. 4), and Alliare (refs. 5 and 14). The recent trend is to shift to a modification of the bulk flow theory to define more closely a set of equations approximating experimental results [Hirs (ref. 13)].

On many significant recent problems, e.g., the problem on the high-speed rotating machinery for the Space Shuttle Main Engine (SSME) [Ek (ref. 3)], Black's equations were the only analytical representation available for significant computer modeling. Present efforts to extend this work include continuing work by Allaire (ref. 14) at the University of Virginia, Childs (ref. 4) at Texas A&M, and Fleming (ref. 12) of NASA Lewis, as well as experimental work with liquid oxygen and hydrogen at the Rocketdyne Division of Rockwell International.

Figure 1. - Orientation of references axes for seal equations.

This study represents a departure from the general approach being carried on by other investigators in that it explores the effect of pitching moments and angulation in the seal, as shown schematically in Fig. 1.
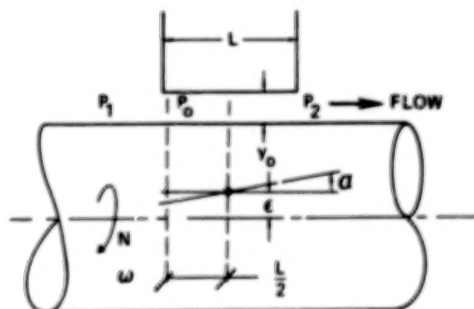
NOMENCLATURE

The nomenclature in general is that employed by Black (ref. 6) and specific nomenclature is introduced as comments in the body of the nomenclature table, in the figures, or presented below. Additional functions are delineated in the text as required.

A-F, a-f = coefficients in force equations

b = gap thickness, $y(x,t)$, inches

D = d/dt, differential operation with regard to time

$\bar{E}$ = shaft elastic modulus

$\bar{F}$ = force on seal, total due to perturbations

I = shaft area moment of inertia, m^4 ($in.^4$)

K = effective bearing spring rate, N/m (lb/in.)

F_n = force on seal, n is defined in the text

H = $PR\pi\sigma/6\lambda(1+\xi+2\sigma)$, general coefficient for moment and force equations $\xi = 0.5$

H_1 = $PR\pi\sigma L/\lambda\gamma$

θ = $\partial F/\partial\varepsilon$, N/m^3 (lb/in.^{3})

ν = kinematic viscosity, m^2/s (in.^{2}/sec)

131

L $\;=\;$ length of seal, m (in.)

$\ell\;=\;$ componen⁺ spacing on rotor, m (in.)

N $\;=\;$ speed of rotation, rpm

P $\;=\;$ total pressure difference across seal, Pa (lb/in.^{2})

p $\;=\;$ pressure within passage, p(x,t), Pa (lb/in.^{2})

R $\;=\;$ shaft radius, m (in.)

$R_a\;=\;$ axial Reynolds No. $2Vy_0/\nu$

$R_r\;=\;$ rotating Reynolds No. $R\omega y_0/\nu$

T $\;=\;$ passage time, L/V, seconds

t $\;=\;$ time, variable, seconds

u $\;=\;$ axial fluid velocity, u(x,t), m/s (in./sec)

V $\;=\;$ mean fluid velocity, m/s (in./sec)

W $\;=\;$ weight of rotor, kg (lb)

x $\;=\;$ axial distance, independent variable, m (in.)

y,z $\;=\;$ radial displacement of rotor mass

$\alpha\;=\;$ angular displacement

$\gamma\;=\;$ $1.5 + 2\sigma$, $\xi = 0.5$

$\delta\;=\;$ weight density, kg/m^3 (lb/m^3)

$\varepsilon\;=\;$ lateral displacement, Y(t), m (in.)

$\lambda\;=\;$ friction coefficient, $\Delta p = \dfrac{\lambda L}{r_n}\dfrac{V^2}{2g}$,

$$r_n = \frac{area}{wetted\ perimeter}, \frac{b}{2}$$

$$= 0.079\,R_a^{-1/4}\left[1 + \left(\frac{7}{8}\frac{R_r}{R_a}\right)^2\right]^{3/8}$$

loss factor per Yamada (ref. 15)

$\mu jk\;=\;$ functions of σ, coefficients for the perturbation terms

$\mu\;=\;$ absolute viscosity, Pa-s (lbf-sec/in.^{2})

$\xi\;=\;$ entry loss coefficient = 0.5 nominally

$\rho\;=\;$ mass density, $\dfrac{\delta}{g}$, kg-s^2/m^4 (lb-sec^2/in.^{4})

$\sigma\;=\;$ $\lambda L/y_0$

$\tau\;=\;$ pitching moment taken about $x = \dfrac{L}{2}$, N-m (lb-in.)

$\tau_0\;=\;$ pitching moment at x = 0, N-m (lb-in.)

$\phi\;=\;$ $\partial F/\partial\alpha$, N/rad (lb/rad)

$\chi\;=\;$ $\partial\tau/\partial\varepsilon$, N (in.-lb/in.)

$\psi\;=\;$ $\partial\tau/\partial\alpha$, N-m (in.-lb/rad)

$\omega\;=\;$ circular frequency, rad/sec

$\bar{\omega}\;=\;$ design speed, rad/sec

ASSUMPTIONS

In the following equations, assumptions are made as follows:

1. The system (shaft within seal) is assumed to be centered.

2. Perturbations about the nominal centered position are small.

3. Whenever two second order terms are multiplied, they are assumed to be higher order, i.e., the product approaches zero.

4. Short seal theory is assumed, i.e., perturbations have negligible effect in the tangential direction.

5. The period of time required for a particle of fluid to travel from the inlet to the discharge is small compared to the frequency of the system.

6. There is no change of properties in the working fluid as it passes through the process.

7. The entrance coefficient into the seal is assumed to be 0.5.

8. The effect of fluid shear variation on the shaft moment is neglected in the fundamental equations.

9. Total linearity is assumed, i.e., any of the effects can be added individually with no interdependence between individual effects.

10. Tangential fluid velocity equal to one-half the shaft tangential velocity is developed immediately at the seal entrance.

11. Perturbations are planar; however, Yamada's (ref. 15) work in defining λ for rotating shaft effects applies.

APPROACH

The process of deriving the fundamental equations departs from that used by Black (ref. 6) in three important respects: (1) clearance is expressed as a function of both x and α, (2) the equations for continuity and velocity are completely rewritten as a consequence of (1), and (3) the order of integration is reversed. In addition, the first derivations lead to a result in which all perturbations, moments, and forces are taken at x = 0. This is done because of great simplification of the boundary conditions. These are then translated to perturbations about x = L/2, and in the case of the moments, τ_o is translated to $\tau|_{L/2}$. Explanations of each step and necessary symbol derivations occur as needed in the text.

DERIVATION OF FUNDAMENTAL EQUATIONS

We first consider two plates of length L and unit width, nominally y in. apart, with the top plate fixed, the bottom plate perturbed: perturbations are positive upward and counterclockwise, as are forces and moments. Flow is positive to the right (Fig. 2). No fluid moves tangentially or normal to the surfaces of the plates.

The steady-state pressure distribution through the flow process is reflected by the following relationships:
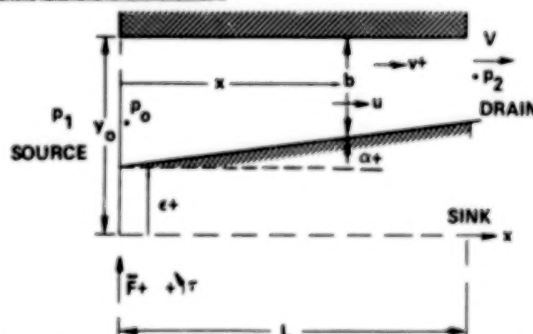

Figure 2. - Derivation of fundamental equations.

$$P = p_1 - p_2 = \rho(1.5 + 2\sigma)\frac{v^2}{2} \tag{2}$$

$$p_1 - p_o = \frac{1.5}{2}\rho v^2 \tag{3}$$

The fundamental equation for head loss through the flow process is

$$\frac{\partial h}{\partial x} = -\frac{\lambda}{b}\frac{u^2}{g} \tag{4}$$

From the Navier-Stokes equations for unsteady flow,

$$-\frac{1}{\rho}\frac{\partial p}{\partial x} = u\frac{\partial u}{\partial x} + \frac{\partial u}{\partial t} + \frac{\lambda u^2}{b} \tag{5}$$

133

If a control volume of length dx, and bounded by the two plates, is now considered, the plates can be thought of as perturbed streamlines. The general continuity equation for an unsteady stream tube of fixed length ds is

$$\frac{\partial(\rho\vec{A})}{\partial t} + \frac{\partial}{\partial s}(\rho\vec{u}\cdot\vec{A}) = 0 \tag{6}$$

Since ρ = constant, $\dot{A} = b$, $\vec{u}\ \vec{A} = ub$, $s = x$,

$$\frac{\partial b}{\partial t} + \frac{\partial(ub)}{\partial x} = 0 \tag{7}$$

or

$$b\frac{\partial u}{\partial x} + u\frac{\partial b}{\partial x} + \frac{\partial b}{\partial t} = 0 \tag{8}$$

Now, approximately

$$\left.\begin{aligned}\frac{\partial u}{\partial x} &= \frac{\alpha}{y_o}u + \frac{\dot{\varepsilon}}{y_o} + \frac{x}{y_o}\dot{\alpha} \\[2mm] \frac{\partial u}{\partial x} - \frac{\alpha}{y_o}u &= \frac{\dot{\varepsilon} + x\dot{\alpha}}{y_o}\end{aligned}\right\} \tag{9}$$

or

and $U(t) = V + v(t)$,

$$u = \frac{1}{y_o}\left(\dot{\varepsilon}x + \frac{x^2}{2}\dot{\alpha}\right) + V + v + \frac{V\alpha x}{y_o} \tag{10}$$

Higher order terms (HOT) are dropped. Now, integrate and set the following boundary conditions:

$$\text{at}\quad x = 0,\ p = p_o = p_1 - \frac{1.5}{2}\rho(V^2 + 2V\sigma)$$

and

$$\text{at}\quad x = L,\ p = p_2$$

$$-\frac{1}{\rho}p = \left(\dot{v} + \frac{2V\lambda}{y_o}v\right)x + \frac{x^2}{2y_o}\ddot{\varepsilon} + \left(\frac{Vx}{y_o} + \frac{\lambda Vx^2}{y_o^2}\right)\dot{\varepsilon}$$

$$+ \frac{\lambda V^2 x}{y_o^2}\varepsilon + \frac{x^3}{6y_o}\ddot{\alpha} + \left(\frac{Vx^2}{y_o} + \frac{\lambda Vx^3}{3y_o^2}\right)\dot{\alpha} \tag{11}$$

$$+ \left(\frac{V^2 x}{y_o} + \frac{3}{2}\frac{\lambda V^2 x^2}{y_o^2}\right)\alpha + \frac{\lambda V^2 x}{y_o} + c(t)$$

Therefore

$$c(t) = -\frac{p_1}{p_o} + \frac{1.5}{2}\rho(v^2 + 2Vv)$$

134

But

$$P_1 - P_2 = P = \rho(1.5 + 2\sigma) \frac{v^2}{2}$$

$$0 = \left[\dot{v} + \frac{V}{L}(1.5 + 2\sigma)v \right] + \frac{\sigma}{2\lambda} \left[\ddot{\varepsilon} + \frac{V}{L} 2(1 + \sigma)\dot{\varepsilon} + \frac{v^2}{L^2} 2\sigma\varepsilon \right]$$

$$+ \frac{L\sigma}{6\lambda} \left[\ddot{\alpha} + \frac{V}{L} 2(3 + \sigma)\dot{\alpha} + \frac{v^2}{L^2} 3(2 + 3\sigma)\alpha \right] \tag{12}$$

If now, $p = p_{steady} + \Delta p(t)$, then Eq. (11) becomes

$$-\frac{\Delta p}{\rho} = \left(\dot{v} + 2 \frac{V\lambda}{y_o} v \right) x + \frac{x^2}{2y_o} \ddot{\varepsilon} + \left(\frac{Vx}{y_o} + \frac{\lambda V x^2}{y_o} \right)\dot{\varepsilon}$$

$$+ \frac{\lambda v^2 x}{y_o^2} \varepsilon + \frac{x^3}{6y_o} \ddot{\alpha} + \left(\frac{Vx^2}{y_o} + \frac{\lambda V x^3}{3y_o} \right)\dot{\alpha} \tag{13}$$

$$+ \left(\frac{v^2 x}{y_o} + \frac{3}{2} \frac{\lambda v^2 x^2}{y_o^2} \right)\alpha + 1.5\, Vv$$

DERIVATION AND SUMMARY OF FORCE AND PITCHING MOMENT EQUATIONS

The symbolism and form of the equations for a shaft is:

$$\left. \begin{array}{l} \tau = A\varepsilon + B\dot{\varepsilon} + C\ddot{\varepsilon} + D\alpha + E\dot{\alpha} + F\ddot{\alpha} \\ \bar{F} = a\varepsilon + b\dot{\varepsilon} + c\ddot{\varepsilon} + d\alpha + e\dot{\alpha} + f\ddot{\alpha} \end{array} \right\} \tag{14}$$

The fundamental assumption of linear independence and superposition is made, i.e.;

$$\left. \begin{array}{l} F_1 = a\varepsilon + b\dot{\varepsilon} + c\ddot{\varepsilon} \\ F_2 = d\alpha + e\dot{\alpha} + f\ddot{\alpha} \\ \tau_1 = A\varepsilon + B\dot{\varepsilon} + C\ddot{\varepsilon} \\ \tau_2 = D\alpha + E\dot{\alpha} + F\ddot{\alpha} \\ \bar{F} = F_1 + F_2 \ , \ \tau = \tau_1 + \tau_2 \end{array} \right\} \tag{15}$$

In the above, all displacements, moments, and forces are taken about $x = L/2$. However, the first solutions will be taken about $x = 0$, and the results transferred to $x = L/2$. The subscript convention at $x = 0$ will be

$$F_o = F_{10} + F_{20} \ , \ \tau_o = \tau_{10} + \tau_{20} \tag{16}$$

For the cases about $x = 0$, certain simplifying parameters will be defined: the resulting form of the equations will be:

$$F_{10} = a_o \epsilon + b_o \dot{\epsilon} + c_o \ddot{\epsilon} = H \ (\mu_{10} \epsilon + \mu_{11} \ T\dot{\epsilon} + \mu_{12} \ T^2 \ddot{\epsilon}) \tag{17}$$

$$F_{20} = d_o \alpha + e_o \dot{\alpha} + f_o \ddot{\alpha} = H \ (\mu_{20} \alpha + \mu_{21} \ T\dot{\alpha} + \mu_{22} \ T^2 \ddot{\alpha}) \tag{18}$$

$$\tau_{10} = A_o \epsilon + B_o \dot{\epsilon} + C_o \ddot{\epsilon} = H_1 \ (\mu_{30} \epsilon + \mu_{31} \ T\dot{\epsilon} + \mu_{32} \ T^2 \ddot{\epsilon}) \tag{19}$$

$$\tau_{20} = D\alpha + E\dot{\alpha} + F\ddot{\alpha} = H_1 \ (\mu_{40} \alpha + \mu_{41} \ T\dot{\alpha} + \mu_{42} \ T^2 \ddot{\alpha}) \tag{20}$$

where $T = L/V$, and H, H_1, and $\mu_{j,k}$ will be defined as part of the derivation.

FORCE AND PITCHING MOMENT EQUATIONS FOR A SHAFT

The definition of pressure perturbations seen in Eq. (13) is for two plates of unit width. Utilizing these, the following force and pitching equations can be written by integrating around a perturbed shaft as in Fig. 1. For example,

$$\frac{F_o}{R\pi\rho} = \int_o^L \Delta p \ dx = - \left\{ \left(\dot{v} + \frac{2V\lambda v}{y_o} \right) \frac{L^2}{2} + \frac{L^3}{6y_o} \ddot{\epsilon} + \left(\frac{VL^2}{2y_o} + \frac{\lambda VL^3}{3y_o} \right) \dot{\epsilon} \right.$$

$$+ \frac{\lambda v^2 L^2}{2 y_o^2} \epsilon + \frac{L^4 \ddot{\alpha}}{24 y_o} + \left(\frac{VL^3}{3y_o} + \frac{\lambda VL^4}{12 y_o} \right) \dot{\alpha}$$

$$\left. + \left(\frac{v^2 L^2}{2y_o} + \frac{\lambda v^2 L^3}{2 y_o^2} \right) \alpha + 1.5 \ VvL \right\} \tag{21}$$

$$\frac{F_o}{R\pi\rho} = - \left\{ \frac{VL}{2} \left[\frac{L}{V} \dot{v} + (2\sigma + 3)v \right] + \frac{v^2 L}{6 y_o} \left[\frac{L^2}{V^2} \ddot{\epsilon} + \frac{L}{V} (3 + 2\sigma) \dot{\epsilon} + 3\sigma \epsilon \right] \right.$$

$$\left. + \frac{v^2 L^2}{24 y_o} \left[\frac{L^2}{V^2} \ddot{\alpha} + \frac{L}{V} (8 + 2\sigma) \dot{\alpha} + 12(1 + \sigma)\alpha \right] \right\} \tag{22}$$

and similarly,

$$\frac{\tau_o}{R\pi\rho} = - \left\{ \frac{VL^2}{3} \left(\frac{L}{V} \dot{v} + 2\sigma v + (1.5)^2 v \right) + \frac{LV^2 \sigma}{8\lambda} \left[\frac{L^2}{V^2} \ddot{\epsilon} + \frac{8L}{V} \left(\frac{1}{3} + \frac{\sigma}{4} \right) \dot{\epsilon} + \frac{8\sigma}{3} \epsilon \right] \right.$$

$$\left. + \frac{L^2 v^2 \sigma}{30\lambda} \left[\frac{L^2}{V^2} \ddot{\alpha} + \frac{30L}{V} \left(\frac{1}{4} + \frac{\sigma}{15} \right) \dot{\alpha} + 30 \left(\frac{1}{3} + \frac{3\sigma}{8} \right) \alpha \right] \right\} \tag{23}$$

After eliminating v, $\dot{v}$ between these equations (23-24) and (12-13), the forces and torques can be defined. This is done piece-wise, then finally superposed.

FORCE DUE TO LATERAL DISPLACEMENTS

This will be expressed in the form

$$F_{10} = a_o \epsilon + b_o \dot{\epsilon} + c_o \ddot{\epsilon} = H (\mu_{10} \epsilon + \mu_{11} T\dot{\epsilon} + \mu_{12} T^2 \ddot{\epsilon}) \tag{24}$$

From Eq. (12), the equation expressing $v, \dot{v}$ as a function of ϵ, $\dot{\epsilon}$, $\ddot{\epsilon}$, is, with $(a, \dot{\alpha}, \ddot{\alpha} = 0)$

$$0 = \left[\dot{v} + \frac{V}{L} (1.5 + 2\sigma)v \right] + \frac{\sigma}{2\lambda} \left[\ddot{\epsilon} + \frac{V}{L} 2(1 + \sigma)\dot{\epsilon} + \frac{V^2}{L^2} 2\sigma\epsilon \right] \tag{25}$$

This can be expressed as

$$0 = [TD + \gamma]v + \frac{V}{L} \frac{\sigma}{2\lambda} [T^2 D^2 + 2(1 + \sigma)TD + 2\sigma]\epsilon \tag{26}$$

Now, from Eq. (19), with α, $\dot{\alpha}$, $\ddot{\alpha} = 0$

$$\frac{F_{10}}{R\pi\rho} = - \left\{ \frac{VL}{2} [TD + (2\sigma + 3)]v + \frac{V^2 L}{6y_o} [T^2 D + (3 + 2\sigma)TD + 3]\epsilon \right\} \tag{27}$$

Eliminating v, $\dot{v}$ between these two equations (26-27) with $TD \ll \gamma$, eliminating (TD) of third and higher power,

$$F_{10} = H \{\mu_{10}\epsilon + \mu_{11} T\dot{\epsilon} + \mu_{22} T^2 \ddot{\epsilon}\} \tag{28}$$

where

$$H = \frac{\sigma\pi RP}{6\lambda\gamma} , \quad \gamma = (1.5 + 2\sigma)$$

$$\mu_{10} = \frac{9\sigma}{\gamma}$$

$$\mu_{11} = \frac{(9 + 12\sigma + 4\sigma^2) \gamma - 9\sigma}{\gamma^2}$$

$$\mu_{12} = \frac{(8\sigma^3 + 18\sigma^2 + 18\sigma)}{\gamma^3}$$

This agrees with Black (ref. 6) except that in μ_{12}, Black has 19σ; 18σ is correct.

FORCE DUE TO AN ANGULAR PERTURBATION

This will be expressed in the form

$$F_{20} = H (\mu_{20}\alpha + \mu_{21} T\dot{\alpha} + \mu_{22} T^2 \ddot{\alpha}) \tag{29}$$

137

Proceeding as before,

$$H = \frac{PR\pi\sigma}{6\lambda\gamma} \quad , \quad \gamma = 1.5 + 2\sigma$$

$$\mu_{20} = \frac{3L(2\sigma^2 + 6\sigma + 3)}{\gamma}$$

$$\mu_{21} = \frac{L}{\gamma^2} [\gamma(2\sigma^2 + 11.5\sigma + 12) - (6\sigma^2 + 18\sigma + 9)]$$

$$\mu_{22} = \frac{L}{\gamma^3} [\gamma^2(4.25 + 2\sigma) - \gamma(2\sigma^2 + 11.5\sigma + 12) + (6\sigma^2 + 18\sigma + 9)]$$

PITCHING MOMENT DUE TO A TRANSLATION

The pitching moment due to a translation will be expressed in the form

$$\tau_{10} = A_o\epsilon + B_o\dot{\epsilon} + C_o\ddot{\epsilon} = H_1 (\mu_{30}\epsilon + \mu_{31} T\dot{\epsilon} + \mu_{32} T^2\ddot{\epsilon}) \tag{30}$$

The equation expressing the boundary condition is (26)

$$0 = [TD+\gamma]v + \frac{V}{L}\frac{\sigma}{2\lambda} [T^2D^2 + 2(1+\sigma)TD + 2\sigma]\epsilon \tag{31}$$

From Eq. (21), $\alpha, \dot{\alpha}, \ddot{\alpha} = 0$,

$$\frac{\tau_{10}}{R\pi\rho} = -\left\{ \frac{VL^2}{3} (TD + 2\sigma + 1.5^2)v \right.$$
$$\left. + \frac{L}{8} v^2 \frac{\sigma}{\lambda} \left[T^2D^2 + 8\left(\frac{1}{3} + \frac{\sigma}{4}\right) TD + \frac{8\sigma}{3} \right] \epsilon \right\} \tag{32}$$

Eliminating $v, \dot{v}$, as before,

$$\tau_{10} = H_1 (\mu_{30}\dot{\epsilon} + \mu_{31} T\dot{\epsilon} + \mu_{32} T^2\ddot{\epsilon}) \tag{33}$$

where

$$H_1 = \frac{R\pi\sigma LP}{\lambda\gamma} \quad , \quad \gamma = 1.5 + 2\sigma$$

$$\mu_{30} = \frac{\sigma}{2\gamma}$$

$$\mu_{31} = \frac{1}{\gamma} \left[\frac{\sigma^2}{3} + \frac{3\sigma}{4} + \frac{1}{2} \right] - \frac{\sigma}{2\gamma^2}$$

$$\mu_{32} = \frac{1}{\gamma} \left(\frac{\sigma}{3} + \frac{3}{8}\right) - \frac{1}{\gamma^2} \left(\frac{\sigma^2}{3} + \frac{3\sigma}{4} + \frac{1}{2}\right) + \frac{\sigma}{2\gamma^3}$$

138

The above pitching moment is about $x = 0$.

TORQUE DUE TO AN ANGULAR PERTURBATION

After proceeding as before, Eq. (20) is expressed in the form

$$\tau_{20} = H_1 (\mu_{40}\alpha + \mu_{41} T\dot{\alpha} + \mu_{42} T^2\ddot{\alpha}) \tag{34}$$

where

$$H = \frac{PR\pi\sigma L}{\gamma\lambda}$$

$$\mu_{40} = \frac{L^2}{45\gamma} [22.5\sigma^2 + 50.67\sigma + 22.5]$$

$$\mu_{41} = \frac{L^2}{45\gamma^2} [\gamma(8\sigma^2 + 39.75\sigma + 33.75) - (22.5\sigma^2 + 50.67\sigma + 22.5)]$$

$$\mu_{42} = \frac{L^2}{45\gamma^3} [8\sigma + 14.25)\gamma^2 - \gamma(8\sigma^2 + 39.75\sigma + 33.75)$$

$$+ (22.5\sigma^2 + 50.67\sigma + 22.5)]$$

TRANSLATION OF EQUATIONS TO $x = L/2$

The translation of the solutions for perturbations about $x = L/2$ can now be written. These involve the α terms only. An x rotation at $\alpha = L/2$, can be considered as the sum of an α perturbation at $x = 0$ plus a displacement of $-\alpha \frac{L}{2}$, so that at $L/2$ there is a pure α perturbation.

$$F_2 = F_{20} - F_{10} \left(-\alpha \frac{L}{2}\right) = d_o\alpha + e_o\dot{\alpha} + f_o\ddot{\alpha} - a_o \frac{L}{2} \alpha - b_o \frac{L}{2} \dot{\alpha} - c_o \frac{L}{2} \ddot{\alpha}$$

$$= \left(d_o - a_o \frac{L}{2}\right)\alpha + \left(e_o - b_o \frac{L}{2}\right)\dot{\alpha} = \left(f_o - c_o \frac{L}{2}\right)\ddot{\alpha} \tag{35}$$

and

$$\tau_{20} = \left(D_o - A_o \frac{L}{2}\right)\alpha + \left(E_o - B_o \frac{L}{2}\right)\dot{\alpha} + \left(F_o - C_o \frac{L}{2}\right)\ddot{\alpha} \tag{36}$$

These are both for α rotated at $x = 1/2$, but the moment is still at $x = 0$. The next step is to translate the resultant force and moment to $x = L/2$. The fundamental relationships are $(F = F_o)$,

$$\tau = \tau|_{L/2} = \tau_o - F \frac{L}{2} = \tau_{10} + \tau_{20} - (F_1 + F_2) \frac{L}{2} \tag{37}$$

To summarize, these become:

Forces:

$$F_1 = a_o\epsilon + b_o\dot{\epsilon} + c_o\ddot{\epsilon} \quad , \quad \text{since } a_o = a, \ b_o = b, \ c_o = c$$

$$F_2 = \left(d_o - a_o \frac{L}{2}\right)\alpha + \left(e_o - b_o \frac{L}{2}\right)\dot{\alpha} + \left(f_o - c_o \frac{L}{2}\right)\ddot{\alpha} \tag{38}$$

139

Moments

$$\tau_1 = \tau_{10} - F_1 \frac{L}{2} = \left(A_o - a_o \frac{L}{2}\right)\varepsilon + \left(B_o - b_o \frac{L}{2}\right)\dot{\varepsilon} + \left(C_o - c_o \frac{L}{2}\right)\ddot{\varepsilon}$$

$$\tau_2 = \tau_{20} - F_2 \frac{L}{2} = \left(D_o - A_o \frac{L}{2} - c_o \frac{L}{2} + a_o \frac{L^2}{4}\right)\alpha$$

$$+ \left(F_o - B_o \frac{L}{2} - e_o \frac{L}{2} + b_o \frac{L^2}{4}\right)\dot{\alpha}$$

$$+ \left(F_o - C_o \frac{L}{2} - f_o \frac{L}{2} + c_o \frac{L^2}{4}\right)\ddot{\alpha} \tag{39}$$

where

$$a_o = H \mu_{10} , \quad b_o = H \mu_{11} T , \quad c_o = H \mu_{12} T^2$$

$$d_o = H \mu_{20} , \quad e_o = H \mu_{21} T , \quad f_o = H \mu_{22} T^2$$

and

$$A_o = H_1 \mu_{30} , \quad B_o = H_1 \mu_{31} T , \quad C_o = H_1 \mu_{32} T^2$$

$$D_o = H_1 \mu_{40} , \quad E_o = H_1 \mu_{41} T , \quad F_o = H_1 \mu_{42} T^2$$

The symbols are previously defined. And finally,

$$\left. \begin{array}{l} \tau = A\varepsilon + B\dot{\varepsilon} + C\ddot{\varepsilon} + D\alpha + E\dot{\alpha} + F\ddot{\alpha} \\ F = a\varepsilon + b\dot{\varepsilon} + c\ddot{\varepsilon} + d\alpha + e\dot{\alpha} + f\ddot{\alpha} \end{array} \right\} \tag{40}$$

where

$$A = A_o - a_o \frac{L}{2} , \quad B = B_o - b_o \frac{L}{2} , \quad C = C_o - c_o \frac{L}{2}$$

$$D = D_o - A_o \frac{L}{2} - d_o \frac{L}{2} + a_o \frac{L^2}{4}$$

$$E = E_o - B_o \frac{L}{2} - e_o \frac{L}{2} + b_o \frac{L^2}{4}$$

$$F = F_o - C_o \frac{L}{2} - f_o \frac{L}{2} + c_o \frac{L^2}{4}$$

and where

$$a = a_o , \quad b = b_o , \quad c = c_o$$

$$d = d_o - a_o \frac{L}{2} , \quad e = e_o - b_o \frac{L}{2} , \quad f = f_o - c_o \frac{L}{2}$$

EVALUATION OF SEAL COEFFICIENTS

The geometry and parameter values shown in Table I were used to evaluate a sample rotor. For comparative purposes, the properties of two fluids, water and steam under supercritical conditions were used.

TABLE I. - GEOMETRY AND PARAMETERS

SEAL

R	- RADIUS	7.62 cm (3 INCHES)
L	- LENGTH	2.54 cm (1 INCH)
Y_0	- CLEARANCE	0.254 mm (0.01 INCH)
N	- SHAFT SPEED	30,000 RPM
p	- PRESSURE DROP	344.6 N/cm² (500 PSI)
μ	- VISCOSITY (STEAM)	2.067×10^{-9} N-S/cm² (3×10^{-9} LB-SEC/IN.²)
δ	- DENSITY (STEAM)	13.84 Kg/m³ (0.0005 LB/IN.³)
μ	- VISCOSITY (WATER)	1.013×10^{-5} N-S/cm² (1.47×10^{-5} LB-SEC/IN.²)
δ	- DENSITY (WATER)	996.5 Kg/m³ (0.036 LB/IN.³)

ROTOR

E	- ELASTIC MODULUS	2.067×10^7 N/cm² (3×10^7 LB/IN.²)
I	- AREA MOMENT OF INERTIA	24.97 cm⁴ (0.6 IN.⁴)
K	- BEARING SPRING RATE	1.75×10^6 N/cm (10^6 LB/IN.)
l	- COMPONENT SPACING	15.24 cm (6 IN.)
W	- ROTOR WEIGHT	36.29 Kg (80 LB)
G	- $l^3 K/EI$	

As indicated in ref. 6, if all dynamic terms are retained in the coefficient formulation, the results are in the form of a frequency-dependent cubic divided by a first-order term. A Taylor's expansion was used for the denominator to obtain a simple polynomial form for the coefficients. Questions remain as to how many terms should be retained and what range of frequencies are allowed before the approximation degrades.

To answer the question of higher order terms, the equations for the seals were established in the cubic form and evaluated for the conditions of Table I. The resulting transfer functions are shown in Table II. From these examples, it is obvious that the only affects that may legitimately be considered are those of stiffness and damping. Only those two affects were considered in the evaluation that follows.

Seal coefficients were evaluated over a wide range of speed by assuming that pressure drop across the seal varied as the square of speed. The density for water was assumed to be constant but the density of steam was assumed to be proportional to pressure drop. The spring rates were found to vary with speed squared for both water and steam. The damping coefficients, however, varied with speed for the case of water and speed squared for steam. The restoring force and torque as a function of shaft translation and angulation are therefore described by

$$\left\{ \begin{array}{c} F(\omega) \\ \tau(\omega) \end{array} \right\} = \left[\begin{array}{cc} \theta & \phi \\ \chi & \psi \end{array} \right] \left\{ \begin{array}{c} \epsilon \\ \alpha \end{array} \right\}$$

141

TABLE II. - SUMMARY OF SEAL COEFFICIENTS AT 30,000 rpm

WATER

θ (N/cm) = 7.84 × 10⁴ $\left(1 + \frac{s}{5483}\right)\left(1 + \frac{s}{7347}\right)\left(1 + \frac{s}{12100}\right)\Big/\left(1 + \frac{s}{7936}\right)$ ≈ 7.84 × 10⁴ + 150.2s

ϕ (N) = 6.806 × 10⁵ $\left(1 + \frac{s}{5053}\right)\left(1 + 1.948\left(\frac{s}{10440}\right) + \left(\frac{s}{10440}\right)^2\right)\Big/\left(1 + \frac{s}{7936}\right)$ ≈ 6.806 × 10⁵ + 264.1s

χ (N) = -3.323 × 10⁴ $\left(1 + \frac{s}{7948}\right)\left(1 + \frac{s}{1057}\right)\Big/\left(1 + \frac{s}{7936}\right)$ ≈ -3.323 × 10⁴ -31.43s

ψ (N-cm) = -1.2308 × 10⁵ $\left(1 - \frac{s}{4482}\right)\left(1 + \frac{s}{8318}\right)\left(1 + \frac{s}{14811}\right)\Big/\left(1 + \frac{s}{7936}\right)$ ≈ -1.2308 × 10⁵ + 19.76s

STEAM

θ (N/cm) = 9.327 × 10⁴ $\left(1 + \frac{s}{5336}\right)\left(1 + \frac{s}{46219}\right)\left(1 + \frac{s}{85632}\right)\Big/\left(1 + \frac{s}{42063}\right)$ ≈ 9.327 × 10⁴ + 18.29s

ϕ (N) = 1.0163 × 10⁶ $\left(1 + \frac{s}{26295}\right)\left(1 + 1.872\left(\frac{s}{64795}\right) + \left(\frac{s}{64795}\right)^2\right)\Big/\left(1 + \frac{s}{42063}\right)$ ≈ 1.0163 × 10⁶ + 25.71s

χ (N) = -3.949 × 10⁴ $\left(1 + \frac{s}{6880}\right)\left(1 + \frac{s}{45388}\right)\Big/\left(1 + \frac{s}{42063}\right)$ ≈ -3.949 × 10⁴ - 8.524s

ψ N-cm = 3.536 × 10⁵ $\left(1 + \frac{s}{41200}\right)\left(1 - \frac{s}{80463}\right)\left(1 + \frac{s}{233796}\right)\Big/\left(1 + \frac{s}{42063}\right)$ ≈ -3.536 × 10⁵ + 2.688s

where $s = j\omega$

Where operating point variations are described by

$$\begin{bmatrix} \theta & \phi \\ \chi & \psi \end{bmatrix} = \left(\frac{\omega}{|\omega|}\right)^2 \begin{bmatrix} a & d \\ A & D \end{bmatrix} + \left(\frac{\omega}{|\omega|}\right)^2 \begin{bmatrix} b\frac{d}{dt} & e\frac{d}{dt} \\ B\frac{d}{dt} & E\frac{d}{dt} \end{bmatrix}_{steam} + \left(\frac{\omega}{|\omega|}\right)\begin{bmatrix} b\frac{d}{dt} & e\frac{d}{dt} \\ B\frac{d}{dt} & E\frac{d}{dt} \end{bmatrix}_{water}$$

ROTOR MODEL

A simple rotor model was necessary that would exhibit both translation and angulation at the seals. A flexible massless shaft was chosen with a mass load at the center. Seals were placed at each end of the shaft and an ideal bearing was located halfway between each seal and the central mass. Properties for the rotor model are contained in Table I.

The restoring force due to the shaft, bearings, and seals due to the lateral deflection (Y or Z) at the mass is given by

$$\bar{F}/Y = \bar{N}/\bar{D} \tag{41}$$

where

$$\bar{N} = -2K\left[1 + \left(1 + \frac{4}{3}G\right)\frac{\theta}{K} + \frac{3}{2}\frac{G}{\ell K}(\phi + \chi) + \frac{2G}{\ell^2 K}\psi + \frac{5}{12}\left(\frac{G}{\ell K}\right)^2(\theta\psi - \phi\chi)\right]$$

$$\bar{D} = \left(1 + \frac{G}{3}\right) + \left(\frac{8}{3} + \frac{7}{36}\, G\right) \frac{G\theta}{K} + \left(2 + \frac{1}{4}\, G\right) \frac{G}{\ell K}\, (\phi + \chi)$$

$$+ \left(2 + \frac{5}{12}\, G\right) \frac{G\phi}{\ell^2 K} + \left(\frac{2}{3} + \frac{G}{18}\right)\left(\frac{G}{\ell K}\right)^2 (\theta\psi - \phi\chi)$$

Inserting values for the structural properties and for the frequency dependent journal coefficients, we obtain a dynamic force-deflection relation at the mass.

$$\frac{\bar{F}}{Y} = -\left[\frac{a_1 + b_1 \dfrac{d}{dt} + c_1 \dfrac{d^2}{dt^2}}{d_1 + e_1 \dfrac{d}{dt} + f_1 \dfrac{d^2}{dt^2}} \right] \tag{42}$$

Since the journal equations were developed for a condition where the flow is ostensibly axial, we assume that they are fixed to Couette coordinates. These equations must be transformed to rotor coordinates to determine the whirl orbit. Now assume, steady circular motion of the shaft in the y-z plane. Transforming the force-deflection equations to coordinates rotating with the shaft, we obtain

$$\begin{bmatrix} d_1 - \dfrac{\omega^2}{4} f_1 & + \dfrac{\omega}{2} e_1 \\[2ex] - \dfrac{\omega}{2} e_1 & d_1 - \dfrac{\omega^2}{4} f_1 \end{bmatrix} \begin{Bmatrix} F_y \\ F_z \end{Bmatrix} = \begin{bmatrix} -\left(a_1 - \dfrac{\omega^2}{4} c_1\right) & -\dfrac{\omega}{2} b_1 \\[2ex] + \dfrac{\omega}{2} b_1 & -\left(a_1 - \dfrac{\omega^2}{4} c_1\right) \end{bmatrix} \begin{Bmatrix} Y \\ z \end{Bmatrix} \tag{43}$$

The equations for the rotor with the central mass unbalanced a distance Δ from the axis of rotation in the y direction are

$$-\omega^2 \frac{W}{g}\, y = F_y + \Delta \frac{W}{g}\, \omega^2$$

$$-\omega^2 \frac{W}{g}\, z = F_z \tag{44}$$

Solutions for shaft motion due to the unbalanced mass at a particular speed (ω) are obtained by first scaling the seal coefficients that were obtained at design speed ($\bar{\omega}$). Then solutions of equations (41-44) produce the normalized orbit radius, or amplification ratio

$$\frac{\sqrt{Y^2 + z^2}}{\Delta}$$

EVALUATION OF ROTOR RESPONSE

Normalized rotor deflection vs shaft speed is shown in Fig. 3 and 4 for the steam and water journals, respectively. Rotor response considering only the translation coefficient (α) is shown for reference. The rotor response with the complete
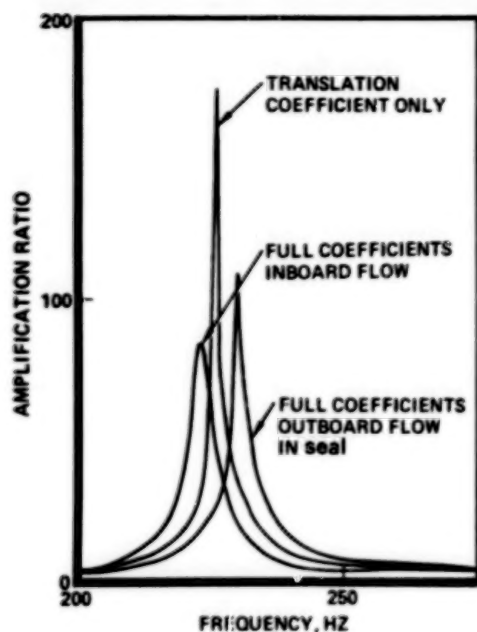
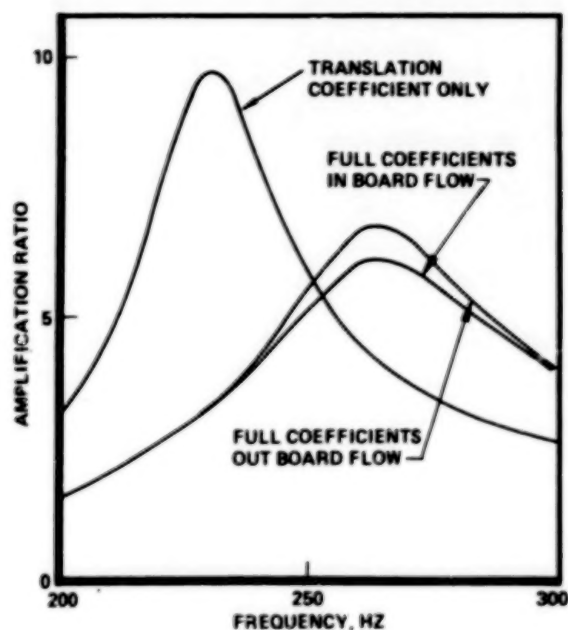Figure 3 - Rotor response with steam as fluid.

Figure 4. - Rotor response with water as fluid.

set of forces are shown for cases where the flow is outboard through the seals and where the flow is reversed. Reversed flow (inboard flow direction) was simulated by changing the sign of the off diagonal coefficients (ϕ and ψ).

To evaluate sensitivity of the various coefficients, cases with the off-diagonal terms increased by 10 percent were run as well as a case where the diagonal coefficient (ψ) was increased by 10 percent. A summary of these cases in terms of critical speed and effective damping (ξ/ξ_{cr}) are contained in Table III.

TABLE III. - SUMMARY OF CRITICAL SPEED CALCULATIONS

SEAL STIFFNESS MATRIX	STEAM		WATER	
	SPEED (RPM)	DAMPING	SPEED (RPM)	DAMPING
$\begin{bmatrix} 0 & 0 \\ 0 & 0 \end{bmatrix}$	13266	0.0%	13266	0.0%
$\begin{bmatrix} \theta & 0 \\ 0 & 0 \end{bmatrix}$	13585	0.28%	13780	5.12%
$\begin{bmatrix} \theta & \phi \\ \chi & \psi \end{bmatrix}$	13807	0.46%	15540	7.58%
$\begin{bmatrix} \theta & -\phi \\ -\chi & \psi \end{bmatrix}$	13323	0.60%	15510	8.47%
$\begin{bmatrix} \theta & 0 \\ 0 & \psi \end{bmatrix}$	13584	-1.2%	14880	-11.2%
$\begin{bmatrix} \theta & 1.1\phi \\ 1.1\chi & \psi \end{bmatrix}$	13830	0.77%	15900	6.36%
$\begin{bmatrix} \theta & \phi \\ \chi & 1.1\psi \end{bmatrix}$	13806	0.32%	15410	7.67%

DISCUSSION OF THE RESULTS

When angulation affects are included, as well as the translation, the critical speed is shifted slightly and the whirl radius is significantly reduced.

Off diagonal seal coefficients are very significant; without them, the effect of angulation is destablilzing. This indicates that the centers of pressure for rotation and for translation do not coincide. Reversing the journal flow (to the inboard direction) actually increased effective damping for the cases investigated.

The second order "mass" affects of the journals were negligible and for whirl the mass affects may be deleted.

For the two fluids that were considered in the journal, spring rates were very similar but damping coefficients were an order of magnitude higher with water. This is evidenced by an order of magnitude increase in damping at critical speed for that journal. For both fluids the spring rate varies with seal pressure drop and therefore speed squared. The damping coefficient varies with speed for an incompressible fluid and the square of speed for a compressible fluid.

CONCLUDING REMARKS

From a study of the results, the following conclusions have been reached:

1. Journal forces associated with the second time derivative of shaft motion should be ignored. The coefficients are very small and are significant only in a frequency range where the approximations required to obtain them are questionable.

2. Forces associated with the first-time derivative are very important.

3. Pitching moments and angulation effects are as significant as translation.

4. The net effect of moment and angulation is a slight shift in critical speed and a significant decrease in peak amplitude.

5. While the partial of moment with respect to angulation appears to be de-stabilizing, off diagonal coefficients result in net stabilization. This result is due to a lack of coincidence between the centers of pressure for translation and rotation.

6. Seals, where the flow is outboard, showed lower damping than where the seal flow was inboard. Higher critical speeds, where a different mode shape is involved, may not exhibit the same trend.

7. Damping forces at speeds below the design value are reduced more for a compressible fluid than for an incompressible one.

8. Moments due to variation in fluid shear along the shaft surface are very small.

9. Coefficient accuracy is not known in the absence of experimental data. Specifically this approach assumes full turbulent flow with a rotation at $\omega/2$ throughout the seal. Black (ref. 11) and Hirs (ref. 13) comment on this. For short seals, a significant error may occur because of the slow development of tangential velocity.

REFERENCES

1. Rothe, K.: "Turbopump Configuration Selection for the Space Shuttle Main Engine," ASME Paper No. 74 FE-23, Joint Fluid Engineering Conference, Montreal, Canada, May 1974.

2. Alford, J. S.: "Protecting Turbomachinery From Self-Excited Rotor Whirl," Journal of Engineering for Power, Trans. ASME, Series A, October 1965, pp. 333-344.

3. Ek, M. C.: "Solving Subsynchronous Whirl in the High-Pressure Hydrogen Turbomachinery of the SSME," Journal of Spacecraft and Rockets, Vol. 17, No. 3, May-June 1980, p. 208.

4. Childs, D. W.: "The Space Shuttle Main Engine High-Pressure Fuel Turbopump Rotordynamic Instability Problem," Gas Turbine Conference, Philadelphia, Pa, 27-31 March 1977, ASME Paper No. 77-GT-49.

5. Allaire, P. E., Lee, C. C., and Gunter, D. J.: "Dynamics of Short Eccentric Plain Seals With High Axial Reynolds Number," Journal of Spacecraft and Rockets, Vol. 15, No. 6, 1978, pp. 341-347.

6. Black, H. F.: "Effects of Hydraulic Forces in Annular Pressure Seals on the Vibrations of Centrifugal Pump Rotors," Journal of Mechanical Engineering Science, Vol. 11, No. 2, 1969, pp. 206-213.

7. Black, H. F. and Jenssen, D. N.: "Effects of High Pressure Ring Seals on Pump Rotor Vibrations," Fluids Engineering Division, ASME, 71-WA/FE-38, 1971.

8. Black, H. F. and Jenssen, D. N.: "Dynamic Hybrid Bearing Characteristics of Annular Controlled Leakage Seals," Institution of Mechanical Engineers, Vol. 184, Pt. 3N, 1970, pp. 92-100.

9. Black, H. F. and Cochrane, E. A.: "Leakage and Hybrid Bearing Properties of Serrated Seals in Centrifugal Pumps," Paper G5, 6th International Conference on Fluid Sealing, Munich, 1973, pp. 61-70.

10. Black, H. F.: Lateral Stability and Vibrations of High-Speed Centrifugal Pump Rotors," Dynamics of Rotors, International Union of Theoretical and Applied Mechanics Symposium, Lyngby/Denmark, 12-16 August 1974.

11. Black, H. F., Allaire, P. E., and Barrett, L. E.: "Inlet Flow Swirl in Short Turbulent Annular Seal Dynamics," 9th International Conference on Fluid Sealing, BHRA Fluid Engineering, Leeuwenhorst, Netherlands, April 1981.

12. Fleming, D.: "Effective Spring Rates of Tapered Seals," NASA Lewis Turbomachinery Work Shop, March 1981.

13. Hirs, G. G.: "A Bulk Flow Theory for Turbulence in Lubricant Films," Journal of Lubrication Technology, Trans. ASME, Series F, Vol. 95, No. 2, April 1973, pp. 137-146.

14. Allaire, P. E., Gunter, E. J., Lee, C. C., and Barrett, L. E.: "Load Capacity and Hybrid Coefficients for Turbulent Interstage Seals," Report No. UVA/528; 49/ME76/103, September 1976.

15. Yamada, Y., "Resistance of Flow Through an Annulus With an Inner Cylinder Rotating," Bulletin JSME, Vol. 5, No. 18, 1962, pp. 302-310.

MEASUREMENT OF INTERSTAGE FLUID-ANNULUS DYNAMICAL PROPERTIES

M. L. Adams
University of Akron
Akron, Ohio 44325

E. Makay
Energy Research & Consultants Corporation
Morrisville, Pennsylvania 19067

I. A. Diaz-Tous
EPRI
Palo Alto, California 94303

ABSTRACT

The work described in this paper is part of an Electric Power Research Institute sponsored effort to improve rotor vibrational performance on power plant feed water pumps. A major objective of this effort is to reduce vibration levels by devising inter-stage sealing configurations with optimized damping capacity, realizing that the typical multi-stage centrifugal pump has several more inter-stage fluid annuli than it has journal bearings. Also, the fluid annuli are distributed between the journal bearings where vibration levels are highest and can therefore be "exercised" more as dampers than can the bearings. Described in this paper is a test apparatus which has been built to experimentally determine fluid-annulus dynamical coefficients for various configurations of inter-stage sealing geometry.

INTRODUCTION

As originally cited in an Electric Power Research Institute survey on feedwater pump outages, Reference (1), excessive vibration is responsible for many power plant forced outages. The major cause of this excessive vibration is now widely recognized as the fluid dynamical forces generated within high-head centrifugal pump flow passages. These dynamical forces are a natural by-product of the high rate of energy transfer to the fluid within a relatively small space and the fact that this transfer of energy cannot, of course, take place at 100 percent efficiency. The farther away from the best efficiency flow a feed pump is operated, the stronger these dynamical forces become, particularly under the low-flow conditions required at part-load operation. Hydraulic excitation forces will remain an inherent feature of feed pumps. Further research on pump hydraulics may possibly reduce their intensity, but their elimination as an important practical consideration would appear to be unlikely. The most promising approach is to optimize system damping, the classical approach when the dynamical forces are not adequately controllable.

One of the approaches presently being pursued is to devise high-damping inter-stage fluid-annulus configurations, Reference (2). The typical multi-stage centrifugal pump has several more inter-stage fluid annuli than it has journal bearings (see Figure 1). Also, the fluid annuli are distributed between the journal bearings where vibration levels are highest and can therefore be exercised more as dampers than can the bearings.

As shown in Reference (3), wear-ring geometry is already known to be a potentially major influence on critical speeds. Currently used geometries are shown in Figure 2, with some type of serrations often preferred to accommodate rubs. However, some pump manufacturers have employed smooth or shallow groove geometries to utilize the resulting radial stiffening effect which can raise the first critical speed considerably above the operating speed. However, as also shown in Reference (3) (see Figure 3), this stiffening effect (called "Lomakin" effect) deteriorates with wear, which can cause high vibration levels after several hours of normal operation. In spite of the attention this potential stiffening effect has received, practically no attention has been given to the potential damping capacity of interstage fluid annuli. Raising or lowering critical speeds can not circumvent the undesireable effects of large hydraulic excitation forces but properly adjusted damping can.

ROTOR VIBRATION DAMPING EVALUATION

A linearized vibration mathematical model is generally the appropriate starting point to study and understand rotor vibration characteristics. In the presence of vibration, an interactive dynamic radial force occurs where there is a close running clearance filled with a liquid or gas (e.g., journal bearings, seals, wear-ring clearances). Such interactive forces are commonly characterized in a linear model as shown in the following matrix equation.

$$\begin{Bmatrix} f_x \\ f_y \end{Bmatrix} = - \begin{bmatrix} D_{xx} & D_{xy} \\ D_{yx} & D_{yy} \end{bmatrix} \begin{Bmatrix} \ddot{x} \\ \ddot{y} \end{Bmatrix} - \begin{bmatrix} B_{xx} & B_{xy} \\ B_{yx} & B_{yy} \end{bmatrix} \begin{Bmatrix} \dot{x} \\ \dot{y} \end{Bmatrix} - \begin{bmatrix} K_{xx} & K_{xy} \\ K_{yx} & K_{yy} \end{bmatrix} \begin{Bmatrix} x \\ y \end{Bmatrix} \tag{1}$$

Here, $[K]$, $[B]$ and $[D]$ are the stiffness, damping and virtual mass matrices, respectively, of the entrapped fluid within the close-running radial clearance. (x,y) is the instantaneous rotor-to-stator radial displacement vector with respect to static equilibrium and (f_x, f_y) the instantaneous radial dynamic force vector. Presently, there is little reliable information on the dynamic matrix coefficients for feed pump fluid annuli.

To evaluate and compare damping capacity of various fluid-annulus geometries, it is a considerable simplification if harmonic motions are used. First of all, this provides a convenient way to absorb the $[D]$ matrix into the $[K]$ matrix as commonly done.

$$[\bar{K}] = [K] - \Omega^2[D] \tag{2}$$

Here, Ω is the frequency of the orbital vibration (see Figure 4). As described in Reference (4), the $[B]$ and $[K]$ matrices are non-symmetric for journal bearings and other fluid annuli contained within a rotating and non-rotating boundary. To separate out conservative and non-conservative (damping) effects, the $[B]$ and $[K]$ matrices are decomposed into symmetric and skew-symmetric parts.

$$[B_{ij}^s] = \frac{1}{2}[B_{ij} + B_{ji}] \text{ , symmetric (positive damping)}$$

$$[B_{ij}^{ss}] = \frac{1}{2}[B_{ij} - B_{ji}] \text{ , skew-symmetric (contributes no damping)}$$

$$[K_{ij}^S] = \frac{1}{2} [K_{ij} + K_{ji}] \text{ , symmetric (contributes no damping)}$$

$$[K_{ij}^{SS}] = \frac{1}{2} [K_{ij} - K_{ji}] \text{ , skew-symmetric (negative damping)} \tag{3}$$

The instantaneous non-conservative interactive force vector on the rotor can there-fore be expressed as follows.

$$\{P\} = - [B^S]\{\dot{X}\} - [K^{SS}]\{X\} \tag{4}$$

The net energy imparted to the rotor (at a fluid annulus) per cycle of orbital motion can therefore be expressed by evaluating the integral of the non-conservative force vector, $\{P\}$, with the differential radial displacement over one period of harmonic motion, expressed as follows.

$$E_{cyc} = \oint \{P\} \cdot \{dX\}$$
$$= - \pi [\Omega(B_{xx}^S X^2 + B_{yy}^S Y^2) - 2K_{xy}^{SS} \sin (\theta_x - \theta_y)] \tag{5}$$

Here, x and y are the principal coordinates of $[B^S]$, and X and Y the corresponding single-peak amplitudes, and (θ_x, θ_y) the respective phase angles.

For any co-rotational orbit $\sin (\theta_x - \theta_y) > 0$. Furthermore, if as with journal bearings, B_{xx}^S, B_{yy}^S and K_{xy}^{SS} are all positive, one sees the presence of both positive and negative damping effects on forward whirls. It is clear from equation (5) why rotor-bearing instability always occurs as a co-rotational or forward whirling vibration.

A compact way to evaluate the net damping capacity of a fluid annulus (or journal bearing) is to determine E_{cyc} as a function of vibration-to-speed frequency ratio. For example, trends of journal bearing damping (E_{cyc}) are shown in Figure 5, which is an alternate way of explaining why rotor-bearing instability occurs when the lowest rotor-bearing resonance frequency is below the zero-damping cross-over frequency ratio. A similar approach for evaluating net damping capacity of interstage fluid annuli could be employed if the dynamic coefficients were known. Also, predictive analyses of feed pump vibration in general would be considerably advanced with reliable dynamic coefficients. A test rig has been designed and built to experimentally determine the [D], [B] and [K] matrix coefficients under operating conditions in feed water pumps.

TEST RIG AND GOVERNING EQUATIONS

Under Electric Power Research Institute sponsorship, a test rig has been designed and built to experimentally determine the dynamic coefficients of currently used and newly devised inter-stage fluid-annulus configurations. Testing is currently in progress and the results will be published when the work is completed.

A conceptual sketch of the test rig is shown in Figure 6, and a detail layout of the actual rig is shown in Figure 7. The concept employed in the design of this rig follows directly from the governing equations which relate the interactive

dynamic force components and the components of relative radial harmonic motion. As developed in Appendix A of this paper, twelve independent equations are needed which relate the force and motion parameters to the twelve dynamic coefficients. These equations are summarized below for the harmonic circular orbit, which is the vibration mode built into the test rig eccentric-spindles design.

$$(F_x \cos \theta_x)/R = - K_{xx} - \Omega_j B_{xx} + \Omega_j^2 D_{xx} - \Omega_j B_{xy}$$

$$(F_x \sin \theta_x)/R = - \Omega_j B_{xx} + K_{xy} - \Omega_j^2 D_{xy}$$

$$(F_y \cos \theta_y)/R = - K_{yx} + \Omega_j^2 D_{yx} - B_{yy} \Omega_j$$

$$(F_y \sin \theta_y)/R = - \Omega_j B_{yx} - K_{yy} - \Omega_j^2 D_{yy}$$

(6)

where, $j = 1,2,3$

The controlled parameters are X and Y, the single-peak vibration amplitudes and their respective phase angles ϕ_x and ϕ_y. The measured parameters are F_x and F_y, the single-peak dynamic force amplitudes and their respective phase angles, θ_x and θ_y. As implied by equations (6), test data is needed at three different vibration frequencies for a given operating condition. That is, one needs twelve independent equations to solve for twelve unknowns. This necessitates independent control over rotational speed and vibration orbit frequency.

There are basically two experimental approaches one could take: (i) impose dynamical forces and measure displacements, or (ii) impose dynamical displacements and measure the forces. With currently available measurement techniques, the second approach is potentially more accurate, and has been used in our design. The test rig is configured around a double-spool spindle, with the inner spindle having an adjustable run-out or eccentricity with the outer spindle (Figures 6 and 7). Rotation of the outer shaft therefore causes the rotational centerline of the inside shaft to experience a circular orbit with a precession frequency of the outside shaft's rotational speed. The rotational speed of the inside shaft is the test rotational speed. Independent control over vibration frequency and test speed is therefore accomplished. The same approach is now being used (see Reference (5)) to experimentally determine the linearized spring and damping coefficients for low specific speed centrifugal pump stages. As the shaft-to-shaft eccentricity is adjusted, it can be measured with extreme accuracy using an LVDT or even a precision dial indicator while slowly rotating the outer shaft by hand.

The test ring is rigidly supported in the radial plane by four piezoelectric load cells (see Figures 6 and 7), two in each of the x and y mutually perpendicular directions which allow variation of orbit-center eccentricity. The necessary advantage of piezoelectric load cells is that they are extremely stiff and therefore keep test ring vibration amplitudes negligible and therefore unnecessary to measure. Strain gauge load cells would not be a feasible option here because they require displacement to sense load.

The test ring is contained within a pressurized chamber. The test ring divides the chamber into high and low pressure compartments. The difference in pressure between these two compartments is controlled to the desired test pressure drop

across the fluid annulus, with a maximum axial pressure drop of 500 psi through the test annulus. The test ring is supported axially on fluid film hydrostatic thrust faces which introduce no extraneous radial loads. The test ring is attached to the four load cells by four leaf springs which are soft in the circumferential direction but stiff in the radial and axial direction. This type of construction allows the fluid reaction torque on the test ring to be equilibrated by the test ring support, without introducing extraneous radial forces on the test ring. The closure head of the pressurized chamber is easily removed as is the test ring and test journal. This provides for quick interchange of the various fluid annulus configurations to be tested and modified.

It is essential that the radial run-out of the test journals which results from inner shaft rotation be as close to zero as is possible to manufacture. This was accomplished in the final machining operation on the test journals by grinding them while they were rotated (inner shaft rotated, outer shaft fixed) in the final assembled double-shaft spindle.

For any given annulus configuration (i.e., diameter, axial width, clearance and surface geometry) the basic operating parameters are rotational speed, water temperature, static eccentricity and axial pressure drop across the test annulus. The effects of each of these parameters will be determined by varying them through ranges encountered in actual feed pump applications.

CONCLUSIONS

The importance of inter-stage fluid annuli to rotor dynamical performance of high-head feed water pumps warrants developmental efforts by the pump manufacturers in this area. The test rig described in this paper has recently come on-line and is just beginning to provide reliable data on inter-stage fluid-annulus dynamic coefficients. Currently used configurations as well as newly devised high-damping configurations are being tested. By the end of this year, we anticipate the completion of the testing that is presently planned. We expect to be able to recommend inter-stage clearance geometries which will provide considerable additional rotor vibrational damping capacity for feed water pump and other multi-stage centrifugal pump applications.

REFERENCES

1. Makay, E. and Szamody, O., "Survey of Feed Pump Outages", EPRI Publication FP-754, April 1978.

2. Adams, M. L. and Makay, E., "Development of Advanced Rotor-Bearing Systems for Feed Water Pumps, Phase 2", EPRI Publication CS-2027, September 1981.

3. Makay, E., "How Close Are Your Feed Pumps to Instability - Caused Disaster?", Power, McGraw-Hill, December 1980.

4. Adams, M. L. and Padovan, J., "Insights into Linearized Rotor Dynamics", Journal of Sound and Vibration, Vol. 76(1), May 1981.

5. Brennen, C. E., Acosta, A. J. and Caughey, T. K., "A Test Program to Measure Fluid Mechanical Whirl-Excitation Forces in Centrifugal Pumps", Proc. Texas A & M Workshop (May 1980) on Instability Problems in High-Performance Turbomachinery, NASA Conference Publication 2133, pp 229-235.

Appendix A

GOVERNING EQUATIONS WHICH RELATE EXPERIMENTAL MEASUREMENTS
TO FLUID-ANNULUS DYNAMIC COEFFICIENTS

A.1 DEVELOPMENT OF GOVERNING FORCE DISPLACEMENT EQUATION

Postulating harmonic motion, equations for rotor system vibrations can be expressed using phasor notation as follows.

$$f_x = F_x e^{i(\Omega t + \theta_x)} \quad , \quad f_y = F_y e^{i(\Omega t + \theta_y)}$$

$$x = X e^{i(\Omega t + \theta_x)} \quad , \quad y = Y e^{i(\Omega t + \theta_y)}$$

$$\dot{x} = i\Omega x \quad , \quad \dot{y} = i\Omega y \tag{A-1}$$

$$\ddot{x} = -\Omega^2 x \quad , \quad \ddot{y} = -\Omega^2 y$$

For the general linear case, the force-motion equations are given in expanded form as follows.

$$f_x = -K_{xx}x - B_{xx}\dot{x} - D_{xx}\ddot{x} - K_{xy}y - B_{xy}\dot{y} - D_{xy}\ddot{y}$$

$$f_y = -K_{yx}x - B_{yx}\dot{x} - D_{yx}\ddot{x} - K_{yy}y - B_{yy}\dot{y} - D_{yy}\ddot{y} \tag{A-2}$$

Using harmonic motion, equations (A-1), the force-motion equations (A-2) then can be simplified as follows.

$$f_x = (-K_{xx} - i\Omega B_{xx} + \Omega^2 D_{xx})x + (-K_{xy} - i\Omega B_{xy} + \Omega^2 D_{xy})y$$

$$f_y = (-K_{yx} - i\Omega B_{yx} + \Omega^2 D_{yx})x + (-K_{yy} - i\Omega B_{yy} + \Omega^2 D_{yy})y \tag{A-3}$$

Using the phasor form, (A-1), and dividing through by $e^{-i\Omega t}$ gives the following.

$$F_x e^{i\theta_x} = (-K_{xx} - i\Omega B_{xx} + \Omega^2 D_{xx})X e^{i\phi_x} +$$

$$(-K_{xy} - i\Omega B_{xy} + \Omega^2 D_{xy})Y e^{i\phi_y}$$

$$F_y e^{i\theta_y} = (-K_{yx} - i\Omega B_{yx} + \Omega^2 D_{yx})X e^{i\phi_x} + \tag{A-4}$$

$$(-K_{yy} - i\Omega B_{yy} + \Omega^2 D_{yy})Y e^{i\phi_y}$$

Recalling from basic phasor convention, $e^{i\theta} = \cos\theta + i\sin\theta$. Therefore, equations (A-4) take the following form.

$$F_x (\cos \theta_x + i \sin \theta_x) = (- K_{xx} - i\Omega B_{xx} + \Omega^2 D_{xx})X$$

$$(\cos \phi_x + i \sin \phi_x) = (- K_{xy} - i\Omega B_{xy} + \Omega^2 D_{xy})Y$$

$$(\cos \phi_y + i \sin \phi_y)$$

$$F_y (\cos \theta_y + i \sin \theta_y) = (- K_{yx} - i\Omega B_{yx} + \Omega^2 D_{yx})X$$

$$(\cos \phi_x + i \sin \phi_x) + (- K_{yy} - i\Omega B_{yy} + \Omega^2 D_{yy})Y$$

$$(\cos \phi_y + i \sin \phi_y) \qquad\qquad (A-5)$$

The two complex equations of (A-5) can be segregated by real and imaginary parts to obtain four real equations. Since there are twelve unknowns (i.e., the stiffness, damping and inertia coefficients), experimentally measured inputs to these equations must be obtained at three different vibration frequencies (i.e., Ω_j, $j = 1,2,3$) for a given operating condition. This leads to the following general form of the governing equations.

$$F_x \cos \theta_x = [(\Omega_j^2 D_{xx} - K_{xx}) \cos \phi_x + B_{xx}\Omega_j \sin \phi_x]X$$

$$+ [(\Omega_j^2 D_{xy} - K_{xy}) \cos \phi_y + B_{xy}\Omega_j \sin \phi_y]Y$$

$$F_x \sin \theta_x = [(\Omega_j^2 D_{xx} - K_{xx}) \sin \phi_x - B_{xx}\Omega_j \cos \phi_x]X$$

$$+ [(\Omega_j^2 D_{xy} - K_{xy}) \sin \phi_y - B_{xy}\Omega_j \cos \phi_y]Y$$

$$F_y \cos \theta_y = [(\Omega_j^2 D_{yx} - K_{yx}) \cos \phi_x + B_{yx}\Omega_j \sin \phi_x]X$$

$$+ [(\Omega_j^2 D_{yy} - K_{yy}) \cos \phi_y + B_{yy}\Omega_j \sin \phi_y]Y$$

$$F_y \sin \theta_y = [(\Omega_j^2 D_{yx} - D_{yx}) \sin \phi_x - B_{yx}\Omega_j \cos \phi_x]X$$

$$+ [(\Omega_j^2 D_{yy} - K_{yy}) \sin \phi_y - B_{yy}\Omega_j \cos \phi_y]Y \qquad\qquad (A-6)$$

where, $j = 1,2,3$.

As explained in the main text of this paper, the test rig has been designed to provide a controlled harmonic circular orbit of radius R. That is,

$$X = Y = R \text{ and } \phi_y = \phi_x - \frac{\pi}{2}$$

Therefore, $\cos \phi_y = \sin \phi_x$ and $\sin \phi_y = -\cos \phi_x$. Furthermore, all phase angles can be referenced to the x-component of vibration (i.e., $\phi_x \equiv 0$). Implementing all these simplifications, reduces equations (A-6) to the following.

$$(F_x \cos \theta_x)/R = -K_{xx} - \Omega_j B_{xx} + \Omega_j^2 D_{xx} - \Omega_j B_{xy}$$

$$(F_x \sin \theta_x)/R = -\Omega_j B_{xx} + K_{xy} - \Omega_j^2 D_{xy}$$

$$(F_y \cos \theta_y)/R = -K_{yx} + \Omega_j^2 D_{yx} - B_{yy}\Omega_j$$

$$(F_y \sin \theta_y)/R = -\Omega_j B_{yx} - K_{yy} - \Omega_j^2 D_{yy} \tag{A-7}$$

where, $j = 1,2,3$

A.2 EXPERIMENTAL ERROR CONSIDERATIONS

Equations (A-7) provide twelve equations in twelve unknowns. The orbit of vibration, R, and its frequency are controlled by the design of the test rig. The single-peak dynamic force amplitudes (F_x, F_y) and the associated dynamic force phase angles (θ_x, θ_y) are measured. The remaining twelve unknowns are the dynamic coefficients. Close examination of equations (A-7) will reveal that the first two sets of equations are coupled only to each other, while the third and fourth sets of equations are individually decoupled from the other equation sets. This is a result of the basic approach of using a controlled circular orbit vibration. An additional advantage is thereby provided since one does not have to actually solve a single system of twelve equations. Instead, solution requires individual solution of one system of six equations and two systems of three equations. This simplification tends to reduce the affinity for amplification of experimental error in the equation solution step of the overall scheme for determining the dynamic coefficients.

As fully shown, experimental data is required at three different frequencies for a specific operating condition in order to recover the twelve dynamic coefficients from the governing equations. Therefore, in theory, any three sufficiently different frequencies should yield the same dynamic coefficients for a given operating condition. The experimental setup therefore inherently provides a means for determining the overall inaccuracy of the experimentally determined coefficients. That is, one can obtain data at say ten (or more) different vibration frequencies and then determine the dynamic coefficients with the data from all unique combinations of three different frequencies out of the total of ten (or more) frequencies available. The difference in answers between the different combinations is the experimental spread or error. Experimental error will come from two basic sources: (i) measurement inaccuracies, and (ii) non-linearity in the actual force-displacement phenomenon. These two sources of error will tend to work in opposition. That is, measurement inaccuracies can be minimized by using "larger" vibration amplitudes, thus making the measured response forces larger and therefore easier to measure accurately. However, the larger the vibration amplitude, the more significant becomes the non-linearities, which are neglected in the governing equations. Therefore, for each operating condition there will be an optimum orbital vibration radius which minimizes the experimental error, being large enough to obtain good measurements, but not too large to produce significant non-linearities. The test rig spindle is designed to that the orbital vibration radius can be varied, specifically so that error can be minimized.
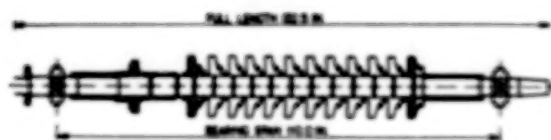
Figure 1. - Twelve-stage boiler feed
pump rotor; cane run no. 6 station,
Louisville gas and electric.

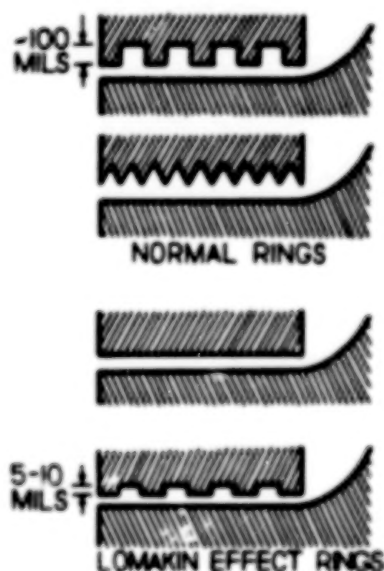NORMAL RINGS

LOMAKIN EFFECT RINGS

Figure 2. - Currently used feed pump
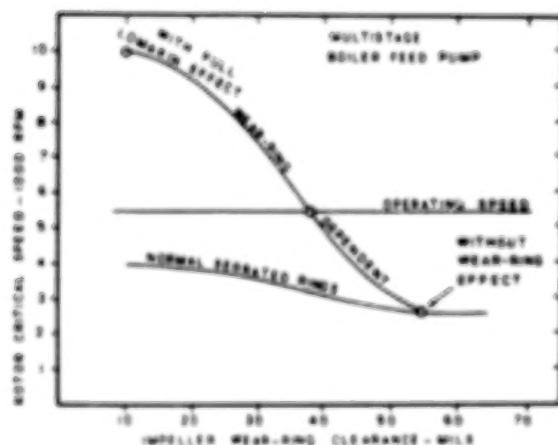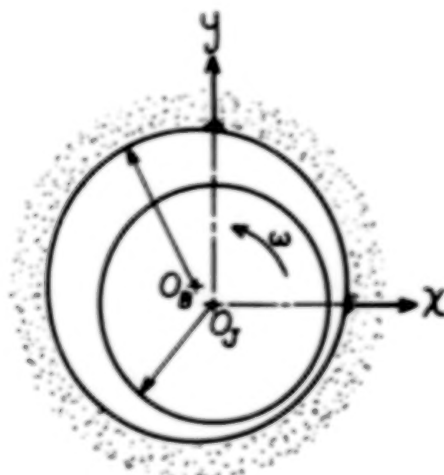wear ring geometries, reference (3).

Figure 3. - Lomakin effect on first
critical speed of a typical feed
water pump, reference (3).

$$x = X \sin[\Omega t + \theta_x]$$
$$y = Y \sin[\Omega t + \theta_y]$$

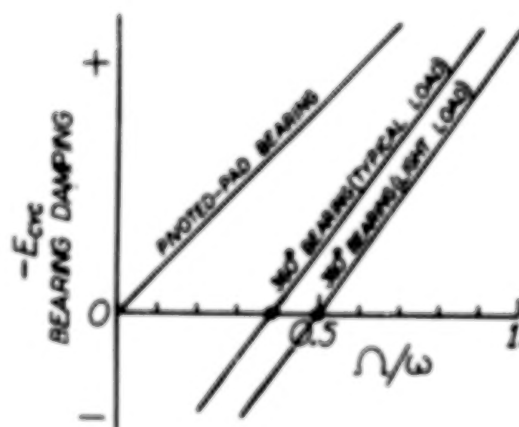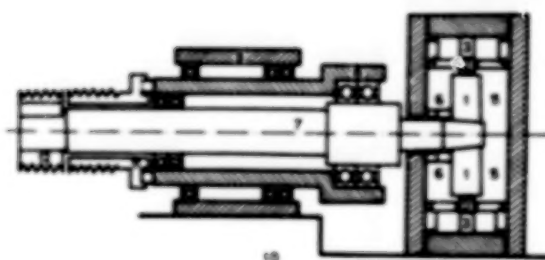Figure 4. - Single-frequency harmonic
orbital vibration of rotor with
respect to stator.

Figure 5. - Trends of journal bearing
net damping per cycle of harmonic
motion. Ω/ω is vibration
frequency-to-speed ratio.

BEST DOCUMENT AVAILABLE

Legend:

1 - Test rotating element
2 - Test annulus ring
3 - Piezoelectric load cell
4 - Hydrostatic axial ring support
5 - High-pressure compartment
6 - Low-pressure compartment

7 - Inner spindle rotor
8 - Outer spindle rotor
9 - Spindle housing
10 - Support base
11 - V-belt pulley
12 - V-belt pulley

Figure 6. - Conceptual sketch of double-spool spindle fluid-annulus test rig.
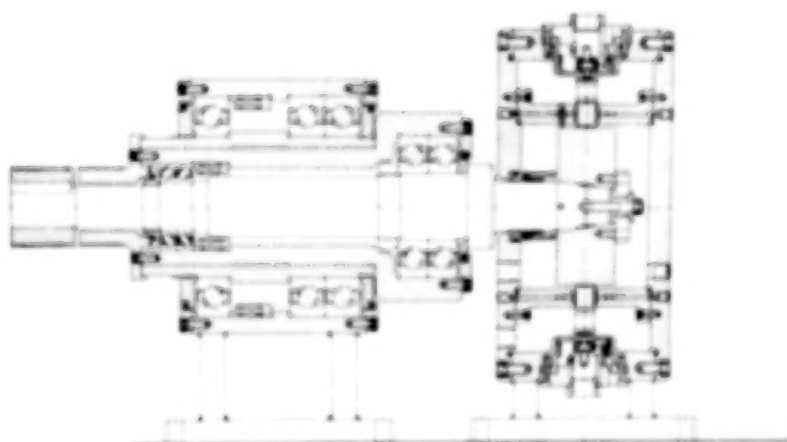
Figure 7. - Detail layout of double-spool spindle fluid-annulus test rig.

TESTING OF TURBULENT SEALS FOR ROTORDYNAMIC COEFFICIENTS

Dara W. Childs
Department of Mechanical Engineering
Texas A&M University
College Station, Texas 77843

John B. Dressman
Department of Mechanical Engineering
The University of Louisville
Louisville, Kentucky 40208

SUMMARY

A facility has been developed for dynamic testing of straight and convergent-tapered seals with the capability of measuring the radial and tangential force components which result from a circular centered orbit. The test apparatus causes the seal journal to execute small-eccentricity centered circular orbits within its clearance circle. Dynamic measurements are made and recorded of the seal-displacement-vector components, and of the pressure field. The pressure field is integrated to yield seal tangential and radial reaction-force components. Representative test data are provided and discussed for straight seals.

NOMENCLATURE

A : amplitude of orbital motion (L)

C_r : radial clearance (L)

$\tilde{C}, \tilde{c}$: nondimensional, direct and cross-coupled damping coefficients, introduced in Eq. (4)

C, c : direct and cross-coupled damping coefficients, introduced in Eq. (6), (FT/L)

H : clearance function (L)

$\tilde{K}, \tilde{k}$: nondimensional, direct and cross-coupled stiffness coefficients, introduced in Eq. (4)

K, k : direct and cross-coupled stiffness coefficients, introduced in Eq. (6), (F/L)

L : seal length (L)

$\tilde{M}, \tilde{m}$: nondimensional, direct and cross-coupled added-mass coefficients, introduced in Eq. (4)

M, m : direct and cross-coupled added mass coefficients introduced in Eq. (6), (M)

ΔP : seal differential pressure, (F/L^2)

r_X, r_Y : components of seal-displacement vector, introduced in Eq. (4), (L)

R_X, R_Y : component of seal reaction force, introduced in Eq. (4), (F)

R : seal radius, (L)

$R_a = 2VC/\nu$: nominal, leal axial Reynolds number

$R_c = R\omega C/\nu$: nominal, seal circumferential Reynolds number

$T = L/V$: transit time of fluid through seal, (T)

V : nominal flow velocity of fluid through seal, (L/T)

λ : friction factor, defined in Eq. (3)

ν : fluid kinematic viscosity, (L^2/T)

ξ : entrance loss factor, introduced in Eq. (1)

σ : friction loss factor defined in Eq. (2)

ρ : fluid density (M/L^3)

ω : shaft angular velocity (T^{-1})

INTRODUCTION

Black [1,2,3,4], in a series of publications incorporating theoretical and experimental results, has demonstrated that the rotordynamic behavior of pumps is critically dependent on forces developed by neck-rings and interstage seals illustrated in Figure 1. Subsequent experience [5] has demonstrated that the stability of cryogenic turbopumps is comparably dependent on seal forces. The test program discussed here was stimulated by stability difficulties encountered in developing ʌhe turbopump of [5], and has the objective of measuring radial and tangential force components for straight and convergent-tapered seals over a range of axial and circumferential Reynolds numbers.

Seal Analysis: Leakage and Dynamic Coefficients

Black [1,2,3,4] is largely responsible for developing models for constant clearance seals. Black's analysis yields a definition of the force acting on a rotor due to its motion at a seal location, and is based on the following leakage relationship from Yamada [6] for flow between concentric rotating cylinders:

$$\Delta P = (1 + \xi + 2\sigma)\rho V^2/2 \qquad (1)$$

where ξ is a constant entry-loss coefficient, ρ is the fluid density, V is the average fluid velocity, and σ is a friction-loss coefficient defined by

$$\sigma = \lambda L/C_r \quad . \tag{2}$$

In the above, L is the seal length, C_r is the radial clearance, and λ has been defined by Yamada to be the following function of the axial and circumferential Reynolds numbers (R_a , R_c)

$$\lambda = 0.079 \, R_a^{-\frac{1}{4}}[1+ (\frac{7R_c}{8R_a})^2]^{3/8} \quad , \quad R_a = 2VC_r/\nu, \quad R_c = R\omega C_r/\nu, \tag{3}$$

where ν is the fluid's kinematic viscosity, R is the seal radius, and ω is the rotor's rotational speed. The friction law definition of Eq. (3), Yamada's definition for λ, is based on an assumed 1/7 power velocity distribution, and fits the Blasius equation for pipe friction.

From a rotordynamic viewpoint, the objective of seal analysis is the definition of seal force coefficients, i.e., stiffness, damping, and added mass terms. In nondimensional form, the force/motion relationship for a seal may be stated

$$-\frac{\lambda}{\pi R \Delta P} \begin{Bmatrix} R_X \\ R_Y \end{Bmatrix} = \begin{bmatrix} \tilde{K} & \tilde{k} \\ -\tilde{k} & \tilde{K} \end{bmatrix} \begin{Bmatrix} r_X \\ r_Y \end{Bmatrix} + T \begin{bmatrix} \tilde{C} & \tilde{c} \\ -\tilde{c} & \tilde{C} \end{bmatrix} \begin{Bmatrix} \dot{r}_X \\ \dot{r}_Y \end{Bmatrix} + T^2 \begin{bmatrix} \tilde{M} & \tilde{m} \\ -\tilde{m} & \tilde{M} \end{bmatrix} \begin{Bmatrix} \ddot{r}_X \\ \ddot{r}_Y \end{Bmatrix} \tag{4}$$

where ($\tilde{K}$, $\tilde{C}$, $\tilde{M}$) and ($\tilde{k}$, $\tilde{c}$, $\tilde{m}$) are, respectively, the direct and cross-coupled stiffness, damping, and added-mass terms.

Prior Analytical Results for Constant-Clearance Seals

Test results for the constant-clearance geometry seals are presented and discussed here. Comparable results for convergent-tapered seal geometries will be presented subsequently. The contents of this section are provided to briefly review theoretical and experimental results and procedures for this seal configuration.

Seal analyses which have been published to-date use bulk-flow models in which the raial variation of the velocity and pressure fields across the fluid film are neglected. Governing equations consist of axial and circumferential momentum equations, and the continuity equation for the axial and circumferential velocity components, $U_z(Z,\theta), U_\theta(Z,\theta), p(Z,\theta)$, which are averaged with respect to the radial coordinate, r. Most reported analyses of seals use a perturbation analysis in the eccentricity ratio of the form

$$H = H_0 + \epsilon H_1, U_\theta = U_{\theta O} + \epsilon U_{\theta 1}$$

$$U_Z = U_{ZO} + \epsilon U_{Z1}, \quad p = p_O + \epsilon p_1 \tag{5}$$

where H is the clearance function, and ϵ is the eccentricity ratio. Governing equations for p_O, $U_{\theta O}$, U_{ZO} define the centered, zero-eccentricity flow field, while the first-order equations for the variables $U_{\theta 1}$, U_{Z1}, p_1 define the flow fields which result from small motion about a centered position defined by the clearance function $H_1(t,\theta)$. A "short-seal" solution results if $U_{\theta 1}$, "the pressure-induced circumferential flow, " is assumed to be negligible in comparison to the shear-induced term $U_{\theta O}$. Black [1] initially developed an analytic short-seal solution,

but then with Jensen [2] developed a numerical finite-length solution. Correction factors were developed by Black and Jensen from the finite-length solution to be used in adjusting the short-seal solution to account for finite L/D ratios. Black's second refinement of the original theory was to account for the influence of a change in clearance on local Reynolds numbers [3].

Finally, Black et al. [4] examined the influence of inlet swirl on seal coefficients. In previous analyses, a fluid element entering a seal was assumed to instantaneously achieve the half-speed tangential velocity, $U_\theta = R\omega/2$. The results in [4] demonstrate that a fluid element may travel a substantial distance along the seal before asymptotically approaching this limiting velocity. For interstage seals in which the inlet tangential velocity is negligible, the practical consequences of accounting for this "swirl" effect is a marked reduction in predictions for the cross-coupled stiffness coefficient, k. Black's experimental results show clear evidence of the influence of swirl. A short-seal analysis is used in [4], and the perturbation in Reynolds number due to a local change in clearnace introduced in [3] is not included.

One of the authors [7,8] has recently completed two analyses based on Hirs' turbulent lubrication model [9]. Short and finite-length solutions are developed in [7] and [8], respectively, including all of the various influences introduced in Black's initial analyses [1-4]. The results resemble, but do not coincide with, Black's.

Prior Seal Testing Procedures and Results

The pertinent data which must be measured to confirm the seal leakage model of Eqs. (1) through (3) are ΔP, V, (from flow rate), ω, and the axial pressure gradient within the seal. This latter measurement yields σ which in turn yields λ. Yamada's model for the friction factor was based on testing for these variables over the Reynolds number range $(200 < R_a < 40,000; 0 < R_c < 40,000)$ and clearance to radius ratios of $(.0106 \leq C_r/R \leq .0129)$.

Various approaches can be taken to the measurement of rotordynamic coefficients of Eq. (4). For example, if the journal segment of the seal is stationary (i.e., $r_X = r_Y = \dot{r}_X = \dot{r}_Y = 0$), Eq. (4) can be inverted to obtain

$$\begin{Bmatrix} r_X \\ r_Y \end{Bmatrix} = \frac{\lambda}{R\rho\Delta P K_e^2} \begin{bmatrix} \tilde{K} & -\tilde{k} \\ \tilde{k} & \tilde{K} \end{bmatrix} \begin{Bmatrix} R_X \\ R_Y \end{Bmatrix} , \quad \tilde{K}_e^2 = \tilde{K}^2 + \tilde{k}^2 .$$

Hence, by applying the static load definition ($F_X = F_s$, $F_Y = 0$), and measuring the displacement components, r_X and r_Y, one obtains a combined measure of the direct and cross-coupled stiffness coefficients. This is predominantly the type of testing performed by Black, who cites results in the form of "receptance magnitudes," i.e.,

$$|r|/F_s = \lambda \{\tilde{K}^2 + \tilde{k}^2\}^{\frac{1}{2}}/R\Delta P .$$

The relative magnitudes of the direct $\tilde{K}$ and cross-coupled $\tilde{k}$ stiffness coefficients depend on the relative magnitudes of the axial and radial Reynolds numbers.

Specifically, at zero running speeds, $\bar{k}$ is zero, but increases with R_c and can exceed K.

Most of Black's testing [2,3,10,11] has been of the static nature cited above. The second type of test cited consists of analytically modelling a test rotor including the theoretically predicted seal dynamics, and comparing the dynamic characteristics of the model with test data. For example, in [2], the test rotor was rapped and a correlation was made with the observed logarithmic decrement on the decay curve. In [3], known imbalances were applied to the test rotor, and a comparison was made with synchronous amplitudes and phase, critical speed location, and onset speed of instability. Comparisons between rotor model results and tests, of this nature, are helpful in deciding whether the general seal model is reasonable. However, this type of test-correlation yields limited specific information about the individual dynamic coefficients. Further, discrepancies in synchronous amplitude and phase results could result from an inadequate initial balance.

A summary of the test results of references [2,3,10,11] is provided in Table 1. The correlation in these tests ranges from "good" to "fair." The nature and results of the test support the following general conclusions concerning the adequacy of Black's dynamic seal model:

(a) Over the Reynolds number range tested, the prediction of the direct stiffness coefficient K is adequate for plain and serrated seals, although less accurate for serrated seals. Black's test results indicate a divergence between tests and theory for the direct damping coefficient C as the axial Reynolds number is increased.

(b) Although the data cited generally supports Black's dynamic seal model over the Reynolds number range considered, it is inadequate to specifically verify the proposed relationships [Eq. (4)] for the dynamic coefficients as functions of the axial and radial Reynolds numbers.

THE UNIVERSITY OF LOUISVILLE DYNAMIC SEAL TEST PROGRAM

Test Section Design

Figure 2 illustrates the test-section design employed in the current seal test program. Water enters the center of the section and flows axially across the two rotating test seals exiting at the bottom of the test section. The seal journals (L = 4 in = 10.16 cm, D = 2 in = 5.08 cm) are mounted eccentrically on the shaft with a constant eccentricity, A = .005 in = 1.27 x 10^{-4} m. The nominal seal clearance is C_r = .020 in = 5.08 mm, which yields C_r/R = .010. Accordingly, shaft rotation causes the seal journals to execute circular centered orbits at the nominal eccentricity ratio ε = 0.25. Axial and circumferential Reynolds numbers may be specified over the range $R_a \varepsilon$[5,000,30,000], $R_c \varepsilon$[0,11,000] by varying the shaft rotational speed (0-4,000 rpm) and flowrate. Shaft-speed is measured by a once-per-revolution counter, while turbine flowmeters separately measure flowrate through each seal.

The rotor of Figure 2 is supported in Torrington hollow roller bearings[1][12]. These precision bearings are preloaded radially, have zero internal clearances, and an accurately predictable radial stiffness. The first rotor-bearing critical speed

161

is predicted to be approximately 12,500 rpm. The end thrust bearing is provided to react the small axial load developed by the opposed test-seal design.

Instrumentation and Data Analysis

The dynamic instrumentation illustrated in Figures 2 and 3 consists, for each seal, of Bently eddy-current motion transducers and five piezo-electric pressure transducers which are distributed both axially and circumferentially along and around the seal. The circumferential "clocking" of the pressure transducers is provided primarily as a matter of convenience, since the transducers are provided exclusively to define the time history of the axial pressure distribution. Since the seal journal is forced to execute a closed circular orbit at constant speed ω within its journal, the steady-state pressure distribution is constant with respect to an observed fixed to the shaft, and the circumferential pressure distribution at time t, $p(z,\theta)$ is definable in terms of either past or future time measurements $p(z,t)$ at a fixed value of θ. The direct extraction of circumferential pressure distributions from pressure time histories also permits the "reconstruction" of a pressure time history at a given circumferential location (e.g., $\theta=0$), despite the fact that the transducers are distributed circumferentially around the seal as illustrated in Figure 3.

The seal reaction forces at a given time, $t = \bar{t}$, are defined by the integrals:

$$R_X(\bar{t}) = -\int_0^{2\pi} \int_0^{L} p(\theta,z) \sin \theta \ R \ d\theta dt = -RL \int_0^{2\pi} \sin \theta \ \bar{p}(\theta) \ d\theta$$

$$R_Y(\bar{t}) = -\int_0^{2\pi} \int_0^{L} p(\theta,z) \cos \theta \ R \ d\theta dz = -RL \int_0^{2\pi} \cos \theta \ \bar{p}(\theta) \ d\theta$$

(6)

where $\bar{p}$ is the average axial pressure defined by

$$\bar{p}(\theta) = \frac{1}{L} \int_0^{L} p(\theta,z)dz.$$

The integral of Eq. (6) is evaluated numerically from pressure time histories corresponding to $\theta = 0$ measurements, and denoted $p_i*(\theta)$. The axial spacing of the pressure transducers has been chosen from Gauss-Legendre quadrature formulas [13] to minimize the error involved in evaluating this integral. The quadrature formula for integration with respect to z is;

$$p(\theta) = \frac{1}{2}[A_1 p_1*(\theta) + A_2 p_2*(\theta) + A_3 p_3*(\theta) + A_2 p_4*(\theta) + A_1 p_5*(\theta)]$$

where

$$A_1 = 0.23603, \quad A_2 = 0.47862, \quad \text{and } A_3 = 0.56889.$$

Data Analysis Procedure

The dimensional form of Eq. (4) is

$$\begin{bmatrix} M & m \\ -m & M \end{bmatrix} \begin{Bmatrix} \ddot{r}_X \\ \ddot{r}_Y \end{Bmatrix} + \begin{bmatrix} C & c \\ -c & C \end{bmatrix} \begin{Bmatrix} \dot{r}_X \\ \dot{r}_Y \end{Bmatrix} + \begin{bmatrix} K & k \\ -k & K \end{bmatrix} \begin{Bmatrix} r_X \\ r_Y \end{Bmatrix} = - \begin{Bmatrix} R_X \\ R_Y \end{Bmatrix} \qquad (7)$$

The nature of the test rig is such that steady synchronous motion of the form

$$r_X = A \cos \omega t , \quad r_Y = A \sin \omega t \qquad (8)$$

results, and for this type of motion, the six coefficients of Eq. (7) can not be separately identified. In fact, only two independent numbers result from the steady-state, harmonic test data $(r_x(t), r_y(t), R_x(t), R_y(t))$ which is generated by the test rig for a given axial and circumferential Reynolds number set (R_a, R_c). For the present study, the two numbers chosen for presentation are the radial and circumferential components of the reaction force. From Eqs. (7) and (8), these components may be stated

$$R_\theta / A = \frac{|\bar{r} \times \bar{R}|}{A^2} = k - C\omega - m\omega^2$$

$$\qquad (9)$$

$$R_r / A = \frac{\bar{r} \cdot \bar{R}}{A^2} = M\omega^2 - c\omega - K .$$

TEST RESULTS AND DISCUSSION

Test Results

Static test results for the seals consists of leakage. Dynamic test results are the radial and circumferential force components, $(R_r/A, R_\theta/A)$, of Eq. (9) as a function of Reynolds numbers (R_a, R_c). Table 2 contains both static and dynamic test results. With respect to static results, for $\xi = 0.5$, the coefficient

$$C_d = 1 + \xi + 2\sigma$$

of Eq. (1) is approximately -5% in error at the higher R_a range ($R_a \cong 24,000$) and +3% in error at the lower R_a range ($R_a \cong 4,600$). Hence, leakage is generally well predicted by Eq. (1).

An inspection of the Reynolds number sets of Table 2 demonstrates that R_a is held nominally constant, while R_c is varied, with the result that the Reynolds number pairs (R_a, R_c) are clustered about the nominal axial Reynolds numbers [24,760; 18,850; 9,040; 4,580]. These results were obtained by holding the seal-leakage rate constant while varying the rotational speed ω.

The dashed lines of Figures 4 and 5 connect the test data points of Table 2 for the radial (R_r/A) and tangential force components (R_θ/A) as a function of the circumferential Reynolds number, R_c. The test results reflect both the small changes in R_a about the nominal value $\bar{R}_a$ and the obvious changes in R_c resulting from changes in ω.

163

Discussion of Radial-Force Component Results

Initial discussions of the test results will deal with results for radial-force components of Figure 4, and the comparison of these results to various theoretical predictions of references [7] and [8]. The experimental and theoretical results of interest are denoted as follows in Figure 4:

------*   Experimental results.

°——°——°   Finite-length solution, reference [8].

△——△——△   Short-seal solution, reference [8].

+—+—+   Short-seal solution, reference [7].

◊—◊—◊   K from reference [8].

The theoretical results of reference [8] would, presumably, provide the best prediction of the radial force component; however, the results of Figures 4(a) through (e) show that: (1) measured radial forces are roughly twice as large as predicted values, and (2) the magnitudes of measured forces tend to increase with increasing R_c, while theoretical predictions show a decreasing magnitude.

As noted in the introduction, short-seal solutions are obtained by neglecting the "pressure-induced" circumferential flow, while including the shear-induced flow. Short-seal solutions yield larger radial force predictions, and, as expected, reduce the discrepancy between theory and experiments of Figure (4). The short-seal solution of reference [8] is developed under less restrictive assumptions than that of reference [7], and agrees better with the test data. The direct stiffness prediction of these two solutions are comparable; however, reference [7] predicts values for M and c that are approximately twice as large as those of reference [8]. The large value for M explains why this solution diverges from both the experimental data and the remaining theoretical solutions with increasing R_c.

In fact, all solutions predict magnitudes for M which are excessive in comparison to either test results or experience with predictions of pumps. An overprediction of M would explain why the theory predicts a reduction in R_θ with increasing R_c, while test results show the opposite. The short-seal theoretical results show that M and c arise from the same momentum terms in the governing equations; hence, if the theory overpredicts M, one would assume that c is comparably overpredicted. If both these terms are eliminated from Eq. (90), only the direct stiffness K remains. This coefficient is illustrated in Figures 4(a) through (e) for the short-seal solution of reference [8].

The coefficient K from the short-seal solution generally behaves the same way as the test results for changes in R_a and R_c, and provides a much better prediction for the radial force component R_θ than the other approaches of Figure 4. However, it underpredicts the test results on the average by about twenty percent.

Discrepancies between theory and experiment illustrated in Figures 4(a) through (e) may be explained as a combination of the following factors:
(a) The theoretical developments are based on a perturbation analysis which assumes that the seal-orbit amplitude A is small compared to the radial clearance C_r, and that second-order terms in A/C_r are negligible. However, for the current apparatus, $A/C_r = 0.25$, and second-order effects may be influencing test results. This may provide part of the explanation for the

seals being stiffer than predicted.

(b) The fundamental bulk-flow model, as presented by the momentum and continuity equations, is, in some sense, deficient. An explanation of this nature is required to explain the apparent major overprediction of the direct added-mass and cross-coupled damping coefficients.

Discussion of Tangential Force Components

Theoretical results for the cross-coupled, added-mass coefficient m typically indicate a negligible contribution to the tangential force component, i.e.,

$$R_\theta/A \cong k - C\omega .$$

Further, in the test apparatus, the shaft rotates in a clockwise sense and the tangential force would be defined by

$$R_\theta/A \cong -k + C\omega . \tag{10}$$

A comparison of the test results with the finite-length solution predictions in Figures 5(a) through (e) shows generally good agreement. If the test results were curvefitted by a linear curve of the form predicted by Eq. (10), one would reach the following conclusions:

(a) The cross-coupled coefficient k is smaller than predicted, and the difference between theory and experiment increases with increasing R_a. This conclusion is supported by noting that measured values for R_θ/A are smaller than predicted at low values of R_c.

(b) The damping coefficient C is slightly smaller than predicted. The generally steeper slopes for the experimental data curve supports this conclusion.

The finite-length solution of [8] generally provides a better correlation with experimental data than either of the short-seal solutions. All of these solutions include the influence of "swirl." Specifically, in contrast to typical hydrodynamic-bearing analyses in which the fluid is assumed to have an average circumferential velocity of $R\omega/2$, the acceleration of a fluid particle due to shear forces is accounted for. For short-seals with high axial fluid velocities, this means that a fluid particle may exit the seal without acquiring a substantial tangential velocity. Since the test rig of Figure 2 provides negligible pre-rotation of fluid entering the seal, the theory assumes that the inlet circumferential velocity is zero. Predictions of k are substantially reduced by including the influence of swirl; hence, test results of Figure 5 provide an additional verification of the influence of swirl.

SUMMARY AND CONCLUSIONS

The test results presented support the following general conclusions:

(a) Leakage is reasonably well predicted by Yamada's model.

(b) The circumferential force, which primarily represents the direct damping coefficient C and cross-coupled stiffness coefficient k, is adequately predicted by the finite-length theory of reference [8].

(c) The radial force is substantially underpredicted (40 to 50%) by the finite-length theory. The direct, added-mass coefficient M appears to be much smaller than predicted by theory. By inference, the cross-coupled damping coefficient c is probably also much smaller than predicted.

(d) The direct stiffness K from the short-seal solution of reference [8] has the

165

same form as the measured radial force component but is approximately 20% less than measured values.

A conclusive explanation for the discrepancies between the theory and experimental results for the radial force component is not possible; however, it may result from either (a) nonlinearities due to the size of the seal orbits relative to the radial clearance, or (b) basic inadequacies in the bulk-flow model.

On the basis of the present results, the following reduced model for seal reaction forces is recommended for modelling seals in rotordynamics analysis of pumps:

$$
- \left\{ \begin{array}{c} R_X \\ R_Y \end{array} \right\} = \left[\begin{array}{cc} K & k \\ -k & K \end{array} \right] \left\{ \begin{array}{c} X \\ Y \end{array} \right\} + \left[\begin{array}{cc} C & 0 \\ 0 & C \end{array} \right] \left\{ \begin{array}{c} \dot{X} \\ \dot{Y} \end{array} \right\} .
$$

Note that the added-mass and cross-coupled coefficients have been discarded. The coefficients of k and C are adequately predicted by the finite-length solution of reference [8]. The best prediction for K is provided by the short-seal solution of reference [8]; however, this prediction is approximately 20% lower than test results.

REFERENCES

1. Black, H. F., "effects of Hydraulic Forces in Annular Pressure Seals on the Vibrations of Centrifugal Pump Rotors," J. M. Eng. Sci., vol. 11, No. 2, pp. 206-213, 1969.

2. Black, H. F. and Jensen, D. N., "Dynamic Hybrid Properties of Annular pressure Seals," Proc. J. Mech. Engin., vol. 184, pp. 92-100, 1970.

3. Black, H. F. and Jensen, D. N., "Effects of High Pressure Ring Seals on Pump Rotor Vibrations," ASME Paper No. 71-WA/FF-38, 1971.

4. Black, H. F., Allaire, P.E., and L. E. Barrett, "The Effect of Inlet Flow Swirl on the Dynamic Coefficients of High-Pressure Annular Clearance Seals, "Ninth International Conference in Fluid Sealing, BHRA Fluids Engineering, Leeuwenhorst, The Netherlands, April 1981.

5. Childs, D. W., "The Space Shuttle Main Engine High-Pressure Fuel Turbopump Rotordynamic Instability Problem," ASME Transactions for Power, pp. 48-57, January 1978.

6. Yamada, Y., "Resistance of Flow through Annulus with an Inner Totating Cylinder, "Bul. J.S.M.E., vol. 5, No. 18, pp. 302-310, 1962.

7. Childs, C. W., "Dynamic Analysis of Turbulent Annular Seals Based on Hirs' Lubrication Equation," accepted for publication, ASME Trans., J. of Lubrication Technology.

8. Childs, D. W., "Finite-Length Solution for Turbulent Annular Seals," Accepted for publications, ASME Trans., J. of Lubrication Technology.

9. Hirs, G. G., "A Bulk-Flow Theory for Turbulence in Lubricant Films," ASME J. Lubrication Technology, pp. 137-146, April 1973.

10. Black, H. F., "Empirical Treatment of Hydrodynamic Journal Bearing Performance in the Superlaminer Regime," J. Mech. Engine. Sci., vol. 12, no. 2, pp. 116-122, 1970.

11. Black, H. F. and Cochrane, E. A., "Leakage and Hybrid Bearing Properties of Serrated Seals in Centrifugal Pumps," Paper G5, 6th International Conference on Fluid Sealing, February 27-March 2, 1973, Munich German Federal Republic.

12. Bowen, W. L. and Bhateje, R., "The Hollow Roller Bearing," ASME Paper No. 79-Lub-15, ASME-ASLE Lubrication Conference, Dayton, Ohio; 16-18 October 1979.

13. Fröberg, Introduction to Numerical Analysis, Second Edition, Addison Wesley, 1969.

TABLE 1. - PRIOR DYNAMIC SEAL TESTS

REF.	R_a	R_c	L/D	$(C_r/R) \times 10^3$	Seal type	Cited Results
[2]	[6,000, 14,000]	[0, 3,500]	.25 , .5, 1.	10.5 , 12.9	plain	a, b, c
[3]	[3,000, 20,000]	[0, 6,000]	.5, 1.	7.23, 10.3	plain	d, e
[10]	10,000	[0, 8,000]	1.	10.7	plain	f
[11]	[3,000, 12,000]	[0, 6,000]	.232, .5, 1.	7.1	Serrated	d

a. Static force-deflection curves for $0 \le \epsilon \le 0.8$.

b. Resultant stiffness F_s/r for centered position and $\omega = 0$.

c. Rotordynamic modelling to correlate with test data on the direct damping coefficient $\bar{c}$.

d. Receptance magnitudes for centered position.

e. Rotordynamic modelling to correlate with synchronous test results. Correlation includes amplitude, phase, critical speed, and onset speed of instability.

f. Receptance magnitude and phase at centered position.

TABLE 2. - EXPERIMENTAL RESULTS FOR A CONSTANT-CLEARANCE SEAL,
L = R = 2 in. (5.08 cm), C_r = 0.020 in. (0.508 mm)

	R_a	R_c	ΔP(psi)	Leakage (gpm)	ω(rpm)	R_r/A(lbs/in)	R_θ/A(lbs/in)
1	24,580	3,160	113.	62.0	1,149.	-13,950.	3,507.
2	23,550	5,800	99.	58.5	2,105.	-13,190	6,800.
3	26,780	7,950	121.	66.51	1,885.	-16,150.	11,870.
4	25,330	8,840	113.	62.9	3,209.	-15,500.	12,790.
5	23,545	10,360	106.	58.5	3,762.	-15,090.	16,540.
6	18,140	2,878	62.0	45.1	1,054.	- 7,886.	2,344.
7	19,990	5,860	65.0	47.1	2,178.	- 8,507.	5,821.
8	18,730	8,260	65.0	46.5	3,000.	- 8,790.	9,250.
9	18,560	10,660	71.0	46.1	3,871.	-11,120.	12,750.
10	13,330	3,040	34.0	33.1	1,103.	- 4,125.	2,503.
11	13,510	6,360	36.0	33.6	2,308.	- 5,014.	4,360.
12	13,060	8,880	35.0	32.4	3,226.	- 6,030.	4,802.
13	13,610	9,860	41.0	33.8	3,582.	- 7,430.	9,170.
14	9,010	2,920	17.0	22.4	1,060.	- 2,276.	1,597.
15	8,850	5,840	19.0	22.0	2,120.	- 2,240.	3,210.
16	9,260	8,610	21.0	23.0	3,125.	- 2,095.	5,715.
17	4,750	2,700	5.0	11.8	980.4	- 670.	812.
18	4,410	4,920	3.0	11.0	1,786.	- 645.	1,475.
19	4,750	8,220	4.0	11.8	2,985.	- 578.	2,763.
20	4,410	10,630	5.0	11.0	3,859.	- 417.	3,492.
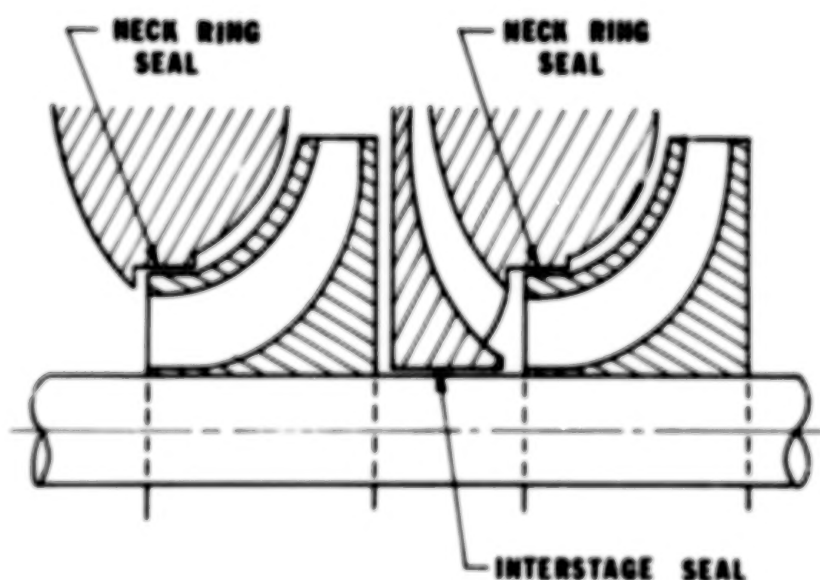
Figure 1. - Neck-ring and interstage seals for pumps.
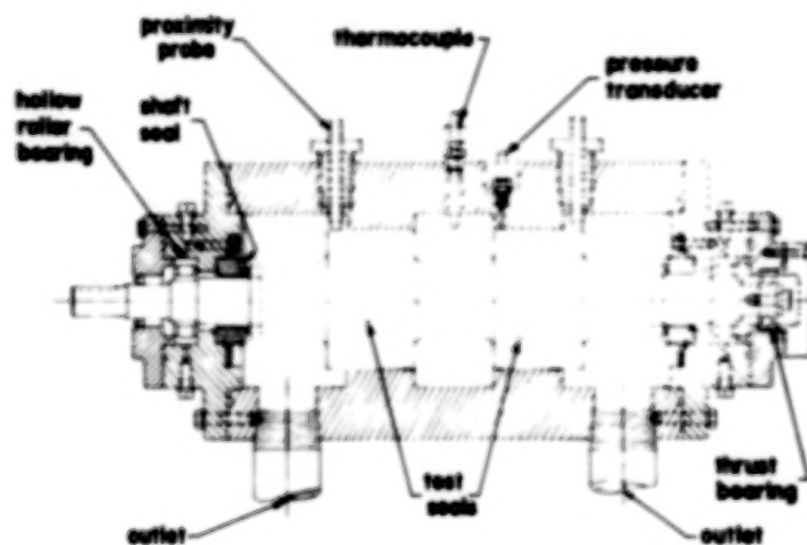
Figure 2. - Test-section layout.
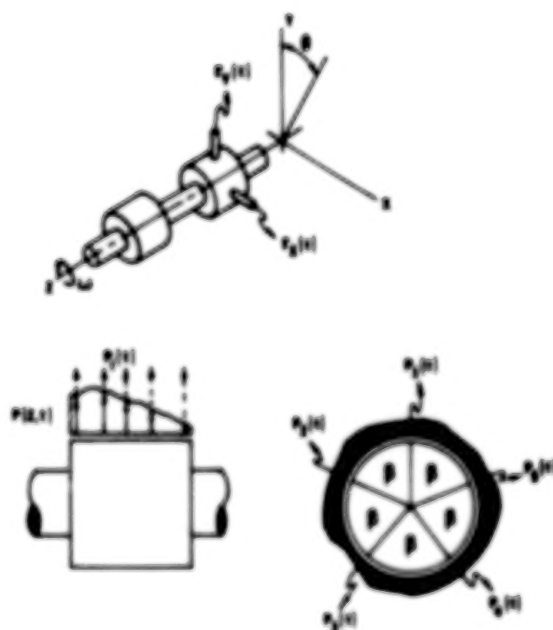
Figure 3. - Instrumentation.

169
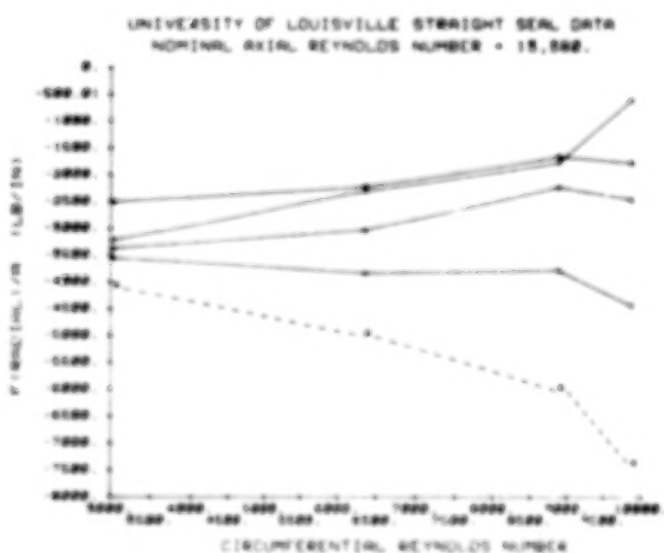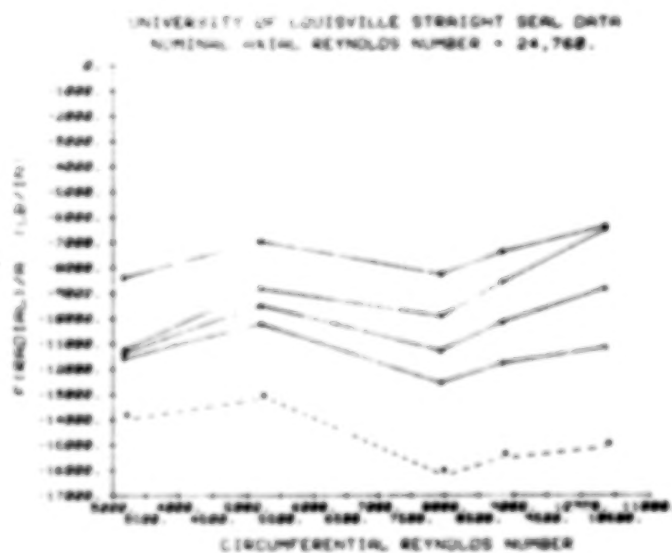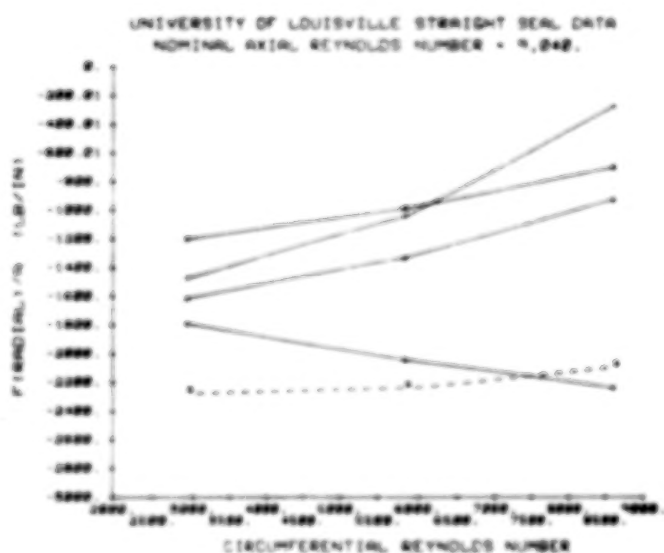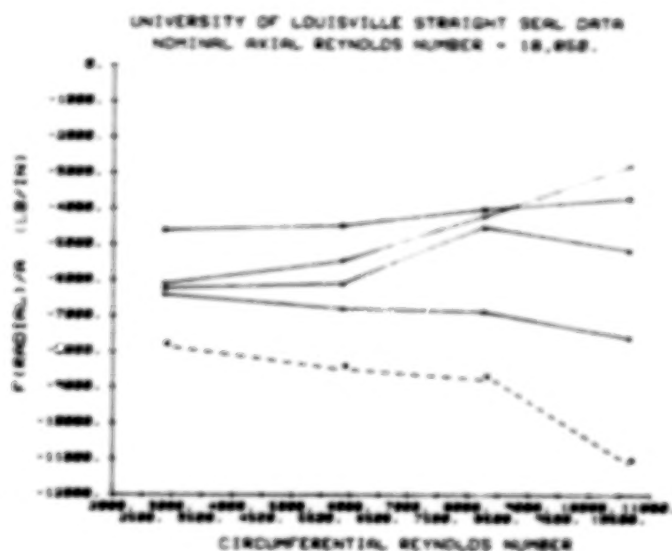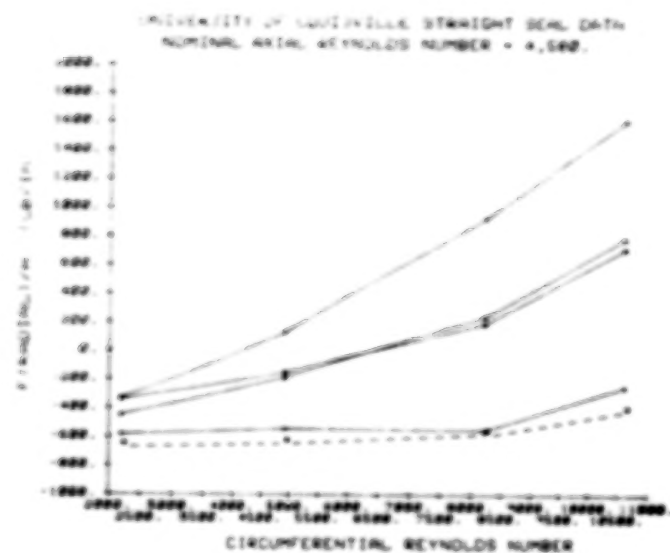
Figure 4. - Seal radial-force component versus axial and circumferential
Reynolds numbers.
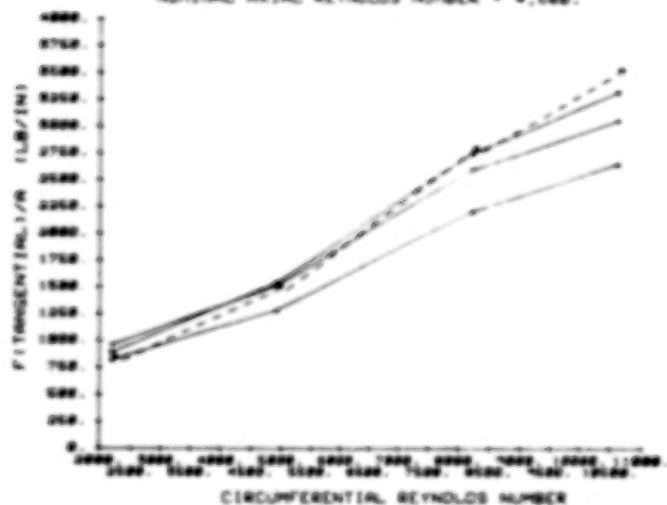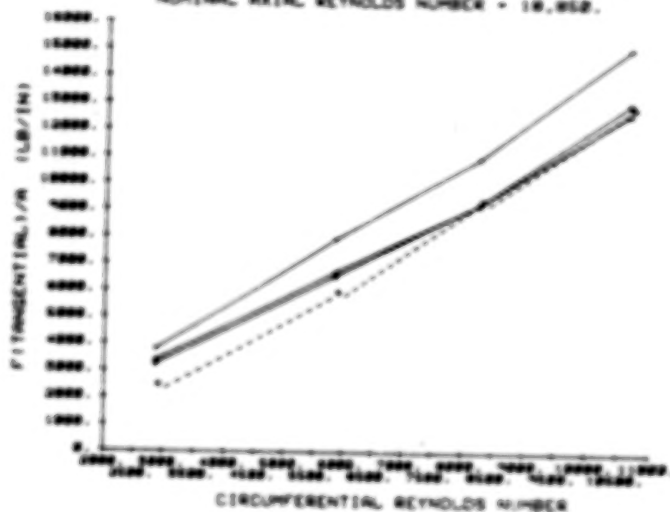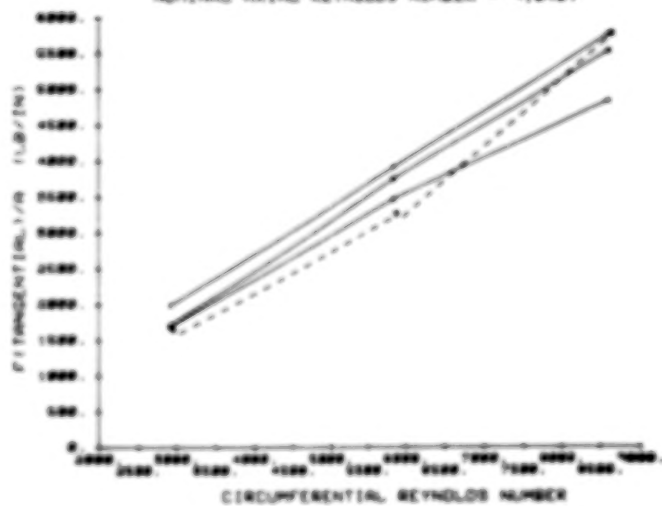
170
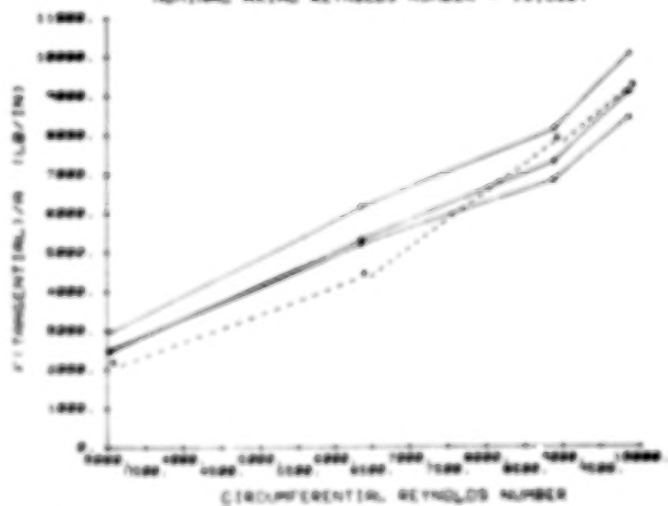
Figure 5. - Seal tangential-force component versus axial and circumferential Reynolds numbers.

BEST DOCUMENT AVAILABLE

A HIGH-REYNOLDS-NUMBER SEAL TEST FACILITY: FACILITY DESCRIPTION

AND PRELIMINARY TEST DATA*

Dara W. Childs, Clayton Nelson, and Ted Noyes
Department of Mechanical Engineering
Texas A&M University.
College Station, Texas 77843

John B. Dressman
Department of Mechanical Engineering
The University of Louisville
Louisville, Kentucky 40229

ABSTRACT

A facility has been developed for testing the leakage and rotordynamic characteristics of interstage-seal configurations for the HPFTP (High Pressure Fuel Turbopump) of the SSME (Space Shuttle Main Engine). Axial Reynolds numbers on the order of 400,000 are realized in the test facility by using a Dupont freon fluid called Halon ($CBrF_3$). The kinematic viscosity of Halon is of the same order as the liquid hydrogen used in the HPFTP. Initial testing has focused on the current flight configurations (a three-segment, stepped unit) and a convergent-taper candidate.

INTRODUCTION

The HPFTP development program experienced considerable difficulty with subsynchronous, unstable vibration problems [1]. As originally designed, the HPFTP was violently and destructively unstable at running speeds above approximately 20,000 rpm. The remedy for this situation consisted of the following steps: (a) the original soft bearing carriers were replaced by stiff bearing carriers, and (b) the grooving was removed from the original stepped interstage seal design. With these modifications, the HPFTP has been stable over its design speed range. The essential contribution of the seal modification to the elimination of the rotor instability was underlined by tests in 1979 on an HPFTP unit which whirled enthusiastically after the interstage seal clearances were deliberately enlarged.

From a rotordynamics viewpoint, seal analysis has the objective of predicting the influence-coefficients of the following equations:

$$-\begin{Bmatrix} R_X \\ R_Y \end{Bmatrix} = \begin{bmatrix} K & k \\ -k & K \end{bmatrix} \begin{Bmatrix} r_X \\ r_Y \end{Bmatrix} + \begin{bmatrix} C & c \\ -c & C \end{bmatrix} \begin{Bmatrix} \dot{r}_X \\ \dot{r}_Y \end{Bmatrix} + \begin{bmatrix} M & m \\ -m & M \end{bmatrix} \begin{Bmatrix} \ddot{r}_X \\ \ddot{r}_Y \end{Bmatrix} \tag{1}$$

as a function of seal operating conditions. Initial analyses and testing for inter-
stage and wearing seals were published by Black et al. [2-5]. Black used the
following leakage relationship from Yamada [6]:

$$\Delta P = \frac{\rho V^2}{2} [1+\xi+2\sigma]$$

(2)

where ξ is a constant entry-loss coefficient, V is the average fluid velocity, and
σ is the friction-loss coefficient defined by;

$$\sigma = \frac{\lambda L}{C_r} .$$

(3)

In this relationship, L is the seal length, C_r is the radial clearance, and λ is
the following function of the axial and circumferential Reynolds numbers (R_a, R_c):

$$\lambda = 0.079 \ R_a^{-\frac{1}{4}} [1+(\frac{7R_c}{8R_a})^2]^{3/8}$$

(4)

$$R_a = 2VC_r/\nu, \ R_c = R\omega C_r/\nu$$

where ν is the fluid's kinematic viscosity, R is the seal radius, and ω is the
rotor's rotational speed.

Childs has subsequently developed analyses [7,8] for constant clearance seals
based on Hirs' turbulent lubrication equations [9]. These results are similar to
Black's, but differ in some respects. Their principal advantage is in a direct
derivation from a single set of governing equations.

Fleming [10] proposed that the direct stiffness of seals could be increased
by either (a) introducing a step in a constant-clearance seal, or (b) using a
convergent-taper geometry. Childs [11] completed an analysis for convergent-tapered
seals which defined all of the dynamic coefficients, and demonstrated that the
seal taper significantly reduces the seal damping and cross-coupled stiffness
terms, while increasing the direct stiffness. Hendricks [12] found in testing
straight and convergent tapered seals at large eccentricities in liquid hydrogen
that a slight taper reduced local seal cavitation at the seal exit, and eliminated
the possibility of a local negative stiffness developing.

Black's analysis was used initially in predicting the rotordynamic coefficients
of the HPFTP interstage seals [1]. His experimental results were for plain
(constant-clearance) seals having smooth and serrated surfaces, and extended out
to axial Reynolds numbers on the order of 20,000, as compared to 500,000 for the
HPFTP. Given that the HPFTP seals differ substantially from those tested by Black
in both configuration and operating conditions, the decision was made to implement
a test program to directly measure the forces developed by seals, which are geo-
metrically similar to the HPFTP seals and operating at the same Reynolds number
conditions. The development of a facility to make these measurements together
with a discussion of some preliminary results is the subject of this report.

FACILITY DESCRIPTION

Test Section

The test section design is an extension of an earlier design used in a University of Louisville test program [13], and is illustrated in Figure 1. Fluid enters in the center and discharges axially across the two test seals. The seals on the right and left illustrate, respectively, the current stepped configuration and a proposed convergent-tapered configuration for the HPFTP interstage seals. The current test section differs from that employed earlier [13] in that it assembles in a mid-plane position, which permits testing of the "slingers" shown in the figure.

The test-section rotor is supported in Torrington hollow-roller bearings* [14], which are extremely precise, radially preloaded, and have a predictable and repeatable radial stiffness. The test seals are mounted eccentrically to the test rotor; hence, rotor rotation develops a rotating pressure field that is constant with respect to a rotor-fixed observer. Axially-spaced kulite strain-gauge pressure transducers are used to measure the pressure field which is developed by seal rotation. Seal motion is measured by MTI capacitance probes in the vertical and horizontal planes. Inlet and discharge measurements are made of temperature and pressure for use in defining the density and viscosity of the test fluid.

A 10-hp variable-speed electric motor is used to drive the test section from five rpm to 5300 rpm. A motion transducer, actuated by a rotating ten-toothed wheel, provides a signal for a counter which defines the rpm of the test section.

John Dressman of the University of Louisville designed the test section and supervised its construction.

Test-Fluid Selection

The very high Reynolds numbers encountered in the HPFTP result from (a) the extremely low kinematic viscosity of liquid hydrogen, (b) the high-shaft rotational speed, and (c) the very large ΔP's developed by the HPFTP stages. The average properties of hydrogen within the HPFTP interstage seals are

$$\mu = 1.16 \times 10^{-5} \text{ Ns/m}^2, \; \rho = 71.2 \text{ kg/m}^2$$
$$\nu = 1.63 \times 10^{-7} \text{ m}^2/\text{sec.}$$

For comparison, the nominal properties of water at 25°C are

$$\mu = 8.9 \times 10^{-4} \text{ Ns/m}^2, \; \rho = 1000 \text{ kg/m}^3$$
$$\nu = 8.9 \times 10^{-7} \text{ m}^2/\text{sec.}$$

Since the Reynolds numbers are inversely proportional to ν, an ideal test fluid should have a low absolute viscosity and a high density.

---

* These bearings were made available from Torrington, Incorporated through the courtesy of W. L. Bowen.

The test fluid selected to meet these criteria is bromotrifluoromethane, $CBrF_3$, which is manufactured as a fire extinguisher fluid (Dupont FE 1301 or Halon) and refrigerant (Freon 13B1). Its fluid properties at 25°C are [15,16]

$$\mu = 1.54 \times 10^{-4} \text{ Ns/m}^2, \quad \rho = 1570 \text{ kg/m}^3,$$

$$\nu = 1.0 \times 10^{-7} \text{ m}^2/\text{s}.$$

This liquid actually has a lower kinematic viscosity than liquid hydrogen, and has the additional advantage of being nonflammable and nontoxic. The vapor pressure of Halon is approximately 200 psi at room temperature.

Seal Geometry

As illustrated in Figure 1, the current flight geometry uses three constant-clearance seal segments separated by two steps. The dimensions of the test seal segments are

L_i (cm)	R_i (cm)	C_{ri} (mm)
1.4986	5.0292	0.5080
1.5265	4.9682	0.5080
1.8034	4.9098	0.4826

The dimensions of the tapered seal are

$$L = 4.996 \text{ cm}, \quad R = 5.0292,$$

$$C_{ro} = 0.5715 \text{ mm}, \quad C_{ri} = 0.4572 \text{ mm}$$

where C_{ro} and C_{ri} are the entrance and exit clearances, respectively. These dimensions yield the following definition for the tapered parameter:

$$q = (C_{ro} - C_{ri})/(C_{ro} + C_{ri}) = 0.111.$$

Relatively speaking, this is a slight taper which should [11] slightly increase K, while slightly decreasing the remaining coefficients.

Mechanical System Layout

Figure 2 illustrates the flow loop used to provide specified flowrates through the test-section seals. A six-stage Goulds pump provides the flowrate required. Loop flow rate discharges from the pump, and then may split with part of the flow going through the test section, and the remainder proceeding through control valves 1 and 3. Two control valves in series are required to absorb the full output pressure of the pump without cavitation. The bypass flow mode is used for total test-section flowrate less than 100 gpm, which represents the lowest flowrate operating point for the pump. Valve 4 is closed in the bypass mode. As the required flowrate increases above 100 gpm, valve 1 is closed and valves 2 and 3 are progressively opened. Valve 4, which has a larger capacity than the remaining valves, is opened to achieve maximum flow conditions. Flowrate through the test section seals is measured by Fischer-Porter vortex flowmeters.

The test-section fluid is circulated through a heat exchanger, which is supplied chilled water by a Trane chiller. The chiller capacity is augmented by a 2000 gallon water tank which is buried outside the test facility.

The ambient system pressure is maintained by the accumulators illustrated in Figure 2. They are also used to remove liquid Halon from the test section for replacement of rotors. Similar accumulators are used to transfer fluid back and forth from the 2000 lb Dupont delivery tank. In fact, all of the Halon can be pumped back into the delivery tank using the accumulators.

The filters illustrated in Figure 2 have a ten micron limit for particles. The complete flow system is stainless steel except for the pump body and the heat exchanger so that particle contamination in the test fluid is minimized.

Control System

The axial and circumferential Reynolds numbers are the quantities to be controlled in the seals. These variables are determined by the pressure and temperature measurements within the seal (which define ρ and μ), the seal rotational speed ω, and the flowrates through the seals. Control is supplied by means of a Data General Nova computer. Control signals are generated, based upon the difference between a measured R_a and a specified $\bar{R}_a$, and cause a change in the Masoniellan control values. Active control is not entirely closed-loop. The operator specifies the number of control cycles to be evaluated by the computer. The computer calculates the running speed that is required to achieve a specified $\bar{R}_c$, and the specified test section speed is set manually.

DATA ACQUISITION AND ANALYSIS

Data Acquisition System

The transient test data to be recorded consists of the seal motion $r_x(t)$, $r_y(t)$ and the pressure measurements $p_i(t)$. Five pressure measurements are made for the tapered seal, with their spacing specified by a Gauss-Legendre quadrature formula [13]. Four additional pressure measurements are made on the stepped seals to measure the pressure immediately upstream and downstream of the steps. These data are recorded using a 17-channel Physical Data, Inc. recorder. Each channel of this unit has its own A/D converter with a sampling rate up to 2×10^6 Hz, and 4096 storage locations.

The physical data system is controlled from the D. G. Nova computer, which enables the recorder, commands data capture, and then controls dumping of the data into disk memory of the Nova. Transient data for control of the system is obtained directly through A/D units on the Nova.

Data Analysis

As outlined in [13], transient data analysis consists of alignment of the pressure signals (which are measured at various circumferential locations), and integrating the pressure signals to obtain the seal force components. The test rig causes a synchronous precession of the seals, and the resultant motion may be stated:

$$r_x = A \cos \omega t, \quad r_y = A \sin \omega t \tag{5}$$

The six coefficients of Eq. (1) can not be separately identified for this type of motion. In fact, if Eq. (5) is substituted into Eq. (1), and the coefficients of $\sin \omega t$ and $\cos \omega t$ on both sides of Eq. (1) are equated, only two independent numbers can be identified. For the present study, the two numbers chosen for presentation are the radial and circumferential components of the reaction force. From Equations (1) and (5) these components may be stated:

$$R_\theta/A = \frac{|\overline{r \times R}|}{A^2} = k - C\omega - m\omega^2$$

$$R_r/A = \frac{|\overline{r \cdot R}|}{A^2} = M\omega^2 - c\omega - K . \tag{6}$$

Since the coefficients depend on σ, which in turn depends on $R_c = R\omega C_r/\nu$, one can not generally vary ω to obtain additional independent equations for the solution of the coefficients. Stated differently, changing ω also changes the coefficients. An exception to this rule is provided by very high values of R_a for which σ is insensitive to changes in ω.

TEST SERIES

Three rotors were initially manufactured for use in testing the general seal configurations of Figure 1, viz , the current flight configuration and a tapered-seal alternative. These rotors differ only in the nominal seal eccentricity; specifically, they have the following eccentrities and eccentricity ratios:

(a) Rotor 1, A = .005 in, A/C_r = 0.25,

(b) Rotor 2, A = .010 in, A/C_r = 0.50, and

(c) Rotor 3, A = 0.0 in, A/C_r = 0.0.

The zero eccentricity rotor provides static leakage and pressure gradients only. Rotors 1 and 2 provide insight as to the influence of seal dynamic eccentricity on test results. The above rotors have been tested over the following nominal axial and circumferential Reynolds number ranges:

R_a: 50,000, 75,000, 150,000, 325,000, 400,000

R_c: 40,000, 65,000, 90,000, 115,000, 140,000

More specifically, a matrix of tests has been carried out such that all of the five values of R_c are obtained for each value of R_a.

Theoretical results [5,7,8] have demonstrated that the cross-coupling terms of Eq. (1), i.e., k, c, m, depend on the fluid tangential velocity entering the seal. The standard test rig provides minimal pre-rotation of the fluid entering the seal. Hence, rotor 2 was mofified by shrinking on an active "slinger" at the entrance to both seals to provide significant fluid pre-rotation. Slingers incorporated radial slots and an axial clearance of 0.010 in. for a radial distance

177

of 0.75 inches prior to seal entry. The power requirements to rotate this rotor are considerably higher than the other rotors, and data can only be taken for axial Reynolds numbers out to 150,000.

Two additional rotors have been manufactured to examine the influence of surface roughness on both sealing capability and the seal reaction-force components. These rotors have an "almost" circumferential grooving pattern with a nominal depth of 0.001 and 0.002 inches, respectively. The original, zero eccentric rotor, was machined to yield an 0.002 inch surface roughness pattern. All of these rotors have been tested over the complete Reynolds number range.

Additional planned tests include machining surface roughness into the housing, with the first and second machining operations yielding depths of 0.001 and 0.002 inches, respectively. The following rotors will be tested in these two surface-roughened housings:

(a) Rotor 1 (smooth); A = 0.005 in.,
(b) Rotor 4 (0.001 inches depth); A = 0.003 in.,
(c) Rotor 5 (0.002 inches depth); A = 0.005 in., and
(d) Rotor 3 (0.002 inches depth); A = 0.0 in.

Testing of helically grooved seals is proposed for the coming year which will include a systematic variation in taper angles, nominal clearances, and groove depths. Initial testing for these seals will be at zero eccentricities.

PRELIMINARY RESULTS
Reduction of the test data is still in a preliminary stage; hence, the results which are available for discussion are limited at present to some static data (ΔP - leakage and pressure gradients) and force magnitude results for the two seals of rotor 1.

Static Results
Static results were obtained for the stepped and tapered seals of rotor 3, viz., the zero-eccentricity rotor. Figures 3 and 4 illustrate the steady-state pressure gradients for the stepped and tapered seals, respectively, for a range of axial and circumferential Reynolds numbers. Each frame of these figure sets illustrates the influence of changes in R_c with R_a held constant. The strain-gauge pressure transducers used to obtain these results have an accuracy specifications of .1% of full scale, which amounts to approximately 1 psi. This lack of accuracy is much more noticeable at low flow rates and shallow pressure gradients than at high flow rates. To some extent, this explains the more "ragged" nature of the pressure gradients in the low flow conditions of figures 3 and 4 as compared to high flow conditions. Each data point in these figures corresponds to an average of 200 samples.

The pressure gradients of figures 3 and 4 are seen to be more sensitive to changes in R_c at low values of R_a, becoming relatively independent of R_c at higher values of R_a. This result would be expected, since from Eqs. (2) and (3)

$$\frac{\partial \sigma}{\partial R_c} = .045 \ (\frac{L}{C}) R_a^{-9/4} [1 + (\frac{7R_c}{8R_a})^2]^{-5/8},$$

which shows a marked drop in sensitivity with increasing R_a.

An apriori analysis of the stepped seal for leakage would use Eq. (1) for each step yielding the results

$$\Delta P_i = \frac{\rho V_i^2}{2} (1 + \xi_i + 2\sigma_i); \quad i = 1, 2, 3$$

$$\Delta P = \sum_{i=1}^{3} \Delta P_i$$

$$w = \rho V_i A_i ; \quad i = 1, 2, 3$$

where A_i is the area of each annulus. Normally, one assumes that the entrance loss factors are constant, independent of R_a and R_c, and range between 0.1 and 0.5. At the inlet, the term $(1 + \xi_1)\frac{\rho V^2}{2}$ represents a velocity head loss due to fluid acceleration plus an entrance loss represented by ξ_i. The following numbers for $(1 + \xi_1)$ were obtained from the data of Figure 3.

Stepped Seal Data

R_a	$(1 + \xi_1)$	$(1 + \xi_2)$	$(1 + \xi_3)$
382,000	1.129	.435	.484
323,000	1.129	.432	.531
150,000	1.255	.432	.371
75,000	1.681	.537	-.178
50,000	1.913	.916	.999

These results are fairly regular and constant over the higher Reynolds number sets, but tend to be erratic over the two lower Reynolds number sets. The results for R_a = 75,000 and 50,000 should be viewed with some skepticism because of the previously mentioned accuracy of the pressure transducers. The most unexpected result from Figure 3 is the relatively small pressure gradient across step 1, the entry step, as compared to the remaining two steps. Figures 3(a) and 3(b) show a small pressure rise immediately before the first step, while figure 3(c) shows a flat pressure gradient across the first step. A zero pressure gradient, $\sigma = 0$, would yield a prediction of zero stiffness contribution from the first step.

For a tapered seal, the steady-state leakage relationship is [11]

$$\Delta P = \frac{\rho V^2}{2} \left[\frac{1+\xi}{(1+q)^2} + 2\sigma + 4q \right]$$

for small q. The experimental results from figures 4(a) - (c) yield the following entrance-loss result:

R_a	$1 + \xi$
434,000	0.926
325,000	0.996
150,000	0.878

While these losses are constant, independent of R_c, this is not the case in figures 4(d) and 4(e) where the losses increase steadily with R_c. In fact, an inlet pressure increase was measured for $R_c = 16,890$ and $R_c = 49,981$. The tapered-seal results above for high Reynolds numbers are consistent with Fleming's assumption [10] of zero ξ.

Dynamic Results

Only a very limited number of dynamic data sets have been reduced. The only immediate conclusion which has been drawn from these results is that the force magnitude $|R| = (R_0^2 + R_T^2)^{\frac{1}{2}}$ is comparable for both the current stepped seal configuration and the proposed tapered seal. A comparison of their radial and tangential forces and a comparison to theory will be forthcoming shortly.

CLOSING STATEMENTS

A test facility has been developed which has the capability for testing annular seals at Reynolds numbers which are comparable to those developed in cryogenic turbopumps. Generally speaking, the facility works the way it was expected to and is beginning to yield the types of static and dynamic test data that are required to support theoretical predictions of seal rotordynamic coefficients and leakage.

REFERENCES

1. D.W.Childs, "The Space Shuttle Main Engine High Pressure Fuel
    Turbopump Rotordynamic Instability Problem," ASME Trans.J of
    Engineering for Power,pp. 48-57, Jan. 1978

2. H.F.Black, "Effects of Hydraulic Forces in Annular Pressure Seals
    on the Vibrations of Centrifugal Pump Rotors," J.M.Eng. Sci.,
    Vol.11, no.2,pp.206-213,1969

3. H.F.Black and D.N.Jensen, "Dynamic Hybrid Properties of Annular
    Pressure Seals, " Proc. J.MECH. Engin., Vol. 184,pp.92-100,1970

4. H.F. Black and D.N.Jensen,"Effects of High Pressure Ring Seals
    on Pump Rotor Vibrations,"ASME Paper No. 71-WA/ff-38, 1971.

5. H.F.Black, P.Allaire, and L. Barrett, "The Effect of Inlet Flow
    Swirl on the Dynamic Coefficient of High-Pressure Annular Seals,"
    Ninth International Conference in Fluid Sealing, BHRA Fluid Engineer
    Engineering, Leeuwenhurst, The Netherlands, April, 1981.

6. Y.Yamada, "Resistance of Flow through Annulus with an Inner Rotating
    Cylinder,"Bul.J.S.M.E., Vol.5, no.18,pp.302-310,1962.

7. D.W.Childs, "Dynamic Analysis of Turbulent Annular Seals Based on
    Hirs' Lubrication Equations," accepted for publication, ASME
    Trans.J. of Lubrication Technology.

8. D.W.Childs,"Finite-Length Solutions for Rotordynamic Coefficients
    of Turbulent Annular Seals," accepted for publication, ASME Trans.J.
    of Lubrication Technology.

9. G.G.Hirs, "A bulk-Flow Theory for Turbulence in Lubricant Films,"
    ASME J. Lubrication Technology, pp. 137-146, April 1973.

10. D.P.Fleming, "High Stiffness Seals for Roter Critical Speed Control,"
    ASME Paper 77-DET-10,Design Engineering Technical Conference,
    Chicago,IL., 26-30 September 1977.

11. D.W.Childs,"Convergent-Tapered Annular Seals: Analysis for Rotor-
    dynamic Coefficients," Fluid Structure Interactions in Turbomachinery
    presented at the ASME winter annual meeting, 15-20 November 1981.

12. R.C.Hendricks,"Some Flow Characteristics of Conventional and Tapered
    high-Pressure-Drop Simulated Seals," ASLE preprint No.79-LC-3B-2,
    presented at the ASLE/ASME Lubrication Conference, Dayton, Ohio;
    16-18 October 1979

13. D.W. Childs, J.B.Dressman, and S.B.Childs, "Testing of Turbulent
    Seals for Rotordynamic Coefficients," NASA Conference Publication
    2133,Rotordynamic Instability Problems of High Performances
    Turbomachinery, proceedings of a workshop held at Texas A&M Univ.,
    12-14 May 1980, pp. 121-138, proceedings published September 1980,

14. W.L. Bowen, and R. Bhateja, "The Hollow Roller Bearing,"ASME Paper
    No. 79-Lub -15, ASME-ASLE Lubrication Conference; Dayton,Ohio; 16-18
    October 1979.

15. H. Stephen and K.Lucas, <u>Viscosity of Dense Fluids,</u> p.59,Plenum Press,
    New·York-London

16. Anon., T-1301,Thermodynamic Properties, Dupont Fire Extinguisher
    Properties, E.I. Dupont DeNemours&Co., Wilmington, Del; 1966.
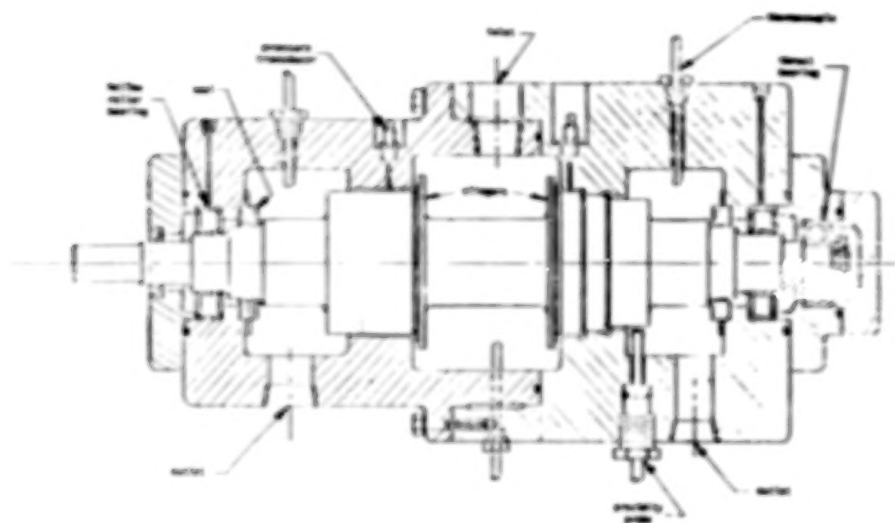
Figure 1. - Test-rig assembly.
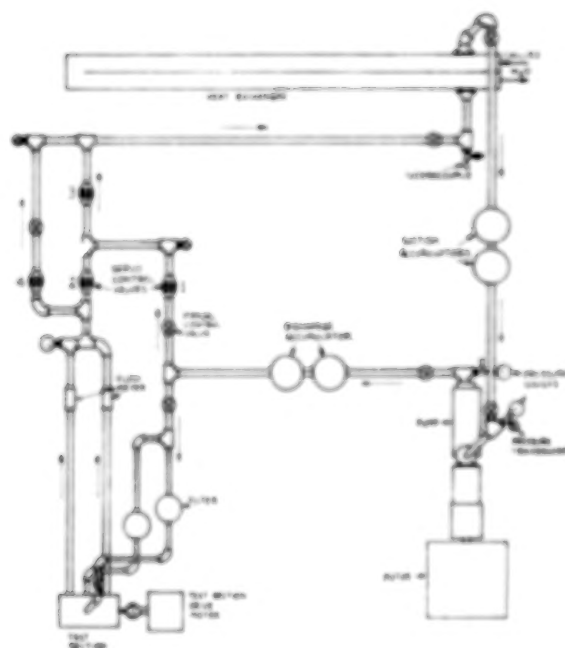
Figure 2. - Test-facility layout.

SEAL 1 DATA

Figure 3(a).

SEAL 1 DATA
AVG AXIAL REYNOLDS • : 323001.

SEAL 1 DATA
AVG AXIAL REYNOLDS • : 75905.

SEAL 1 PROFILE

AXIAL LOCATION (IN)

Figure 3(b).

Figure 3(d).

SEAL 1 DATA
AVG AXIAL REYNOLDS • : 149168.

SEAL 1 DATA
AVG AXIAL REYNOLDS • : 49927.

SEAL 1 PROFILE

AXIAL LOCATION (IN)

Figure 3(c).

SEAL 1 PROFILE

AXIAL LOCATION (IN)

Figure 3(e).

184

Figure 4(a).

Figure 4(c).

Figure 4(b).

Figure 4(d).

185

SEAL 2 DATA
AVG AXIAL REYNOLDS • = 49212.

○ FILE:SEAL231032.RD   RC = 140537   RA = 49552
▲ FILE:SEAL241032.RD   RC = 114619   RA = 47769
+ FILE:SEAL251032.RD   RC = 90015   RA = 50082
✕ FILE:SEAL261032.RD   RC = 64890   RA = 48676
◇ FILE:SEAL271032.RD   RC = 40108   RA = 49981

Figure 4(e).

186
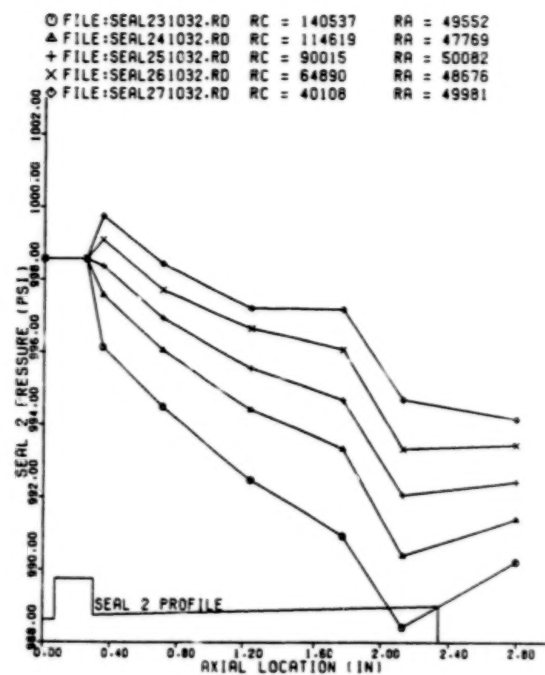
VIBRATION AND DESTABILIZING EFFECTS OF FLOATING RING SEALS IN COMPRESSORS

Mark F. Emerick
Compressor and Custom Pump Division
Allis-Chalmers Corporation
Milwaukee, Wisconsin 53201

I. INTRODUCTION

Operating experience on a compressor commissioned 12 years ago has presented an interesting history of sporadic increases in shaft vibration. Initial operation was satisfactory with low levels of vibration. However, after some time the shaft vibration level increased to several mils. Initially this was believed to be due to rotor unbalance from deposits formed in the passages due to process upsets. After cleaning up the rotor, operation was again satisfactory. In time the vibration level again increased. It was then found that the rotor vibration was primarily subsynchronous. Further investigation revealed that the original seal design was subject to wear and was no longer properly pressure balanced. A modified seal design was installed and it has operated successfully for the past six years.

Subsequent analysis has provided a better understanding of the seal destabilizing effects on the rotor and motion of the seal which has been confirmed by test data on the current seal design. These will be briefly presented.

NOMENCLATURE

MW	molecular weight
P	pressure
K_{yx} K_{xy}	cross coupled stiffness damping properties for seals
C_{xx} C_{yy}	principle damping properties for seals
ω	angular velocity (rad/sec)
D	diameter
μ	oil viscosity
L	seal or bearing length
c	clearance
F_p	force, radial
F_A	force, axial

μ	coefficient of friction
Q	aerodynamic or seal destabilizing
δ	logarithmic decrement

II COMPRESSOR DESIGN

The subject machine is a 5-stage, vertically-split, centrifugal compressor with floating ring oil film seals in refinery service. (See Figure 1) The gas is a diesel distillate (MW = 8.2) and the process conditions are as follows:

Inlet Pressure P_1 = 2896. K Pa (420 PSIG)

Discharge Pressure P_2 = 4178 K Pa (606 PSIG)

Flow   = 322 Kg/min (739 LB/MIN)
Driver Size   = 1118.6 KW (1500 HP)

The compressor has 38.1 cm (15") diameter impellers and operates at 12,320 RPM in 8.89 cm (3.5") diameter tilting pad journal bearings. The seal diameter is 11.43 cm (4.5 in.)

III OPERATING HISTORY

Commissioned in 1970, the machine had a history of minor, occasional vibration problems. A pattern developed which was noted by the Allis-Chalmers Field Service and Repair Group:

.   The machine generally operated smoothly following service or maintenance.

.   Increased shaft vibration would develop over time (6 months). Seal oil flows would sometimes increase substantially, resulting in operation of the auxiliary seal pump to keep up with the increased flow.

.   Upon disassembly, the unit would be fouled with ammonium chloride deposits in the aerodynamic passages. (See Figure 2) The presence of the deposits and the resulting unbalance was initially believed to be the cause of the vibration.

    The floating bushing would be quite worn on the axial face resulting in high axial forces on the seal housing. (See Figure 3 for arrangement.)

Finally, in 1975 the operator reported that vibration levels had become unacceptable and noted that the machine behaved differently with each of the two rotors (main and spare). One rotor performed smoothly with enlarged radial seal clearances (8 mils vs. 2-3 mils design), even though it was fouled and a balance check indicated it was out of balance. The other rotor ran rough with design seal clearances, despite a touch-up balance. The apparent contradiction between vibration experience and the

machine balance condition strongly suggested that the vibration problem was non-synchronous in nature. The Allis-Chalmers service group discussed the problem with the Compressor Engineering group and a study was initiated.

Field vibration spectra were obtained by Allis-Chalmers on the balanced rotor at several locations using displacement probes and accelerometers. See Figure 4a.

The data showed:

1. A subsynchronous vibration signal was present at all locations checked. (See Figure 4b & c)

2. The frequency which would change with a slight variation in bearing and seal oil temperature, varied slightly from 80.6 to 81.6 hz, (4836 to 4906 CPM).

3. Accelerometer data (integrated to yield displacements) showed casing motions which were significantly lower than shaft amplitudes indicating that the probes were measuring actual shaft motion, and not a foundation resonance.

Vibration amplitudes at various locations are shown in Table 1.

TABLE I. - VIBRATION AMPLITUDES AT 4850 CPM (FILTERED)

AMPLITUDE	A_1	IB_1	A_2	OB_1	OB_2
mm	.0127	.051	.009	.009	.074
(mils)	(.5)	(2.0)	(.35)	(3.5)	(2.9)

The synchronous component of shaft vibration was less than .0127 mm (.5 mils). This coincided with the customers comments about the performance of the two rotors. An increase in the synchronous vibration of the out-of-balance rotor could still result in lower overall vibration levels if the sub-synchronous component present in the well balanced rotor were eliminated.

IV ANALYSIS OF PROBLEM

At the time the machine was designed, analysis was limited to undamped critical speeds, so an updated rotor dynamics analysis was performed using improved rotor dynamics programs in use at Allis-Chalmers in 1975 which included:

. Undamped critical speed map showing intersection of undamped critical speeds with bearing stiffness curves.
. Mode shapes.
. Elliptical orbit synchronous response analysis.
. Stability analysis.

189

The critical speed analysis indicated that the machine was operating between the 2nd and 3rd modes, see Figure 5a. The mode shapes show substantial motion at the bearings for the second mode indicating it should be well damped (see Figure 5b). This is confirmed by the response analysis (Figure 5c), note that the 2nd mode is well damped and that the amplitudes produced by an unbalance distribution based on the API residual unbalance limit are quite low (less than .002 mm, [.8 mils]). The response analysis showed a 1st resonance at 4100 RPM, and the 1st critical speed on test was 4086 RPM.

Baseline (no destabilizing) stability analysis showed acceptable stability with a log decrement of .169 at 3845 CPM for the 1st Y-mode in forward precession. (See Figure 5d.)

Since the machine was stable under baseline conditions it was then desired to evaluate the rotor's sensitivity to destabilizing forces approximate their destabilizing effect the stiffness and damping p ties of the seal ring were estimated by assuming that the seal sto ing the shaft ("locks up") and behaves as a non-cavitated concentri sleeve bearing.

Under these assumptions the properties are given approximately by:

$$K_{xy} = K_{yx} = \frac{\pi}{4}\, \omega\, D\mu \left(\frac{L}{c}\right)^3$$

$$\omega\, C_{xx} = \omega\, C_{yy} = 2\, K_{xy}$$

From this calculation the properties developed for design conditions are:

- $K_{xy} = K_{yx} = 1077$ N/CM   (6.148×10^5 lb/in.)
  $C_{xx} = C_{yy} = 1681$ N-S/CM   (960 lb-sec/in.)

The principle stiffness terms K_{xx} and K_{yy} for a concentric seal are negligible. Note that these properties are highly sensitive to variations in clearance (inversely proportional to C^3), and that quadrupling the clearance reduces the properties by a factor of 64. Thus the enlarged clearances at the seals found on disassembly could have allowed operation even if the seals were locked up. This explains why the unbalanced rotor with enlarged clearances operated with less vibration than the balanced rotor with design clearances which had bounded whirl.

More sophisticated calculation schemes exist to develop the seal complete stiffness and damping matrices for various assumptions about the seal lock-up eccentricity. However, the results are sensitive to the assumptions about whether lock-up results in increased or decreased journal loading. Reduced journal loading will change the natural frequency of the rotor because the effective bearing span changes with transfer of the load to the seals. Due to the uncertainties associated with the assumption of a lock-up eccentricity, the simple concentric seal properties were used in this case.

Various values of seal destabilizing were input into the stability analysis to evaluate the system sensitivity. See Figure 5e. The stability analysis shows zero log decrement with aerodynamic destabilizing of 2329 N/CM (1330 lb/in) distributed among the impellers and 38,530 N/CM (22,000 lb/in) at each seal. This is substantially less destabilizing than would be produced by the locked up seals with original design clearance. Thus the seals can produce sufficient destabilizing to drive the rotor into bounded whirl under lock-up conditions.

The frequency of the analytically predicted unstable mode was 3850 CPM as opposed to 4850 CPM in the field. Phase information from the field test data indicated that the shaft ends were in phase, so it was concluded from the limited available information about frequency and mode shape that the 1st 'Y' mode of the rotor was unstable (bounded whirl) and was being driven by the seals. Several other conclusions can be drawn from the operating experience and analysis:

1. Stable operation of this rotor with the design seal clearances is only possible if the seal "tracks" the shaft and doesn't lock-up. This implies that any destabilizing produced under tracking conditions must be substantially less than that present under lock-up, in fact less than 38,530 N/CM (22,000 lb/in).

2. Stable operation is possible if the seal locks up, if the seal clearances are abnormally large (resulting in much smaller hydrodynamic destabilizing forces).

3. The difference in the frequency of the unstable mode between analysis and field data is possibly due to the development of principle stiffness terms (Kxx, Kyy) at the seals due to an eccentric lock-up of the seal ring which transfers bearing load to the seals, thus reducing the effective bearing span of the rotor, and raising its natural frequency from 3850 to 4850

4. The frictional force (F_R) which restrains the seal from moving radially (and determines lock-up eccentricity) is a function of the pressure induced axial forces (F_A) on the seal ring and the coefficient of friction (γ) between the seal and its housing.

$$F_R = \gamma F_A$$

Review of the axial forces (F_A) on the seal at the design pressure with no seal wear show a relatively small value. See Figure 6A.

$$F_A = P(\frac{\pi}{4}) \quad (D_2^2 - D_1^2) = 792 \text{ N} \ (178 \text{ lbs.})$$

However, as wear occurred on the axial face of the seal, the outer diameter of the contact face (D_2) increased. For example, if axial wear on the ring was .0254mm (.001") one fourth of the chamfer would be removed, and D_2 would increase from 11.53 cm (4.54 in.) to 13 cm (5.118 in.).

At this point the axial force would be 8985 N (2020 lbs.) or 11.3 times the original seal design value. The radial force could increase by more than this if the coefficient of friction increased with wear.

Thus the original design was highly sensitive to both the friction coefficient and wear so that following some initial wear, the wear rate would accelerate until lock-up occurred.

4. Since the seal parts had shown substantial wear during earlier maintenance and service inspections, the compressor performed well after maintenance, and the stability analysis showed good correlation with experience, seal modification was selected as the best method of resolving the problem.

V   SOLUTION:

Such a seal-induced instability can be solved by two types of seal modifications:

1. Allow the seal to lock up, but reduce the hydrodynamic forces produced by changing the geometry of the seal in the following ways:

   a. Reduce seal effective length - reducing the effective length by adding grooves to the seal surface reduces the stiffness and damping produced but this is at the expense of reduced film thickness and therefore seal centering capability which can increase the possibility of seal rubs.

   b. Increase seal clearances - This reduces the stiffness and damping properties but increases oil flows dramatically which is undesirable.

      Increased clearance due to wear allowed operation in this case despite a locked-up bushing. The auxiliary seal pump ran all the time. In addition the customer added a third pump to keep up.

2. Balance the axial forces on the seals as closely as possible so that the seal doesn't lock up to begin with. Reduction in axial forces makes the seal less sensitive to the coefficient of friction between the seal and its housing (which can increase with wear) and reduces the seals tendency to wear.

The second type of modification was used to solve this problem. Figure 6a and 6b show the original and modified seal bushings.

Note that the following modifications were made.

1. The residual axial force on the bushing was reduced by balancing the pressure induced axial force.

a.   O-ring was removed from bushing end reducing friction.

b.   Face relief was remachined to better control pressure
      equalization.

c.   Pressure balancing axial hole added.

d.   The taper was removed to make the new design
      insensitive to wear.

2. These changes don't affect the hydrodynamic performance (i.e., leak-
   age or film thickness) of the seal, only the force required to move it
   radially (FR).

Since the new seal has been installed, seal wear has been negligible and
the sub-synchronous vibration problems have been eliminated. The modified
seal has performed successfully for over 6 years.

Allis-Chalmers has over 20 years experience in the design and application
of oil film seals. The current Allis-Chalmers standard "Trapped Bushing
Seal" features:

.   A "dual" bushing which encompasses both the inner and outer seal
     in one ring for reduced axial length. (See Figure 7)

.   Low residual axial force on the seal which effectively reduces
     the potential for lock-up and seal sensitivity to friction and
     wear. (See Figure 8)

VI   SEAL VIBRATION TEST PROGRAM

A test program was subsequently conducted in the Allis-Chalmers test
facility to verify the motion of the A-C standard dual bushing at design
pressure level to insure that the bushing tracks the shaft without
lock-up.   All seal vibration data were provided by Mr. P. G. Shay, the
Supervisor of the Allis-Chalmers Compressor Test Facility. Two displace-
ment probes were mounted 90° apart in the cage surrounding the bushing to
determine the amplitude of bushing motion and the relative phase lag
between the shaft motion and bushing motion. (See Figure 9, note the
epoxy-filled relief around the probe tips.) The oscilloscope traces show
the seal orbit to be circular with a phase lag of 45° behind shaft motion
and amplitudes slightly less than the shaft amplitude (See Figure 10.)
The vibration spectra show the seal motion to be predominently synchronous
with only small traces of non-synchronous motion. Shaft vibration is
entirely synchronous. (See Figures 11A-D.)

Based on this information, it may may concluded that this arrangement
results in minimal destabilizing effects as the bushing is able to freely
track the shaft motion. Seal induced hydrodynamic forces are dissipated
in seal motion and not applied to the shaft. The seal is also insensitive
to wear on the axial faces.

VII CONCLUSIONS:

1. Residual axial forces in seals can influence seal and shaft vibration. Some small level should be present. However, seal lock-up should be avoided.

2. Restraint ("lock up") of bushing results in high levels of destabilizing forces and it is therefore better to err on the low side with respect to axial (pressure induced) forces in the event that seal wear increases the friction coefficient significantly.

3. Normally tracking seals exert only minor destabilizing effects.

4. The seal design should be relatively insensitive to wear on its axial face to prevent accelerating wear rates.

REFERENCES:

1. Rouch, K. E., Kao, J. S., "Reduction in Rotory Dynamics by the Finite Element Method". ASME Paper 79-DET-70.

2. Alford, J. S., "Protecting Turbomachinery From Self-Excited Rotor Whirl", Journal of Engineering and Power, Trans. ASME Series A, Vol. 87, October 1965, pp. 333-339.

3. Lund, J. W., "Stability and Damped Critical Speeds of a Flexible Rotor in Fluid Film Bearings", ASME Paper 73-DET-103 - 1973.

4. Kirk, R. G., Miller, W. H. "The Influence of High Pressure Oil Seals on Turbo-Rotor Stability ASLE Preprint 77-LL-3A-1.

ACKNOWLEDGEMENTS:
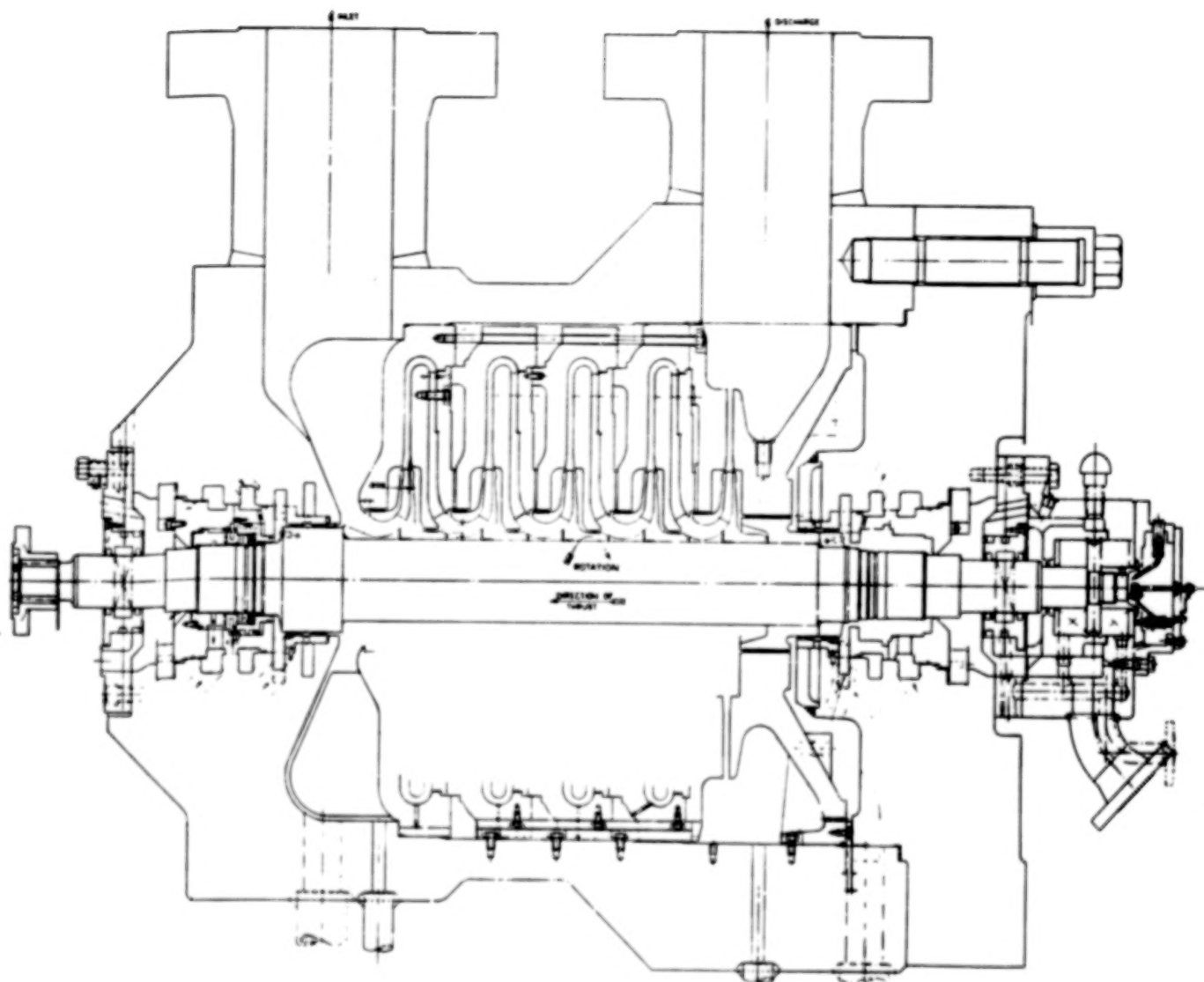
Figure 1. - 5 stage barrel compressor.

Figure 2. - Fouling deposits in compressor.

1 - BUSHING
2 - DIAPHRAGM
3 - IMPELLER
4 - STATOR
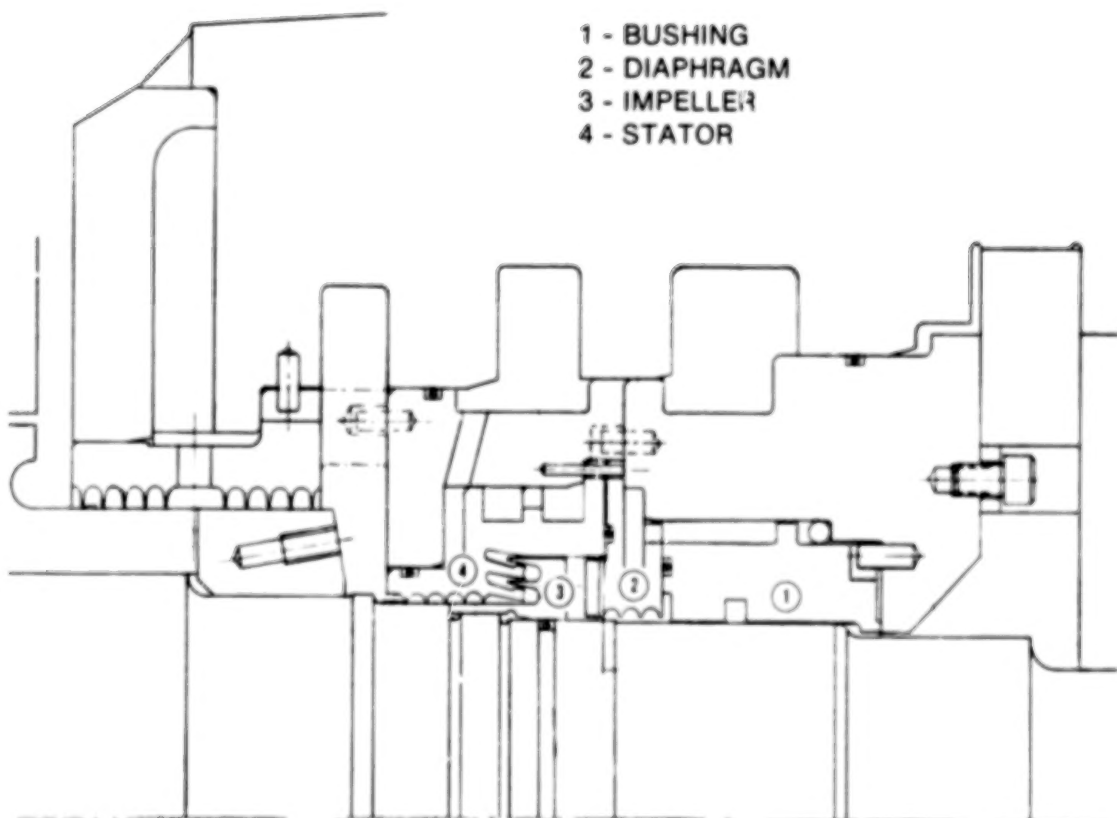
Figure 3. - Seal arrangement.

196

Accelerometers:
A₁ Vertical on coupling guard
A₂ Vertical on outboard bearing cap
A₃ Vertical on compressor casing inlet end
A₄ Vertical on gear box

Displacement:
IB₁ 30° clockwise from vertical as viewed from motor end
OB₁ 30° clockwise from vertical as viewed from motor end
OB₂ 60° counterclockwise from vertical as viewed from motor end
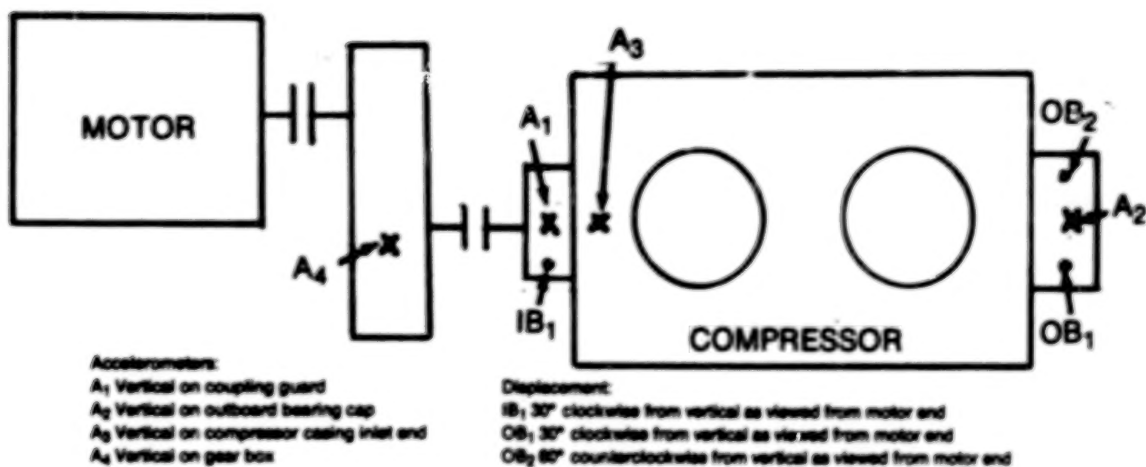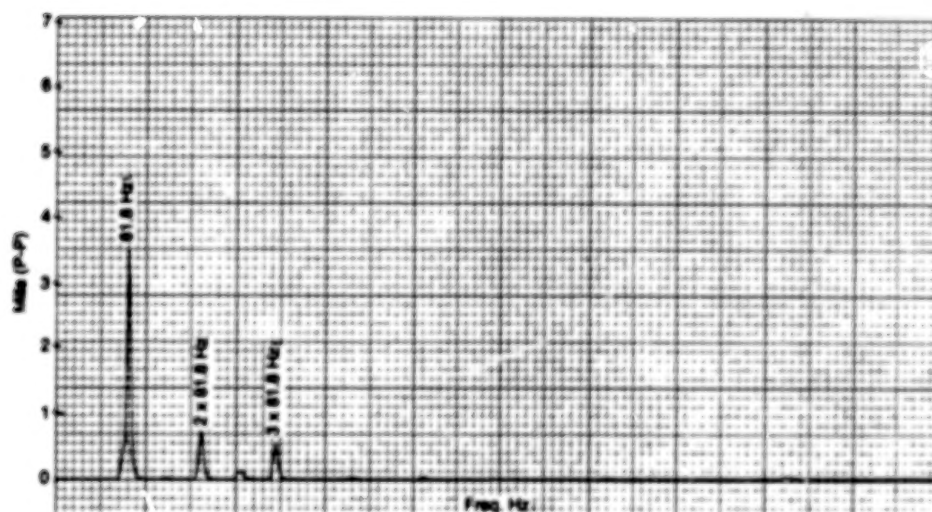
Figure 4(a).

Figure 4(b). - Vibration spectrum inboard probe 1.
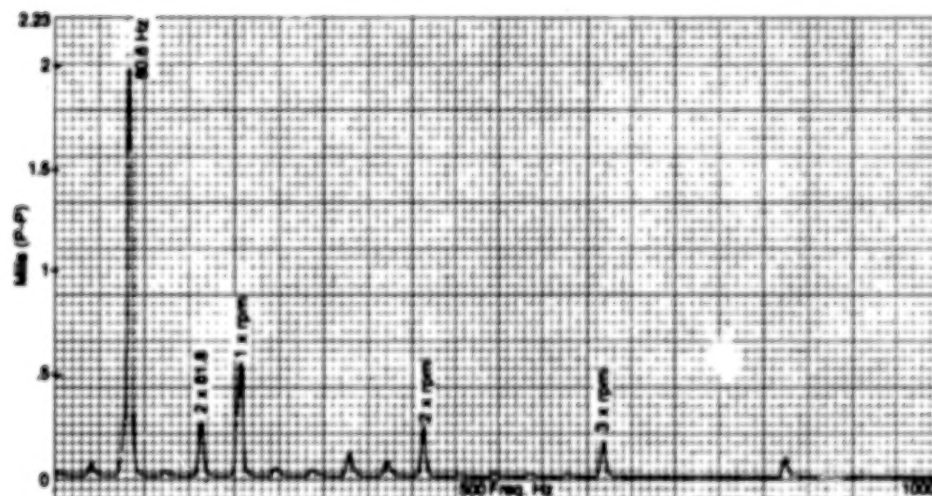
Figure 4(c). - Vibration spectrum outboard probe 1.

197
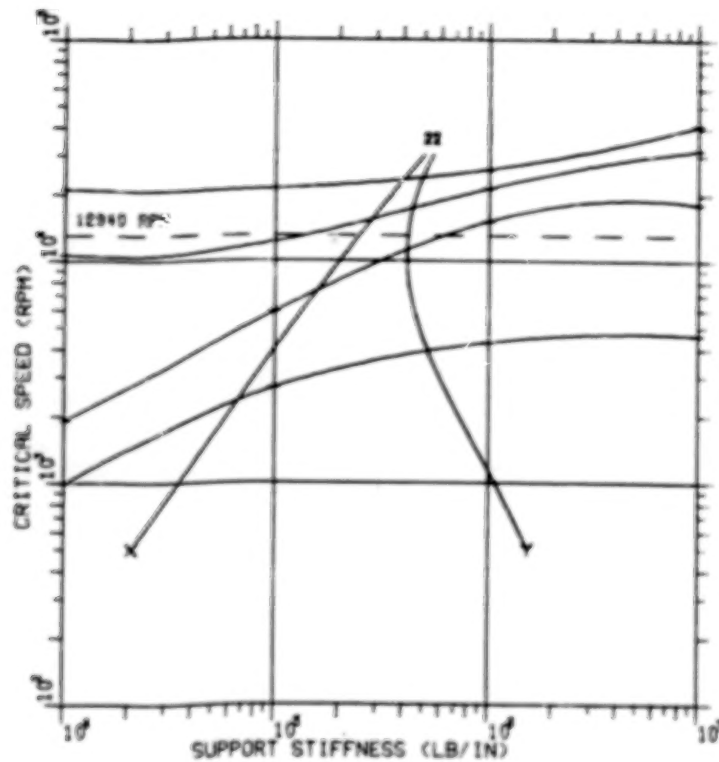
CRITICAL SPEED MAP

Figure 5(a). - Critical speed map.

ROTOR MODE SHAPE AT CRITICAL SPEED
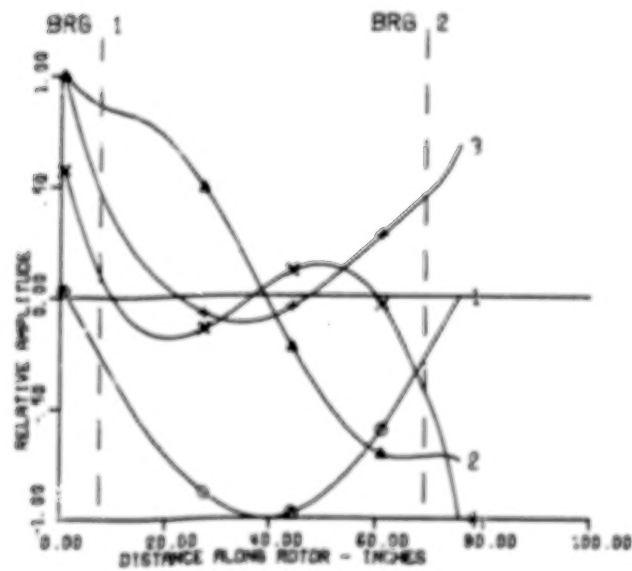
BRG	BRG		CRITICAL	SPEED	
NO.	STIFF	1	3926	RPM	●
1 4.50X10⁵		2	11593	RPM	▲
2 4.50X10⁵		3	17043	RPM	+
		4	22607	RPM	×

Figure 5(b). - Mode shapes.

198

STR *1 THRUST BRG. END

STR * COUPLING END

STATION	UNBALANCE	ANGLE	LOCATION
2	.197	0.	Coupling
14	.134	16.	1st Stage
18	.037	90.	2nd Stage
22	.037	90.	3rd Stage
26	.037	90.	4th Stage
30	.037	90.	5th Stage
32	.134	164.	Balance Piston
45	.120	180.	Thrust Collar
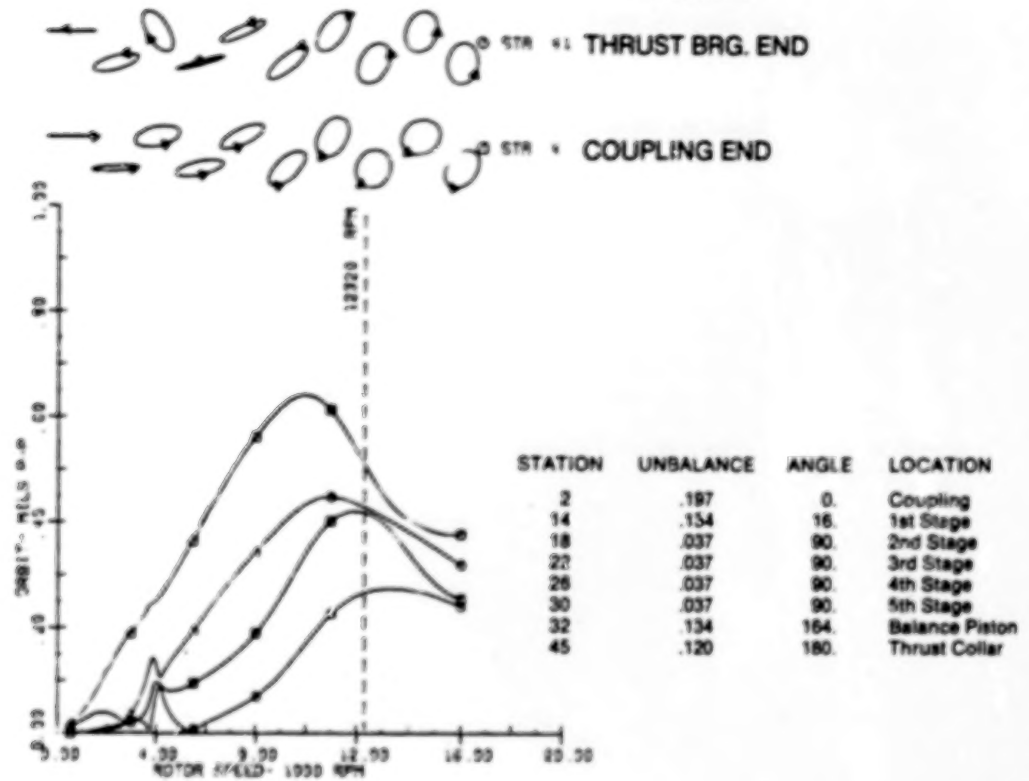
Figure 5(c). - Synchronous response.

MODE 2   LOG DECREMENT = .17   RPM = 3847   FWD
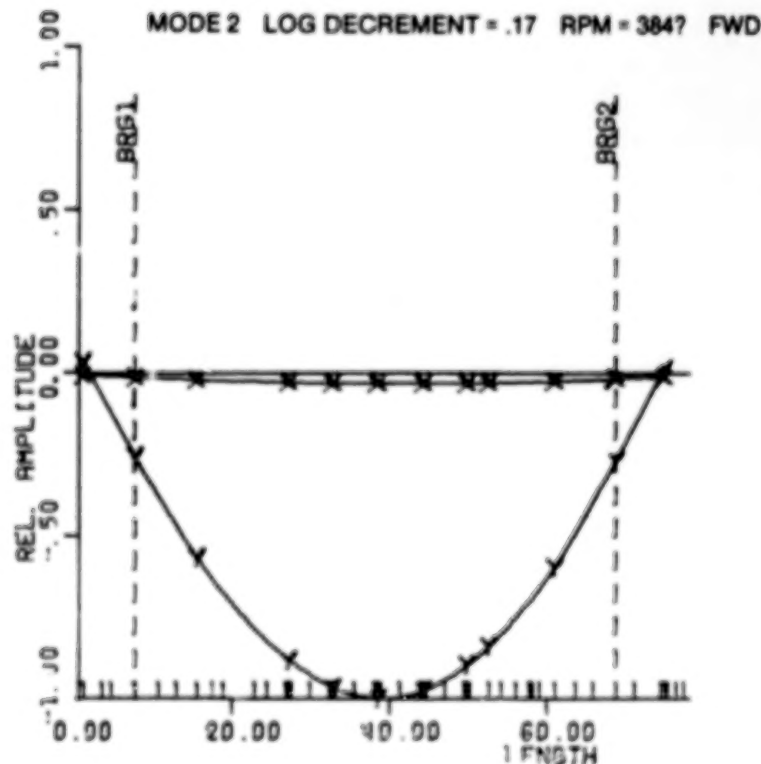
Figure 5(d). - Shaft whirl mode.

199

BEST DOCUMENT AVAILABLE
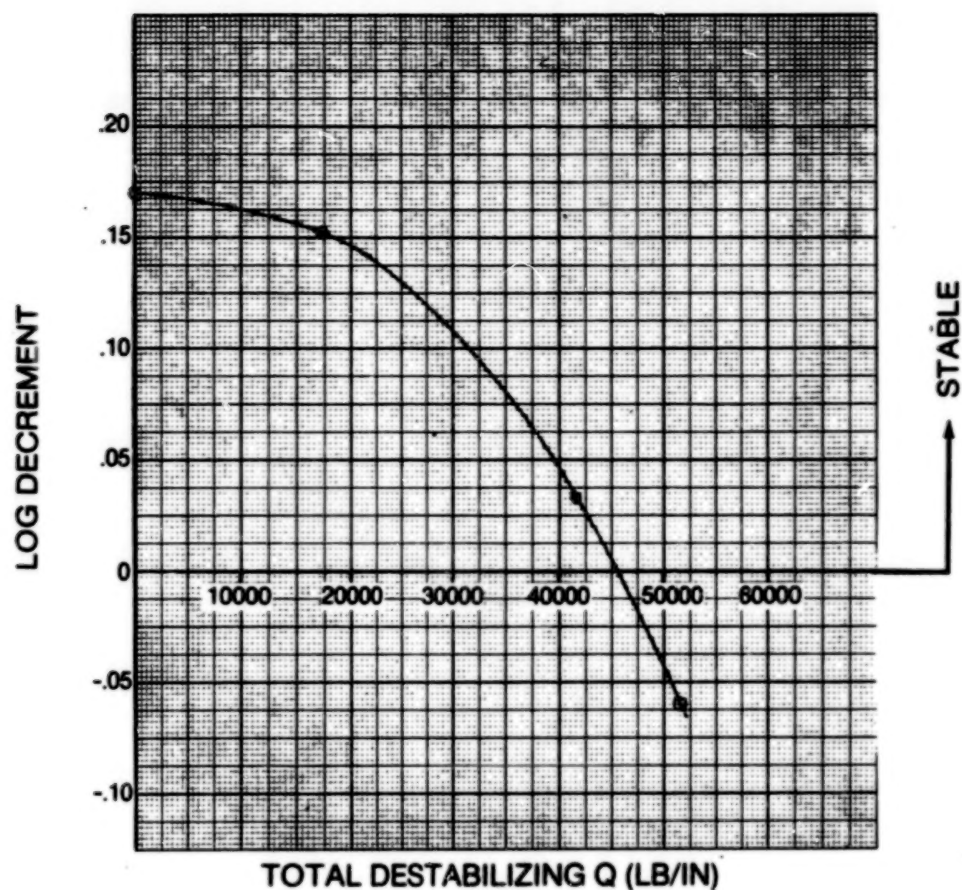
Figure 5(e). - Log decrement vs. destabilizing.
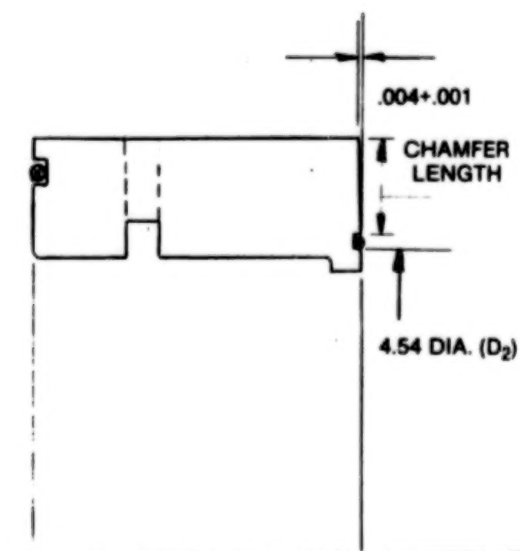
Figure 6(a). - Original bushing.
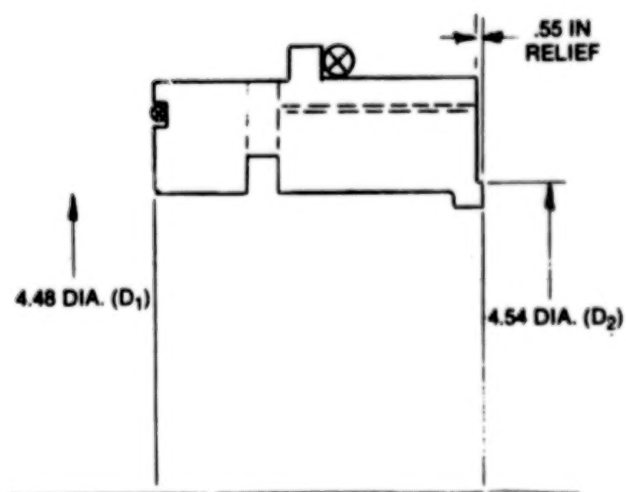
Figure 6(b). - Modified bushing.

200

Compact Design — allows shorter bearing spans for higher critical speeds of the compressor rotor.
Sleeve (impeller) with interference fit under bushing — protects shaft and simplifies assembly and disassembly. Requires only a jack/puller bolt ring.
Spacer fit at initial assembly — no field fitting of parts.

ITEM	DESCRIPTION
1	Shaft
2	Impeller
3	Stator
4	Stepped Dual Bushing
5	Bushing Cage
6	Nut
7	Shear Ring
8	Oil/Gas Baffle
9	Spacer Ring
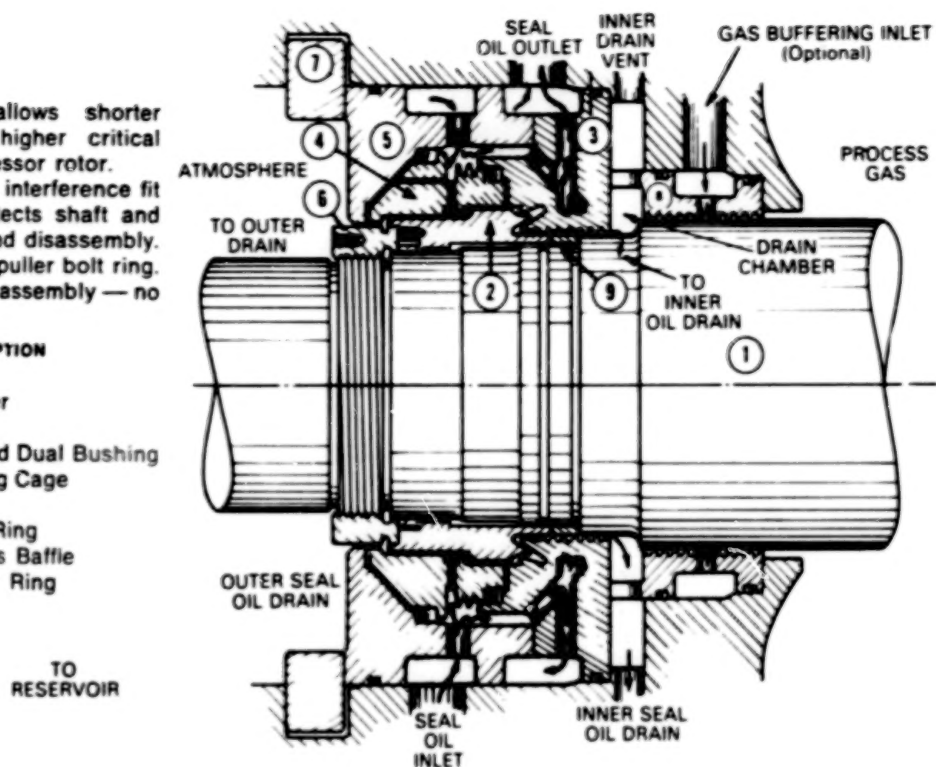
Figure 7. - Trapped bushing seal arrangement.

P_s

TOTAL FORCES ON DUAL BUSHING
RESIDUAL FORCES ON DUAL BUSHING
P_s - SEAL OIL SUPPLY PRESSURE
P_D - OUTER LEAKAGE PRESSURE
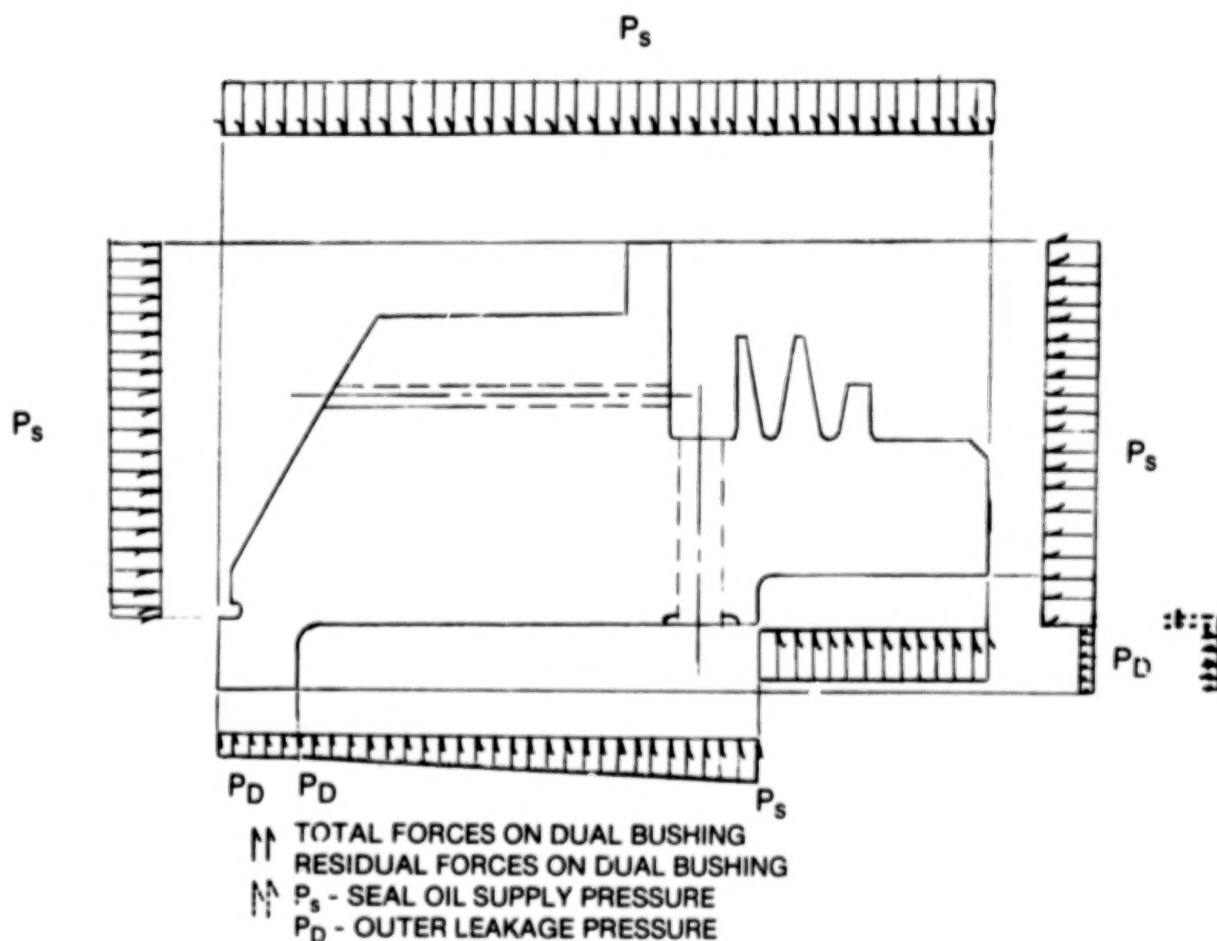
Figure 8. - Pressure induced forces on dual bushing.

201
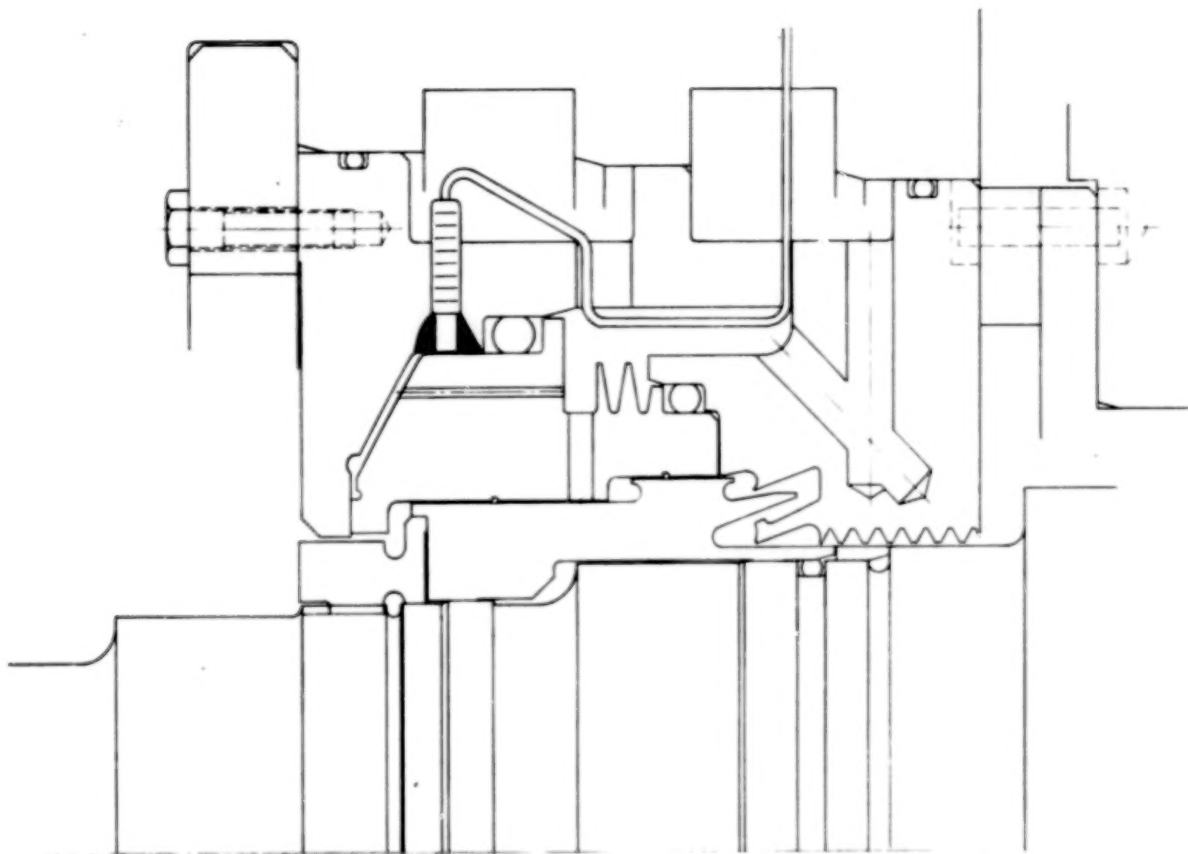
Figure 9. - Probe arrangement for trapped bushing seal vibration test.

Upper:	Bushing	Orbit
Lower:	Shaft	Orbit

Upper:	Bushing	X
	Vibration	Y
Lower:	Shaft	X
	Vibration	Y

1 Mil

1 Mil

13050 rpm 1 MIL Per Division
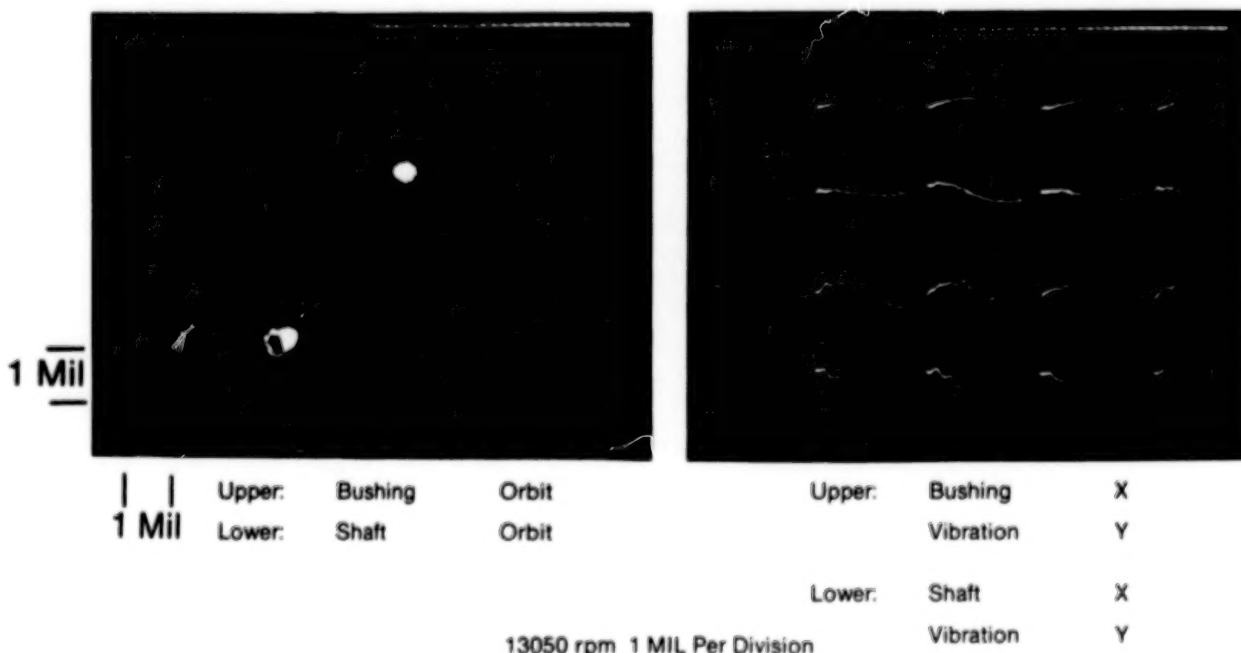
Figure 10. - Shaft and dual bushing vibration data.

202
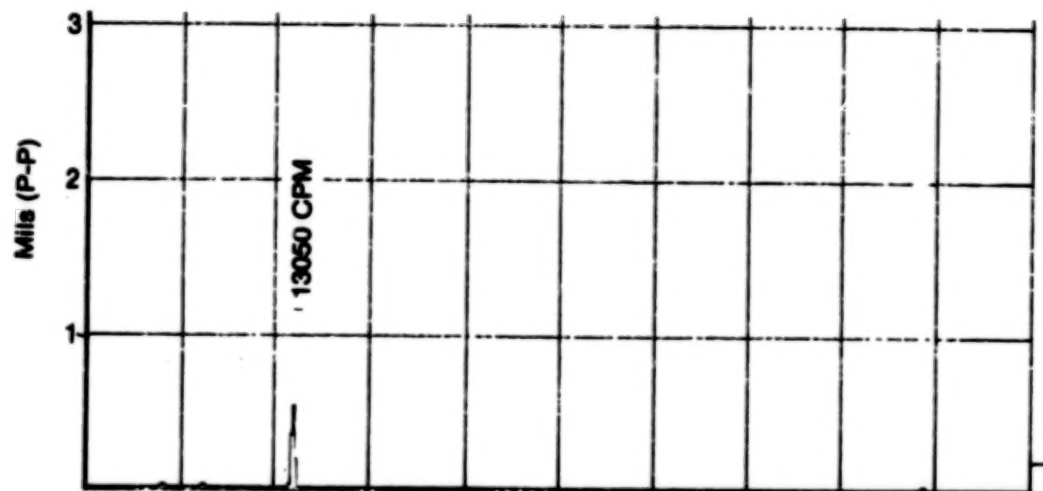
Figure 11(a). - Vibration spectrum - shaft (horizontal).
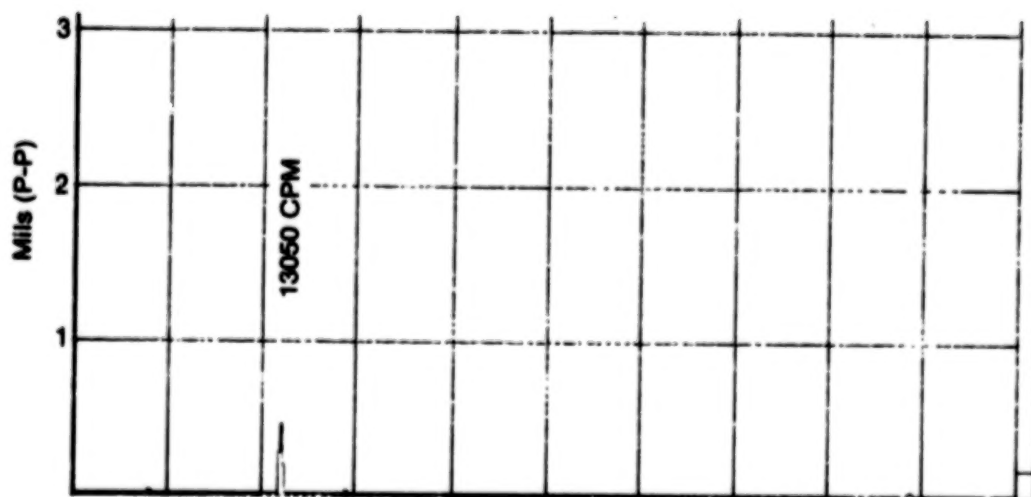
Figure 11(b). - Vibration spectrum - shaft (vertical).

203
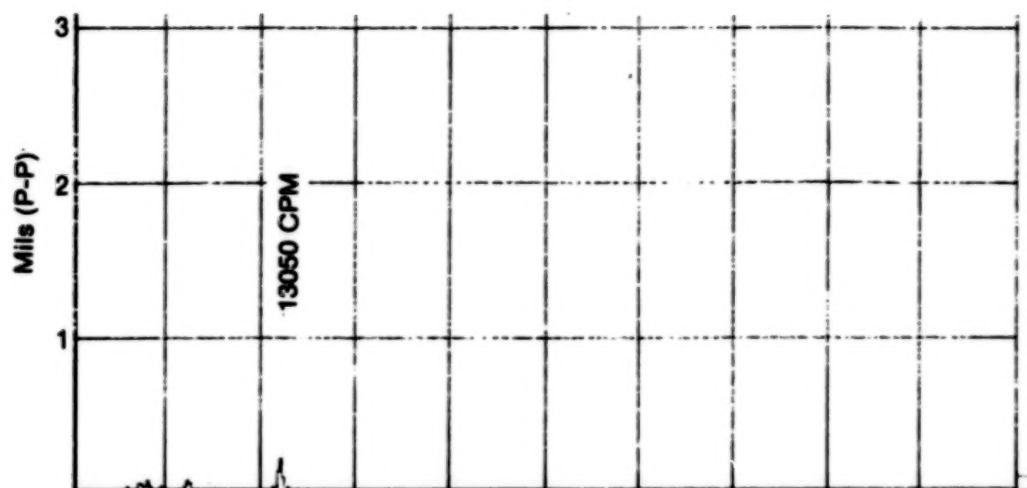
Figure 11(c). - Vibration spectrum - seal (horizontal).
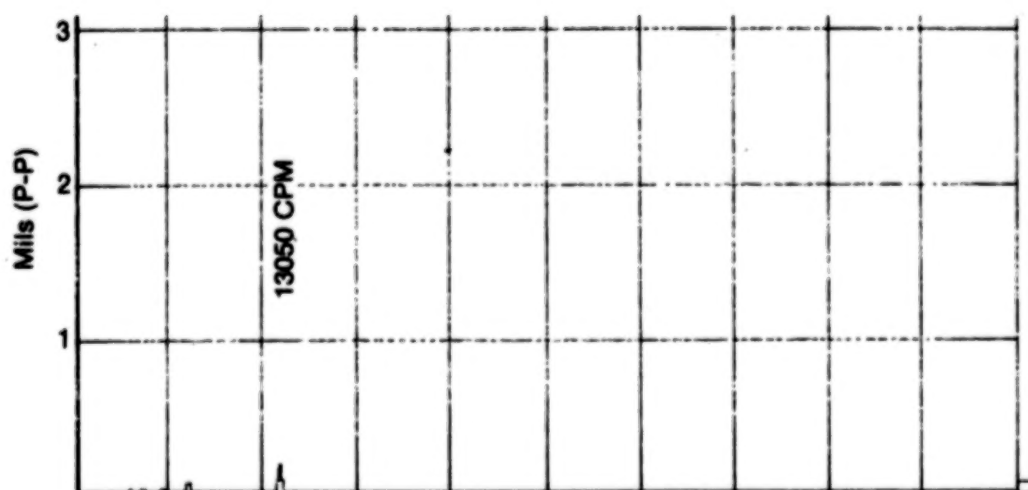
Figure 11(d). - Vibration spectrum - seal (vertical).

204

FLOW INDUCED FORCE OF LABYRINTH SEAL

Takuzo Iwatsubo, Naoto Motooka,
and Roji Kawai
Faculty of Engineering, Kobe University
Rokko, Nada, Kobe, 657 Japan

SUMMARY

This paper deals with theoretical analysis of flow induced instability
force due to labyrinth seal. That is, a approximate solution is given for the
partial differential equation representing the flow in labyrinth seal and it is
compared with the finite difference method which was proposed in the previous
report in order to verify the accuracy of both methods. Then the effects of
difference of inlet and outlet pressures of the seal, deflection of pressure and
mass flow from the steady state, rotor diameter, seal clearance, seal interval
and seal number on the flow induced force of the seal are investigated and it is
known that some of these factors are very influential on the flow induced force.

INTRODUCTION

In the previous report (1), the fundamental equation of flow in the labyrinth
seal was derived by considering the effect of the variation of gland cross section.
The equation is numerically solved by using the finite difference method. Then
the spring and damping coefficients of the labyrinth seal are calculated, and by
using the result, the stability of a rotor system having labyrinth seal is
discussed on this coefficient by using the energy concept. Furthermore, experi-
ments are executed to observe the flow pattern in the gland and to study the
characteristics of the flow induced forces in the labyrinth seal.

However, further theoretical investigations are required for the accuracy of
numerical calculation and more detail description of labyrinth seal behaviour.
Then in this paper the equation is solved by another method and the calculated
results are compared with the solution of finite difference method. After that
influences of deflection of steady state, pressure difference between inlet and
outlet, labyrinth seal radius, seal clearance, seal pitch, number of seal cham-
ber, seal strip height and divergence and convergence seal on the flow induced
force, phase angle and leakage flow rate are investigated.

SYMBOLS

t time

$w = R_s \varphi$

R_s radius of labyrinth seal

p pressure in seal chamber

c	peripheral velocity in seal chamber
ρ	density of gas
q	mass flow rate in axial direction
φ	angle from x axis
f	cross section of seal chamber
ℓ	length of strip pitch
h	strip height
δ	radial clearance of seal
τ'	friction shear stress of stator surface
τ''	friction shear stress of rotor surface
U'	length of acting surface of shear stress (stator)
U"	length of acting surface of shear stress (rotor)
R	gas constant
T	absolute temperature of gas in seal
γ	specific weight of gas
ψ	flow coefficient
n	ratio of specific heat
ω	rotating speed of rotor
ω_n	critical speed of rotor system
$u = \omega R_s$	peripherical velocity of rotor
K	coefficient of viscosity
ν	coefficient of kinematic viscosity
R_e	Reynold's number
λ'	friction coefficient (stator)
λ''	friction coefficient (rotor)
subscript *	steady state

EQUATION OF MOTION

Derivation of Equation of Motion

Derivation of the equation which describes the labyrinth seal flow is followed the previous report (1), where the following assumptions are taken and schematic flow is shown in Fig.1;

(1) Fluid in labyrinth seal is assumed to be gas and its behavior is assumed to be ideal.

(2) Temperature of the fluid in the labyrinth seal is assumed to be constant.

(3) Cross section area of the seal gland is assumed to be constant in spite of the deflection of rotor and time derivative of cross section area is only considered.

(4) Change of flow state in the gland is assumed to be isentropic change. Thus the fundamental equations with respect to continuity and momentum for the ith seal element are as follows;

$$\frac{\partial(\rho_i f_i)}{\partial t} + f_i \frac{\partial(\rho_i C_i)}{\partial W} + (g_{i+1} - g_i) = 0 \tag{1}$$

$$f_i \frac{\partial(\rho_i C_i^2)}{\partial W} + \frac{\partial(\rho_i f_i C_i)}{\partial t} + (g_{i+1} C_i - g_i C_{i-1}) + \tau_i' U_i' - \tau_i'' U_i'' = -\frac{\partial P_i}{\partial W} f_i \tag{2}$$

As temperature of each gland is constant, the equation of state in the ith gland is given as;

$$P_i = \gamma_i R T \tag{3}$$

where

$$\gamma_i = \rho_i g$$

Next, denoting the gas flow velocity through labyrinth nozzle (seal clearance) S, the relation between axial flow rate and pressure in the gland is given by the thermodynamical energy equilibrium condition as,

$$S = \sqrt{2g \frac{n}{n-1} P_I v_I \left[1 - \left(\frac{P_0}{P_I}\right)^{\frac{n-1}{n}} \right]} \tag{4}$$

where n is isentropic exponent, v specific volume and subscripts I and 0 mean inlet and outlet of nozzle, respectively. Assuming that the flow is adiabatic change, i.e. $v_0 = (P_I / P_0)^{\frac{1}{n}} v_I$, the flow rate through the nozzle G [kgf/sec] is given as;

$$G = \alpha \frac{F \cdot S}{v_0} = \alpha \frac{F \cdot S}{v_I} \left(\frac{P_0}{P_I}\right)^{\frac{1}{n}} = \alpha F \sqrt{2g \frac{n}{n-1} \frac{P_I}{v_I} \left[\left(\frac{P_0}{P_I}\right)^{\frac{2}{n}} - \left(\frac{P_0}{P_I}\right)^{\frac{n+1}{n}} \right]} \tag{5}$$

where F is nozzle cross area (area of seal clearance) and subscripts (i,0) correspond to the gland number of the labyrinth seal. Applying the above relation to flow in the labyrinth seal, we assume that the labyrinth seal is a series of the nozzle, pressure difference between each gland is small and enthalpy of each gland is nearly equal. Then leakage flow rate through labyrinth seal G (kgf/sec) is given by using the relation
$P_1 v_1 = P_2 v_2 = \cdots = P_i v_i$ as;

$$G_L = \alpha F \sqrt{\frac{g}{RT}} \sqrt{P_1^2 - P_0^2} \tag{6}$$

Applying Eq.(6) to the flow through the ith seal element, mass flow rate for unit area is given as;

$$\frac{q_i}{\delta_i} = \frac{G_L}{F \cdot g} = \frac{\alpha}{\sqrt{gRT}} \sqrt{P_{i-1}^2 - P_i^2} \tag{7}$$

Rewriting Eq.(7), the following equation is obtained;

$$P_{i-1}^2 - P_i^2 = \frac{q_i^2}{\mu^2 g_i} \tag{8}$$

where

$$\frac{1}{\mu^2} = \frac{gRT}{\alpha^2} \tag{9}$$

Linearization of Fundamental Equation

For the linearization of the equation, the perturbations of pressure, peripheral velocity and flow rate from those of the steady state and also mean value and perturbation of seal clearance are introduced as

$$
\begin{aligned}
P_i &= P_{*i}(1 + \xi_i) & C_i &= C_{*i}(1 + \iota_i) \\
q_i &= q_{*i}(1 + \zeta_i) & \delta_i &= \delta_{*i}(1 + \psi_i)
\end{aligned} \tag{10}
$$

where p_{*i}, c_{*i} and q_{*i} are pressure, peripheral velocity and axial flow rate of steady state in the ith gland and ξ_i, ι_i and ζ_i are nondimensional perturbation terms of pressure, peripheral velocity and axial flow rate. Also δ_{*i} and ψ_{*} are mean value and perturbation of seal clearance.

Assuming that the rotor is whirling along elliptical orbit, ψ_i is represented as

$$\psi_i = -\frac{a_i}{\delta_{*i}} \cos \omega t \cos \varphi - \frac{b_i}{\delta_{*i}} \sin \omega t \sin \varphi \tag{11}$$

Then the cross section area in the ith gland is represented as

$$f_i = \left\{ h_i + \delta_{*i}(1 + \psi_i) + h_{i+1} + \delta_{*i+1}(1 + \psi_{i+1}) \right\} \frac{\ell}{2} \tag{12}$$

As the change of state in the gland is isentropic, the following relations are obtained;

$$\frac{P_{*i}}{\rho_{*i}^n} = \frac{P_i}{\rho_i^n} = A \tag{13}$$

therefore

$$\frac{\partial P_i}{\partial t} = n \frac{P_i}{\rho_i} \frac{\partial \rho_i}{\partial t} \tag{14}$$

Substituting Eqs.(10) - (14) into Eqs.(1) and (2), and denoting the time derivative $\frac{\partial}{\partial t}$ and spatial derivative $\frac{\partial}{\partial y}$ $(\dot{\ })$ and $(\cdot)'$, respectively, the following equations are obtained for the ith seal element;

$$\frac{f_{*i}}{n} \dot{\xi}_i + \frac{C_* f_{*i}}{n R_s} \xi'_i + \frac{C_* f_{*i}}{R_s} \zeta'_i - \frac{g R T P_{*i}^2 \delta_{*i+1}^2 \mu^2}{g_* P_{*i}} \xi_{i+1} + \frac{g R T \mu^2 P_{*i}}{g_*}(\delta_{*i+1}^2 + \delta_{*i}^2)\xi_i$$

$$- \frac{g R T P_{*i-1}^2 \delta_{*i}^2 \mu^2}{g_* P_{*i}} \xi_{i-1} + \frac{g R T \mu^2 \delta_{*i+1}^2}{2 P_{*i} g_*}(P_{*i}^2 - P_{*i+1}^2) - \frac{g R T \mu^2 \delta_{*i}^2 P_{*i-1}^2}{2 P_{*i} g_*}(P_{*i-1}^2 - P_{*i}^2)$$

$$= - \frac{g R T \mu^2}{g_* P_{*i}} \delta_{*i+1}(P_{*i}^2 - P_{*i+1}^2)\left\{ a_{i+1} \cos \omega t \cos \varphi + b_{i+1} \sin \omega t \sin \varphi \right\}$$

$$- \frac{g R T \mu^2}{g_* P_{*i}} \delta_{*i}(P_{*i-1}^2 - P_{*i}^2)\left\{ a_i \cos \omega t \cos \varphi + b_i \sin \omega t \sin \varphi \right\}$$

$$+ \frac{\ell}{2}\left\{ -a_i \omega \sin \omega t \cos \varphi + b_i \omega \cos \omega t \sin \varphi - a_{i+1} \omega \sin \omega t \sin \varphi + b_{i+1} \omega \cos \omega t \sin \varphi \right\} \tag{15}$$

$$\frac{f_{*i}}{n} \dot{\xi}_i + f_{*i} \dot{\zeta}_i + \frac{f_{*i}}{R_s}\left(\frac{g R T}{C_{*i}} + \frac{C_{*i}}{n} \right)\xi'_i + \frac{C_{*i} f_{*i}}{R_s} \zeta'_i - \frac{g R T \mu^2 \delta_{*i+1}^2 P_{*i+1}^2}{g_* P_{*i}} \xi_{i+1}$$

$$+ \left\{ \frac{g R T \mu^2 \delta_{*i+1}^2 P_{*i}}{g_*} + \frac{g R T \mu^2 \delta_{*i}^2 P_{*i}}{g_*} + \frac{\lambda'_i C_{*i} U'_i}{2} - \frac{\lambda''_i U''_i}{2 C_{*i}}(u - C_{*i})^2 \right\}\xi_i$$

$$+ \left\{ \frac{g R T g_*}{P_{*i}} + \lambda'_i C_{*i} U'_i + \lambda''_i U''_i(u - C_{*i}) \right\}\zeta_i - \frac{g R T \mu^2 \delta_{*i} P_{*i-1}}{g_* P_{*i}} \xi_{i-1} - \frac{g R T g_*}{P_{*i}} \zeta_{i-1}$$

$$+ \frac{\lambda'_i C_{*i} U'_i}{2} - \frac{\lambda''_i U''_i}{2 C_{*i}}(u - C_{*i})^2 + \frac{g R T \mu^2}{2 g_*}\left(\delta_{*i+1}^2 P_{*i} - \delta_{*i+1}^2 \frac{P_{*i+1}^2}{P_{*i}} - \delta_{*i}^2 \frac{P_{*i-1}^2}{P_{*i}} + \delta_{*i}^2 P_{*i} \right)$$

$$= \frac{g R T \mu^2}{g_*}\left[(\delta_{*i} P_{*i} - \delta_{*i+1} \frac{P_{*i+1}^2}{P_{*i}})(a_{i+1} \cos \omega t \cos \varphi + b_{i+1} \sin \omega t \sin \varphi) \right.$$

$$\left. - (\delta_{*i} \frac{P_{*i-1}^2}{P_{*i}} - \delta_{*i} P_{*i})(a_i \cos \omega t \cos \varphi + b_i \sin \omega t \sin \varphi) \right] + \frac{\ell}{2}(-a_i \omega \sin \omega t \cos \varphi$$

$$+ b_i \omega \cos \omega t \sin \varphi - a_{i+1} \omega \sin \omega t \cos \varphi + b_{i+1} \omega \cos \omega t \sin \varphi) \tag{16}$$

209

For the n stage labyrinth seal, Eqs.(15) and (16) are represented in matrix form as;

$$T\ddot{u} + V u' + A u = G_1\left[a_*\cos(\varphi+\omega t) + a_*\cos(\varphi-\omega t) - b_*\cos(\varphi+\omega t)\right.$$

$$\left. + b_*\cos(\varphi-\omega t)\right] + G_2\left[-a_*\sin(\varphi+\omega t) + a_*\sin(\varphi-\omega t) + b_*\sin(\varphi+\omega t)\right.$$

$$\left. + b_*\sin(\varphi-\omega t)\right] + G_3\left[\theta_a\cos(\varphi+\omega t) + \theta_a\cos(\varphi-\omega t) - \theta_b\cos(\varphi+\omega t)\right.$$

$$\left. + \theta_b\cos(\varphi-\omega t)\right] + G_4\left[-\theta_a\sin(\varphi+\omega t) + \theta_a\sin(\varphi-\omega t) + \theta_b\sin(\varphi+\omega t)\right.$$

$$\left. + \theta_b\sin(\varphi-\omega t)\right] \tag{17}$$

where $P_{*0} = P_0$ (inlet pressure) and $P_{*n} = P_n$ (outlet pressure).

ANALYSIS

Analysis of Steady State

Setting the perturbation terms ξ_i and $\mathfrak{l}_i$ zero in Eqs.(15) and (16) in order to obtain the pressure and peripheral velocity of each seal stage in steady state,

$$q_{i+1} = q_i = q_* \tag{18}$$

$$q_{i+1}\omega_i - q_i\omega_{i-1} + \tau'U_i' - \tau''U_i'' = 0 \tag{19}$$

As the multi labyrinth stage is considered as a serial nozzle, the axial flow rate in the steady state is obtained as follows

$$q_i = \alpha \delta_i \sqrt{\frac{2n}{n-1} P_{i-1}' S_{i-1}' \left[\left(\frac{P_i}{P_{i-1}}\right)^{\frac{2}{n}} - \left(\frac{P_i}{P_{i-1}'}\right)^{\frac{n+1}{n}}\right]} \tag{20}$$

where P_{i-1}' is the pressure of $(i-1)$th chamber which is taken into account of draughty flow. The pressure is given by Ref.(3) as;

$$P_i' = P_i + (P_0 - P_{*1})(1 - A_i^2)\xi_p \mathfrak{l}_p \ , \quad \mathfrak{l}_p = \frac{2A_i}{A_i+1} \tag{21}$$

where A_L is determined by the shape of labyrinth seal;

$$A_i = \frac{\frac{\delta_i}{t}C_c}{\frac{\varsigma}{t}C_c + \tan\theta} \tag{22}$$

where C_c is coeffi... of vena contracta.
From these equations, state variables i.e. the pressure and flow rate satisfied the equilibrium condition, is obtained by iterating Eqs.(18) and (19). The peripheral velocity is obtained by using Eq.(19) in the same manner.

210

Referring to the left term in Eq.(17), the solutions are assumed as follows

$$P_i = P_{*i} + P_{*i}\{A_{+i}\sin(\varphi+\omega t)+B_{+i}\cos(\varphi+\omega t)+A_{-i}\sin(\varphi-\omega t)+B_{-i}\cos(\varphi-\omega t)\} \tag{23}$$

$$C_i = C_{*i} + C_{*i}\{E_{+i}\sin(\varphi+\omega t)+F_{+i}\cos(\varphi+\omega t)+E_{-i}\sin(\varphi-\omega t)+F_{-i}\cos(\varphi+\omega t)\} \tag{24}$$

Representing the above coefficients in matrix form as

$$\alpha_1 = \begin{bmatrix} A_{+1} \\ E_{+1} \\ \vdots \\ A_{+n} \\ E_{+n} \\ O \end{bmatrix} \quad, \quad \alpha_2 = \begin{bmatrix} A_{-1} \\ E_{-1} \\ \vdots \\ A_{-n} \\ E_{-n} \\ O \end{bmatrix} \quad, \quad \beta_1 = \begin{bmatrix} B_{+1} \\ F_{+1} \\ \vdots \\ B_{+n} \\ F_{+n} \\ O \end{bmatrix} \quad, \quad \beta_2 = \begin{bmatrix} B_{-1} \\ F_{-1} \\ \vdots \\ B_{-n} \\ F_{-n} \\ O \end{bmatrix}$$

the solution is written as;

$$U = \alpha_1 \sin(\varphi+\omega t)+\beta_1\cos(\varphi+\omega t)+\alpha_2\sin(\varphi-\omega t)+\beta_2\cos(\varphi-\omega t) \tag{25}$$

Substituting Eq.(25) into Eq.(17), and separating it to the elements $\cos(\varphi+\omega t)$, $\sin(\varphi+\omega t)$, $\cos(\varphi-\omega t)$ and $\sin(\varphi-\omega t)$, the coefficients are represented as follows;

$$\omega T\alpha_1 + V\alpha_1 + A\beta_1 = G_1 a_* + G_3\theta_a + G_5 b_* + G_7\theta_b \tag{26}$$

$$-\omega T\beta_1 - V\beta_1 + A\alpha_1 = G_1 a_* + G_4\theta_a + G_6 b_* + G_8\theta_b \tag{27}$$

$$-\omega T\alpha_2 + V\alpha_2 + A\beta_2 = H_1 a_* + H_3\theta_a + H_5 b_* + H_7\theta_b \tag{28}$$

$$\omega T\beta_2 - V\beta_2 + A\alpha_2 = H_{12}a_* + H_{14}\theta_a + H_{16} b_* + H_{18}\theta_b \tag{29}$$

where $G_1 \sim G_8$ and $H_1 \sim H_8$ are coefficient matrices which is composed of the matrices B, C, F and G. Solving Eqs.(26),(27) and Eqs.(28), (29) simultaneously, $\alpha_1, \beta_1, \alpha_2$ and β_2 are obtained. Then velocity and pressure in the gland is calculated by substituting the coefficients into Eq.(23), and the flow induced force for whole seal is obtained by integrating the pressure for each gland. Representing the x and y direction force by P_x and P_y,

$$P_x = -R_s\sum_{i=1}^{n}\int_0^{2\pi} P_{*i}\,\xi_i\,l\cos\varphi\,d\varphi$$

$$P_y = -R_s\sum_{i=1}^{n}\int_0^{2\pi} P_{*i}\,\xi_i\,l\sin\varphi\,d\varphi \tag{30}$$

The flow induced force F and phase angle from x axis are described as

$$F = \sqrt{P_x^2 + P_y^2} \qquad \phi = \tan^{-1}\frac{P_y}{P_x} \tag{31}$$

Spring coefficients and damping coefficients are obtained from Eqs.(30) and (31) in the following matrix form;

211

$$\begin{bmatrix} K_{xx}K_{xy} & 0 \\ K_{yx}K_{yy} & \\ & K_{\theta xx}K_{\theta xy} \\ 0 & K_{\theta yx}K_{\theta yy} \end{bmatrix}\begin{bmatrix} x \\ y \\ \theta_x \\ \theta_y \end{bmatrix} + \begin{bmatrix} C_{xx}C_{xy} & 0 \\ C_{yx}C_{yy} & \\ & C_{\theta xx}C_{\theta xy} \\ 0 & C_{\theta yx}C_{\theta yy} \end{bmatrix}\begin{bmatrix} \dot{x} \\ \dot{y} \\ \dot{\theta}_x \\ \dot{\theta}_y \end{bmatrix} \tag{32}$$

When Eqs.(30) and (31) are rewritten to Eq.(32) in the above, the following form is used as ξ_i,

$$\xi_i = \xi_{1i}\, a_* \cos\omega t + \xi_{2i} a_* \sin\omega t + \xi_{3i} b_* \cos\omega t + \xi_{4i} b_* \sin\omega t + \xi_{5i}\theta_a \cos\omega t$$
$$+ \xi_{6i}\theta_a \sin\omega t + \xi_{7i}\theta_b \cos\omega t + \xi_{8i}\theta_b \sin\omega t$$

Using the above expression, the following relations are obtained between coefficients;

$$K_{xx} = K_{yy} \quad K_{\theta xx} = K_{\theta yy} \quad K_{xy} = -K_{yx} \quad K_{\theta xy} = K_{\theta yx}$$
$$C_{xx} = C_{yy} \quad C_{\theta xx} = C_{\theta yy} \quad C_{xy} = -C_{yx} \quad C_{\theta xy} = -C_{\theta yx} \tag{33}$$

NUMERICAL EXAMPLE AND DISCUSSIONS

The labyrinth seal having three teeth, which is shown in Fig.2, is used as a numerical model. Details of the labyrinth seal is shown in Table 1 and for the parameter survey each element of seal dimension is independently changed in order to investigate the influence of its seal size on the flow induced force. In order to evaluate the seal force, circular orbit ($a_* = b_*$ in Eq.(17)) are used as a whirling of labyrinth seal, and its radius $a_* = 0.1$mm. For the calculation the following equation is used as the friction coefficient between rotor and stator;

for stator surface;

$$R'_{ei} = \frac{D(U - C_{*i})}{\nu}$$

where D is wetted perimeter length considered the rotating Reynold's Number

$$R'_{ei} < 1200, \quad \lambda'_i = 64/R'_{ei}, \quad R'_{ei} \gtrsim 1200, \quad \lambda'_i = 0.3164\, R_e^{-0.25}$$

for rotor surface;

$$R''_{ei} = \frac{D(U - C_{*i})}{\nu}, \quad R''_{ei} < 1200, \quad \lambda''_i = 64/R'_{ei}, \quad R''_{ei} \gtrsim 1200, \quad \lambda''_i = 0.3164\, R_e^{-0.25}$$

Two methods are used for the numerical calculation, one is the method which is shown in previous section, the other is one which is the finite diference method that was proposed in Ref.(1). At first calculated results for these two methods are compared with and as the result it is known that these two results agree. Then parameter surveys of labyrinth seal are carried out to see the influence on the flow induced force which exits the instability.

In this paper critical speed of a rotor system is assumed to be 5000 rpm, and rotating speed of the rotor is represented in nondimensional expression as $\omega/\omega_n(\omega$ (rpm):rotating speed of the rotor). F and FAI shown in figures mean the absolute value of the force induced by labyrinth seal and its phase angle from x axis.

a) Accuracy of Two Calculation Method

Fig.3 shows the spring coefficients and damping coefficients which are obtained by two methods i.e. approximate method and finite difference method. In the figure, full line and broken line show the coefficients for inlet pressure P_0 =196.13(KPa) and 147.1(KPa) respectively and outlet pressure Pn=98.07(Kpa) which are obtained by the approximate method and doted line shows the coefficient for inlet pressure P_0=196.13(KPa) and outlet pressure P_3=98.0(KPa) which is obtained by the finite difference method. Also sign (-) on line means negative value. From this figure full line and dotted line coincide very well so each calculation method has good accuracy.

b) Influence of Deflection of Steady

In this paper pressure, peripheral velocity and flow rate in steady state are iteratively calculated, however, Kostyuk and other authors obtain them by another method and there are some discrepancies between both steady state values. Moreover, steady state values in field and the calculated values may have discrepancies. So it is important to investigate the influence of deflection from steady state on the accuracy of the induced force. Then Fig.4 shows the flow induced force and its phase angle when pressure is a little deflected from steady state where the number on lines correspond to the number in Table 3. The calculated data are shown in table 2. From the calculated result, it is known that even if the flow rate is deflected 20% from the steady state, flow induced force and phase angle are not so influenced, and these curves become like one line, so this figure is neglected. On the other hand if the pressure is deflected 0.5% from steady state value, they are influenced very much. Also it is known that the induced force is not influenced by rotating speed of rotor but if it is separated to component, influence of rotating speed is remarkable as shown in Fig.5. From the above discussions it is concluded that in the calculation of flow induced force, steady state values must be calculated with high accuracy.

c) Influence of Pressure Difference Between Inlet and Outlet

Fig.6 shows the influence of pressure difference between inlet and outlet on the flow induced force when inlet (entrance) pressure is kept constant value (209 atm) and outlet (exit) pressure is changed. The figure shows that as the outlet pressure becomes large, i.e. the pressure difference between inlet and outlet becomes small, the flow induced force becomes small. As the flow rate decreases, the induced force proportionally decreases.

d) Influence of Labyrinth Seal Radius

Fig.7 shows the influence of labyrinth seal radius on the flow induced force, where the seal radius is valiable and other dimensions are fixed at constant values. Here flow rate means total flow rate as shown in the expression;

From the figure the flow induced force proportionaly increases as the seal radius increases. Therefore, the flow induced force due to labyrinth seal can be easily evaluated by the similarity law, when the seal radius is known.

e) Influence of Seal Clearance

Fig.8 shows the relation between seal clearance and the flow induced force and the leakage flow rate (leakage mass flow rate per unit length), where as the clearance increases, the induced force F decreases and the flow rate increases proportionally.

213

f) Influence of Seal Pitch

Fig.9 shows the influence of seal pitch on the flow induced force, when strip height is kept constant. From the figure it is known that as the seal pitch increases, the induced force increases, but the leakage flow rate q does not so much changed. Thus the large pitch is not good from the view point of the flow induced force.

g) Influence of Number of Seal Chamber

Fig.10 shows the influence of chamber number on the induced force and the leakage flow rate, where inlet and outlet pressure is constant and each chamber dimension is also same. From the figure the induced force increases like hyperbolic as the chamber number increasing. On the other hand leakage flow rate decreased like exponentially. Therefore optimum number of chambers may be determined when inlet and outlet pressure are known.

h) Influence of Seal Strip Height

Fig.11(a)(b) shows the influence of seal strip height. In this case the induced force, phase angle and leakage flow rate do not influenced so much. But if this result is represented in the spring and damping coefficients, the influence due to the strip height is remarkable. Fig 11(c) shows the spring coefficients k_{xx} and k_{xy}.

i) Influence of Divergence and Convergence Type Labyrinth Seal

Fig.12 shows a comparison of seal types, that is, comparison of straight through type, convergence type and divergence type. In this calculation there is little discrepancies of the flow rate q, so its figure is neglected. From Fig.12(a), it is known that the flow induced force for the convergence type is the smallest of all and divergence type is the largest inspite of the same leakage flow rate. From Fig.12(c), the flow induced coupling stiffness k_{xx} is similar characteristics, but convergence type is excellent from the viewpoint of stability.

CONCLUSION

In this report the flow induced force due to labyrinth seal which is sometimes the cause of instability is studied for the special model. That is, the labyrinth seal of shroud of steam turbine is used as an example and its flow induced force and stiffness and damping coefficients are theoretically calculated by two method. Then influences of deflection of steady state, pressure difference between inlet and outlet, labyrinth seal radius, seal clearance, seal pitch, number of seal chamber and seal strip height on the flow induced force and leakage flow rate are investigated. As the results, it is known that the above factors are very influential on the flow induced force. However further theoretical and experimental investigation are required in order to obtain a more precise description of labyrinth seal characteristics.

REFERENCES

1. Iwatsubo, T. : Evaluation of Instability Forces of Labyrinth Seals in Turbines or Compressors. NASA 2133, May 12-14, 1980.

TABLE 1. - LABYRINTH SEAL DIMENSIONS FOR NUMERICAL EXAMPLE

SEAL RADIUS	Rs	1	(m)
ROTOR NATURAL FREQUENCY	ω_n	5000	(rpm)
STRIP HEIGHT	h	10	(mm)
SEAL CLEARANCE	δ	1.3	(mm)
STRIP PITCH	ℓ	30	(mm)
NUMBER OF CHAMBER	N	2	
SEAL TYPE		straight-through type	

TABLE 2. - GAS CONDITION FOR NUMERICAL EXAMPLE

OPERATING LIQUID		air	
LIQUID TEMPERATURE	T	784.15	(K)
ENTRANCE PRESSURE	P_O	20482.0	(kPa)
EXIT PRESSURE	P_n	19678.4	(kPa)

TABLE 3. - DEFLECTION OF PRESSURE AND FLOW RATE FROM STEADY STATE

		PRESSURE OF EACH STAGE (kPa)				FLOW RATE
		PO	P1	P2	P3	(kg s/m^2)
STEADY STATE VALUE	(1)	20482.0	20166.3	19936.7	19678.4	6.8443
DEFLECTION OF	(2)	20482.0	20267.2	20036.4	19678.4	6.8443
PRESSURE P1,P2	(3)	20482.0	20065.5	19836.9	19678.4	6.8443
DEFLECTION OF	(2)	20482.0	20166.3	19936.7	19678.4	7.5287
FLOW RATE	(3)	20482.0	20166.3	19936.7	19678.4	6.1599

215
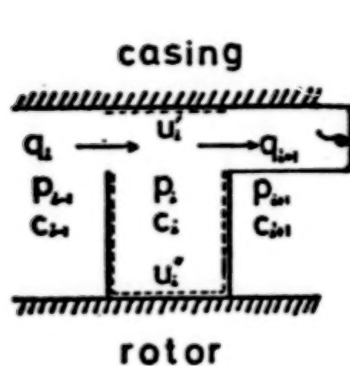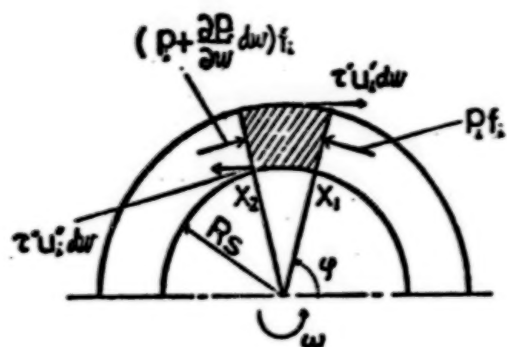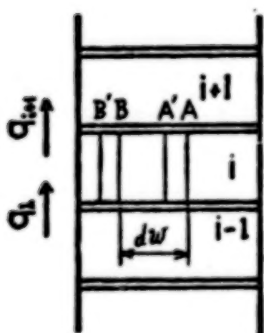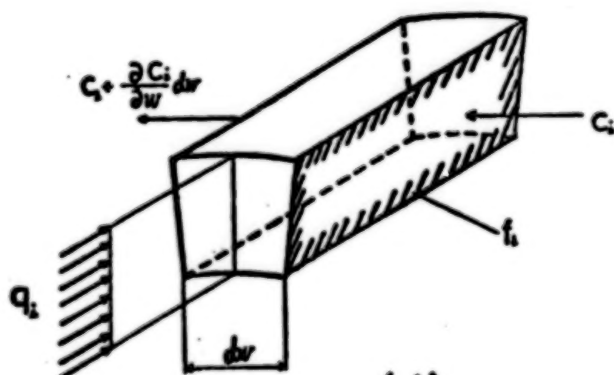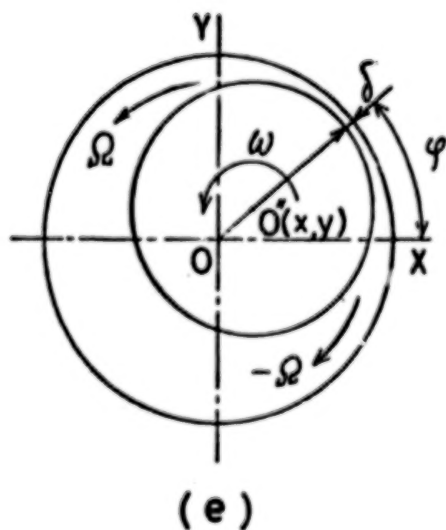
Figure 1. - Cross section of labyrinth seal
and definition of the coordinate.
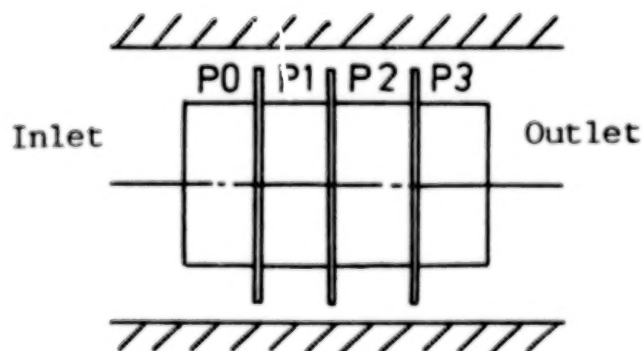
Figure 2. - Labyrinth seal model
for numerical example.

216
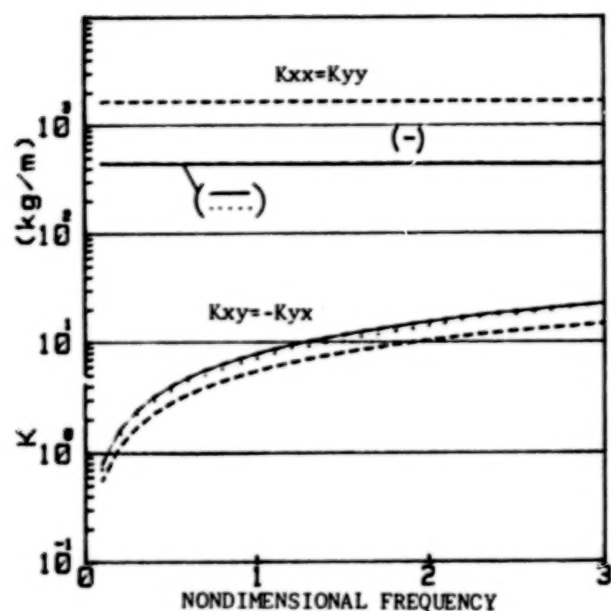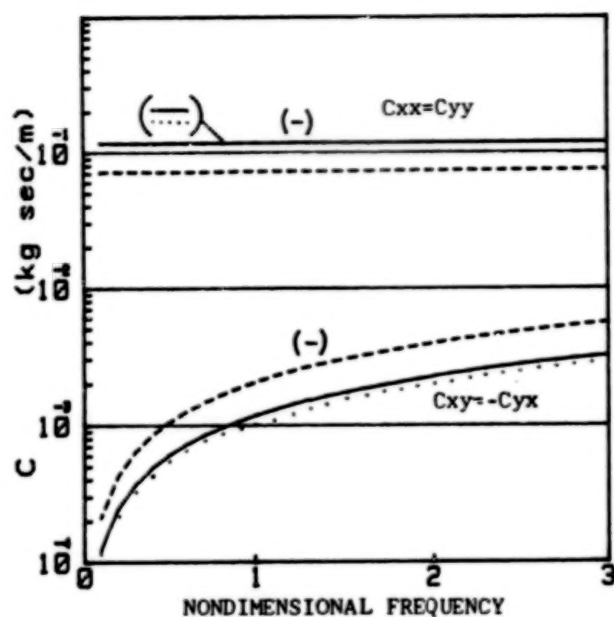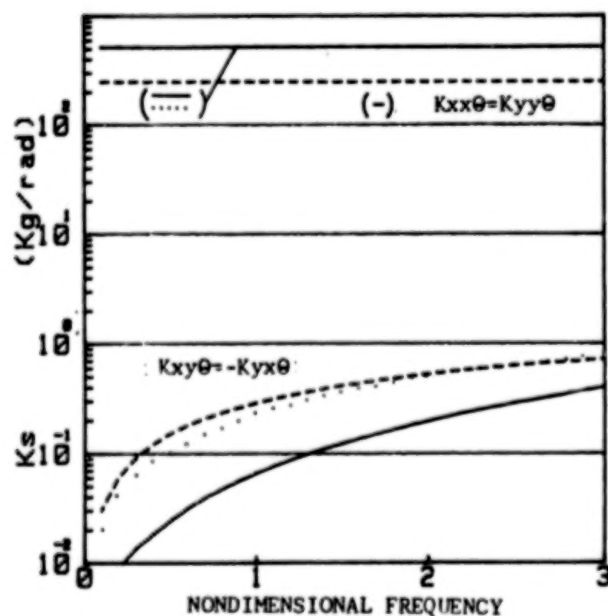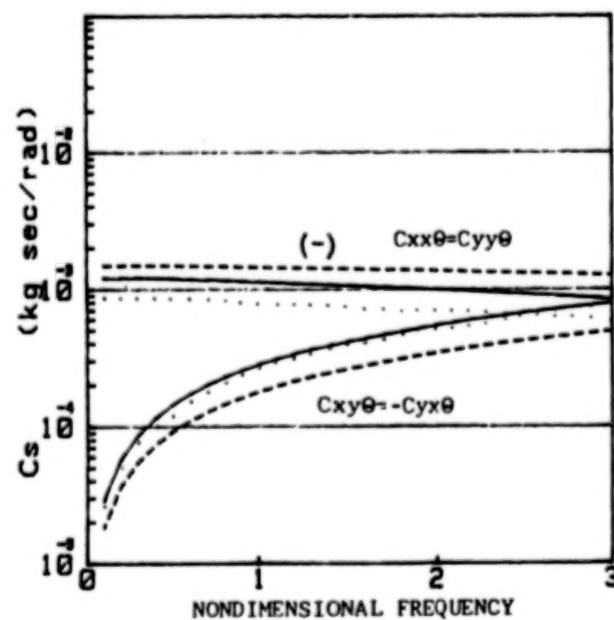
Figure 3. - Accuracy of two calculating methods and influence of pressure difference between inlet and outlet.

217
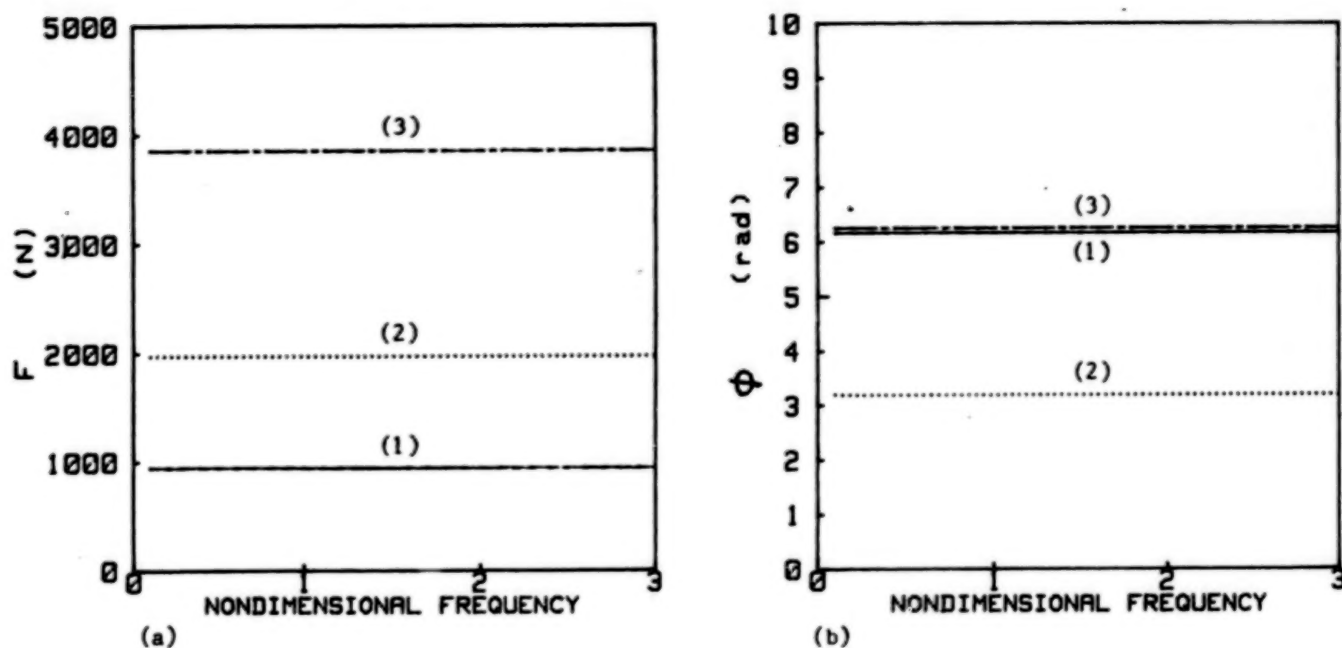
Figure 4. - Influence of pressure deflection from steady state on the flow induced force.
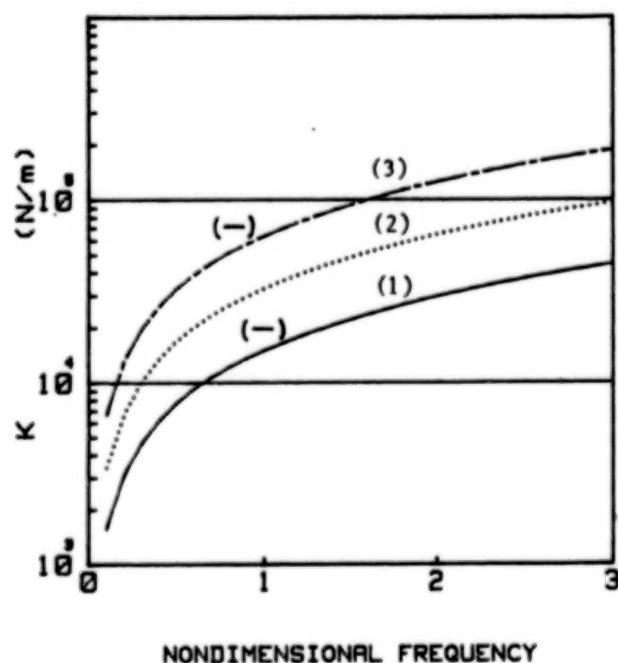
Figure 5. - Influence of pressure deflection from steady state on the cross coupling stiffness.

218

BEST DOCUMENT AVAILABLE
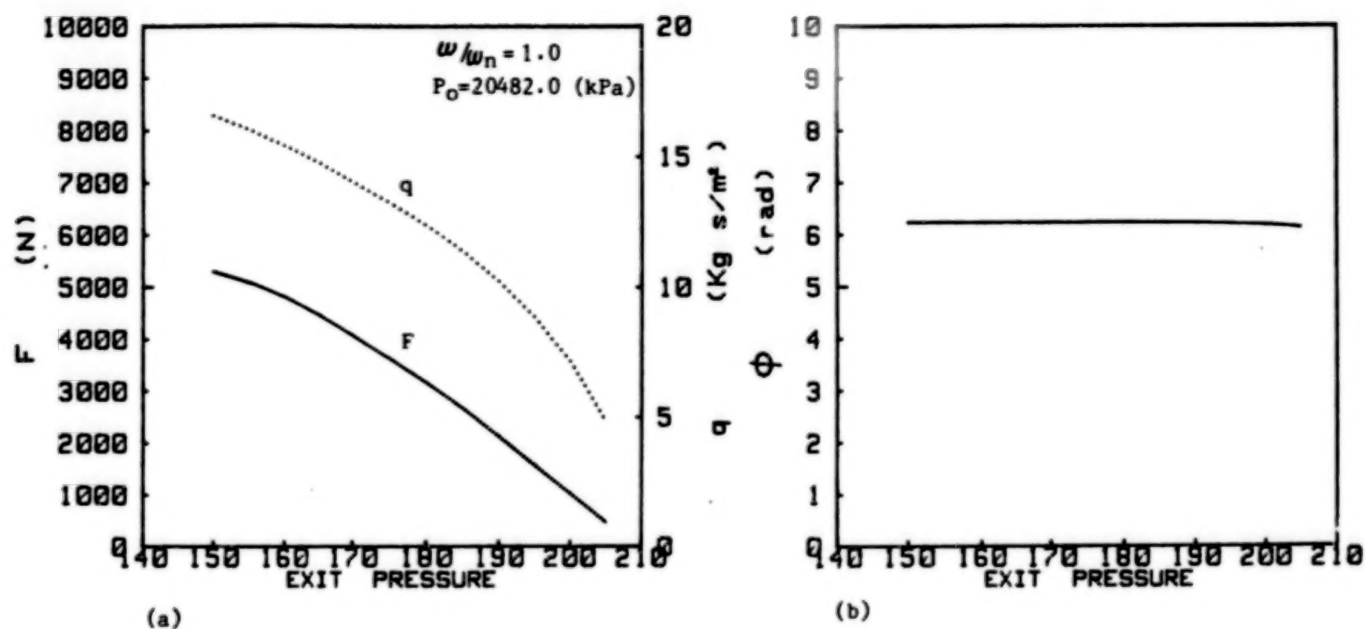
Figure 6. - Influence of pressure difference between inlet and outlet.
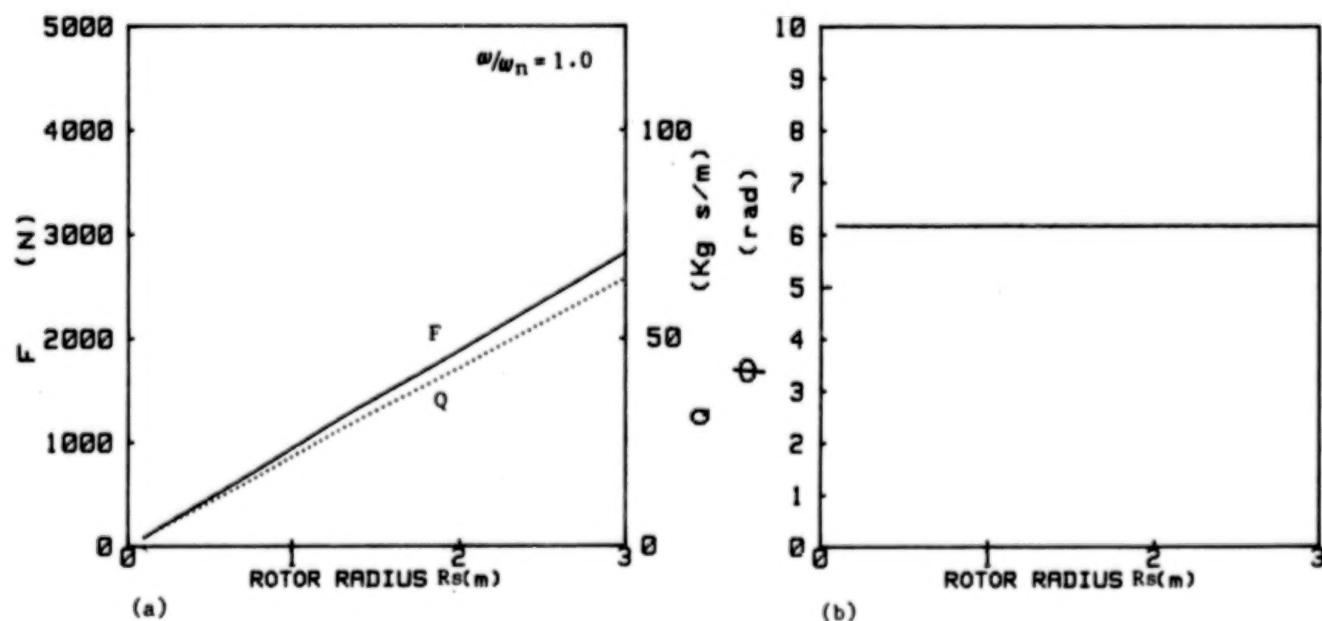
Figure 7. - Influence of labyrinth seal radius.

BEST DOCUMENT AVAILABLE
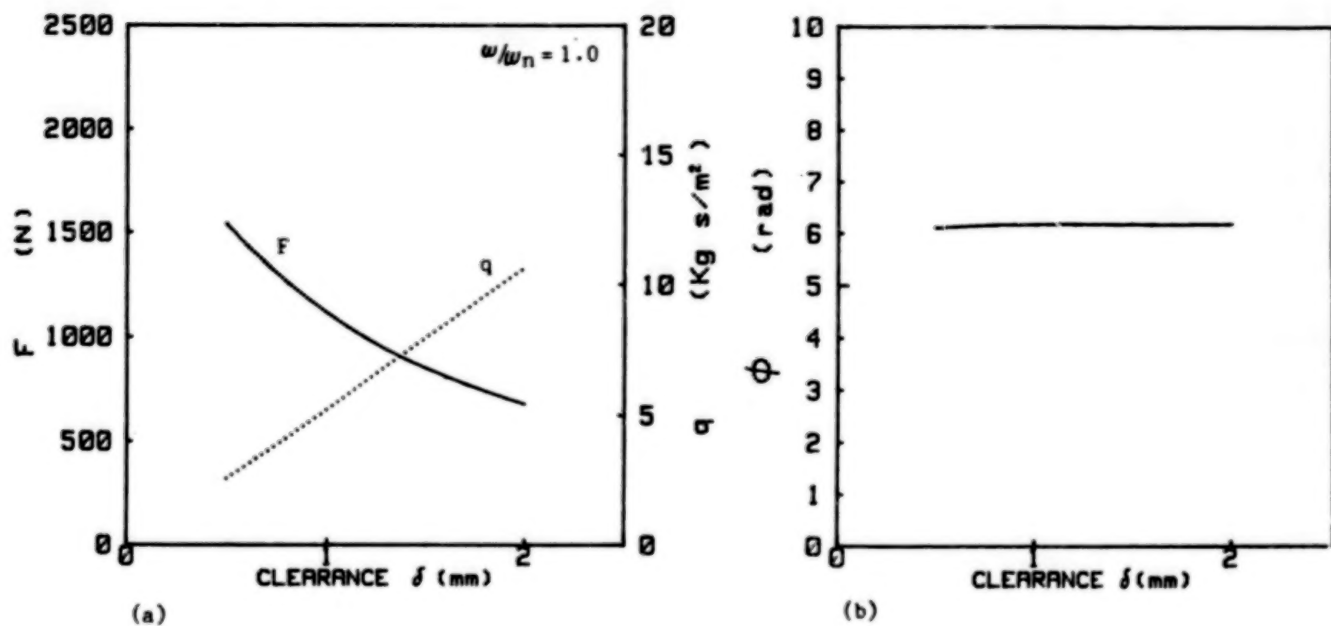
Figure 8. - Influence of seal clearance.
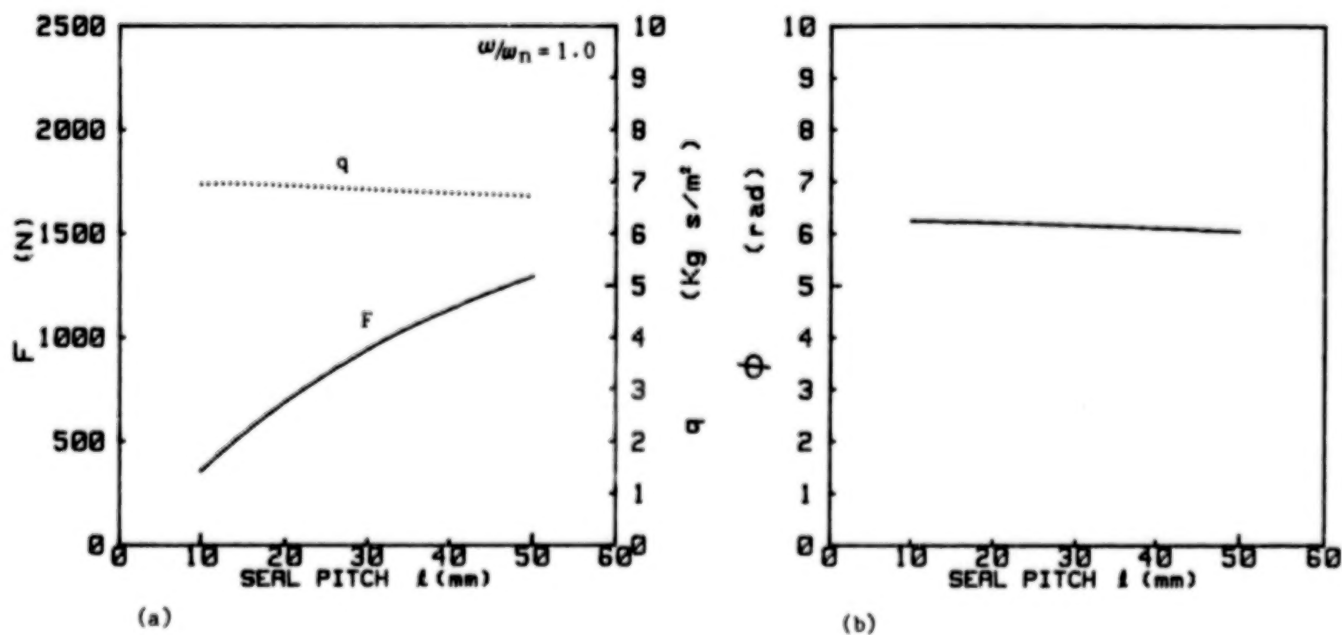
Figure 9. - Influence of seal pitch length.

220
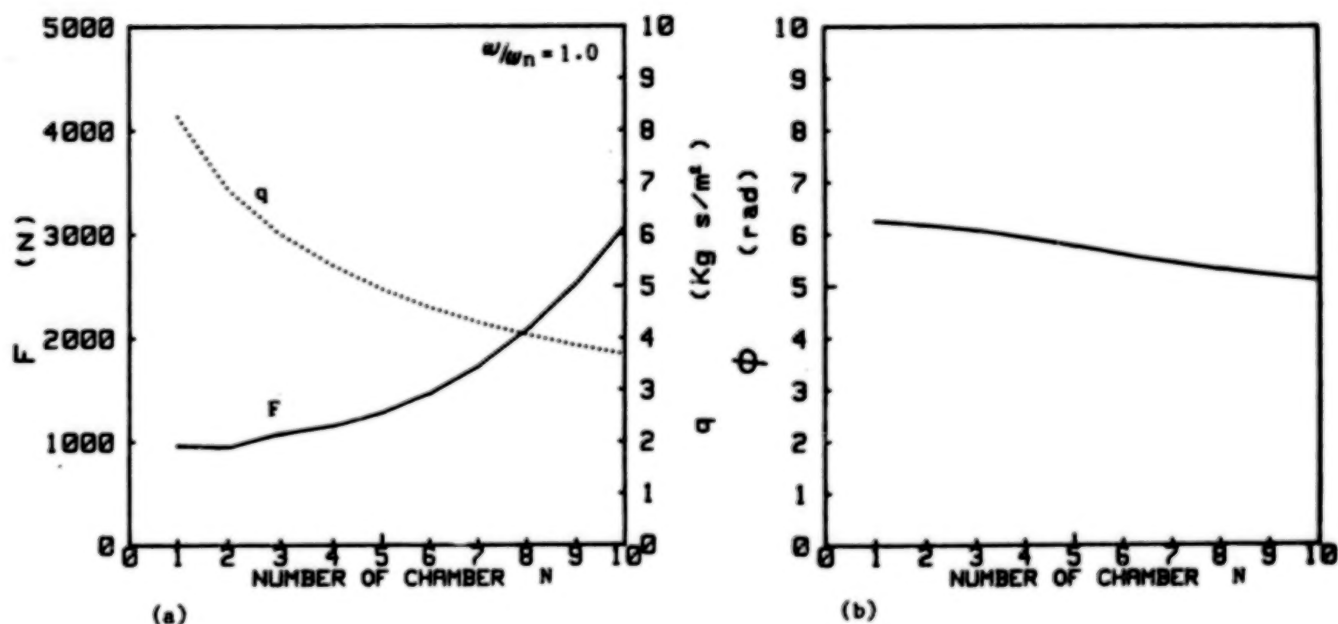
Figure 10. - Influence of number of seal chamber.
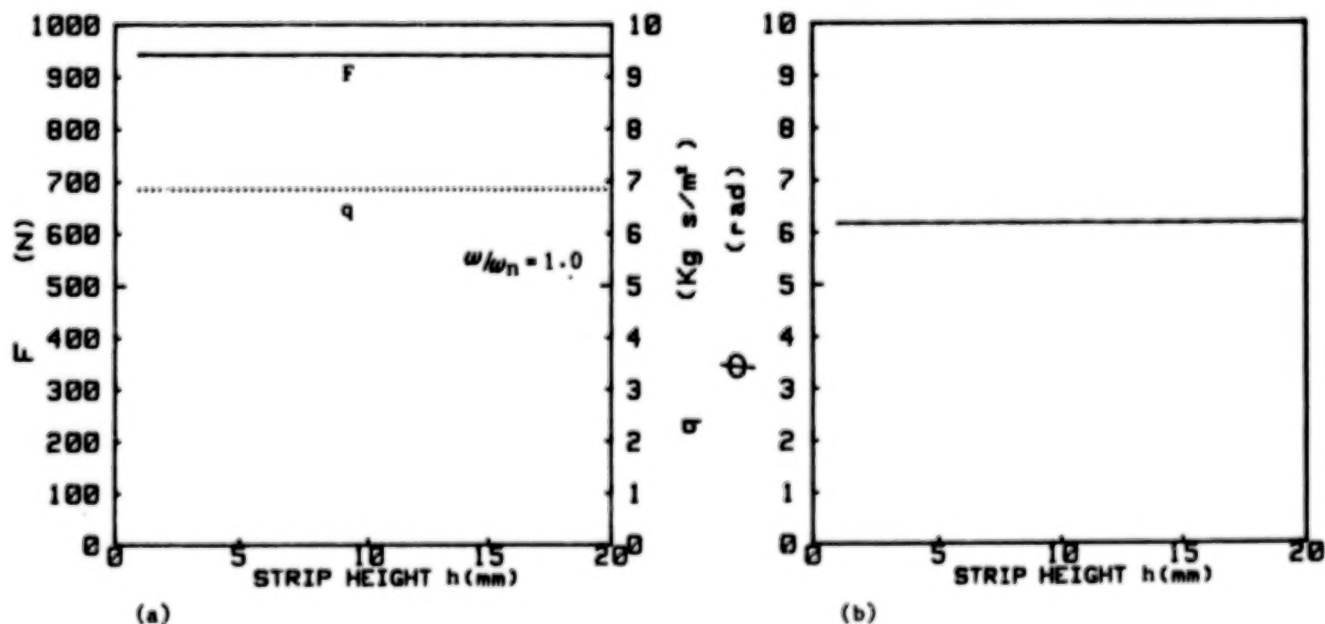
Figure 11. - Influence of seal strip height on the flow induced
force and phase angle.

221
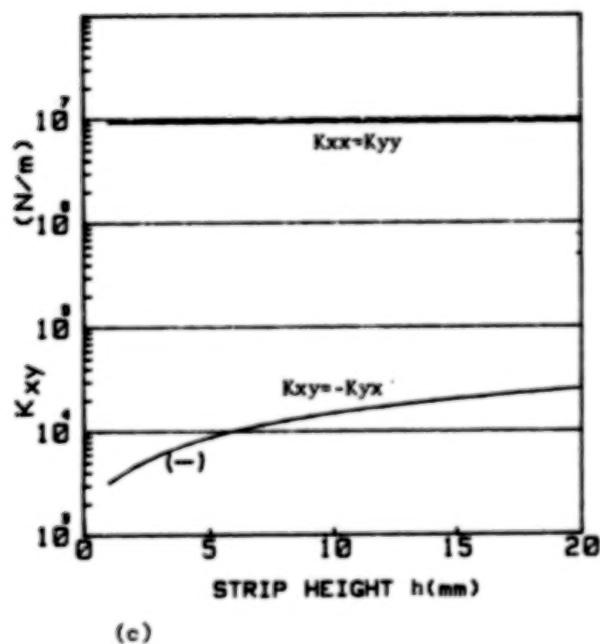
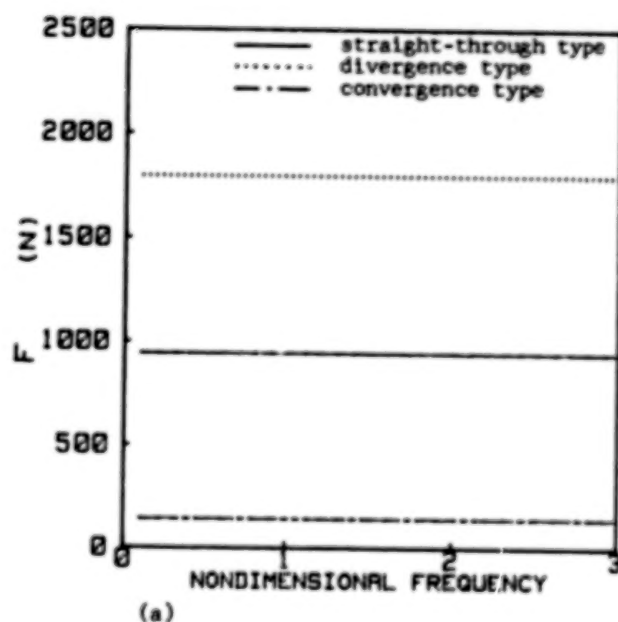Figure 11. - Influence of seal strip
height on flow induced cross-coupling.
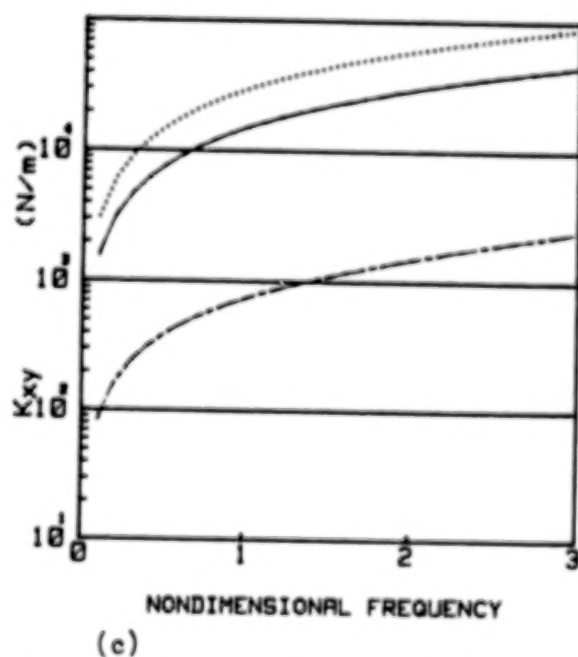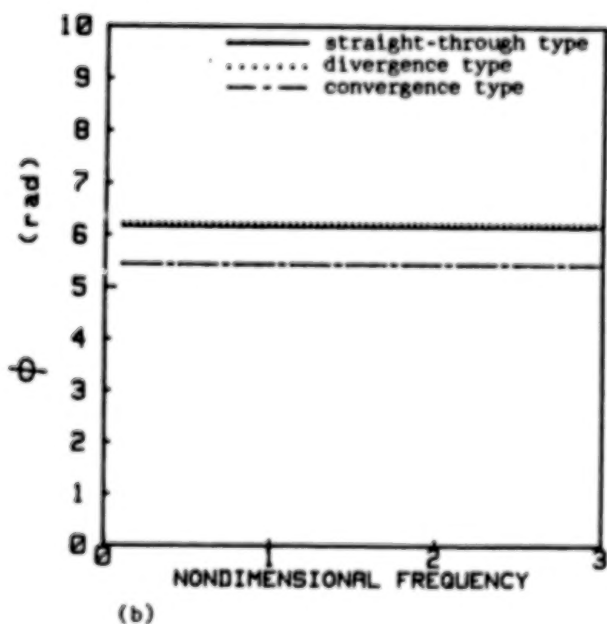
Figure 12. - Influence of divergence and convergence type labyrinth seal.

CIRCUMFERENTIAL PRESSURE DISTRIBUTIONS IN A MODEL LABYRINTH SEAL

Y. M. M. S. Leong and R. D. Brown
Heriot-Watt University
Riccarton, Edinburgh EH 14 4AS
Scotland

SUMMARY

Leakage flow through labyrinth glands had long been known to affect rotor stability but its effects have been often underestimated. A research programme to isolate and study this cause of instability has been initiated. Circumferential pressure distributions are measured in the labyrinth glands with geometry appropriate to the high pressure labyrinths in large steam turbines. Knowledge of this pressure distribution is essential as it is this unequal pressure field that results in the destabilising force. Parameters that are likely to affect the pressure distributions are incorporated into the test rig. Some preliminary pressure profiles are presented.

INTRODUCTION

Over the last few decades the development of steam turbines and gas turbo compressors has resulted in a steady increase in the energy density of the working fluid. Thus the energy available for various mechanisms leading to unstable motion also increases. The increase in power implies an increase in length of turbine-generator sets as these machines operate at a fixed speed (3000 or 3600 rpm). This makes the machine less rigid and the operational speed often lies above the first and second criticals. High level nonsynchronous vibrations have often been attributed to instability arising from lightly loaded bearings. The light loads instability problem is accentuated by the presence of a large number of bearings supporting a typical rotor with rigid couplings. Operational practice ensures that each bearing takes a load and/or the use of more stable bearing configurations, e.g. lemon-bore. In extreme cases tilting pad bearings may be used. If the instability arises in the bearings then the problem will be eliminated. However, there are other sources of instability which may prove to be significant. Steam whirl associated with differential clearance at the periphery of a blade row has long been suggested as a possible source. The possibility of labyrinth seals inducing instability has not been given the same weight of attention. The destabilising forces were considered by Pollman to be insignificant (ref.1). Furthermore it has been concluded that instability arises if and only if the labyrinths converge, Alford (ref.2); or diverge Spurk (ref.3) which of course led many to conclude as highly unlikely to occur in practice. It is also argued that the pressure in the labyrinths would equalise and hence cannot maintain the unequal pressure field which is essential in producing the lateral forces acting on the rotor.

Recent experience has indicated that the dynamic effects have been under-estimated. Based on operational steam turbines, Greathead (ref. 4,5) has brought

to light the influence of the labyrinth sealing glands, in particular at the high pressure end adjacent to the working fluid inlet, on the rub-synchronous response and the instability threshold. The response is strongly load dependent and has a major frequency component greater than half speed. Evidently the resultant destabilising force re-excites the lower criticals. A further interesting observation here was that the replacement of the standard journal bearings with tilting pad journal bearings had detrimental consequences on the response. This indicates that an instability which does not originate from the bearings cannot be eliminated by the use of tilt pad bearings.

NOTATION

p	absolute pressure	n	number of labyrinth stages
p_o	absolute pressure at entry	ϵ	eccentricity ratio
p_n	absolute pressure at exit	r	radius of rotor
q^*	mean axial flow	U	rotor surface velocity
q	axial flowrate per unit circumference	c	circumferential velocity of fluid in gland
μ	flow coefficient	v	axial velocity of fluid
ν	kinematic viscosity	Re	circumferential Reynolds number $(= (U-\bar{c})h/2\nu)$
$\Delta\mu_{1,2}$	change of flow coefficient at narrow, widest clearance	Re_a	axial Reynolds number $(= 2v\,\bar{\delta})/\nu)$
ρ	density	Ta	Taylor number $(= Re\sqrt{(h/r)})$
R	gas constant	θ	peripheral angle, measured from widest clearance
T	temperature	x	horizontal coordinate $(= r\theta)$
δ	radial clearance	z	axial coordinate
h	height of labyrinth fin		
f	cross-sectional area of gland	Subscripts	
L'	wetted perimeter of gland per unit circumference	i	i-th gland
L''	wetted perimeter of rotor per unit circumference	$-$	mean value

CURRENT STATE OF ART

Reports on labyrinth induced instabilities date back as early as the 1950's
(ref.6). A physical explanation of the occurance of self-excited vibrations through
clearance flows at the blade tips and interstage glands was presented by Thomas
(ref.7). It is already recognised that these vibrations were very much load
dependent. Alford introduced further understanding to the problem in his report on
aerodynamic exciting forces on jet turbo compressors and turbines (ref.2). The
occurrence of a circumferential variation of static pressure acting on the cylindri-
cal surface of a rotor particularly within labyrinth seals was put forward. The
whirl frequency was identified as the fundamental frequency of the rotor and rotor
support system whose whirl speed was about 40 to 50 percent rotational speed. The
whirl amplitude increases with power output. It is concluded that unequal radial
clearances at entry and discharge have significant effect on the excitation. Based
on a single chamber labyrinth a stability criteria was arrived at, with converging
labyrinth glands being destabilising. This stability criterion was contradicted by
Spurk (ref.3) in that diverging labyrinths are destabilising instead. In common with
Alford the rotational motion of rotor is neglected in the stability analysis and the
reason given for the contradiction is due to the further neglect of circumferential
flow within the labyrinth by Alford. Further literature (ref. 8,9) indicates that
lateral forces can be produced by parallel clearances when eccentricity exists, with
or without the occurence of spiral flow; and these lateral forces lead to unloading
of radial bearings.

Until 1975 approximately comprehensive experimental work on multi-stage laby-
rinths is non-existent, and at best the destabilising forces are only defined
qualitatively. Among the first attempts to analytically quantify these forces
in multi-stage labyrinths was by Kostyuk (ref.10). A set of fundamental equations
correlating leakage flow, circumferential flow and pressure distribution was arrived
at by applying compressible gas dynamics and conservation of energy and momentum.
Simplified solution to the equations was forwarded for cases with tilt although the
form of solution arrived at predicts no unequal pressure distribution for cases of
parallel eccentricity between rotor and labyrinths. The application of Kostyuk's
equations were extended by Iwatsubo and Kurohashi et al (ref. 11, 12). Iwatsubo
applied a finite difference method on the equations with the spring and damping
coefficients of the labyrinths numerically determined. With a simpler approach
Kurohashi et al applied an equivalent clearance to take into account of the variable
flow coefficient through the annular clearance of the labyrinths to arrive at a
pressure distribution and set of stiffness and damping coefficients. No swirl or
spiral flow was assumed nor considered. Although some experimental work was
performed the published data were found to be rather limited especially on the
pressure distributions. Pressure measurements were made at only two opposite
locations within a labyrinth chamber hence with the assumption that the pressure
peaks at such location.

The experimental work of Benckert and Wachter (ref. 13,14,15) represents the
first serious attempt to investigate the leakage flow induced forces on multi-stage
labyrinths. It was an extensive experimental programme on labyrinths on a high
pressure air rig. Various geometry, number of stages, inlet conditions, eccentricity
and realistic peripheral velocity of rotor were catered for. Pressure profiles were
indeed obtained on cases with a parallel eccentricity through the labyrinths and
swirl has an increased forcing effect on the rotor. However the published results
were mainly of integrated forces and only few pressure distributions were published,

pressure distributions with rotor rotation were not presented. As the interest of the authors was towards gas turbo compressors the published work was based on geometry and dimensions not appropriate to steam turbines.

It is this lack of directly applicable experimental results in open literature based on realistic seal geometry with full rotational speeds that necessitates the need for further research. This research programme on labyrinth seals was a natural extension of existing work on rotor dynamics in the Department of Mechanical Engineering at Heriot-Watt University. Work on rotordynamic instability included the effects of high pressure ring seals on turbomachinery vibrations, fluid force induced vibrations, boiler feed pump instability and a general rotor dynamic computer programme evaluating forced response and stability. It is ultimately hoped that the programme would incorporate labyrinth seal forces to extend its range of applicability.

OBJECTIVE

The main objective of the rig is to isolate the labyrinth induced effects from other rotor dynamic effects that can possibly arise. A rotor diameter approximately half that of a typical steam turbine shaft is used. Nevertheless the rotor and labyrinth dimensions should meet the requirement that the flow parameter of Reynolds number and Taylor number are of the same order of magnitude both in the axial and circumferential direction. As it is felt that the rotor peripheral velocity is of importance in the shearing of the leakage flow, a realistic velocity must be attained on the rig, in this case of 100 m/s as in operational steam turbines. Consultation on the above data and seal geometries had been made with United Kingdom based manufacturers and public utilities.

The approach taken is to measure the static pressure distributions in the labyrinth chambers as the flow passes through the labyrinth and to match these measured distributions with theoretical predictions. An alternative method is to attempt to measure overall force and/or stiffness coefficients directly. However the literature has a number of examples where considerable scatter was demonstrated in attempts to measure stiffness and damping coefficients. Moreover circumferential pressure distributions give a better insight into the nature of the problem. It is interesting to know how these pressure distributions are affected by eccentricity, clearance, speed and a host of other parameters. When an adequate match has been achieved between experimental and theoretical circumferential pressures, the required dynamic coefficients can be obtained theoretically. The integrated pressure force for overall perturbed conditions yield the appropriate stiffness and damping coefficients.

DESCRIPTION OF RIG

The experimental rig consists of a main casing enclosing the rotor and labyrinth assembly, figures 1,2,3. The main casing is made up in two sections with the upper section easily removable to enable the labyrinth assembly, especially combination and stepped labyrinths, be built up conveniently. Slots are milled on the casing adjacent to the labyrinth assembly to facilitate the mounting of pressure tappings in the labyrinth. A vertical rotor is mounted on roller ball bearings

226

226

0

0

0

0

0

0

0

0

0

0

0

0

0

0

0

0

0

0

0

0

within the casing. The top bearing housing is bolted on to the main top cover plate and the bottom bearing housing on the main platform on which the casing is bolted. Drive is by means of a horizontally mounted 8.5 kW variable speed DC motor, with the driving shaft attached to a 1:1 right angle conversion gear box. The rotor is driven by a timing belt from the gear box with the necessary step up in speeds achieved through the pulleys giving speed ranges from 0 to 7600 rpm.

Consistent with the need to isolate other rotor dynamic effects a rigid rotor is used. This eliminates the influence of hydrodynamic bearings as well as making it easy to preset and maintain predetermined eccentricities. Mounting it vertically eliminates the need to consider gravitational effects in the experiments and subsequent theoretical work. Grease lubricated self aligning ball bearings are used at the top to allow for small relative misalignment between the rotor and main casing for tilt investigations. To take the high downwards thrust a matched pair of angular contact ball bearings is used in tandem. The bottom bearings are oil lubricated from nozzles directed on to the cages and races allowing them to be used at the higher speeds. A high pressure thrust compensating dummy piston could have been incorporated into the design but was not as conservation of the available working fluid was a major consideration. In order to achieve the peripheral velocity of 100 m/s, a drum of 240mm in diameter is mounted on to the main shaft to form part of the rotor. The drum is interchangeable and the experiments will involve the use of a plain drum and grooved drum for various labyrinth combinations. The axial length of the drum is 160mm to accommodate the axial length of a complete labyrinth assembly. The main shaft and drum are first balanced individually and finally as a completed assembly to ISO G 1.0 (1 gm-mm per kg rotating mass).

The working fluid is fed into a diffusion box in the main casing. Within the diffusion box deflection vanes and perforated holes spread the flow. From here the flow enters a plenum chamber where the flow is further settled. The working fluid used is compressed air at a gauge pressure of 5.52 bar although higher pressure or higher density compressed gas can easily be adapted for use on the rig. The flow rate through the rig is measured by an annubar. It has four dynamic pressure sensing holes facing the stream, and the dynamic pressure being averaged by means of an interpolating inner tube. A further pressure sensing hole measures the static pressure less the suction pressure which eventually gives a differential pressure representing the mean velocity along the tube. This measured flow rate is compared with the extensively used and tested semi-empirical labyrinth leakage equation of Vermes (ref.16) as well as equation 1. (ref. 10,12). Axial and circumferential Reynolds number and Taylor number of 33×10^3, 63×10^3 and 17×10^3 respectively can be attained on the rig as compared to typical values of 222×10^3, $124 \times 10^3 - 216 \times 10^3$ and $14 \times 10^3 - 35 \times 10^3$ respectively on operational United Kingdom steam turbines. Nevertheless one of the main current constraints on the rig is due to the limitations of output from the compressors of the Department. Just prior to entry into the labyrinths the flow enters a set of swirl ring mounted on top of the labyrinth assembly. These rings are interchangeable with vane angles of 45°, 30°, 15° and 0°. These swirl rings can hence pre-induce a spiral flow prior to entry into the labyrinth assembly. As the rotational direction of the rotor can be reversed the case of the pre-swirl in opposite direction to the rotation of the rotor is also possible. The 0° vanes are used as a flow straightener when no pre-swirl is required.

Depending on dimensions, the labyrinth assembly is built up from interlaying individual seal fin and chamber or as in integral individual labyrinth, figures 4,5. This allows interchangeability of seals with different geometry, sizes and

227

clearance. The current sizes used for straight through labyrinths are 4.064mm (height) x 6.350mm (axial length) and 9.525mm x 9.525mm being the largest size to be used; with clearances of 0.254mm - 0.635mm. Stepped and combination seals of 4.064mm/4.620mm x 6.350mm are also used. Further combination of labyrinth dimensions can be catered for by mere manufacture of the fins required. The number of stages can be altered by removing or adding appropriate individual fins. The current number of stages considered total up to 12 labyrinth chambers, although more can be added. Custom made pressure fittings are mounted on recesses in the individual labyrinth fins to measure static pressure circumferentially at 30° intervals in each and every stage down the labyrinth stack.

The eccentricity of the rotor with respect to the labyrinths can be set at any predetermined location. The labyrinth assembly together with the main casing as a whole is moved laterally across the main table platform, with the rotor and its bearings housings being fixed in its original location. The movement is achieved by means of lateral finely threaded jack screws, with the main casing moving in guide blocks. To minimise the effort required to move the job, four sets of ball bearing thrust pads are brought into play raising the main casing and assembly off the table platform whilst being moved. Lateral adjustable pre-compressed springs are mounted against the casing to eliminate any backlash on such small movements. The eccentricity is checked by means of displacement proximators as well as dial gauges. Other than parallel eccentric movement a relative tilt between the rotor and labyrinths can be set. Here again the rotor is left undisturbed and the main casing with the labyrinth assembly tilted. This is so achieved by raising the main casing off the platform and an angled tilt pad inserted between the main casing and platform.

The experimental parameters are

(i)   seal geometry and types: straight through, stepped and combination labyrinths
(ii)   number of stages
(iii)   relative tilt between labyrinths and rotor
(iv)   flow rate and inlet conditions, including swirl
(v)   eccentricity
(vi)   rotational speed of shaft.

At each setting of these parameters static pressure measurements are taken as the leakage flows through the labyrinths. The current total of 144 pressure distribution measurements of the labyrinth assembly as well as static and dynamic pressure measurements at the inlet and outlet are fed to a bank of mechanical rotary switches. These switches allow 5 pressure lines, on the inlet ports, to be served by 1 pressure transducer at the outlet port of the switches. At each inlet port setting a scan of all the pressure transducers are taken and sequential switching of open inlet ports gives a complete pressure mapping. As static pressure measurements are of interest here this arrangement would be more cost effective than electronics based scanning valves. The working fluid inlet and outlet temperature from the labyrinth assembly are also monitored by thermocouples to validate the theoretical assumption that the two temperatures are constant. The scanning of the pressure transducers as well as thermocouples and proximators are activated via a data transfer unit, giving output in forms of readings on the digital voltmeter and paper tape for final processing on a digital computer.

228

SUMMARY OF THEORY

Assuming an isothermal process in a multi-stage labyrinth glands and the working fluid to be a perfect gas, Kostyuk (ref.10) derived a set of fundamental equations as follows:

$$P_{i-1}^2 - P_i^2 = \frac{q_i^2 \, RT}{\mu_i^2 \, \delta_i^2} \tag{1}$$

$$\frac{\partial \rho_i}{\partial t} + \frac{\partial(\rho_i c_i)}{\partial x} = \frac{1}{f_i} \, (q_i - q_{i+1}) \tag{2}$$

$$\rho_i \frac{\partial c_i}{\partial t} + \rho_i c_i \frac{\partial c_i}{\partial x} + \frac{q_{i+1}}{f_i} \, (c_{i+1} - c_i)$$

$$+ \, K' \rho_i c_i^2 - K'' \, \rho_i (U - c_i)^2 = - \, \frac{\partial p_i}{\partial x} \tag{3}$$

$$K' = \frac{\lambda' L'}{2f_i} \ \text{sign } c_i \quad , \quad K'' = \frac{\lambda'' L''}{2f_i} \ \text{sign } (U - c_i) \tag{4}$$

$$\lambda' = fn(Re') \quad , \quad \lambda'' = fn(Re'') \tag{5}$$

$$Re' = \frac{c_i h_i}{2\nu} \quad , \quad Re'' = \frac{(U - c_i)h_i}{2\nu}$$

$$p_i = \rho_i \, RT \tag{6}$$

The analytical solution to the above set of equations is simplified by defining an equivalent clearance change (ref.12)

$$y_{(e)} = (1 + \xi_i)y_i \tag{7}$$

$$\text{where} \quad \xi_i = \frac{\overline{\delta}_i (\Delta\mu_2 - \Delta\mu_1)}{2 \, \overline{\mu}_i y_i} \tag{8}$$

229

BEST DOCUMENT AVAILABLE

Subsequently giving a pressure distribution

$$p_i(\theta) - \bar{p}_i = - \frac{\dot{D}r_i^{\,2}}{f_i} \cos\theta + \frac{\bar{c}\, Dr_i}{f_i} \sin\theta$$

$$- 2\left[K'c +.K'' (U - \bar{c}) \right] \frac{Dr_i^{\,2} \cos\theta}{f_i} \qquad (9)$$

where $D = \dfrac{q^*}{2\pi r_i} \left[\dfrac{y_{(e)i+1}}{\bar{\delta}_{i+1}} - \dfrac{y_{(e)i}}{\bar{\delta}_i} \right]$ \qquad (10)

A possible alternative approach is to apply modified bearing theory to labyrinth chambers. Pinkus and Etison (ref.17) has shown that the Reynolds Equation in a modified form can be used for finite cylinders rotating within moderate clearance ratios, say between 10^{-3} to 10^{-1} which cover likely values for labyrinths.

ADDITIONAL MATERIAL PRESENTED AT THE WORKSHOP

All experimental data presented in figures 6-17 are for straight through seals with mean radial clearance 0.635mm, axial pitch 9.525mm and labyrinth depth 9.525mm. Figure 6 shows the pressure reduction as the working fluid is throttled for a concentric rotor. The resulting circumferential pressure distributions are shown in Figure 7. The expected unbiased pressure distributions are obtained except for slight deviation in chambers 6 and 7. This indicates that any biased pressure profiles would be due to eccentricity, speed or other experimental parameters and can be taken as significant.

Figures 8-11 give the circumferential pressure distribution down the stages for cases of parallel eccentricities; $\epsilon = 0.4$, 0.6 and u = 94.3, 37.7, 0 m/s. A restoring force type of pressure distribution with a slight trough is observed in the first chamber. However subsequent chambers give a distribution with minimum pressure just before the minimum gap. These give rise to radial negative spring forces. The profiles are similar in form but with values scaling up with increased eccentricity. Apparently peripheral speeds do not affect the distributions except for the first chamber where the trough increases with speed. Figure 12 shows the pressure ratio for all chambers on an absolute scale for a case seen earlier $\epsilon = 0.6$, 94.3 m/s. It is pointed out here that the experimental points are averaged values of readings taken continuously for each pressure measurement. Scatter are within $\pm 2\frac{1}{2}\%$ and extremely good repeatability is obtained. It is obvious here that unequal pressure field does exist for parallel eccentricity cases. The obtaining of pressure profiles beyond the first chamber shows the limitation of the 'equivalent clearance' pressure prediction of Kurohashi which gives a zero differential pressure field beyond the first chamber.

If the pressure distributions are numerically integrated as defined in the sign convention, figure 13, radial and transverse forces can be obtained. Note that with the sign convention adopted a positive F_y indicates a negative spring force.

230

Figure 14 gives the radial and transverse forces in individual labyrinth chambers for u = 94.3 m/s and ε = 0.4, 0.6. The first chamber has a restoring radial force, and beyond this chamber negative spring forces are evident in all stages. These radial forces vary with stage number and eccentricity in a consistent manner, in particular an axial wave variation is clearly present. The transverse force tends to be small and fairly insensitive to eccentricities.

The pressure distributions, as seen earlier, are fairly insensitive to speed and obviously so would the resulting forces, figure 15. Figure 16 gives the radial and transverse forces for several eccentricities. The radial forces are dependent on eccentricity and the transverse forces much less so. Figure 17 gives the summation of radial and transverse forces plotted against eccentricity with the linear relationship of F_y with eccentricity seen.

The above results presented are some of the experiments done with the recent commissioning of the test rig. Obviously the full experimental schedule is yet to be undertaken and it is hopeful that meaningful results will be obtained. The effects of these forces will be incorporated into a model of a real rotor using the rotordynamic computer programme of the Department in the near future.

REFERENCES

1. Pollman, E., Schwerdtfeger, H. and Termuehlen, H.: Flow Excited Vibrations in High Pressure Turbines (Steam Whirl). Trans. ASME, J.Engng. Power, April 1978, pp. 219-228.

2. Alford, J.S.: Protecting Turbomachinery from Self-Excited Rotor Whirl. Trans. ASME, J. Engng. Power, October 1965, pp. 333-344.

3. Spurk, J.H. and Keiper, R.: Self-Excited Vibration in Turbomachines resulting from Flow through Labyrinth Glands. C.E. Trans. 6785. Translated from Ingenieur Archiv. Vol. 43 (1974), pp. 127-135.

4. Greathead, S.H. and Bastow, P.: Investigations into Load Dependent Vibrations of the High Pressure Rotor on Large Turbo-Generators. I.Mech.E. Conference on Vibrations in Rotating Machinery. September 1976.

5. Greathead, S.H. and Slocombe, M.D.: Further Investigations into Load Dependent Low Frequency Vibration of the High Pressure Rotor on Large Turbo-Generators. I.Mech.E. Conference on Vibrations in Rotating Machinery, September 1980.

6. Den Hartog, J.P.: Mechanical Vibrations, McGraw-Hill Book Co. Inc., New York, fourth edition, pp. 295- 296.

7. Thomas, H.J.: Unstable Oscillations of Turbine Rotors due to Steam Leakage in the Clearances of the Sealing Glands and Blading, C.E. Trans. 6281. Translated from A.I.M. Bull. Sci. (1958) Vol. 71, Nos. 11, 12.

8. Rosenberg, C.S., Orlik, W.G. and Marshenko, U.A.: Investigating Aerodynamic Transverse Forces in Labyrinth Seals in Cases Involving Rotor Eccentricity. C.E. Trans. 7083. Translated from Energomashinostrojenie Vol. 8, 1974, pp. 15-17.

9. Orlik, W.G., et al: The Centring Effect in Labyrinth Type Seals and its Effect on Low Frequency Vibration of Turbo-Machines. C.E. Trans. 7104. Translated from Energomashinostrojenie Vol. 10, 1975, pp. 25-29.

10. Kostyuk, A.G.: A Theoretical Analysis of the Aerodynamic Forces in the Labyrinth Glands of Turbomachines. Thermal Engineering Vol. 19 1972 (11), pp. 39-44 (Teploenergetika 1972, 19 (11) pp. 29-33).

11. Iwatsubo, T.: Evaluation of the Instability Forces of Labyrinth Seals in Turbines or Compressors. Symposium - Workshop on Rotordynamic Instability Problems in High-Performance Turbomachinery. Texas A&M Univ., May 1980. NASA Conference Publication 2133.

12. Kurohashi, M., Inoue, Y., Abe, T. and Fujikawa, T.: Spring and Damping Coefficients of the Labyrinth Seals. I,Mech.E. Conference on Vibrations in Rotating Machinery. September 1980.

13. Benckert, H. and Wachter, J.: Investigations on the Mass Flow Induced Forces in Contactless Seals of Turbomachines. Proceedings of the 6th Conference on Fluid Machinery, Budapest 1979, pp. 57-66.

14. Benckert, H. and Wachter, J.: Flow Induced Coefficients of Labyrinth Seals for Application in Rotordynamics. Symposium - Workshop on Rotordynamic Instability Problems in High Performance Turbomachinery, Texas A&M Univ., May 1980, NASA Conference Publication 2133.

15. Benckert, H. and Wachter, J.: Flow Induced Constants of Labyrinth Seals. I.Mech.E. Conference on Vibrations in Rotating Machinery, September 1980.

16. Vermes, G.: A Fluid Mechanics Approach to the Labyrinth Seal Leakage Problem. Trans. ASME, J.Engng. Power, April 1961, pp. 161-169.

17. Pinkus, O. and Etsion, I.: Analysis of Finite Cylinders Rotating Within Moderate Clearance Ratios. Trans. ASME, J. Fluids Engng., June 1976, pp. 156-162.
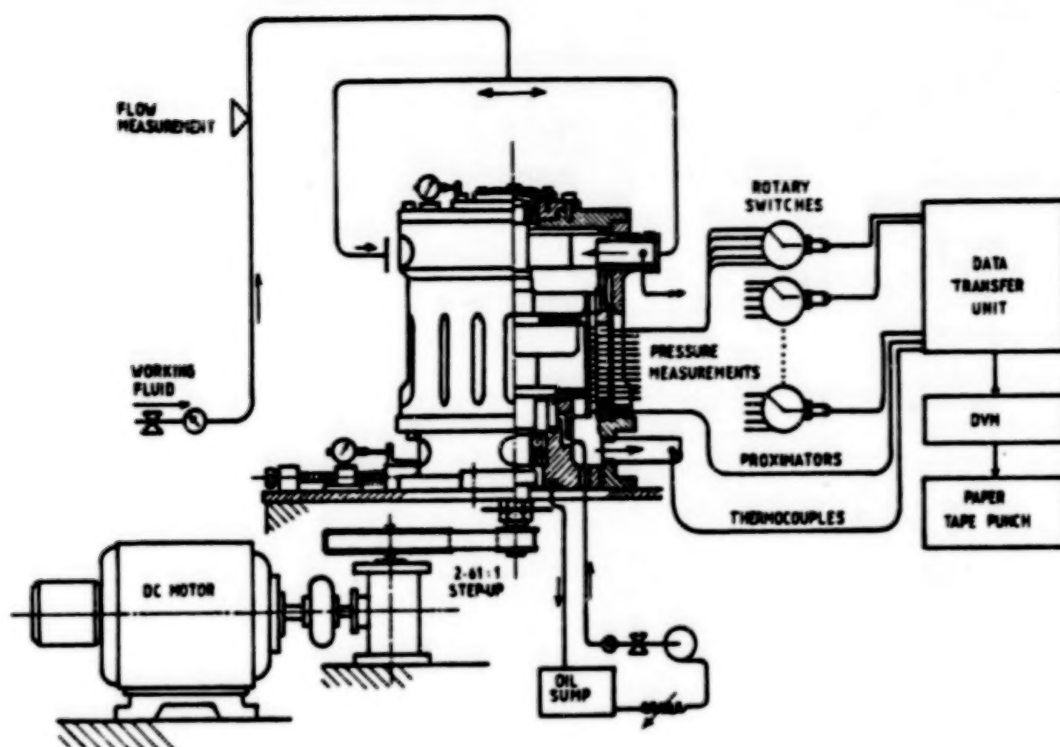
Figure 1. - Schematic layout of test rig and instrumentations.
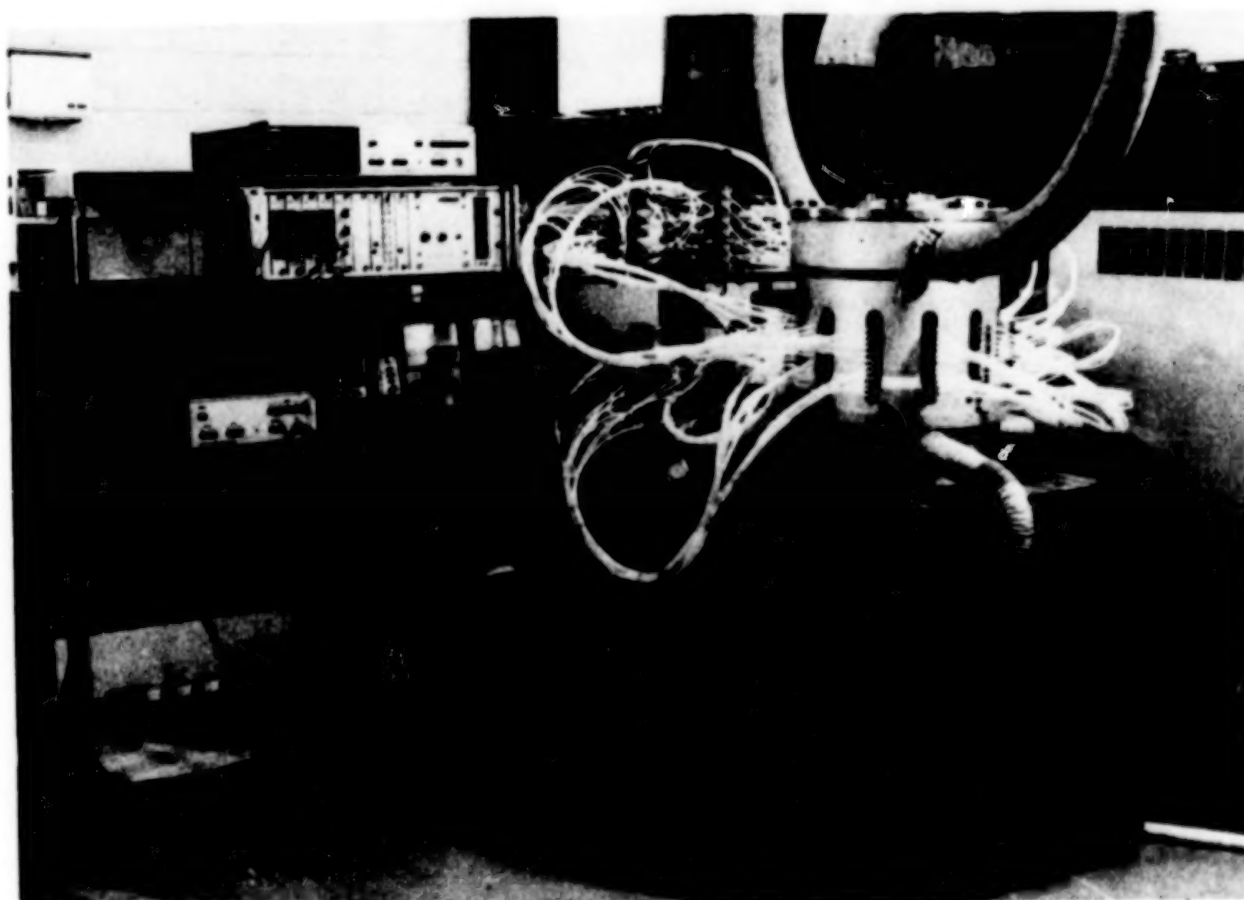
Figure 2. - View of overall test rig.

233
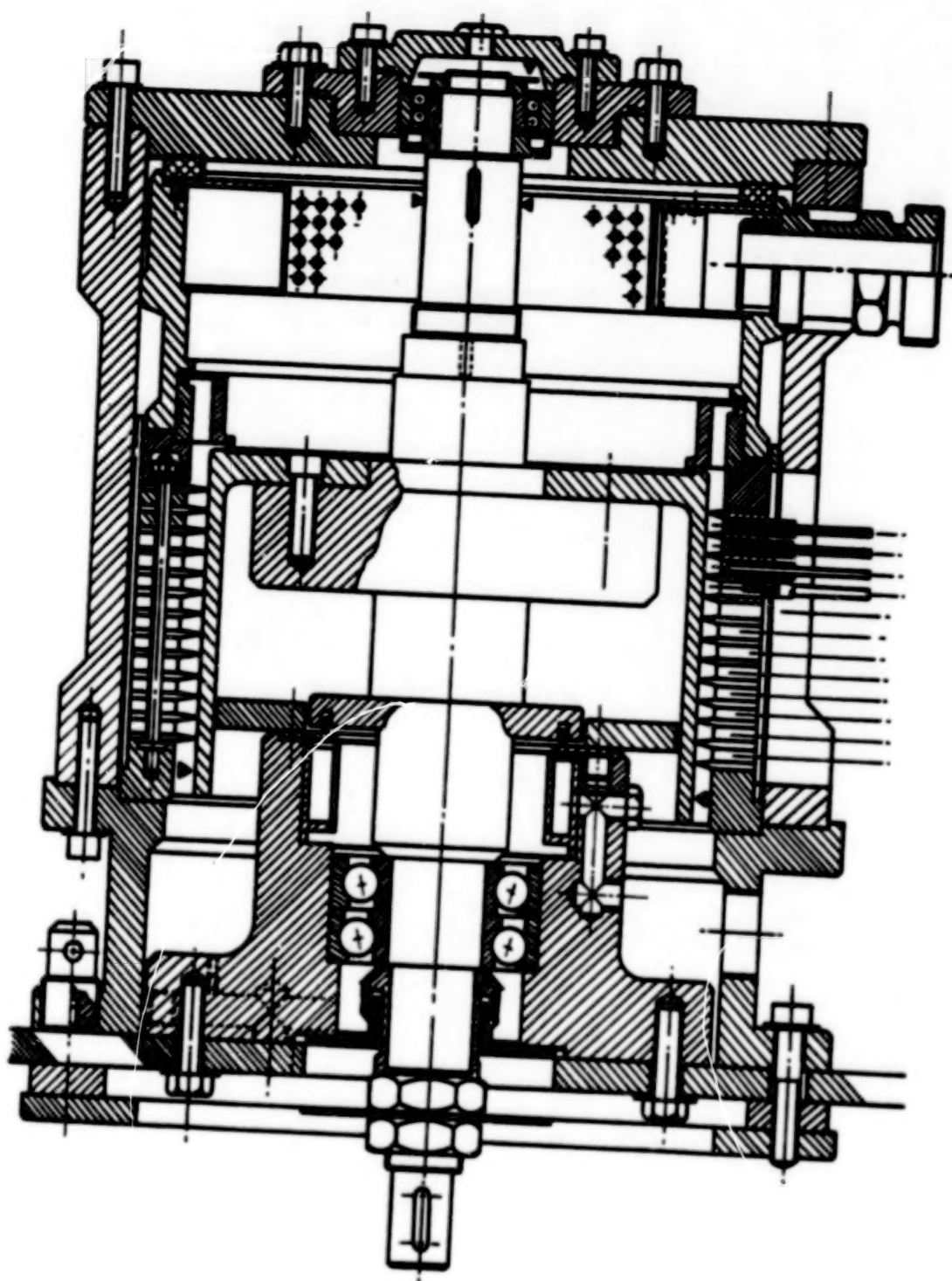
Figure 3. - Sectioned assembly drawing of test rig (main assembly).

234
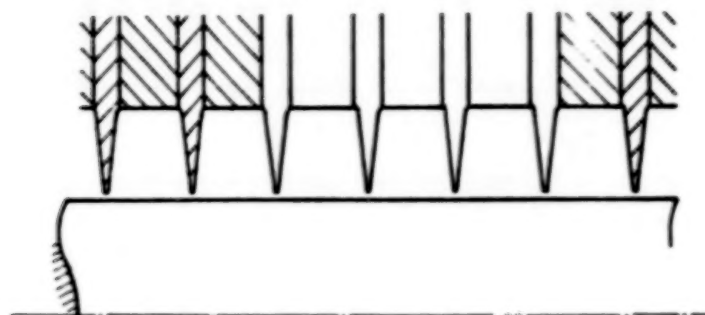
(a). - Straight through labyrinths.
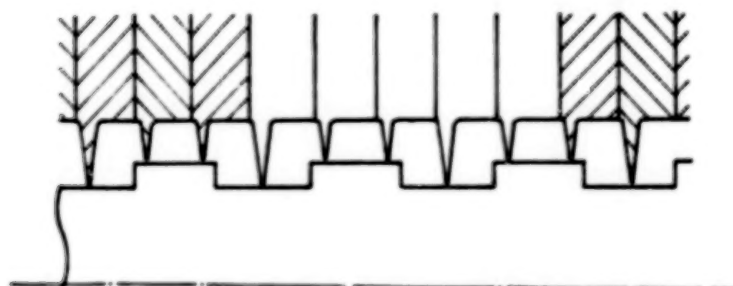
(b). - Combination labyrinths.

Figure 4. - Types of built-up labyrinth stack.
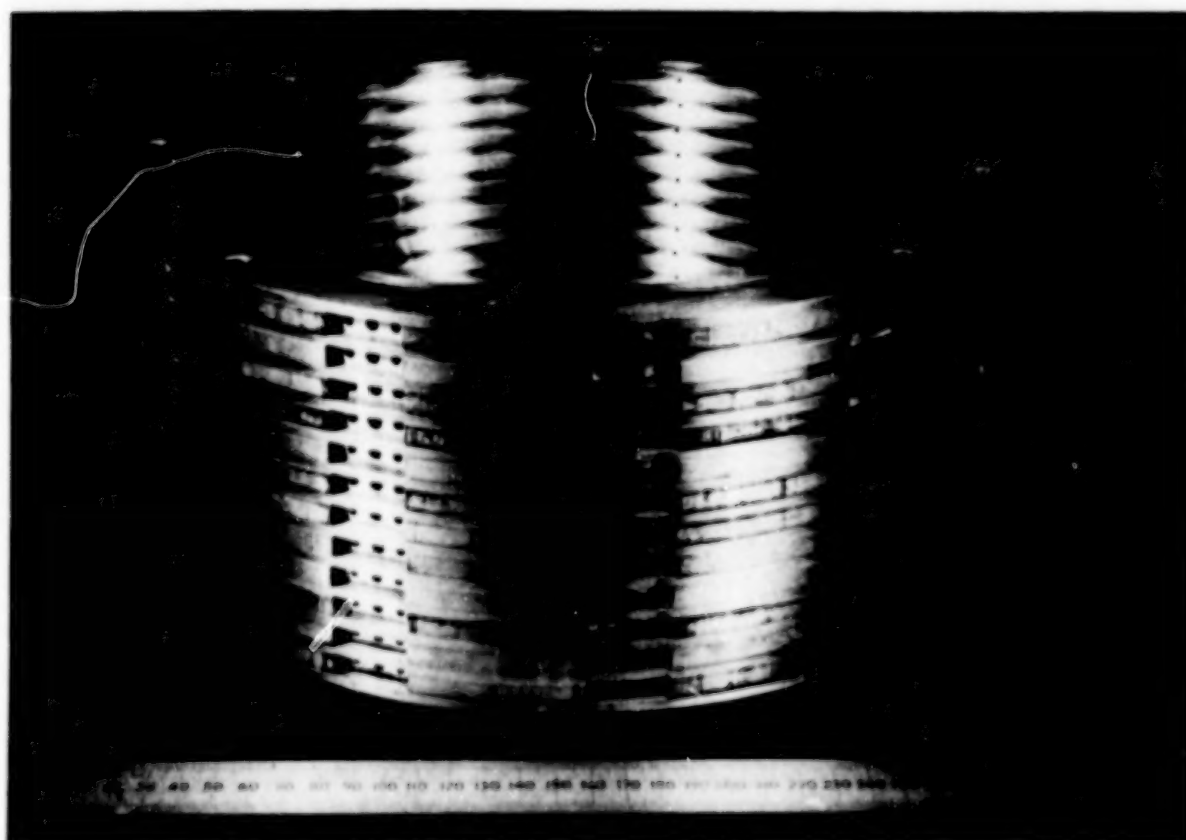
Figure 5. - View of built-up straight through labyrinths.

235

236
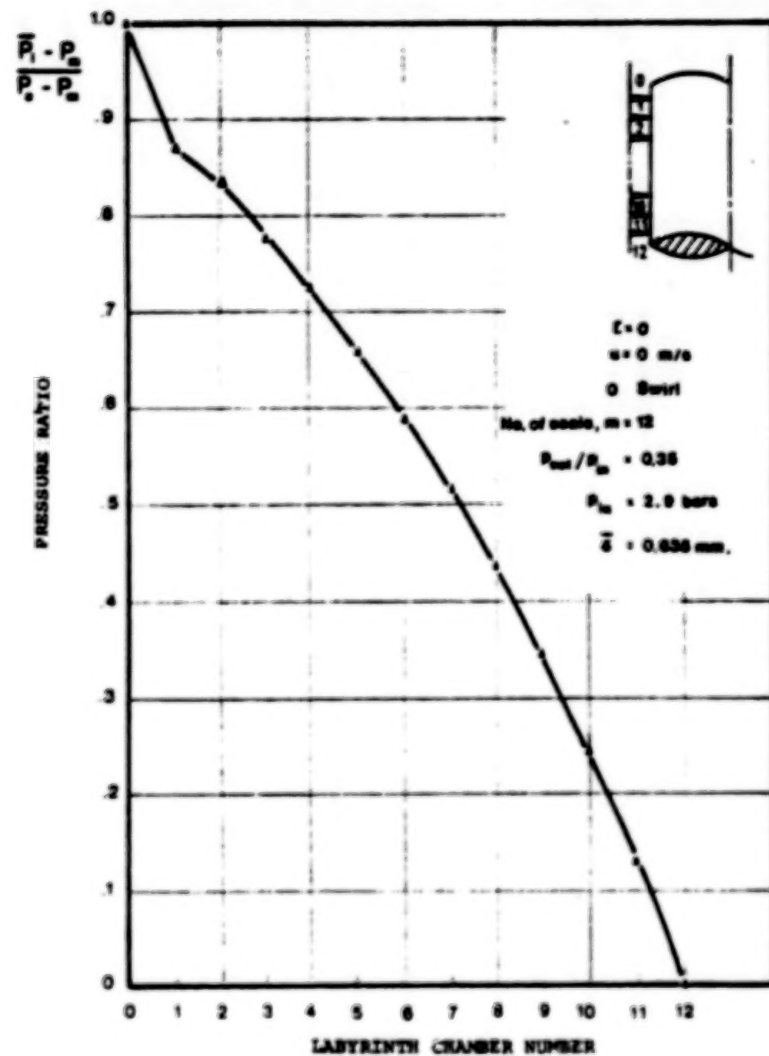
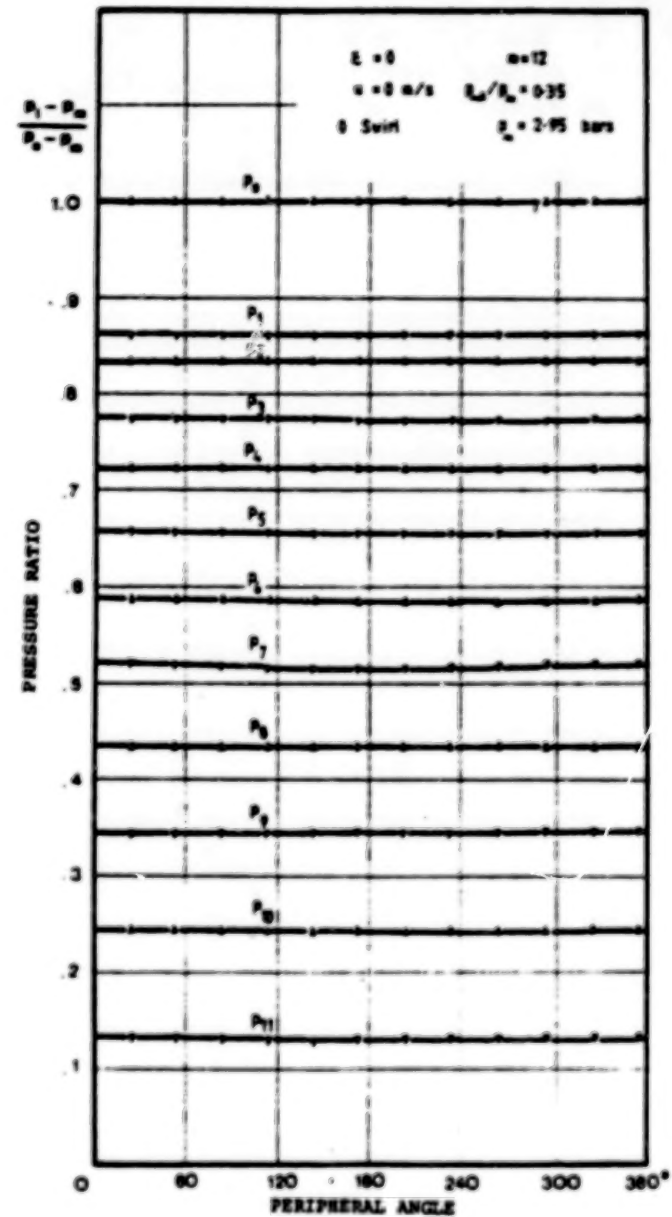Figure 6. - Pressure expansion through
the stages, concentric rotor

Figure 7. - Pressure distribution, concentric rotor.

236
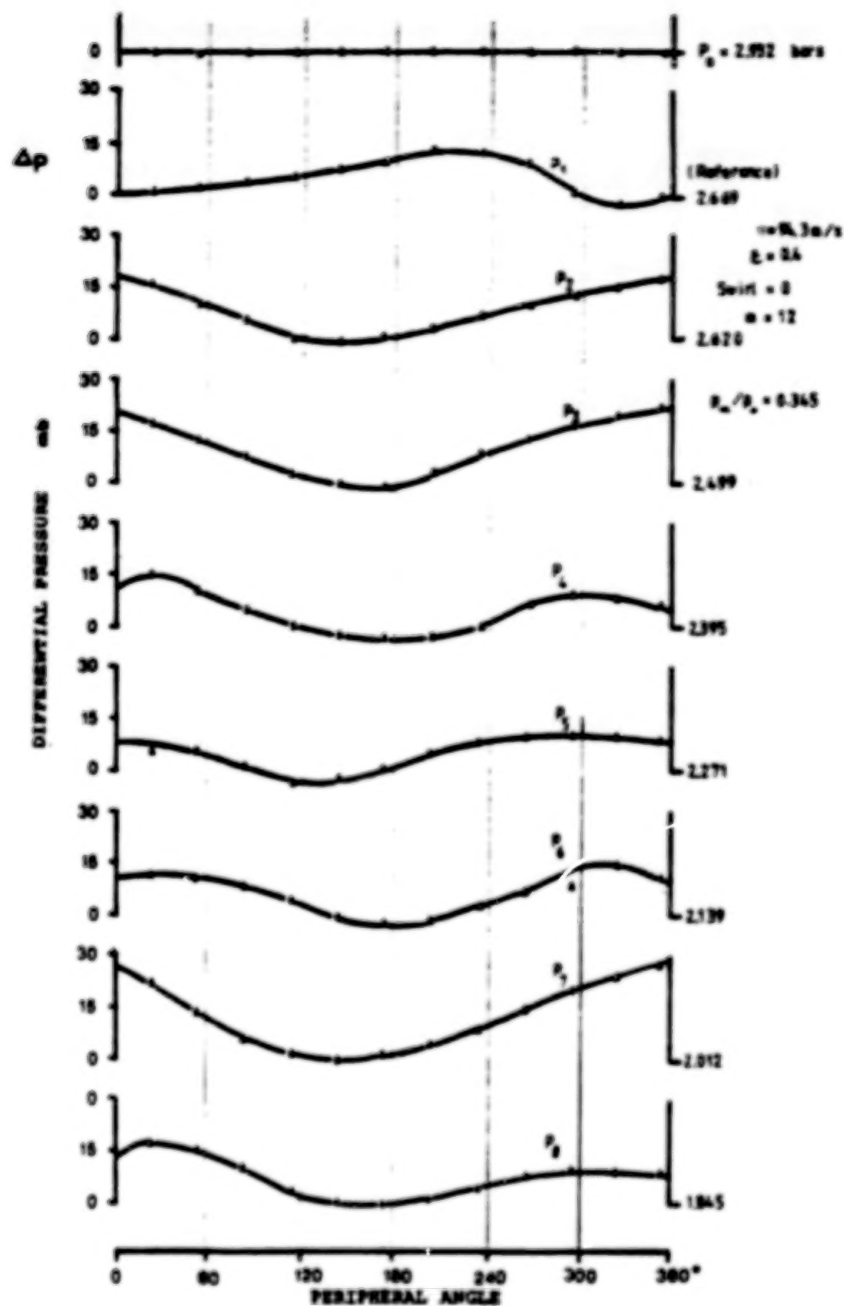
Figure 8. - Pressure distribution, parallel eccentricity.
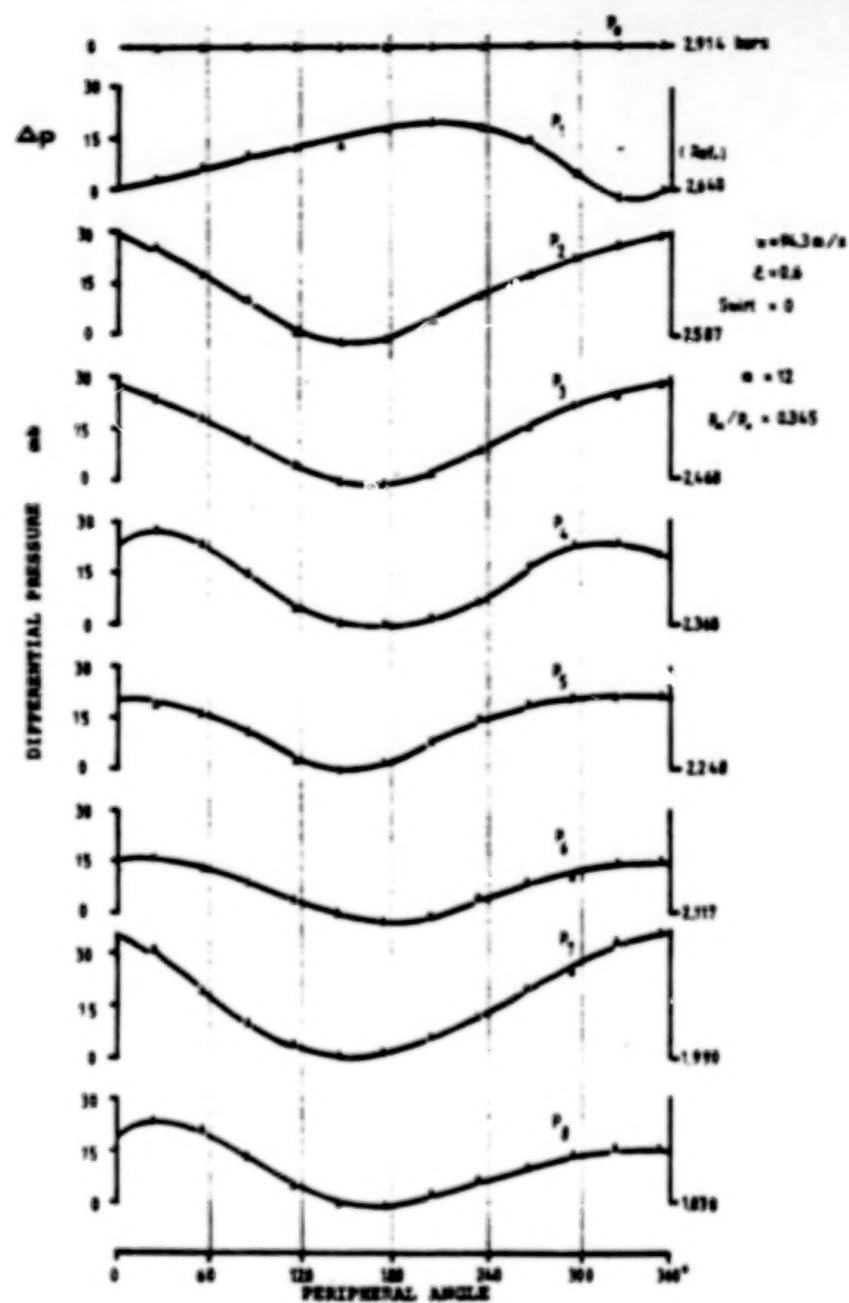
Figure 9. - Pressure distribution, parallel eccentricity.

237

237

238
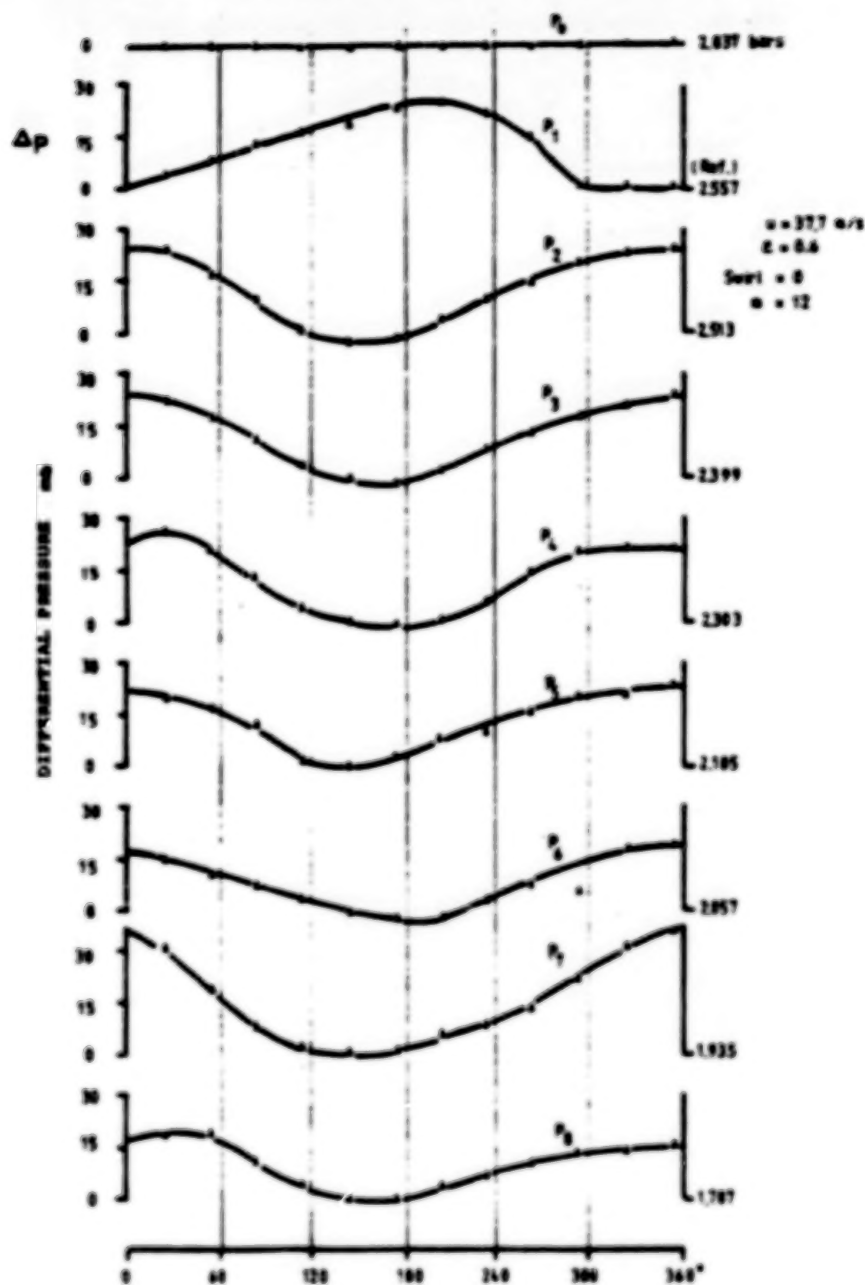
Figure 10. - Pressure distribution, parallel
eccentricity.
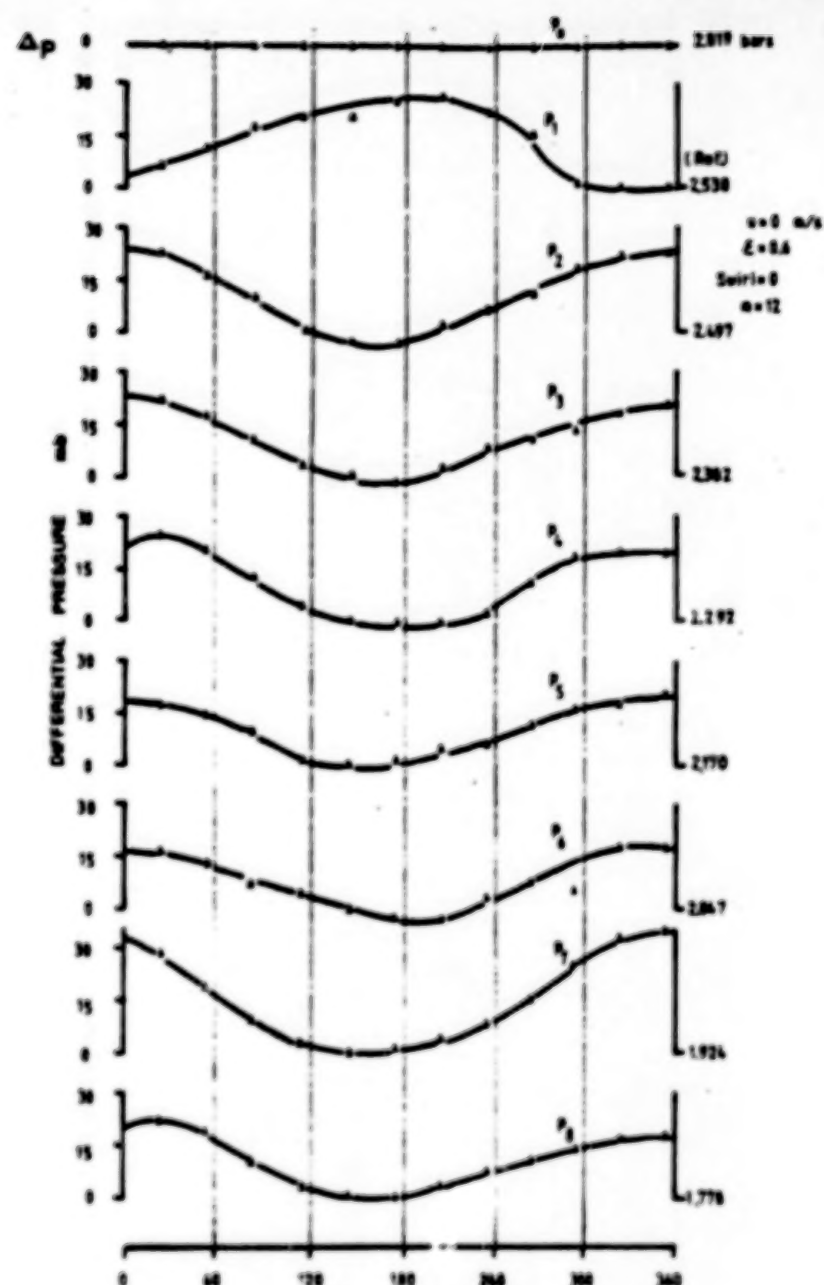
Figure 11. - Pressure distribution, parallel
eccentricity.

938

239

$$\frac{P_i - P_\infty}{P_o - P_\infty}$$

$\mathcal{E} = 0.6$ $n = 12$

$u = 94.3 \text{ m/s}$ $P_o/P_\infty = 0.345$

Swirl $= 0$ $P_o = 2.91 \text{ bars}$

$i = 0$

PRESSURE RATIO

PERIPHERAL ANGLE

Figure 12.

$$F_Y = \int_0^{2\pi} r \, L \, p \, \text{Cos} \, \theta \, d\theta$$

$$F_X = \int_0^{2\pi} r \, L \, p \, \text{Sin} \, \theta \, d\theta$$
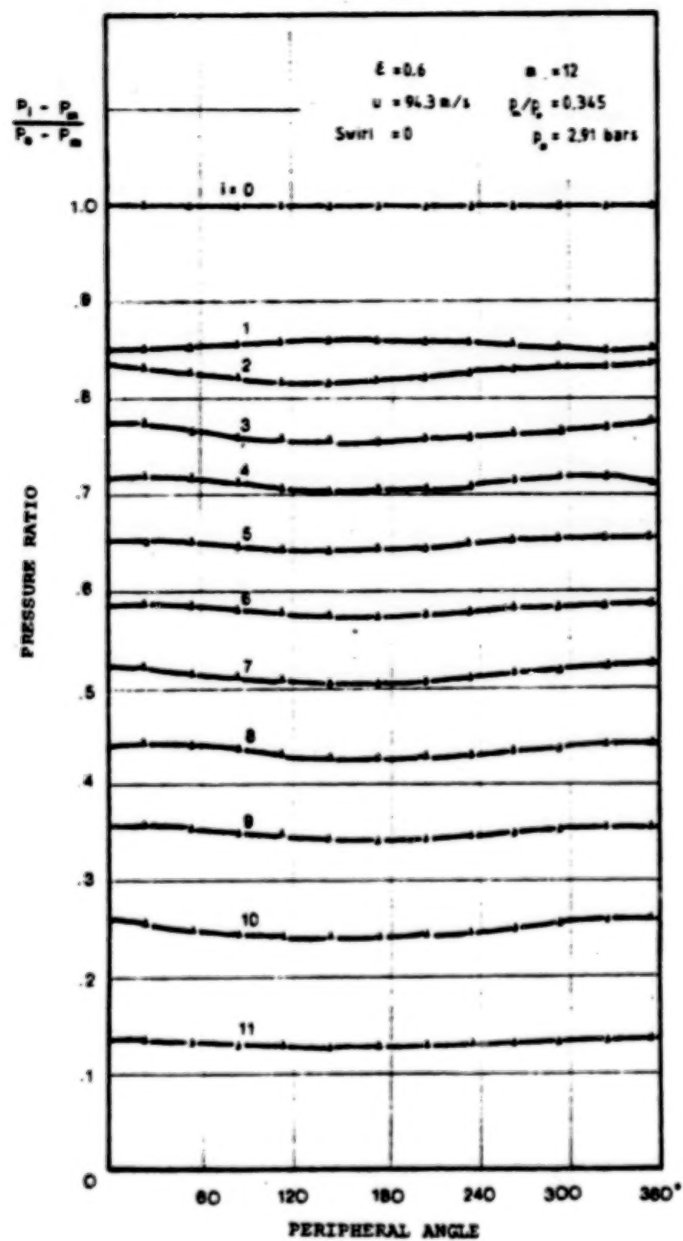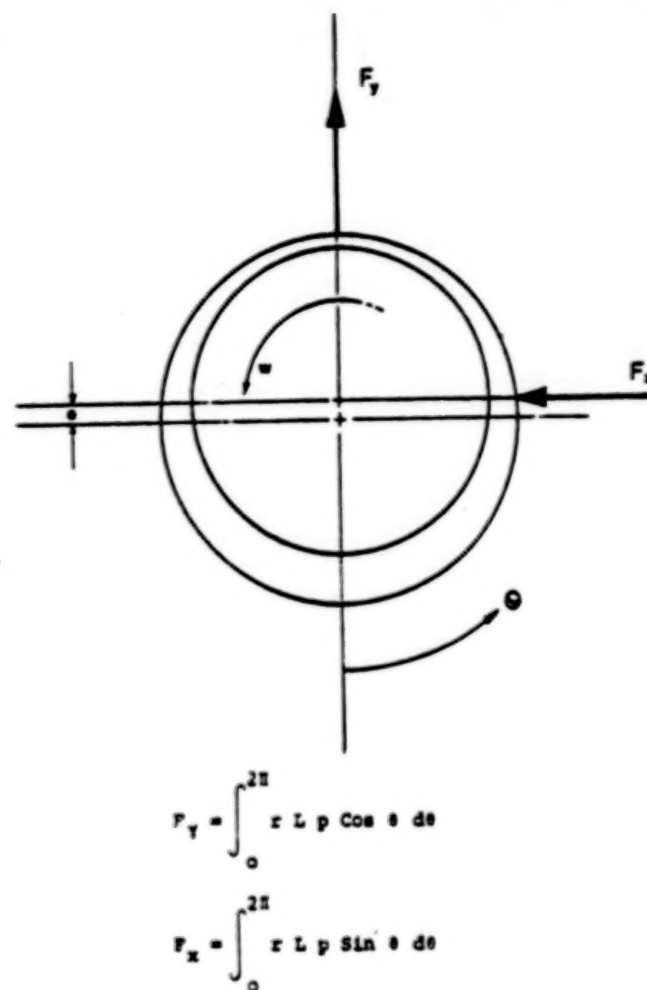
Figure 13. - Sign convention for eccentricity and forces.

239
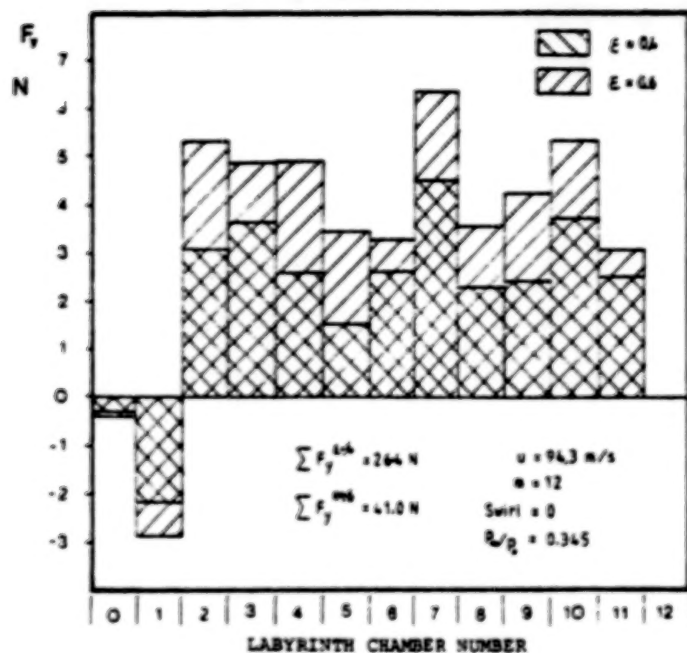
RADIAL FORCE IN INDIVIDUAL LABYRINTH CHAMBER
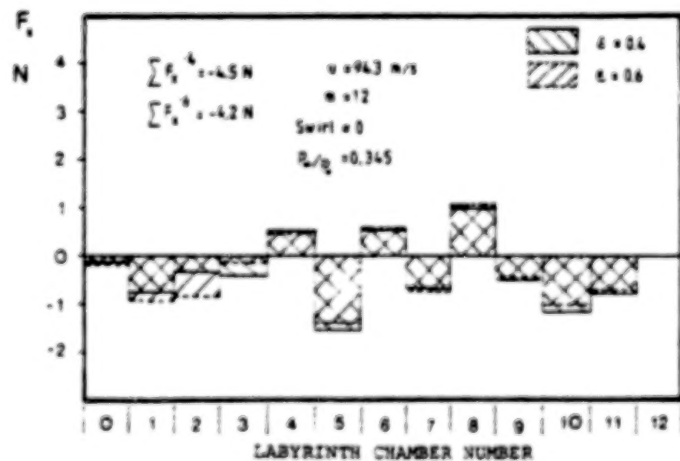
Figure 14. - Transverse force in individual labyrinth chamber.
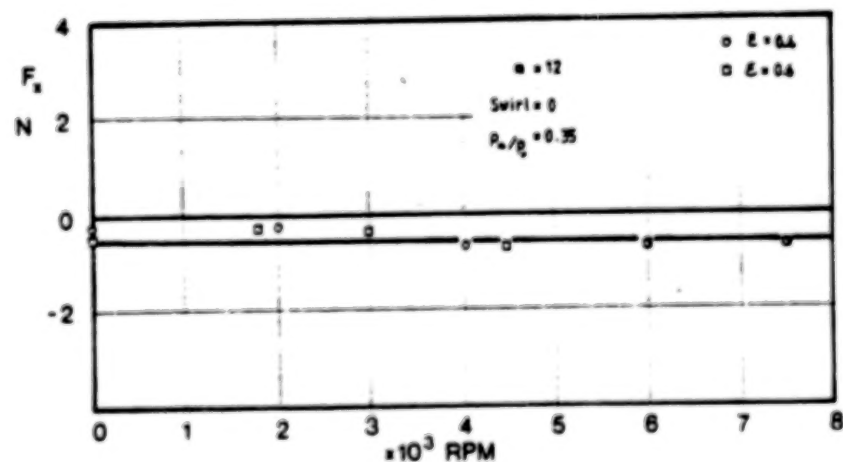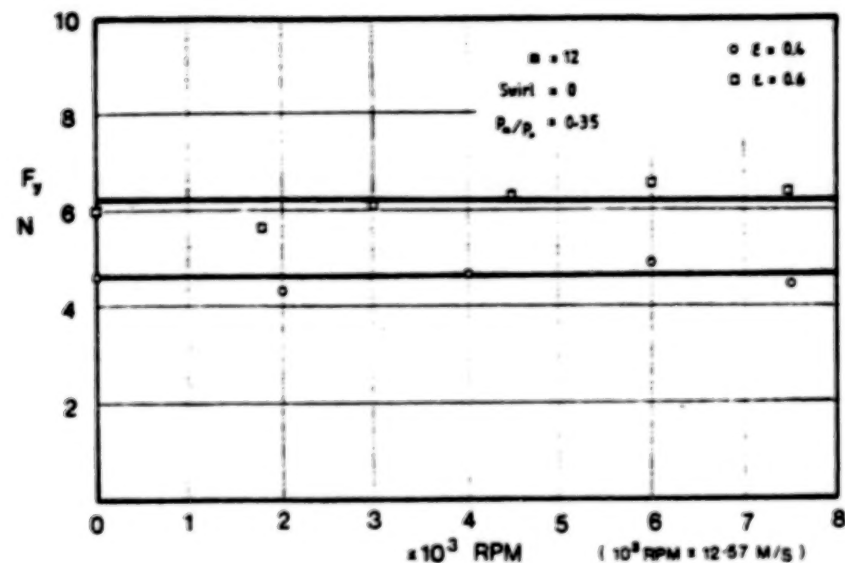
Figure 15. - F_y, F_x in typical chamber (chamber 7) versus speed.
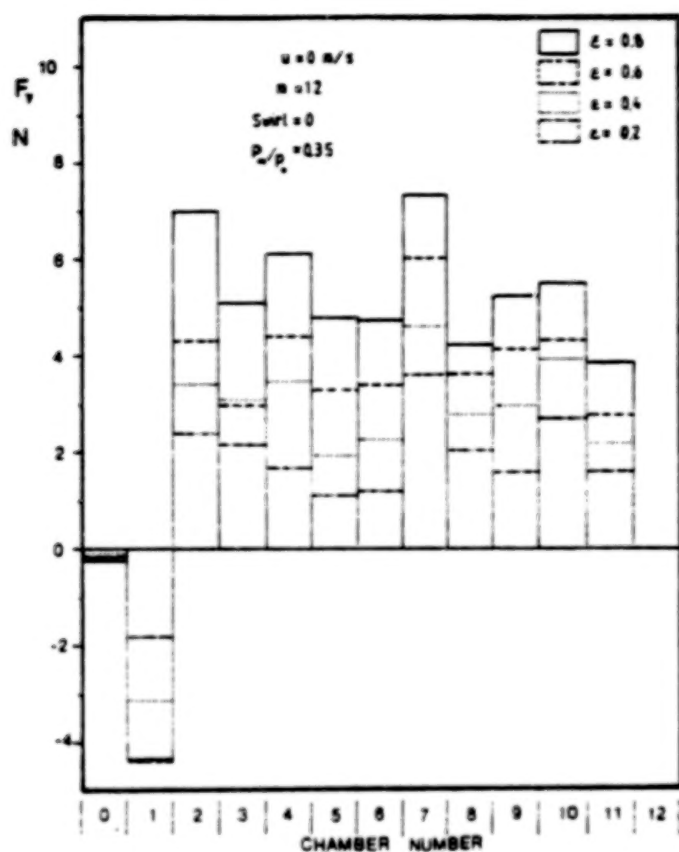
(a). - Radial force.
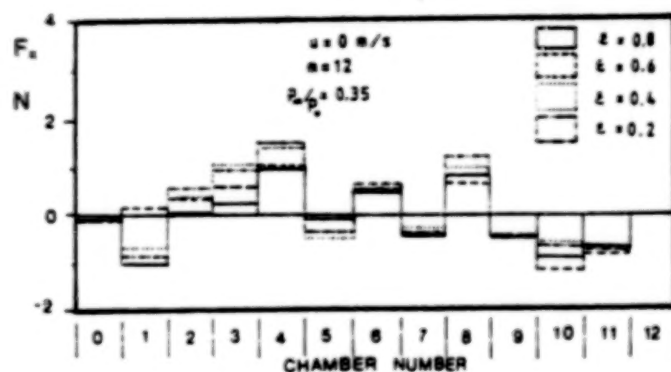
(b). - Transverse force.

Figure 16. - Radial and transverse forces in individual labyrinth chamber.
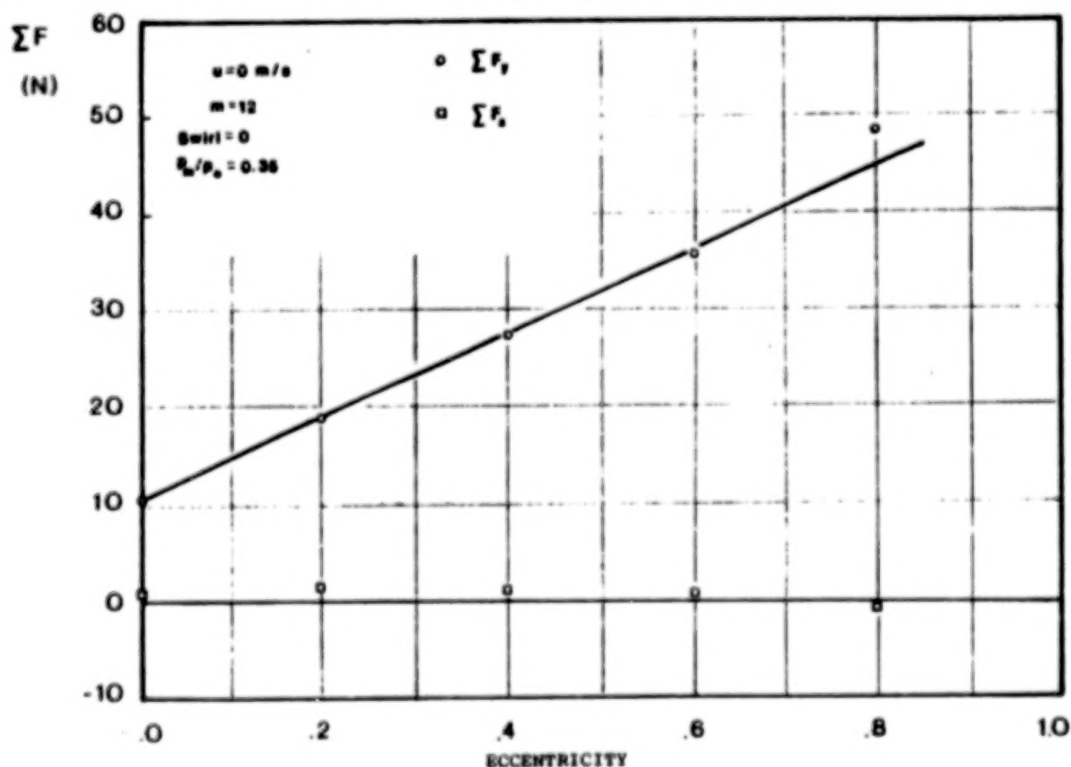

Figure 17. - ΣF_y, ΣF_x vs. eccentricity.

MEASUREMENT AND EVALUATION OF SWIRL-TYPE FLOW IN LABYRINTH SEALS

OF CONVENTIONAL TURBINE STAGES

L. Hauck
Institut für Thermische Kraftanlagen
Technische Universität München
8000 München 2, Feoeral Republic of Germany

SUMMARY

Previous studies of rotor whirl instability pointed out two different
mechanisms inducing lateral forces within non-contacting labyrinth-type
seals. Evaluating the part of exciting forces that results from leakage
losses is possible by means of variable flow contraction in the gap of
a seal with variable clearance at the circumference. The dominating
part of exciting forces has its origin in unequal pressure distributions
at the circumference of the seal with a shaft in out-of-centre position.
The pressure distribution is mainly influenced by swirl-type flow at seal
entry.

The installation of a computer controlled cantilevered pitot cylindre
within the seals of two different test stages enables the measurement
of flow conditions within every cavity of the labyrinth. The effects of
load factor and rotor eccentricity were determined on flow conditions in
test series for both stages. The results indicate that swirl-type entry
flow follows the rules of potential swirl. Within the labyrinth cavities
two spatial separated flow areas are to consider. A dominating flow in
peripheral direction nearly fills the space between the sealing strips
and the ceiling of the cavity. Below this flow, an area of axial mass
transport is situated, with a slight peripheral component, limited on
the nearest surroundings of the seals gap and the rotor surface. Between
both flows, an exchange of energy takes place. Within the gaps, flow
direction depends on axial velocity and therefore on variable flow
contraction. A balance of energy within the seal and the cavities
interprets the results of lateral force measurements as an influence
of friction at the sealing strips surface and the rotating shaft surface.
Stages with their blades put together in buckets by means of shrouding
segments are particularly influenced by the rotating speed of the shrouding.

One method to describe the flow conditions more closely is dividing
the leakage flow in stream tubes with varying cross sections at the circum-
ference. This enables a one-dimensional view on the flow along every
stream tube. Additionally, two flow areas within every cavity must be taken
into account. Therefore, the local profile of the tube is unequal to the
geometric boundary of the labyrinth. Other effects, as rotating shaft, flow
contraction and compressible flow through the labyrinth may be considered
as well.

INTRODUCTION

Non-contacting seals are already known as a possible reason of self-excited rotor vibrations in turbomachinery. A large number of papers (ref. 1,2,3,4), based on theoretical approaches and experimental results, pointed out two different mechanisms as origin of exciting lateral forces.

Exciting Forces due to Leakage Losses

A change of leakage losses at the circumference, caused by the variable gap resulting from rotor eccentricity, leads to a change of blade force at the circumference (ref. 1). The resultant exciting force is given by the integral of local blade force dU at the circumference

$$Q_2^S = \int_0^{2\pi} dU \cos\varphi = -\frac{U_{is}}{2\pi} \int_0^{2\pi} \xi_{sp}(\varphi) \cos\varphi \, d\varphi \tag{1}$$

where φ is the circumference angle. Following equation (1) tangential forces can be expressed by isentropic tangential force U_{is} and the leakage loss ξ_{sp}. The leakage loss is determined by the geometric boundary of the seal and the performance of the stage at a certain operating point. This is taken into account by the constant factor C.

$$\xi_{sp} = C \alpha s \tag{2}$$

Additional, the leakage losses depend on local clearance s and the flow contraction factor α. Both change at the circumference.

While geometric clearance can be easily put up, the determination of varialbe flow contraction is still difficult. Therefore, flow contraction is set up as a global constant factor α^* applying to centric rotor position. Flow contraction causes a higher uniformity of gap clearance at the circumference with a rotor in out-of-centre position. This is considered by the effective eccentricity e_{eff}.

$$e_{eff} = v_F e \tag{3}$$

The uniformity factor v_F (ref. 5) is put up using flow contraction in the narrowest and the widest gap.

$$v_F = (\alpha_{0°} s_{0°} - \alpha_{180°} s_{180°})/(2e) \tag{4}$$

According to these relations, exciting force can be calculated by using the isentropic tangential force, the eccentricity, the uniformity factor and the flow contraction.

$$Q_2^s = -\frac{U_{is}}{2} C\dot{\alpha}\dot{v}_F e \qquad\qquad\qquad (5)$$

Exciting Forces due to Pressure Distribution

If fluid flow through the labyrinth is superimposed by a peripheral flow component, a dominating lateral force arises from the pressure distribution in shrouded stages (ref. 3,6,7,8). With dp for the local pressure, z the coordinate in axial direction and b the width of the shrouding, the exciting force is given by

$$Q_2^D = -\int_0^b\int_0^{2\pi} dp \, \sin\varphi = -\int_0^b\int_0^{2\pi} p(z,\varphi) \, \sin\varphi \, r \, d\varphi \, dz \qquad (6)$$

Calculating the pressure distribution is problematic, since the location of maximum pressure depends on swirl-type flow at seal entry. A complete solution, like in the case of leakage losses, is not yet possible.

DESCRIPTION OF TEST APPARATUS

Investigated Stages

The flow patterns within the labyrinth seals of two test stages were measured, to check existend methods of calculation and set up better resolutions of calculating exciting forces.

Figure 1 shows the investigated turbine stages. The stage marked with the number I is a reaction type stage. As may be seen from the blades profile, stage II is a impulse type one. Besides this, the shrouding of stage II is closed, while the blades of stage I are put together in buckets of three or four blades. Further data of the investigated stages are gathered in table I. Both stages have stepped seals that are similar in its geometric shape.

Distribution of Measuring Positions

Figure 2 shows the labyrinth seal of one stage. The cantilevered pitot cylindre illustrated in the figure was used for flow measurements. The revolving cylindre drive was fixed in ball-bearings and designed to measure flow patterns in every cavity of the labyrinth seal. The structure of the drive can be seen in figure 3. The gear box includes two different drives. Revolving the cylindre is done by drive (c), while drive (d) moves the cantilevered pitot cylindre to its axial position. Moving from one cavity to the next is done by drive (a). Before revolving the gear box, the pitot cylindre must be lowered into the box. Then the whole drive is raised by three pneumatic motors, revolved by drive (a) to the next position and moved back by the pneumatic motors.

In this way, a net of measuring positions is distributed over a sectional area in the seal. Figure 4 shows the position of the measuring points within the seal. Several eccentric positions of the rotor could be adjusted at the inves-

244

tigated stages. The resulting variable gap clearance at the circumference influences the number of measuring positions. The whole net of measuring positions can be divided in two areas as shown in picture 4. Those positions, that are located within the cavity are used for all measurements. Previous studies supposed a fundamental influence of flow in the clearance on the whole flow patterns in the seal. Therefore, additional measuring positions were provided in the surroundings of every throttle gap. The number of positions depends on the adjusted eccentricity. The geometric clearance varies between 0,1 and 0,7 mm (0,004 and 0,027 inch). To enable the measurement of flow conditions as exact as possible, measuring positions were distributed over the clearance with a distance of 0,1 mm (0,004 inch) from each other.

Cantilevered Pitot Cylindre

As already mentioned, a cantilevered pitot cylindre was used for the measurements of flow conditions. The cylindres diameter is 1 mm (0,039 inch), that of the measuring hole is 0,1 mm (0,004 inch). Figure 5 shows the structure of the measuring unit. It consists of the pitot cylindre, a miniature pressure transducer and the cylindre carrier. Measurement is done by revolving the cylindre and picking up pressure data simultaneously. The position and the level of the total pressure in the stagnation point, as well as the static pressure at the measuring position is obtained from the pressure distribution. Thus, intensity and direction of flow velocity can be derived in an area perpendicular to the cylindre.

Test results may be influenced by a wall close to the cylindre. Therefore, tests were made in a special prepared wind tunnel. Deviations of the results due to a nearby wall have been taken into account. The whole test apparatus was controlled and watched by a desktop computer. In addition, this computer gathered test and position data.

IMPULSE TYPE STAGE

The result of a test period can be seen in figure 6 with the rotor in centric position. The figure shows the measured vectors of flow velocity in each position, described by arrows. Measuring areas are illustrated by dashed linies in the labyrinth scheme. The arrows length shows the level of velocities. Its direction is equivalent to the flow direction of the measured cylindre flow. The entry flow into the first cavity follows the rules of potential swirl.

Spatial Distribution of Velocity

Figure 7 shows the spatial distribution of flow velocities in a qualitative illustration. As shown in the figure, a dominating flow in peripheral direction fills the labyrinth cavities. This core flow is overlapped by a heavy, screw-like flow near the walls of the labyrinth. The three dimensional distribution of the flow velocity is determined by measurements over the height of the cavity, because only two dimensional velocities are measured

by the pitot cylindre. The directions of flow velocity near the ceiling of the cavity and the rotors surface, together with the rules of mass continuity point out a "vortex-screw" rotating with high peripheral velocity within the cavity. The rotating direction of the vortex is determined by the leakage flow and the geometric boundary of the cavity. In the second cavity of a stepped seal, as illustrated in the figure, the leakage flow dashes against the step of the shrouding. The flow is turned round at this point and raises, until it touches the ceiling of the cavity. The "vortex-screw" revolves counter clockwise due to the additional pressure drop to the next cavity. Caused by the set-back of the shrouding in the third cavity, the expansion of the leakage flow is limited on the nearest surroundings of the rotor surface. Above this flow, a dominating tangential flow nearly fills the space between the sealing strips and the ceiling of the cavity. A "vortex-screw" revolving clockwise in this cavity, grows by jet mixing and impulse exchange.

Axial Flow in the cavities

Figure 8 shows the distribution of axial velocities in the cavities of the labyrinth. Measurements were made near the ceiling, in the middle of the cavity and at the shrouding by changing the eccentricity of the rotor. Up stream velocities are marked by negative axial flow components. They are caused by "vortex-screws". The rotating direction of the vortex is determined by velocity near the shrouding and the ceiling of the cavity. The influence of rotor eccentricity on flow patterns in this region is unimportant.

Velocities at the Gap Clearance

Near the gap clearance, velocity distribution depends hard on rotor eccentricity. Especially the distribution of axial velocities along the clearance is modified, while tangential velocity is not influenced by rotor position. Figure 9 shows the distribution of axial velocity and flow angle in the gap clearance. The first measuring position is not situated within the clearance, because a minimum distance to the rotating surface must be regarded to secure the pitot cylindre. For the same reason, the velocity close to the shrouding could not be measured. The influence of the seal clearance on the velocity can be seen in the figure. Additional the security distance to the cylindre is shown, with a rotor that is 0,3 mm (0,012 inch) out of centre. The velocity distribution in the smallest clearance, according to e = - 0,2 mm (0,008 inch), changes continuously with increasing clearance. This points out the influence of varying flow contraction. The flow angles, an important factor of calculation, are shown in the lower figure. As already mentioned, tangential flow does not change by eccentricity. Therefore, flow angles are essential determined by axial velocity and can be evaluated using leakage flow and flow contraction.

Exitation Coefficient of Impulse Type Stage

Exciting forces can be defined as dimensionless coefficient too.

$$K2 = K_2^D \cdot K_2^S = \frac{Q_2^D/U_{is}}{e/l''} \cdot \frac{Q_2^S/U_{is}}{e/l''}$$
(7)

The exitation coefficient K2 is given by the quotient of related exciting force Q/U_{is} and relative eccentricity $e/1''$, where $1''$ is the length of the rotor blade.

In figure 10, this coefficient is plotted over the power of the stage, represented by the load factor $\Psi = 2\Delta h_{is}/u^2$, with Δh_{is} as the isentropic enthalpy difference and u the circumferential speed. The resulting force on the rotor of impulse-type stage is illustrated in curve (a). Forces due to pressure distributon and to leakage losses are both included. The exitation coefficient induced by pressure distribution was measured and is shown in curve (b). The part of leakage losses cannot be measured directly. Therefore, curve (c) shows the calculated exitation coefficent of leakage losses. Near load factor 3.5, a remarkable behaviour of excitation coefficient can be seen. A close examination of this behaviour points out that the speed of rotation is equal to the peripheral flow at labyrinth entry. Beyond this point, velocities of labyrinth flow and the speed of rotation are different. Thus, the course of exitation coefficient can be explained as influence of shrouding friction. This effect has not yet been regarded as important, especially for seals with short axial length.

Balance of Energy

Based on the results of measurements, a balance of energy within the seal and the cavities is set up. Figure 11 illustrates this balance of energy for different operating points of the impulse type stage. A clear supply of energy by the shrouding can be seen at load factor 2 and 3, whereas elimination of energy dominates at load factor 4. Calculating the losses as well as the velocities and the pressure in the cavities, enables the evaluation of energy flow. Friction losses can be determined from the mass flow of the "vortex-screw" and the pressure drop caused by friction. The distribution of energy losses in the cavities and the shrouding, shown in the picture, base on this evaluation.

REACTION TYPE STAGE

The energy supply of the labyrinth is influenced by the construction of the shrouding. The blades of reaction type stage are put together in buckets of three or four blades by means of shrouding segments that are separated from each other by a gap.

Figure 12 shows the flow pattern within the labyrinth seal of this stage. Because of the similar geometric shape the flow in this seal can be compared with stage II. A dominating tangential flow overlapped by a "vortex-screw" results as well. But it is additionally influenced by a jet flow that injects perpendicular to the shrouding. This jet flow reaches to the ceiling of the cavity and causes pressure oscillations picked up during additional measurements. The oscillations at high frequency level do not influence the force due to pressure distribution directly, but the jet flow, injected from the gaps of the shrouding, works like a rotating blade. Thus the swirl of flow in the cavities is influenced.

Exitation Coefficient of the Reaction Type Stage

As the jet flow depends on the rotating speed of the shrouding, the influence of shrouding velocity on exciting forces increases. In figure 13, the exitation coefficient is plotted over the load factor of the reaction type stage. Because of the slight entry swirl, exitation coefficients are generally lower. In spite of this, a heavy influence of shrouding velocity on measured resulting exitation is to be seen. Near load factor four, the measured tangential flow is equal to the rotating speed of the shrouding. The lowest exitation coefficient is measured at this load. Obviously, the injection flow is able to accelerate the swirl of entry flow in a way, that raises the exciting forces by lowering power. At high load factors, influence of injection flow on entry swirl prevents an increase of exitation with the load number.

CONCLUDING REMARKS

As shown by the results of investigations, high tangential velocities, varying flow contraction together with its influence on flow angles, and the effect of friction on the shrouding are to be especially considered by the calculation of exciting forces. A method that considers these influences ic given by ref (9). In this case, the labyrinth flow is described by dividing the leakage flow in stream tubes that are joint against one another at the circumference.

The shape of a stream tube is principally illustrated in figure 14. At every cross section, the equations of impulse and energy are resolved iteratively, using the continuity of mass flow. A part of the working fluid is branched at the entry of the seal. The shape of the stream tubes within the seal depends on various conditions. The leakage flow is added to the working fluid at outlet of the seal. This kind of view gives a description of complete flow patterns, as usually present in labyrinth seals, by means of a one-dimensional flow.

The test results enable an extension of this method. Two different flow areas, relating to the flow within the cavity and the leakage flow are to consider. New statements are needed to describe the local profile of the stream tubes that are not identical with the geometric boundary of the labyrinth. Additionally, the influence of shrouding velocity must be considered by friction and velocity at the rotor surface. Besides this, the change of flow angles due to flow contraction is important. Because of a slight pressure drop within every cavity, calculation in the cavity can be done using the rules of incompressible flow. The pressure drop from one cavity to the next however must be considered. Therefore, compressible flow should be supposed for calculations in the gap. Using these additional considerations, the accuracy of this method would raise essentially. Actual work is done on this topic and will be described in a later paper.

REFERENCES

1. Thomas, H.-J.: Instabile Eigenschwingungen von Turbinenläufern, angefacht durch die Spaltenströmung in Stopfbuchsen und Beschaufelungen. Bull. de L'AIM (1958) Nr. 11/12, S. 1039-1063

2. Alford, J. S.: Protecting Turbomachinery From Selfexited Whirl. Jornal of Engineering for Power, Trans. ASME, Series A, 38 (1965) pp333-344

3. Lomakin, A. A.: Die Berechnung der kritischen Drehzahl und der Bedingung für Sicherung der dynamischen Stabilität des Läufers von hydraulischen Hochdruck-Maschinen unter Berücksichtigung der Kräfte, die in den Dichtungen entstehen. Energomasinostroenie 4 (1958) H. 4, S. 1-5

4. Thomas, H.-J.: Urlichs, K.; Wohlrab, R.: Läuferinstabilität bei thermischen Turbomaschinen infolge Spalterregung. VGB Kraftwerkstechnik 56 (1976) H. 6, S. 377-383

5. Hauck, L.: Vergleich gebräuchlicher Turbinenstufen hinsichtlich des Auftretens spaltströmungsbedingter Kräfte. Konstruktion 33, (1981) H. 2, S. 59-64

6. Childs, D. W.: Dressman, J. B.: Testing of Turbulent Seals for Rotordynamic Coefficient. NASA Publication 2133, May 1980

7. Benckert, H.; Wachter, J.: Flow Induced Coefficients of Labyrinth Seals for Application in Rotordynamics. NASA Conference Publication 2133, (1980)

8. Jenny, R.: Labyrinthe als Ursache selbsterregter Rotor-Schwingungen bei Radialverdichtern. Technische Rundschau Sulzer (1980) H. 4, S. 149-156

9. Urlichs, K.: Durch Spaltströmungen hervorgerufene Querkräfte an den Läufern thermischer Turbomaschinen, Diss. TU München 1975; s.a. Ing.-Arch. 45 (1976) H.3, S. 193-208

TABLE I. - DATA OF INVESTIGATED STAGES

		stage I	stage II
Speed	min⁻¹	4000	5000
Diameter of stage	mm	420	420
Number of blades			
nozzle vanes		50	63
wheel blades		50	99
Length of blades			
nozzle vanes	mm	40.6	38.6
wheel blades	mm	42.0	40.0
Flow angles			
a_1	degrees	17.3	12.9
β_2	degrees	17.3	20.1
Clearance			
nozzle vanes	mm	0.48	0.40
wheel blades	mm	0.43	0.40
Width of shrouding			
nozzle vanes	mm	22.4	36.0
wheel blades	mm	19.0	27.0
Degree of reaction		0.45	0.20
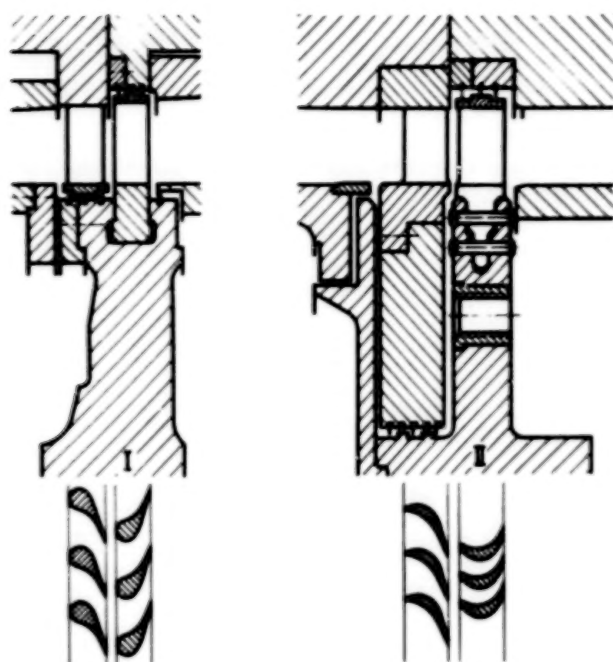
Figure 1. - Investigated stages.
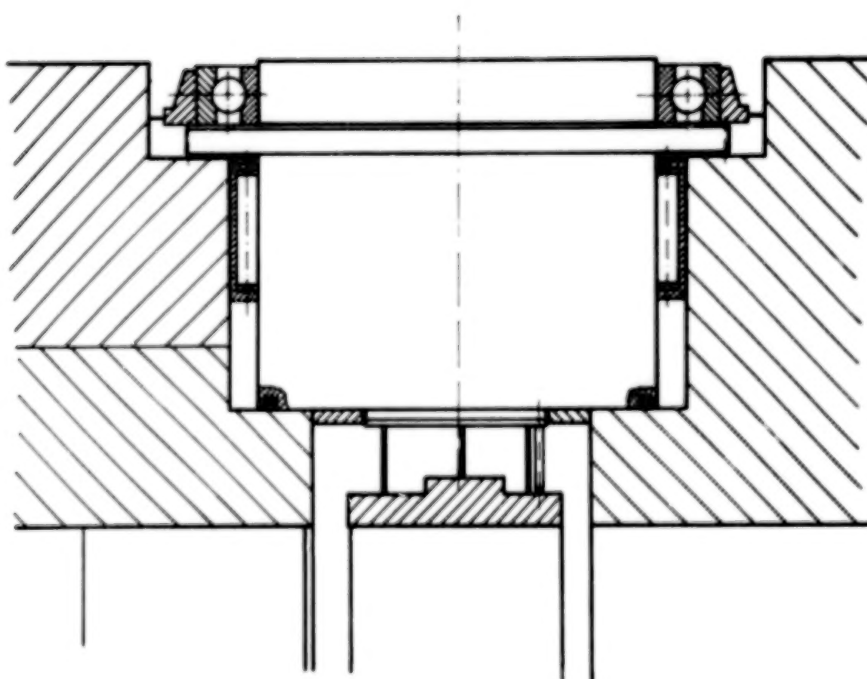
Figure 2. - Labyrinth seal and measuring unit.
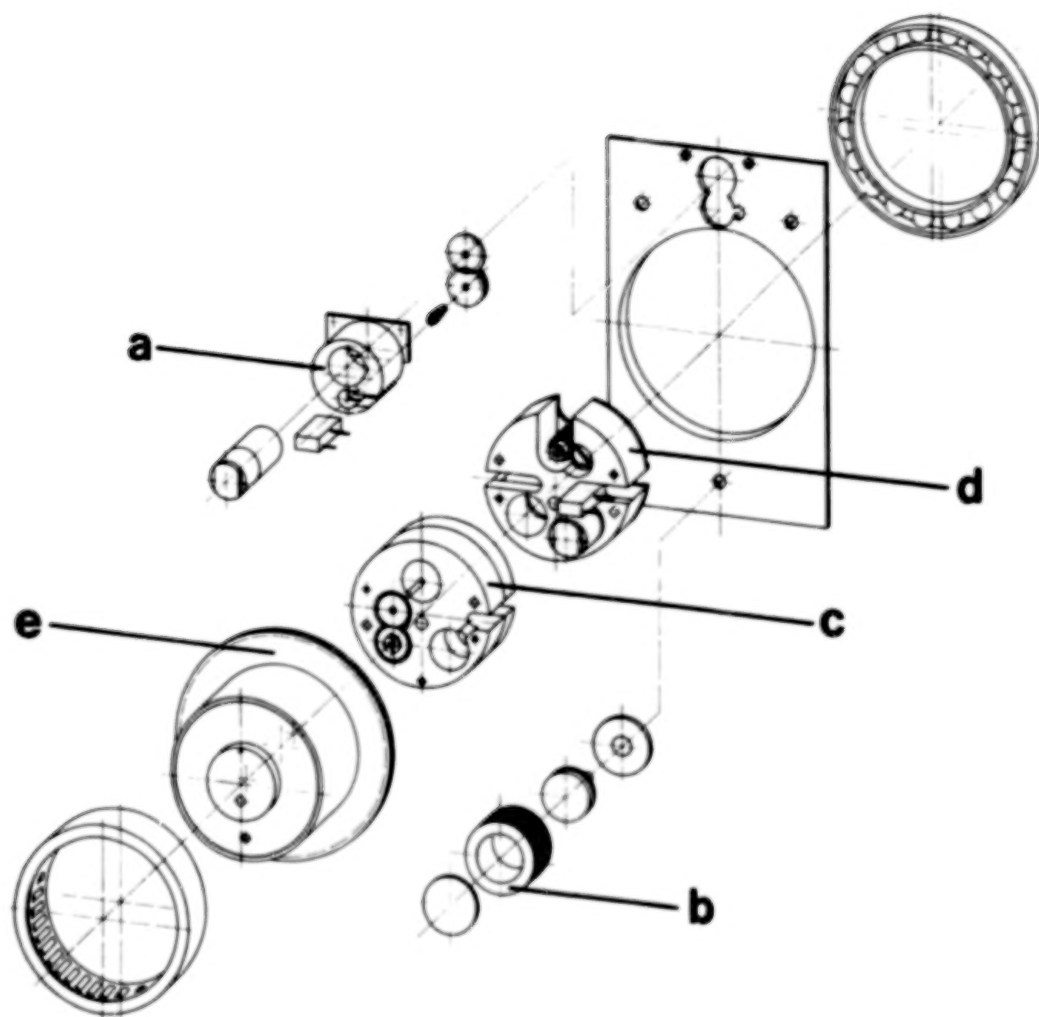
a revolving drive
b pneumatic motor
c revolving drive
d axial moving drive
e housing

Figure 3. - Structure of the gear box.

a smallest clearance
b widest clearance
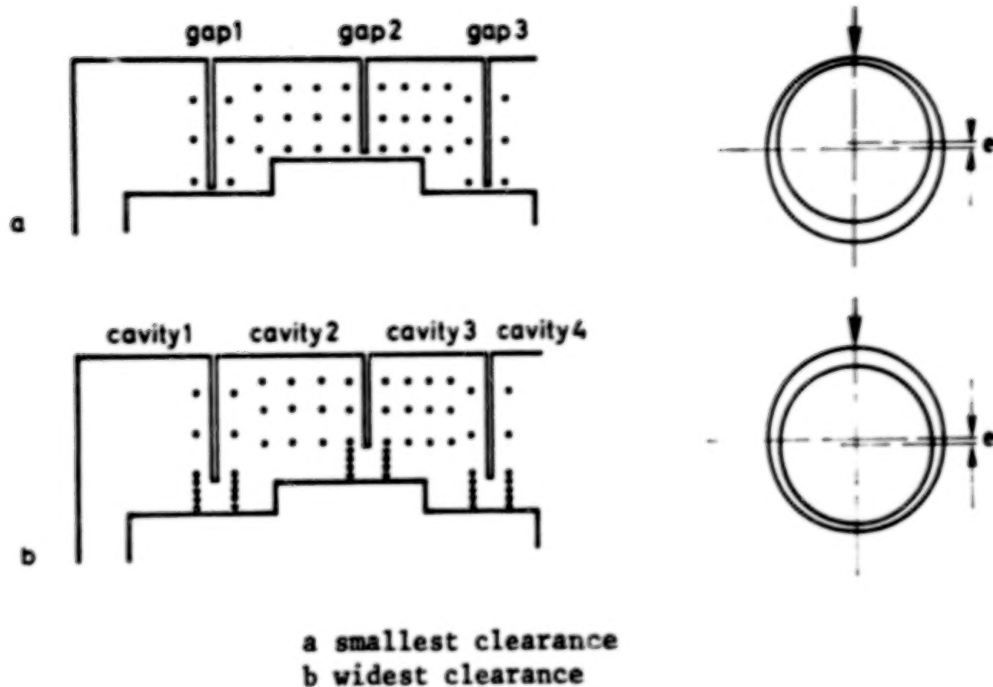
Figure 4. - Distribution of measuring positions.

a pitot cylindre
b cylindre carrier
c pressure transducer
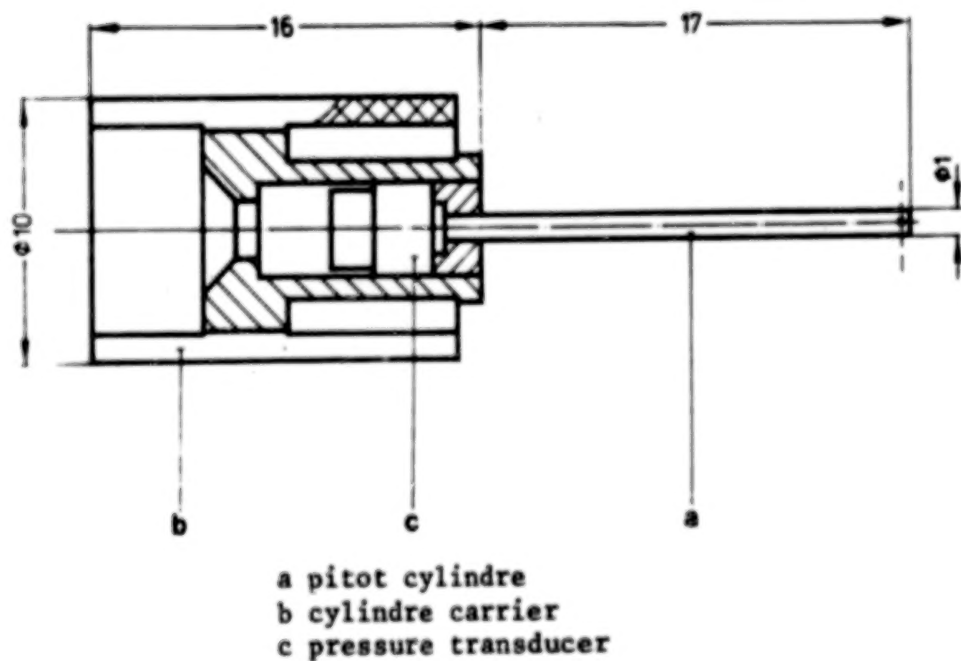
Figure 5. - Structure of the measuring unit.

253
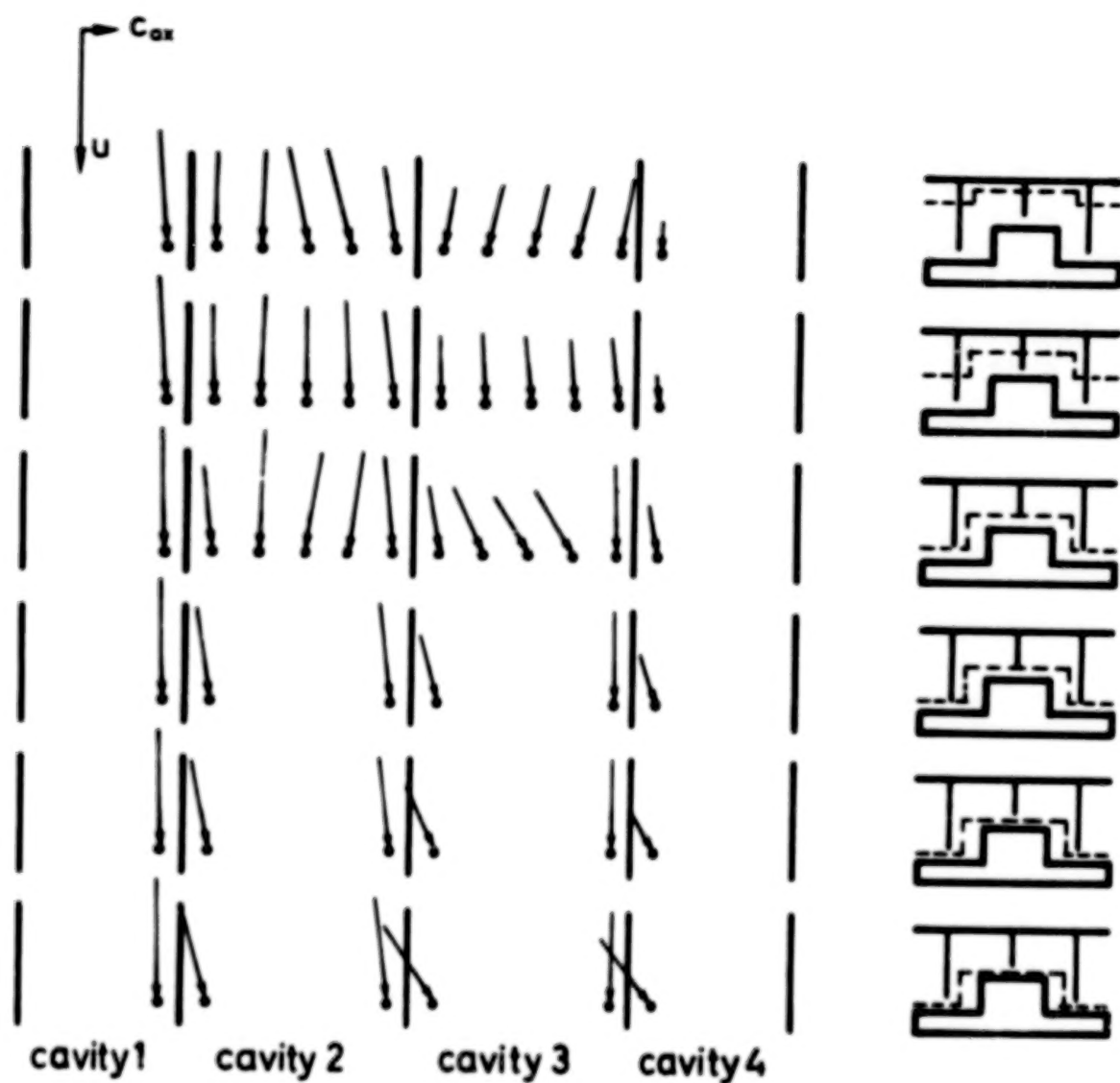
Figure 6. - Flow velocity within the cavities (measured).

254
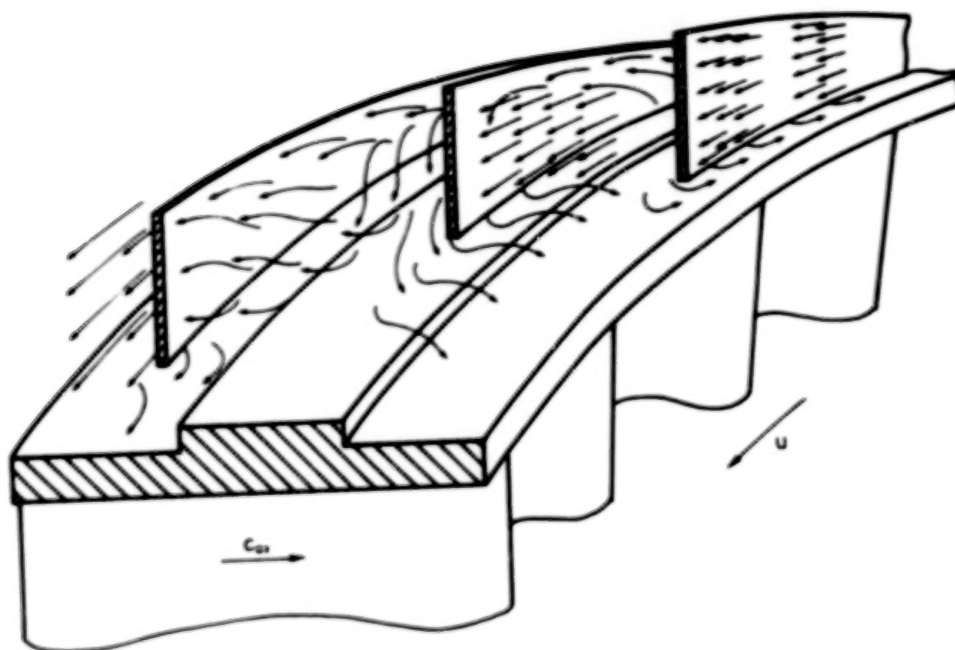
Figure 7. - Spatial distribution of flow velocities (stage II).
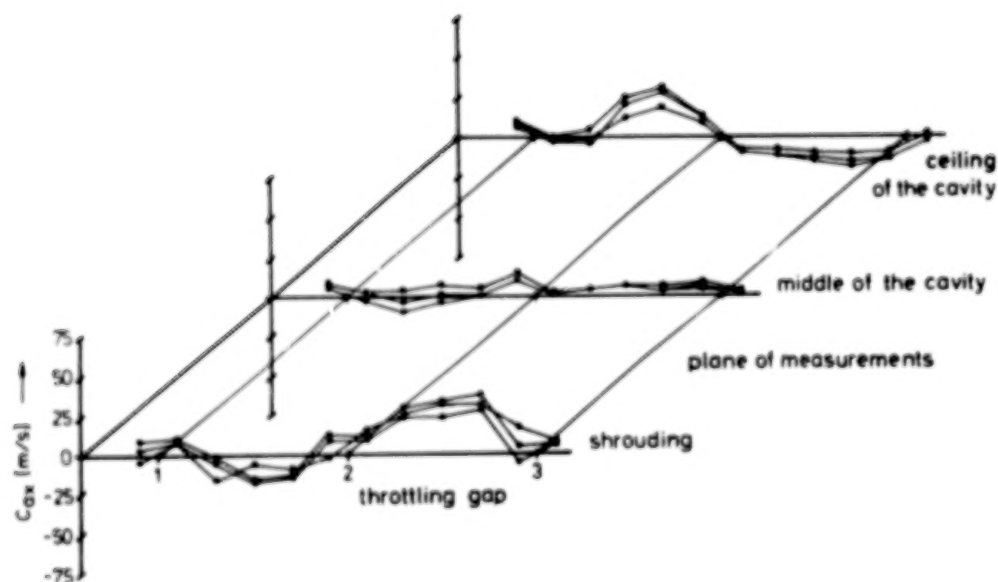
Figure 8. - Distribution of axial velocity in the cavities (measured).

255
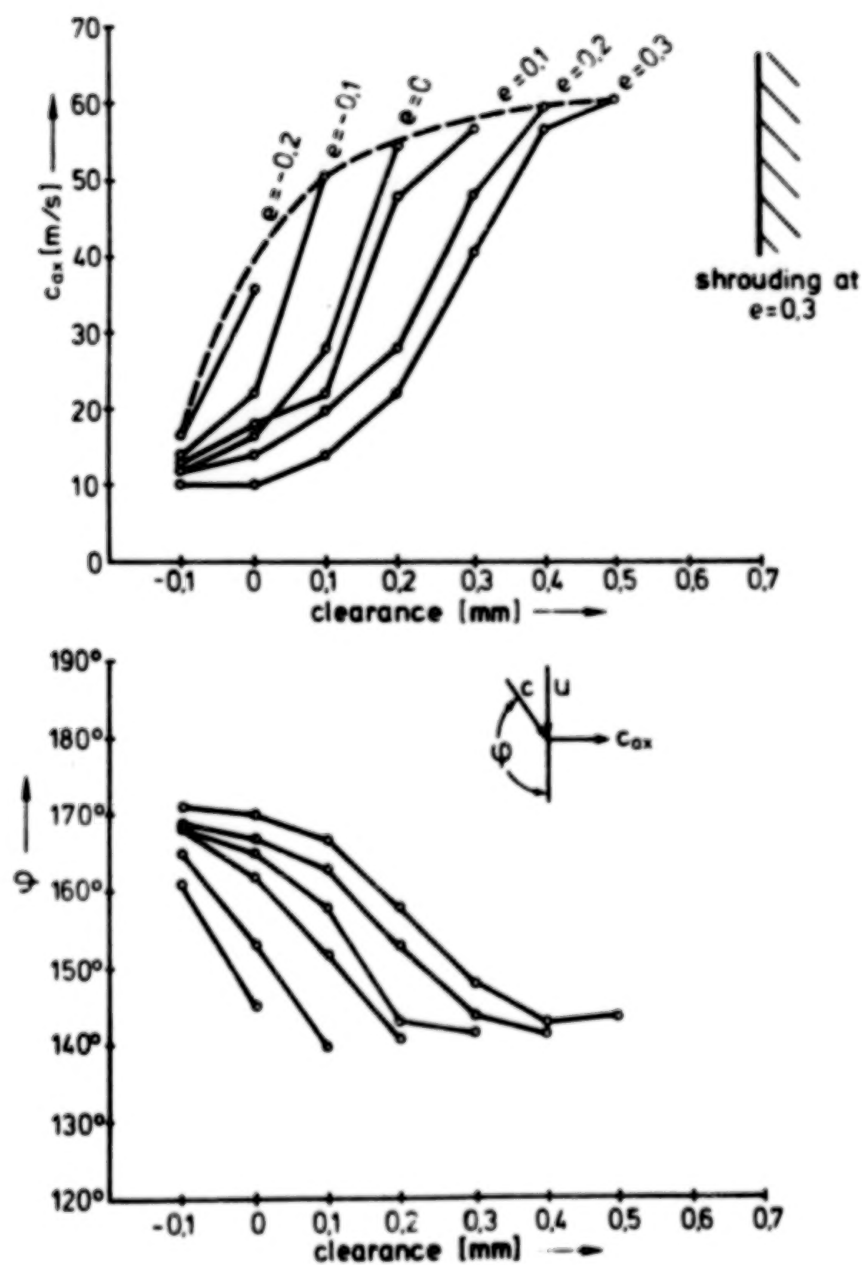
Figure 9. - Axial velocity and flow angle in the gap (measured).
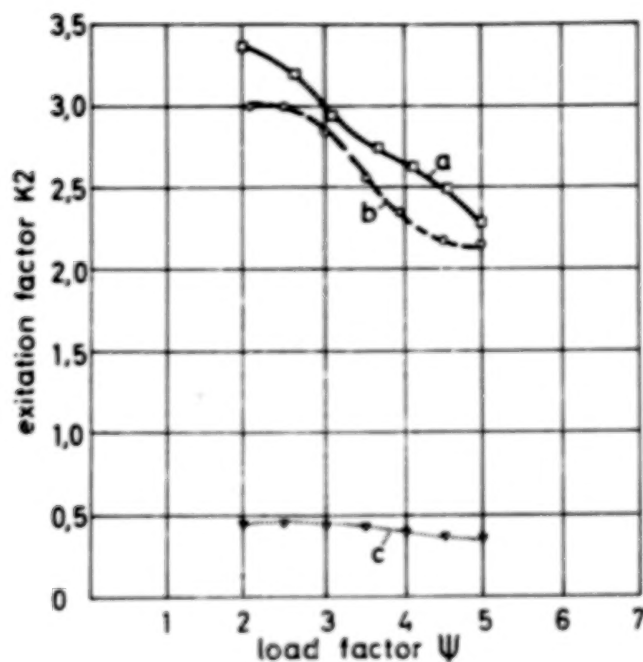
256

a resulting exitation (measured)
b exitation by pressure distribution (measured)
c exitation by leakage losses (calculated)
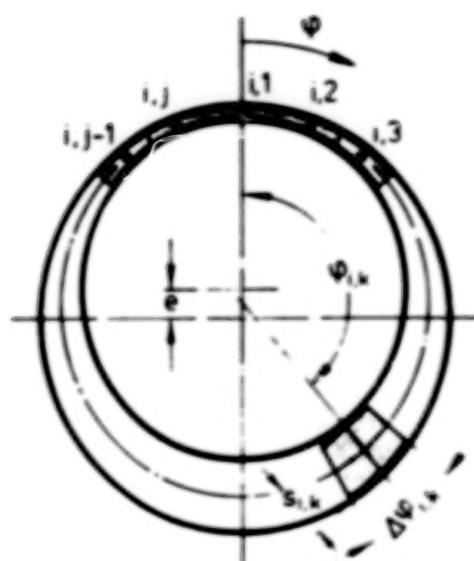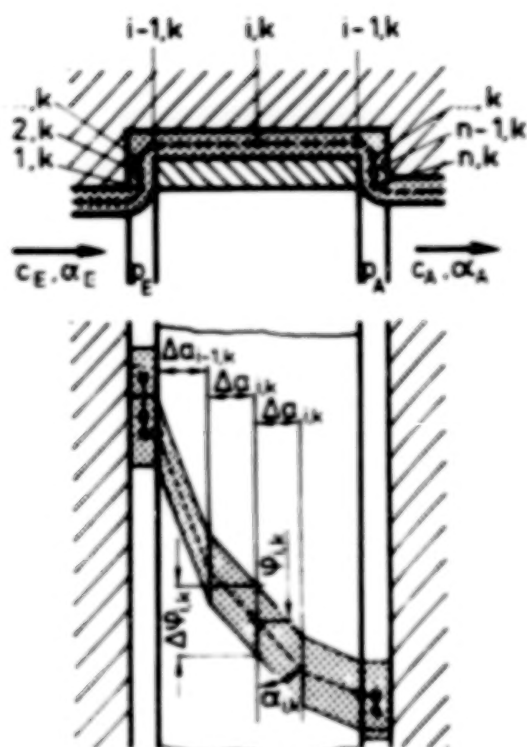
Figure 10. - Exitation factor and load factor (stage II).
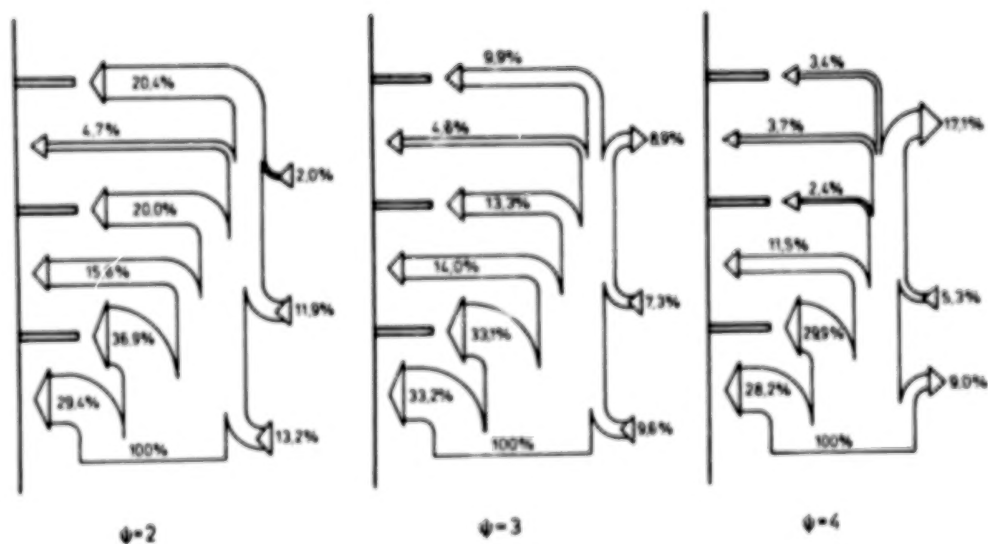
Figure 11. - Balance of energy and load factor (stage II).
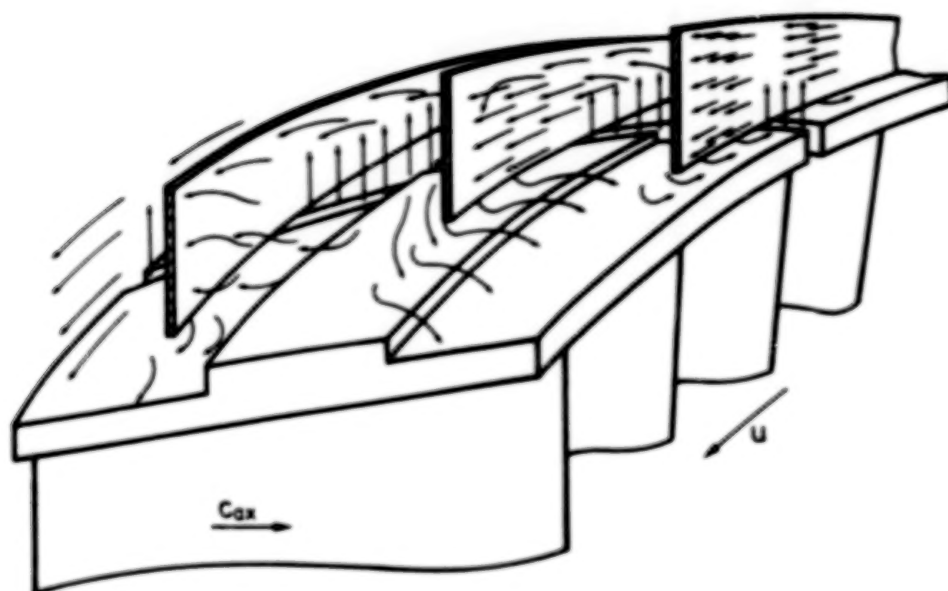
Figure 12. - Spatial distribution of flow velocities (stage 1).
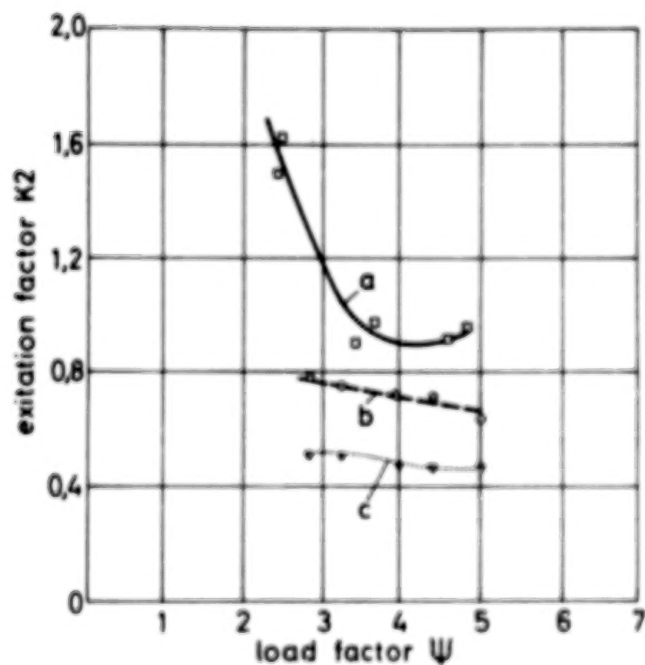
a resulting exitation (measured)
b exitation by pressure distribution (measured)
c exitation by leakage losses (calculated)

Figure 13. - Exitation factor and load factor (stage 1).

258

Figure 14. - Shape of stream tube.

EXPERIMENT MEASUREMENT OF ALFORD'S FORCE

IN AXIAL-FLOW TURBOMACHINERY

John M. Vance
Department of Mechanical Engineering
Texas A&M University
College Station, Texas 77843

Frank J. Laudadio
Motorola Corporation
Fort Lauderdale, Florida 33322

ABSTRACT

In 1965, J. S. Alford published a theory and mathematical model [1] which pre-
dicts that circumferential variation of blade-tip clearances in axial-flow turbo-
machinery will produce cross-coupled (normal to the eccentricity) aerodynamic forces
on the rotor. Ever since then, the theory has been used (without experimental veri-
fication) by rotor dynamicists as one of the few mathematical models available to
calculate the cross-coupled aerodynamic stiffness coefficients required for rotor-
dynamic stability analysis.

This paper presents the results of experimental measurements made on a small,
high speed, axial flow test apparatus to verify the existence of Alford's force and
to investigate the validity of his mathematical prediction model.

INTRODUCTION

There are many mechanisms which cause rotordynamic instabilities in turbines
and compressors. An instability in turbomachinery occurs when the shaft precesses
about the bearing centerline (whirling) with unacceptable amplitudes, at frequencies
nonsynchronous with shaft speed. Instabilities can become a costly problem since
they limit the operation of the turbomachinery by reducing the allowable speed.
They can be destructive if the instability threshold speed is exceeded.

There are documented cases showing the severity of instabilities in turbo-
machinery. Doyle [2] presents two cases where an instability has required exten-
sive rotor modification, resulting in lost production and heavy maintenance expen-
ditures. One of the cases mentioned is the 1964 Ekofisk gas reinjection problem
which has become a classical example of how costly an instability can become. A
centrifugal compressor was designed to reinject the gas by-product from crude oil
production. Oil production was stopped for several months due to the instability
problem with this compressor.

In mathematical terms an instability occurs when an eigenvalue of the equation that describes the motion of the rotor has a positive real component. In engineering terms, the nonsynchronous amplitude of rotor whirl (any amplitude which has a frequency not equal to running speed) grows with time until the system exceeds its operating limits. In many instances the rotor orbits can be large enough to destroy bearings and seals.

Computer programs are now available [3] which can predict whirling frequencies and threshold speeds, provided that accurate values for the destabilizing coefficients are used as input. The destabilizing coefficients usually take the form of a linearized cross-coupled stiffness term [4], but sometimes are expressed as negative damping [5], depending on the mechanism producing the instability.

One mechanism, which is a type of self-excited instability, is the aerodynamic excitation due to circumferential variation of blade clearance in axial-flow compressors and axial-flow turbines. An objective of the work reported here was to quantify a term in the mathematical equation due to Alford which predicts the magnitude of the aerodynamic cross-coupled stiffness, along with verifying the form of the equation.

Alford actually presented two mechanisms which can cause severe rotor whirl in axial flow compressors and turbines. One is due to the circumferential variation of static pressure action on the cylindrical surface of a rotor, particularly within labyrinth seals. The other is due to circumferential variation of blade-tip clearance (the topic of this paper). Alford presented both seal deflection criteria and bladed-disk torque deflection criteria for use as design guides for a stable rotor system.

Investigations of rotordynamic problems in steam turbines have shown that unbalanced moments on wheels and shafts, caused by steam forces, are a source for nonsynchronous rotor whirl. Steam whirl was first described by Thomas [6] in 1958 and is similar to the phenomenon hypothesized by Alford. Winter [7] performed model tests in 1968. He used ball bearings in his test rig to eliminate the shaft whipping due to hydrodynamic bearings, and applied external damping elements to the bearings since ball bearings have little inherent damping. Winter proved the presence of a load-dependent instability but was not able to quantify his results.

THE TEST APPARATUS

The test apparatus used in the experiment consists of a flexibly mounted bladed rotor driven by a variable speed electric motor, and a movable shroud (see Figure 1). The blade O. D. is 6". The motor is rated 1/7 HP at 10,000 rpm.

An offset of the bladed rotor within the shroud clearance circle is produced by translating the shroud laterally. The shroud is mounted on slides, and is translated laterally by turning a threaded rod.

The lateral stiffness of the rotor bearing support is made low enough so that very low levels of Alford's force (3-10 grams) produce a measurable rotor deflection. The rotor deflection is measured with an eddy-current proximity probe and

calibrated to lateral force in grams/mil. One of the most challenging and time-consuming aspects of the project was the measurement of rotor deflection (DC signal) in the presence of a relative large AC signal produced by rotor runout, synchronous vibration, and ball bearing roughness. This was finally accomplished by passing the probe signal through a very effective low-pass filter.

The speed of the rotor can be varied independently from the torque, over a range of 0 to 7000 rpm, by changing the voltage supplied to the electric motor. The torque is varied by adjusting the air velocity at the rotor inlet with an auxiliary blower. This method allows the rotor speed to be changed while holding the torque constant, or vice versa. Many combinations of speed, torque, and shroud eccentricity can thus be obtained.

Rotor speed is measured by feeding a once-per-revolution keyphaser signal into an electronic counter.

The aerodynamic torque is measured with a strain gage dynamometer. The driving torque of the electric motor is entirely reacted by a steel rod in torsion, with torsional strain gages calibrated to torque.

EXPERIMENTAL PROCEDURE

For each set of data taken, a base measurement was made with the shroud in the center position (i.e. with the lateral eccentricity nominally zero). With the shroud in this position, the rotor was run up to the selected measurement speed and measurements were made of rotor deflection, speed, and torque.

Immediately after completing the base measurements, an eccentricity was imparted to the shroud (adjusting screws translate the shroud laterally) and new values of rotor deflection and torque were measured at the same speed as for the base measurement. Since the direction, as well as the magnitude, of shroud offset was found to have an effect on the measurements, the procedure was repeated for an equal shroud eccentricity in the negative (opposite) direction.

Large quantities of data were taken and averaged, since the repeatability was found to be relatively poor (typically ±20% for two successive measurements of the same variable under the same conditions). The poor repeatability was partially due to apparent aerodynamic instabilities (surging) under some conditions of speed and torque.

RESULTS

The results of the experiments are shown in Figures 2 through 13. The lines connecting the points in the figures were derived using a least squares fit.

Figures 2 and 3 show how the measured Alford force varied with rotor eccentricity. The only difference between the two graphs is in the direction that the eccentricity was imparted. Figures 4 and 5 show the magnitude of the efficiency facor, β, and how it varies with rotor eccentricity. Again, the differnce between the two figures is the direction that the eccentricity was imparted. The efficiency

factor β was calculated using Alford's equation which gives the aerodynamic force as proportional to a radial deflection which is normal to the force. The constant of proportionality is called cross-coupled stiffness. Thus we have

$$F_y = \frac{\tau \beta x}{D_p H} = K_{yx} X \qquad (1)$$

The cross-coupled stiffness is seen to be $K_{yx} = \frac{\tau \beta}{D_p H}$.

Equation (1) implies that β remains constant for varying eccentricity. Figure 5 confirms this. Therefore it was felt that the point on Figure 4 corresponding to 20 mils eccentricity was not representative, and should not be included in the least squares fit.

Figures 6 and 7 show how Alford's force and β vary with torque. Again β was calculated using equation (1). Figure 8 shows how the measured Alford force varied with speed holding the rotor torque constant. Figure 9 was derived from figures 6 and 8. The curve corresponding to 5000 rpm was derived using a least squares fit to the data from all 3 tests in Figure 6. The four remaining curves on Figure 9 were derived from this one curve and Figure 8, using extrapolation techniques. Figures 10, 11, 12 and 13 show how the measured Alford force varied with rotor speed and torque. These figures help support the empirical equation of Alford's force to be presented below. They show how the developed rotor torque varies with the speed.

AN IMPROVED PREDICTION MODEL

One of the remarkable features of Alford's theory is its simplicity. Figures 2, 3, and 6 verify the predicted linearity of Alford's force with rotor eccentricity and stage torque. However, Figure 6 shows that Alford's force does not appear at all until a certain level of stage torque is reached: then it suddenly appears and increases steeply with torque. Alford mentions, in reference [1], that "large power inputs to the compressor rotor appear to increase the hazard of whirl. The vibration problem was encountered only at the full 100 percent power rating of the engine." Figure 6 is compatible with this observation.

Figures 7 and 8 also reveal certain limitations of equation (1), principally that the efficiency factor β actually varies with the aerodynamic load torque and that the developed Alford's force is speed-dependent as well as torque-dependent. Also, extrapolation of the curves for Alford's force versus torque (e.g. Figure 6) shows that the y-intercept is not zero as equation (1) predicts.

To obtain an improved prediction model, the speed must be included as a pertinent variable. Dimensional analysis shows that if the speed is pertinent, then the inlet velocity is also pertinent. In dimensionless groups, the prediction equation takes the form

$$\frac{F_y D_p}{\tau} = f\left(\frac{x}{H}, \frac{D_p}{H}, \frac{V}{N D_p}\right) \qquad (2)$$

where N = speed, rpm
V = inlet velocity, fps
and the other variables are as previously defined.

In the experiments reported here, measurements of the inlet velocity V were not made. Therefore the improved prediction model at this stage must be purely empirical, to fit the available test data.

Equation (1) is modified to include a y-intercept, which gives

$$F_y = \frac{\tau \beta x}{D_p H} + C \qquad (3)$$

where the constant C is evaluated as C = -17.37 from Figure 9.

In addition, Figure 9 shows that the slope of the curve is affected by the rotor speed. A relationship can be calculated between the rotor speed and the slope $x/(D_p H)$, as follows:

$$\frac{\beta x}{D_p H} = -10.54 \times 10^{-3} \, (N) + 89.33 \qquad (4)$$

Substituting equation (4) into equation (3) gives

$$F_y = (-10.54 \times 10^{-3} \, (N) + 89.33) \, \tau - 17.37 \qquad (5)$$

In a more general form; factoring out $x/(D_p H)$ where x = 40 mils, D_p = 4.875 in., and H = 0.875 in. gives

$$F_y = \left\{ (-1.12(N) + 9526.42) \, \tau - 1852.35 \right\} \frac{x}{D_p H} \qquad (6)$$

where
F_y = Alford force, grams
τ = developed rotor torque, in-lb
N = rotor speed, rpm
x = eccentricity, in
D_p = blade diameter, in
H = bucket height, in

If the units of Alford force are taken to be pounds (lb), the equation becomes

$$F_y = \left\{ (-2.47 \times 10^{-3}(\text{rpm}^{-1}) \times (N) + 21.0) \, \tau - 4.08(\text{in-lb}) \right\} \frac{x}{D_p H} \qquad (7)$$

Equation (6) reasonably approximates all of the curves presented in this paper that show Alford's force as a function of developed rotor torque, rotor speed, and eccentricity. It is a purely empirical equation which fits the measured data for the described test rig.

CONCLUSIONS AND SUGGESTIONS FOR FUTURE RESEARCH

Due to the size of the test rig and the lack of measurement capability for aerodynamic velocities and pressures, the conclusions which can be made from this research are quite limited in scope. They are as follows:

1. The aerodynamic force postulated by Alford for axial flow turbomachinery does exist, and can be measured experimentally.

2. Alford's force is speed-dependent as well as torque-dependent, and is probably also a function of the gas velocity entering the stage.

3. Although the relationship of Alford's force to the stage torque is fairly linear at a given speed, the y-intercept is not zero. That is, no aerodynamic force is generated until a certain level of stage torque is reached.

The authors believe that these conclusions are significant, since rotordynamics engineers have used Alford's theory for years with no experimental verification.

However, it is easy to see why rotordynamic stability thresholds cannot be reliably predicted at present by computer analyses which use Alford's equation as a model for the destabilizing coefficients. In order to do this, it will be necessary to develop more accurate prediction models for the aerodynamic force, which will require experimental measurements on full scale turbomachinery components, such as an axial flow stage from the compressor in a turbojet aircraft engine, or an industrial process compressor.

REFERENCES

1. Alford, J. S., "Protecting Turbomachinery from Self-Excited Rotor Whirl," Journal of Engineering for Power, Vol. 87, Series A, No. 4, October 1965, pp. 333-334.

2. Doyle, H. E., "Field Experiences with Rotordynamic Instability in High-Performance Turbomachinery," Proceedings of a Workshop held at Texas A&M University, May 1980, NASA Conference Publication 2133.

3. Murphy, B. T., "Computer Programs for Critical Speeds and Stability Analysis," Rotordynamics of Turbomachinery Short Course, Texas A&M University, May 18-20, 1981.

4. Vance, J. M. and Laudadio, F. J., "Rotordynamic Instabilities in Centrifugal Compressors - Are all the Excitations Understood?", ASME Journal of Engineering for Power, April 1981, pp. 288-293.

5. Vance, J. M., "Instabilities in Turbomachinery", Proceedings of the 5th Annual Vibration Institute Seminar on Machinery Vibration Analysis, April 9, 1981, New Orleans, La.

6. Thomas, H. J., "Unstable Oscillations of Turbine Rotors Due to Steam Leakage in the Clearances of the Sealing Glands and the Buckets," Bulletin Scientifique, A. J. M. 71, 1958, pp. 1039-1063.

7. Winter, C. J., "Instabile Bewegungen von Turbinenlaeufern infolge lastabhaengiger Erregerkraefte," Energie and Technik, January 1969, pp. 7-13.
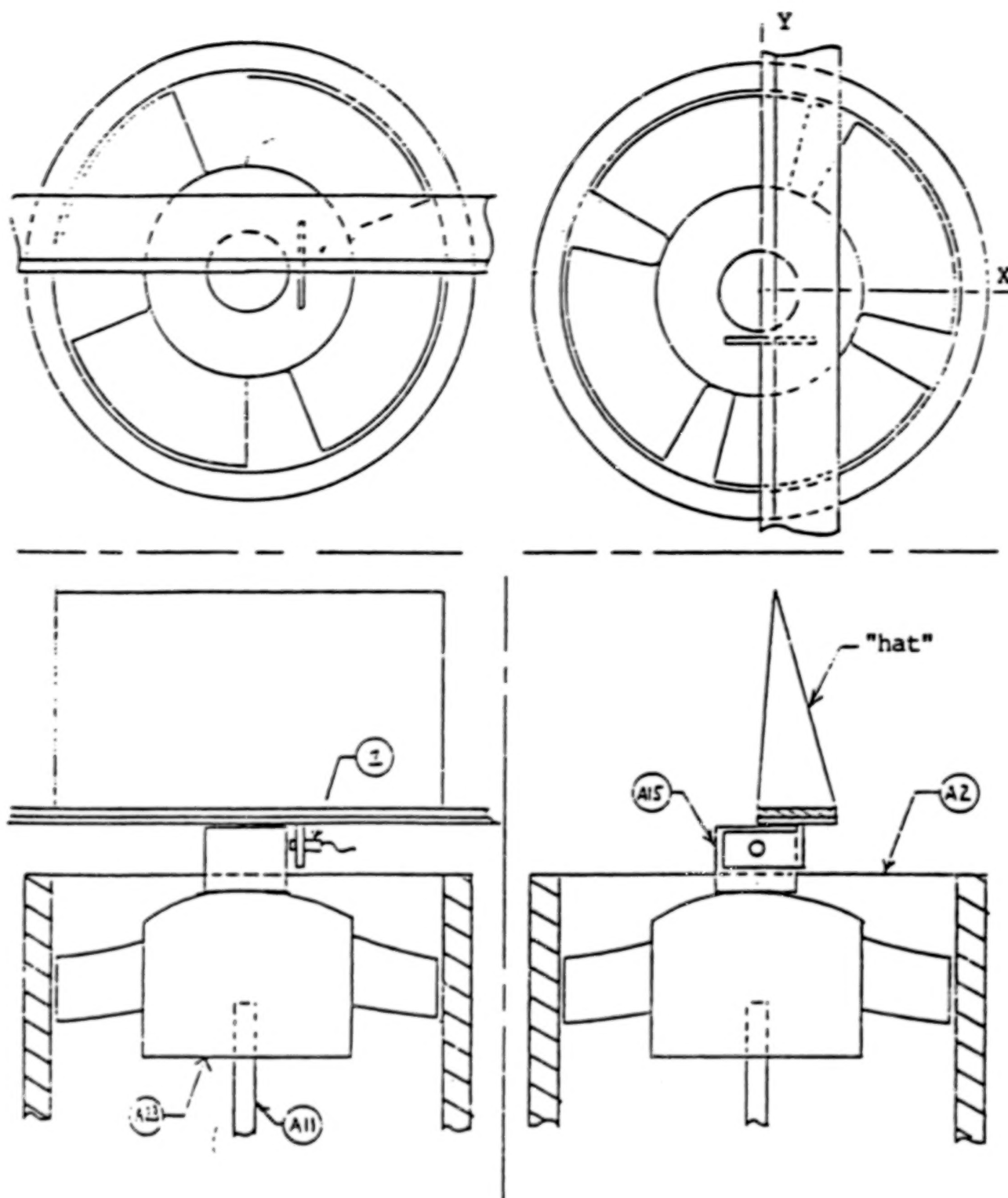
Figure 1. - Drawing of top of test rig showing inlet configuration and coordinate system.
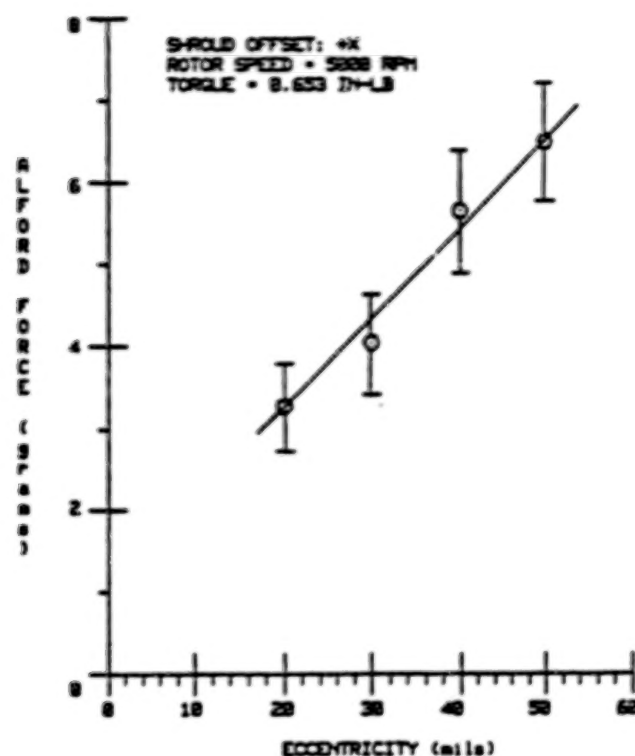
Figure 2. - Alford force as function of rotor eccentricity, showing ±2 standard
deviations (shroud offset: +X).
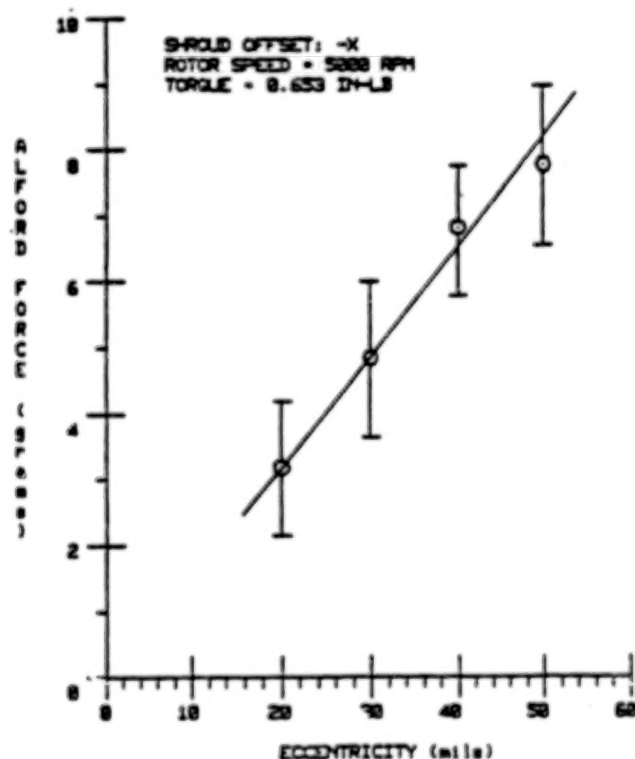
Figure 3. - Alford force as function of rotor eccentricity, showing ±2 standard
deviations (shroud offset: -X).

268
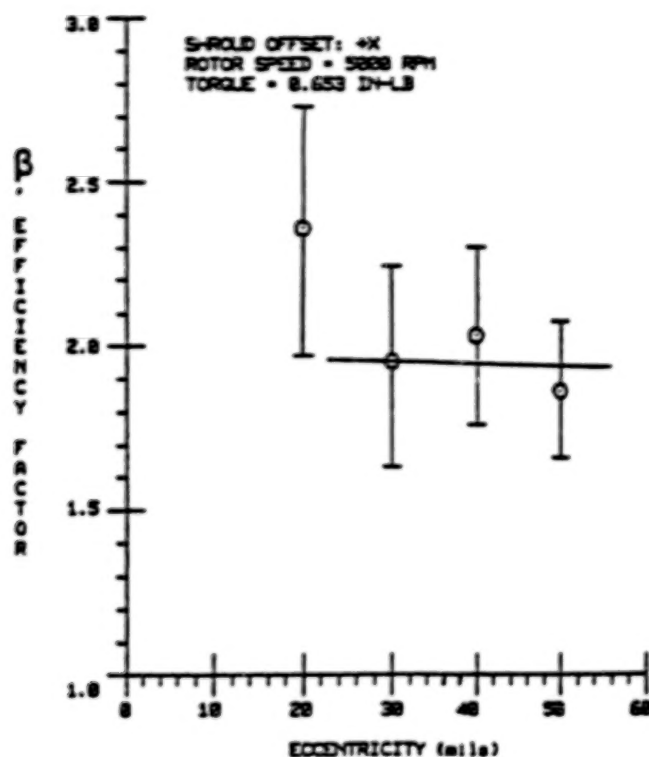
Figure 4. - Efficiency factor, β, as function of rotor eccentricity, showing ±2 standard deviations (shroud offset: +X).
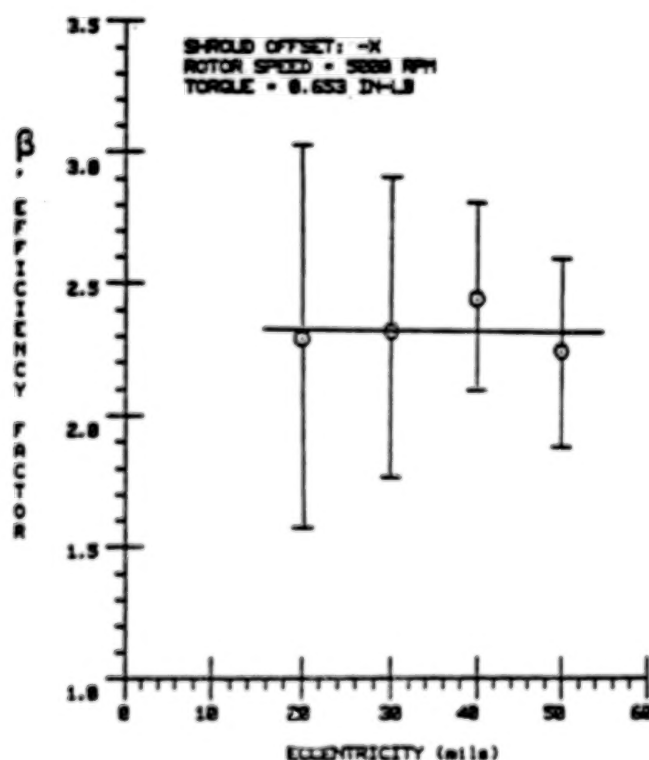
Figure 5. - Efficiency factor, β, as function of rotor eccentricity, showing ±2 standard deviations (shroud offset: -X).

269
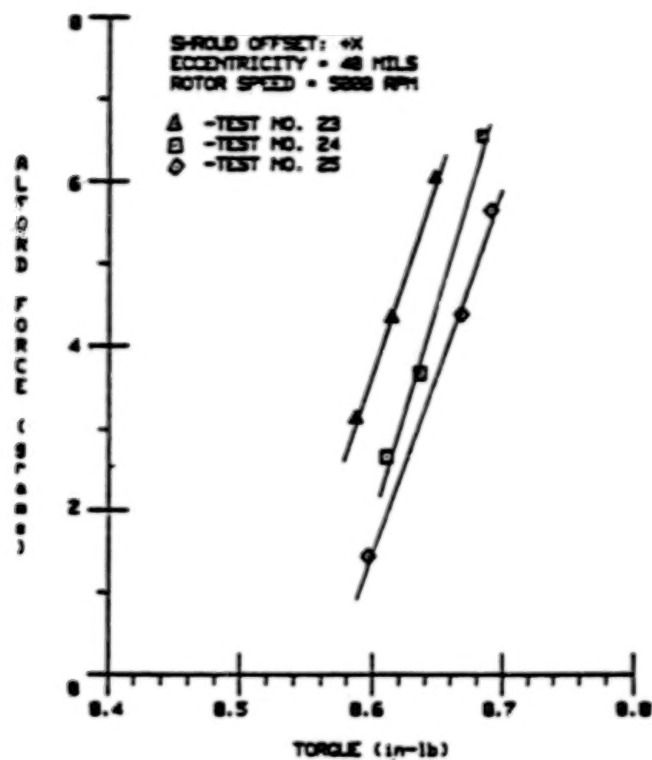
Figure 6. - Alford force as function of developed rotor torque (for three different tests).
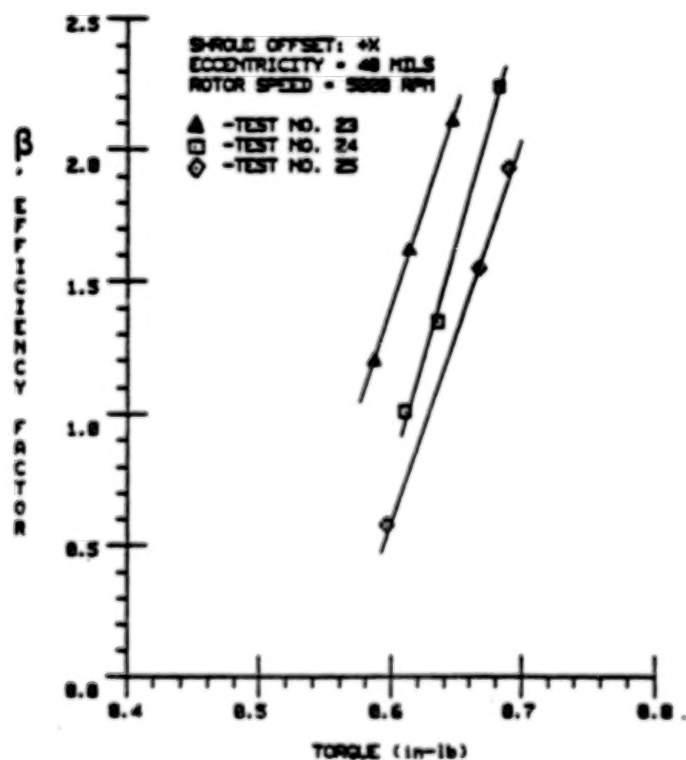
Figure 7. - Efficiency factor, β, as function of developed rotor torque (for three different tests).

BEST DOCUMENT AVAILABLE
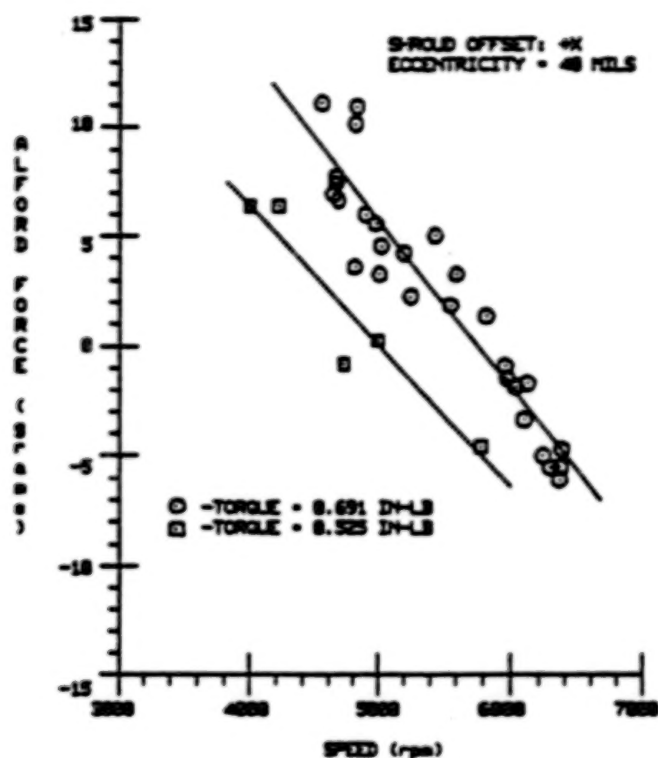
Figure 8. - Alford force as function of rotor speed (for two different values of torque).
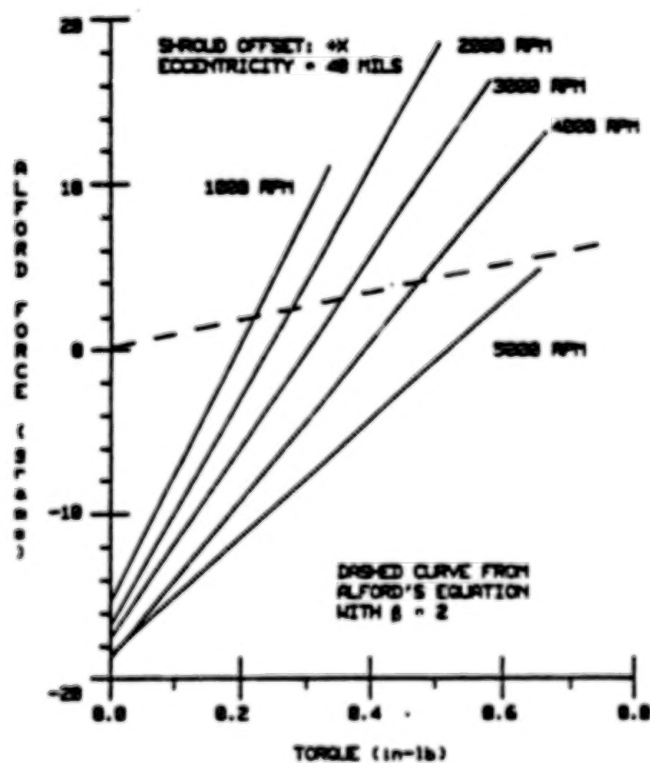
Figure 9. - Alford force as function of developed rotor torque (for different values of speed).
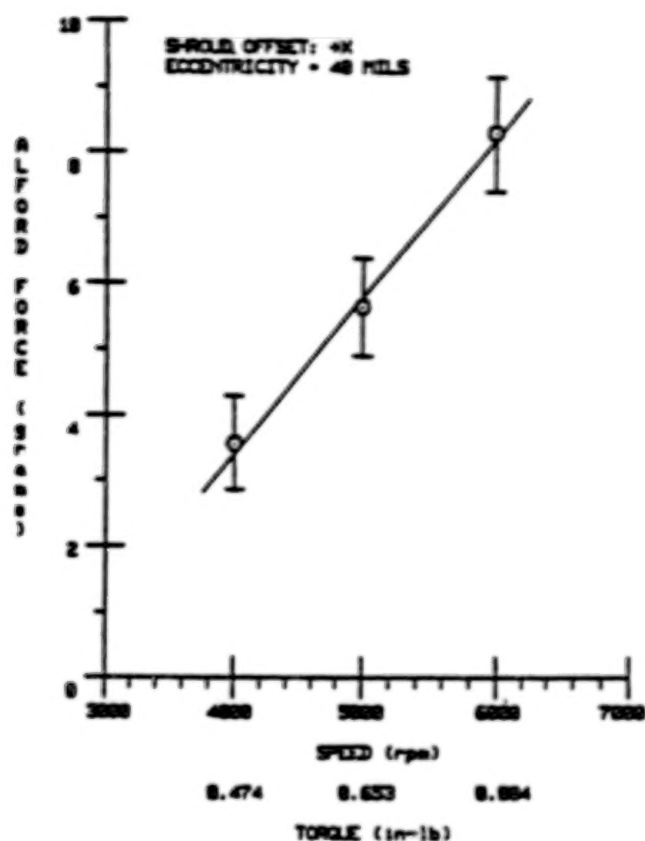
271

Figure 10. - Alford force as function of developed rotor torque and rotor speed, showing ±2 standard deviations (shroud offset: +X).
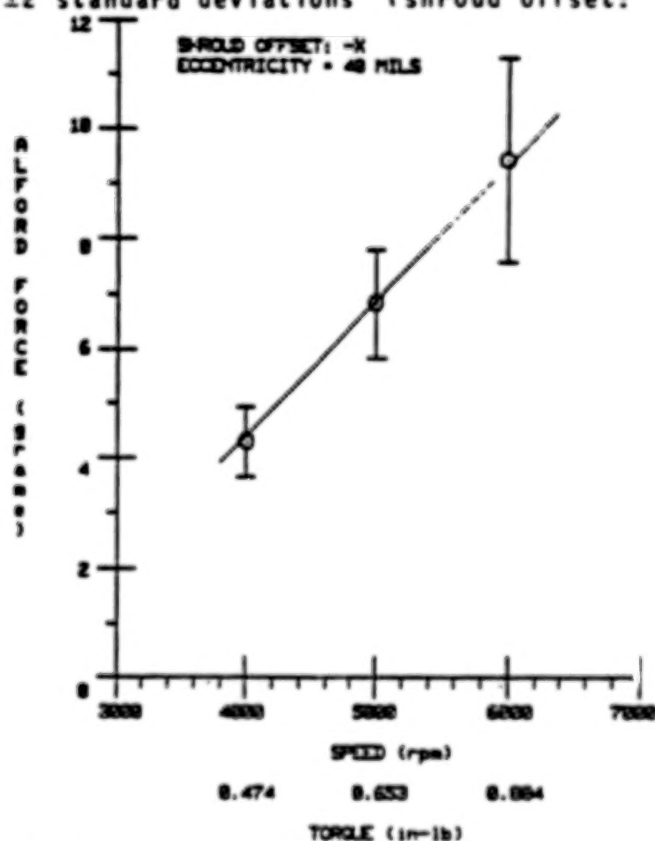

Figure 11. - Alford force as function of developed rotor torque and rotor speed, showing ±2 standard deviations (shroud offset: -X).
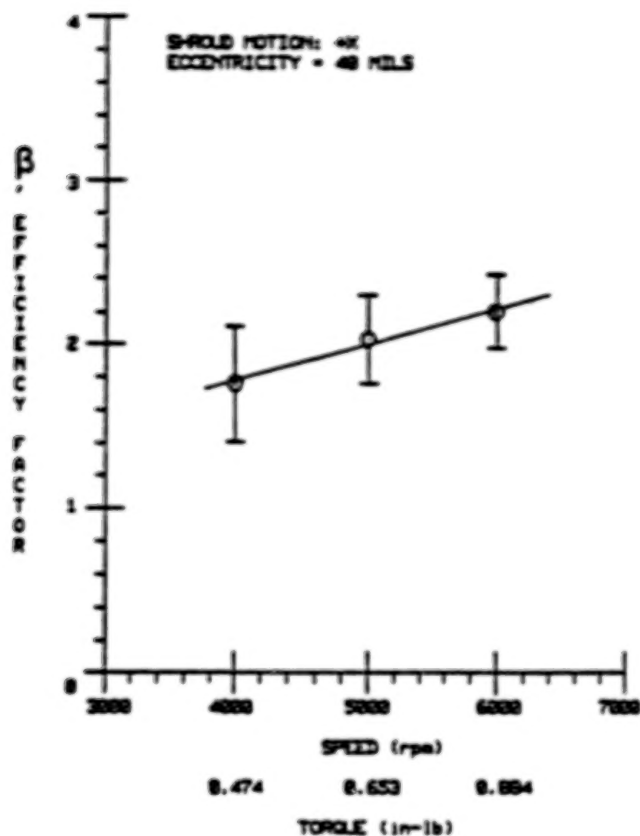
Figure 12. - Efficiency factor, β, as function of developed rotor torque and rotor speed, showing ±2 standard deviations (shroud offset: +X).
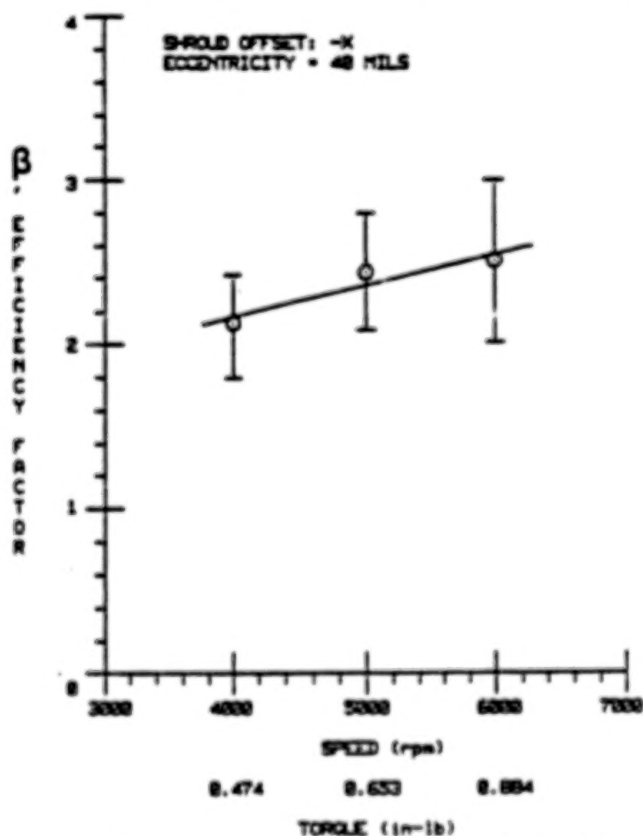

Figure 13. - Efficiency factor, β, as function of developed rotor torque and rotor speed, showing ±2 standard deviations (shroud offset: -X).

273

HEURISTIC EXPLANATION OF JOURNAL BEARING INSTABILITY

Stephen H. Crandall
Massachusetts Institute of Technology
Cambridge, Massachusetts 02139

SUMMARY

A fluid-filled journal bearing is viewed as a powerful pump circulating fluid around the annular space between the journal and the bearing. A small whirling motion of the journal generates a wave of thickness variation progressing around the channel. The hypothesis that the fluid flow drives the whirl whenever the mean of the pumped fluid velocity is greater than the peripheral speed of the thickness-variation wave is discussed and compared with other simple explanations of journal-bearing instability. It is shown that for non-cavitating long bearings the hypothesis predicts instability onset correctly for unloaded bearings but gradually overpredicts the onset speed as the load is increased.

INTRODUCTION

One of the important causes for high speed rotor instability is the oil whip phenomenon in hydrodynamically lubricated journal bearings. It was first reported in 1925 by Newkirk and Taylor (ref. 1) who described several experiments and gave a simple explanation of why a lightly loaded journal whirls at half the frequency of rotation. In the present paper Newkirk and Taylor's argument is reexamined and compared with a heuristic hypothesis briefly suggested (ref. 2) in the first Workshop on Rotordynamic Instability in High Performance Turbomachinery in 1980. When compared with conventional dynamic stability analysis both arguments are incomplete. Nevertheless, both arguments predict the instability onset speed correctly for unloaded full circular bearings. The heuristic hypothesis can additionally be applied to loaded bearings for which it makes useful approximate predictions of instability onset speeds for moderate loads. For simplicity the discussion is centered on the case of a full circular bearing with two-dimensional non-cavitating flow. To set the stage, the classical Sommerfeld analysis (ref. 3) for equilibrium under a constant load is reviewed. After this the problem of whirling stability is discussed, first for an unloaded bearing, and then for a loaded bearing.

SOMMERFELD'S ANALYSIS

The idealized case treated by Sommerfeld (ref. 3) in 1904 is sketched in Fig. 1. A journal of radius R rotates at a fixed angular rate Ω within a full circular bearing of radius $R + h_0$ where the radial clearance h_0 is very small in comparison to R. The annular space between journal and bearing is filled with an incompressible fluid lubricant with uniform viscosity μ. The fluid flow is taken to be two-dimensional; i.e., axial flow is assumed to be negligible. In addition it is assumed
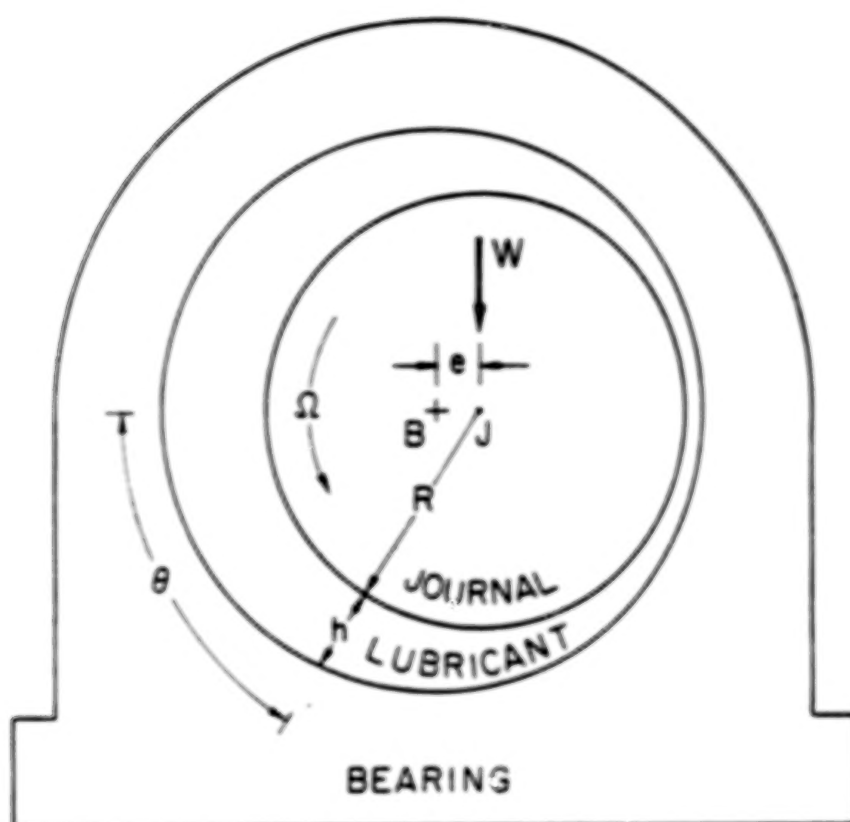
274

Figure 1. - Equilibrium configuration of journal rotating at rate Ω under load W. Journal center J displaced distance e with respect to bearing center B.

that cavitation does not occur. The width of the bearing normal to the plane of the figure is b.

Sommerfeld's principal result is that in the equilibrium position under a vertical load W the journal is eccentrically displaced by a distance e in the horizontal direction. Because of the eccentricity e the film thickness h varies with position θ around the annular space. For $h_o \ll R$ the approximate relation is

$$h = h_o + e \cos \theta = h_o(1 + a \cos \theta) \tag{1}$$

where $a = e/h_o$ is the eccentricity ratio. Under the assumptions of laminar viscous flow with no pressure variation across the thickness of the film, the only possible flow patterns that satisfy the requirements of fluid mechanics in a uniform channel of thickness h are combinations of the two basic patterns shown in Fig. 2. Here x is distance along the channel and y is distance across the channel with $0 < y < h$. The fluid velocity (in the x-direction at position y) is denoted by u. The volume flow rate across a section of the channel of width b normal to the plane of the figure is denoted by Q and $\partial p/\partial x$ is the pressure gradient along the channel. For the linear profile at the left of Fig. 2 the pattern depends on the parameter U which is the velocity of the upper channel wall (the velocity of the lower channel wall is taken to be zero). For the parabolic profile at the right of Fig. 2 the pattern depends on the parameter A which is a velocity whose magnitude is four times the peak velocity in the profile or six times the average velocity. While the

275

$$u = U\ y/h \qquad\qquad u = A(y/h - y^2/h^2)$$

$$Q = U\ bh/2 \qquad\qquad Q = A\ bh/6$$

$$\frac{\partial p}{\partial x} = 0 \qquad\qquad \frac{\partial p}{\partial x} = -2A\mu/h^2$$
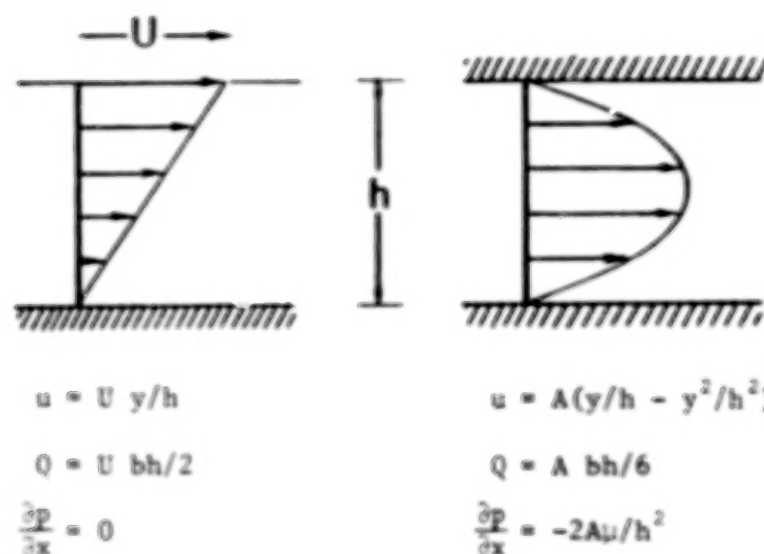
Figure 2. - Component laminar flows in narrow channel with uniform pressure across channel. Either linear or parabolic velocity profiles.

relations in Fig. 2 are strictly correct only for steady state flows with constant values of the parameters h, U, and A, the Reynold's theory of lubrication extends them to apply to slow variations, both in time t and space x, of these parameters.

In application to the bearing of Fig. 1, the component flows of Fig. 2 are superposed, with $x = R\theta$ and $U = R\Omega$, with h given by (1), and the undetermined parameter A to be fixed by the requirements of continuity $[\partial Q/\partial \theta = 0]$ and uniqueness of pressure $[p(\theta) = p(\theta + 2\pi)]$. The value of A so determined is

$$A_1 = R\Omega\left[\frac{6(1 - a^2)}{2 + a^2}\ \frac{1}{1 + \varepsilon \cos \theta} - 3\right] \tag{2}$$

and the total volume flow rate is

$$Q_1 = R\Omega bh_o\ \frac{1 - a^2}{2 + a^2} \tag{3}$$

The pressure gradients of the component flows in Fig. 2 are superposed and integrated to obtain the pressure distribution $p(\theta)$ acting on the journal. The resultant of the pressures acting on width b of the journal is a force, acting vertically upwards through the journal center J, of magnitude

$$W_1 = \frac{12\pi\mu bR^3\Omega}{h_o^2}\ \frac{a}{(2 + a^2)(1 - a^2)^{\frac{1}{2}}} \tag{4}$$

276

The viscous shearing stresses acting on the boundary of the journal also produce a resultant force on the journal but its magnitude is smaller than the pressure resultant (4) by a factor of order h_0/R, and thus may be neglected. The force (4) must then be equal and opposite to the applied load W for the journal to be in equilibrium.

The remarkable property of the Sommerfeld bearing model is that the equilibrium displacement is at right angles to the applied load. This characteristic implies that an unloaded bearing is unstable with respect to slow forward whirling motions of the journal. To see this, imagine that an external agent moves the center of the journal J of Fig. 1 in a circular path of radius e in the counterclockwise sense about the bearing center B. When the journal passes through the position shown in Fig. 1 if the motion is slow enough the lubricant flow and pressure distribution will be very nearly the same as for the equilibrium configuration shown there, which means that the fluid will be exerting a force very nearly equal and opposite to W on the journal. This force, in the same direction as the velocity of the journal center J in its circular path does positive work on the whirling motion. The Sommerfeld bearing thus promotes whirling instability for very slow forward whirling rates. To consider more rapid whirling rates it is necessary to extend the Sommerfeld analysis to include motion of the journal center J.

WHIRLING STABILITY OF UNLOADED BEARING

According to (4) the equilibrium position for an unloaded bearing (W = 0) has zero eccentricity (a = 0, = 0). In this configuration the parameter A_1 of Eq. (2) vanishes and the lubricant flow pattern is simply the linear profile shown on the left of Fig. 2. The stability of this configuration is discussed, first by describing Newkirk and Taylor's explanation of half-speed whirl (ref. 1) and the
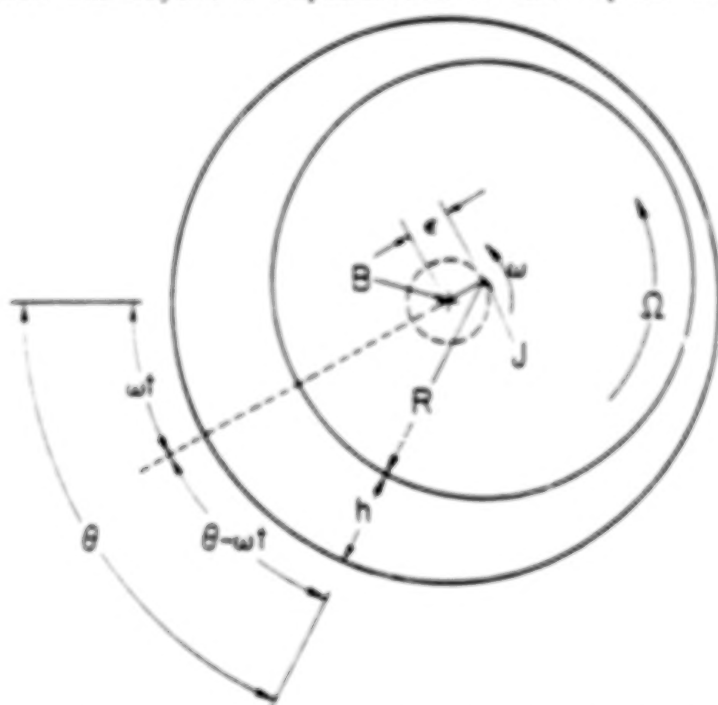

Figure 3. - Traveling wave of lubricant film thickness variation circling channel when center of rotating journal J whirls at frequency ω around circle of radius ε.

277

new heuristic hypothesis (ref. 2), and then by performing a conventional whirling stability analysis which sheds light on the preceding arguments. The bearing kinematics are displayed in Fig. 3 for the case where the journal center J whirls at the steady angular rate ω in a circle of radius ϵ about the equilibrium position in which J and B coincide. Note that the diametrally opposite sections of maximum and minimum film thickness advance around the bearing at the rate ω. At the location θ the film thickness is

$$h(\theta,t) = h_o + \epsilon \cos(\theta - \omega t) \tag{5}$$

Note that the dependence of h on space θ and time t is that of a _progressive wave_ circling the annular channel with an angular phase velocity of ω or a linear phase velocity of $R\omega$.

The Newkirk and Taylor explanation (ref. 1) is based on an application of the continuity requirement to the flow in a channel whose thickness varies according to (5). The continuity requirement applied to a differential arc of length $Rd\theta$ is

$$\frac{\partial Q}{R\partial\theta} + b\,\frac{\partial h}{\partial t} = 0 \tag{6}$$

Newkirk and Taylor assumed that the lubricant flow retains the linear profile of Fig. 2 so that $Q = R\Omega b h/2$ which reduces (6) to

$$\frac{\Omega}{2}\frac{\partial h}{\partial\theta} + \frac{\partial h}{\partial t} = 0 \tag{7}$$

When $h(\theta,t)$ from (5) is substituted in (7) the result is that continuity cannot be satisfied unless

$$\omega = \frac{\Omega}{2} \tag{8}$$

Newkirk and Taylor took this to provide analytical verification of the half-frequency whirl phenomenon which they observed in a vertical shaft running in a bearing with plentiful oil supply. It also appeared to explain the "Oil Resonance" peak in response when the rotation rate was twice the natural frequency of the system. The simple result (8) was less satisfactory in explaining the oil-whip phenomenon where the whirling frequency remains at the natural frequency as the rotation rate Ω is increased, although it was noted that the onset of whipping always occured at speeds equal to or greater than twice the natural frequency.

In the heuristic hypothesis (ref. 2) the rotating journal is considered to be a pump impeller which maintains the lubricant flow pattern with linear profile when the journal is unloaded and centered. The fluid velocity varies linearly from u = 0 at the bearing to u = $R\Omega$ at the journal. This flow can be decomposed into a mean flow with uniform velocity u = $R\Omega/2$ and no vorticity plus a residual flow with zero mean velocity and large vorticity. It is assumed that the mean flow is available to encourage (or discourage) small whirling perturbations of the centered configuration. If a whirl involving a thickness variation wave of the form (5) is imposed the heuristic hypothesis (ref. 2) postulates that energy will be pumped into the whirl if the mean flow velocity $R\Omega/2$ is greater than the phase velocity $R\omega$ of the whirl around the periphery of oil film. Conversely energy will be removed from the whirl if the phase velocity of the whirl is greater than the mean velocity of the lubricant. Neutral stability occurs when these velocities are equal; i.e., when $\omega = \Omega/2$. This

hypothesis thus "explains" half-frequency whirls and oil whip for a system which has an unloaded bearing with plentiful oil supply. If the system provides little restraint on the journal its motion will be primarily determined by the fluid film forces acting on it. When a low frequency whirl ($\omega < \Omega/2$) is accidently started energy will be pumped into the whirl, accelerating the whirl until ω gets sufficiently close to $\Omega/2$ that the energy pumped into the whirl just balances the system energy losses in a steady "half-frequency" whirl. If the system provides considerable restraint on the journal and only permits appreciable whirling motion at a natural frequency the fluid film in the bearing will remove energy from accidental whirls at a natural frequency ω whenever $\Omega < 2\omega$. However, when $\Omega > 2\omega$ the fluid film will pump energy into any such whirl. Whether or not oil whip occurs depends on whether the energy supplied by the fluid film is sufficient to overcome the system losses.

Both of the previous explanations are incomplete in the sense that they do not make use of all the physical requirements involved. Both arguments use the flow pattern of the underlying steady centered flow and both use the kinematics of a small whirling perturbation. The Newkirk and Taylor argument also makes explicit use of the continuity requirement for the perturbation but neither explanation explicitly invokes any consideration of the pressures developed in the oil film.

Historically, the first complete dynamic analysis of the whirling stability of an unloaded bearing was given by Robertson in 1933 (ref. 4). The development which follows is essentially just a linearized version of Robertson's analysis. We consider the whirl defined by the eccentricity ε ($\varepsilon \ll h_o$) and the frequency ω to be a small perturbation on the underlying centered rotation in which the flow distribution is simply

$$u = R\Omega \, y/h_o, \quad 0 < y < h_o \tag{9}$$

When the journal is whirling the flow pattern will be a superposition of the two profiles of Fig. 2. To fit the conditions of Fig. 3 we take

$$u = R\Omega \, y/h + A(y/h - y^2/h^2) \tag{10}$$

where $h(\theta,t)$ is given by (5) and A is to be determined from the continuity require-ment (6) and the requirement of single-valued pressure $[p(\theta) = p(\theta + 2\pi)]$. Using a linear perturbation analysis we neglect terms of order $(\varepsilon/h_o)^2$ in comparison with terms of order ε/h_o and find

$$A = -6R \, \frac{\varepsilon}{h_o} \, (\frac{\Omega}{2} - \omega) \, \cos(\theta - \omega t) \tag{11}$$

The corresponding total volume flow rate for the lubricant film is

$$Q = R\Omega bh/2 - \varepsilon R(\frac{\Omega}{2} - \omega)b \, \cos(\theta - \omega t)$$

$$= R\Omega bh_o/2 + \varepsilon Rb\omega \cos(\theta - \omega t) \tag{12}$$

The pressure distribution is obtained by integrating the pressure gradient given in Fig. 2. To first order in ε/h_o

$$p(\theta,t) - p_o = 12\mu R^2 \frac{\varepsilon}{h_o^3}\left(\frac{\Omega}{2} - \omega\right)\sin(\theta - \omega t) \tag{13}$$

The resultant force acting on the journal due to these pressures is directed at right angles to the journal displacement ε and has the magnitude

$$F = 12\pi\mu\varepsilon b\,\frac{R^3}{h_o^3}\left(\frac{\Omega}{2} - \omega\right) \tag{14}$$

The sense is such that when $\Omega/2 > \omega$, F has the same direction as the instantaneous velocity V_J of the journal center. The rate at which the fluid film forces do work on the journal (i.e., the power flow into the whirl) is

$$FV_J = 12\pi\mu b\,\frac{R^3}{h_o^3}\,\varepsilon^2\omega\left(\frac{\Omega}{2} - \omega\right) \tag{15}$$

This analysis shows that the amplitude A of the component flow with parabolic profile, the pressure in the fluid film, the resultant force on the journal, and the power flow into the whirl all are proportional to the factor $(\Omega/2 - \omega)$. Low speed whirls are encouraged and high speed whirls are discouraged. The whirling frequency of neutral stability is $\omega = \Omega/2$.

These results can be compared with the two simplified arguments considered previously. The assumption in the Newkirk and Taylor argument that the velocity profile remains linear is equivalent to assuming that the parameter A in Fig. 2 vanishes, which according to (11) implies that ω must equal $\Omega/2$. Furthermore the vanishing of A implies an absence of pressure gradient and consequently an absence of resulting force so that at the particular whirl frequency $\omega = \Omega/2$ the fluid film neither retards or advances the whirl. This is the neutral stability condition. The heuristic hypothesis (based simply on the flow pattern of the underlying centered configuration and the kinematics of the whirl perturbation) that the mean flow drives the whirl whenever the mean fluid velocity is greater than the phase velocity of the whirl is essentially a qualitative statement equivalent to the quantitative statement represented by eqn. (15). It happens that for an unloaded bearing the frequency of neutral whirl is given correctly by the heuristic hypothesis. For loaded bearings it is difficult to see how the Newkirk and Taylor argument can be extended to predict any other frequency of neutral whirl than $\omega = \Omega/2$. The heuristic hypothesis is however easily extended. It no longer predicts the exact frequency of neutral whirl but it provides useful approximations for moderate loads.

WHIRLING STABILITY OF LOADED BEARINGS

In this section a linear perturbation analysis is made to determine the whirling stability of the equilibrium configuration of Fig. 1. The heuristic hypothesis is then applied to predict an approximate value of the whirling frequency for neutral stability. We consider a small whirling motion of the journal centered about the equilibrium position of Fig. 1 where the journal center whirls with angular velocity ω in a counter-clockwise sense about a circle of radius

280

ε centered on the equilibrium position which lies a distance e to the right of the bearing center. In the equilibrium configuration the film thickness h, the parameter A_1, the volume flow rate Q_1, and the load W_1 are given by eqns. (1), (2), (3), and (4) respectively. When the whirling motion is added the film thickness becomes

$$h(\theta,t) = h_o + e \cos \theta + \varepsilon \cos (\theta - \omega t) \tag{16}$$

With this value of h the velocity profile is taken to have the form of eqn. (10) with the parameter A to be determined anew from the continuity requirements (6) and the requirements of single-valued pressure $[p(\theta) = p(\theta + 2\pi)]$. Using a linear perturbation analysis with respect to ε/h_o (but including terms of all order with respect to $a = e/h_o$) we find

$$A = A_1 + \frac{\varepsilon}{h_o} \frac{6R}{1 + a \cos \theta} [\Omega f(\theta,t) + \omega g (\theta,t)] \tag{17}$$

where

$$f(\theta,t) = -\frac{1 - a^2}{2 + a^2} \frac{\cos(\theta - \omega t)}{1 + a \cos \theta} - \frac{6a}{(2 + a^2)^2} \cos \omega t$$

$$\tag{18}$$

$$g(\theta,t) = \cos(\theta - \omega t) + \frac{3a}{2 + a^2} \cos \omega t$$

Note that (17) reduces to (2) when $\varepsilon = 0$ and to (11) when $a = e/h_o = 0$. The corresponding total volume flow rate is

$$Q = Q_1 - \varepsilon Rb \left[6\Omega \frac{a}{(2 + a^2)} \cos \omega t - \omega g(\theta,t) \right] \tag{19}$$

which reduces to (3) when $\varepsilon = 0$ and to (12) when $a = 0$. The corresponding pressure gradient from Fig. 2 when integrated gives the pressure distribution in the lubricant film. The resultant force acting on the journal due to these pressures has horizontal and vertical components given by

$$H = -\frac{12\pi\mu bR^3}{h_o^3(1-a^2)^{3/2}} \left[\frac{1 - a^2}{2 + a^2} \Omega - \omega \right] \varepsilon \sin \omega t$$

$$\tag{20}$$

$$V = W_1 + \frac{12\pi\mu bR^3}{h_o^3(1-a^2)^{3/2}} \left[\frac{1 - a^2}{2 + a^2} \Omega - \omega + 3a^2 \frac{a^2\Omega + (2+a^2)\omega}{(2 + a^2)^2} \right] \varepsilon \cos \omega t$$

which reduce to (4) and (14) respectively when $\varepsilon = 0$ and when $a = 0$. The forces (20) may be decomposed into three forces: the steady-state load $W_1 = W$, a force proportional to $[(1 - a^2)\Omega/(2 + a^2) - \omega]$ which whirls in phase with the velocity of the journal center, and an oscillating vertical force whose magnitude is small when

a is small. The total work done on the journal by these forces during one whirling cycle; i.e., the energy per cycle ΔE imparted to the whirl is

$$\Delta E = \frac{12\pi^2 \mu b R^3 \epsilon^2}{h_o^3 (2+a^2)(1-a^2)^{3/2}} \left[\frac{4 - 2a^2 + a^4}{2 + a^2} \Omega - (4 - a^2)\omega \right] \tag{21}$$

The lubricant film forces are once more destabilizing for slow whirls and stabilizing for rapid whirls. The neutral stability whirl frequency

$$\omega = \frac{4 - 2a^2 - a^4}{8 + 2a^2 - a^4} \Omega = \frac{3 + (1-a^2)^2}{9 - (1-a^2)^2} \Omega \tag{22}$$

varies from $\omega = \Omega/2$ at $a = e/h_o = 0$ for an unloaded bearing to $\omega \to \Omega/3$ when the load approaches infinity and the eccentricity ratio a approaches unity. The variation of ω/Ω according to (22) is represented by the curve labeled A in Fig. 4.
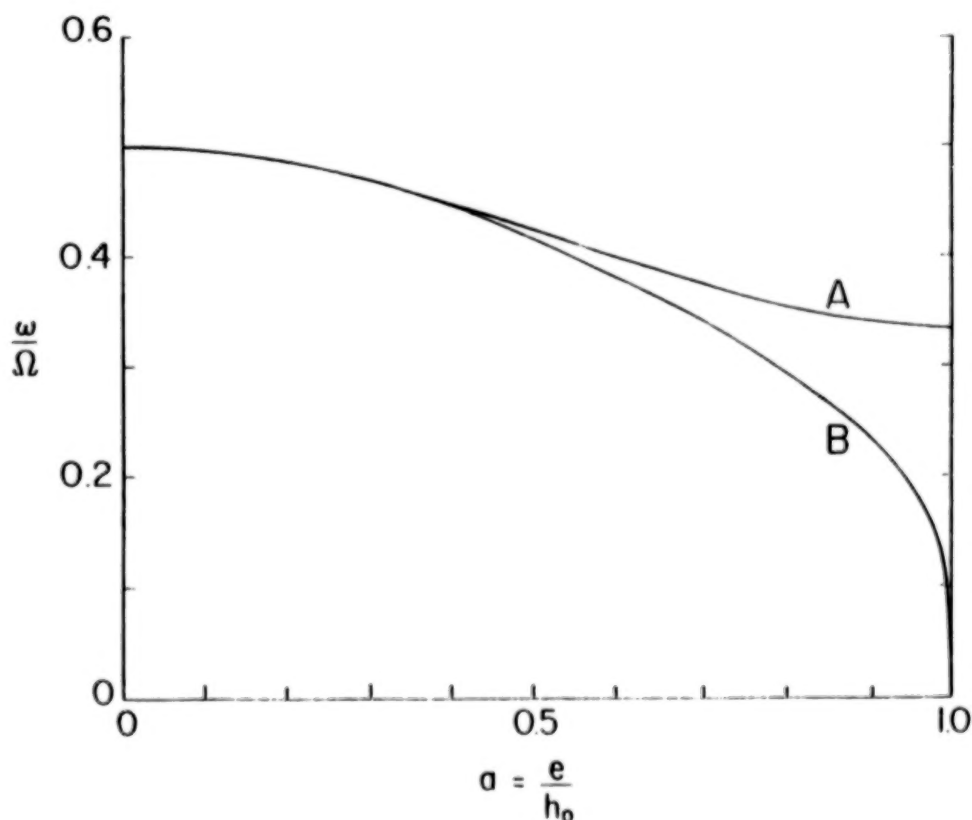
Figure 4. - Frequency ω of neutral stability whirl as function of steady state eccentricity ratio: A, according to complete stability analysis (22); B, according to heuristic proposal (25).

Turning now to the heuristic hypothesis that the lubricant flow pumps energy into the whirl whenever the mean flow velocity is greater than the phase velocity $R\omega$ of the thickness variation wave, we recall that in the equilibrium configuration

282

of Fig. 1 the film thickness h is given by (1) and the volume flow rate Q_1 is given by (3). The mean velocity

$$\bar{U} = \frac{Q_1}{bh} = \frac{R\Omega}{1 + a \cos \theta} \frac{1 - a^2}{2 + a^2} \tag{23}$$

varies with location around the annulus. To obtain a single velocity to compare with the phase velocity of the thickness variation wave, we propose to take the root-mean-square average of $\bar{U}$. The heuristic criterion for neutral stability then becomes

$$R\omega = \bar{U}_{rms} = \left[\frac{1}{2\pi} \int_0^{2\pi} \bar{U}^2 \, d\theta\right]^{1/2} \tag{24}$$

Evaluating the integral, we obtain

$$\omega = \frac{(1-a^2)^{1/4}}{2 + a^2} \Omega \tag{25}$$

as the neutral stability whirl frequency according to the proposed heuristic hypothesis. The variation of this frequency with eccentricity ratio a is represented by the curve B in Fig. 4. The heuristic prediction (25) is not identical to (22) obtained from the dynamic stability analysis, but it provides a useful approximation for values of the steady state eccentricity ratio that are less than $a = 0.5$.

REFERENCES

1. B.L. Newkirk and H.D. Taylor, Shaft Whipping Due to Oil Action in Journal Bearings, General Electric Review 28, 559-568 (1925).

2. S.H. Crandall, Physical Explanations of the Destabilizing Effect of Damping in Rotating Parts, pp. 369-382 in Proc. Workshop on Rotordynamic Problems in High Performance Turbomachinery, NASA CP 2133, 1980. See Appendix.

3. A. Sommerfeld, Zur hydrodynamischen Theorie der Schmiermittelreibung, Zeitschr. für Math. und Physik 50, 97-155 (1904).

4. D. Robertson, Whirling of a Journal in a Sleeve Bearing, Phil. Mag. [7] 15, 113-130 (1933).

INFLUENCE OF PARAMETER CHANGES TO STABILITY BEHAVIOR OF ROTORS

Claus P. Fritzen and Rainer Nordmann
Department of Mechanical Engineering
University of Kaiserslautern
Kaiserslautern, Federal Republic of Germany

SUMMARY

The occurence of unstable vibrations in rotating machinery requires corrective measures for improvements of the stability behavior. Before a measure will be realized, different possibilities should be investigated. In this paper a simple approximate method is represented, to find out the influence of parameter changes to the stability behavior. The method is based on an expansion of the eigenvalues in terms of systemparameters. Influence coefficients show in a very intuitive way the effect of structural modifications. The method first of all was applicated to simple nonconservative rotor models. Furthermore it was approved for an unsymmetric rotor of a test rig.

INTRODUCTION

The occurence of instability in rotating machinery may be caused by different effects, for example oil film forces in journal bearings, forces in seals, unsymmetric shafts, internal damping etc. A machine designer wants to know, whether a rotor will run stable during operation and what size the stability threshold speed will have. Furthermore he needs information about the parameters influencing the stability behavior.

Important informations about the stability of a linear rotor system can be obtained by calculations in the design stage. Because of uncertain input data for calculation, the results have to be considered critically. It is possible, that unstable vibrations may occur during operation, although the calculation was predicting a stable machine. On the other hand parameters may change during operation leading to increasing oscillations. In such cases suitable corrective measures for improvements of the stability behavior are required. Before a measure will be realized, different possibilities should be investigated finding out the simplest and most effective one. For that it would be very useful, to have approximate formulas, expressing the sensitivity of the dynamic behavior to changes of system parameters.

In linear rotor systems with nonconservative effects the stability can be valuated by means of the system eigenvalues. The real parts of the eigenvalues determine, whether the natural motion is decreasing or increasing. If the variations of eigenvalues caused by variations of systemparameters (mass-, damping-, stiffness-coefficients) are known, an estimation of system modifications to the stability behavior is possible. Such sensitivities, respectively influence coefficients, expressing the change of eigenvalues to changes of systemparameters are presented here.

Lund (ref. 1) has developed a method to calculate sensitivities of the critical speeds (eigenfrequencies) of a conservative rotor to changes in the design. Dresig (ref. 2) gives a more general development for conservative mechanical structures. The basic idea in his method is an expansion of the eigenvalues in terms of the system parameters. In Taylor's expansion derivatives of the eigenvalues to the system parameters are needed. Such derivatives were developed from Plaut and Huseyin (ref. 3) and from Fox and Kapoor (ref. 4).

Based on Taylor's expansion for complex eigenvalues in this paper an improvement of the method is presented for rotor systems with nonconservative mechanisms (oil film bearings, seals ets.) Linear, quadratic or higher order formulas are obtained, depending on the order of the derivatives taken into consideration in the expansion. With the linear formula very simple influence coefficients can be defined, pointing out the influence of special parameters to an eigenvalue. Superposition of different parameter changes is possible in this special case. Using the formulas the eigenvalues, the left-hand and right-hand eigenvectors of the original system (without parameter changes) must be known.

The application of the method is demonstrated for simple nonconservative rotor models, investigating the effects of stiffness and damping coefficients to the stability behavior. Furthermore the influence of the mass variation to the eigenvalues of an unsymmetric rotor is determined. The predicted vibration behavior caused by parameter variations could be confirmed by measurements.

NATURAL VIBRATIONS OF LINEAR ROTORS

A turbomachine consisting of a high pressure turbine, a generator and an exciter is shown in figure 1. The power of the machine is 110 MW and the operating speed 3000 rpm. Contrary to nonrotating structures the dynamic behavior of such rotating machines is influenced by additional effects. Of great importance are selfexciting and damping effects (nonconservative effects), caused by the oil film forces of journal bearings, forces in seals etc.

In linear rotor dynamics the natural vibrations can be described by linear equations of motion, usually derived by means of the finite element method.

$$\underline{M}\ddot{\underline{q}} + \underline{C}\dot{\underline{q}} + \underline{K}\underline{q} = \underline{0} \tag{1}$$

$\underline{M}$ mass matrix (order NxN)

$\underline{C}$ damping matrix (order NxN)

$\underline{K}$ stiffness matrix (order NxN)

$\underline{\tilde{q}}$ displacement vector

The equations express the equilibrium of inertia, damping, and stiffness forces. Because of the nonconservative effects damping and stiffness matrix contain also skewsymmetric and nonsymmetric terms besides the symmetric ones. Furthermore some of the matrix elements depend on the operating conditions of the machine (speed, power, pressure etc.).

Investigating the natural motion (stability) of a rotor equation (1) has to be solved. The solution has the form

$$\tilde{\underline{q}}(t) = \underline{q} \, e^{\lambda t} \tag{2}$$

Substitution yields the quadratic eigenvalue problem

$$\{\lambda^2 \underline{M} + \lambda \underline{C} + \underline{K}\} \, \underline{q} = \underline{O} \tag{3}$$

with 2N eigenvalues λ_n and corresponding eigenvectors (natural modes) $\underline{q}_n$. The eigenvalues as well as the eigenvectors mainly occur in conjugate complex pairs

$$\text{eigenvalues:} \quad \lambda_n = \alpha_n + i\omega_n \, , \quad \bar{\lambda}_n = \alpha_n - i\omega_n \tag{4}$$

$$\text{eigenvectors:} \quad \underline{q}_n = \underline{s}_n + i\underline{t}_n \, , \quad \bar{\underline{q}}_n = \underline{s}_n - i\underline{t}_n \tag{5}$$

The part of the solution, which belongs to such a conjugate complex pair, can be written as

$$\tilde{\underline{q}}_n(t) = B_n \, e^{\alpha_n t} \{\underline{s}_n \sin(\omega_n t + \gamma_n) + \underline{t}_n \cos(\omega_n t + \gamma_n)\} \tag{6}$$

ω_n is the circular natural frequency and α_n the damping constant (decay constant). The damping constant, respectively the real part of the eigenvalue determines, whether the solution $\tilde{\underline{q}}_n(t)$ decreases ($\alpha_n < 0$) or increases ($\alpha_n > 0$).

The four lowest natural frequencies and the corresponding damping constants of the turbomachine (figure 1) are plotted versus the running speed in figure 2. The eigenvalues are changing with speed, especially the damping constants α_1 and α_3. The diagram shows that the rotor instability onset speed is 3400 rpm determined by the zero value of α_1. The relative distance between the instability onset speed and the operating speed is very low. Therefore unstable vibrations may occur if additional destabilizing forces are acting on the rotor. If such calculated results are known in a machines design stage, corrective measures improving the stability behavior should be arranged. If instability occurs in

operating machines similar problems have to be solved. Approximate formulas, respectively influence coefficients expressing the influence of parameter changes to the eigenvalues (stability behavior) may be very useful for the above mentioned requirements.

<div align="center">INFLUENCE OF PARAMETER CHANGES TO THE</div>

<div align="center">STABILITY BEHAVIOR</div>

Eigenvalue Problem and Modal Parameters

Our aim is to find formulas for an approximate calculation of eigenvalue variations caused by system modifications (parameter changes). Besides the designed parameter changes this formulas will contain modal parameters of the initial dynamic system, that means eigenvalues λ, left-hand eigenvectors $\underline{\ell}$ and right-hand eigenvectors $\underline{q}$ of the system without parameter changes. Normally they are known from calculations (ref. 5).

Complementary to the eigenvalue problem (eq. (3)) the corresponding left-hand-eigenvalue problem with transposed matrices

$$\{\lambda^2 \underline{M}^T + \lambda \underline{C}^T + \underline{K}^T\} \, \underline{\ell} = \underline{O} \tag{7}$$

has the same eigenvalues λ, but the mentioned left-hand eigenvectors ℓ. Working with the procedure of inverse vector iteration for complex eigenvalues (ref. 5) a desired number of the modal parameters λ, $\underline{q}$, $\underline{\ell}$, can be calculated effectively. For further derivations we suppose that the interesting modal parameters of the initial system are given.

Taylor's Expansion for the Eigenvalues

The basic idea of the approximate method is an expansion (Taylor's series) of the eigenvalues in terms of the generalized system parameters p_k $(k = 1, 2, \ldots K)$

$$\lambda_n = \lambda_{no} + \sum_r \frac{1}{r!} \left(\frac{\partial}{\partial p_1}\bigg|_o \Delta p_1 + \frac{\partial}{\partial p_2}\bigg|_o \Delta p_2 + \ldots \frac{\partial}{\partial p_K}\bigg|_o \Delta p_K \right)^r \lambda(p_1, p_2, \ldots p_K) \tag{8}$$

in which the p_k may be mass, damping, or stiffness parameters. λ_n is the changed eigenvalue after a parameter variation. λ_{no} is the corresponding eigenvalue of the initial system. The derivatives of the eigenvalues to the system parameters are expressed in operational notation. r is the order of the derivative.

<div align="center">287</div>

Truncating equation (8) after a desired derivative, the changed eigenvalue may be calculated approximately. Easy to handle is a linear formula with first derivatives. A more exact expression can be obtained if an additional quadratic term is taken into account.

Linear Approximate Formula

Taylor's expansion (eq. (8)), truncated after the first derivatives leads to the following linear approximate equation (9)

$$\lambda_n = \lambda_{no} + \left.\frac{\partial \lambda_n}{\partial p_1}\right|_o \Delta p_1 + \left.\frac{\partial \lambda_n}{\partial p_2}\right|_o \Delta p_2 + \cdots \left.\frac{\partial \lambda_n}{\partial p_K}\right|_o \Delta p_K = \lambda_{no} + \sum_k \left.\frac{\partial \lambda_n}{\partial p_k}\right|_o \Delta p_k \quad (9)$$

For determination of λ_n, respectively $\Delta\lambda_n = \lambda_n - \lambda_{no}$ the first partial derivatives $\partial\lambda_n/\partial p_k$ are required.
Using the standard subscript notation for partial derivatives

$$\lambda_{n,k} = \frac{\partial \lambda_n}{\partial p_k} \quad q_{n,k} = \frac{\partial q_n}{\partial p_k} \quad \underline{M}_{,k} = \frac{\partial \underline{M}}{\partial p_k} \quad \underline{C}_{,k} = \frac{\partial \underline{C}}{\partial p_k} \quad \underline{K}_{,k} = \frac{\partial \underline{K}}{\partial p_k} \quad (10)$$

the differentiation of equation (3) with respect to p_k yields

$$\{\lambda_n^2 \underline{M} + \lambda_n \underline{C} + \underline{K}\} q_{n,k} + \{2\lambda_n \lambda_{n,k}\underline{M} + \lambda_{n,k}\underline{C} + \lambda_n^2\underline{M}_{,k} + \lambda_n\underline{C}_{,k} + \underline{K}_{,k}\} \underline{q}_n = 0 \quad (11)$$

We premultiply equation (11) by $\underline{\ell}_n^T$ to obtain the scalar expression

$$\underline{\ell}_n^T \{\lambda_n^2 \underline{M} + \lambda_n \underline{C} + \underline{K}\} \underline{q}_{n,k} + \underline{\ell}_n^T \{2\lambda_n\underline{M} + \underline{C}\} \underline{q}_n \lambda_{n,k}$$

$$= - \underline{\ell}_n^T \{\lambda_n^2 \underline{M}_{,k} + \lambda_n \underline{C}_{,k} + \underline{K}_{,k}\}\underline{q}_n \quad (12)$$

The first term in this equation is zero, it represents the left-hand eigenvalue problem, multiplied with $q_{n,k}$. Furthermore it is assumed that $\underline{q}_n$ and $\underline{\ell}_n$ are normalized in a way to satisfy the relation

$$\underline{\ell}_n^T \{2\lambda_n\underline{M} + \underline{C}\} \underline{q}_n = 1 \quad (13)$$

It follows that

$$\lambda_{n,k} = \frac{\partial \lambda_n}{\partial p_k} = - \underline{\ell}_n^T \{\lambda_n^2 \underline{M}_{,k} + \lambda_n \underline{C}_{,k} + \underline{K}_{,k}\} \underline{q}_n \quad (14)$$

288

Substitution of this result into equation (9) yields

$$\Delta\lambda_n = (\lambda_n - \lambda_{no}) = -\sum \underline{\ell}_n^T \{\lambda_{no}^2 \underline{M},_k + \lambda_{no} \underline{C},_k + \underline{K},_k\} \underline{q}_n \Delta p_k = \sum_{k=1}^{K} g_{nk} \Delta p_k \quad (15)$$

with the influence coefficients g_{nk}.
Finally we introduce Δ-matrices

$$\Delta\underline{M} = \sum_{k=1}^{K} \Delta\underline{M}_k = \sum_{k=1}^{K} \underline{M},_k \Delta p_k$$

$$\Delta\underline{C} = \sum_{k=1}^{K} \Delta\underline{C}_k = \sum_{k=1}^{K} \underline{C},_k \Delta p_k \quad (16)$$

$$\Delta\underline{K} = \sum_{k=1}^{K} \Delta\underline{K}_k = \sum_{k=1}^{K} \underline{K},_k \Delta p_k$$

expressing the change of mass, damping, and stiffness matrices and we obtain the linear expression

$$\Delta\lambda_{n\ LIN} = (\lambda_n - \lambda_{no})_{LIN} = -\underline{\ell}_n^T \{\lambda_{no}^2 \Delta\underline{M} + \lambda_{no}\Delta\underline{C} + \Delta\underline{K}\} \underline{q}_n \quad (17)$$

This approximate equation is a good tool for calculation in many cases, pointing out the influence of parameter changes to the stability behavior of rotors. As above mentioned for application of the formula the modal parameters of the initial system are needed besides the parameter changes. Derivatives of the eigenvectors do not appear in equation (17).

Influence Coefficients

In equation (15) we have defined influence coefficients g_{nk}

$$g_{nk} = \frac{\partial\lambda_n}{\partial p_k}\bigg|_o = -\underline{\ell}_n^T \{\lambda_{no}^2 \underline{M},_k + \lambda_{no}\underline{C},_k + \underline{K},_k\} \underline{q}_n \quad (18)$$

This differential quotient, respectively differential sensitivity yields the influence on the eigenvalue λ_n of an infinitesimal change of a particular parameter p_k. It can be used as a meaningful approximation for finite parameter changes, when the considered modifications are relatively small.

$$g_{nk} \approx \frac{\Delta\lambda_n}{\Delta p_k} = \frac{\Delta\alpha_n}{\Delta p_k} + i \frac{\Delta\omega_n}{\Delta p_k} \quad (19)$$

Influence coefficients are complex numbers. They depend on the modal parameters of the initial system.

Changing the stiffness k_k of a spring with one end fixed and the other end free (see Table 1), we obtain with $\underline{M}_{,k} = 0$ and $\underline{C}_{,k} = 0$

$$g_{nk} = - \underline{\ell}_n^T \underline{K}_{,k} \, \underline{q}_n \tag{20}$$

The derivation $\underline{K}_{,k}$ leads to a unity main diagonal element $K_{kk} = 1$ with all other elements zero and therefore the influence coefficient of the spring is

$$g_{nk} = - \ell_{nk} \, q_{nk} = - (\ell_k q_k)_n \tag{21}$$

Table 1 contains further influence coefficients for the most important elements in rotor dynamics like springs, dampers, masses, oil film bearings and seals.

Quadratic Approximate Formula

Taking into consideration the quadratic terms in Taylor's expansion too, we obtain the following expression

$$\lambda_n = \lambda_{no} + \sum_{k=1}^{K} \left.\frac{\partial \lambda_n}{\partial p_k}\right|_o \Delta p_k + \frac{1}{2} \sum_{k=1}^{K} \sum_{\ell=1}^{K} \left.\frac{\partial^2 \lambda_n}{\partial p_k \partial p_\ell}\right|_o \Delta p_k \Delta p_\ell \tag{22}$$

in this improved formula the second derivatives $\lambda_{,k\ell}$ are needed besides the first derivatives and the given parameter changes. The determination of the second derivative is shown in the appendix. The expression is more complicated than the first derivative, but all quantities can be determined from the initial system.

PARAMETER CHANGES AT SIMPLE ROTOR MODELS

We applicate the method at simple rotor models to show the influence of particular parameter changes to the stability behavior. Naturally these simple examples can be solved also exactly, on the other hand they are suitable to demonstrate the approximate formulas. A comparison of the results with exact solutions is possible.

Rigid Rotor with Flexible Supports and Clearance Excitation

The first example is an elastically supported rigid rotor with mass m (fig. 3). The supports have the stiffnesses k_{11} in horizontal direction and k_{22} in vertical direction. A clearance excitation force acts in the middle of the rotor. For instance such excitation forces appear in steam turbines. They result from the unsymmetrical fluid flow through the radial clearances at rotor and blading which appears according to the eccentricity between rotor and casing. The clearance excitation force acts rectangular to the displacement direction (fig. 3).

$$\begin{bmatrix} \tilde{F}_1 \\ \tilde{F}_2 \end{bmatrix} = \begin{bmatrix} 0 & -k \\ k & 0 \end{bmatrix} \begin{bmatrix} \tilde{q}_1 \\ \tilde{q}_2 \end{bmatrix} \tag{23}$$

The coefficient k depends on the power of a turbomachine, increasing with power.

Investigating the translatory natural motion we employ the coordinates q_1 and q_2 .

Equations of Motion, Eigenvalues and Eigenvectors

The equations of motion for the rigid rotor with elastic supports are

$$\begin{bmatrix} m & 0 \\ 0 & m \end{bmatrix} \begin{bmatrix} \ddot{\tilde{q}}_1 \\ \ddot{\tilde{q}}_2 \end{bmatrix} + \begin{bmatrix} 2k_{11} & k \\ -k & 2k_{22} \end{bmatrix} \begin{bmatrix} \tilde{q}_1 \\ \tilde{q}_2 \end{bmatrix} = 0 \tag{24}$$

or with the definitions

$$\omega_o^2 = 2k_{11}/m \qquad \tau = \omega_o t \qquad (\ )' = d(\ )/d\tau$$

$$\gamma = k_{22}/k_{11} \qquad \text{stiffness ratio of support} \tag{25}$$

$$\beta = k/2k_{11} \qquad \text{dimensionless clearance excitation coefficient}$$

in dimensionless form

$$\begin{bmatrix} 1 & 0 \\ 0 & 1 \end{bmatrix} \begin{bmatrix} \tilde{q}_1'' \\ \tilde{q}_2'' \end{bmatrix} + \begin{bmatrix} 1 & \beta \\ -\beta & \gamma \end{bmatrix} \begin{bmatrix} \tilde{q}_1 \\ \tilde{q}_2 \end{bmatrix} = 0 \tag{26}$$

The corresponding eigenvalue problem is ($\mu = \lambda/\omega_o$)

$$\begin{bmatrix} 1 + \mu^2 & \beta \\ -\beta & \gamma + \mu^2 \end{bmatrix} \begin{bmatrix} q_1 \\ q_2 \end{bmatrix} = 0 \qquad (27)$$

with the characteristic equation

$$\mu^4 + (1+\gamma)\,\mu^2 + \gamma + \beta^2 = 0 \qquad (28)$$

we obtain the solutions $Z = \mu^2$ from

$$Z_{1,2} = -\frac{1+\gamma}{2} \pm \sqrt{\frac{(1-\gamma)^2 - 4\beta^2}{4}} \quad , \qquad (29)$$

respectively the four eigenvalues μ_n as a function of γ and β.

Figure 4 shows the real part and imaginary part of the essential eigenvalue with positive damping constant. The system is unstable within the range of $(1-2\beta) \leq \gamma \leq (1 + 2\beta)$. This range increases with increasing values of the clearance excitation coefficient β. Isotropy ($\gamma = 1$) of the supports is the most disadvantageous case. An increase of the anisotropy stabilizes the rotor system. For $(1 - 2\beta) \geq \gamma \geq (1 + 2\beta)$ the real part of the eigenvalue is zero and the natural frequencies are split.

The amplitude ratio of the right-hand eigenvector corresponding to an eigenvalue μ can be determined with equation (27), the left-hand eigenvector has the opposite sign

$$\frac{q_2}{q_1} = -\frac{1+\mu^2}{\beta} \quad , \quad \frac{\ell_2}{\ell_1} = \frac{1+\mu^2}{\beta} \qquad (30)$$

Parameter Variations

To demonstrate the approximate formulas we choose an initial system with parameters $\gamma = 1.1$ and $\beta = 0.1$ (fig. 5) and investigate variations of γ, β and an additional damping ΔD. With normalized eigenvectors the particular expressions for eigenvalue changes are

-variation of γ with increment $\Delta\gamma$

$$\Delta\mu = -[\ell_1, \ell_2] \begin{bmatrix} 0 & 0 \\ 0 & \Delta\gamma \end{bmatrix} \begin{bmatrix} q_1 \\ q_2 \end{bmatrix} = -\ell_2 q_2 \,\Delta\gamma$$

-variation of β with increment $\Delta\beta$

$$\Delta\mu = - [\ell_1, \ell_2] \begin{bmatrix} o & \Delta\beta \\ -\Delta\beta & o \end{bmatrix} \begin{bmatrix} q_1 \\ q_2 \end{bmatrix} = - (\ell_1 q_2 - \ell_2 q_1) \Delta\beta$$

-additional modal damping $\Delta D = c/2m\omega_o$

$$\Delta\mu = - \mu [\ell_1, \ell_2] \begin{bmatrix} 2\Delta D & o \\ o & 2\Delta D \end{bmatrix} \begin{bmatrix} q_1 \\ q_2 \end{bmatrix} = - 2\mu (\ell_1 q_1 + \ell_2 q_2) \Delta D$$

The linear approximate formula points out the stabilizing effect of anisotropic supports ($\Delta\gamma$ positive in fig. 5b). Figure 5a shows an increase of frequency caused by stiffening the system from γ to $\gamma + \Delta\gamma$.

For special cases the linear approximate formula has disadvantages, for instance in the isotropic case ($\gamma = 1$) with horizontal tangent line. Then better results will be obtained with the quadratic formula (fig. 5b).

The destabilizing effect of increasing clearance excitation coefficient β and the stabilizing effect of additional damping ΔD are presented in figure 5c.

Rigid Rotor in Journal Bearings

Figure 6 shows a rotor of a test rig. Compared to the bearings the stiffness of the shaft is very high, therefore it can be regarded as a rigid rotor supported in two equal bearings (cylindrical bearings B/D = 0.8), rotating with the rotational speed Ω. The rotor has a mass m = 72 kg, the distance between the bearings is 660 mm. The statical bearing load F_{stat} is equal to 353 N. Each journal has a diameter of 50 mm, the values for the radial clearance and for the oil viscosity are Δr = 210 μm, respectively 3.35 Ns/m^2.

The dynamic behavior of journal bearings can be characterized by four stiffness - and four damping coefficients k_{ik} and c_{ik}, respectively by the non-dimensional quantities

$$\gamma_{ik} = k_{ik} \frac{\Delta r}{F_{stat}}, \quad \beta_{ik} = c_{ik} \frac{\Delta r \, \Omega}{F_{stat}} \tag{31}$$

They are functions of the Sommerfeld number. The pure translatory motion can be described by means of the coordinates q_1 and q_2.

Equations of Motion, Eigenvalues and Eigenvectors

The following equations of motion for a rigid rotor in two journal bearings describe the equilibrium of forces in the case of pure translatory motion and without external loads.

$$
\begin{bmatrix} m & o \\ o & m \end{bmatrix}
\begin{bmatrix} \ddot{\tilde{q}}_1 \\ \ddot{\tilde{q}}_2 \end{bmatrix}
+2
\begin{bmatrix} c_{11} & c_{12} \\ c_{21} & c_{22} \end{bmatrix}
\begin{bmatrix} \dot{\tilde{q}}_1 \\ \dot{\tilde{q}}_2 \end{bmatrix}
+2
\begin{bmatrix} k_{11} & k_{12} \\ k_{21} & k_{22} \end{bmatrix}
\begin{bmatrix} \tilde{q}_1 \\ \tilde{q}_2 \end{bmatrix}
= 0
$$

(32)

Defining

$$
\omega_o^2 = g/\Delta r, \quad \tau = \omega_o t, \quad w = \Omega/\omega_o, \quad ( )' = d ( ) / d\tau
$$

the equations of motion can be written in the nondimensional form

$$
\begin{bmatrix} 1 & o \\ o & 1 \end{bmatrix}
\begin{bmatrix} \tilde{q}_1'' \\ \tilde{q}_2'' \end{bmatrix}
+ \frac{1}{w}
\begin{bmatrix} \beta_{11} & \beta_{12} \\ \beta_{21} & \beta_{22} \end{bmatrix}
\begin{bmatrix} \tilde{q}_1' \\ \tilde{q}_2' \end{bmatrix}
+
\begin{bmatrix} \gamma_{11} & \gamma_{12} \\ \gamma_{21} & \gamma_{22} \end{bmatrix}
\begin{bmatrix} q_1 \\ q_2 \end{bmatrix}
= 0
$$

(33)

The statement for the natural motions

$$
\tilde{q}_i = q_i e^{\lambda t} = q_i e^{\mu\tau}, \quad \mu = \lambda/\omega_o
$$

(34)

yields the eigenvalue problem

$$
\begin{bmatrix}
\gamma_{11} + \dfrac{\beta_{11}}{w}\mu + \mu^2 & \gamma_{12} + \dfrac{\beta_{12}}{w}\mu \\[2ex]
\gamma_{21} + \dfrac{\beta_{21}}{w}\mu & \gamma_{22} + \dfrac{\beta_{22}}{w}\mu + \mu^2
\end{bmatrix}
\begin{bmatrix} q_1 \\ q_2 \end{bmatrix}
= 0
$$

(35)

The four eigenvalues μ_n are i. g. conjugate-complex quantities. If the eigenvalues are known, the corresponding eigenvectors can be calculated from equation (35).

Figure 7 shows the eigenvalue that causes the instability in dependence of the dimensionless rotational speed w. Also the eigenvalue that belongs to a rotatory motion is plotted, but it has no meaning for the stability behavior of the rotor. The real part of the eigenvalue will come to zero at $w = 2.66$. At this rotational speed the stability threshold is reached. The Sommerfeld number here has the value $So = 0.563$. The corresponding circular natural frequency ω/ω_o is 1.435.

294

Influence of Parameter Changes at the Stability Threshold

We start from the stability threshold and we investigate how particular parameters effect the stability behavior. Therefore we take the linear approximate formula (17). First we ask about the influence of the single coefficients γ_{ik} and β_{ik}/w. It can be judged by the influence coefficients in Table 1. Figure 8 shows the influence coefficients in the complex plane. For example, one can see that an increase of γ_{12} is labilizing or that an increase of the damping coefficients β_{11}/w and β_{22}/w is stabilizing the rotor motion.

If we change the rotational speed, the Sommerfeld number and the stiffness and damping coefficients also will change. Figure 9 shows the variation of the eigenvalue in dependence of the rotational speed calculated by the approximate formula. The formula figures the tangent line to the eigenvalue curve at the expansion point. An increase of the rotational speed causes instability.

Finally in figure 9 the influence of the oil viscosity is shown. If we increase the oil temperature from 38°C to 44°C, the oil viscosity will decrease. The real part of the eigenvalues becomes negative and there is a stabilizing effect.

ELASTIC ROTOR WITH FLEXIBLE SUPPORTS AND SEAL FORCES

A more complicated rotor-system, an elastic turbopump rotor with flexible supports, an impeller and two plain seals is shown in figure 10. Between the bearings where the basic shaft diameter is 64 mm, the shaft carries the impeller mass of 55 kg. Two plain seals are mounted besides the impeller with a seal length of 40 mm and a radial clearance of 0.3 mm. The dynamic characteristics of the seals are given by the stiffness, damping and inertia coefficients K, k, C, c, m* (fig. 10). The shaft is supported in two identical bearings, each one having a horizontal stiffness $k_{11} = 1.0\ 10^7$ N/m and a vertical stiffness $k_{22} = .75\ 10^7$ N/m. The distance between the bearings is equal to 1.2 m.

First of all eigenvalues and eigenvectors were calculated for the described original system in a speed range from 2000 rpm to 8000 rpm. In figure 11 two damping constants (decay constants) are plotted versus rotational speed. One of the damping constants crosses the zero axis, pointing out the instability onset speed of 5200 rpm, which is above the operating speed.

In order to improve the stability behavior, some parameter changes were investigated, starting from the initial system with a rotational speed of 5000 rpm. Figure 11 shows the results, especially the influence of seal stiffness and damping coefficients. All coefficients were changed 20 per cent. An increase of K and C stabilizes; an increase of k has a destabilizing effect.

Furthermore it is shown that a positive change of k_{22} in direction to isotropic bearings is disadvantageous.

VARIATION OF THE MASS OF A TEST RIG ROTOR

WITH UNSYMMETRIC FLEXIBLE SHAFT

The test rig rotor shown in figure 12 consists of a flexible shaft with rectangular cross section 8 x 12 mm^2. It is running in two ball bearings which are comparatively stiff. In the middle between the bearings a disk is supported, having a mass of 0.89 kg. The nonrotating shaft has two different natural frequencies 24.6 Hz and 35.1 Hz concerning to the different stiffnesses in two rectangular planes.

It is well known that in rotors with unequal moments of inertia different dynamic effects may occur, for instance vibrations caused by the rotor weight and unstable vibrations (ref. 6). Con erning the stability behavior in this case a variation of the disk mass was investigated by calculations (exact results and approximate formulas) and for control by measurements at the test rig. Theoretical results for the eigenvalues of the undamped shaft are plotted in figures 13a and 13b versus the rotational speed and the mass of the disk. The eigenvalues defined for the rotating coordinate system are either pure imaginary (fig. 13a) or pure positive real (fig. 13b). The last one occur in a rotational speed range between the two natural frequencies of the nonrotating shaft. That means that the rotor motion is unstable in this range.

In order to show the utility of the approximate formula the change of the eigenvalues (rotating system) caused by a positive 25 per cent variation of the disk mass was investigated for the three different running speeds 1200 rpm, 1800 rpm and 2400 rpm. The three figures 14a, 14b, 14c show the variation of the natural frequency, respectively the damping constant, in dependence of the mass. The mass of the original system is 0.89 kg, the changed mass is 1.1 kg. The three diagrams contain the exact, the linear and the quadratic approximate solution. Furthermore the results from measurements are plotted in figures 14a and 14c. There is a good agreement of the results. For 1200 rpm the mass change decreases the frequency (destabilizing effect), for 2400 rpm the mass change increases the frequency (stabilizing effect). A stabilizing effect is also given at the running speed 1800 rpm, where the decay constant α is lowered by the mass change.

REFERENCES

1. Lund, J.W., "Sensitivity of the Critical Speeds of a Rotor to Changes in the Design," J. of Mech. Design, Vol. 102, pp. 115-121, 1980.

2. Dresig, H., "Methode zur Berechnung des Einflusses von Parameteränderungen auf die Eigenfrequenzen von Schwingungssystemen", Maschinenbautechnik 26, pp. 427-430, 1977.

3. Plaut, R.H. and Huseyin, K., "Derivatives of Eigenvalues and Eigenvectors in Non-Self-Adjoint Systems", AIAA-Journal, Vol. 11, No. 2, pp. 250-251, 1973.

4. Fox, R.L. and Kapoor, M.P., "Rates of Change of Eigenvalues and Eigenvectors", AIAA-Journal, Vol. 6, No. 12, pp. 2426-2429, 1968.

5. Nordmann, R., "Eigenschwingungen von Maschinenwellen mit Dämpfungen und Anfachungen," VDI-Bericht, Nr. 221, pp. 157-164, 1974.

6. Gasch, R. and Pfützner, H., "Rotordynamik", Springer Verlag Berlin, Heidelberg, New York, 1975.

APPENDIX

Calculation of the Second Derivatives of the Eigenvalues

First we have to express the right- and lefthand eigenvalue problem (eq. 3), (eq. 7) in the following form:

$$(\underline{A} - \lambda_n \underline{B}) \, \underline{x}_n = 0 \tag{A 1}$$

$$\underline{y}_n^T (\underline{A} - \lambda_n \underline{B}) = 0 \tag{A 2}$$

where the matrices $\underline{A}$, $\underline{B}$ and the vectors $\underline{x}_n$ and $\underline{y}_n$ are defined as

$$\underline{A} = \begin{bmatrix} \underline{M} & \underline{0} \\ \underline{0} & -\underline{K} \end{bmatrix} \quad ; \quad \underline{B} = \begin{bmatrix} \underline{0} & \underline{M} \\ \underline{M} & \underline{C} \end{bmatrix} \tag{A 3}$$

$$\underline{x}_n = \begin{bmatrix} \lambda_n \underline{q}_n \\ \underline{q}_n \end{bmatrix} \quad ; \quad \underline{y}_n = \begin{bmatrix} \lambda_n \underline{\ell}_n \\ \underline{\ell}_n \end{bmatrix} \tag{A 4}$$

The vectors $\underline{x}_m$ and $\underline{y}_n$ satisfy the biorthogonality relation

$$\underline{y}_n^T \underline{B} \, \underline{x}_m = \delta_{nm} \tag{A 5}$$

where δ_{nm} is the Kronecker delta. The first derivative of λ_n with respect to the parameter p_j has the form

$$\lambda_{n,j} (\underline{y}_n^T \cdot \underline{B} \, \underline{x}_n) = \underline{y}_n^T (\underline{A}_{,j} - \lambda_n \underline{B}_{,j}) \, \underline{x}_n \tag{A 6}$$

For the calculation of the second derivatives of λ_n , we need the derivatives of the eigenvectors $\underline{x}_n$ and $\underline{y}_n$. The vectors $\underline{x}_{n,j}$ and $\underline{y}_{n,j}$ can be represented as a linear combination of $\underline{x}_n$ and $\underline{y}_n$:

$$\underline{x}_{n,j} = \sum_{i=1}^{2N} c_{nji} \, \underline{x}_i \qquad \underline{y}_{n,j} = \sum_{i=1}^{2N} d_{nji} \, \underline{y}_i \tag{A 7}$$

Using the equations (A1), A2), (A5) and (A7), Plaut and Huseyin (ref. 3) obtain the following expressions for the coefficients c_{nji} and d_{nji}

$$c_{njn} + d_{njn} = - \underline{y}_n^T \underline{B},_j \underline{x}_n$$

$$c_{nji} = \frac{\underline{y}_i^T (\underline{A},_j - \lambda_n \underline{B},_j) \underline{x}_n}{\lambda_n - \lambda_i}$$

$$d_{nji} = \frac{\underline{y}_n^T (\underline{A},_j - \lambda_n \underline{B},_j) \underline{x}_i}{\lambda_n - \lambda_i}$$
for $n \neq i$
(A 8)

In order to get the second derivative of λ_n with respect to p_j and p_ℓ we must differentiate eq. (A6) with respect to p_ℓ. With eq. (A1), (A2), (A5) and (A7) we obtain for $\lambda_{n,j\ell}$ (ref. 3)

$$\lambda_{n,j\ell} = \underline{y}_n^T (\underline{A},_{j\ell} - \lambda_n \underline{B},_{j\ell}) \underline{x}_n$$

$$+ (c_{njn} + d_{njn}) \lambda_{n,\ell} + (c_{n\ell n} + d_{n\ell n}) \lambda_{n,j}$$

$$+ \sum_{\substack{i=1 \\ i \neq n}}^{2N} (\lambda_n - \lambda_i) [d_{nji} c_{n\ell i} + d_{n\ell i} c_{nji}]$$
(A 9)

where c_{nji} and d_{nji} can be calculated by eq. (A8).

If we go back to our initial problem with the matrices $\underline{M}$, $\underline{C}$ and $\underline{K}$ and the eigenvectors $\underline{\ell}$ and $\underline{q}$, we get by substituting $\underline{A}$, $\underline{B}$, $\underline{x}$ and $\underline{y}$ for the second derivative

$$\lambda_{n,j\ell} = \frac{\partial \lambda_n}{\partial p_j \partial p_\ell} = - \underline{\ell}_n^T (\lambda_n^2 \underline{M},_{j\ell} + \lambda_n \underline{C},_{j\ell} + \underline{K},_{j\ell}) \underline{q}_n$$

$$- \{ \underline{\ell}_n^T (2\lambda_n \underline{M},_j + \underline{C},_j) \underline{q}_n \} \lambda_{n,\ell}$$

$$- \{ \underline{\ell}_n^T (2\lambda_n \underline{M},_\ell + \underline{C},_\ell) \underline{q}_n \} \lambda_{n,j}$$

$$+ \sum_{\substack{i=1 \\ i \neq n}}^{2N} \frac{(\underline{\ell}_n^T \underline{G}_{nj} \underline{q}_i)(\underline{\ell}_i^T \underline{G}_{n\ell} \underline{q}_n) + (\underline{\ell}_n^T \underline{G}_{n\ell} \underline{q}_i)(\underline{\ell}_i^T \underline{G}_{nj} \underline{q}_n)}{(\lambda_n - \lambda_i)}$$

where $\underline{G}_{nj}$ means
(A 10)

$$\underline{G}_{nj} = \lambda_n^2\, \underline{M}'_j + \lambda_n \underline{C}'_j + \underline{K}'_j \tag{A 11}$$

The second derivative with respect to a single parameter p_j can be obtained by replacing the subscript ℓ in eq. (A10) by the subscript j.

Element	Force-motion-relation	Influence coefficient g_{nk}
Spring	$\tilde{F}_k = k_k\, \tilde{q}_k$	$g_{nk} = \left.\dfrac{\partial \lambda_n}{\partial k_k}\right|_o = -\,(\ell_k q_k)_n$
Damper	$\tilde{F}_k = c_k\, \dot{\tilde{q}}_k$	$g_{nk} = \left.\dfrac{\partial \lambda_n}{\partial c_k}\right|_o = -\,\lambda_{n_o}(\ell_k q_k)_n$
Mass	$\tilde{F}_k = m_k\, \ddot{\tilde{q}}_k$	$g_{nk} = \left.\dfrac{\partial \lambda_n}{\partial m_k}\right|_o = -\,\lambda_{n_o}^2(\ell_k q_k)_n$
Journal bearing	$\begin{bmatrix}\tilde{F}_i\\ \tilde{F}_k\end{bmatrix} = \begin{bmatrix}c_{ii} & c_{ik}\\ c_{ki} & c_{kk}\end{bmatrix}\begin{bmatrix}\dot{\tilde{q}}_i\\ \dot{\tilde{q}}_k\end{bmatrix} + \begin{bmatrix}k_{ii} & k_{ik}\\ k_{ki} & k_{kk}\end{bmatrix}\begin{bmatrix}\tilde{q}_i\\ \tilde{q}_k\end{bmatrix}$	$g_{nc_{ik}} = -\,\lambda_{n_o}(\ell_i q_k)_n$ $g_{nk_{ik}} = -\,(\ell_i q_k)_n$
Seals of Pumps	$\begin{bmatrix}\tilde{F}_i\\ \tilde{F}_k\end{bmatrix} = \begin{bmatrix}C & c\\ -c & C\end{bmatrix}\begin{bmatrix}\dot{\tilde{q}}_i\\ \dot{\tilde{q}}_k\end{bmatrix} + \begin{bmatrix}K & k\\ -k & K\end{bmatrix}\begin{bmatrix}\tilde{q}_i\\ \tilde{q}_k\end{bmatrix}$	$g_{nC} \quad -\lambda_{n_o}(\ell_i q_i + \ell_k q_k)_n$ $g_{nc} \quad -\lambda_{n_o}(\ell_i q_k - \ell_k q_i)_n$ $g_{nK} \quad -\,(\ell_i q_i + \ell_k q_K)_n$ $g_{nk} \quad -\,(\ell_i q_k - \ell_k q_i)_n$
Clearance Excitation	$\begin{bmatrix}\tilde{F}_i\\ \tilde{F}_k\end{bmatrix} = \begin{bmatrix}o & k\\ -k & o\end{bmatrix}\begin{bmatrix}\tilde{q}_i\\ \tilde{q}_k\end{bmatrix}$	$g_{nk} = \quad -\,(\ell_i q_k - \ell_k q_i)_n$

300

High Pressure Turbine   Generator   Exciter

Oil Film Forces

Clearance Excitation Forces
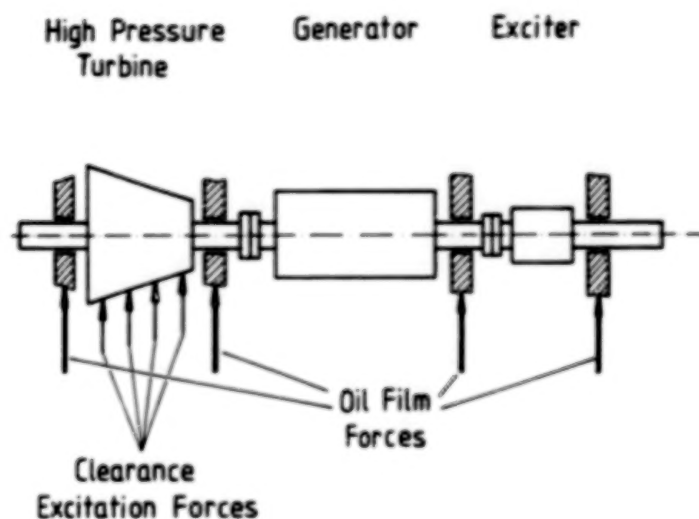
Figure 1. - Rotor of turbomachine.
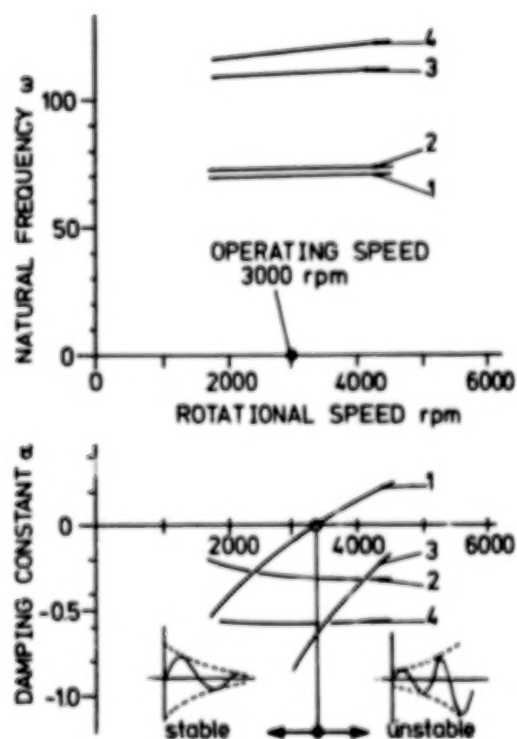
Figure 2. - Eigenvalues of turbomachine rotor.
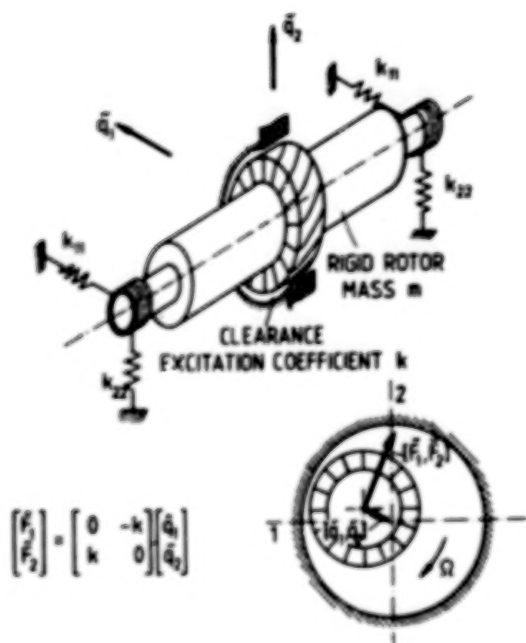
Figure 3. - Rigid rotor with flexible
supports and clearance excitation.
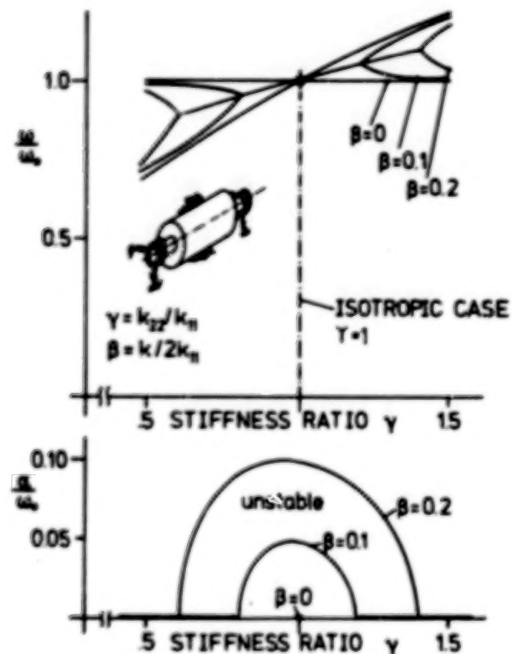
Figure 4. - Eigenvalues of rigid
rotor with flexible supports
and clearance excitation.
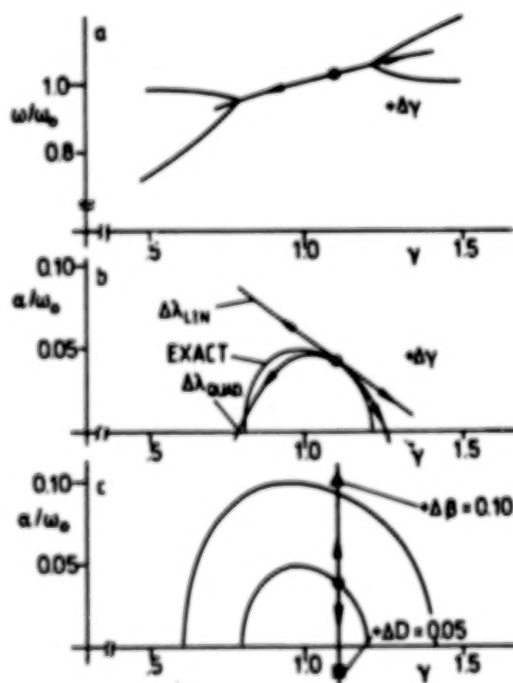
Figure 5. - Parameter variations at rigid rotor with flexible supports and
clearance excitation.
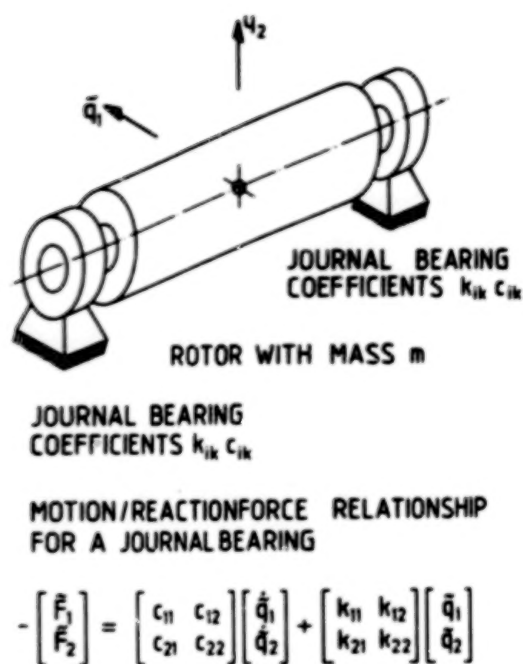
Figure 6. - Rigid rotor in journal
bearings.
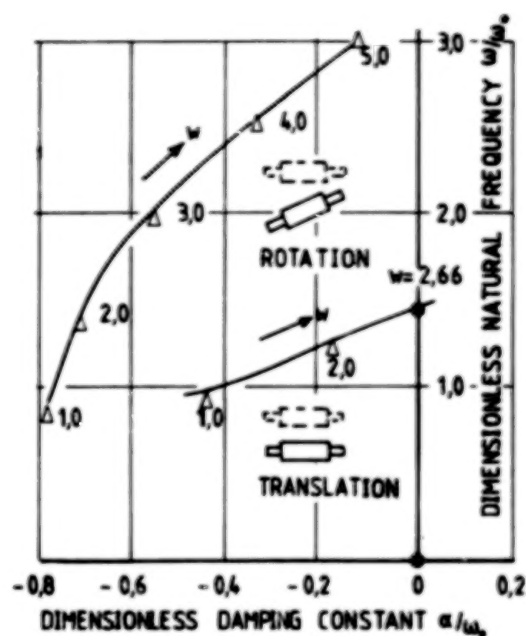
Figure 7. - Eigenvalues of rigid
rotor in journal bearings.
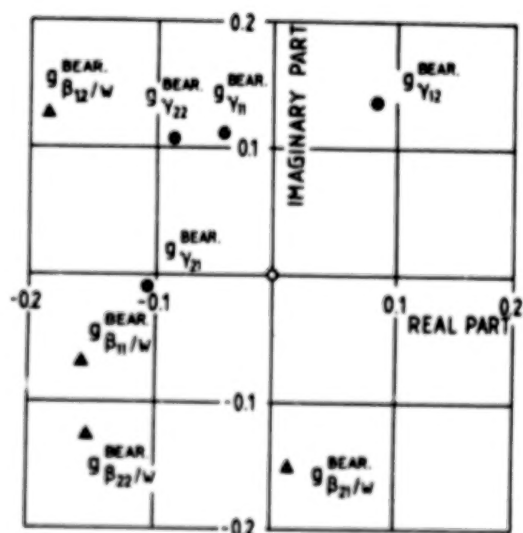
Figure 8. - Influence of bearing
coefficients to stability
behavior.
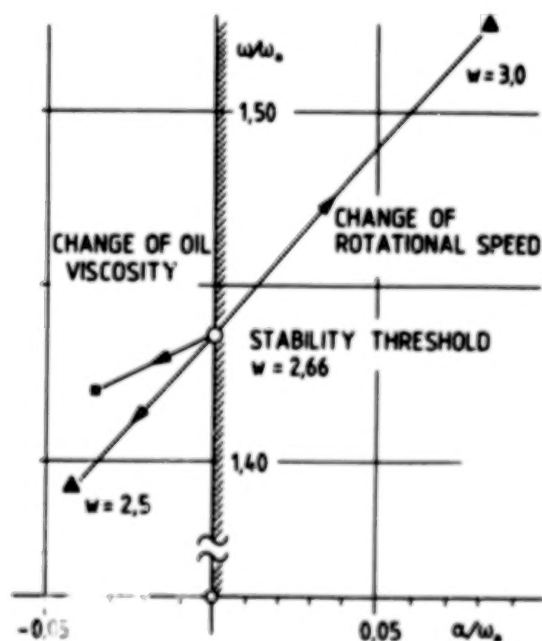
Figure 9. - Variation of rotational
speed and oil viscosity.

303
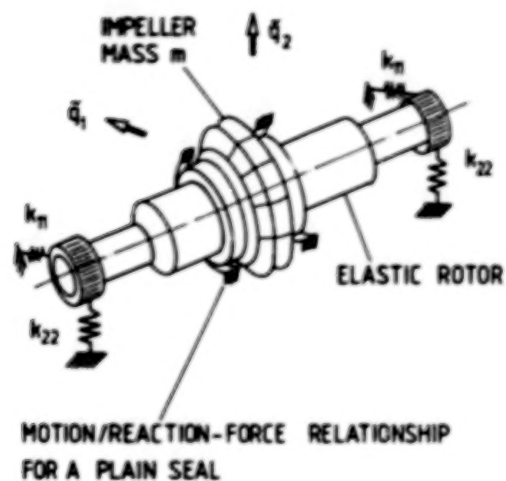
$$-\begin{bmatrix} \bar{F}_1 \\ F_2 \end{bmatrix} = \begin{bmatrix} m^* & \\ & m^* \end{bmatrix}\begin{bmatrix} \ddot{q}_1 \\ \ddot{q}_2 \end{bmatrix} + \begin{bmatrix} C & c \\ -c & C \end{bmatrix}\begin{bmatrix} \dot{q}_1 \\ \dot{q}_2 \end{bmatrix} + \begin{bmatrix} K & k \\ -k & K \end{bmatrix}\begin{bmatrix} q_1 \\ q_2 \end{bmatrix}$$

Figure 10. - Elastic turbopump rotor.
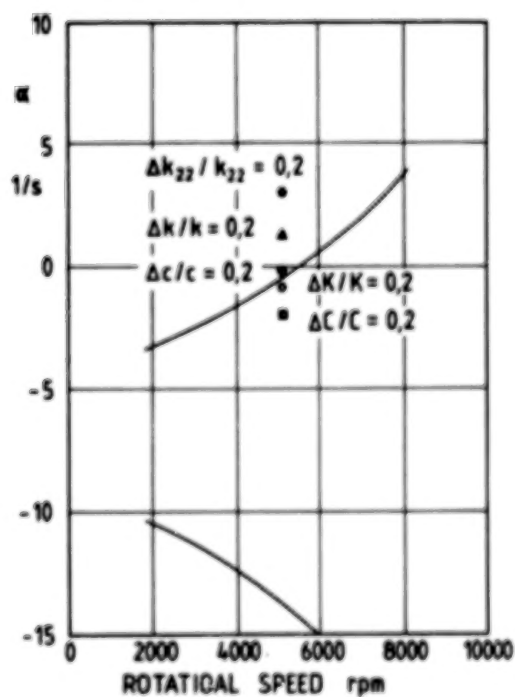
Figure 11. - Influence of seal stiffness and damping coefficients
to stability behavior of turbopump rotor.

304
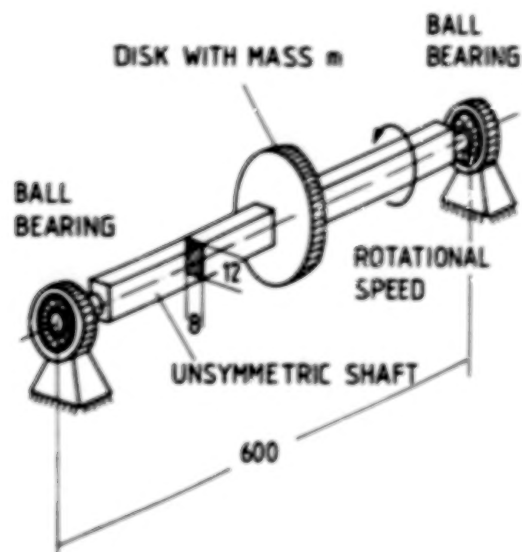
Figure 12. - Test rig rotor with unsymmetric shaft.
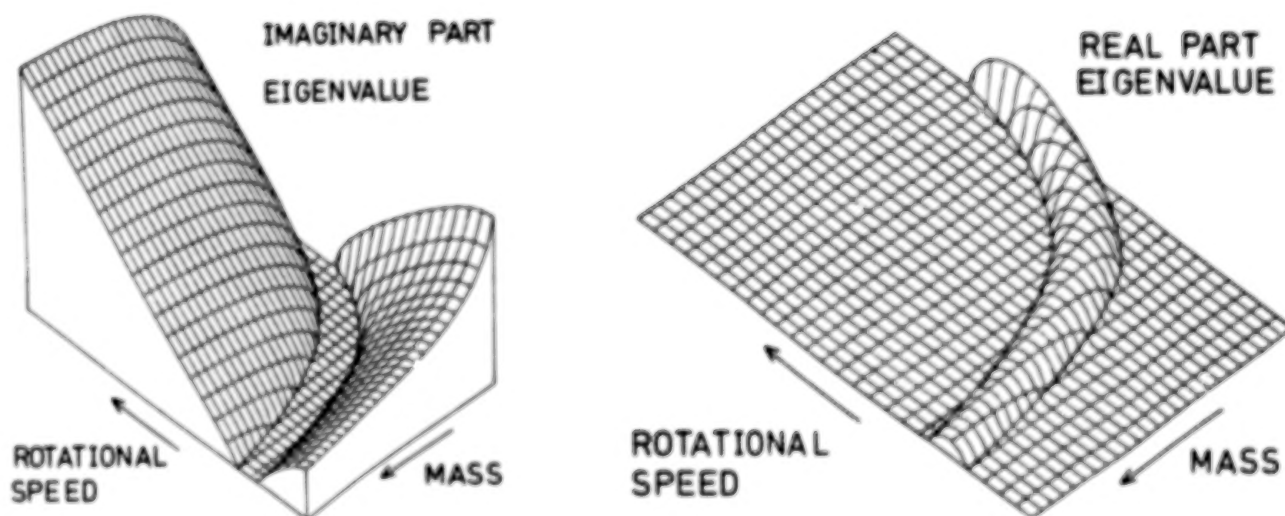
Figure 13. - Eigenvalues of rotor with unsymmetric shaft.
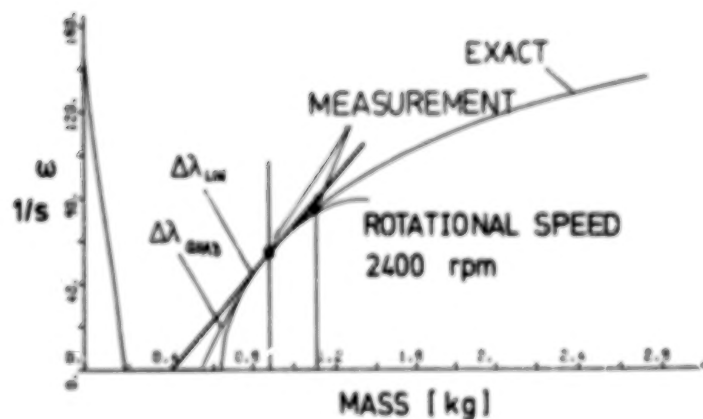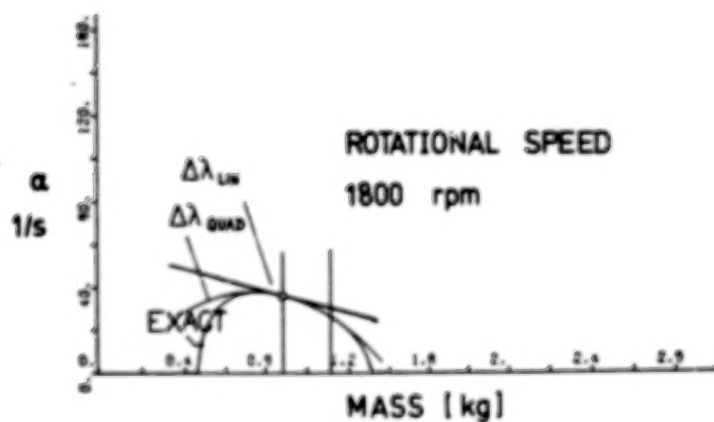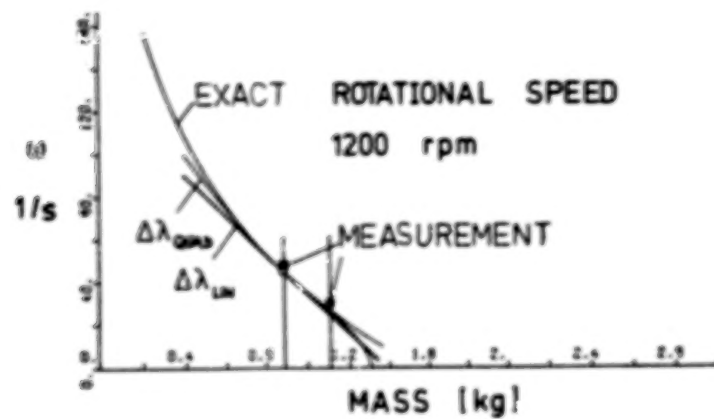
Figure 14. - Variation of eigenvalues in dependence of mass change.

STABILITY EVALUATION OF ROTOR/BEARING SYSTEM

BY PERTURBATION TESTS

Donald E. Bently and Agnieszka Muszynska
Bently Nevada Corp.
P.O. Box 157
Minden, Nevada 89423

SUMMARY

The paper presents the stability study of rotor/bearing systems. Even though it was limited to study of a fully lubricated bearing subject to oil whirl, and further limited to low eccentricity region for linearity and with only one type of lubricant, it can be seen that the perturbation methodology, together with the sorting of the impedance terms into direct and quadrature with respect to input force can be very useful to the general study of stability. Further, the concept of active feedback should assist to increase knowledge in rotor system stability. While there remains a large amount of study to be accomplished, perhaps some more tools are available to assist this field of analysis.

INTRODUCTION

The problem of rotor vibration in plain fluid bearing becomes more and more serious as operating speeds of turbomachinery continually increase. Two of the most significant sources of vibrations are fluid lubricated bearings and seals. Despite the high interest of field engineers and researchers which has followed the widespread application of oil/gas bearings and seals, the problems created by their hydrodynamic actions in turbomachines are still not solved completely [1-18].

This paper shows that the dynamic behavior of a rotor and its stability can be modeled as an active feedback mechanism, which should greatly help in clarifying the stability problems of rotor system. It further shows testing and data techniques for bearings and seals, and the evaluation of the performance of a perturbation test bearing.

The principal observed dynamic phenomena due to the lubricant action during shaft rotation are known as oil whirl and oil whip. Oil whirl appears at rotational speeds lower than twice the first bending critical speed of the rotor (corresponding to its first natural frequency), as a forward circular motion of the journal with the frequency nearly equal to half the speed of rotation. This motion is related to a loss of stability of a pure rotational motion (about a central position of the journal in the bearing, or more generally - an equilibrium position, determined by the static load) and creation of a stable steady circular motion with an amplitude affected by nonlinear factors of the oil film. In the performance of real machines, oil whirl may cause serious machine damage since the level of the steady-state whirling amplitude may exceed admitted tolerances of vibration.

Oil whip also has the character of forward motion, but unlike oil whirl, is locked to the frequency of the first self balance resonance (critical speed) of the rotor. The rotational speed must be of at least twice the resonance speed for oil whip instability to occur. Sometimes the rotor goes unstable in oil whirl, then converts

to oil whip when higher rotative speeds are reached. Oil whirl is not known to occur at higher speeds than oil whip.

In earlier years it was believed that for all of the forward circular instabilities that the range of rotative speeds from 2 to 2.5 times the self-balance resonance speed was required. However, more recent works [1] show that such instabilities may occur at any rotative speed ratio with respect to balance resonances, depending on the type of instability. Some machines in the field with severe gas whip problems show that this instability cannot be cured with the machine rotational speed below the first self balance resonance.

The literature on oil whirl/whip phenomena is quite rich [1-18]. The results concerning the loss of stability of the pure rotational rotor motion are usually presented in the form of stability charts describing the behavior of the rotor in the vicinity of the steady equilibrium position for different variable parameters. The stability rules indicated by different authors rarely agree in detail. This is not surprising - rotor response is very sensitive to slight variations in parameters (e.g., a change of temperature by a few degrees, or minor geometric asymmetry in the bearing may stabilize the rotor), and it has not been recognized that the active feedback is involved.

Classical analysis of the rotor/bearing systems usually starts from the very general Euler-Navier-Stokes equations. The solution of these equations, which may supply information concerning magnitude and functional relationship of hydrodynamic forces is unfortunately not easy to obtain. Analytical solutions require a lot of simplfying assumptions (such as idealized boundary conditions, neglecting thermal effects, ideal characteristics of lubricant, assumed pattern of the pressure distribution, neglecting curvature and capillarity effects of the lubricant, laminar flow, etc.). The resulting solution represents, then, only a rough approximation, as some of the neglected factors may happen to be dominant.

Numerical solutions of the Euler-Navier-Stokes equations, requiring, just as much, a number of simplifying assumptions, involve a lot of time-consuming computations [6] and can solve only some particular problems. Progress in computer facilities and numerical techniques, however, improves the possibility of achieving solutions, which allow for rotor/bearing coupling of motion and further parametric analysis. Parallel to the progress in computer sciences, a remarkable progress in experimental techniques and measurement facilities has been observed. The experimental results bring better understanding of dominating phenomena occurring during rotor/bearing motion. This, in turn, will clarify eventually the simplifying assumptions introduced in theoretical analyses.

In the present paper an experimental method of identifying the hydrodynamic forces in a plain cylindrical bearing during the oil whirl condition will be dicussed. The results are applicable to rotor/bearing or rotor/seal systems. The approach, based on analysis of forced response of the perturbed system, presents a continuation of previous research [7,8,9,12,13]. The mathematical model of the system considered is based on the linear theory of the rotor motion and fluid flow effects, as this series of tests have been deliberately run at low eccentricity numbers (generally less than 0.5).

The agreement of the experimental results and the predicted motion is very good. The method of investigation is shown to be very effective and sensitive to any parametric variation, so that it can be highly recommended in many applications.
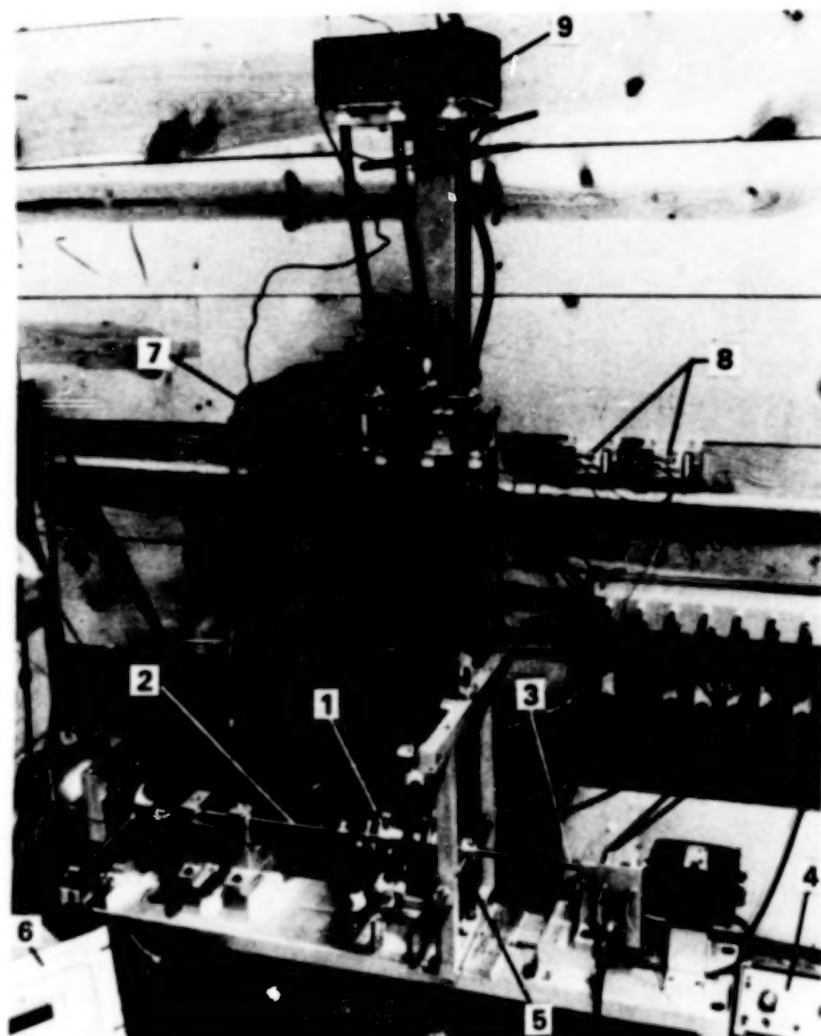
Figure 1. - Rotor test rig. 1 - Bearing, 2 - Main shaft, 3 - Perturbing shaft, 4 - Perturbing speed controller, 5 - Additional springs, 6 - Main shaft tachometer, 7 - Thermometer, 8 - Proximitors, 9 - Perturbed Reservoir.

The experimental rig to perform the perturbation test consists of two shafts with circular cross sections (Figs. 1,2). The main shaft rotates at the constant speed ω_R (being quite well below the first critical speed) in a rolling, pivoting bearing and in a plain cylindrical oil bearing with diameter D=2" axial length L=1.5" and radial clearance C=0.015". The second shaft rotating at perturbing speed ω_p in a pivoting bearing and a rolling antifriction bearing, is attached to the journal of the main shaft at the oil bearing. The transparent bearing, fed by blue dyed oil type ISO-VG-32 from an outboard tank with a constant pressure $p=7100$ N/m^2 permits direct observation of the distribution of the lubricant within the bearing .

Both shafts are driven by separate electric motors (0.75 HP for the main rotor, 0.1 HP for the perturbing one) through a flexible rubber coupling. For compensating weight of two shafts, a pulling vertical force is introduced in such a manner that during rotation of the main shaft, its response is a pure rotating motion in the center of the bearing. For this purpose, the main shaft is also straightened and balanced. At the same section of the shaft the additional symmetric springs can be introduced. The perturbing force is created by a controlled unbalance at the second shaft (calibrated unbalance masses attached to a single light disk mounted on the shaft). The unbalance inertia force is then proportional to the square of the perturbing speed ω_p .

The motion of the shaft journal is observed by two displacement motion, noncontacting probes (vertically and horizontally located) plus a Keyphasor probe to provide accurate phase and speed signals. Additionally the constant rotational speed of the main shaft and slowly variable rotation speed of the perturbing shaft are recorded. A special device designed to control constant angular acceleration of the perturbing shaft was used. The Keyphasor, horizontal and vertical probe signals, filtered to

the main (perturbing) frequency, were continuously observed on the oscilloscope monitor (orbits and time variable displays) and stored in the computer. The computer then provides numerical results and graphical representation of the amplitude/phase/ frequency relationships, or their derivatives ("Direct" and "Quadrature" Impedances, see expressions (9) and (10)). The physical model of the system is presented in Fig 2.

MATHEMATICAL MODEL OF THE SYSTEM
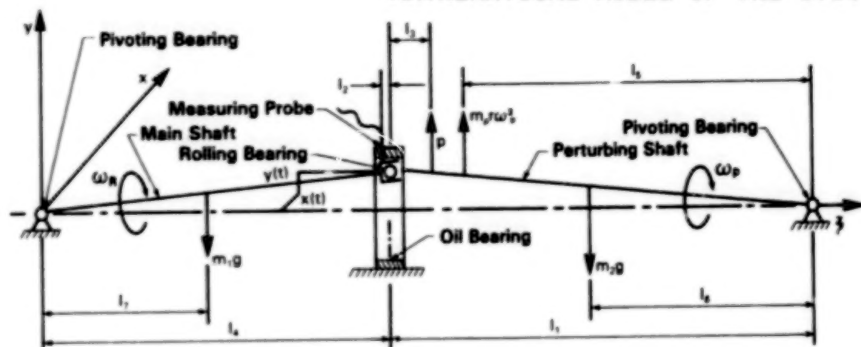
Figure 2. - Physical model of system.

The mathematical model is based on the assumption of "small" deflections, allowing for linerization. The angular motions of the shafts are then approximated by their linear radial deflections. The hydrodynamic forces are introduced in the oil bearing are introduced in their linear approximation. It was assumed that the system has only two degrees of freedom (horizontal (x) and vertical (y) deflections of the main shaft, as seen by the probes). The shafts are supposed rigid. External damping is neglected. With these assumptions, the equation of motion of the system is as follows:

$$M\ddot{z} + (J_1 w_R + J_2 w_p)i\dot{z} + Kz + F = U w_p^2 e^{iw_p t} + i P_1 , \tag{1}$$

where:

$$M = I_1/\ell_4{}^2 + I_2/\ell_1{}^2, \qquad J_1 = I_{1z}/\ell_4{}^2, \tag{2}$$
$$J_2 = I_{2z}/\ell_1{}^2, \qquad U = (\ell_4-\ell_2)\ell_5 m_p r/\ell_1\ell_4,$$
$$P_1 = (\ell_4-\ell_2)[P(\ell_1-\ell_3) - g (\ell_1 m_1\ell_7/\ell_4 + m_2\ell_6)]/\ell_1\ell_4$$

and

$$z = x + iy, \qquad i = \sqrt{-1} \tag{3}$$

combines in a complex variable the horizontal (x) and vertical (y) deflections of the journal; I_1, I_2, I_{1z}, I_{2z} are moments of inertia of the main (1) and perturbing (2) shafts (about the x or y and z axis), $\ell_1....,\ell_7$, are corresponding lengths (Fig. 2); w_R is main shaft rotational speed, w_p - perturbing shaft rotation speed, K - stiffness coefficient of the additional springs; m_p, r-mass and radius of the controlled unbalance, P - vertical constant pulling force, m_1, m_2 - masses of the main and perturbing rotors, g- gravity acceleration. F represents the hydrodynamic force in the bearing:

$$F = (m + m_t i)\ddot{z} + (d_r-d_t i)\dot{z} + (k_r-w_R k_t i)z , \tag{4}$$

where m, m_t, d_r, d_t, k_r and k_t are bearing coefficients.

The full symmetric linear two degree of freedom model of hydrodynamic forces is taken into consideration.

SOLUTION OF THE MATHEMATICAL MODEL

We simplify the mathematical model (1)+(4) neglecting gyroscopic terms ($J_2=J_2=0$) and the coupling "fluid inertia" term ($m_t=0$).

310

If the condition of stability is satisfied,

$$- |f_2| < \omega_R k_t / d_r < |f_1| ,$$ (5)

where f_1, f_2 are natural frequencies of the free vibration (see Appendix for details), then the dominating solution of (1) will be the forced response:

$$z = A e^{i(\omega_p t + \gamma)} + B,$$ (6)

where amplitude A and phase angle γ are

$$A = U \omega_p^2 / (D^2 + Q^2)^{\frac{1}{2}},$$ (7)

$$\gamma = \arctan (- Q/D),$$ (8)

with

Direct Impedance: $D = -(M + m) \omega_p^2 + d_t \omega_p + k_r + K$ (9)
and
Quadrature Impedance: $Q = d_r \omega_p - k_t \omega_R.$ (10)

Figure 3. - Phase frequency and amplitude/frequency responses of system.

Note that the phase angle γ corresponds to the attitude angle of the bearing.

The static displacement in the solution (6) is

$$B = \frac{P_1(i(k_r + K) - \omega_R k_t)}{(K + k_r)^2 + k_t^2 \omega_R^2} .$$ (11)

It will serve for evaluation of the stiffness coefficients by a preload test with no perturbation ($\omega_p = 0$). During the perturbation test (variable ω_p) the preload was eliminated ($P_1 = 0$).

TEST RESULTS.   IDENTIFICATION OF THE IMPEDANCES AS FUNCTIONS OF ROTATIONAL SPEED.   STABILITY CHECK

The experimental tests produced a set of results for the response amplitude A and phase angle γ versus (slowly varying) perturbation speed. The parameters of the set were rotational speed and temperature. The tests were performed for three cases: with additional springs (System "S"), with additional springs and mass (System "SM") and without

311

them (original system "0"). Fig. 3 presents an example of the test results for a rotational speed ω_R =200 rad/s. For a perturbation speed slightly less than half of the rotational speed, a well pronounced resonance was observed. This pattern repeated for all values of the rotational speed. In the resonance vicinity, the phase angle sharply changes values between zero and -90°. This behavior corresponds well to the predicted model of the system (see expressions (7), (8)).
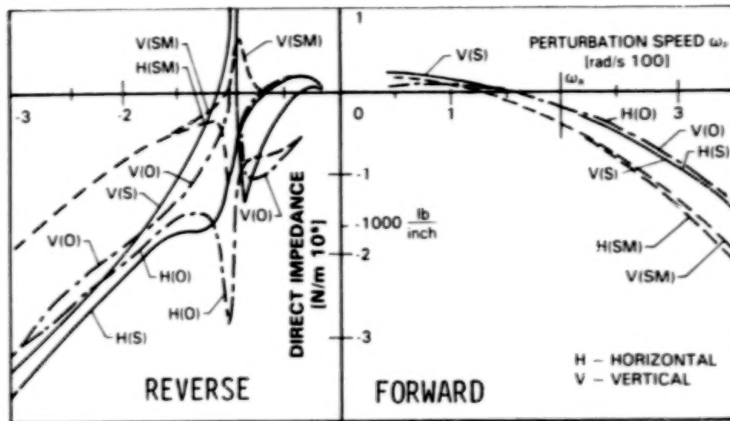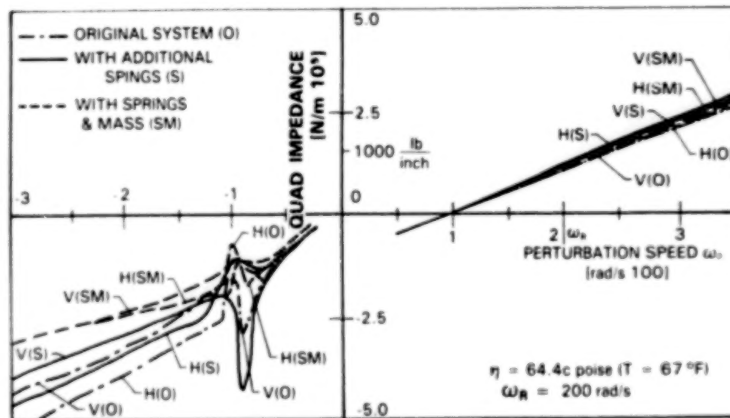
The system without additional springs and mass shows the highest resonance amplitude. An addition of springs lowers the amplitude considerably.

For the reverse perturbation speed resonance has not been observed although the system attempts to whirl forward. The amplitudes of vibration slowly increase with negative frequency, the phase angle slightly changes at the frequency corresponding to minus half ω_R. Major differences in horizontal and vertical phase angles are due to the 90° difference in probe readings. We observe however, some nonsymmetricity in the system, especially in the $-1/2\omega_R$ frequency region.

Figure 4. - Impedances versus perturbation speed for three cases.

The experimental data stored in the computer were transformed into the Direct and Quadrature Impedances:

$$D = U \, \omega_p^2 \, \cos\gamma \, /A \, , \qquad\qquad Q = -U \, \omega_p^2 \, \sin\gamma \, /A \qquad\qquad (12)$$

An example of the computer generated relationship between Impedances and perturbation speed for ω_R = 200 rad/s is given in Fig. 4. The graphs correspond to the results presented in Fig. 3. In all three cases the symmetry of the system for the forward perturbation speed was maintained - the amplitudes and phases showed to be the same for vertical and horizontal responses, the orbits were circular. At the reverse perturbation speed, we observed differences in horizontal and vertical Impedances.

Figure 5 presents a set of results of the response of the original system "0" for variable rotational speed. All other parameters of the system were kept constant during this test. The Direct Impedances have a roughly parabolic shape, while the Quadrature Impedances are nearly straight lines.

312
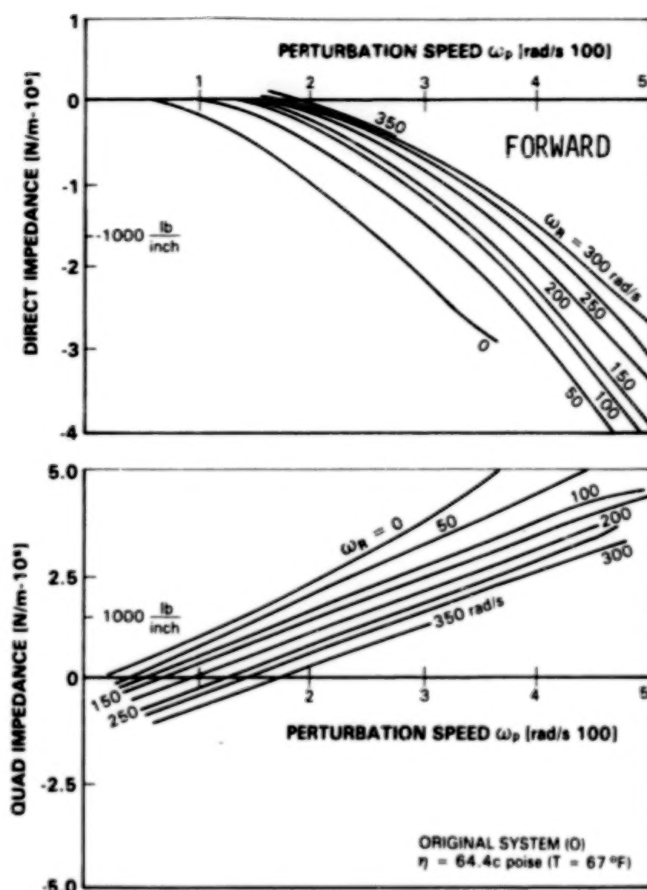
Figure 5. - Impedances versus perturbation speed for variable rotational speed.

The data taken from Fig. 5 served to obtain the cross relation for the Direct Impedance versus rotational speed with the perturbation speed as a parameter (Fig. 6). An analytical approximation to the Direct Impedance as straight line function of the rotational speed has been adapted:

$$D = C_1 \omega_R - C_2.$$

The next step of identification was an evaluation of the coefficients C_1 and C_2 as functions of the perturbation speed ω_p. For this purpose, the values of the Direct Impedance at zero perturbation speed and the slopes of the straight lines present in Fig. 6 were crossplotted as functions of the perturbation speed.

For both of these curves the parabolic approximation has been adapted [15]:

$$C_1 = -1.8 \cdot 10^{-3} \omega_p^2 - 2.5 \omega_p - 200 \ [kg/s]$$

$$C_2 = +0.25 \omega_p^2 - 950 \omega_p - 9.5 \cdot 10^4 \ [N/m]$$

Finally the Direct Impedance is described by for the following analytical form:

$$D/0.77 = -(1.8 \cdot 10^{-3} \omega_R + 0.25)\omega_p^2 - \omega_p (2.5\omega_R - 950) - 200 \omega_R + 9.5 \cdot 10^4, \tag{13}$$

where 0.77 was not yet taken into account the dimensional factor. Comparing this expression with the expression (9) derived from the mathematical model of this system and introducing M=0.4 kg, K=0, the identification of the parameters of the rotor can be completed:

$$m = m(\omega_R) = (1.4 \cdot 10^{-3} \omega_R - 0.21) \ [kg]$$

$$d_t = d_t(\omega_R) = -(1.9 \omega_R - 730) \ [kg/s] \tag{14}$$

$$k_r = k_r(\omega_R) = (7.3 \cdot 10^4 - 150 \omega_R) \ [N/m].$$

The Quadrature Impedances (Fig. 5) were identified as the straight lines; varying with rotational speed.

$$Q = (970 - 0.69\omega_R)(\omega_p - \lambda\omega_R), \tag{15}$$

where

$$\lambda = \frac{\omega_p|Q=0}{\omega_R} \tag{16}$$

313

Figure 6. - Direct impedance versus rotational speed
and variable perturbation speed.

is the ratio of the perturbation speed for which the Quadrature Impedance has a zero value to the rotational speed ω_R. The parameter λ appeared to be nearly constant for all performed tests: $\lambda = 0.48$.

Its value agrees with the oil whirl ratio observed in practice. The value $\lambda\omega_R$ corresponds to the average oil velocity.

The comparison between the expressions (10) and (15) leads to the identification of the system parameters:

$$d_r = d_r(\omega_R) = (970-0.69\ \omega_R)\ [kg/s]$$

$$k_t = k_t(\omega_R) = (470 - 0.33\ \omega_R)\ [kg/s] = \lambda d_r(\omega_R) \tag{17}$$

and $m_t = 0$, as it has been already assumed.

As we notice, all parameters of the system are functions of the rotational speed ω_R. It was not possible to obtain test results for very low values of the perturbation speed. For this reason a "displacement" test was performed. The main shaft rotating at constant speed was perturbed by a constant pulling force P. The probes measured vertical and horizontal displacements. The force-response characteristics showed to be linear in relatively wide range of displacements, however, their slopes varied considerably with the rotational speed. The formula (11) served for the identification the parameters k_r and k_t (K=0 in this test*):

$$k_r = 4000\ N/m\ (for\ 0 < \omega_R \leq 150\ rad/s) \tag{18}$$
$$k_t^r = (\ 490-0.27\omega_R)\ [kg/s].$$

The evaluation of the coefficient k_r was not very precise. However, its relatively

---

* The calculation of the coefficients k_r and k_t was performed indirectly. First the slopes of the straight lines corresponding to the pulling force P_1 versus horizontal (x) and vertical (y) displacements were evaluated for different values of the rotational speed.
The slopes are equal to "directional" stiffnesses $K_x = P_1/x$, $K_y = P_1/y$, corresponding to x and y. Taking (6) and (11) into account the stiffness coefficients

$$k_r = K_y\ /\ (1+(K_y/K_x)^2), \qquad k_t\omega_R = k_r K_y/K_x$$

were then calculated for each value of the rotational speed.

small value was noticed especially for higher ω_R. The agreement with the previously evaluated coefficient k_t (expression (17)) is very good.

Having evaluated the parameters of the system the stability check has been possible.

Introducing the expressions (14) and (17) into the stability criterion (5) and rearranging terms, we obtain the cubic polynomical inequality:

$$1.29\ \omega_R^3 + 3030\ \omega_R^2 - 6.17 \cdot 10^5 \omega_R - 2.29 \cdot 10^8 < 0 \tag{19}$$

The polynominal (19) has one positive root ω_R = 366 rad/s. The stability criterion, then, has the form: $\omega_R < 366$ rad/s.

Figure 7. - Perturbation speed at zero impedances and stability margins.

During the experiment it was observed that for rotational speeds higher than 350 rad/s the rotor became unstable, which is consistant with the above analysis.

We notice that the value of amplitude peaks is closely related to the difference between perturbation speeds at which Direct Impedance and Quadrature Impedance equal to zero (Figs. 3 and 4). This difference is referred to as the stability safety margin Δ (see Appendix). In Fig. 7 the values of perturbation speed for zero impedances have been plotted. The margin of stability decreases with the rotational speed. For the considered systems ("O","S", and "SM") the zeros of the Quadrature Impedance remain the same. The additional springs and mass have influence on the Direct Impedance only.

At the reverse perturbation speed, the Quadrature Impedance is negative for all speeds (compare (10) for ω_p negative, see also Figs. 4 and 5). It does not cross zero; the system is very stable.

Figure 8 presents the impedances for the squeeze film test (ω_R=0). We notice the symmetric parabolic shape of the Direct Impedance and antisymmetric (straight line) for the Quadrature Impedance. (Slight displacement of the lines from zero at ω_p=0 is due to very low input force level). As expected, tangential stiffness, being related to the rotational speed, equals zero when ω_R=0.

In the squeeze film test the Quadrature Impedance contain then only the radial damping term d_r (see (10)), which appears to be positive. The condition of stability (5) is satisfied for all rotational speeds. The displacement of the

315
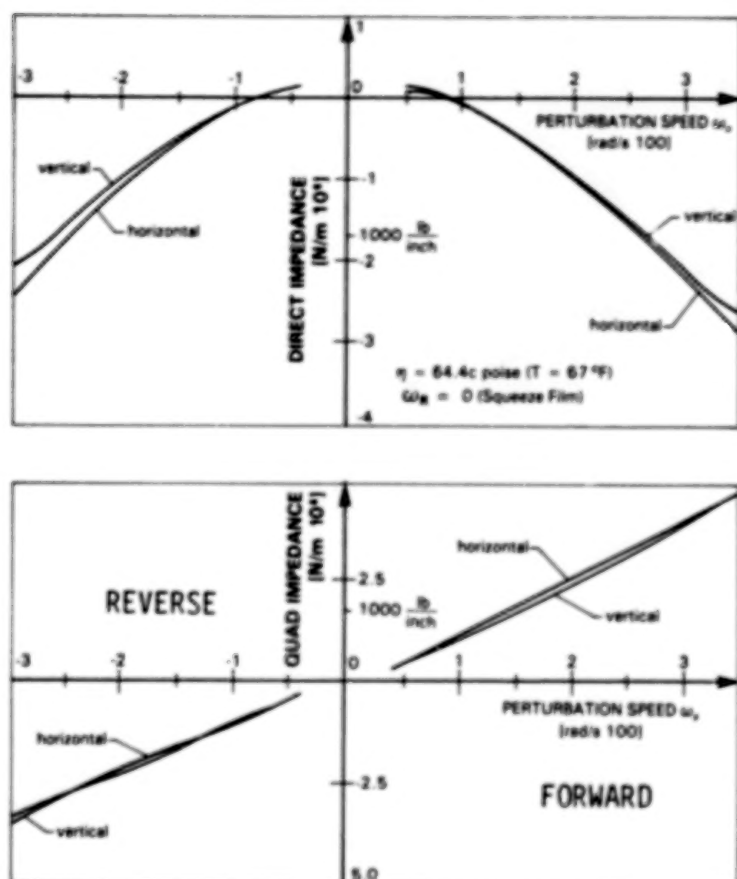
Figure 8. - Impedances versus rotational speed for squeeze film.

Direct Impedance parabole from the symmetric position for $\omega_R=0$ into the region of positive perturbation speeds for $\omega_p>0$ indicates a relationship of the tangential damping d_t with rotational speed. $d_t=0$ for $\omega_R=0$ and $d_t>0$ for $\omega_R>0$ within the investigated range of speed. (See (14) for comparison).

The Fig. 9 presents the Direct and Quadrature Impedances for variable oil temperature. The variations of the Quadrature Impedance are quite significant while the Direct Impedance remains nearly invariable in the wide temperature range, especially for lower values of the perturbation speed. Let us evaluate the Quadrature Impedance as a function of temperature. From the graphs Fig. 9 the relation between the slope of the Quadrature Impedance versus temperature and the speed ratio λ can be obtained. Finally the Quadrature Impedance is evaluated as follows [15]:

$$Q/0.77 = (1700 - 10T) \; [\omega_p - \lambda(T)\omega_R] \; [N/m],$$

$$\lambda(T) = 0.48 \; (1.1 - 1.8 \cdot 10^{-3} T),$$

where T is temperature in Farenheit degrees. Further we derive the relationship between temperature and oil viscosity (measured by Cannon-Fenske Viscosimeter 200), so that the Quadrature Impedance can be expressed in terms of the oil viscosity. If the Direct Impedance is known for any temperature, then a correcting factor can be introduced for the value of Direct Impedance corresponding to any different temperature [15].

Summarizing the test results, we see that the predicted model well reflects the main dynamic features of the system. The Direct and Quadrature Impedances can be identified easily as a function of the system parameters and in particular, as a function of the rotational speed.

ACTIVE SERVOMECHANISM CONCEPT

The ability of a lubricated bearing to support both steady-state and dynamic loads by forming a springy cushion consisting of a fluid wedge is well known. It is also well known that a 360° lubricated bearing has a propensity for instability known as oil whirl/whip. In fact, even before the outstanding work of Newkirk and Taylor [10] or Hull [11-13], Harrison [14] predicted in 1919 that the full lubricated bearing would be unstable.

316

BEST DOCUMENT AVAILABLE

Figure 9. - Impedances versus perturbation
speed with variable viscosity (temperature)
of the oil.

The study of rotor instability has generated a vocabulary including such expressions as cross springs, cross damper, (and even cross masses), negative damping, etc. Such cross actions exist as effects, unlike gyroscopic action which is a genuine cross coupling physical law. The reason why these cross coupling bearing and seal effects occur is that such elements clearly have a behavior much more complex than any possible passive systems. These machine elements contain active feedback, in which exists a mechanism transferring rotational energy into lateral vibration energy. This is true for every identifiable rotor instability of the forward circular whirl and whip category, including shaft internal friction, aerodynamic cross coupling or steam whip. In particular, the behavior of a 360° lubricated bearing is analyzed herein. The situation in any gas or liquid seal is also generally in the 360 degree category so that the results can then be extended to any seal or bearing dynamic behavior. To show in simple description that such systems are actually closed loop servomechanisms, observe the performance of the bearing in response to a steady-state load.

Apply a downward pressure to a shaft rotating anticlockwise with no initial dynamic or steady-state preload. The obvious and well known result is that the shaft moves downward very slightly, and moves strongly to the right. This motion, of course, provides the converging lubricant wedge to support the applied downward load. Since lubricant has virtually no spring effect of its own, the action generates the spring cushion synthetically. Applying a downward steady-state load as a step function, the first effect is for the shaft to move downward in response to passive direct (radial) damping (d_r) . The result of this downward action is to create a restriction of oil flow at the bottom. This in turn creates a converging wedge on the left, which forces the shaft to the right. This process continues (usually with some damped whirling), until the shaft reaches an equilibrium position in which forces are balanced. This position to the right is sufficient to create the constriction which provides the wedge to support the shaft against the input force because the input to the active element is motion and the output is force, as previously described.

The dimensions of the active elements are that of impedance. It then seems reasonable to present the rotor/bearing system as a servomechanism with a feedback loop containing active elements of the system (Fig. 10). The general transfer

function of the system (described by Eqs. (1) and (4)) is given in the Appendix. As it has been shown in the previous section, the parameters related to the bearing depend directly on rotational speed - they represent active elements. The term "active" refers to the mechanism of transformation of rotational energy into vibration energy, which provides the major reaction to input forces.

The input to the system is represented by the exciting periodic force as well as static load ($\phi(\omega_p i)$ - see Appendix).

The output is the motion - vertical and horizontal displacements of the main shaft ($z(i\omega_p)$).

The output motion with respect to the input force shows all of the active and passive terms in simple series (see (A8)). As such, it could be optional which ones are put in the active category, with the remaining ones left in the passive category. However, the static loading test provides a perturbation speed of $\omega_p=0$ so that all terms con-

Figure 10. - Rotor-bearing active feedback diagram.

taining ω_p as a multiplier are deleted. These terms deleted entirely are the passive terms. Further, the squeeze film tests, where rotative speed $\omega_R=0$ deletes all terms containing ω_R as a multiplier. The terms which are deleted entirely can be considered as the active terms. These observations indicate the proper location of the terms.

If a further check is desired, since it is fundamental that springs with negative stiffness cannot exist as real passive impedances, any negative stiffness term component necessarily represents the active portion of the feedback loop. Since spring force is motion times spring coefficient, in order to supply the restoring force against input force the elastic force must be at nearly 90 degrees with respect to motion, because the motion itself is nearly 90 degrees with respect to input force (Fig. 11).

As a result, the so called "cross spring" is actually the very real (but synthetically manufactured by feedback) restoring spring force. In review of the active behavior of such a bearing it is at the same time extremely simple with only one moving part, as well as extremely complex, because this one working part performs several functions.

Figure 11. - Force diagram for rotational speed below resonance.

Summarizing these considerations we describe the transfer function of the active feedback loop in the following form (Fig. 10):

$$\bar{k}_r - i\omega_R \tilde{k}_t \sin\alpha = \tilde{k}_t \omega_R (\cos\alpha - i\sin\alpha) = \tilde{k}_t \omega_R e^{-i\alpha},$$

(20)

where $\bar{k}_r = \tilde{k}_t \cos\alpha$, $k_r = \bar{k}_r + \bar{\bar{k}}_r$, $k_t = \tilde{k}_t \sin\alpha = \lambda d_r$.

The active loop then contains a fraction of the ω_R dependent coefficient k_r (radial stiffness) and full tangential stiffness coefficient. The last one is entirely the result of oil wedge formation. As it was identified in the previous section, the radial stiffness contains a constant term and a term varying with the rotational speed. However, a precise identification was difficult in view of its relatively small value.

It is supposed that the terms located in the feedback loop are directly responsible for the transfer of rotational energy into vibrations. The angle α represents the angle between the observed motion and the active force (Fig. 11). This angle is usually a little less than 90 degrees for 360° fluid bearing. For other types of bearings it is nearer 0 degrees (e.g. for sleeve bearings with stable void islands in the thick film region, generally referenced to as "180 Degree" or "Half Sommerfeld" bearings).

In the present study it has been found that the radial spring coefficient has a low value, for $\alpha \cong 90°$ $\cos\alpha$ is very small - this is reflected in the expression (20). However, at this time we have not found a means to measure directly the angle α.

All other terms of the rotor system are located in the "passive" part of the servomechanism model (Fig. 10). Being functions of the rotational speed, they may also modify the rotor response in some "active" way, however to a lower degree than the ones related to stiffnesses.

A rotating shaft in a bearing does (1) have passive impedance, (2) transfers energy from input torque by dragging lubricant around, (3) moves sidewise of the input force (as best it can) to provide a restriction of flow to the lubricant to build a converging wedge for support, and finally (4) synthetically builds a force to counteract the input force.

Rotor systems, as currently configured, are rarely well stabilized because (1) their basic algorithims are complex, nonlinear and nonsymmetric, and (2) there has been lack of recognition and knowledge of this feedback nature of rotor behavior. The present paper throws some light on these problems, however much more research is needed to provide answers to all questions related to the rotor/bearing/seal stability.

REFERENCES

1. Tondl A., "Some Problems of Rotor Dynamics", Czechoslovak Academy of Sciences, Prague 1965.
2. Vibrations in Rotating Machinery, Proc. of the Conference, University of Cambridge, The Institution of Mechanical Engineers, Cambridge, U.K., 1976.
3. Rieger, N.F., "Rotor-Bearing Dynamics: State of the Art 1976", Shock and Vibration Digest, v. 9, No. 5, 1977.
4. "Rotordynamic Instability Problems in High Performance Turbomachinery", Proc. of a Workshop, Texas A & M University, College Station, Texas, 1980.
5. Tribology International, 0301-979X/80/050233, JPC Business Press, October 1980.

6. Hankey, W.L., "Self Excited Oscillation in Fluid Flow", University of Dayton Research Institute Seminar, May 1981.

7. Bently, D.E., Bosmans, R.F., "Oil Whirl Resonance", Trans ASME, April 1979.

8. Bently, D.E., "The Parameters and Measurement of the Destabilizing Actions of rotating Machines and the Assumptions of the 1950's", in [4].

9. Kanaki, H., Mitsubishi Heavy Industries, LTD, Takasayo, Private communication, 1981.

10. Newkirk, B.L., Taylor, H.D., "Shaft Whipping Due to Oil Action in Journal Bearings", G.I. Review, v. 28, 1925.

11. Hull, E.H., "Oil Whip Resonance", Trans ASME, October 1958, pp. 1490-1496.

12. Hull, E.H., "Journal Bearing Behavior Under Periodic Loading", G.I. Research Laboratory, Rep. No. 55-RL-1354, Schenectady, New York, 1955.

13. Hull, E.H., Darrow K.A., "Hydrodynamic Oil Film Stiffness", G.I. Research Laboratory, Rep. No. 59-RL_2217, Schenectady, New York, 1959.

14. Harrison, W. J., "The Hydrodynamic Theory of the Lubrication of a Cylindrical Bearing Under Variable Load", Trans Cambridge Philos. Soc., v. 22, 1919.

15. Bently, D.E., Muszynska, A., "Stability Analysis of Cylindrical 360° Bearing Oil Whirl", Bently Nevada Report, 1982 (to appear).

16. Adams, M.L., Padovan J., "Insights Into Linearized Rotor Dynamics", Journal of Sound and Vibration, 76 (1), 1981.

17. Lund, J.W., Thomsen, K.K., "A calculation Method and Data for the Dynamic Coefficients of Oil Lubricated Journal Bearings", Topics in Fluid Film Bearing and Rotor Bearing System Design and Optimization, ASME, 1978.

18. Childs, D.W., Dressman, J.B., "Testing of Turbulent Seals for Rotor Dynamic Coefficients," in [4].

APPENDIX

AI. EIGENVALUE PROBLEM FOR THE EQUATIONS (1) AND (4)

The homogeneous equation (1) with hydrodynamic forces (4) has the following eigenvalues:

$$\lambda_{1,2,3,4} = (-d_r \pm i(d_t - J_1\omega_R - J_2\omega_p))/(2M+2m) \pm (\alpha_1 + i\alpha_2), \tag{A1}$$

where

$$\alpha_j = \left[(-1)^j \left((d_t - J_1\omega_R - J_2\omega_p)^2 - d_r^2 + 4((M+m)k_r + m_t k_t \omega_R)\right) + \right.$$

$$+ \left(((d_t - J_1\omega_R - J_2\omega_p)^2 - d_r^2 + 4((M+m)k_r + m_t k_t \omega_R))^2 + \right. \tag{A2}$$

$$\left. + 4 (d_r(d_t - J_1\omega_R - J_2\omega_p) + 2(m_t k_r - (M+m)k_t \omega_R))^2 \right)^{\frac{1}{2}} \right]^{\frac{1}{2}} / (\sqrt{8}(M+m)), \quad j=1,2.$$

The condition of stability (negative real parts of the equinvalues (A1) is as follows:

$$d_r((M+m)k_r + m_t k_t \omega_R) - d_r(d_t - J_1\omega_R - J_2\omega_p)(m_t k_r - (M+m)k_t \omega_R) - (m_t k_r - (M+m)k_t \omega_R)^2 > 0. \tag{A3}$$

For $J_1 = J_2 = m_t = 0$ it reduces to

$$-(M+m)(k_t \omega_R/d_r)^2 + k_t \omega_R d_t/d_r + k_r > 0 , \tag{A4}$$

or after transformation to

$$-|f_2| < \omega_R k_t/d_r < |f_1| , \tag{A5}$$

where

$$f_j = \pm \left[d_t/(2M+2m) + (-1)^j ((d_t/(2M+2m))^2 + k_r/(M+m))^{\frac{1}{2}} \right], \quad j=1,2 \tag{A6}$$

are natural frequencies of the system at the limit of stability, i.e., when instead of inequality (A4) we have the equation. As we can easily check f_1 and f_2 are also the roots of the Direct Impedance (9).

For $k_t > 0$ the quantity

$$\Delta = f_1 - \omega_R k_t/d_r > 0 \tag{A7}$$

gives a margin of safety for the stability. As the value $\omega_R k_t/d_r$ is the root

of the Quadrature Impedance (10), the stability of the perturbed system is assured if the zero of the Quadrature Impedance appears at a lower perturbation speed ω_p than the zero of the Direct Impedance.

AII. FOURIER TRANSFORMATION OF THE EQUATIONS (1) and (4).

The mathematical model of the system can be presented applying the Fourier transformation and the control theory formalism. From (1) and (4) we get then

$$z (i\omega_p) [D (i\omega_p) + iQ (i\omega_p)] = L [\emptyset (i\omega_p)] \tag{A8}$$

where $z (i\omega_p)$ is the Fourier transformation of the variable $z(t)$ (2), $i\omega_p$ is

the Fourier operator, $D(i\omega_p)$, $Q(i\omega_p)$ are given by (9),(10), $L [\emptyset (i\omega_p)]$ is

the Fourier transformation of the input forces $\emptyset = U\omega_p^2 e^{i\omega_p t} - iP_1$. $[D(i\omega_p) +$

$+iQ (i\omega_p)]$ is the transfer function of the system.

NOTATION

A	Amplitude of the response
C	Bearing radial clearance (0.015"=3.8 10^{-4} m)
d_r, d_t	Radial and tangential bearing damping coefficients
D	Direct Impedance
g	Acceleration of gravity
I_1, I_2	Moments of inertia of the main (1) and perturbing (2) shafts about x or y axis (24.8 gm^2, 6.7gm^2; I_1=50 gm^2 for the case of additional mass)

321

Symbol	Description
I_{1z}, I_{2z}	Moments of inertia of the main and perturbing (2) shafts about the axis of rotation (0.0650gm^2, 0.03gm^2; $I_{1z}=0.0652\text{gm}^2$ for case of additional mass)
k_r, k_t	Radial and tangential bearing stiffness coefficients
K	Equivalent stiffness coefficient of the additional springs (33100 N/m=189 lb/inch)
l_1	Length of the perturbing shaft (9.5"=0.241m)
l_2	Distance from the center of bearing to the probe (0.625"=0.0159m)
l_3	Distance from the bearing center to the pulling force section (2"=0.0508m)
l_4	Length of the main shaft (11.75"=0.298m)
l_5	Distance to the position of the perturbing force (7.7"=0.195m)
m_1, m_2	Masses of the main and perturbing shafts with accessories (280g, 150g)
m_p	Perturbing unbalance mass (4g)
m_r, m_t	Radial and tangential bearing "fluid inertia" coefficients
"O"	Original system
P	Pulling force
Q	Quadrature Impedance
r	Radius of the controlled unbalance (33/32"=0.0262m)
R	Radius of the shaft journal (1.00"=0.0254m)
"S"	System with additional springs
"SM"	System with additional springs and mass
γ	Phase of the response – Attitude angle
Δ	Stability margin
η	Dynamic viscosity of oil (poise)
λ	Oil rotation speed ratio
ω_p	Perturbation speed (perturbing shaft)
ω_R	Rotation speed (main shaft)

AERODYNAMIC STIFFNESS OF AN UNBOUND ECCENTRIC WHIRLING CENTRIFUGAL

IMPELLER WITH AN INFINITE NUMBER OF BLADES

Paul E. Allaire
Department of Mechanical and Aerospace Engineering
University of Virginia
Charlottesville, Virginia   22901

Lyle A. Branagan
Pacific Gas and Electric
San Ramon, California   94583

John A. Kocur
Department of Mechanical and Aerospace Engineering
University of Virginia
Charlottesville, Virginia   22901

ABSTRACT

This paper considers an unbounded eccentric centrifugal impeller with an infinite number of log spiral blades undergoing synchronous whirling in an incompressible fluid. The forces acting on it due to coriolis forces, centripetal forces, changes in linear momentum, changes in pressure due to rotating and changes in pressure due to changes in linear momentum are evaluated.

NOMENCLATURE

Symbol	Definition
$\vec{a}$	Vector acceleration
a	Impeller perturbation
b	Thickness of two-dimensional impeller
$\vec{F}_P$	Vector pressure forces
$\vec{F}_s$	Vector surface forces on control volume
$\vec{F}_{SHAFT}$	Vector force of the shaft on the fluid
ΔF_{ij}	Change in force in i direction due to perturbation in j direction
K_{xx}	Principal stiffness
$\bar{K}_{xx}$	Dimensionless principal stiffness, $(K/\rho U_{R_1} R_1)$
K_{yx}	Cross-coupled stiffness
$\bar{K}_{yx}$	Dimensionless cross-coupled stiffness
n	Number of blades

323

0	Center of flow field
$0'$	Geometric center of impeller
$\bar{R}$	Dimensionless radii ratio, (R_2/R_1)
R_1	Inner radius of impeller
R_2	Outer radius of impeller
R_B	Radius of impeller with respect to center of flow field
U_{R1}	Average radial inlet velocity in fixed coordinate frame
U_B	Radial velocity at point B
V_B	Relative velocity of rotating coordinate system at point B
$\vec{V}$	Analytic velocity expression for force equation
W_B	Velocity in rotating coordinate system at point B
$\vec{W}_{TOT}$	Vector velocity at any point in rotating coordinate system
β	Blade angle ($\tan\beta = U_{R_1}/\omega R_1$)
ε	Dimensionless eccentricity
θ	Angle measured from x axis
θ_1	Entrance angle
θ_2	Exit angle
θ_b	Blade sweep angle ($\theta_b = \cot\beta \ln(R_2/R_1)$)
θ'	Angle of fluid particle along blade
ρ	Fluid density
ω	Angular speed of the impeller

1. INTRODUCTION

The analysis of turbomachinery requires a combination of solid mechanics and fluid dynamics. Vibrations of a centrifugal pump or compressor are controlled by the bearings, by the shaft geometry, by fluid forces on the impeller, by seals, and other factors. Often the nature and magnitude of the forces and stiffnesses generated by bearings and shaft geometry are fairly well understood and can, in general, be accurately modeled. Those forces acting on the impeller can rarely be adequately determined as yet. These forces arise from the interaction of the impeller with the driven fluid, and are often called "aerodynamic forces," "aerodynamic stiffnesses" or "aerodynamic cross-coupling".

Much of the large body of work on incompressible flows in impellers assumes a centered impeller with varying degrees of complexity. A few examples include one-dimensional velocity vectors [1], two-dimensional considerations [2,3], and full three-dimensional analysis [4,5,6]. These are not discussed further.

Calculation of aerodynamic forces was first reported by Alford [7], considering circumferential variations of static pressure and efficiency in axial compressors.

Work by Black [8], Barrett and Gunter [9], Lund [10], and Gunter, et al. [11], have demonstrated the importance of aerodynamic forces to the safe operation of turbo-machinery, but have not, in general, addressed the calculation of these forces, or their associated stiffnesses. Further, in the work by Barrett [9] and Gunter [11], these forces are modeled by their cross-coupled stiffness only; consideration is not given to the principal stiffness of the fluid-impeller interaction.

Several recent papers have sought to more accurately quantify these forces. Colding-Jorgensen [12] used a simple source and vortex flow model for the impeller along with a series of vortex sheets representing the pump volute. He then super-imposed a uniform flow over this model, without clear physical explanation, to deter-mine the forces on the volute, as a function of the volute spiral angle. The flow field emerging from the impeller is assumed to correspond with the typical one-dimen-sional analysis, except that its location is perturbed. The force calculated by this method is the total force acting on the entire impeller/volute model for uniform flow - not the force on the impeller.

The work by Shoji and Ohashi [13] considers an ideal impeller whirling about its geometric center. Blades are modeled by vortex sheets using unsteady potential theory with shockless entry to predict the flow field within the impeller. Forces on the blades are summed from the pressures calculated by an unsteady Bernoulli equation. The calculation is two-dimensional without volute or vaned diffuser effects but does allow for a whirl frequency other than the rotational speed.

The papers by Thompsen [14,15] outline the assumptions and general theory con-tained in a proprietary program. The technique uses unsteady flow theory and deter-mines the stability of the rotor stage based on nonsynchronous fluid excitations. The proprietary nature of the program limits the discussion of the details of the procedure. An actuator disc method for calculating forces is currently being used by Chamieh et al. [16]; however, the work is incomplete and detailed results are lacking.

A paper by Jenny and Wyssmann [17] suggests the aerodynamic excitation is approximately two orders of magnitude smaller than other destabilizing mechanisms. Their simplified analysis, however, considers only the variation in radial clearance, while neglecting the change in momentum of the fluid. In a radial flow machine, the change in force due to clearance variations should be negligible compared to changes in force due to momentum variations since the former are perpendicular to the main flow path.

A paper by Washel and von Nimitz [18] gives an empirical formula for aerodynamic cross coupling forces in compressor impellers. It is used for comparison to the theory developed in this work.

The purpose of this paper [19] is to consider the nature and magnitude of aero-dynamic cross-coupling forces and stiffnesses as generated by the change in fluid momentum in an eccentric impeller. The approach is to perform a control volume analysis on a perturbed, infinite bladed impeller undergoing a steady orbit at the rotational speed of the shaft. This assumes incompressible, ideal flow without volute or diffuser effects. It further assumes that the impeller consists of an infinite number of infinitely thin blades of simple geometry; the use of which allows an analytic expression for the aerodynamic forces to be obtained. Boundary layer development separation, and secondary flows, however, are not considered. The forces calculated are generated by a perturbation of the impeller about the flow center and thus are related to principal and cross-coupled stiffness terms. A

separate analysis using a perturbation velocity would have to be performed in order to determine principal damping terms for the impeller.

2. VELOCITIES IN AN ECCENTRIC IMPELLER

Figure 1 shows a perturbed centrifugal impeller where $0'$ is the geometric center of the impeller and 0 is the center of the steady flow field. It is assumed that the flow enters through an inlet pipe centered at 0 and the radial velocity varies inversely with radius away from this point. The eccentricity a is small such that the dimensionless eccentricity

$$\varepsilon = \frac{a}{R_1}$$

is much less than unity. For this analysis terms of order ε^2 and higher will be neglected. The impeller consists of an infinite number of infinitely thin logarithmic spiral blades with angle β. The blades are backward curved with a blade angle θ_b, an inner radius R_1, and outer radius R_2.

The analysis is to be performed in a coordinate system rotating at rotor speed ω about the center of the impeller. Only synchronous whirling about the flow center 0 will be considered. The fluid is assumed to follow the shape of the blades through the impeller passage and to exit parallel to the blades. The particle path in the absolute reference frame is shown in Figure 2. The impeller is purely two-dimensional and ideal, incompressible flow is assumed.

The radial inflow to a centered impeller in the fixed (non-rotating) coordinate system centered at 0 is

$$u = U_{R1} \frac{R_1}{r} \tag{1}$$

where the average inlet velocity is

$$U_{R1} = \frac{1}{2\pi} \int_0^{2\pi} u(R_1, \theta_1) d\theta_1$$

Here θ_1 is the angle of a fluid particle measured along $r = R_1$. The impeller rotates with angular velocity ω. The blade angle is given by

$$\tan \beta = \frac{U_{R1}}{\omega_{R1}}$$

From Fig. 1, the length R_B is

$$R_B = R_1 + a \cos\theta_1$$

Thus, along an eccentric impeller centered at $0'$, the inlet velocity is

$$u = \frac{U_{R1} R_1}{(R_1 + a \cos\theta_1)} = U_{R1} \frac{1}{1 + \varepsilon \cos\theta_1} \tag{2}$$

From the binomial approximation

$$\frac{1}{1 + \varepsilon \cos\theta_1} \simeq 1 - \varepsilon \cos\theta_1$$

which leads to

$$u = U_B = U_{R1} \, (1 - \varepsilon \cos\theta_1) \tag{3}$$

This is the assumed form of the flow entering the eccentric impeller at a point B around the impeller.

From the geometry of the eccentric impeller, this velocity can be resolved into components normal to and tangential to the impeller (shown in Fig. 3)

$$U_{BN} = U_B \cos\delta \simeq U_{R1}(1 - \varepsilon \cos\theta_1)$$

$$U_{BT} = -U_B \sin\delta \simeq -U_{R1} \, (1 - \varepsilon \cos\theta_1) \, \varepsilon \sin\theta_1 \simeq -U_{R1} \, \varepsilon \sin\theta_1$$

for $\delta << 1$. The relative velocity of the rotating impeller is

$$V_B = \omega R_B = \omega R_1 (1 + \varepsilon \cos\theta_1)$$

along the inner radius of the impeller. Resolving this velocity into normal and tangential components gives

$$V_{BN} = V_B \sin\delta \simeq \omega R_1 \, \varepsilon \sin\theta_1 = \omega \, a \, \sin\theta_1$$

$$V_{BT} = V_B \cos\delta \simeq \omega R_1 \, (1 + \varepsilon \cos\theta_1)$$

In the rotating coordinate system, the velocity of point B is $W_B = U_B - V_B$ or in components

$$W_{BN} = U_{R1}(1 - \varepsilon \cos\theta_1 - \varepsilon \cot \beta \, \sin\theta_1) \tag{4}$$

$$W_{BT} = -\omega_{R1} \, (1 + \varepsilon \cos\theta_1 + \varepsilon \tan \beta \, \sin\theta_1) \tag{5}$$

Since the tangential velocity does not enter the control volume, it will be neglected in this analysis.

From continuity, the radial velocity must vary inversely with r in the interior of the impeller. Let θ' denote the angle of the fluid particle as it travels along the log spiral blade relative to the x axis in the rotating coordinate system. The relative velocity of the fluid is then

$$W_N = U_{R1} \, \frac{R_1}{r} \, (1 - \varepsilon \cos\theta' - \varepsilon \cot \beta \sin\theta') \tag{6}$$

Let θ_2 denote the angle of the fluid particle at the exit of the impeller. Figure 2 shows that, in the rotating coordinate system, the fluid which enters the impeller at angle θ_1 also leaves the impeller at angle $\theta_1 - \theta_b$. Thus

$$\theta_2 = \theta_1 - \theta_b$$

The relative velocity at the exit of the impeller is, at $\theta' = \theta_2$,

$$W_{N2} = U_{R1} \frac{R_1}{R_2} (1 - \ddot{\varepsilon} \cos\theta_2 - \varepsilon \cot \beta \sin\theta_2)$$

For flow along a blade, the relative magnitude is given by

$$W_{TOT} = \left[W_N^2 + W_T^2 \right]^{1/2}$$

It is assumed that the number of blades is infinite so the streamlines follow the log spiral blade exactly.

$$\tan \beta = -\frac{W_T}{W_N} =$$

Then the magnitude becomes

$$W_{TOT} = \left[1 + (\tan \beta)^2 \right]^{1/2} W_N \tag{7}$$

where W_N is obtained from Eq. (6). While an exact representation of the variation of θ' with radius would be logarithmic, the approximation of a linear variation will be used to facilitate the development of an analytic expression. It is

$$\theta' = \theta - \frac{r - R_1}{R_2 - R_1} \theta_b$$

The total relative velocity vector has the angle β taken from the tangent to a circle of radius r. Thus the x and y components of $\vec{W}_{TOT}$ are given by

$$\vec{W}_{TOT} = W_{TOT} \left[\sin (\theta + \beta)\vec{i} - \cos (\theta + \beta)\vec{j} \right]$$

The general velocity expression becomes

$$\vec{W}_{TOT}(r,\theta) = U_{R1} \frac{R_1}{r} \left[1 + (\tan\beta)^2 \right]^{1/2} \left\{ 1 - \varepsilon \cos \left(\theta - \frac{r - R_1}{R_2 - R_1} \right) \right. \tag{8}$$
$$\left. - \varepsilon \cot \beta \sin \left(\theta - \frac{r - R_1}{R_2 - R_1} \right) \right\} \left[\sin (\theta + \beta)\vec{i} - \cos (\theta + \beta)\vec{j} \right]$$

328

3. FORCE ON THE WHIRLING IMPELLER

The linear momentum equation for an accelerating control volume [20] is

$$\vec{F}_s - \int_{cv} [\vec{a} + 2\vec{\omega} \times \vec{V} + \vec{\omega} \times (\vec{\omega} \times \vec{r}) + \dot{\vec{\omega}} \times \vec{r}]\rho \, dv$$

$$= \frac{\partial}{\partial t} \int_{cv} \vec{V} \rho \, dv + \int_{cs} \vec{V} \rho(\vec{V} \cdot d\vec{A})$$

where

$\vec{F}_s$ = net surface forces acting on the control volume

$\vec{a}$ = rectilinear acceleration of the moving reference frame with respect to the fixed frame

$\vec{\omega}$ = angular velocity of the moving reference frame

$\vec{V}$ = velocity of a particle in the moving reference frame

$\dot{\vec{\omega}}$ = angular acceleration of the moving reference frame

$\vec{r}$ = position of a particle in the moving reference frame

For a reference frame rotating with constant angular velocity, this expression reduces to

$$\vec{F}_s = \int_{cv} [2\vec{\omega} \times \vec{V} + \vec{\omega} \times (\vec{\omega} \times \vec{r})] \rho \, dv + \int_{cs} \vec{V} \rho(\vec{V} \cdot d\vec{A}) \tag{9}$$

The surface forces consist of two parts

$$\vec{F}_s - \vec{F}_{SHAFT} + \vec{F}_p$$

where

$\vec{F}_{SHAFT}$ = force of shaft on control volume

$\vec{F}_p$ = pressure force acting on control volume

Bernoulli's equation for a rotating reference frame is

$$P - \frac{\rho}{2} |\vec{\omega} \times \vec{r}|^2 + \frac{\rho}{2} |\vec{V}|^2 = CONST$$

The pressure force on the control volume is given by

$$\vec{F}_p = - \int_{cs} P \, d\vec{A}$$

329

or, from Bernoulli's equation

$$\vec{F}_p = -\int_{cs} \left[\frac{\rho}{2}|\vec{\omega} \times \vec{r}|^2 - \frac{\rho}{2}|\vec{v}|^2 \right] dA$$

The final expression for the force exerted by the shaft (impeller) on the fluid in the control volume is

$$\vec{F}_{SHAFT} = \int_{cv} \left[\rho\, 2\, \vec{\omega} \times \vec{V} + \rho\vec{\omega} \times (\vec{\omega} \times \vec{r}) \right] dv$$

$$+ \int_{cs} \vec{V} \rho \vec{V} \cdot d\vec{A} + \int_{cs} \left[\frac{\rho}{2}|\vec{\omega} \times \vec{r}|^2 - \frac{\rho}{2}|\vec{v}|^2 \right] dA$$

The desired force here is the force exerted by the fluid on the shaft. It is the negative of the above expression.

$$\vec{F}_{ON\ SHAFT} = \underbrace{-\int_{cv} \rho\, 2\, \vec{\omega} \times \vec{V}\, dv}_{\text{Coriolis Force}} - \underbrace{\int_{cv} \rho\vec{\omega} \times (\vec{\omega} \times \vec{r})\, dv}_{\text{Centripital Force}}$$

$$\underbrace{-\int_{cs} \vec{V} \rho \vec{V} \cdot d\vec{A}}_{\substack{\text{Change in Linear} \\ \text{Momentum}}} - \underbrace{\int_{cs} \frac{\rho}{2}|\vec{\omega} \times \vec{r}|^2\, dA}_{\substack{\text{Change in Pressure} \\ \text{Due to Rotation}}} \qquad (10)$$

$$\underbrace{+\int_{cs} \frac{\rho}{2}|\vec{v}|^2\, dA}_{\substack{\text{Change in Pressure Due} \\ \text{to Change in Linear} \\ \text{Momentum}}}$$

where

$$\vec{r} = (r + a\cos\theta)(\cos\theta\, \vec{i} + \sin\theta\, \vec{j})$$

$$\vec{\omega} = \omega\vec{k}$$

$$\vec{V} = \vec{W}_{TOT} = U_{R1} \frac{R_1}{r} \left[1 + (\tan\beta)^2 \right]^{1/2} \left[1 - \varepsilon\cos\theta' \right.$$

$$\left. - \varepsilon\cot\beta\sin\theta' \right] \left[\sin(\theta + \beta)\vec{i} - \cos(\theta + \beta)\vec{j} \right]$$

$$d\vec{A} = (\cos\theta\, \vec{i} + \sin\theta\, \vec{j})\, rd\theta\, dz$$

$$(\vec{V} \cdot d\vec{A}) = W_N - U_{R_1} \frac{R_1}{r} (1 - \varepsilon\cos\theta' - \varepsilon\cot\beta\sin\theta')$$

330

$dv = r\, d\theta\, dr\, dz$

Integration is taken over the control volume from R_1 to R_2, and from 0 to 2π. On the control surface, integration is performed both at $r = R_2$ and at $r = R_1$ over θ from 0 to 2π. The thickness of the impeller is assumed to be the constant b.

For convenience in evaluation, the force acting on the shaft (impeller) due to the fluid is evaluated as five parts.

$$\vec{F}_{\substack{ON \\ SHAFT}} = - ①_{cv} - ②_{cv} - ③_{cs} - ④_{cs} + ⑤_{cs} \tag{11}$$

After integration, they are

Coriolis Force

$$① = 2\pi\, a\omega^2\rho\, b\, R_1 \left[\frac{R_2 - R_1}{\theta_b}\right] \tan\beta \left[1 + (\tan\beta)^2\right]^{1/2}$$

$$\times \left\{ [-\sin(\theta_b + \beta) + \sin\beta - \cot\beta \cos(\theta_b + \beta) + \cot\beta \cos\beta]\vec{i} \right.$$

$$\left. + [\cos(\theta_b + \beta) - \cos\beta - \cot\beta \sin(\theta_b + \beta) + \cot\beta \sin\beta]\vec{j} \right\}$$

Centripetal Force

$$② = -\frac{1}{2}\pi a\, \omega^2\rho b\, (R_2{}^2 - R_1{}^2)\vec{i}$$

Change in Linear Momentum

$$③ = 2\pi a\omega^2\rho b\, R_1{}^2 \sin\beta\, (\tan\beta)^2 \left[1 + (\tan\beta)^2\right]$$

$$\times \left\{ -\left[\frac{R_1}{R_2} \sin(\theta_b + \beta) - \frac{R_1}{R_2}\cot\beta \cos(\theta_b + \beta) + \sin\beta \right.\right.$$

$$\left. + \cot\beta \cos\beta \right]\vec{i} + \left[\frac{R_1}{R_2}\cos(\theta_b + \beta) - \frac{R_1}{R_2}\cot\beta \sin(\theta_b + \beta) \right.$$

$$\left.\left. - \cos\beta + \cot\beta \sin\beta \right]\vec{j} \right\}$$

Change in Pressure Due to Rotation

$$\text{(4)} \quad = \pi\, a\omega^2 \rho b(R_2{}^2 - R_1{}^2)\,\vec{i}$$

Change in Pressure Due to Change in Linear Momentum

$$\text{(5)} \quad = \pi\, a\omega^2 \rho b\, R_1{}^2 (\tan\beta)^2 \,[1 + (\tan\beta)^2]$$

$$\times \left\{ \left[-\frac{R_1}{R_2}\cos\theta_b + \frac{R_1}{R_2}\cot\beta\,\sin\theta_b + 1 \right]\vec{i} \right.$$
$$\left. + \left[-\frac{R_1}{R_2}\sin\theta_b - \frac{R_1}{R_2}\cot\beta\,\cos\theta_b + \cot\beta \right]\vec{j} \right\}$$

The physical significance is indicated above each term.

The five parts can be summed together yielding the vector force acting on the shaft. Dividing the force into components gives F_{xx} and F_{yx}. A similar impeller eccentricity along the y axis would yield the forces F_{xy} and F_{yy}. What is of interest here is the stiffness obtained from

$$K_{ij} = -\frac{F_{ij}}{a}$$

The principal stiffness is

$$K_{xx} = -\pi\omega^2\rho b\, R_1{}^2 \left(\boxed{1} + \boxed{2} + \boxed{3} + \boxed{4} + \boxed{5} \right) \tag{12}$$

where

$$\boxed{1} = -2\,\frac{1}{\theta_b}(\bar{R} - 1)\tan\beta\,[1 + (\tan\beta)^2]^{1/2}$$

$$\times [-\sin(\theta_b + \beta) + \sin\beta + \cot\beta\,\cos(\theta_b + \beta) + \cot\beta\,\cos\beta]$$

$$\boxed{2} = \frac{1}{2}(\bar{R}^2 - 1)$$

$$\boxed{3} = -2\sin\beta\,(\tan\beta)^2\,[1 + (\tan\beta)^2]$$

$$\times \left[-\frac{1}{R}\sin(\theta_b + \beta) - \frac{1}{R}\cot\beta\,\cos(\theta_b + \beta) + \sin\beta + \cot\beta\,\cos\beta \right]$$

$$\boxed{4} = -(\bar{R}^2 - 1)$$

$$\boxed{5} = (\tan\beta)^2\,[1 + (\tan\beta)^2]$$

$$x \left[-\frac{1}{\bar{R}} \cos\theta_b + \frac{1}{\bar{R}} \cot\beta \sin\theta_b + 1 \right]$$

The cross-coupled stiffness is

$$K_{yx} = -\pi\omega^2\rho b\, R_1^{\,2} \left(\triangle_1 + \triangle_2 + \triangle_3 \right) \tag{13}$$

where

$$\triangle_1 = -2\,\frac{1}{\theta_b}(\bar{R}-1)\tan\beta\,[1 + (\tan\beta)^2]^{1/2}$$

$$x\,[\cos(\theta_b + \beta) - \cot\beta\,\sin(\theta_b + \beta)]$$

$$\triangle_2 = -2\sin\beta\,(\tan\beta)^2\,[1 + (\tan\beta)^2]$$

$$x\,[\frac{1}{\bar{R}}\cos(\theta_b + \beta) - \frac{1}{\bar{R}}\cot\beta\,\sin(\theta_b + \beta)]$$

$$\triangle_3 = (\tan\beta)^2\,[1 + (\tan\beta)^2]$$

$$x\,[-\frac{1}{\bar{R}}\sin\theta_b - \frac{1}{\bar{R}}\cot\beta\,\cos\theta_b + \cot\beta]$$

Note that both principal and cross-coupled stiffnesses are obtained. In a rotor dynamics analysis, the other stiffnesses would be given by

$$K_{yy} = K_{xx}$$

$$K_{xy} = -K_{yx}$$

For comparison with other works and convenience in plotting results, the stiffnesses have been made dimensionless in the following manner

$$\bar{K}_{ij} = \frac{K_{ij}}{\rho U_{R_1}^{\,2} R_1} = \frac{K_{ij}}{\rho\omega^2 R_1^{\,3}\tan^2\beta}$$

The resulting expressions are

$$\bar{K}_{xx} = -\pi\,\frac{b}{R_1}\,\frac{1}{\tan^2\beta}\,(\triangle_1 + \triangle_2 + \triangle_3 + \triangle_4 + \triangle_5)$$

$$\bar{K}_{yx} = -\pi\,\frac{b}{R_1}\,\frac{1}{\tan^2\beta}\,(\triangle_1 + \triangle_2 + \triangle_3)$$

The dimenionless stiffnesses are functions of the ratio b/R_1, the radius ratio $\bar{R}$, the blade angle β, and angular sweep of the blade θ_b. The terms $\bar{R}$, β, and θ_b are

related to one another so actually only two are independent. Also the term b/R_1 appears only as a multiplicative constant. Thus only the radius ratio $\bar{R}$ and the blade angle β need be varied for these stiffnesses.

4. RESULTS

Figure 4 shows a plot of the dimensionless stiffnesses $\bar{K}_{xx}$ and $\bar{K}_{yx}$ vs. blade angle β for a radius ratio $\bar{R} = 1.5$. For plotting purposes b/R_1 has been set to unity. It shows that the blade angle has a strong influence on both the magnitude and sign of the stiffnesses. The principal stiffness is large and positive for low blade angles. Pumps generally have a low blade angle so they fit in this category. The cross-coupled stiffness is negative for this level of blade angle. The large positive principal stiffness is generally a stabilizing effect while the negative $\bar{K}_{yx}$ term is destabilizing. In the range of pump blade angles, 10 to 20 degrees, the principal stiffness term is larger than the cross-coupled stiffness probably leading to an overall stabilizing effect. Compressors generally have large blade angles (as defined in this paper), perhaps in the range of 60 to 80 degrees. With a radius ratio $\bar{R} = 1.5$, both the principal stiffness and cross-coupled stiffness are negative indicating destabilizing effects. Field results indicate that pumps are usually stable while compressors are sometimes unstable. Thus the theory developed here appears to agree, at least qualitatively, with results from actual machines.

A semi-empirical formulation for the cross-coupled stiffness was developed in [18] of the form

$$K_{yx} = - \frac{6300 \ HP \ (Mol \ Wt) \rho_o}{N D h \rho_s}$$

where

HP = pump horsepower

Mol Wt = fluid molecular weight

ρ_o = discharge density

ρ_s = suction density

N = speed in RPM

D = impeller diameter

h = restrictive dimension in flowpath

While this expression was developed for compressible flow, it can be reduced to incompressible flow. Non-dimensionalizing this reduced expression gives

$$\bar{K}_{yx} = -0.6\pi \ (b/R_1) \ n \ \cot\beta \ \bar{R}(\bar{R}-1)$$

where

n = the number of blades

$$HP = (\omega R_2)^2 - \omega U_{R_1} R_1 \cot\beta$$

The curve for this expression was added to Figure 4 with a blade number of eight. Another choice of number of blades will move the curve up or down somewhat without changing the overall shape of the curve. The plot of $\bar{K}_{yx}$ from the theory developed in this paper agrees fairly well with the semi-empirical formula.

Figure 5 gives the results for a radius ratio $\bar{R} = 2.0$. Again the principal stiffness is large for small blade angles. At larger blade angles, it decays to zero but does not go negative as it did for $\bar{R} = 1.5$. The cross-coupled stiffness is negative and fairly large over the blade angle range of 15 to 75 degrees. The semi-empirical formula gives a somewhat larger negative coefficient than the theory.

One of the purposes of this study is to examine the effects of various terms on the stiffnesses. Table 1 gives the five terms involved in the principal stiffness vs. blade angle for $\bar{R} = 1.5$. At low blade angles, the dominant effect is the change in pressure due to rotation. This term arises in Bernoulli's equation due to the rotating coordinate system. At larger blade angles, the dominant terms become the linear momentum ones. Now the other term from Bernoulli's equation is the largest but it is nearly balanced by the change in linear momentum. Table 2 shows the three terms in the cross-coupled stiffness vs. blade angle for $\bar{R} = 1.5$. At low blade angles, the Coriolis force produces the cross-coupled stiffness effect. At higher blade angles, the linear momentum terms become dominant. Tables 3 and 4 give the numerical values for $\bar{R} = 2.0$.

It is sometimes difficult to obtain a physical feel for the results of an analysis when dimensionless parameters are used. In an effort to impart a better idea of the numerical values developed from the theory here, some sample impellers were chosen. The results are given in Table 5. Generally small pumps will have very small stiffnesses while large pumps such as boiler feed pumps can have fairly large stiffness acting on them. The stiffness value here $K_{xx} = 124,000$ lbf/in is the same order of magnitude expected from the seals in a pump. A small compressor, even at high speed, produces a relatively small cross-coupling stiffness. Large compressors have somewhat larger coefficients. Often such a compressor will have eight or ten stages with a fairly flexible shaft. The cumulative effect can produce an instability.

5. CONCLUSIONS

The theoretical solution for a simple impeller model shows the principal and cross-coupled stiffnesses to be of about the same order of magnitude. For blade angles (β) less than thirty degrees, common for water pumps. the flow seems to provide tabilization for the shaft, while for the larger blade angles, common for compressors, the impeller is generally destabilizing. Since the magnitude of K_{xx} and K_{yx} are nearly the same, it would be important to include both terms in any rotor dynamics analysis of the shaft, rather than incorporating just the cross-coupling terms.

· Though this work does not fully resolve the nature of aerodynamic forces on centrifugal machines, it does offer more understanding of these forces. An important element of any future work, however, is the availability of experimental data for verification. As of the present, no such data exists, although efforts are being perused in this area.

6. REFERENCES

1. Shepherd, D. G., Principles of Turbomachinery, MacMillan Publishing Co., New York, 1956.

2. Acosta, A. J., "An Experimental and Theoretical Investigation of Two-Dimensional Centrifugal Pump Impellers," Transactions of the ASME, July, 1954, p. 749-763.

3. Balje, O. E., "A Flow Model for Centrifugal Compressor Rotors," Transactions of the ASME, Vol. 100, Jan., 1978, p. 148-158.

4. Howard, J. H. G. and Lennemann, E.,"Measured and Predicted Secondary Flows in a Centrifugal Impeller," Journal of Engineering for Power, Trans. ASME, Jan., 1971, p. 126-131.

5. Lennemann, E. and Howard, J. H. G., "Unsteady Flow Phenomena in Rotating Centrifugal Impeller Passages," Journal of Engineering for Power, Trans. ASME, Jan. 1970, p. 65-72.

6. Moore, J., "A Wake and an Eddy in a Rotating Radial Flow Passage," Journal of Engineering for Power, Trans. ASME, July 1973, p. 205-219.

7. Alford, J. S., "Protecting Turbomachinery from Self-Excited Rotor Whirl," Journal of Engineering for Power, Trans. ASME, Oct. 1965, p. 333-344.

8. Black, H. F., "Lateral Stability and Vibration of High Speed Centrifugal Pump Rotors," IUTAM Dynamics of Rotors Symposium, Lyngby, Denmark, Aug. 1974, p. 56-74.

9. Barrett, L. E. and Gunter, E. J., "Stabilization of Aerodynamically Exicted Turbomachinery with Hydrodynamic Journal Bearings and Supports," Proceedings of NASA/ARO Workshop on Rotordynamic Instability Problems in High Performance Turbomachinery, College Station, Texas, May 1980.

10. Lund, J. W., "Some Unstable Whirl Phenomena in Rotating Machinery," The Shock and Vibration Digest, Vol. 7, No. 6, June 1975, p. 5-12.

11. Gunter, E. J., Barrett, L. E., and Allaire, P. E., "Stabilization of Turbomachinery with Squeeze Film Dampers - Theory and Application," I. Mech. E., Proceedings of Conference on Vibrations in Rotating Machinery, Cambridge, England, C233/76, Sept. 1976.

12. Colding-Jorgensen, J., "Effect of Fluid Forces on Rotor Stability of Centrifugal Compressors and Pumps," Proceedings of NASA/ARO Workshop on Rotordynamic Instability Problems in High-Performance Turbomachinery, College Station, Texas, May 1980.

13. Shoji, H. and Ohashi, H., "Fluid Forces on Rotating Centrifugal Impeller with Whirling Motion," Proceedings of NASA/ARO Workshop on Rotordynamic Instability Problems in High-Performance Turbomachinery, College Station, Texas, May 1980.

14. Thompson, W. E., "Vibration Exciting Mechanisms Induced by Flow in Turbomachine Stages," Proceedings of NASA/ARO Workshop on Rotordynamic Instability Problems in High-Speed Turbomachinery, College Station, Texas, May 1980.

15. Thompson, W. E., "Fluid Dynamic Excitation of Centrifugal Compressor Rotor Vibrations," Journal of Fluids Engineering, Vol. 100, March 1978, p. 73-78.

16. Chamieh, D. and Acosta, A. J., "Dynamic Forces on a Whirling Centrifugal Rotor," Proc. 6th Conference on Fluid Machinery, Akademiai Kiado, Budapest, Hungary, 1979.

17. Jenny, R. and Wyssmann, H. R., "Lateral Vibration Reduction in High Pressure Centrifugal Compressors," Proceedings of the Ninth Turbomachinery Symposium, Texas A&M University, Dec. 1980, p. 45-56.

18. Wachel, J. C. and von Nimitz, W. W., "Assuring the Reliability of Offshore Gas and Compression Systems," Proceedings of the European Offshore Petroleum Conference Vol. 1, EUR205, October, 1981, pp. 559-568.

19. Branagan, L. A., "Aerodynamic Forces on an Unbound Centrifugal Impeller: Effects of Change in Fluid Momentum," M.S. Thesis, University of Virginia, January, 1982.

20. Fox, R. W. and McDonald, A. T., Introduction to Fluid Mechanics, John Wiley & Sons, New York, 1978, p. 166.

TABLE 1. - EFFECT OF VARIOUS TERMS ON PRINCIPAL STIFFNESS FOR $\bar{R} = 1.5$

Blade Angle	Coriolis Force	Centripetal Force	Change In Linear Momentum	Change In Pressure Due To Rotation	Change In Pressure Due To Change In Linear Momentum	Principal Stiffness
ß	[1]	[2]	[3]	[4]	[5]	$\bar{K}_{xx}$
10.00	-.75	.63	-.09	-1.25	.03	144.75
15.00	-.67	.63	-.15	-1.25	.08	59.67
20.00	-.57	.63	-.21	-1.25	.15	29.76
25.00	-.50	.63	-.30	-1.25	.26	16.74
30.00	-.45	.63	-.44	-1.25	.44	10.05
35.00	-.42	.63	-.65	-1.25	.73	6.15
40.00	-.40	.63	-.98	-1.25	1.20	3.62
45.00	-.40	.63	-1.55	-1.25	2.00	1.80
50.00	-.41	.63	-2.55	-1.25	3.44	.33
55.00	-.43	.63	-4.46	-1.25	6.20	-1.05
60.00	-.47	.63	-8.44	-1.25	12.00	-2.59
65.00	-.53	.63	-17.78	-1.25	25.75	-4.66
70.00	-.63	.63	-43.96	-1.25	64.53	-8.04
75.00	-.81	.63	-140.25	-1.25	207.92	-14.94
80.00	-1.18	.63	-714.71	-1.25	1066.62	-34.20

TABLE 2. - EFFECT OF VARIOUS TERMS ON CROSS-COUPLED STIFFNESS FOR $\bar{R} = 1.5$

Blade Angle	Coriolis Force	Change In Linear Momentum	Change In Pressure Due To Change In Linear Momentum	Cross-Coupled Stiffness	Cross-Coupled Stiffness
θ	△	△	△	$\bar{K}_{xy}$	Wachel [18]
10.00	.33	.03	.06	-42.96	-64.14
15.00	.71	.10	.09	-39.32	-42.21
20.00	.91	.18	.12	-28.73	-31.07
25.00	1.07	.27	.15	-21.52	-24.25
30.00	1.23	.38	.18	-16.84	-19.59
35.00	1.41	.53	.19	-13.69	-16.15
40.00	1.64	.74	.19	-11.46	-13.48
45.00	1.95	1.05	.11	-9.78	-11.31
50.00	2.37	1.53	-.11	-8.40	-9.49
55.00	3.00	2.32	-.70	-7.10	-7.92
60.00	3.96	3.71	-2.31	-5.62	-6.53
65.00	5.57	6.45	-6.93	-3.47	-5.27
70.00	8.52	12.65	-22.29	.47	-4.12
75.00	14.90	30.06	-87.79	9.66	-3.03
80.00	33.13	101.59	-533.98	39.00	-1.99

TABLE 3. - EFFECT OF VARIOUS TERMS ON PRINCIPAL STIFFNESS FOR $\bar{R}$ = 2.0

Blade Angle	Coriolis Force	Centripetal Force	Change In Linear Momentum	Change In Pressure Due To Rotating	Change In Pressure Due To Change in Linear Momentum	Principal Stiffness
ø	1	2	3	4	5	$\bar{K}_{xx}$
10.00	-.89	1.50	-.09	-3.00	.03	247.42
15.00	-1.53	1.50	-.22	-3.00	.08	138.95
20.00	-1.58	1.50	-.35	-3.00	.15	77.74
25.00	-1.50	1.50	-.51	-3.00	.26	46.85
30.00	-1.42	1.50	-.73	-3.00	.44	30.17
35.00	-1.36	1.50	-1.06	-3.00	.73	20.43
40.00	-1.33	1.50	-1.59	-3.00	1.20	14.35
45.00	-1.33	1.50	-2.46	-3.00	2.00	10.35
50.00	-1.37	1.50	-4.00	-3.00	3.44	7.60
55.00	-1.45	1.50	-6.92	-3.00	6.20	5.64
60.00	-1.58	1.50	-12.95	-3.00	12.00	4.22
65.00	-1.79	1.50	-27.08	-3.00	25.75	3.16
70.00	-2.15	1.50	-66.57	-3.00	64.53	2.37
75.00	-2.76	1.50	-211.50	-3.00	207.92	1.77
80.00	-4.05	1.50	-1074.58	-3.00	1066.62	1.32

TABLE 4. - EFFECT OF VARIOUS TERMS ON CROSS-COUPLED STIFFNESS FOR $\bar{R}$ = 2.0

Blade Angle	Coriolis Force	Change in Linear Momentum	Change In Pressure Due To Change In Linear Momentum	Cross-Coupled Stiffness	Cross-Coupled Stiffness
ø	⚠	⚠	⚠	$\bar{K}_{xy}$	Wachel [18]
10.00	-.37	-.02	.09	30.89	-171.04
15.00	.44	.04	.14	-26.93	-112.56
20.00	1.12	.14	.19	-34.58	-82.86
25.00	1.63	.26	.25	-31.07	-64.68
30.00	2.07	.41	.33	-26.49	-52.24
35.00	2.52	.61	.41	-22.65	-43.07
40.00	3.03	.88	.50	-19.69	-35.94
45.00	3.69	1.28	.59	-17.44	-30.16
50.00	4.57	1.89	.64	-15.71	-25.31
55.00	5.84	2.89	.56	-14.31	-21.12
60.00	7.79	4.68	.00	-13.05	-17.41
65.00	11.00	8.18	-2.20	-11.60	-14.06
70.00	16.92	16.11	-10.85	-9.23	-10.98
75.00	29.68	38.40	-51.91	-3.65	-8.08
80.00	66.16	130.04	-353.46	15.36	-5.32

TABLE 5. – NUMERICAL EXAMPLES FOR PUMP AND COMPRESSOR IMPELLERS

Impeller	$\dfrac{\rho}{slug/ft^3}$	$\dfrac{\omega}{rpm}$	$\dfrac{R_1}{in}$	$\dfrac{b}{in}$	$\dfrac{\beta}{degrees}$	$\dfrac{K_{xx}}{lbf/in}$	$\dfrac{K_{yx}}{lbf/in}$
Small Pump	1.94	600	3.0	0.5	15	16.5	-3
Large Pump	1.94	10,000	9.0	1.5	15	124,000	-24,000
Small Compressor	7.5×10^{-3}	30,000	3.0	0.5	60	205	-702
Large Compressor	7.5×10^{-3}	10,000	12.0	0.5	60	720	-2,200
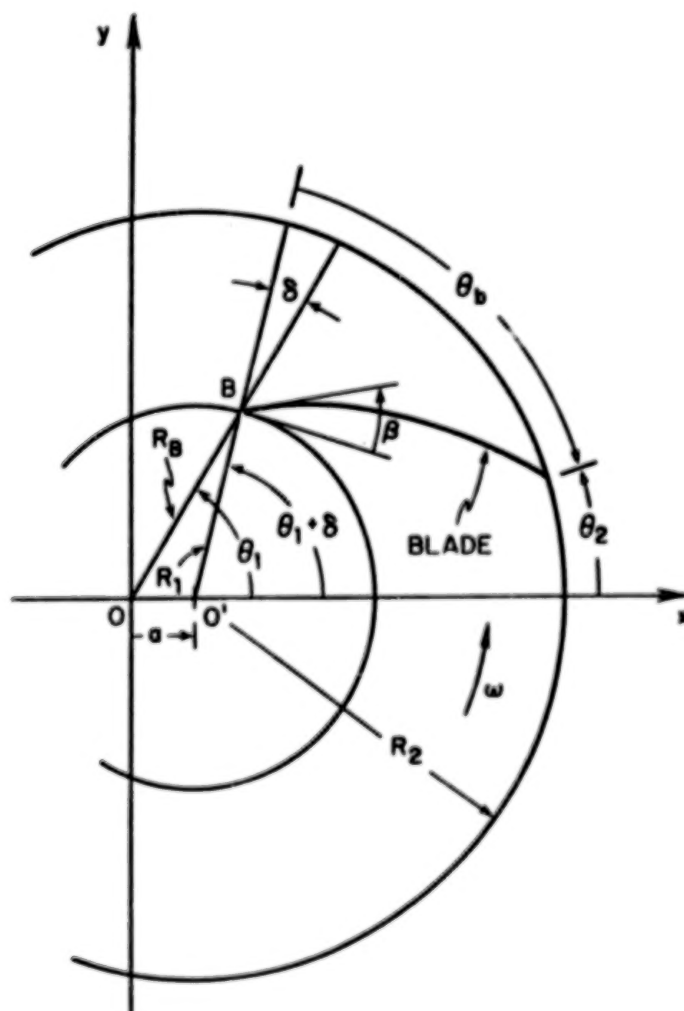
Figure 1. – Geometry of perturbed impeller.

340
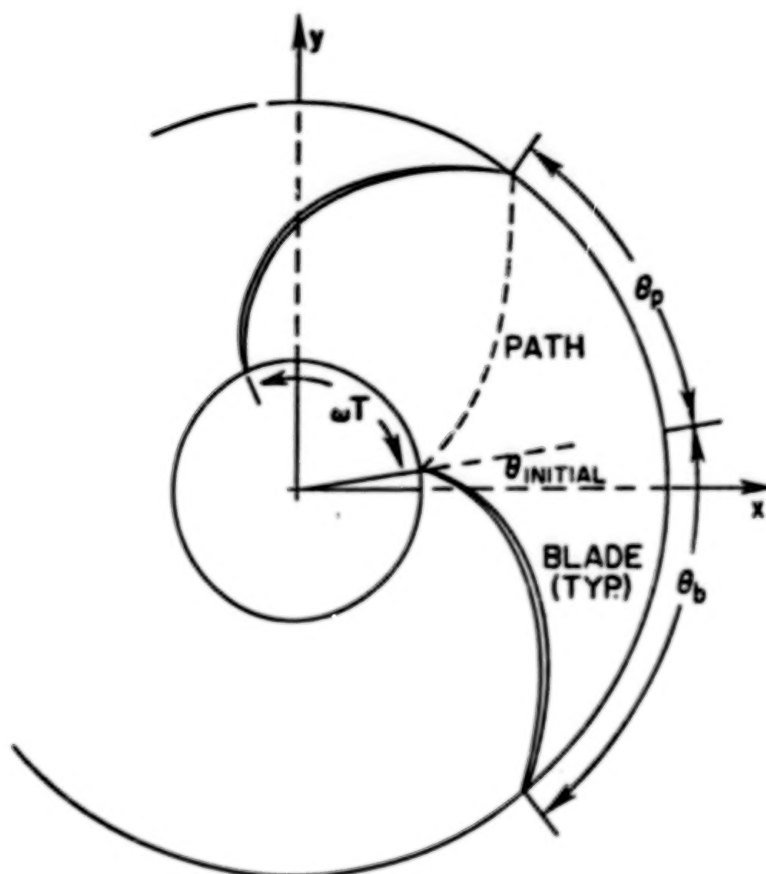
Figure 2. - Fluid path through impeller over passage time (T). Fixed coordinate frame $[\theta_p = \omega T - \theta_b]$.
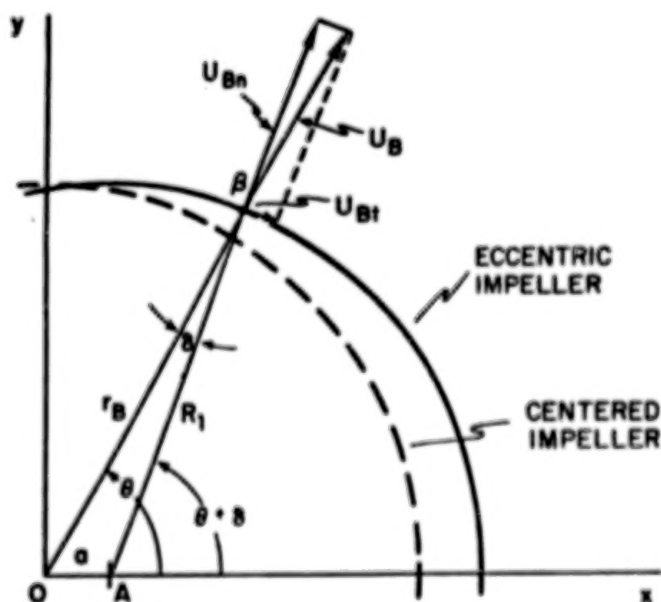
(a). Absolute velocity components at point B.

Figure 3. - Velocity components at impeller inlet.

341
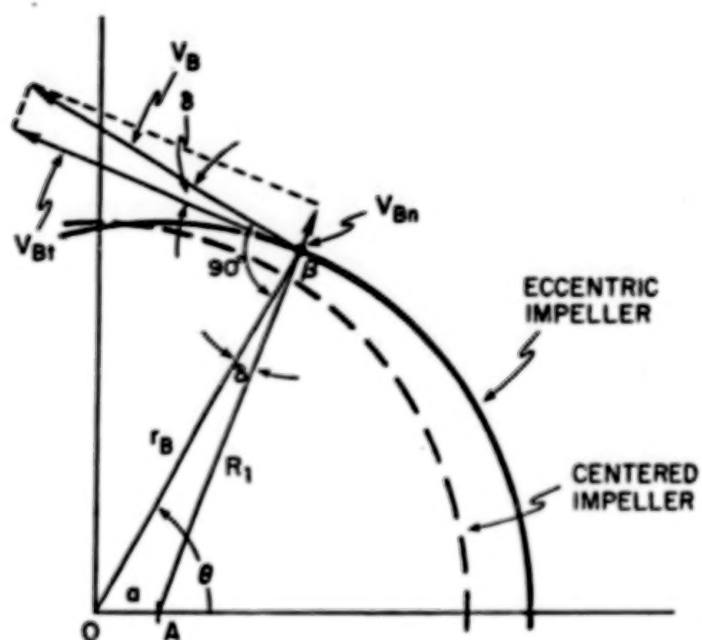
(b). Relative velocity between fluid and impeller.
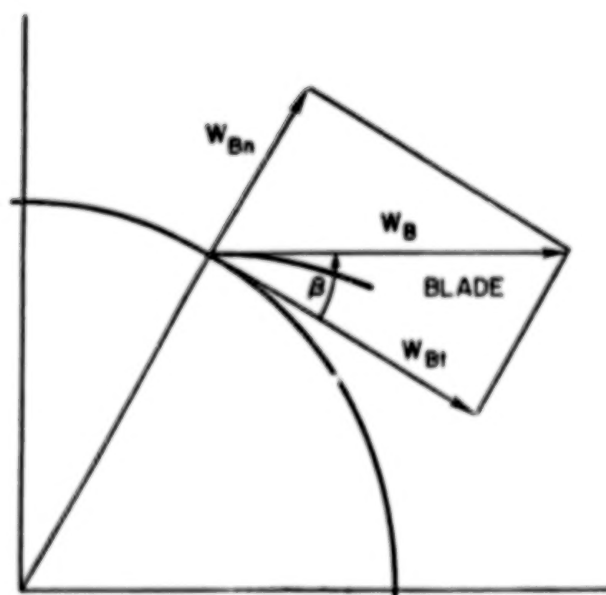
(c). Relative velocity components in rotating coordinate system.

Figure 3. - Concluded.

342
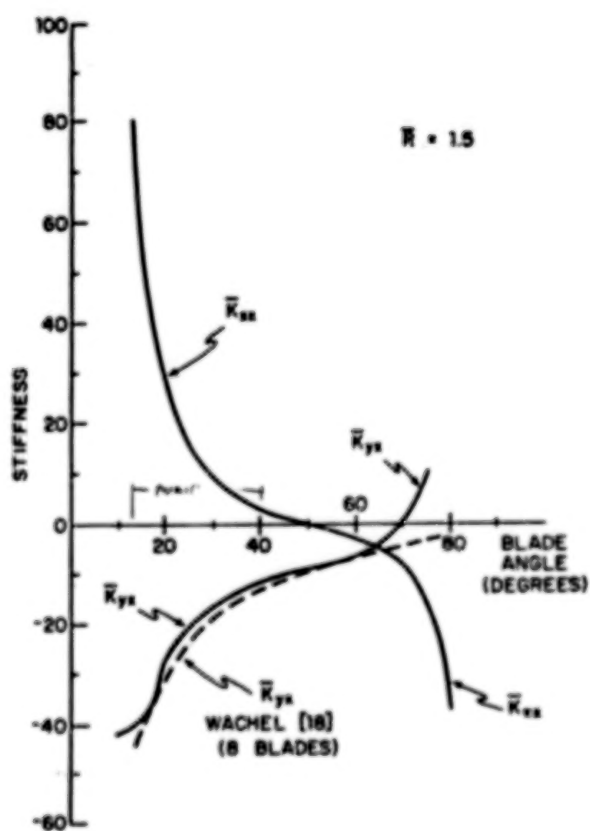
Figure 4. - Dimensionless stiffness
versus blade angle for $\overline{R}$ = 1.5.
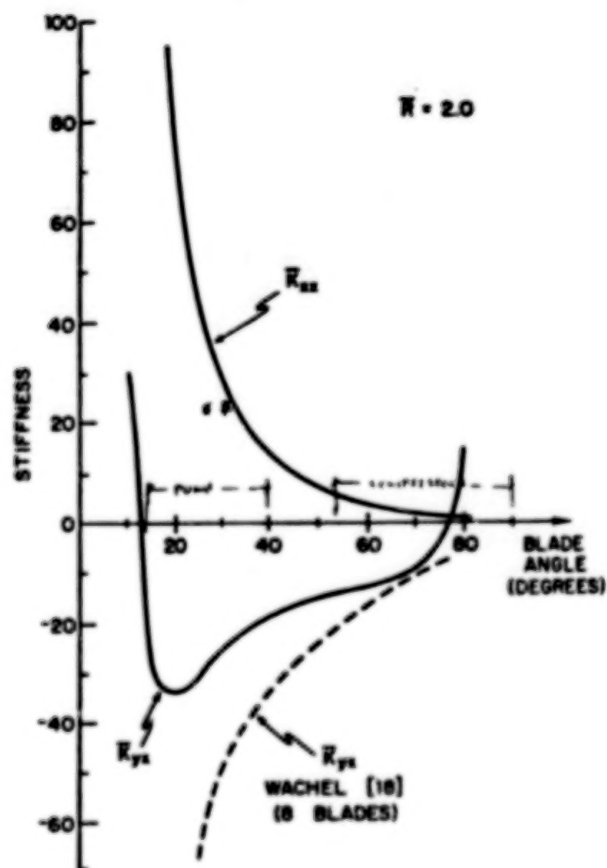
Figure 5. - Dimensionless stiffness
versus blade angle for $\overline{R}$ = 2.0.

343

UNSTEADY FLOW PHENOMENA IN INDUSTRIAL CENTRIFUGAL COMPRESSOR STAGE

L. Bonciani, L. Terrinoni, and A. Tesei
Nuovo Pignone
50127 Florence, Italy

SUMMARY

It is well known that rotating non-uniform flow pattern has a strong influence on high pressure centrifugal compressor vibrations. This paper shows the results of an experimental investigation on a typical centrifugal compressor stage running on an atmospheric pressure test rig. Unsteady flow was invariably observed at low flow well before surge. In order to determine the influence of the statoric components, the same impeller was repeatedly tested with the same vaneless diffuser, but varying return channel geometry. Experimental results show the strong effect exerted by the return channel, both on onset and on the behavior of unsteady flow. Observed phenomena have been found to confirm well the observed dynamic behavior of full load tested machines when gas density is high enough to cause appreciable mechanical vibrations. Therefore, testing of single stages at atmospheric pressure may provide a fairly accurate prediction of this kind of aerodynamic excitation.

INTRODUCTION

Problems which have arisen in past years with high density centrifugal compressors have considerably increased the demand for full load testing (ASME PTC 10, Class 1), mainly aimed at checking the stability of machines under aero-induced excitation forces.

Present experience leaves no doubts that aerodynamic excitation is always present in centrifugal compressors and it is obvious that the forces involved become more marked the greater gas density and machine speed. This is the reason why machines subject to aero-induced vibrations have been found more frequently in natural gas injection or urea synthesis plants than in ammonia synthesis or refinery compressors, even when running at the same pressure levels (ref. 1). Although the action of aerodynamic forces involved leads to subsynchronous vibrations in general, two completely different behaviors have been encountered: self-excited vibrations and forced vibrations. Vibrations belonging to the first category (self-excited vibrations) have been noted in high performance turbo-machinery (ref. 2) including high pressure compressors (ref. 3 and 4), apparently with greater frequency in back-to-back versions of the latter. The vibration frequency observed is normally the fundamental bending natural frequency of the rotor. An explanation commonly given for this phenomenon is based on destabilizing forces caused by the labyrinth seals (ref. 5 and 6). On the other hand vibrations belonging to the second category

(forced vibrations) have been recorded in all high density compressors. They have the following typical behavior (ref. 7 and 8):

. They appear relatively near to surge and are very stable in amplitude.

. Asynchronous frequency is very low (order of magnitude 10% of RPM)

. Asynchronous amplitude depends on tip speed and gas density.

In order to examine this phenomenon more closely a test program was set up with the aim of investigating the amplitude and frequency of pressure oscillations within a centrifugal compressor stage. A standardized low specific speed stage, which is normally utilized in high pressure applications, was slated for testing.

SYMBOLS

R	Radius
p	static pressure
P_e	total pressure
C_r	radial velocity
A	pressure oscillations amplitude
f_s	fundamental frequency of pressure oscillations
Ω	impeller angular velocity
$\hat{A}$	amplitude of pressure oscillations normalized to stage total inlet pressure
$\hat{f}_s$	fundamental frequency of pressure oscillations normalized to impeller speed ($\hat{f}_s = 2\pi f_s / \Omega$)
Mu	tip speed Mach number
R_e	Reynolds number (based on diffuser axial width)
φ	inlet flow coefficient
$\hat{C}_r$	normalized radial velocity ($\hat{C}_r = C_r / \Omega R$)
α	absolute flow angle (referred to tangential direction)
C_p	pressure recovery coefficient

Subscripts:

10	= measured at section 10					
10	=	"	"	"	10'	
20	=	"	"	"	20	

20'	=	"	"	"	20'
30'	=	"	"	"	30'
40	=	"	"	"	40
40'	=	"	"	"	40'
50'	=	"	"	"	50'
60	=	"	"	"	60
60'	=	"	"	"	60'

D = diffuser

RC = return channel

* = onset of unsteady flow

TEST FACILITIES AND INSTRUMENTATION

Tests have been arranged on one of the three test rigs available for the individual stages development (ref. 9). A cross section of the test rig is shown on Fig. 1; the stage consisted of an impeller, a free vortex diffuser, a cross-over and a return channel. The gas utilized was air at atmospheric pressure in an open loop circuit. Speed was adjusted by an hydraulic coupling torque converter while an electrically actuated discharge valve was operated to vary the pressure ratio. Table 1 shows the conventional instrumentation used for industrial stage testing. Table 2 shows the instrumentation utilized to detect pressure oscillations connected with non-stationary flow conditions. The following should be mentioned of the conventional instrumentation:

. The data acquisition system is based on a Solartron system 35 with a PDP 11/03 control unit.

. All pressure readings are connected, through a scannivalve, to a single pressure transducer. The transfer function of the measurement chain has been experimentally tested, to check that the output is the time average of the pressure within the frequency range of interest.

Regarding non-stationary reading we can note that:

. static pressure probes are the Kulite XT-190-50 type

. total pressure probes are the Kulite XB-093-50G type

. probe signals have been recorded on an Ampex PR 2200 tape recorder and finally analized through an Ono-Sokki CF-500 real time spectrum analizer. Data shown for each tested point are the RMS averages of 256 spectra.

Two different stage configurations have been tested: configuration A and configuration B. Both configurations utilize the same impeller and diffuser but different return channels and, of course, cross-overs.

TEST RESULTS

Configuration A

It is necessary to point out that the following procedure was adopted to obtain the data relating to configuration A.

1. Readings were taken of time "average" quantities (i.e. pressures, temperatures etc. at the different measuring sections) with conventional instrumentation.

2. Next, readings were taken of pressure oscillations (remeasuring inlet pressure, flow and RPM) independently of prior readings.

3. Finally some "points" were repeated in regions of particular interest.

Qualitative Description

When flow is reduced at constant speed the following behavior was observed:

. Pressure oscillations started simultaneously on all pressure transducers with very low amplitude and almost sinusoidal shape.

. A small flow reduction resulted in a slight increase in frequency and a considerable increase in amplitude while the signal shape remained sinusoidal.

. If flow was further reduced the phenomena observed was dependent on the tip speed Mach numbers (Mu) as follows:

At $Mu = 0.45$ and 0.60 we noted:

. The shape of the signal suddenly changed from a sinusoid with a frequency of f_s to a signal having frequencies f_s and $f_s/2$ with comparable amplitudes. The onset of the second frequency (i.e. $f_s/2$) is usually very sudden.

. When flow was reduced the f_s and $f_s/2$ frequencies slowly increased and the f_s amplitude component remained almost constant while the $f_s/2$ one rose gradually.

. On rethrottling, the $f_s/2$ signal finally disappeared and the f_s signal had a sudden increase in amplitude.

. Further flow reductions caused a shifting of the f_s frequency while amplitude remained almost constant till full surge.

. On opening the valve and exploring the phenomenon starting from full surge we found that frequencies and amplitudes were repetitive related to flow. A slight hysteresis was noted in the onset region.

At $Mu = 0.75$ and 0.85 we observed that:

. Pressure oscillations might have a sinusoidal shape with f_s frequency till full surge.

347

. With the same inlet flow coefficient it was possible to shift from a single
  frequency signal (f_s) to a dual-frequency signal having the same f_s frequency
  and an additional component at $f_s/2$ frequency. Each one of the amplitudes
  (i.e. at f_s and $f_s/2$) with dual frequency was lower than the amplitude with
  single frequency.

Although the factors governing the shift from one shape to the other were not
discovered, the following observations were made:

a. The shift from a single frequency shape to the other seemed easier when
   increasing the flow from the surge.

b. Sometimes introduction of the conventional instrumentation probes into the
   diffuser was very effective in triggering the shift to the dual-frequency shape.

c. Mantaining a constant opening of the discharge valve and raising the speed from
   low Mu (i.e. Mu = 0.45) with dual frequency shape the signal might retain the
   same shape even if Mu exceeds 0.85.

d. Cases were observed where shifting appeared several minutes after the last
   positioning of the valve.

   Summarizing we believe that the phenomenon can be described as follows:

. The unsteady flow pattern may exhibit two distinct shapes (single frequency
  and dual frequency).

. The dual frequency shape is stable within a range of flows-RPM (or better
  φ - Mu) and metastable in the remaining range.

. When dual frequency exists is may survive in the entire speed range explored.

It will later be seen that the two different signal shape correspond to two
distinct values of the return channel recovery coefficient, based on time average.

Quantitative Description

To keep the length of the paper within reasonable limits we will indicate only the
results obtained at section 20', behavior at all the other measuring sections
being very similar.

Fig. 2 shows the frequencies normalized to the RPM while fig. 3 and 4 show the
amplitudes of the pressure oscillations corresponding to f_s and $f_s/2$ normalized to
the suction pressure. The following can be remarked:

. Amplitudes at section 10' (impeller suction) were always negligible till surging.

. At the different measuring sections pressure oscillations amplitudes exhibited
  shapes similar to those shown for section 20'. The following are the average
  values found:

$A_{30'}$	$\simeq$	80% $A_{20'}$		$A_{30'}$	$\simeq$	81% $A_{20'}$
$A_{40'}$	$\simeq$	60% $A_{20'}$		$A_{40'}$	$\simeq$	60% $A_{20'}$
$A_{50'}$	$\simeq$	60% $A_{20'}$		$A_{50'}$	$\simeq$	17% $A_{20'}$
$A_{60'}$	$\simeq$	9% $A_{20'}$		$A_{60'}$	$\simeq$	9% $A_{20'}$

. Irrespectively of the flow coefficient, the phase difference between static probes at the same radius is 90° for the $f_s/2$ component and 180° for the f_s component with dual frequency signal shape and is 180° for the f_s component when the signal is single-frequency. Therefore it seems that $f_s/2$ is associated with a single stall cell, while f_s is associated with two stall cells.

. The phase difference between static probes at the same angular position was practically independent from the flow coefficient. Typical values measured (in round figures) were: -10°, between sec. 20' and sec. 30', and -20°, between sec. 20' and sec. 40', for the f_s component (with both single or dual frequency shape) and always near 0° for the $f_s/2$ component.

Analysis of Time Averaged Data

Fig. 5, 6 and 7 show the pressure ratios (static to total and total to total) versus flow at three different measuring sections. An appreciable variation in the slope can be noted at the onset of the pressure oscillations followed by a region with a positive slope. At Mu = 0.75 and 0.85 two distinct branches clearly identify the working regions relevant to the two shapes of the signal previously described.

The lack of connection between "average" measurements and instantaneous measurements initially led to considerable confusion. Only later was it realized that the two disturbance shapes have distinct "average" measurements and that the shift from one shape to the other cannot always be triggered at will in the Mu = 0.75+0.85 area. As a result the graphs in fig. 7 and fig. 3 are slightly contradictory: the shift point from one shape to the other at Mu = 0.75 and Mu = 0.85, shown in fig. 3, does not coincide with those indicated in fig. 7. The general shape of the amplitude curve at Mu = 0.75 looks similar to those at Mu = 0.45 and Mu = 0.60 but fig. 7 suggests that this was not always the case.

The flow coefficients corresponding to the onset of the pressure oscillations are related to tip speed Mach numbers. However, if the inlet flow coefficient is plotted versus any of the impeller exit variables, for example $\hat{C}_{r20}$, as shown

on fig. 8, one can note that the onset starts at an almost constant value of such variables. Fig. 9 shows both α_{20} and α_{40} versus $\hat{C}_{r20}$. It can be noted that the unsteady flow condition invariably appears when $\alpha_{20_\bullet} \simeq 10°$ and $\alpha_{40_\bullet} \simeq 13°$. The behavior of the diffuser pressure recovery coefficient, see fig. 10, shows considerable scattering corresponding to the $\alpha_{20_\bullet}$ onset value. Fig. 11 shows that the return channel pressure recovery coefficient exhibits considerable discontinuity in the onset regions.   It is of particular interest to note that the C_{pRC} vs. α_{40} curve is split into two different branches which correspond to dual frequency and single frequency respectively.

Bearing in mind, that pressure oscillations at impeller suction were always negligible and considering the behavior of pressure recovery coefficients, it seems that the phenomenon had its origin from the statoric components. Three different hypothesis can be formulated to explain the onset mechanism:

a. - the phenomenon pertains to the diffuser "in itself" and starts when a "critical" inlet angle is reached.

b. - the phenomenon pertains to the return channel "in itself" and starts when a "critical" incidence angle is reached.

c. - interaction between the vaneless diffuser and return channel is not negligible, therefore a "critical value" of some exit variable exists which cannot be clearly ascribed to each one individually.

It is clear that these hypothesis as they have been formulated are somewhat simplified and that they ignore the fact that the inlet conditions of the stationary components, for a constant value of $\hat{C}_{r20}$, are not strictly similar at different Mu. For instance:

- "average" velocity profiles are not exactly similar

- the diffuser inlet absolute Mach number increases from 0.25 at Mu = 0.45 to 0.43 at Mu = 0.85

- the diffuser inlet Reynolds number varies from R_e = 90,000 at Mu = 0.45 to R_e = 160,000 at Mu = 0.85

However these variations are moderate and fig. 9, fig. 10 and fig. 11 suggest that the influence of these factors is limited within the range explored throughout testing.

Let us assume as a working hypothesis that the phenomenon is mainly influenced by the return channel and starts when a "critical" incidence angle at the leading edge of the return channel blades is reached. In the light of this hypothesis a new return channel was built with identically shaped blades, but a different axial width, to move the onset close to the design flow of the stage.

Configuration B

In order to avoid some confusion experienced when testing configuration A, both time averages and instantaneous measurements were acquired contemporaneously, moreover the tested points were concentrated in the unsteady flow area.

The phenomenon is easier to describe since it is characterized by a single-frequency shape within the tested range of Mu. The onset as well as the growth of the pressure oscillations are similar to those tested on configuration A when the single frequency shape was present. Fig. 12 and fig. 13 show respectively the normalized frequency and the pressure oscillations amplitudes at sec. 20' versus the inlet flow coefficient. The following can be noted:

. Amplitudes at sect. 10' are always negligible till full surge.

. At the different measuring sections pressure oscillations amplitudes are qualitatively similar to those of section 20'. The following are the average values found:

$$A_{30'} \simeq 78\% \; A_{20'}$$

$$A_{40'} \simeq 60\% \; A_{20'}$$

$$A_{50'} \simeq 56\% \; A_{20'}$$

$$A_{60'} \simeq 14\% \; A_{20'}$$

Irrespectively of the flow coefficient, the phase difference between static probes at the same radius is 180° thus indicating a two stall cells configuration.

. The phase difference between static probes at the same angular position was slightly dependent on the flow coefficient. Starting from the onset and reaching the full surge, the phase difference gradually changed (in round figures) from 0° to -10°, between sec. 20', and 30', and from 0° to -20° between sec. 20' and 40', being the phase difference ratio almost constant and near to two. As a consequence, loci of maximum and minimum pressure amplitudes are not radial lines but curves shifted slightly backwards as referred to the direction of rotation.

Analysis of the Time Averaged Data

Fig. 14, 15 and 16 show the pressure ratios (static to total and total to total) versus flow at three different measuring sections. It can be noted that the onset has been shifted to a considerably higher flow as indicated by the hypothesis formulated. As already noted with configuration A, the onset of pressure oscillations starts at an almost constant value of the impeller discharge parameters (see fig. 17 and fig. 18). In this case we had $\alpha_{40*} \simeq 18°$ and $\alpha_{20*} \simeq 14°$.

It can be verified that the onset takes place when there is a practically constant incidence angle at return channel blades while flow angles along the diffuser are considerably different from those of the configuration A. Fig. 20 shows that the pressure recovery coefficient of the return channel again exhibits a sudden drop at the onset of unsteady flows. The C_{pD} too curves downwards, fig. 19, however the drop is less evident, whereas scattering is greatly reduced if compared with configuration A.

TESTS SUMMARY AND CONCLUDING REMARKS

Two different stage configurations were tested to study the behavior of unsteady flows. Configuration A and configuration B had identical impellers and diffusers but different return channels and cross-overs. The following can be concluded on the basis of tests performed:

1. The two configurations tested clearly showed that unsteady flow is caused by the statoric components.

2. With configuration B unsteady flows begin at much higher flow coefficient than those of configuration A.

3. The onset of pressure oscillations takes place with considerably different diffuser flow angles for the two configurations, while the incidence angle at the return channel blades is almost constant.

Therefore it seems that the return channel blades played the most important role in determining both the onset and the growth of the phenomenon.

To conclude, some additional remarks are necessary to give an indication of the general validity of obtained results and some comparison with the behavior of complete machines when gas density is high enough to reveal pressure oscillations in the form of shaft vibrations.

. Tests performed on completely different stages (i.e. several standard stages for average specific speed and one 3-D type typical for pipeline applications) exhibited unsteady flows with frequency-amplitude behavior similar to that of the configurations described in this paper.

. The frequencies of forced asynchronous vibrations, detected in full load testing of high density compressors (ref. 7 and 8) showed a very good correspondence to the frequencies of pressure oscillations of non stationary flows investigated on a single stage test rig.

. Reviewing current literature on this subject the following can be remarked:

   a. The tests referred to with ref. 10, 11, 12 and 13 definitely show that a vaneless radial diffuser may generate self-excited pressure oscillations. The present paper suggests that such data should be used with some caution for an industrial centrifugal stage, having a return channel.

352

b. Test results of the present paper agree to a great extent with ref. 14
   and with some of the data published in ref. 15, both based on testing of
   industrial centrifugal stages with return channels.

REFERENCES

1. Ferrara P.L., Tesei A.: High Pressure Centrifugal Compressors. Inst. Mech. Eng.
   Conference Publications 1978-3 March 1978

2. EK M.C.: Solution of the Subsynchronous Whirl Problem in the High Pressure
   Hydrogen Turbomachinery of the Space Shuttle Main Engine. AIAA/SAE 14-th
   Joint Propulsion Conference. Las Vegas, Nev.-July 25-27, 1978.

3. Geary C.H., Damratowsky L.P., Seyer C.: Design and Operation of the World's
   Highest Pressure Gas Injection Centrifugal Compressor paper No. O.T.C. 2485
   presented at the Offshore Technology Conference, Houston Texas, May 1976.

4. Coletti N.J., Crane M.E.: Centrifugal Compression on the Arun High Pressure
   Injection Project. Inst. mech. Eng. Conference Publications 1981-3 March 1981.

5. Wright D.V.: Air Model Tests of Labyrinth Seal Forces on a Whirling Rotor.
   ASME Book Editor W.G. Steltz 1977.

6. Benckert H., Wachter J.: Flow Induced Spring Coefficients of Labyrinth Seals
   for Application in Rotor Dynamics. NASA Conference Publication 2133-Aug. 1980.

7. Bonciani L., Ferrara P.L., Timori A.: Aero-Induced Vibration in Centrifugal
   Compressors. NASA Conference Publication 2133-August 1980.

8. Sabella D. Terrinoni L., Timori A.: Full Load Testing of Centrifugal Natural
   Gas Injection Compressors. Inst. Mech. Eng. Conference Publication 1981-3 March
   1981.

9. Benvenuti E.: Aerodynamic Development of Stages for Industrial Centrifugal
   Compressors, Part. 1 & 2 - ASME Paper No. 78-GT4 & 5.

10. Jansen W.: Rotating Stall in a Radial Vaneless Diffuser. Transactions of the
    ASME-Journal of Basic Engineering - Dec. 1964 p.p. 750+758.

11. Abdelhamid A.N., Bertrand J.: Distinctions Between Two Types of Self-excited
    Gas Oscillations in Vaneless Radial Diffusers - ASME Paper No. 79-GT-58.

12. Abdelhamid A.N.: Analysis of Rotating Stall in Vaneless Diffusers of Centrifugal
    Compressors. ASME Paper No. 80-GT-184.

13. Abdelhamid A.N.: Effects of Vaneless Diffuser Geometry on Flow Instability in
    Centrifugal Compression Systems. ASME Paper No. 81-GT-10.

14. Abdelhamid A.N., Colwill W.H., Barrows J.F.: Experimental Investigation of
    Unsteady Flow Phenomena in Vaneless Radial Diffusers. ASME Paper No. 78-GT-23.

15. Van Den Braembussche R.A., Frigne P., Roustan M.: Rotating non Uniform Flow in
    Radial Compressors. AGARD C.P. 282-May 1980

TABLE 1.

Measuring sect.	Total pressure probes	Static pressure probes	Thermoel.
Sec. 10 (impeller inlet)	4 Kiel 1 cobra	1	8 (circum. and radially spaced)
Sec. 20 (diffuser inlet)	1 cobra	1	2
Sec. 40 (diffuser exit)	1 cobra	4	
Sec. 60 (return channel exit)	4 Kiel	8 (4+4 st inner and over radius)	8 (circum. and radially spaced)

TABLE 2.

Measuring sect.	Total pressure probes	Static pressure probes
Sec. 10' (Impeller inlet)	1	1
Sec. 20' (Diffuser inlet)	1	2 (90° spaced)
Sec. 30' (Diffuser midspan)	1	2 (90° spaced)
Sec. 40' (Diffuser exit)		2 (90° spaced)
Sec. 50' (Return channel throat area)		2 (90° spaced. Throat area of two sections of the return channel)
Sec. 60' (Return channel exit)		1 (At the exit of one of the two sections of sec. 50)
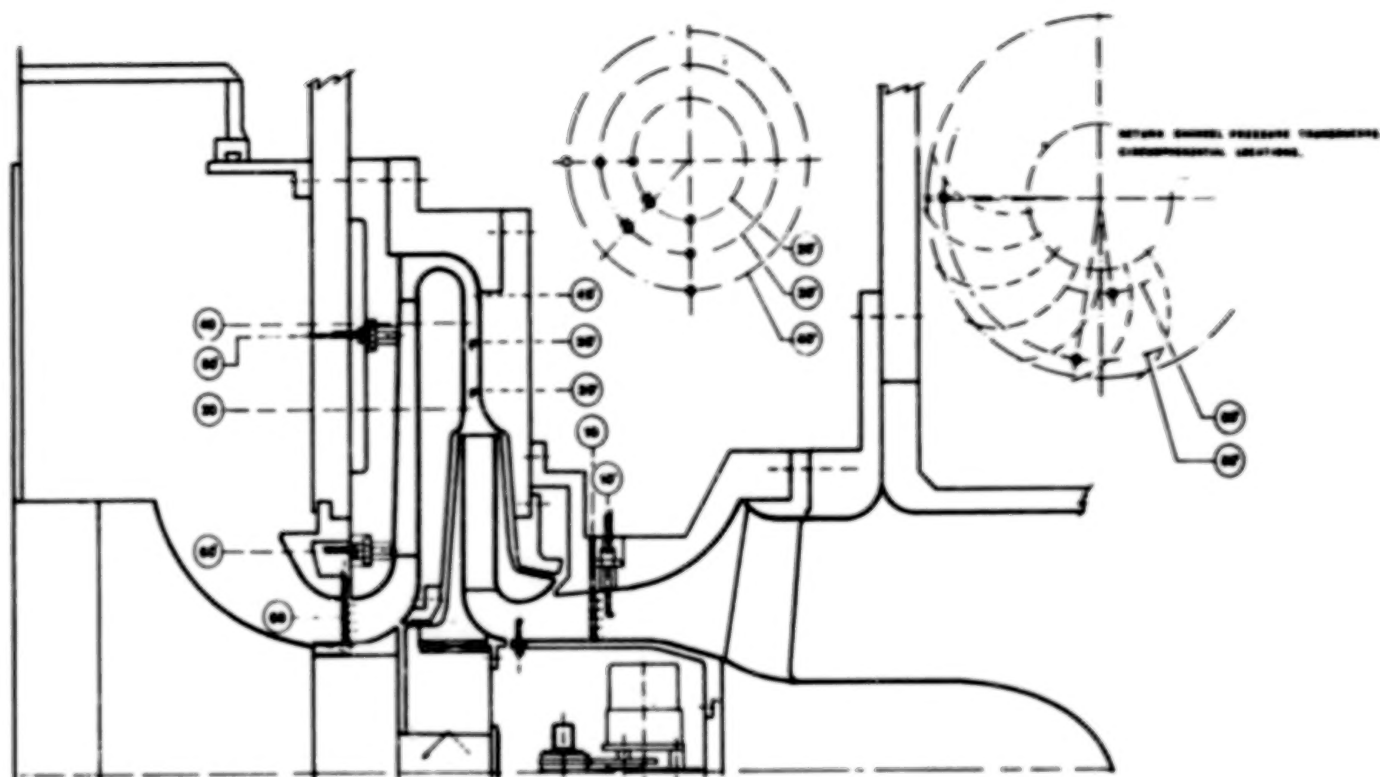
Figure 1. - Cross section of the test rig.
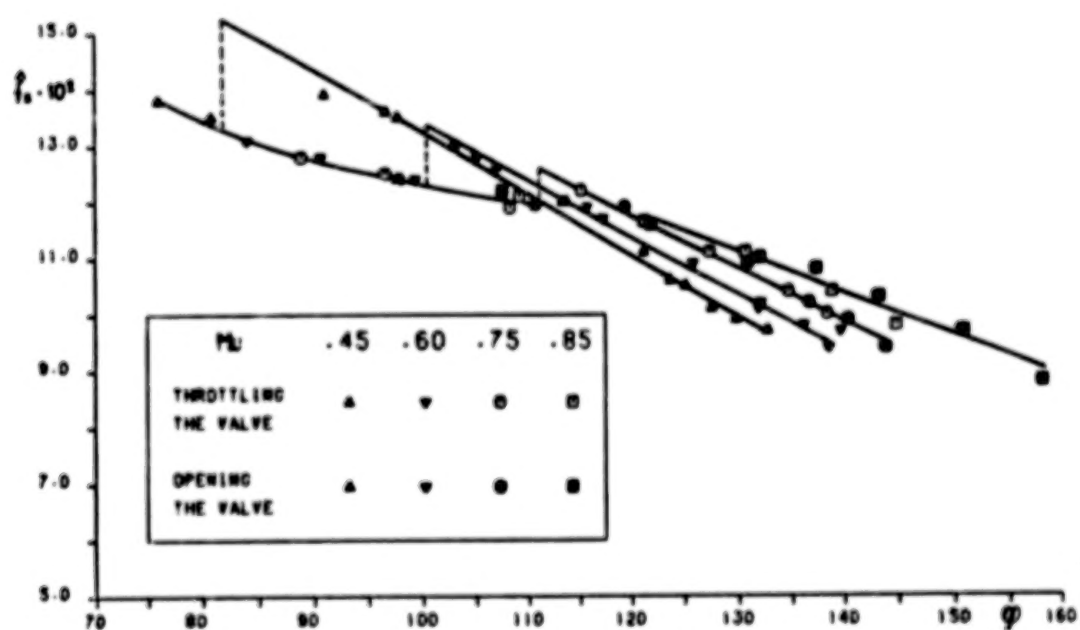
Figure 2. - Normalized observed frequency vs. inlet flow coefficient (configuration A).

356
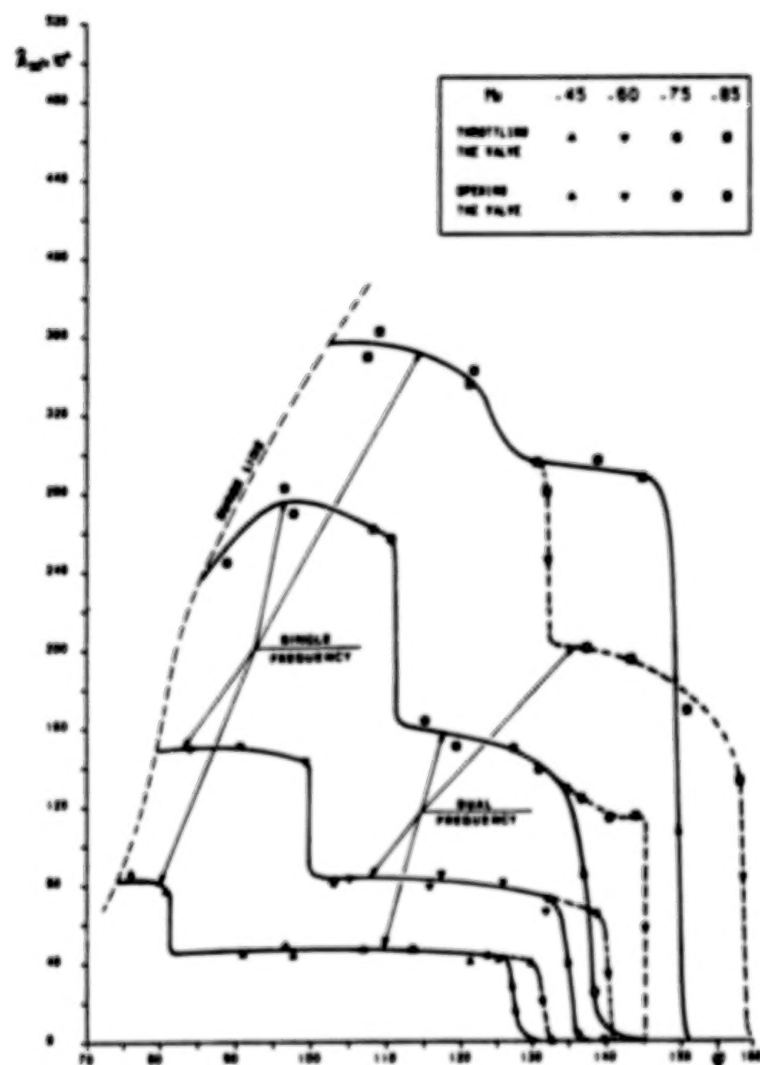
Figure 3. - Static pressure oscillation reduced
amplitude (θ fs) at section 20 vs. inlet flow
coefficient (configuration A).

Figure 4. - Static pressure oscillation reduced
amplitude (θ fs/2) at section 20 vs. inlet flow
coefficient (configuration A).

356
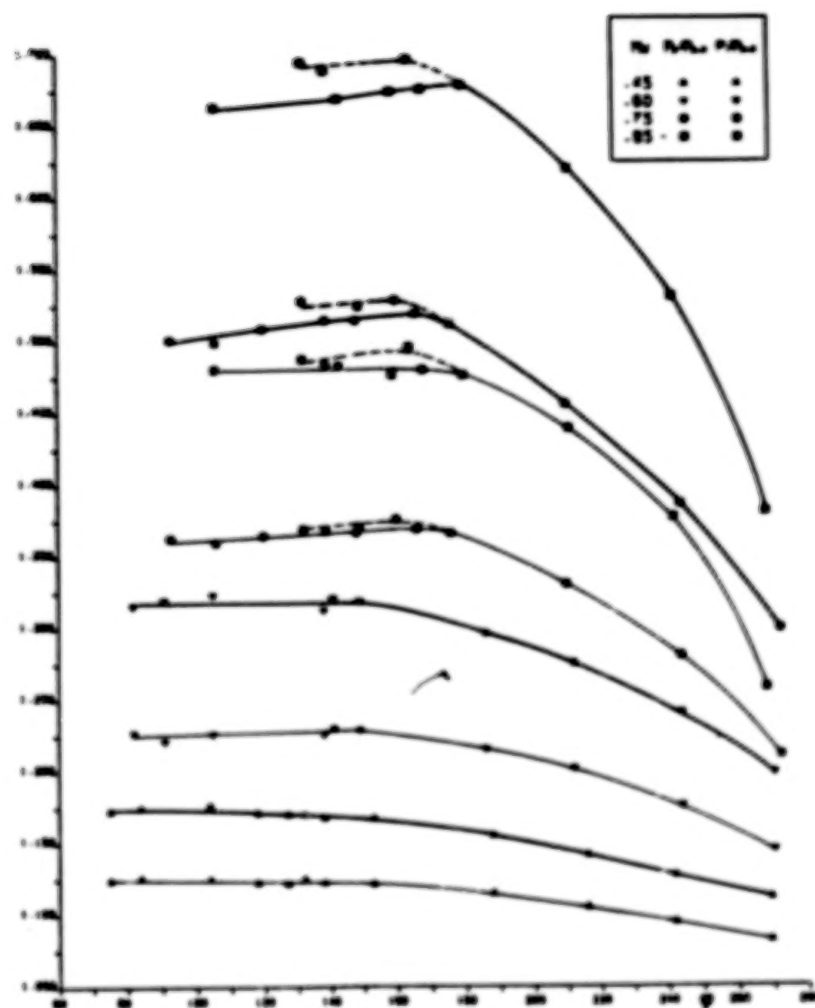
Figure 5. - Static to total and total to total pressure ratios at section 20 vs. inlet flow coefficient at different Mach numbers (configuration A).
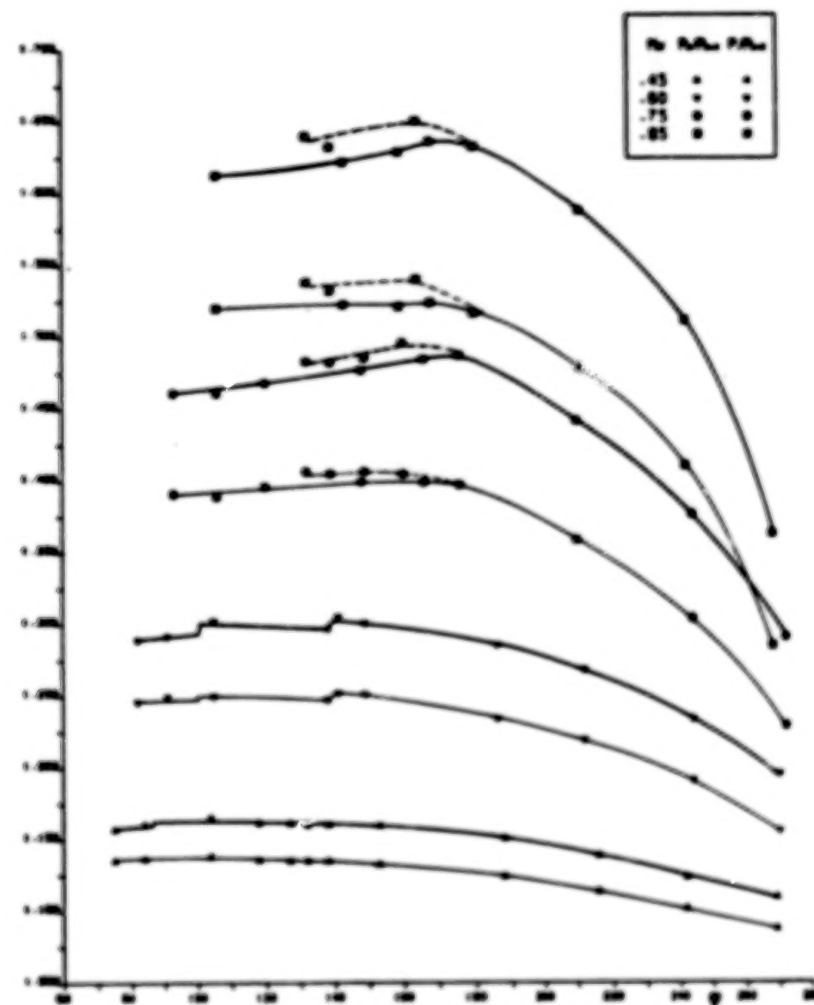
Figure 6. - Static to total and total to total pressure ratios at section 40 vs. inlet flow coefficient at different Mach numbers (configuration A).

357

357

358
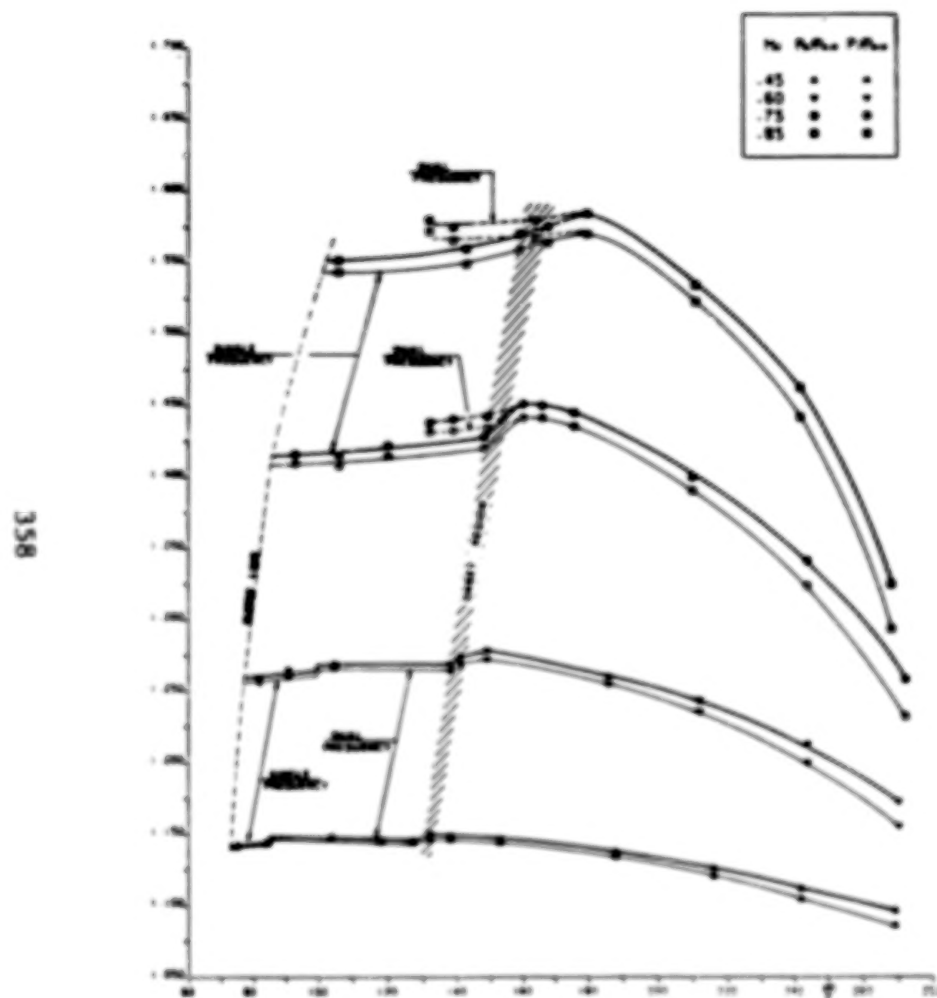
Figure 7. - Static to total and total to total pressure ratios at section 60 vs. inlet flow coefficients at different Mach numbers (configuration A).
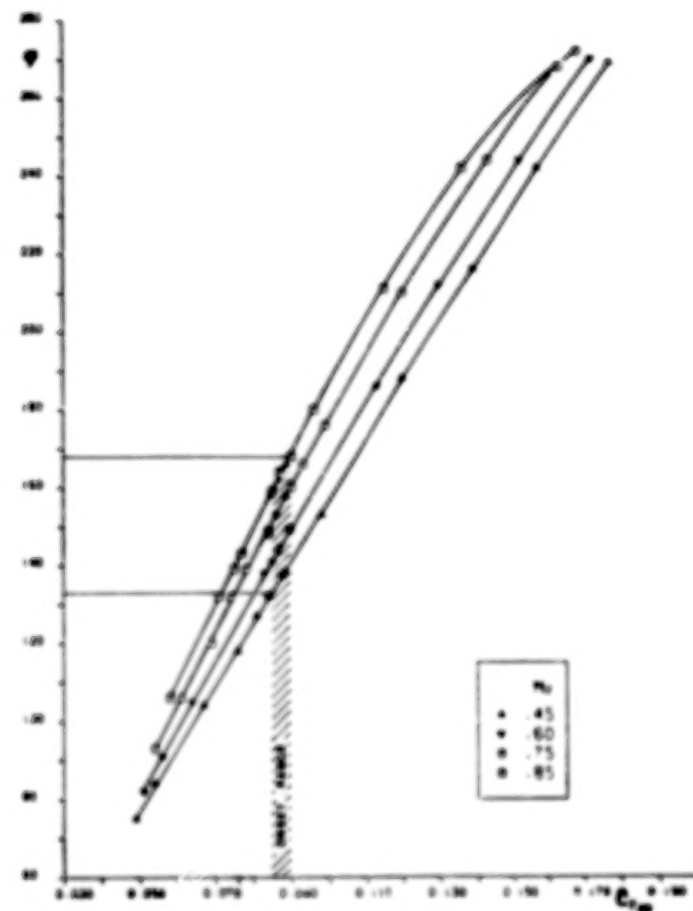
Figure 8. - Flow coefficient versus nondimensional radial speed at section 20, at different Mach numbers (configuration A).
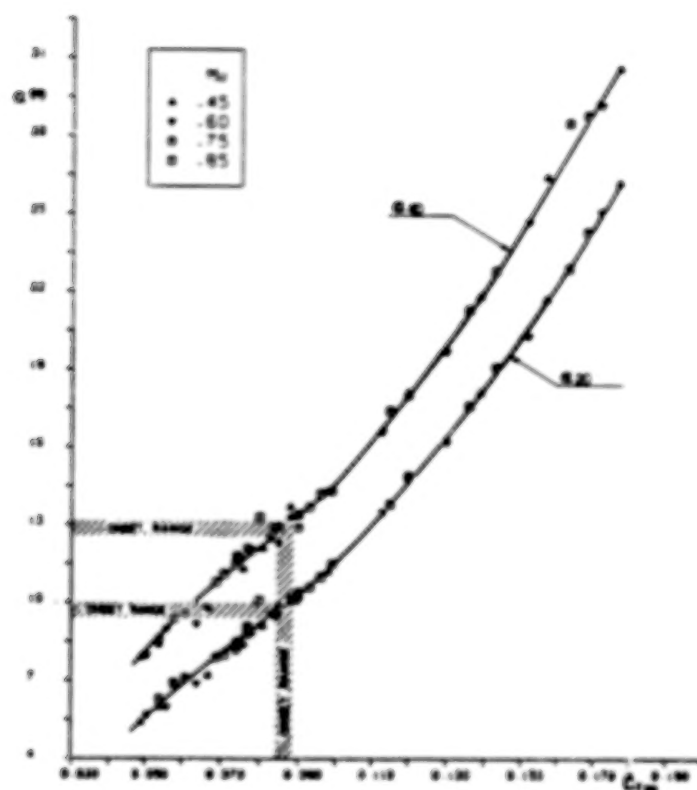
Figure 9. - Absolute flow angles at section 20 and section 40 vs. nondimensional radial speed at section 20 (configuration A).
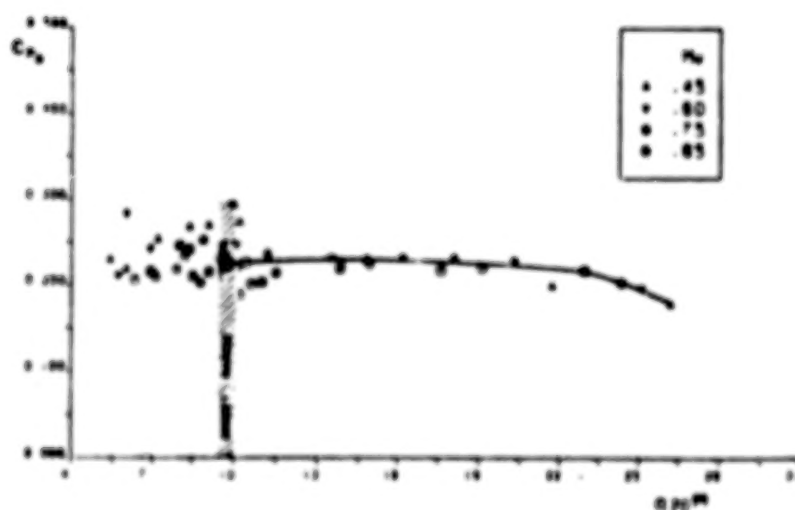
Figure 10. - Vaneless diffuser pressure recovery coefficient vs. absolute flow angle at section 20 (configuration A).
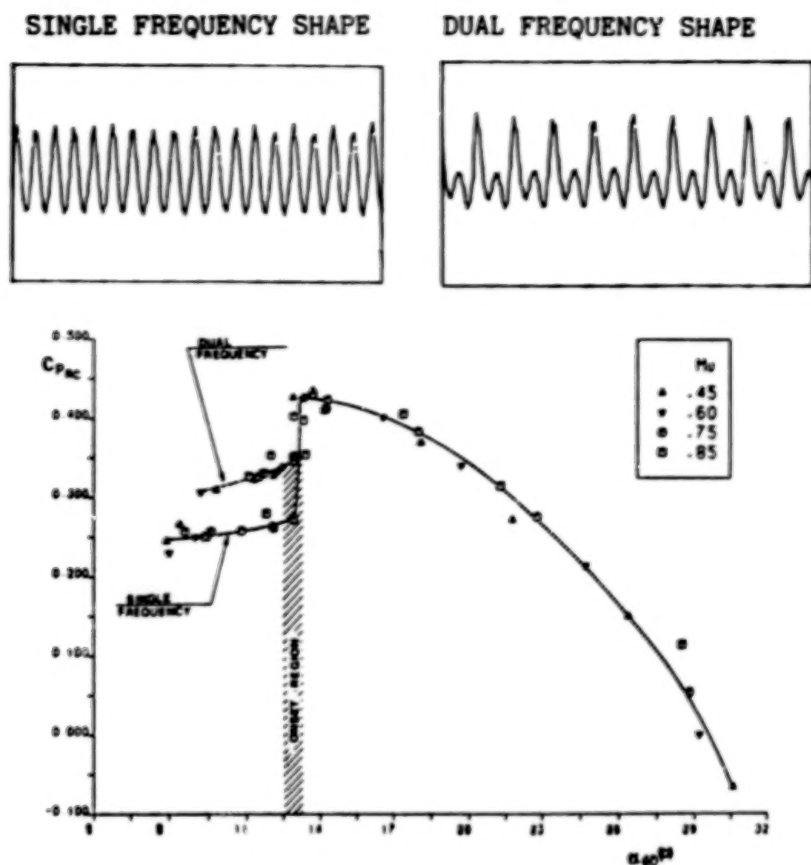
Figure 11. - Return channel pressure recovery coefficient vs. absolute flow angle at section 40 (configuration A).
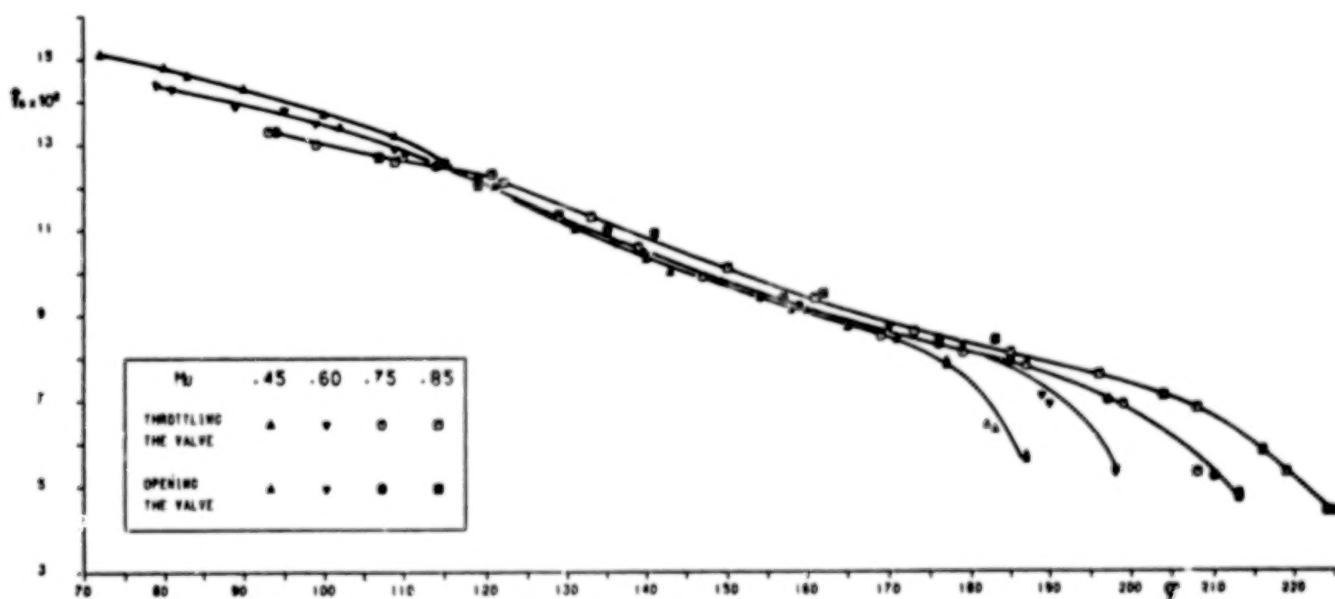
Figure 12. - Normalized observed frequency vs. inlet flow coefficient (configuration B).

360
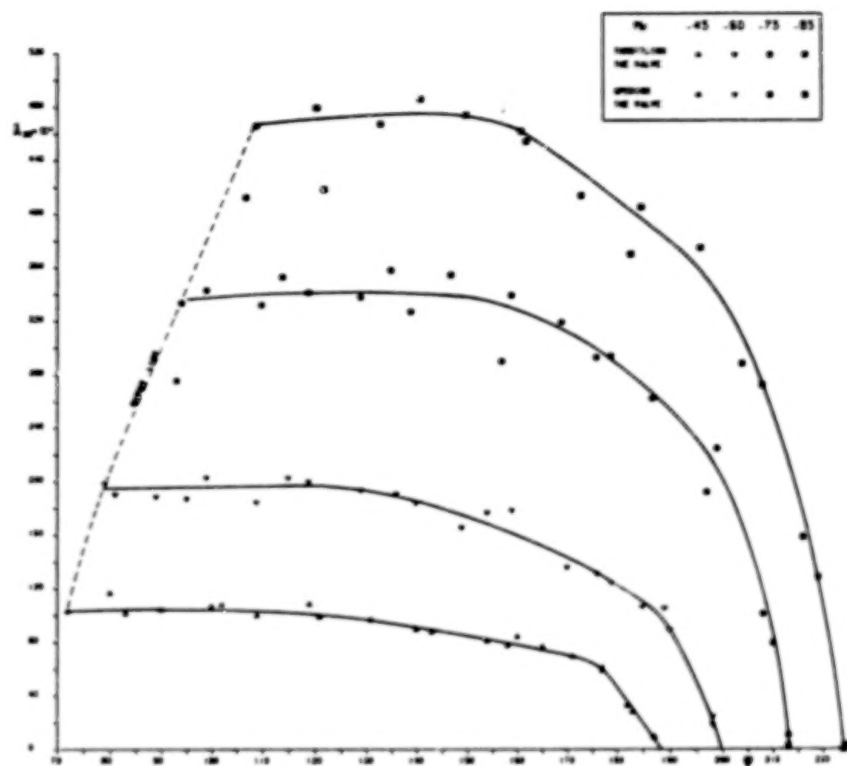
Figure 13. - Static pressure oscillation reduced amplitude (@ fs) at section 20 vs. inlet flow coefficient (configuration B).
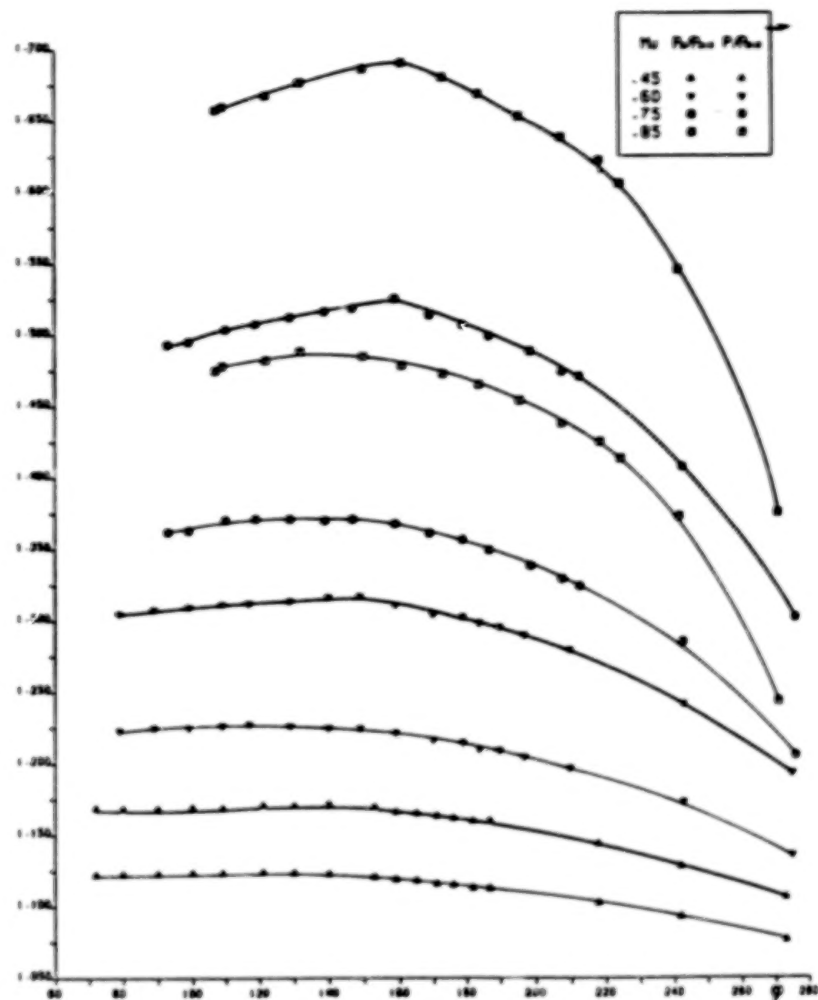
Figure 14. - Static to total and total to total pressure ratios at section 20 vs. inlet flow coefficient at different Mach numbers (configuration B).
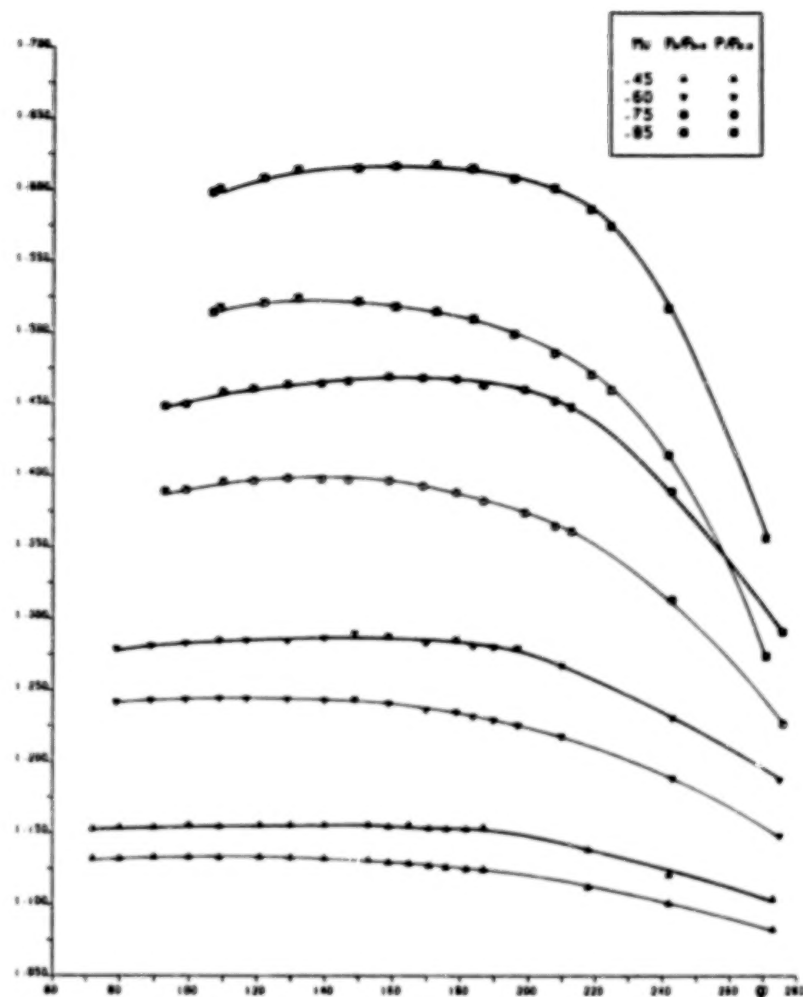
Figure 15. - Static to total and total to total pressure ratios at section 40 vs. inlet flow coefficient at different Mach numbers (configuration B).
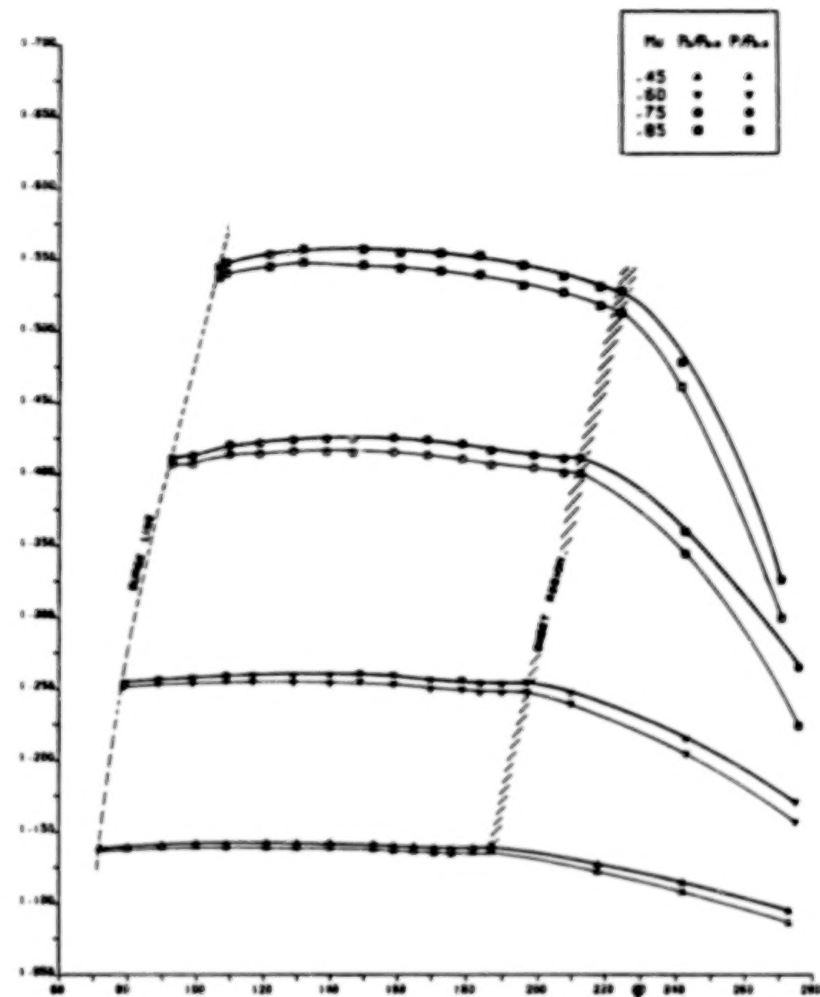
Figure 16. - Static to total and total to total pressure ratios at section 60 vs. inlet flow coefficient at different mach numbers (configuration B).
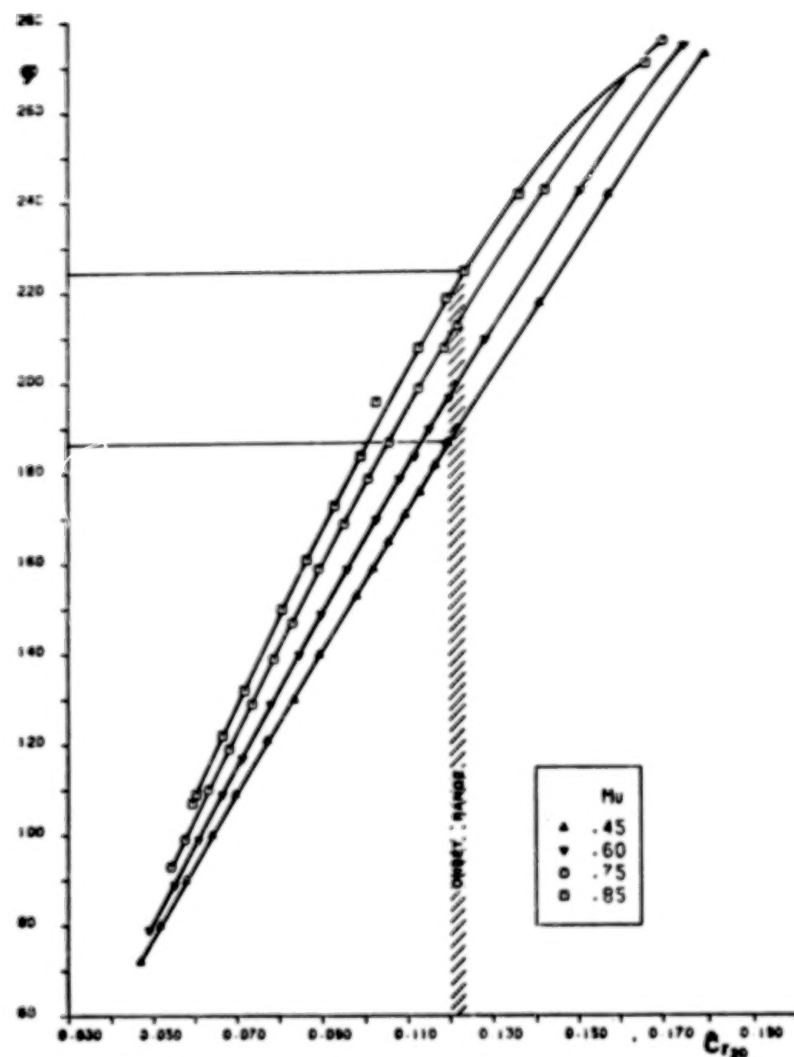
Figure 17. - Flow coefficient versus nondimensional speed at section 20, at different Mach numbers (configuration B).
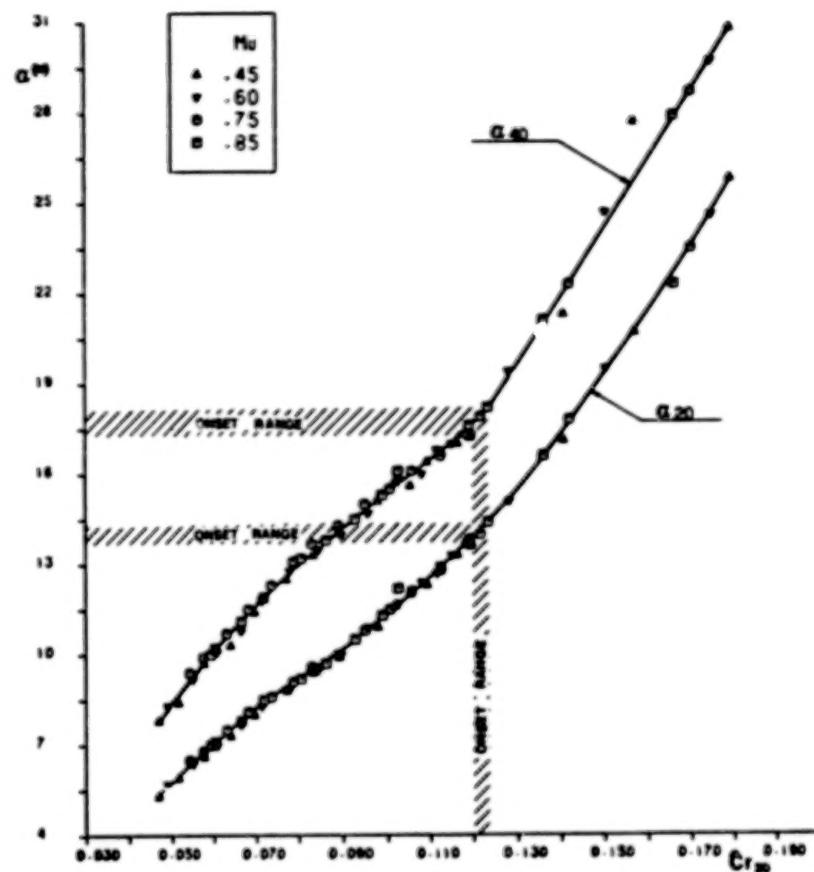
Figure 18. - Absolute flow angles at section 20 and section 40 vs. nondimensional radial speed at section 20 (configuration B).
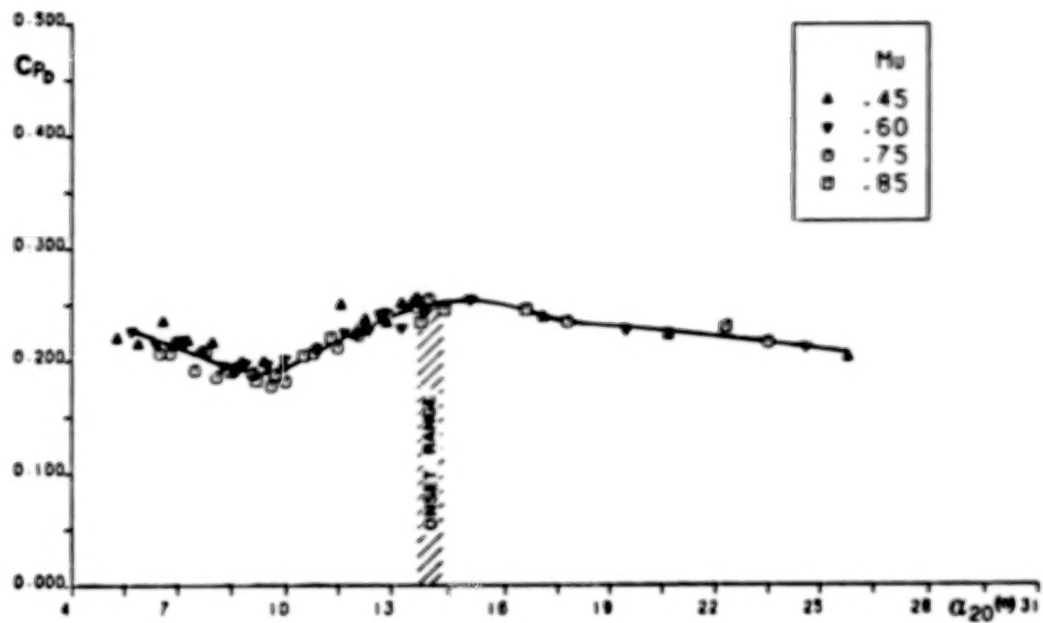
Figure 19. - Vaneless diffuser pressure recovery coefficient vs. absolute flow angle at section 20 (configuration B).
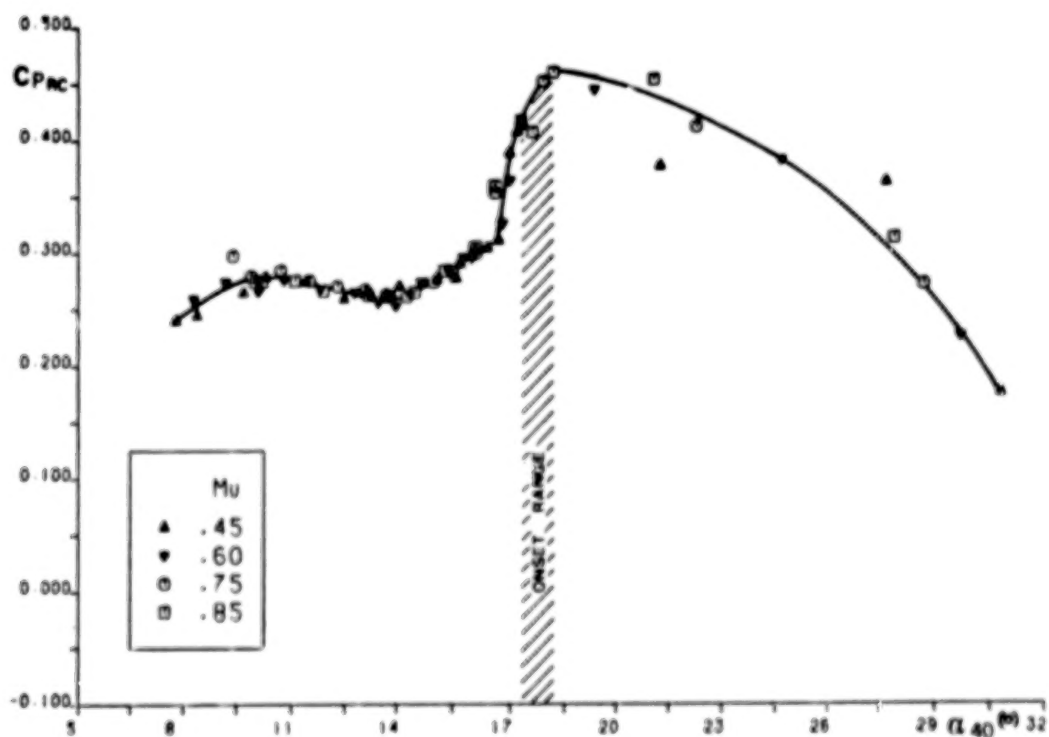
Figure 20. - Return channel pressure recovery coefficient vs. absolute flow angle at section 40 (configuration B).

364

COMPARATIVE STUDY OF SUBSYNCHRONOUS ROTATING FLOW PATTERNS

IN CENTRIFUGAL COMPRESSORS WITH VANELESS DIFFUSERS

P. Frigne*
State University of Gent
9000 - Gent, Belgium

R. Van Den Braembussche
von Karman Institute
1640 - Rhode Saint Genèse, Belgium

SUMMARY

A comparative experimental investigation of the unstable operating modes of a centrifugal compressor is made. Hot wire measurements, in two different compressor configurations, allowed to distinguish between the different unsteady flow pattern. Impeller and/or diffuser rotating stall has been observed, depending on the flow conditions. The measured relative rotational speed of this perturbation is cross-checked with other experimental data and it is shown that the rotational speed is strongly dependent on the type of rotating stall. The diffuser absolute inlet flow angle at the onset of diffuser rotating stall agrees well with the value predicted by an existing stability criterion.

INTRODUCTION

Self excited vibrations of turbomachinery components, due to aerodynamic forces, can be divided into two groups. A first one concerns the vibrations where the destabilizing forces are function of the whirling motion of the rotor. The initial displacement of the shaft influences the flow conditions in the labyrinth seals or creates an asymmetric blade loading on the impeller. The corresponding forces sustain the initial perturbation because of the negative damping.

A second type concerns the vibrations where the main flow is destabilized by hydrodynamic or viscous forces which are independent of the resulting mechanical vibration. They are known as rotating stall and surge. The last ones have also an important influence on compressor performance.

At low pressure levels, the corresponding forces are often too small to have any significant influence on the shaft vibrations, but sometimes result in blade failures. However, at high pressure levels the excitation becomes much larger and very often limits the range of operation because of vibrational problems.

This paper is limited to the study of the second type of destabilization in centrifugal compressors with vaneless diffusers.

---

* Formerly Research Associate at von Karman Institute.

Hot wire measurements have been performed in two different compressor configurations in order to investigate the different unsteady flow pattern.

SYMBOLS

b	diffuser width
C_p	static pressure rise coefficient
i	number of stall cells
P	static pressure
R	radius
Re_{b_2}	Reynolds number, based on diffuser absolute inlet velocity and diffuser width
U	peripheral velocity
V	absolute velocity
α	absolute flow angle, measured from meridional plane
β	blade angle measured from meridional plane
ϕ	mass flow coefficient
ρ	static density
μ	slip factor
ω_s	absolute angular velocity of stall cells
Ω	angular velocity of the impeller

Subscripts

0	settling chamber
1	inducer inlet channel
2	diffuser inlet
3	diffuser outlet
c	critical

DESCRIPTION OF TEST FACILITY AND INSTRUMENTATION

The experiments have been performed in the open loop test facility (Fig. 1a) of the State University of Gent. Mass flow is fed into the settling chamber by a normalized tube which allows for flow control and mass flow measurement. Inlet guide vanes can be installed in the suction pipe if prerotation is required. Flow is discharged at atmospheric pressure after a 180° turning at the diffuser exit.

All measurements have been performed with a vaneless diffuser. Geometrical parameters of the unshrouded impeller (Fig. 2) are listed in Table 1.

Besides the classical pressure and temperature probes, required for overall performance measurements, four hot wire probes are also installed. The hot wires are mounted perpendicular to the mean flow direction. One is installed at impeller inlet (II), one at diffuser inlet (ID) and two at R/R_2 = 1.3 inside the diffuser (MD1 and MD2) at 42° circumferential distance (Fig. 1b). The linearized signals are visualized on an oscilloscope and processed with a HP 3582A two channel Fourier spectrum analyser. This allows to define the power spectrum, coherence function and phase transfer function.

Perturbations rotating in the diffuser will result in periodic signals at MD1 and MD2 with period τ_2. Because of the 42° difference in circumferential position there will be a time lag τ_1 which allows to calculate the number of stall cells i, and the rotational speed ω_s:

i = 360/42 • τ_1/τ_2 (i must be integer)

ω_s = $2\pi/(i\tau_2)$.

TEST RESULTS WITHOUT PREROTATION VANES

The first series of measurements have been obtained with an axial flow at compressor inlet. The overall performances are shown on figure 3. The static pressure rise is not related to the mass flow coefficient ϕ_2 but to the diffuser inlet flow angle α_2. The last parameter is used here because of its important influence on diffuser stability and is defined by

tg α_2 = μ/ϕ_2.

The slip factor is calculated from correlations and is checked against the measured impeller temperature rise. Increasing values of α_2 correspond to decreasing mass flow.

The static pressure rise is non dimensionalized by $\rho_0 U_2^2/2$ to become independent of RPM.

All curves show a maximum at α_2 = 76° which coincides with the onset of unstable flow. At higher RPM, these curves do not continue to the left because of surge. At low RPM, surge occurs only at α_2 = 87°

which leaves a large range of flow conditions where unsteady flow can be observed. The hot wire measurements are therefore made at 2000 RPM for α_1 values between 76° and 87°.

The hot wire traces shown on figure 4a are measured at rotor inlet (II) and diffuser inlet (ID) for α_2 = 76°. The relative amplitude of the oscillations, defined by $(V_{max}-V_{min})/V_{RMS}$, amounts to .14 at rotor inlet and .23 at diffuser inlet. The power spectrum and coherence function, shown on figures 4b and 4c, clearly indicate an instability at 27.2 Hz. Inside the diffuser, at R/R_2 = 1.3, the flow is steady as shown on the power spectrum of probe MD1 (Fig 4d). One can therefore conclude that these instabilities are due to impeller rotating stall, which can be explained by the high positive incidence (12°) at inducer tip for this operating point.

Measurements at α_2 = 78° (Fig. 5a) do not only show an increase in amplitude to .37 at impeller inlet (II), but also an extension of these perturbations downstream inside the diffuser (MD). The hot wire traces MD1 and MD2 (Fig. 5b) have a relative amplitude of .13. The phase lag between both signals indicates the presence on one stall cell rotating at 77% of the rotor speed. The power spectrum and coherence function of the II and MD signal (Figs. 5c, 5d) reveal a decrease of the basic frequency to 25.6 Hz and the presence of important harmonics at 52 and 77 Hz.

Figures 6a and 6b are measured at α_2 = 81° and indicate a further increase in amplitude to 200% at rotor inlet (II) and 18% inside the diffuser (MD). The basic frequency is now 23.2 Hz and ω_S/Ω = .70. The harmonics have almost disappeared at rotor inlet but are unchanged inside the diffuser.

Low frequency oscillations completely suppress impeller rotating stall at α_2 = 87°. The hot wire traces of figure 7a seem to indicate that the frequency at rotor inlet (II) is twice the frequency of oscillations inside the diffuser. However, hot wires read only the velocity component perpendicular to the wire and are insensitive to a 180° change in flow direction. The real flow velocity at rotor inlet changes sign (return flow) and is indicated by the dashed line. Both signals are in phase at 6.4 Hz and indicate compressor surge. The power spectrum on figure 7b shows the presence of several harmonic frequencies as well at rotor inlet as inside the diffuser.

This series of measurements show only one type of rotating stall, originating from the rotor. The oscillations are gradually increasing in amplitude and extending downstream inside the diffuser. They are due to one stall cell rotating at high relative velocity.

TEST RESULTS WITH INLET PREROTATION VANES

According to a stability criterion, developed by the authors (Ref. 1), vaneless diffuser rotating stall should occur at α_2 = 77°. However, only impeller rotating stall has been observed in previous experiments. A possible explanation for this disagreement could be

that diffuser rotating stall is completely suppressed by the impeller rotating stall if the latter one starts first.

In order to verify this hypothesis, inlet guide vanes have been installed in the suction pipe, in order to create 60° prerotation at the impeller inlet. Preliminary calculations indicated that this would delay impeller rotating stall at least to $a_2 = 82°$. In this way a sufficiently broad margin for diffuser rotating stall would be created.

The overall compressor performance map is shown on figure 8. Compared to previous results, one can observe a 6° shift to the left of impeller characteristics. The maximum compressor pressure rise has slightly decreased because of the prerotation. The diffuser pressure rise is almost unchanged.

First instabilities are observed in the diffuser at $a_2 = 77°$ (Fig. 9a). The frequency is 17.6 Hz (Fig. 9b) with a coherence of 55% (Fig. 9c). From the 132° phase shift between MD1 and MD2, one can calculate that three stall cells are rotating at $w_s/\Omega = .176$. These instabilities are not observed at the inducer inlet (Fig. 9d) and one can therefore conclude that they are due to diffuser rotating stall.

These instabilities have a maximum amplitude of .11 at $a_2 = 78°$ but completely disappear at $a_2 = 80°$. They suddenly reappear in the diffuser at $a_2 = 80°5$ with a relative amplitude of .14 and a coherence of 98%.

With the achieved prerotation, the critical flow angle for impeller rotating stall is predicted at $a_2 = 82°$. This is experimentally verified by the power spectra obtained at $a_2 = 82°6$. The power peak at 23.2 Hz is measured at rotor inlet and inside the diffuser. The phase angle of 52° indicates that one stall cell rotates at $w_s/\Omega = .673$. These results are very similar to impeller rotating stall observed with zero prerotation. The power peak at 19.2 Hz is observed only inside the diffuser and the phase angle between MD1 and MD2 indicates that three stall cells are rotating at $w_s/\Omega = .192$. In analogy to the measurements at lower a_2 values, one can conclude that this is diffuser rotating stall.

When closing the throttle valve further to $a_2 = 83°1$, diffuser rotating stall remains unchanged, but impeller rotating stall (23.2 Hz) disappears completely (Fig. 11).

A new type of unstable flow, with a frequency of 8.8 Hz is observed at $a_2 = 83°6$ (Fig. 12a). These instabilities are observed only in the diffuser and correspond to a second type of diffuser rotating stall. Two stall cells are rotating at $w_s/\Omega = 13.2\%$. These high and low frequency diffuser rotating stall patterns do not occur simultaneously but in a rather intermittent mode. This relative amplitude increases further to .22 at $a_2 = 84°7$ (Fig. 12b).

The low frequency oscillations (6.4 Hz), observed at a_2 = 86°, are in phase and due to compressor surge. Rotating stall has disappeared at this point.

COMPARISON OF THE TWO TEST SERIES

Impeller rotating stall can be observed at impeller inlet and inside the diffuser. In both test series, the onset of this type of stall coincides with a 12° positive incidence at impeller tip. Prerotation therefore allows to delay this type of instability to lower mass flow coefficients.

Diffuser rotating stall can only be observed in the diffuser and starts at a_2 = 77°. This value will be compared to other data in the next chapter.

Both types of rotating stall can exist simultaneously if diffuser rotating stall occurs first. This absolute frequency and amplitude is of the same order of magnitude and measurements with one single probe do not allow to distinguish between them. However, the relative rotational speed is quite different as shown in figure 13.

Impeller rotating stall has a relative rotational speed of about .7 and this velocity seems to be unaffected by prerotation. The relative rotational speed of diffuser rotating stall is of the order of .10 to .20 only. This difference is in agreement with experimental observations of Lenneman & Howard (Ref. 2), Misuki et al. (Ref. 3) and Abdelhamid (Ref. 4). This difference could therefore be used to distinguish between impeller and diffuser rotating stall. However, the definition of relative rotational speed not only requires to measure the absolute frequency but also the phase difference between two circumferential positions.

THEORETICAL PREDICTIONS OF VANELESS DIFFUSER
ROTATING STALL

Several stability criteria for vaneless diffusers have been developed and published in the literature. They are based on different assumptions and result in contradictory conclusions.

The stability criterion for vaneless diffusers of C. Rodgers (Ref. 5) is based on theoretical considerations concerning variation of C_p in function of a_2. The critical value of a_{2c}, separating the zone of stable operation from the unstable zone, is function of the non dimensionalized diffuser width b_2/R_2 and radius ratio R_3/R_2.

This conclusion is similar to the one obtained by W. Jansen (Ref. 6). His criterion is based on detailed calculations of the viscous flow in vaneless diffusers. Besides diffuser width (b_2/R_2), radius ratio (R_3/R_2) and flow angle (a_2), stability is now also a function of the Reynolds number. Both theories suggest that the critical flow angle a_{2c} is decreasing for decreasing diffuser width. This

would mean that for a given impeller, an unstable vaneless diffuser cannot always be stabilized by decreasing the diffuser width.

A similar but more precise calculation by Senoo (Ref. 7), however, results in a criterion which shows an opposite trend in terms of α_{2c} as a function of diffuser width. The critical flow angle is now increasing for decreasing diffuser width. An unstable diffuser can therefore be stabilized by decreasing diffuser width. This theory also allows to draw important conclusions in terms of diffuser radius ratio R_3/R_2 and about the influence of non uniform flow at diffuser inlet.

The stability criterion of A. Abdelhamid (Ref. 8) is based on rotor-diffuser interaction and does not account for viscous effects. This criterion relates stall operation to the pressure and tangential velocity fluctuations non dimensionalized by radial velocity fluctuations. This criterion is not easily applicable and stability is independent of diffuser width.

In order to eliminate the contradiction between the different criteria, the authors (Ref. 1) have performed some unsteady flow measurements on different impeller-diffuser combinations. These results and other experimental data from the literature allowed to derive the following correlation. All values of α_{3c} fall within a relatively narrow band as shown on figure 14 after they have been corrected for Reynolds number influence according to figure 15. Points 1 to 5 are experimental data obtained by the authors. Points 6 to 16 are derived from published data.

These experimental data indicate an increase of α_{3c} for decreasing diffuser width and agree very well with the predictions of Senoo. His theoretical results do not indicate an influence of Reynolds number on diffuser stability for values of $b_2/R_2 < .10$. However, the experimentally observed variation of α_{2c} in function of Reynolds number is in agreement with the predictions of Jansen ($\Delta\alpha_2 = 6° =$ between $Re_{b_2} = 10^4$ and $Re_{b_2} = 10^5$).

The flow angles 1 to 16, are calculated from measured temperature rise and slip factor correlations. Therefore, some doubt could exist about the precision by which these angles are defined. Some special tests have been performed in order to evaluate this error. They are made for one impeller-diffuser combination at two different Reynolds numbers. Flow angles at diffuser inlet are measured by a crossed hot wire. The experimental values shown by points 17 and 18 are already corrected for Reynolds number influence.

The observed differences with the theoretical curve are within an acceptable tolerance and therefore provide an additional verification of this correlation.

Point 19 is the value obtained from the present test series and confirms the stability limit for diffuser rotating stall.

CONCLUSION

Measurements described in this paper allow to distinguish between impeller or diffuser rotating stall. The onset of impeller rotating stall can be related to inducer incidence and the relative rotational speed is about .70. Diffuser rotating stall is a function of diffuser inlet air angle and Reynolds number and has a relative rotational speed of .1 to .2.

These experiments provide a criterion to distinguish between both phenomena and indicate which part of the compressor should be modified to achieve stable operation.

Flow conditions at the onset of diffuser rotating stall have been compared with a criterion for diffuser stability and agree very well.

REFERENCES

1. VAN DEN BRAEMBUSSCHE, R.: FRIGNE, P.; ROUSTAN, M.: Rotating non uniform flow in radial compressors.
   AGARD CP 282, pp 12-1 to 12-14.

2. LENNEMAN, E. & HOWARD, J.H.G.: Unsteady flow phenomena in rotating centrifugal impeller passages.
   ASME Transact., Series A : J. Engineering for Power, Vol. 92, No. 1, January 1970, pp 65-72.

3. MISUKI, S.; KAWASHIMA, Y.; ARIGA, I.: Investigation concerning rotating stall and surge phenomena within centrifugal compressor channels.
   ASME Paper 78 GT 9.

4. ABDELHAMID, A.N.: Effects of vaneless diffuser geometry on flow instability in centrifugal compressor systems.
   ASME Paper 81 GT 10.

5. RODGERS, C.: Impeller stalling as influenced by diffusion limitations.
   ASME Transact., Series I : J. Fluids Engineering, Vol. 99, No. 1, March 1977, pp 84-97.

6. JANSEN, W.: Rotating stall in radial vaneless diffusers.
   ASME Transact., Series D : J. Basic Engineering, Vol. 86, No. 6, December 1964, pp 750-758.

7. SENOO, Y. & KINOSHITA, Y.: Limits of rotating stall and stall in vaneless diffuser of centrifugal compressors.
   ASME Paper 78 GT 19.

8. ABDELHAMID, A.N.: Effects of vaneless diffuser geometry on flow instability in centrifugal compression systems.
   ASME Paper 81 GT 10

9. LIGRANI, P.M.; VAN DEN BRAEMBUSSCHE, R.; ROUSTAN, M.: Rotating stall measurements in the vaneless diffuser of a radial flow compressor. ASME Paper 82 GT 257

TABLE 1. - GEOMETRICAL CHARACTERISTICS OF THE COMPRESSOR

R_1^{tip}	= .095	b_3	= .016 m
R_1^{hub}	= .054 m	N	= 20
R_2	= .208 m	β_1^{tip}	= 50°
R_3	= .400 m	β_1^{hub}	= 32°
b_2	= .016 m	β_2	= 0°
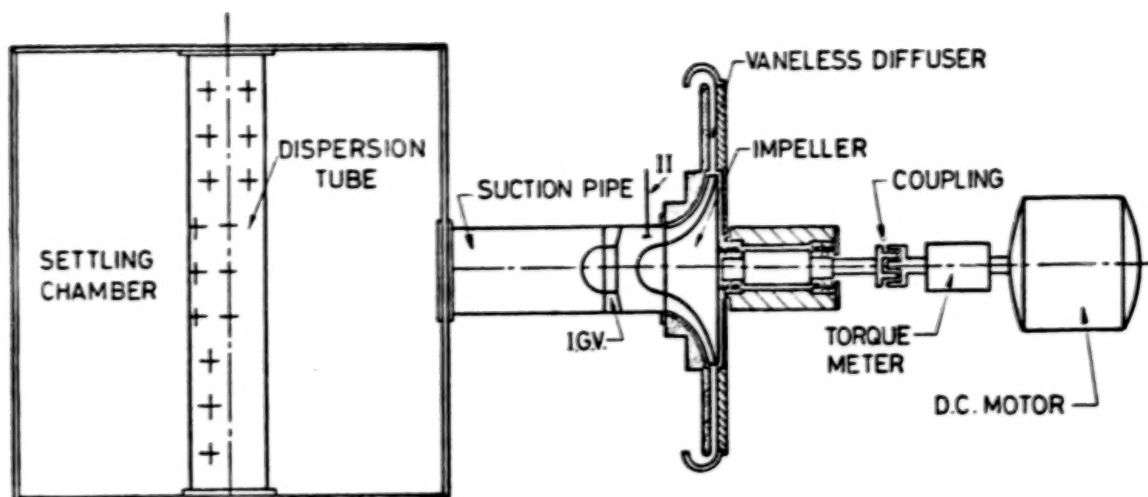
Figure 1(a). - Open loop centrifugal compressor facility.
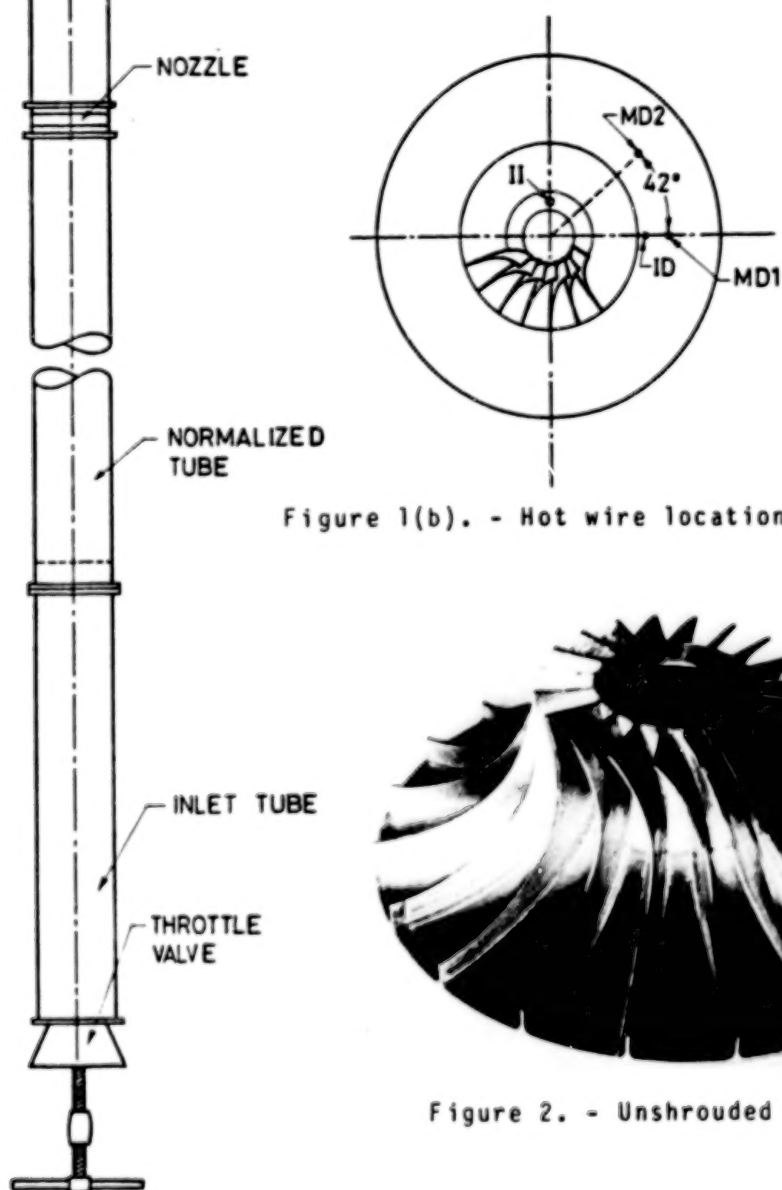
Figure 1(b). - Hot wire locations.
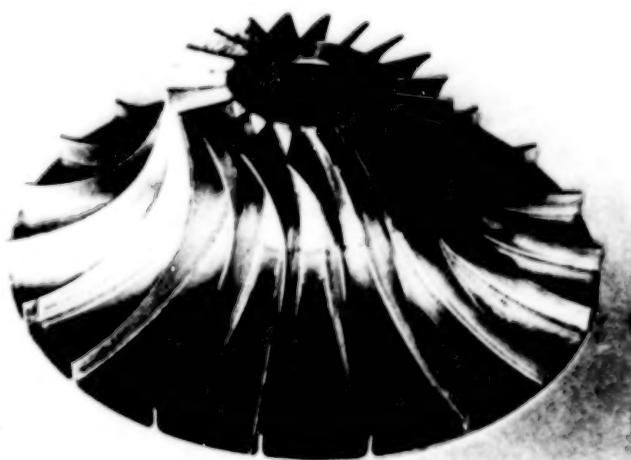
Figure 2. - Unshrouded impeller.

374
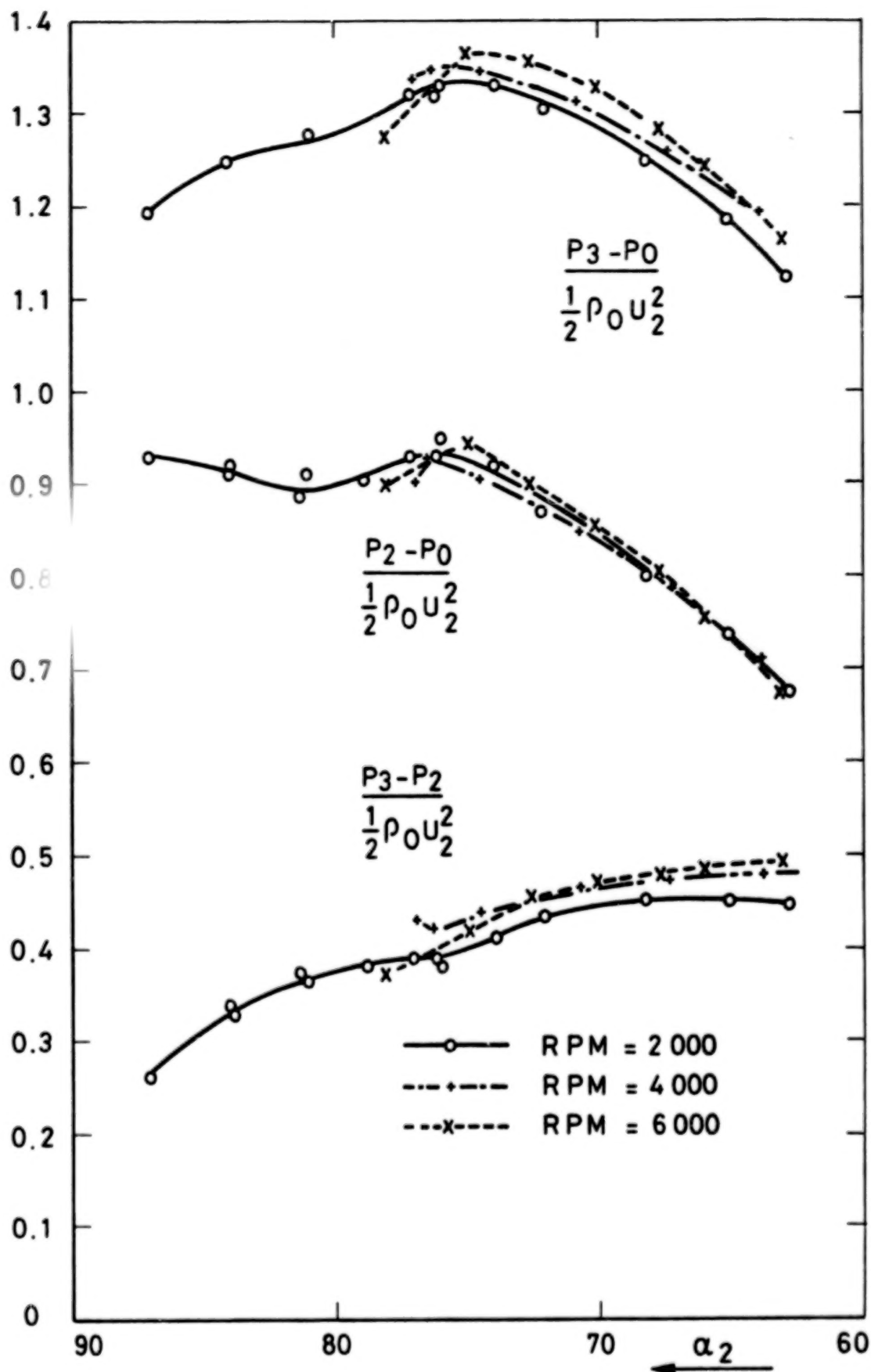
Figure 3. - Compressor performance with zero prerotation.
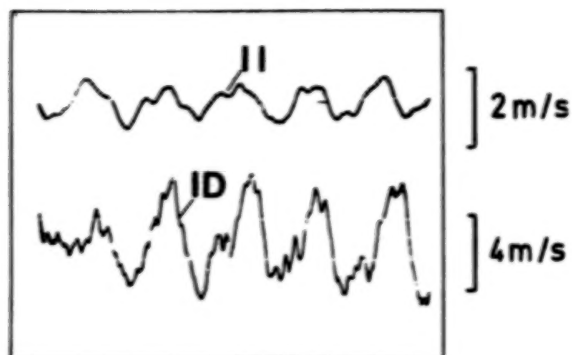
Figure 4(a).
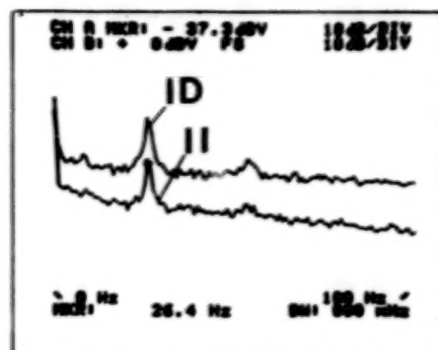
Figure 4(b).
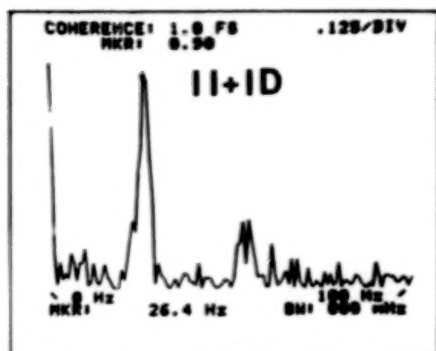
Figure 4(c).
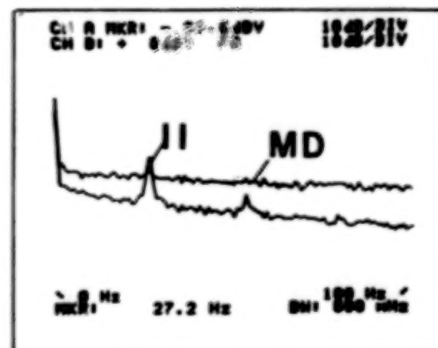
Figure 4(d).
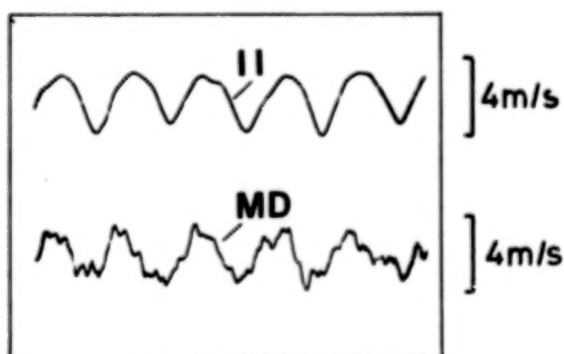
Figure 5(a).
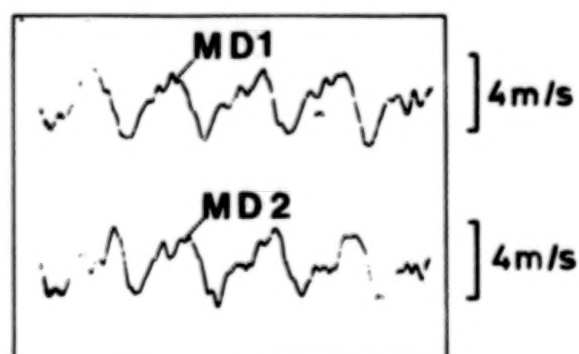
Figure 5(b).

Figure 5(c).

Figure 5(d).

376

II

4 m/s

MD

4 m/s

100 ms

Figure 6(a).

CH A MKR: - 15.6dBV   10dB/DIV
CH B: + 0dBV FS   10dB/DIV

MD

II

MKR: Hz   23.2 Hz   BW: 100 Hz/ mHz

Figure 6(b).

II

10 m/s

MD

10 m/s

100 ms

Figure 7(a).

CH A MKR: - 17.9dBV   10dB/DIV
CH B: + 0dBV FS   10dB/DIV

MD

II

MKR: Hz   13.6 Hz   BW: 100 Hz/ mHz
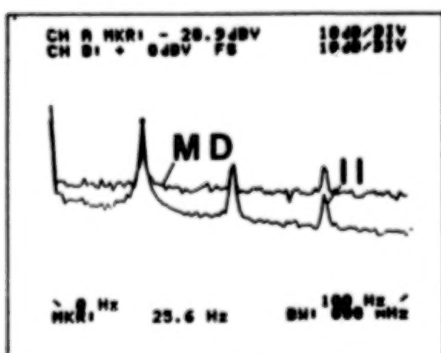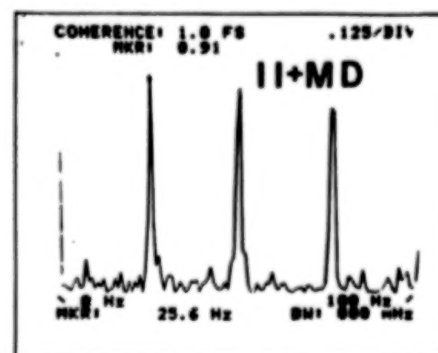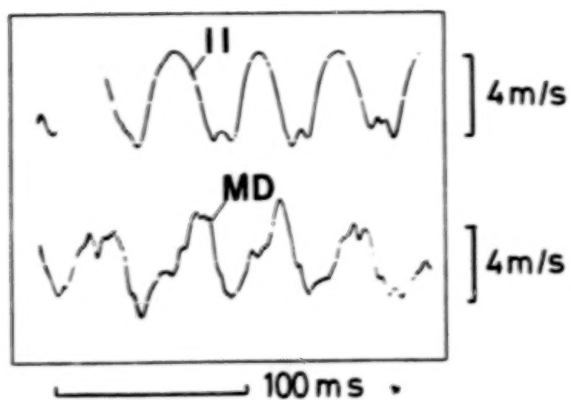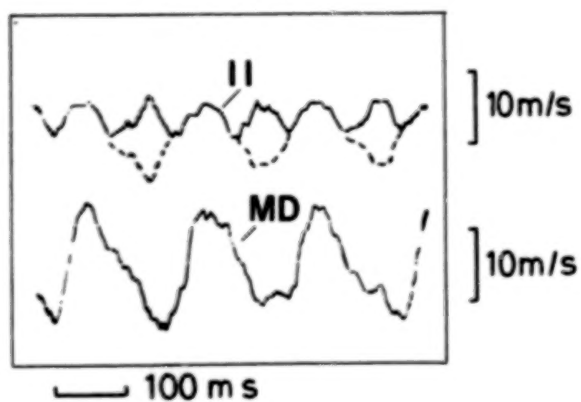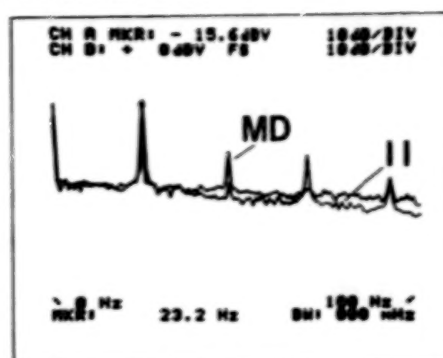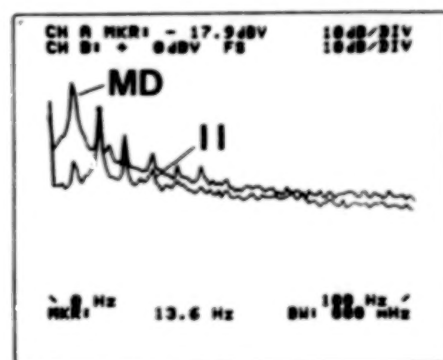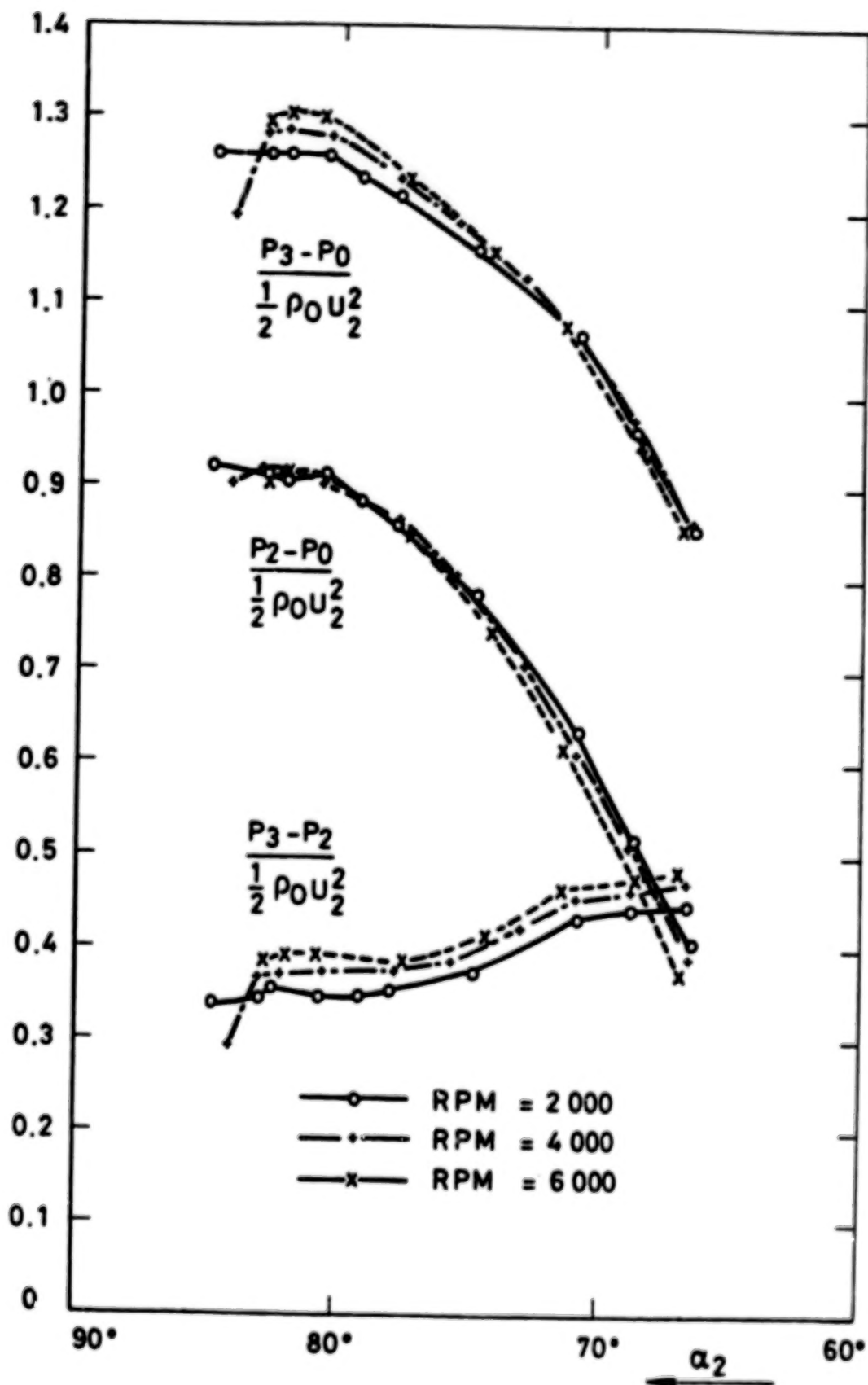
Figure 7(b).

Figure 8. - Compressor performance with 60° prerotation at the inducer tip.

378
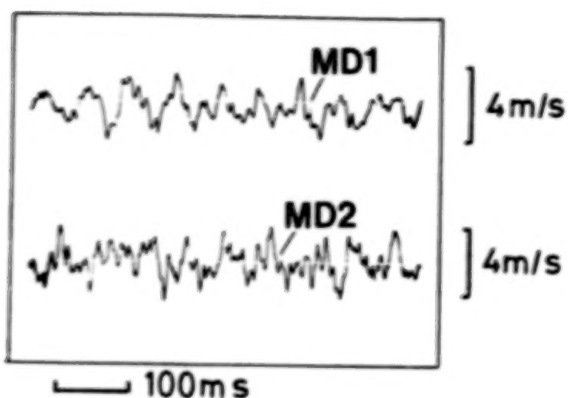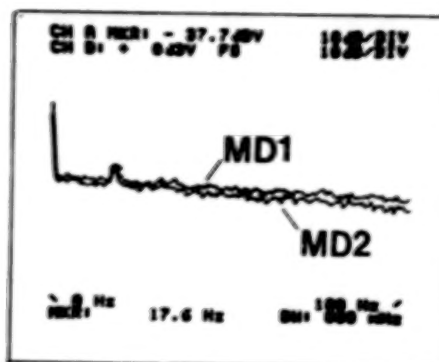
Figure 9(a).

Figure 9(b).
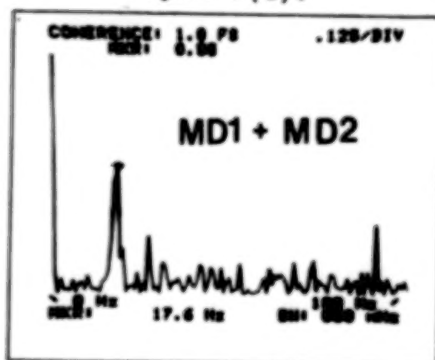
Figure 9(c).
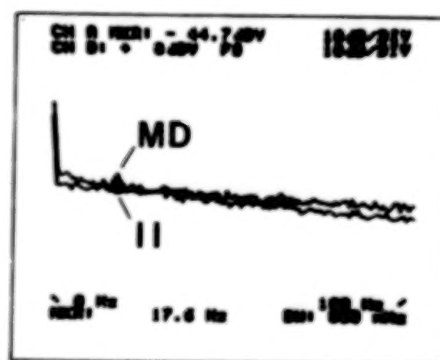
Figure 9(d).
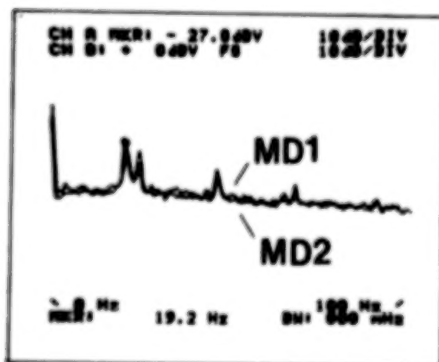
Figure 10(a).
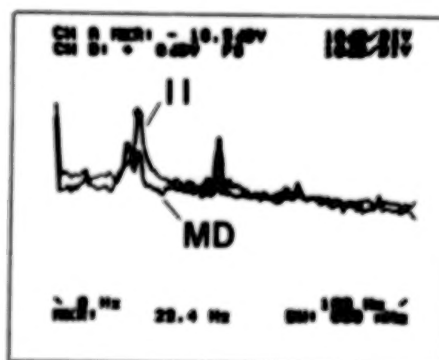
Figure 10(b).
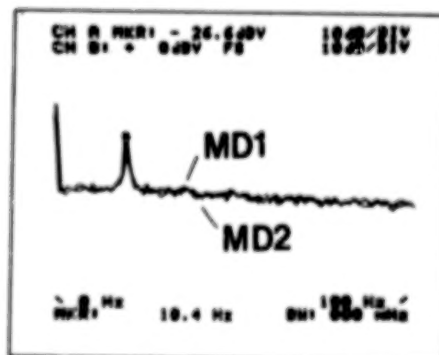
Figure 11.
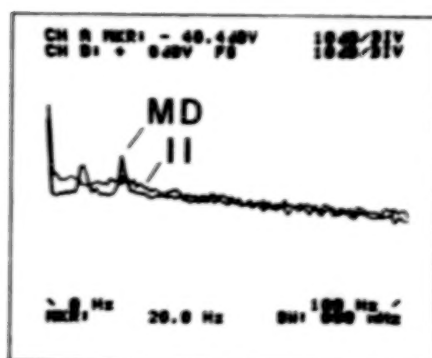
Figure 12(a).
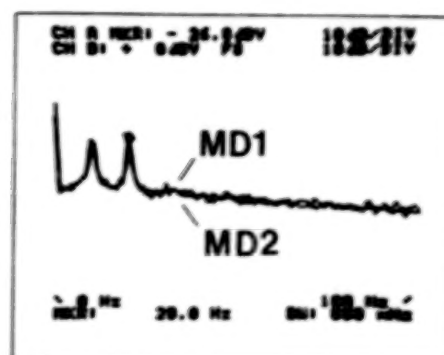
Figure 12(b).
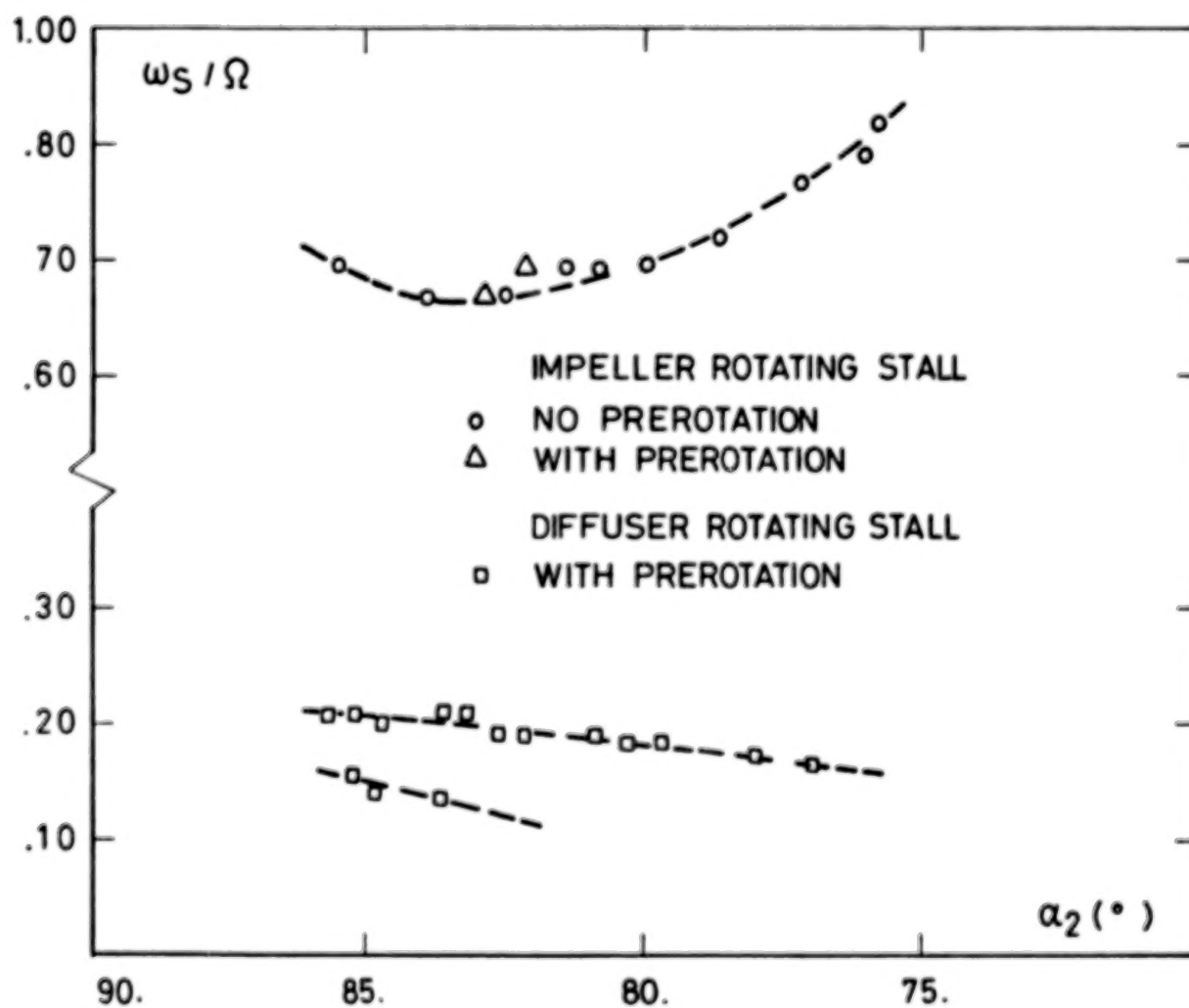
Figure 13. - Relative rotational speed.
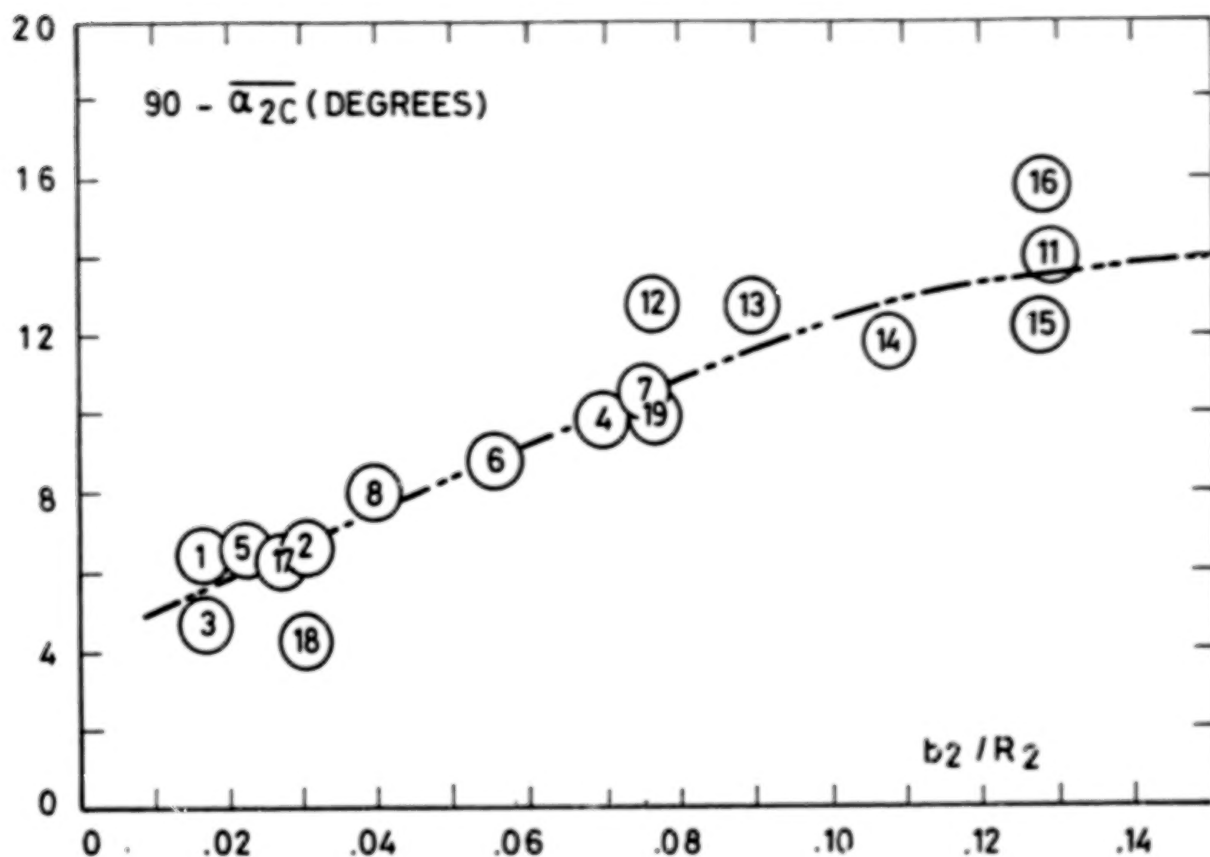
Figure 14. - Critical inlet flow angle complement versus nondimensional diffuser width.
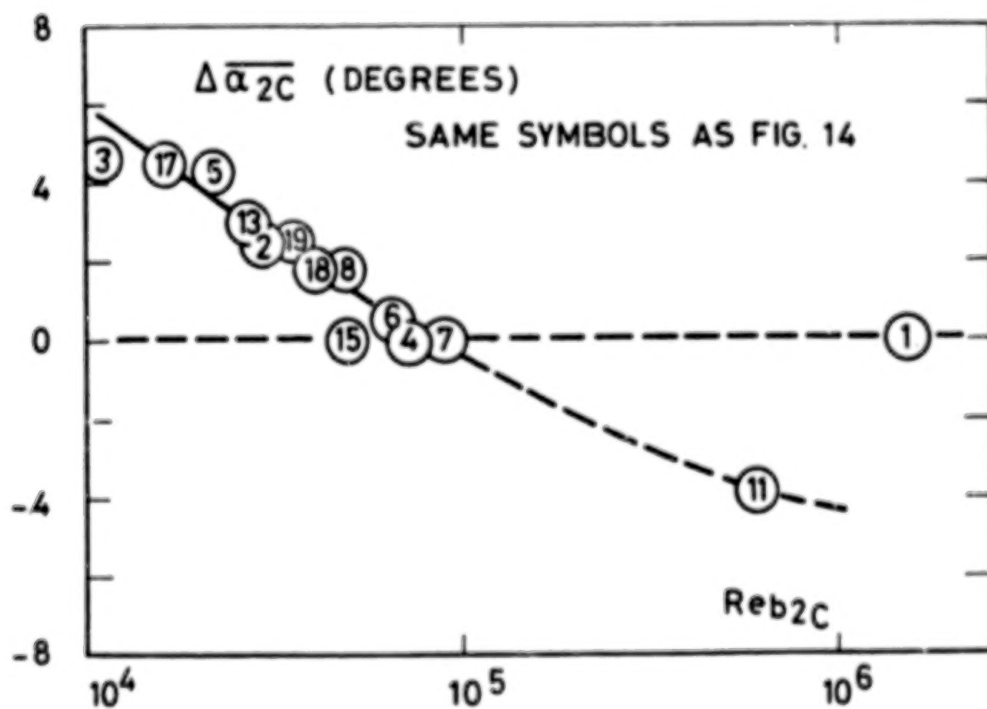
Figure 15. - Critical inlet flow angle correction factor versus Reynolds number.

EXPERIMENTAL MEASUREMENTS OF HYDRODYNAMIC STIFFNESS

MATRICES FOR A CENTRIFUGAL PUMP IMPELLER[*]

D. S. Chamieh, A. J. Acosta, C. E. Brennen, T. K. Caughey, and R. Franz
California Institute of Technology
Pasadena, California 91125

ABSTRACT

The objective of the Rotor Force Test Facility at the California Institute of Technology is to artificially orbit the center of rotation of an impeller enclosed within a volute over a range of frequencies from zero to synchronous and to measure the resulting forces on the impeller. This paper reports preliminary data from the first stage experiments in which the shaft is orbited at low frequency. Steady volute forces along with stiffness matrices due to the change in position of the rotor center are measured. Static pressure taps around the volute are used to obtain volute pressure distributions for various fixed positions of the impeller center and for various flow rates. Static pressure forces are calculated from these pressure distributions allowing a more complete analysis of the components of the impeller forces. Comparison is made with various existing theoretical and experimental results.

INTRODUCTION

It has become evident in the last few years that the main flow through a pump or compressor can contribute to the rotor dynamic inertia, damping and stiffness matrices of the machine in a significar   v (ref.1, 2). Consequently in many applications an accurate rotor dynamic analys   a turbomachine may require inclusion of the components of these matrices resulting from the flow through the impeller as well as the contributions from seals and bearings. In the past the hydrodynamic forces on a radial impeller enclosed in a volute have been primarily studied experimentally and many of the earlier references are based on the semi-empirical relation introduced by Stepanoff (Ref.3). Other experimental papers followed in the same spirit namely those of Domm and Hergt (Ref.4), Agostinelli et al (Ref.5) and Iversen et al (Ref.6). Later as a first step towards studying the whirling problem, Hergt and Krieger (Ref.7) measured radial forces at various eccentricities of the impeller.

Theoretical studies directed toward evaluation of the impeller forces include the work of Domm and Hergt (Ref.4) who modelled the impeller by a source vortex placed within the volute. Their analysis demonstrated the existence of a lateral force on the impeller even in the absence of an orbiting motion of the shaft. Colding-Jorgensen (Ref.8) extended the work of Domm and Hergt (Ref.4) by imposing an orbiting motion on the source/vortex model of the impeller. His results are discussed below. Other more complex methods have also been developed. The actuator disk model, suggested by Chamieh and Acosta (Refs. 9, 10) was used to obtain inertial terms that do not arise in the source-vortex model. More recently both Imaichi, Tsujimoto and Yoshida (Ref. 11) and Shoji and Ohashi (Ref.12) represent the impeller wakes by a finite number of rotating vortex sheets. Imaichi et al (Ref.11) solved the unsteady problem of a fixed impeller inside a volute and Ohashi et al (Ref.12) solved the unbounded whirling problem. However neither were able to formulate the more complex problem of an orbiting impeller enclosed within a volute.

NOMENCLATURE

A_2 Impeller discharge area $= 2\pi R_2 b_2$

b_2 Impeller discharge width

C_p Pressure coefficient, $(p - p_{T2})/\frac{1}{2}\rho U_2^2$

$\underline{e}$ Instantaneous vector displacement of the external balance flexure system

$\{F_o\}$ Average volute force on impeller (vector)

$\{F_o^\star\}$ Non-dimensional average volute force on impeller (vector) $= \{F_o\}/\frac{1}{2}\rho A_2 U_2^2$

$F_x^\star, F_y^\star$ Components of $\{F_o^\star\}$ in X,Y directions (see Fig.4)

$\underline{F}_1, \{F_1\}$ Instantaneous hydrodynamic force on impeller (vector)

$\{F_\Omega\}$ Fundamental harmonic component of $\{F_1\}$

$\{K_s\}$ Stiffness matrix for external balance

$\{K_{ij}\}$ Hydrodynamic force matrix for volute/impeller

$\{K_{ij}^\star\}$ Non-dimensional hydrodynamic force matrix

N, ω Main shaft speed (rpm and radian/sec)

p Static pressure measurement in volute

P_{T2} Discharge total pressure

Q Volume flow rate

R_2 Impeller discharge radius

U_2 Impeller tip speed

t Time

X, Y Cartesian coordinates (Fig.4)

$\underline{\delta}, \{\delta\}$ Instantaneous position of impeller center (vector, Fig.4)

$\{\delta_o\}$ Mean position of impeller center

$\{\delta_\Omega\}$ Fundamental harmonic component of $\{\delta\}$

$\underline{\varepsilon}, \{\varepsilon\}$ Imposed eccentricity of impeller ($|\varepsilon| = 1.26mm$).

λ Logarithmic spiral angle of volute

φ Flow coefficient, $= Q/A_2 U_2$

ψ	Head coefficient = Total pressure rise across pump/ρU_2^2
ρ	Density of water
Ω	Radian frequency of whirl motion
θ	Angular position measured from the tongue (Fig.4)
ω	Radian frequency of impeller rotation

ROTOR FORCE TEST FACILITY

In an earlier paper (Ref.13) the facility was described in detail. We will merely repeat that the objective of the facility is to impose known orbiting motions of radian frequency Ω on the basic rotary motion of a number of typical centrifugal pump impellers (radian frequency, ω, shaft speed, N). Two force balances are incorporated: (a) a simple balance external to the bearings and seals for scoping experiments and the measurement of steady volute asymmetry forces and stiffness matrices at zero whirl frequency ($\Omega = 0$) and (b) an internal balance upon which the impeller is directly mounted for measurements at non-zero whirl frequencies (see Figs. 1, 2 and Ref.13).

This paper reports measurements using the external balance and a 16.2cm diameter five-bladed Byron-Jackson centrifugal impeller (designated Impeller X) with a specific speed of 0.57. A matching logarithmic spiral volute (Volute A) with a spiral angle of 36° was employed with this impeller (other impeller/volute combinations will be tested shortly). The volute was designed in accordance with the assumption of Ref. 3. During the measurements face seals on both sides of the impeller were backed off to prevent interference with the force measurements. Various face seal clearances were investigated. Figure 5 presents the performance characteristic for two seal clearances.

The external balance, consisting of three aluminum flexures (see Figs. 1, 2 and 4) was used with the entire impeller/eccentric drive system floating on soft spring supports attached to the ceiling. Three stainless steel flexures parallel with the shaft maintained the alignment in this configuration. A small D.C. motor was also mounted on the floating assembly to produce a shaft orbit speed of 3 rpm. The purpose of this was to allow continuous sampling of the forces at all locations of the shaft around a circular orbit with a radius of 1.26mm. By comparison with the forces at certain fixed locations it was determined that the dynamic effects of this 3 rpm orbit speed were negligible.

Two of the strain-gaged flexures are mounted horizontally (Figs.2 and 4) for measurement of horizontal force and torque; the other measures the vertical force. Calibrations were performed by known forces applied by systems of wires, pulleys and weights. The linearity of the calibrations was within 1% over the entire range of calibration (-20 to +20kg) and the interactions were less than 1%.

Signal processing was accomplished by means of an eight channel digital signal processor which was phase locked to an optical encoder attached to the shaft of the 3 rpm motor. In this way each of the 8 channels of data (three flexures plus pressure transducers, flow rates, etc) are sampled at 32 equally spaced positions of each rotation of the eccentricity. Furthermore this sampling was continued for 15 or more rotations in order to obtain averages of the forces for each of the 32 geometric positions.

The flexure signals were also recorded on magnetic tape and processed through a digital spectrum analyser to investigate their content. A major peak was observed at the 3 rpm whirl frequency. Much smaller peaks were observed at higher harmonics of this whirl frequency. The largest observed magnitude of the second harmonic was less than 10% of the fundamental indicating that the impeller forces at the small eccentricity employed here vary quite sinusoidally around the circular eccentric orbit. In other words the forces vary linearly with cartesian displacements X and Y and this variation can be accurately represented by a stiffness matrix. In addition to these low frequency components the spectral analysis also showed peaks at the shaft frequency and the higher blade passage frequencies. These represent dynamic forces which are not accurately measured by the external balance and will be the subject of a later paper based on the internal balance measurements.

The geometry and notation of the impeller shaft location, external balance flexures and volute position are shown in Figure 4 (viewed from the pump inlet).

CALCULATION OF IMPELLER VOLUTE FORCES AND STIFFNESS MATRICES

The flexure system, though quite stiff, has some deflection due to the hydrodynamic forces on the impeller; indeed this deflection is monitored by the external balance elements. One consequence of this is that the actual position of the shaft center is a combination of the 1.26mm eccentricity plus the deflection of the flexure system. All of the data on the impeller forces and stiffness matrices were corrected for this effect in the following way (see Fig.4). If $\{\epsilon\}$ is the instantaneous shaft center due to the imposed eccentricity of 1.26mm and $[K_s]$ is the stiffness matrix of the flexure system (measured by loading under conditions of no motion) then the actual position of the shaft (see Fig.4) is

$$\{\delta\} = \{\epsilon\} + \{e\} \ ; \ \{e\} = [K_s]^{-1}\{F_i\} \tag{1}$$

where $\{F_i\}$ is the total force acting on the floating assembly due to the Ω and ω motions. Tare forces were found to be negligible so that, with proper zeroing of the balance, the forces, $\{F_i\}$, are entirely hydrodynamic (see the no-impeller results of Figure 9 for confirmation).

Fourier decomposition of the data yielded average hydrodynamic forces F_0 associated with the mean position of the shaft center and first harmonics, $\{F_\Omega\}$ and $\{\delta_\Omega\}$ at the orbit frequency, Ω (3 rpm). Then the hydrodynamic force matrix, $[K_{ij}]$ is defined as

$$\{F_\Omega\} = [K_{ij}]\{\delta_\Omega\} \tag{2}$$

where $\{\delta_\Omega\}$ is the fundamental of $\{\epsilon + [K_s]^{-1}\{F_i\}\}$ and therefore $[K_{ij}]$ can be calculated since ϵ, $[K_s]^{-1}$ and $\{F_\Omega\}$ are all known. In the present experiments the correction $[K_s]^{-1}\{F_\Omega\}$ could be as large as 10% of δ_Ω.

The forces and force matrices are presented in non-dimensional form using the normalizing factors defined in the nomenclature.

ADDITIONAL MEASUREMENTS

Two types of additional measurements were performed in order to investigate the source of the impeller forces and stiffness matrices. Firstly, measurements of these

quantities were also obtained (i) with different seal clearances (ii) at zero flow rate by total flow blockage exterior to the pump (iii) with the impeller inlet and/or exit blocked by sheet metal attachments (iv) with the impeller removed (v) with a dummy solid impeller having the same exterior shape. Secondly, static pressure distributions within the volute were measured by means of the static pressure taps shown in Fig.3 for four fixed positions of the eccentricity (the positions 'farthest', 'closest', 'right' and 'left' shown in Fig.4) and various flow coefficients. These pressure distributions are presented non-dimensionally using a pressure coefficient, Cp, based on the downstream total pressure and $\rho U_2^2/2$.

FORCE DATA; RESULTS AND DISCUSSION

The reduced data for the average force on Impeller X due to the Volute A when the mean position of the former is coincident with the center of the logarithmic spiral volute is presented in magnitude and direction form in Figs. 6 and 7 and in terms of its cartesian components in Fig.8. The data presented is for seal clearances of 0.14mm. However quite similar results were obtained for clearances of 0.79mm even though the performance characteristic in the latter case is significantly degraded. Some results for both a forward 3 rpm sampling orbit speed $(\Omega > 0)$ and with the direction reversed $(\Omega < 0)$ are shown to confirm that this orbit speed had little effect on the results. The non-dimensionalized force data for different shaft speeds (600 rpm up to 2000 rpm) is in substantial agreement though there would appear to be a slight increase in the magnitude of the force coefficient at low flow coefficients when the speed is increased. It seems likely that this is a Reynolds number effect. From a practical viewpoint it is clear that the Volute A and the Impeller X are well matched at their design flow coefficient $\varphi = 0.092$ since the force on the impeller is virtually zero in this operating state.

Also shown in Figs. 6 and 7 are the experimental results of Agostinelli, Nobles and Mockridge (Ref.5) and Iversen, Rolling and Carlson (Ref.6) for pumps with specific speeds of 0.61 and 0.36 respectively. The former are in close agreement with the present results since the specific speed of the present Impeller X/Volute A combination is 0.57. The results of Iversen et al for a lower specific speed also appear consistent in magnitude with the present results. For clarity a fourth set of experimental results by Domm and Hergt (Ref.4) are presented in Fig.8. These results for a similar volute $(\lambda = 86.3°)$ appear to be in substantial disagreement (lower forces by a factor of 2 or 3) with the results of Fig.6; the reason for this is not clear at the present time.

Finally Fig.8 also presents the theoretical results of both Domm and Hergt (Ref. 4) and Colding-Jorgensen (Ref.8) for volutes with angles close to the 86° of the present set-up. These theories which are based on source/vortex models of the impeller also underpredict the present results by a factor of about two.

Figure 9 present the force coefficient data for a number of tests performed with the objective of assessing the source of the large forces present at conditions of no flow ($\varphi = 0$ in Figs. 6, 7, 8). All of the data of Fig.9 appears to be virtually independent of shaft speed indicating that forces are proportional to the square of the tip speed. The lack of any appreciable force in the absence of the impeller (No impeller points) confirms that these shut-off forces are hydrodynamic in origin. The data for the solid impeller, for Impeller X with the exit blocked off by a sheet of metal and for Impeller X with both the inlet and exit similarly blocked are all similar. Though data is shown for 0.14mm face seal clearances, the data for 0.79mm face seal clearances is very similar in magnitude. We conclude that this force

coefficient component (about 0.04) is due to fluid frictional effects and the induced
pressure gradient acting on the entire exterior surfaces of the impeller. The data
with only the impeller inlet blocked is significantly higher, probably because the
discharge surface (blades and gaps) has greater friction. Finally the force data for
the flow blocked exterior to the pump is significantly higher still. The reason for
this is not entirely clear as yet but the associated observation of substantially
greater prerotation under shut-off conditions may be significant.

HYDRODYNAMIC FORCE MATRICES

Typical non-dimensional hydrodynamic force matrices, $[K^*_{ij}]$, are presented in
Fig.10; these contain all the information on how the forces presented in Figs. 7, 8
and 9 vary as the position of the impeller center changes provided the change is with-
in the linear region. The hydrodynamic stiffness matrix experienced by
the shaft is $[-K_{ij}]$. The data shown in Fig. 10 is for seal clearances of 0.14mm,
various impeller speeds and flow coefficients. We observe that the variation with
N is consistent with that anticipated by the non-dimensionalization and that the
components vary only modestly with flow coefficient, φ, for values above about 0.03.
Data has also been obtained with 0.79mm seal clearances; it is qualitatively similar
to that of Fig. 10 except that the _magnitude_ of all of the components is roughly 0.5
larger for the larger clearances. The theoretical results of Colding-Jorgensen (Ref.
8) based on the source/vortex model of the impeller which are also depicted in Fig.10
exhibit substantial disagreement with the measurements. The diagonal components
K^*_{xx} and K^*_{yy} are different by a factor of 3. The off-diagonal or "cross-coupling"
terms are very different in magnitude and, in the case of K^*_{yx}, the experimental
data do not exhibit the change of sign near the design flow coefficient.

Both the hydrodynamic forces presented in Figs. 6, 7 and 8 and the hydrodynamic
force matrices in Fig.10 imply that the fluid forces will tend to excite a whirl
motion of the impeller. The force matrix could be presented approximately by the
form

$$[K^*_{ij}] = \begin{bmatrix} 2.0 & -0.9 \\ \\ 0.9 & 2.0 \end{bmatrix}$$

at least over the range $0.04 < \varphi < 0.14$. It is therefore a combination of a diagonal
and a skew-symmetric matrix. The former will simply reduce the structural stiffness
matrix and in many cases this hydrodynamic effect will be small. The skew-symmetric
or cross-coupling terms are much more important. Since K^*_{xy} and K^*_{yx} are of op-
posite sign their effect is to tend to destabilize the rotor. The rotordynamic con-
sequences of such excitation will, of course, depend on the damping matrix as well
(see for example Ref.14). However since K^*_{xy} and K^*_{yx} are proportional to N^2
it follows that if the damping increases more slowly with N, then there will always
be a critical speed, N, above which the excitation will exceed the damping. Further-
more it is clear that this whirl will not necessarily be synchronous. Future mea-
surements using the internal balance will examine the hydrodynamic contribution to
the damping and mass matrices; this will allow more quantitative analysis of hydro-
dynamically induced whirl.

Finally, we note that the force matrix data implies a "hydrodynamic center"
within the volute; when the impeller center coincides with this "hydrodynamic center"
the force $\{F_i\}$ is zero. The position of the "hydrodynamic center" for the Impeller
X, Volute A is presented as a function of flow coefficient in Fig.11 where the origin

is the center of the logarithmic spiral volute shape. It is seen that this data is consistent with that of Domm and Hergt (Ref.3) for a similar volute.

STATIC PRESSURE MEASUREMENTS IN THE VOLUTE

Typical static pressure distributions in the impeller discharge flow (measured as described earlier) are presented in Fig.12 for various flow coefficients and for seal clearances of 0.79mm. This data is for the impeller position labeled "closest" in Fig.4. The form and magnitude of the pressure variations are similar to those measured by Iversen et al (Ref.6) and to those predicted theoretically by Kurokawa (Ref.15). The pressure distributions were integrated numerically to obtain static pressure forces on the impeller for each of the four impeller positions indicated in Fig.14. Figure 13 presents the X and Y components of these static pressure forces for one of the four positions and compares them with the total force components on the impeller measured by the external balance for the same impeller location. Note that the static pressure component is not sufficient in itself to explain the measured total force. This is contrary to the result obtained by Iversen et al (Ref.6); they observed significant agreement between the forces. On the other hand we conclude that the discrepancy in the forces presented in Fig.13 is due to a difference in net flux of momentum into and out of the volute. Some measure of the order of magnitude of this momentum flux difference can be obtained by evaluation of the momentum flux discharging from the volute which, when non-dimensionalized in the same manner as the forces leads to a momentum flux in the Y direction of $4.14\varphi^2$. This is of the same order of magnitude as the forces. We conclude that the non-isotropy of the momentum is an important contribution to the impeller forces.

Results similar to Fig.13 were obtained for each of the four positions in Fig.4. Hence hydrodynamic force matrices or stiffness matrices due to the static pressure forces could be evaluated. It transpires that this component represents only about 20% of the magnitude of the total force matrices presented in Fig.10. We therefore conclude that the non-isotropy of the momentum flux is the primary contributor to the stiffness matrix. This fact emphasizes the need for direct measurement of the forces on the impeller.

CONCLUDING REMARKS

This paper has presented measurements of the hydrodynamic forces on a centrifugal pump impeller as a function of position within a logarithmic spiral volute. These correspond to the forces experienced by the impeller at zero whirl frequency. The hydrodynamic force matrices (negative of the hydrodynamic stiffness matrices) derived from these measurements exhibit both diagonal and off-diagonal terms of substantial magnitude. The off-diagonal or cross-coupling terms are of a form which would tend to excite a whirl motion in a rotordynamic analysis of the pump.

Static pressure measurements in the impeller discharge flow show that the hydrodynamic force on the impeller contains a substantial component due to the non-isotropy of the net momentum flux leaving the impeller. Moreover a similar breakdown of the contributions to the stiffness matrices reveals that the major component of these matrices results from the non-isotropy of the momentum flux.

Future plans include measurement of these forces at non-zero whirl frequencies in order to obtain a complete picture of the rotordynamic consequences of these hydrodynamic forces.

REFERENCES

1. Alford, J. S.: Protecting Turbmachinery from Self-excited Rotor Whirl. J. Eng. Power, vol. 87 A, 1965, pp. 333-344.

2. Thompson, W. E.: Fluid Dynamic Excitation of Centrifugal Compressor Rotor Vibrations. J. Fluid Engineering, vol. 100, no. 1, 1978, pp. 73-79.

3. Stepanoff, A. J.: Centrifugal and Axial Flow Pumps. Wiley, New York, 2nd Edition, 1957, pp. 116-123.

4. Domm, H.; and Hergt, P.: Radial Forces on Impeller of Volute Casing Pumps. Flow Research on Blading (L. S. Dzung, ed.), Elsevier, 1970, pp. 305-321.

5. Agostinelli, A.; Nobles, D.; and Mockridge, C. R.: An Experimental Investigation of Radial Thrust in Centrifugal Pumps. Trans, ASME, J. of Eng. for Power, 1960, pp. 120-126.

6. Iversen, H. W.; Rolling, R. E.; and Carlson, J. J.: Volute Pressure Distribution, Radial Force on the Impeller and Volute Mixing Losses of a Radial Flow Centrifugal Pump. Trans. ASME, J. of Eng. for Power, 1960, pp. 136-144.

7. Hergt, P.; and Krieger, P.: Radial Forces in Centrifugal Pumps with Guide Vanes. Proc. Inst. Mech. Engrs., vol. 184, Pt.3N, pp. 101-107,1969-70.

8. Colding-Jorgensen, J.: The Effect of Fluid Forces on Rotor Stability of Centrifugal Compressors and Pumps. Ing. Thesis, Technical University of Denmark, 1979.

9. Chamieh, D.; and Acosta, A. J.: Dynamic Forces on a Whirling Centrifugal Rotor. Proc. 6th Conf. on Fluid Machinery, Akademiai Kiado, Budapest, Hungary, 1979, pp. 210-219.

10. Chamieh, D.: Calculation of the Stiffness Matrix of an Impeller Eccentrically Located within a Volute. Cavitation and Polyphase Flow Forum, Joint ASME – ASCE Solid and Fluid Mechanics Conference, Boulder, Colorado, pp. 51-53, 1981.

11. Imaichi, K.; Tsujimoto, Y.; and Yoshida, Y.: A Two Dimensional Analysis of the Interaction Effects of Radial Impeller in Volute Casing. IAHR/ AIRH Symposium, Tokyo, Japan, 1980, pp. 635-647.

12. Shoji,H.; and Ohashi, H.: Fluid Forces on Rotating Centrifugal Impeller with Whirling Rotors. NASA Conf. Pub. 2133, Texas A & M University, College Station, Texas, 1980, pp. 317-328.

13. Brennen, C. E.; Acosta, A. J.; and Caughey, T. K.: A Test Program to Measure Fluid Mechanical Whirl-Excitation Forces in Centrifugal Pumps. NASA Conference Publication 2133, 1980, pp. 317-328.

14.   Adams, M. L.; and Padovan, J.: Insights into Linearized Rotor Dynamics.
        Journal of Sound and Vibration, 1981, pp. 129-142.

15.   Kurokawa, J.: Theoretical Determinations of the Flow Characteristics in
        Volutes.   IAHR/AIRH Symposium, Tokyo, Japan, 1980, pp. 623-634.
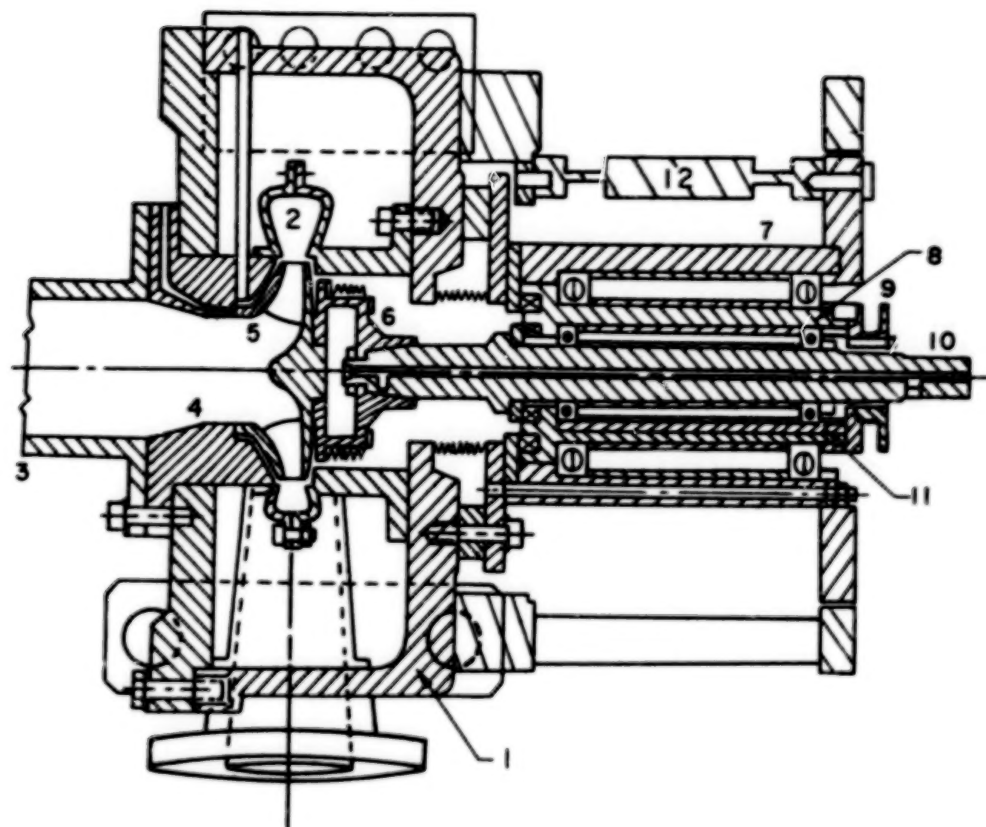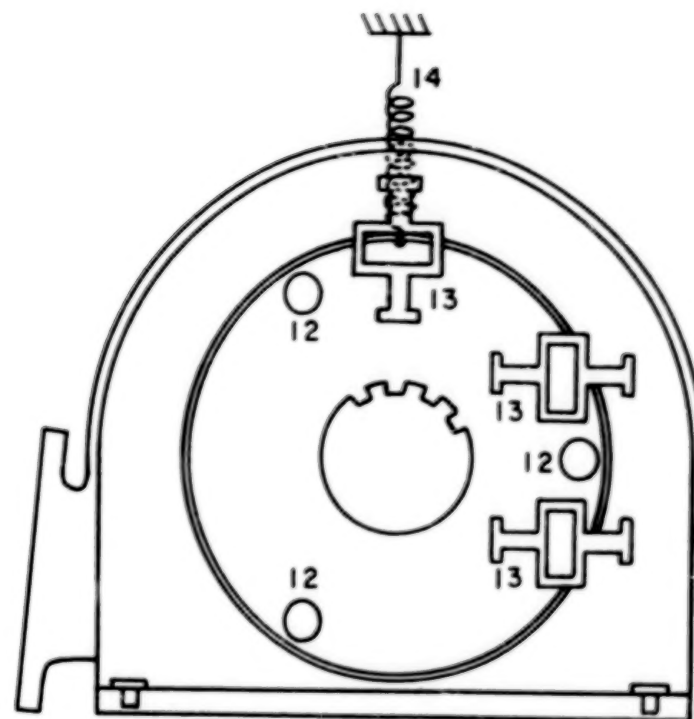
PLAN VIEW   ELEVATION VIEW

Figure 1. - Schematic of pump housing and force balance assembly of rotor test
force test facility. Pump housing (1), volute (2), inlet connection (3),
inlet bell (4), impeller (5), internal balance (6), double bearing system
(7,8,11), orbiting motion sprocket (9), main shaft (10), axial retaining
flexure (12), external balance flexure (13), retaining spring (14).

391
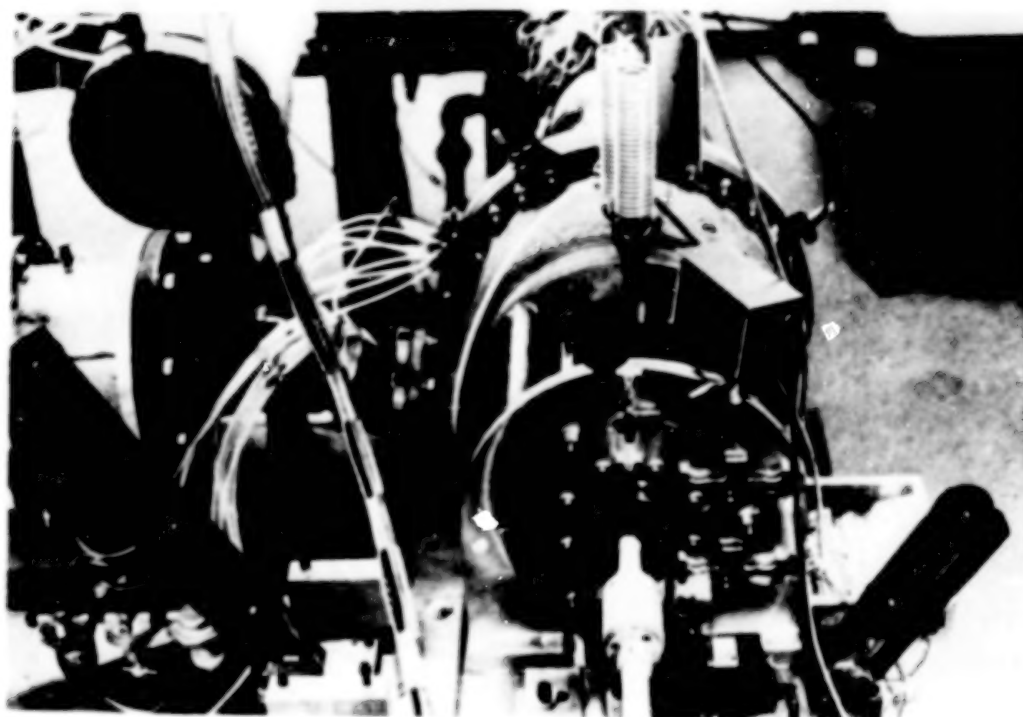
Figure 2. - Photographs of the items shown in Figure 1.
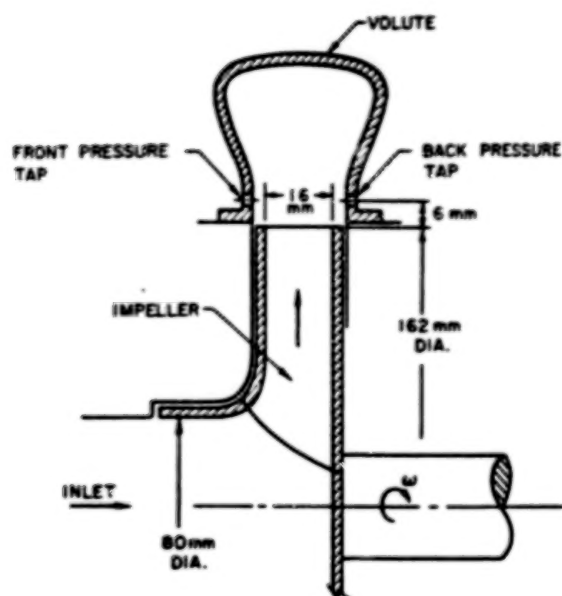
Figure 3. - Schematic showing main dimension and static pressure measurement
points within volute. (Eight pressure taps more or less equally spaced
around volute circumference on front and back.)
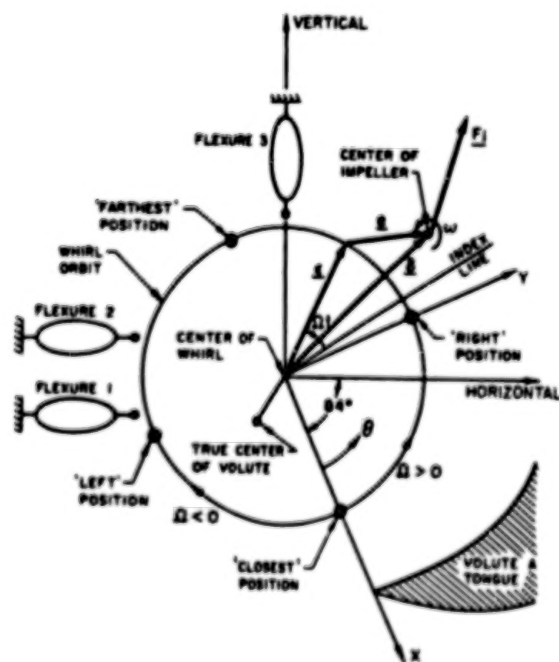
Figure 4. - Schematic of forces and locations within impeller-volute system
as seen from inlet.
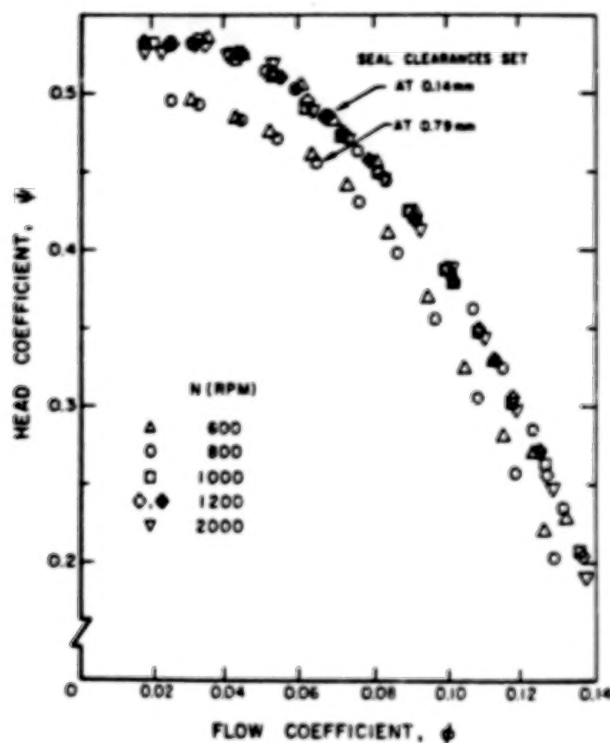
Figure 5. - Performance characteristic of Impeller X inside Volute A for front and back seal clearances of 0.14 and 0.79 mm. (Open and closed symbols represent data for $\Omega > 0$ and $\Omega < 0$ respectively.)
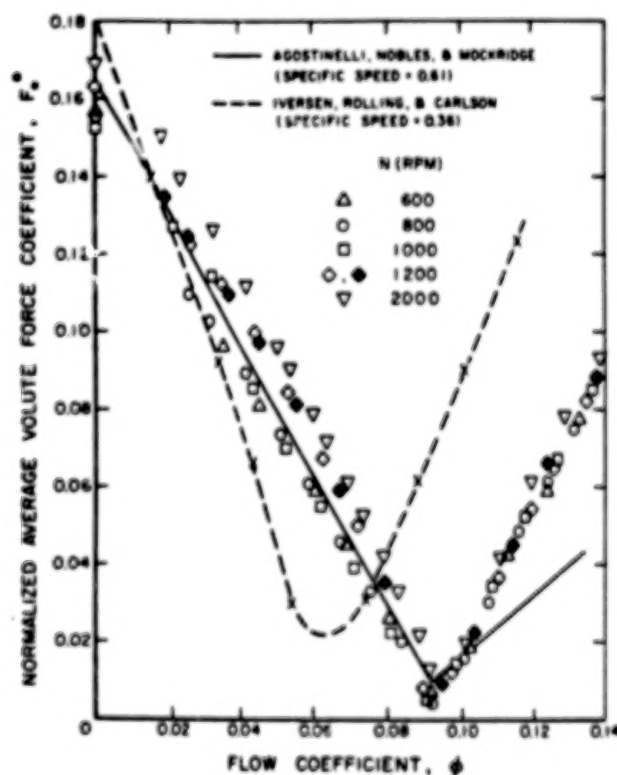
Figure 6. - Normalized average volute force for Impeller X, Volute A, and seal clearances of 0.14 mm. (Open and closed symbols represent data for $\Omega > 0$ and $\Omega < 0$, respectively. Comparison is made with Iversen et al. (ref.6) bearing reactions and Agostinelli et al. (ref.5) experimental data.)

394
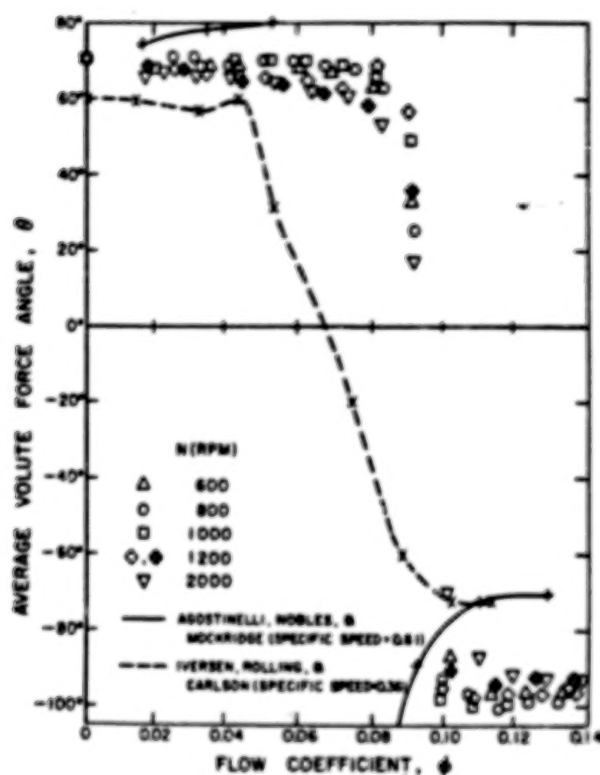
Figure 7. - Direction of average volute force plotted in figure 6 expressed in volute coordinate system. (θ is the angle between the direction of average force and line joining center to tongue of volute.)
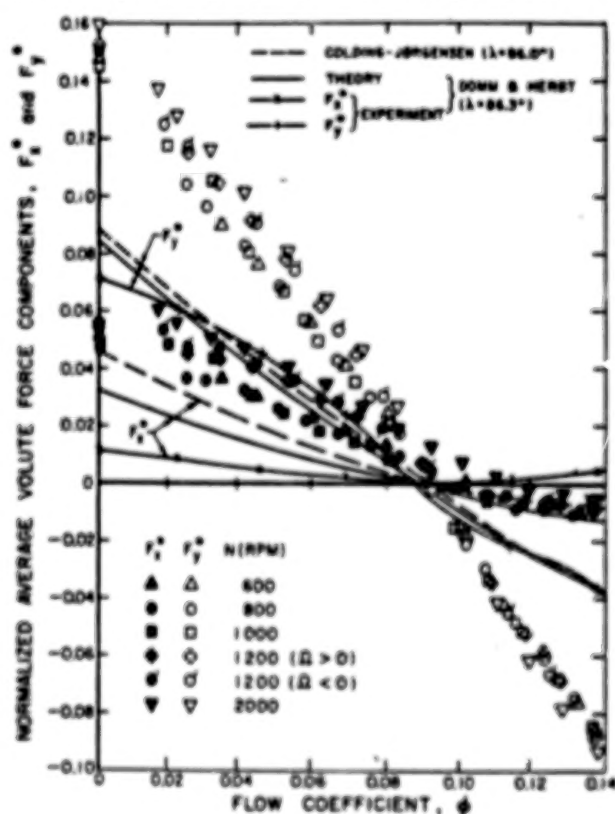
Figure 8. - Comparison of normalized average volute force components of figures 6 and 7 with work of Domm and Hergt (ref.4) and Colding-Jorgensen (ref.8). (Impeller X, Volute A, and seal clearances of 0.14 mm).

395
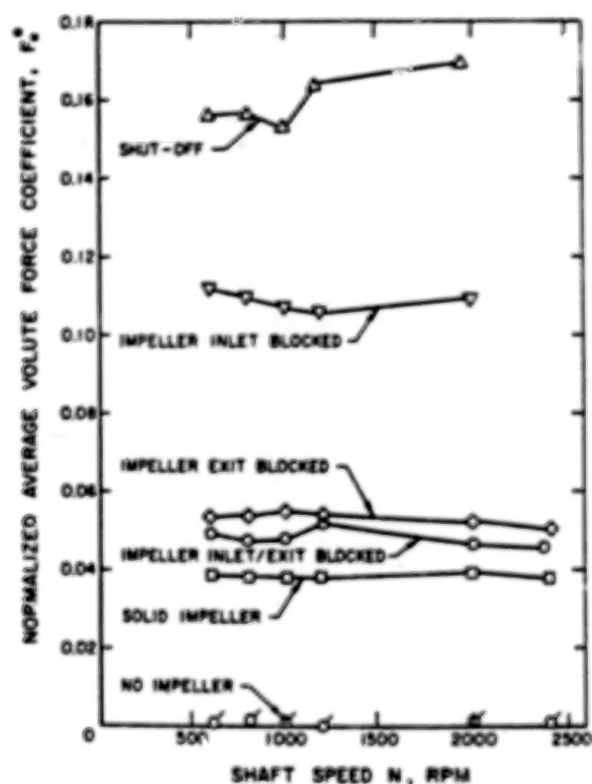
Figure 9. - Normalized average volute force as function of shaft speed for various auxiliary experiments. (Impeller X, Volute A, and seal clearances at 0.14 mm).
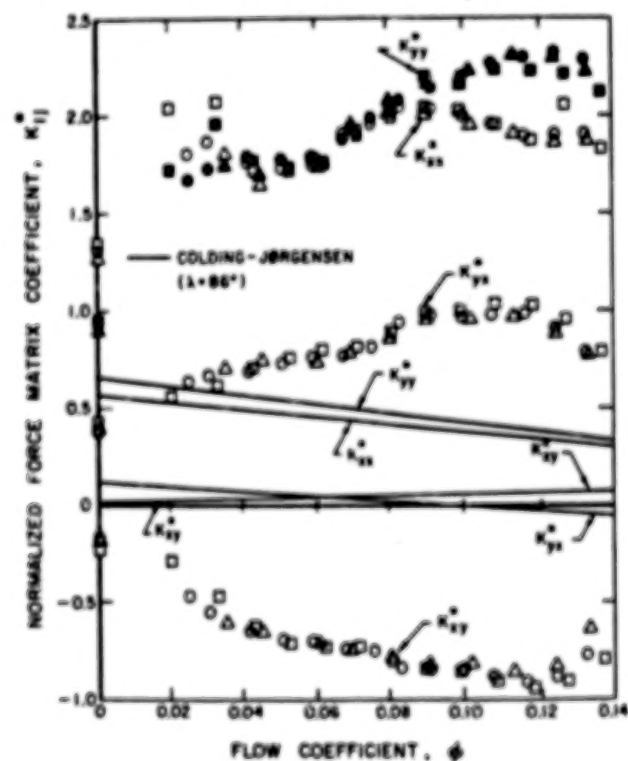
Figure 10. - Force matrix coefficients as defined in text (Impeller X, Volute A, and seal clearances at 0.14 mm), shaft speed = 600 rpm: $\triangle$,$\blacktriangle$; 800 rpm O,$\bullet$; 1000 rpm: $\square$,$\blacksquare$. (Values of K_{xx}^*, K_{xy}^*, and K_{yx}^* are represented by open symbols; values of K_{yy}^* by closed symbols.)
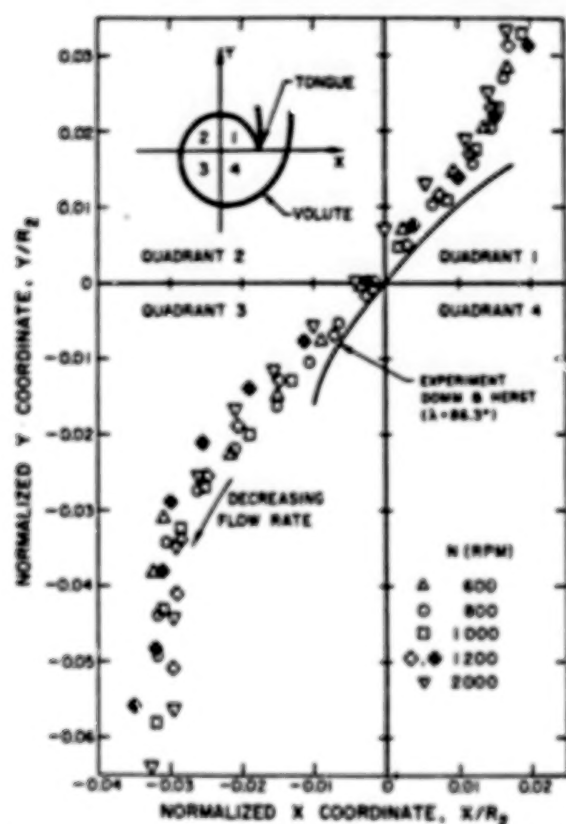
Figure 11. - Equilibrium positions of Impeller X within Volute A for seal clearances of 0.?? mm for various flow rates. Solid line indicates experimental data of Domm and Hergt (ref.4) for $\lambda = 86.3_0$.
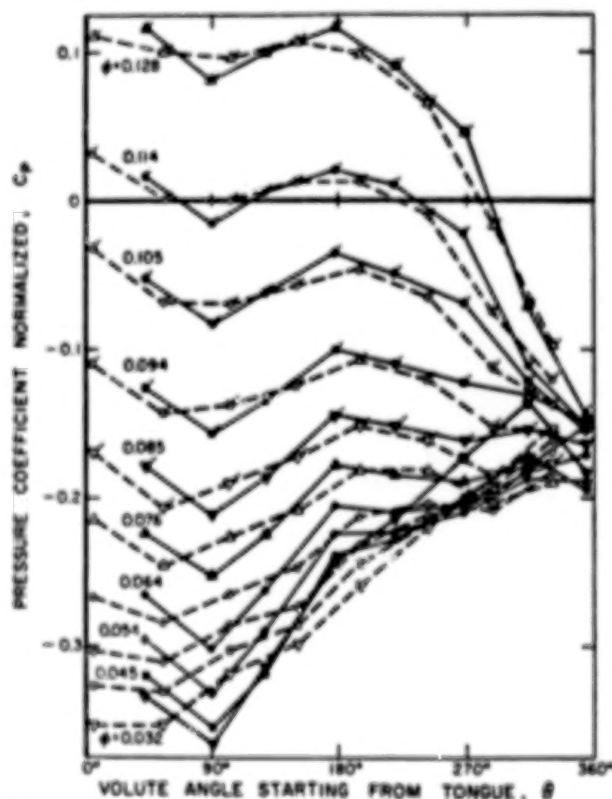
Figure 12. - Pressure coefficient for various flow rates for main shaft speed N = 600 rpm. Impeller X, Volute A, and seal clearances at 0.79 mm. Shaft center position is at 'closest' point (fig.4). Solid lines represent front pressure taps and dashed line back pressure taps of figure 3.
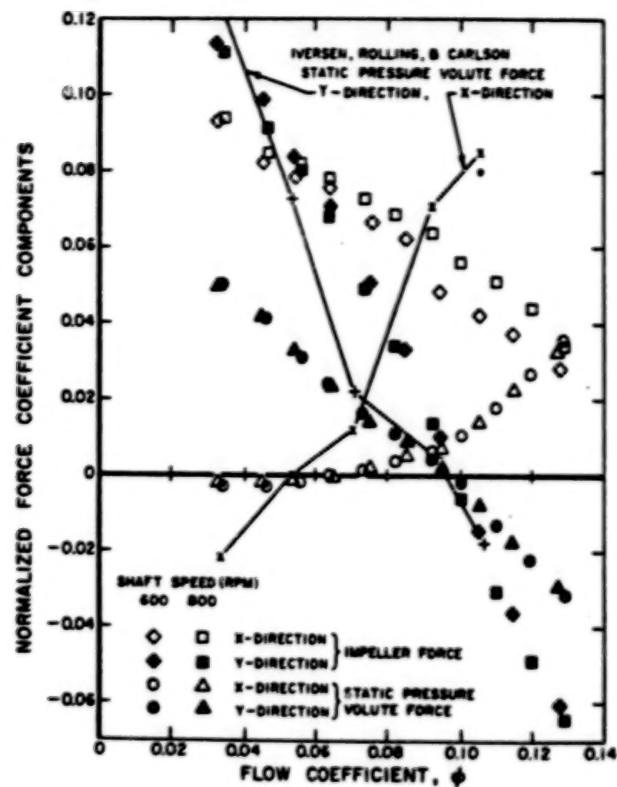
Figure 13. - Normalized impeller forces and static pressure forces of figure 12 shown for main shaft speed N = 600 rpm. Impeller X, Volute A, and seal clearances set at 0.79 mm. Shaft center position is at 'closest' point (fig.4). Comparison is made with Iversen et al. (ref.6) static pressure volute forces.

398

GAS TURBINE ROTOR/CASE STRUCTURAL RESPONSE TO ROTATING STALL:

EXPERIMENTAL DOCUMENTATION AND ANALYTICAL APPROACH*

Philip J. Haley
Detroit Diesel Allison
Division of General Motors Corp.
Indianapolis, Indiana 46206

SUMMARY

This work presents experimental data describing the forcing functions and structural responses characterizing gas turbine rotor/case system vibration due to rotating stall in an axial-flow compressor. Two data sets with fundamentally different response characteristics are presented; one is supersynchronous and the other subsynchronous. Conventional beam-element rotor dynamics analysis is shown to be severely limited in its ability to predict these responses. A new analytical approach, which significantly increases structural response predictive capability for these phenomena, is briefly discussed.

INTRODUCTION AND BACKGROUND

The emphasis on aerothermodynamic performance in the high-performance gas turbine engine of today and tomorrow has focused attention on increased performances from its components, one of which is the axial-flow compressor. Compressor design trends, aimed toward high efficiencies and/ or high aerodynamic loadings, have led to machines that are very sensitive to running tip clearances between blades/vanes and their respective case/ rotor structures. The controlling criterion in the selection of these clearances is often the necessity to accommodate rotor and case excursions associated with surge/stall instabilities. Closely related to clearance selection is the rotor dynamic design of a given machine. The mechanical designer typically has only empirical guidelines based on severely limited data with which to design to accommodate surge/stall deflections and to simultaneously provide minimum running clearances. This paucity of knowledge of structural dynamic response during surge/stall instabilities renders the optimization of tip clearances, rotor/ case flexibility, and bearing placement a difficult and abstract task.

Detroit Diesel Allison (DDA) is currently working under Air Force contract to experimentally document compressor structural response to the rotating stall phenomenon and to improve state-of-the-art analytical techniques for predicting such response. These efforts address some of the deficiencies in knowledge noted above. This paper presents an abbreviation of some of the results of this contractual effort with emphasis on the experimental data.

Rotating stall can be viewed as one or more regions or "cells" of low momentum, low-pressure fluid, each covering some sector of the flow annulus of the compressor. Although rotating stall typically occurs near the compressor surge line, some machines exhibit it away from surge, even near the operating line. The number of cells can vary from one to eight or more. Multiple cells seem to be uniformly spaced circumferentially. In the fully developed rotating stall considered herein, the cells traverse the axial length of the com-

pressor, so can be regarded as "tubes" of low-pressure fluid that are axially twisted or "corkscrewed" through the machine. These stall cells result in net forces exerted on both the compressor rotor and the case, assuming the cell fills the flow passage span. These forces are radial and, if ramp angles are present, can have axial components. The stall pattern rotates in the direction of the compressor rotor but at partial rotor speed, generally between 25% and 75% speed, as viewed from the inertial frame. Thus a single-cell rotating stall at 50% rotor speed acts as a subsynchronous excitation mechanism. A two-cell stall at 50% speed appears as a synchronous force, while a two-cell stall at 60% speed appears supersynchronous.

In contrast to the surge phenomenon, rotating stall can produce quasi-steady, periodic forcing functions which can cause steady-state, periodic rotor/case response manifested as structural dynamic instabilities. Such responses can, based on experience, lead to high amplitude vibration and/or radial excursions beyond the design clearances, causing rub and potential structural failures. This paper presents a classic set of experimental data describing the violent nature of rotating stall-induced rotor/case system vibration. The associated forcing functions are also presented, and Fourier analysis is utilized to gain insight into the forcing function/response relationships. The new analytical approach developed at DDA to calculate stall-induced system response is briefly outlined.

EXPERIMENTAL DATA AND DISCUSSION

The data presented herein were generated at DDA on a large, multistage, axial-flow compressor rig, which is fairly typical of the compressors currently found in high-performance, aircraft-type gas turbines. This rig is sketched in Figure 1. Though not shown in this sketch, the bearing/rotor arrangement of the rig is similar to that of the parent gas generator, of which this compressor is a component. This rig was instrumented to measure the time-variant forcing functions and structural responses associated with rotating stall. The elements of this high-response instrumentation scheme are shown in Figure 2, which depicts the compressor case unwrapped into a plane. These sensors are all mounted on the compressor case in the stationary frame. The dynamic pressure sensors are high-response transducers flush-mounted in the outer gas-path wall. They measure the fluctuating component of endwall pressure, which is assumed to characterize the stall cell at both its inner and outer span. Vibration pickups measure case velocities, while rotor-to-case relative motion is sensed with "whip" pickups, which are proximity probes located over compressor blade tips. Rotor motion can be established by vectorially adding case motion and rotor-to-case relative motion after transforming these measured parameters to compatible units.

Running of this compressor rig produced several rotating stall and/or surge sequences, which were recorded on magnetic tape via the described instrumentation. The phenomenological sequence from which the data presented herein were quantified consists of a high-speed surge followed by two-zone and then single-zone rotating stall patterns. Figure 3 is a time record of the rotor speed excursion showing the onset of surge and the subsequent initiation of the stall patterns. As seen in this figure, the entire sequence of time-variant phenomena lasted approximately 5 seconds, during which time the rotor accumulated over 900 revolutions under the influence of the related rotating forces. The data presented in the subsequent discussion were defined over the two time intervals shown in Figure 3.

Following surge, a two-zone rotating stall pattern was spontaneously established, traveling (one-per-circumference spatial propagation rate) at 57% rotor speed. Time traces of the dynamic signals over the defined analysis interval are presented in Figures 4, 5, and 6. A common timing signal on these plots is used to time-relate events. The responses shown in Figures 5 and 6 show high-amplitude compressor case structural vibration at the frequency of the individual stall cell passage from Figure 4, i.e. at two times the two-zone rotating stall rotational frequency. The whip signals of Figure 6 also indicate rotor-to-case relative motion at the same frequency. These responses and the associated forcing functions thus appear to be supersynchronous.

The two-zone rotating stall pattern evolved into a single-zone pattern (Figure 3) with a propagation rate of 60% rotor speed. Figures 7, 8, and 9 present the traces of dynamic pressure, case vibration, and whip for this stall occurrence. Again, high amplitude structural response is observed. Both the compressor case response and the whip signals visually indicate major components at the subsynchronous passing frequency of the Figure 7 forcing functions. Clearly evident in some of the response signals are additional higher frequency components.

Insight into the nature and relationships of the forcing functions and structural responses characterizing these stall phenomena is afforded by Fourier analysis. The two-zone stall data of Figures 4 through 6 were digitized over the common interval shown on Figure 4, and the single-zone data of Figures 7 through 9 were likewise digitized over the period shown on Figure 7. Digitized data were harmonically analyzed to produce components for each signal according to the cosine Fourier form:

$$\sum_{m=0}^{\infty} U_m \cos (m \Omega t - m\theta + a_m)$$

where:

U_m = amplitude of mth harmonic (harmonic coefficient)
m = harmonic index
Ω = fundamental frequency
θ = circumferential location of sensor
a_m = phase of mth harmonic
t = time

This procedure removes phase differences arising from the different circumferential locations of the various sensors. Note that in Figures 4 through 9, representing fully developed stall patterns, all these dynamic signals, considered to represent transient phenomena in the sense of an operating steady-state turbomachine, are relatively periodic functions.

The Fourier content of the pressure traces is presented in Tables I and II for the two-zone and one-zone phenomena, respectively. Because eight one-per-circumference spatial cycles were digitized (Figures 4 and 7), the first five spatial harmonics of the waveforms correspond analytically to temporal harmonics 8, 16, 24, 32, and 40, as listed. A comparison of Table I with Figure 4 for two-zone stall confirms the predominance of second harmonic content (first

401

harmonic of a single stall cell times two cells per circumference) and indicates a strong fourth harmonic. Comparison of Table II with Figure 7 for one-zone stall shows a predominant first harmonic content with significant higher harmonic content, notably second harmonic.

Table III presents the Fourier content of the measured responses to the two-zone rotating stall pattern. The first five spatial harmonics are listed. The amplitude predominance of second harmonic is seen, followed by fourth (first harmonic of second). This pattern corresponds to that noted in the pressure traces. The highest amplitude forcing functions (pressures) from Table I are seen to be axially toward the rear of the compressor, whereas the highest amplitude case responses from Table III are seen to be in the compressor inlet area, suggesting a proximity to a resonance in the inlet. Comparison of these two tables does clearly show, however, direct structural response to rotating stall. The presence and predominance of second and higher harmonic case response show the importance of localized distortion and "egging" behavior in a flexible gas turbine case. Beam-like behavior, corresponding to first harmonic force and response components, is a relatively minor contributor to case response in these data. Figure 10 further clarifies these descriptions.

Table IV presents the Fourier content of the measured responses to single-zone stall. The amplitude predominance of first harmonic is apparent, along with a strong second harmonic contribution, especially in the inlet. This same pattern is seen in the rotor-to-case whip signal. The relative Fourier contents of these response signals are comparable to those of the forcing functions (Table II), again suggesting the approach of comparing forces and responses on a harmonic basis. These data indicate the primary case response to be beam-like, unlike that observed in the two-zone phenomenon.

As shown in Figure 2, axially-redundant signals were obtained for several parameters. Examination of the Fourier content of these signals in Tables III and IV reveals circumferentially asymmetric responses throughout this compressor in both first and second harmonic components for both case and rotor-to-case signals. The significance of these observations is that the responses of this "axisymmetric" turbomachine to these stall-induced forcing functions are not at all axisymmetric. The asymmetric case response in the first harmonic indicates asymmetric mounting of the case to ground for the beam-like motion. Asymmetric case response in the second and higher harmonics is due to asymmetry in the case itself, caused by holes, split lines, bleed manifolds, and other deviations from pure axisymmetry.

A conclusion from these experimental data is that stall-induced response of the compressor case, an important contributor to system dynamic response and to rotor-to-case clearance response, cannot always be adequately described by first harmonic, beam-like motion. Furthermore, significant circumferential asymmetry is present in the different modes of case response. Obvious from these observations is the fact that the beam-element analytical approach widely used in rotor dynamic analyses is generally inadequate for modeling either of the forced response problems described herein. Since the supersynchronous two-zone stall is seen to have only minor components of forcing functions and responses that can be described by the first spatial harmonic, the beam-element approach is inherently grossly inadequate. Although forcing functions and responses of the subsynchronous single-zone stall have predominant first harmonic content, the higher harmonic components are not negligible but are ignored in beam-element analysis.

NEW ANALYTICAL APPROACH

DDA has developed a capability for predicting rotor/case structural response to dynamic forcing functions. This analysis has been developed specifically for the rotating stall phenomenon in compressors. The analysis includes the ability to predict localized motions of the static structure (i.e., compressor case), including "egging" modes. The approach entails using a beam-element rotor analysis along with an axisymmetric finite-element case analysis. Egging and localized motions are calculated for the case alone and are assumed to be decoupled from the rotor. Beam-like motion is calculated for the coupled rotor/case system using finite-element case modes modally coupled to the conventional beam-element rotor model. Deviations from pure axisymmetry are recognized: (1) in the beam-element calculation, through allowance for asymmetric support modeling, and (2) in the finite-element case analysis, through availability of a discontinuous element for modeling struts, vanes, holes in the case, bleed manifolds, and other variances from pure axisymmetry. This technique has substantially addressed the shortcomings of conventional beam-element rotor dynamics analysis in the modeling of stall-induced response and has produced reasonable analytical simulations of both the subsynchronous and supersynchronous preceding experimental data sets.

TABLE I. - FOURIER DECOMPOSITON OF DYNAMIC PRESSURES FROM TWO-ZONE STALL

				Stage				
_1_	_2_	_3_	_5_	_6_	_7_	_8_	_9_	_10_

Temporal harmonic = 8

	1	2	3	5	6	7	8	9	10
Amplitude	0.2143	0.0346	0.0613	0.0670	0.0562	0.0475	0.1012	0.0924	0.2463
Phase	-103.1	-75.9	97.0	-144.7	135.5	-149.5	-174.5	60.7	77.7

Temporal harmonic = 16

	1	2	3	5	6	7	8	9	10
Amplitude	0.1050	0.1597	0.1961	0.9671	1.784	2.711	2.622	3.878	2.340
Phase	-1.5	-122.6	78.1	-160.2	-176.8	-175.6	159.5	136.4	106.1

Temporal harmonic = 24

	1	2	3	5	6	7	8	9	10
Amplitude	0.0498	0.0334	0.0260	0.0513	0.0620	0.0561	0.0688	0.0974	0.1809
Phase	47.3	18.4	115.3	-74.0	140.6	153.8	166.4	88.4	61.6

Temporal harmonic = 32

	1	2	3	5	6	7	8	9	10
Amplitude	0.1022	0.1339	0.1023	0.1286	0.3121	0.5181	0.4338	0.8993	0.1992
Phase	-22.9	-24.8	-28.0	-164.8	-171.1	-154.2	141.5	102.6	117.0

Temporal harmonic = 40

	1	2	3	5	6	7	8	9	10
Amplitude	0.0380	0.0026	0.0001	0.0311	0.0495	0.0188	0.0526	0.0914	0.0211
Phase	0.0	-180.0	-180.0	0.0	-180.0	0.0	0.0	0.0	0.0

Amplitude in psi.
Phase in degrees.

TABLE II. - FOURIER DECOMPOSITION OF DYNAMIC PRESSURES FROM SINGLE-ZONE STALL

				Stage				
_1_	_2_	_3_	_5_	_6_	_7_	_8_	_9_	_10_

Temporal harmonic = 8

	1	2	3	5	6	7	8	9	10
Amplitude	0.2323	0.2519	0.3808	1.041	1.576	2.222	2.122	2.139	0.7372
Phase	17.3	149.3	176.0	-157.3	-172.7	-173.5	177.1	155.6	128.1

Temporal harmonic = 16

	1	2	3	5	6	7	8	9	10
Amplitude	0.1429	0.0926	0.1158	0.4098	0.7246	1.111	0.9731	0.9519	0.4192
Phase	-7.6	38.3	-108.3	-134.4	-147.7	-155.3	179.7	166.4	108.8

Temporal harmonic = 24

	1	2	3	5	6	7	8	9	10
Amplitude	0.1128	0.0888	0.1165	0.1704	0.3000	0.4062	0.3069	0.2796	0.0043
Phase	-26.2	7.0	-47.2	-146.3	-145.2	-150.8	-164.6	-127.8	169.1

Temporal harmonic = 32

	1	2	3	5	6	7	8	9	10
Amplitude	0.0399	0.0845	0.0883	0.0797	0.1446	0.1212	0.0718	0.1437	0.1235
Phase	-32.8	32.1	-32.6	-124.5	-143.3	176.6	-40.8	-30.1	127.2

Temporal harmonic = 40

	1	2	3	5	6	7	8	9	10
Amplitude	0.0085	0.0129	0.0245	0.0408	0.0491	0.0655	0.0659	0.1723	0.0220
Phase	0.0	0.0	0.0	-180.0	-180.0	-180.0	0.0	0.0	0.0

Amplitude in psi.
Phase in degrees.

TABLE III. - FOURIER COMPONENTS OF EXPERIMENTAL RESPONSE FOR TWO-ZONE ROTATING STALL

Ref. Figures 5 & 6

Signal	Description	U_1	a_1	U_2	a_2	U_3	a_3	U_4	a_4	U_5	a_5
Vibration	Inlet hsg., 0°	0.0441	26	2.286	-28	0.1124	-226	0.1953	-170	0.0276	0
Vibration	Inlet hsg., 270°	0.0706	-174	2.499	-182	0.0835	18	0.1082	-178	0.0165	0
Vibration	Stg. 7 vane, 220°	0.0265	-200	0.6071	-269	0.0141	-105	0.0635	-243	0.0118	-180
Vibration	Stg. 8 vane, 150°	0.0453	-187	0.2829	17	0.0471	-240	0.0682	-137	0.0206	0
Vibration	Stg. 9 vane, 173°	0.0448	-231	0.7128	74	0.0060	-141	0.0275	2	0.0006	-179
Vibration	Stg. 9 vane, 355°	0.0118	2	0.6265	63	0.0129	-111	0.0171	- 45	0.0035	-180
Vibration	Rear comp., 0°	0.0447	6	0.5282	68	0.0171	16	0.0329	-193	0.0129	0
Vibration	Rear comp., 150°	0.0241	-191	0.2541	-4	0.0065	49	0.0441	-268	0.0094	-180
Vibration	Rear comp., 240°	0.0271	-148	0.8876	-209	0.0218	72	0.1112	-96	0.0094	-180
Vibration	Rear comp., 270°	0.0276	-63	0.4035	-108	0.0100	22	0.0429	62	0.0035	-180
Whip	Stg. 9, 240°	0.0014	148	0.0023	201	0.0006	113	0.0002	88	0.0002	-180
Whip	Stg. 9, 150°	0.0007	77	0.0018	46	0.0006	225	0.0011	191	0.0003	0

U_m = amplitude (harmonic coefficient); vibration in in./sec., avg; whip in in., single amplitude.

a_m = phase angle, in degrees.

m = harmonic index.

TABLE IV. - FOURIER COMPONENTS OF EXPERIMENTAL RESPONSE FOR SINGLE-ZONE ROTATING STALL

Ref. Figures 8 & 9

Signal	Description	U_1	a_1	U_2	a_2	U_3	a_3	U_4	a_4	U_5	a_5
Vibration	Inlet hsg., 0°	1.059	63	0.9482	45	0.0553	-257	0.0676	-62	0.0276	0
Vibration	Inlet hsg., 270°	0.6907	-41	0.9385	-133	0.1021	75	0.0388	-58	0.0137	-180
Vibration	Stg. 7 vane, 220°	0.8600	-77	0.3906	-221	0.2041	-150	0.0512	-200	0.0165	0
Vibration	Stg. 8 vane, 150°	0.6681	-104	0.3110	25	0.0269	-182	0.0525	-14	0.0006	-179
Vibration	Stg. 9 vane, 173°	1.038	-107	0.2897	80	0.1545	-181	0.0333	-19	0.0200	0
Vibration	Stg. 9 vane, 355°	0.9588	66	0.4257	-232	0.1152	-89	0.0281	-43	0.0072	-180
Vibration	Rear comp., 0°	0.9194	40	0.3806	-240	0.0576	-110	0.0194	-28	0.0109	-180
Vibration	Rear comp., 150°	0.6627	-135	0.2436	-5	0.0579	-184	0.0657	-44	0.0161	-180
Vibration	Rear comp., 240°	1.485	-88	0.3059	-133	0.0376	-108	0.1682	-225	0.0171	-180
Vibration	Rear comp., 270°	0.5379	-30	0.2448	-48	0.1325	-23	0.0287	-107	0.0096	-180
Whip	Stg. 9, 240°	0.0112	-36	0.0029	-70	0.0011	-100	0.0005	244	0.0001	-180
Whip	Stg. 9, 150°	0.0164	-157	0.0016	61	0.0003	137	0.0006	59	0.0003	0

U_m = amplitude (harmonic coefficient); vibration in in./sec., avg; whip in in., single amplitude.

a_m = phase angle, in degrees.

m = harmonic index.

405
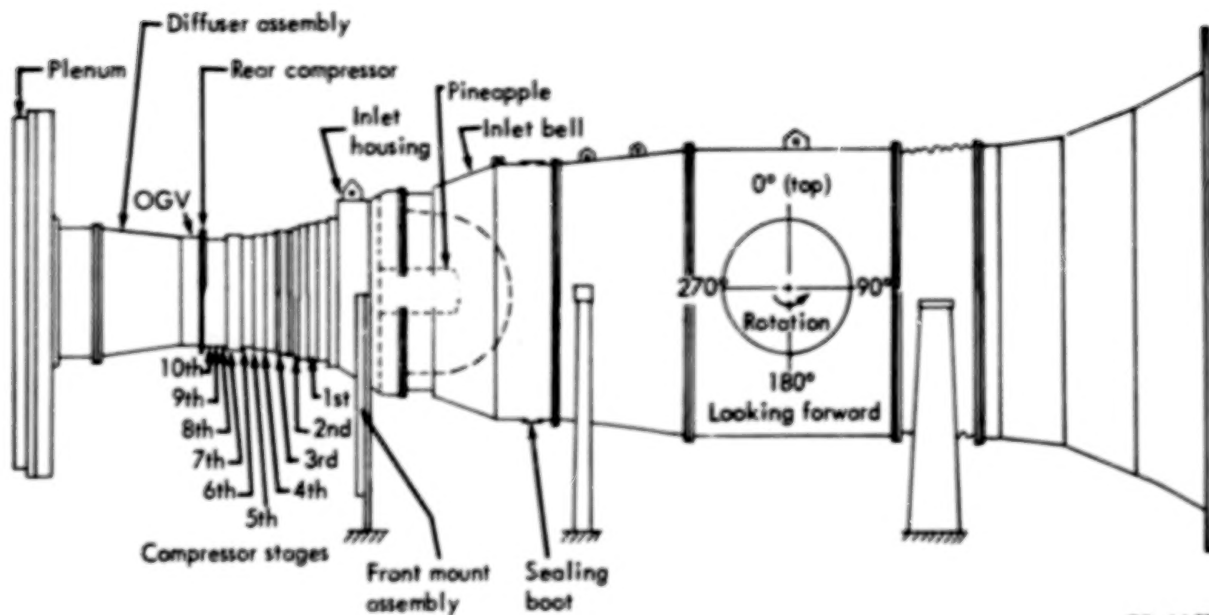
Figure 1. - Compressor rig on test stand.

TE-6657
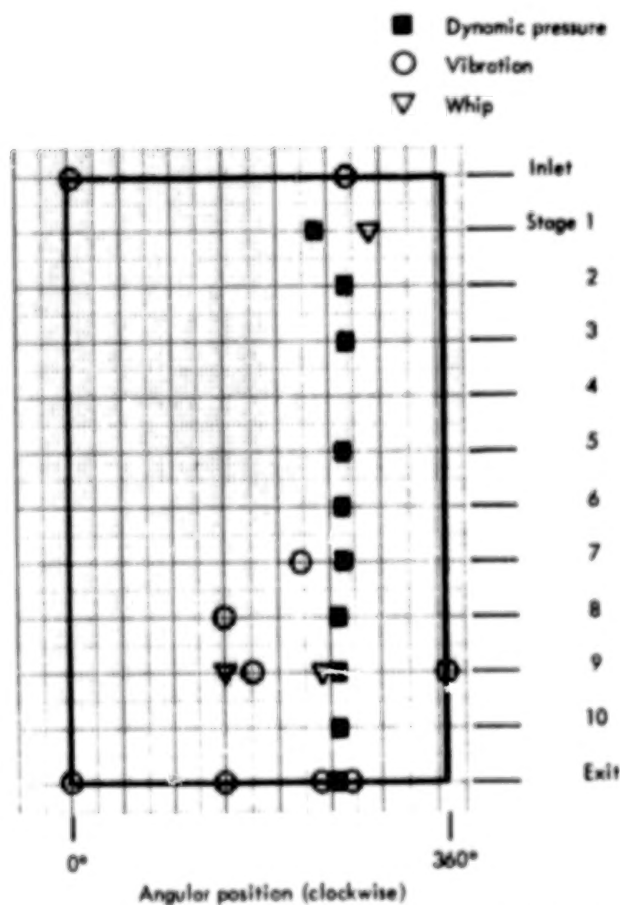
UNCLASSIFIED
TE-6714

Figure 2. - High-response instrumentation scheme.

406
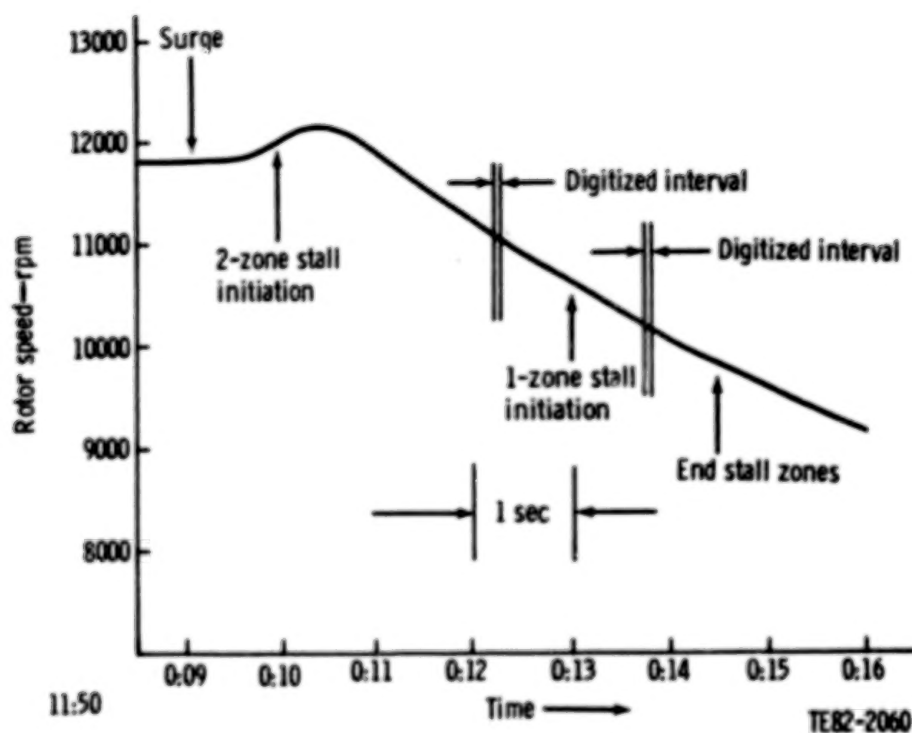
Figure 3. - Sequence of phenomena following surge.

407
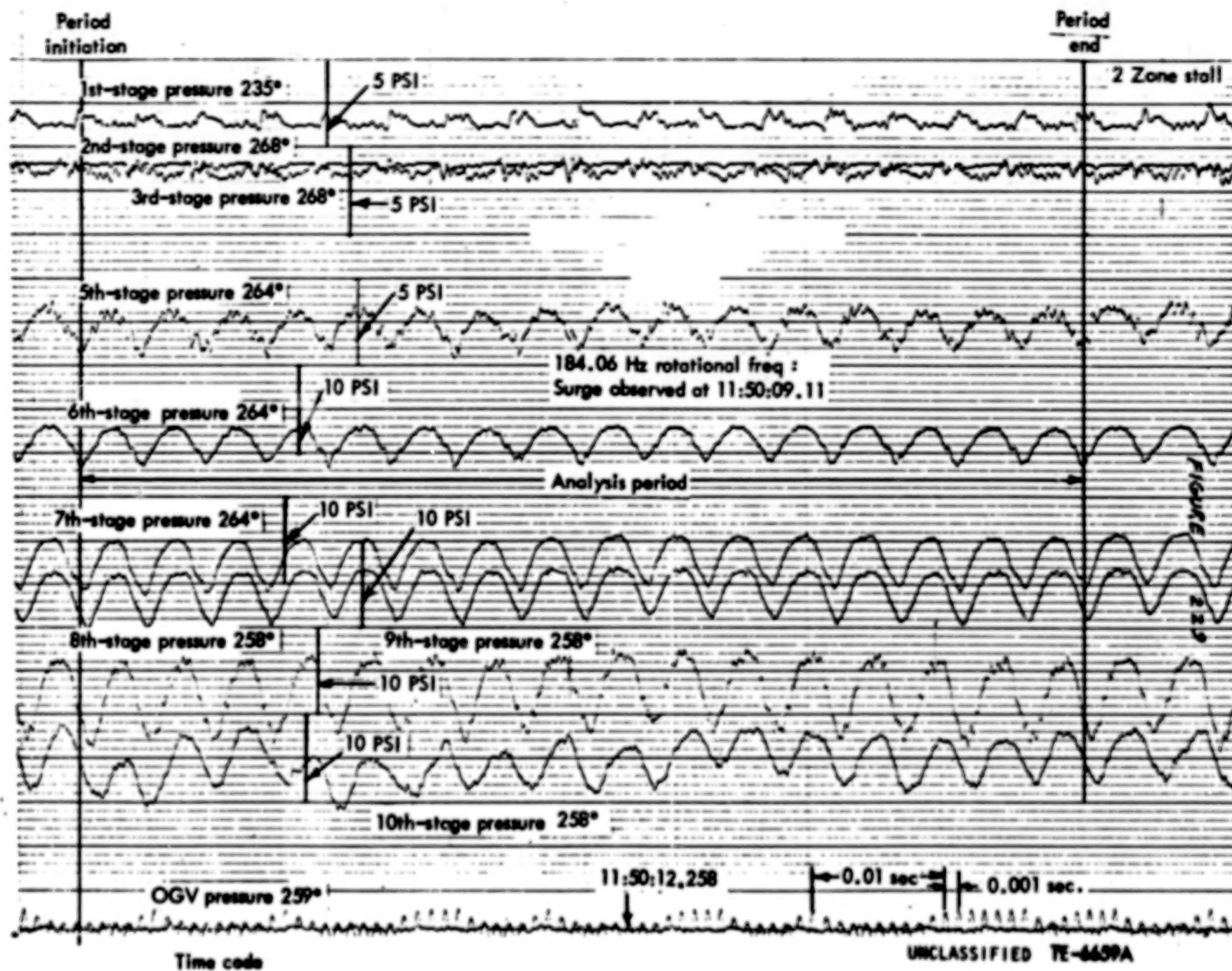
Figure 4. - Pressure data during two-zone stall.

BLANK PAGE

BLANK PAGE

BLANK PAGE

P/A vibration at 195° 4 in/sec

Inlet bell 0° 4 in/sec

Inlet Housing 0° 4 in/sec

Rear bearing support 180° 4 in/sec

P/A vibration at 265° 4 in/sec Surge observed at 11:50:09:11

184.06 Hz rotational freq.

Inlet bell 90° 4 in/sec 2 zone stall

Inlet housing 270° 4 in/sec

4 in/sec

Rear bearing support 283°

4 in/sec

1st-stage whip 293° 11:50:12.258 ⊢0.01 sec⊣ ⊢0.001 sec

Time code

FIGURE 227
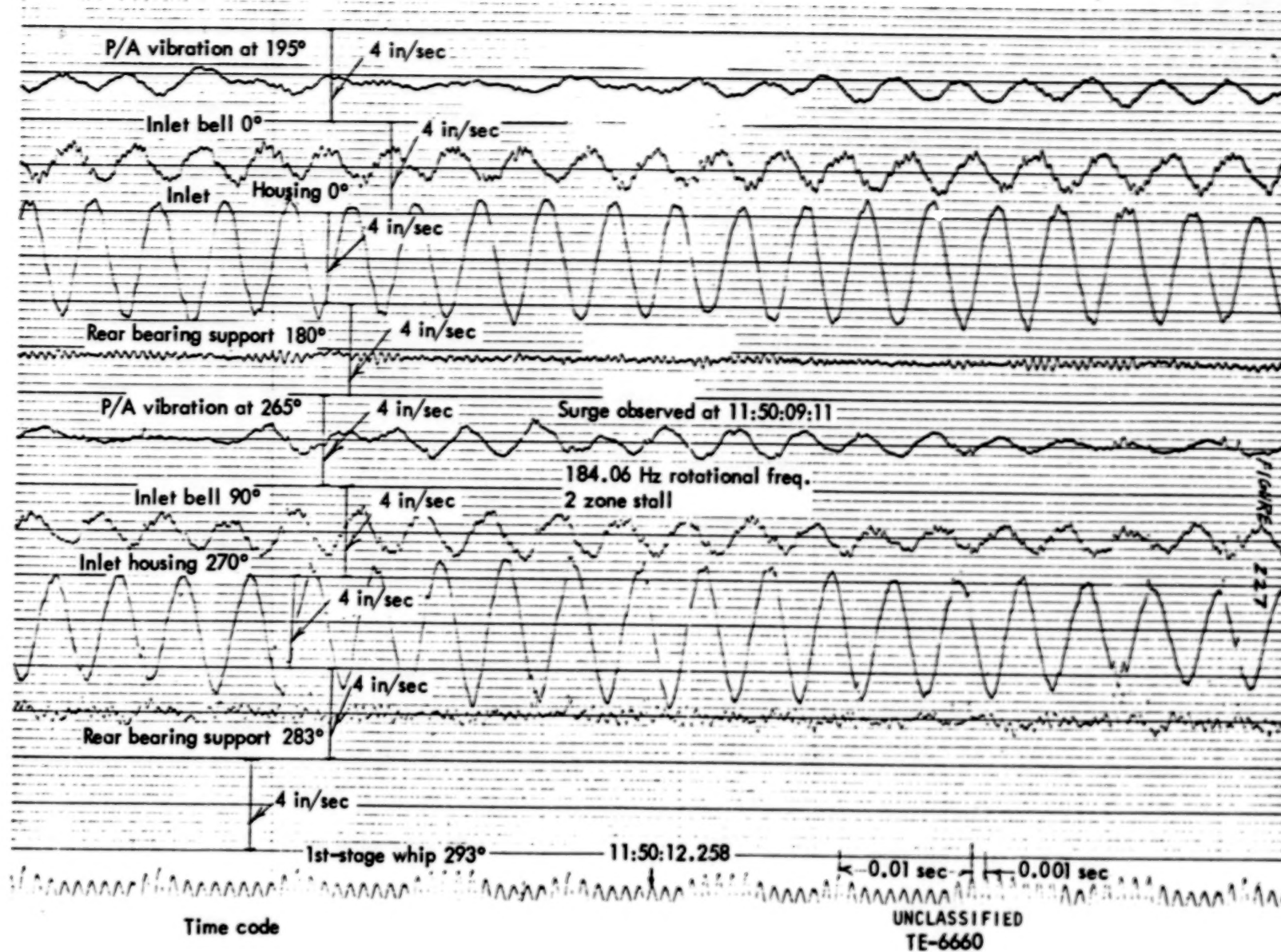
Figure 5. - Vibration induced by two-zone stall.

409
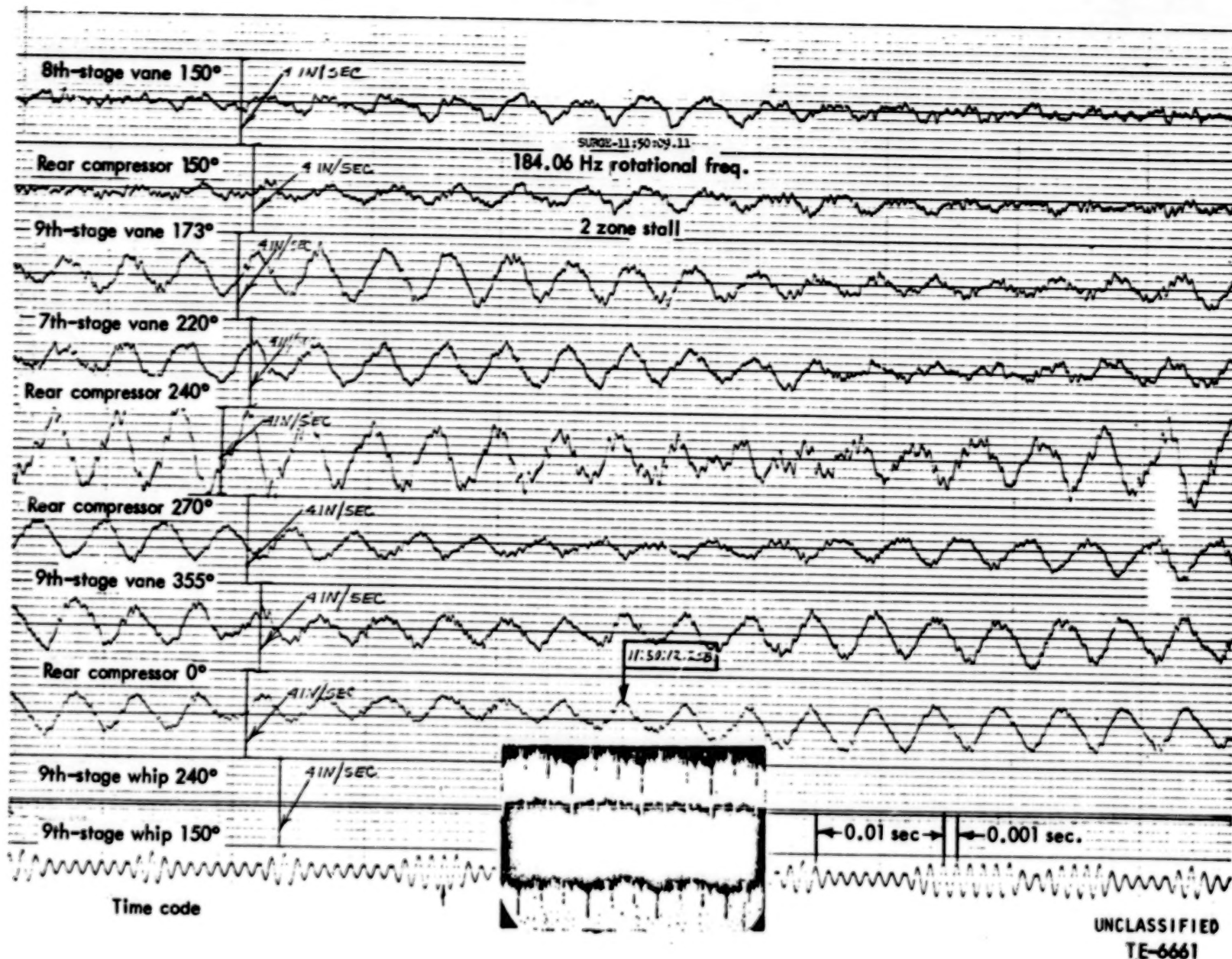
Figure 6. - Vibration induced by two-zone stall.

410

$H10$
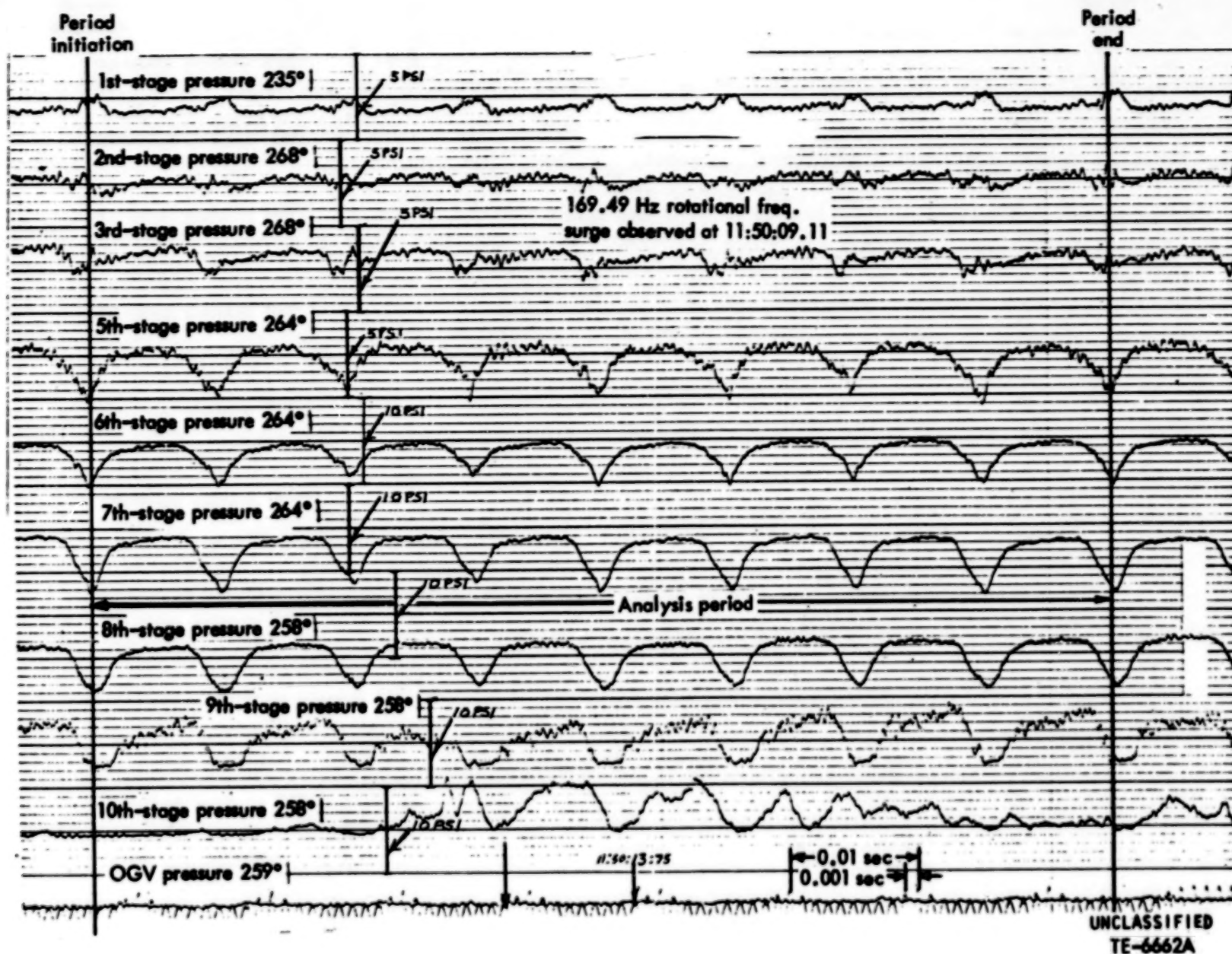
Figure 7. - Pressure data during single-zone stall.

P/A vibration at 195° 4 IN/SEC

Inlet bell 0° 4 IN/SEC

Inlet housing 0° 4IN/SEC

Rear bearing support 180° 4 IN/SEC

P/A vibration at 265° 4 IN/SEC

169.49 Hz rotational freq

Inlet bell 90° 4 IN/SEC

Inlet housing 270° Surge observed at 11:50:09.11

4 IN/SEC

Rear bearing support 283 4 IN/SEC

1st-stage whip 293

4 IN/SEC

|←0.01 sec→|←0.001 sec→|

11:50:13.75

Time code

412

UNCLASSIFIED
TE-6663
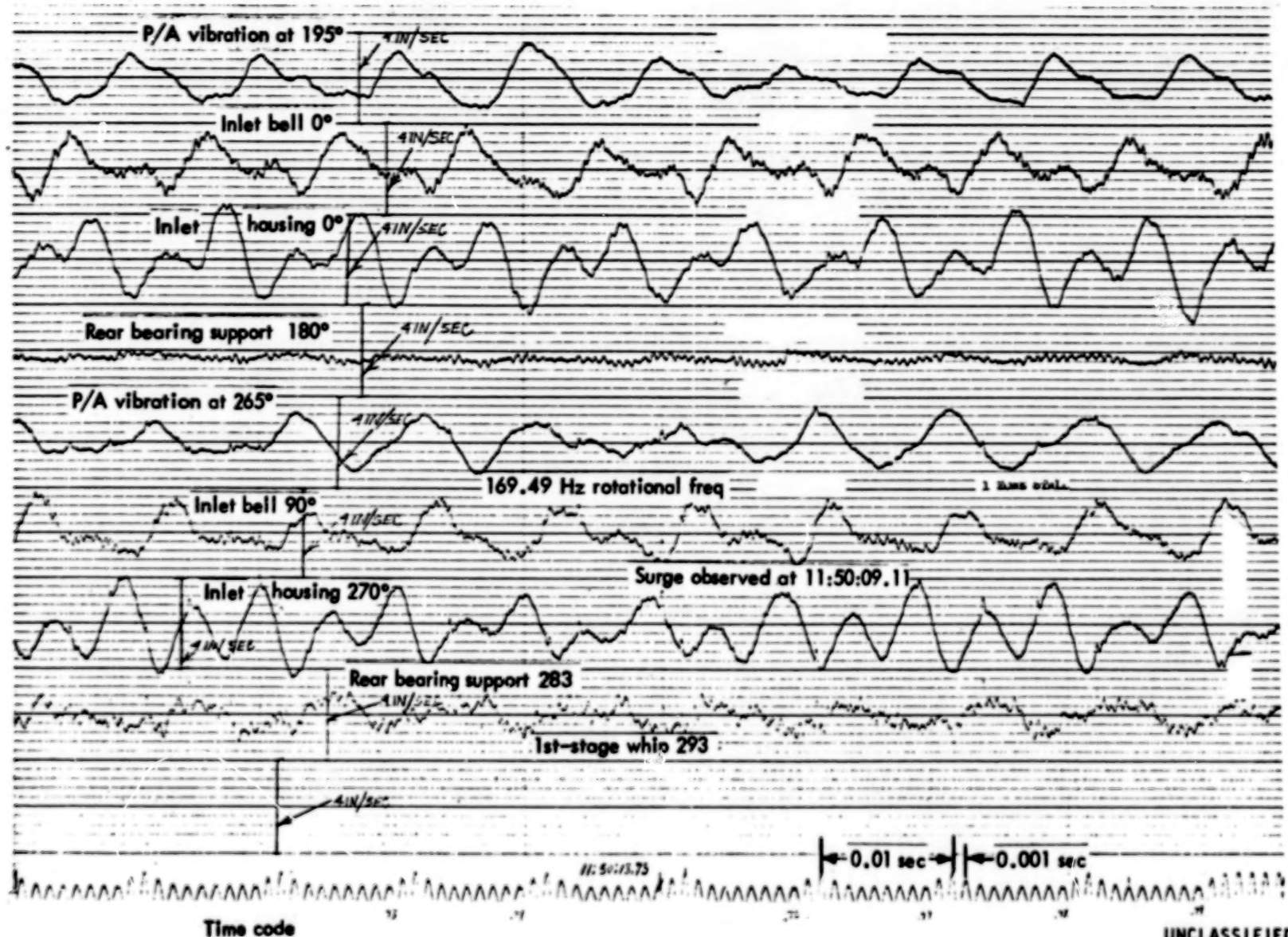
Figure 8. - Vibration induced by single-zone stall.

412
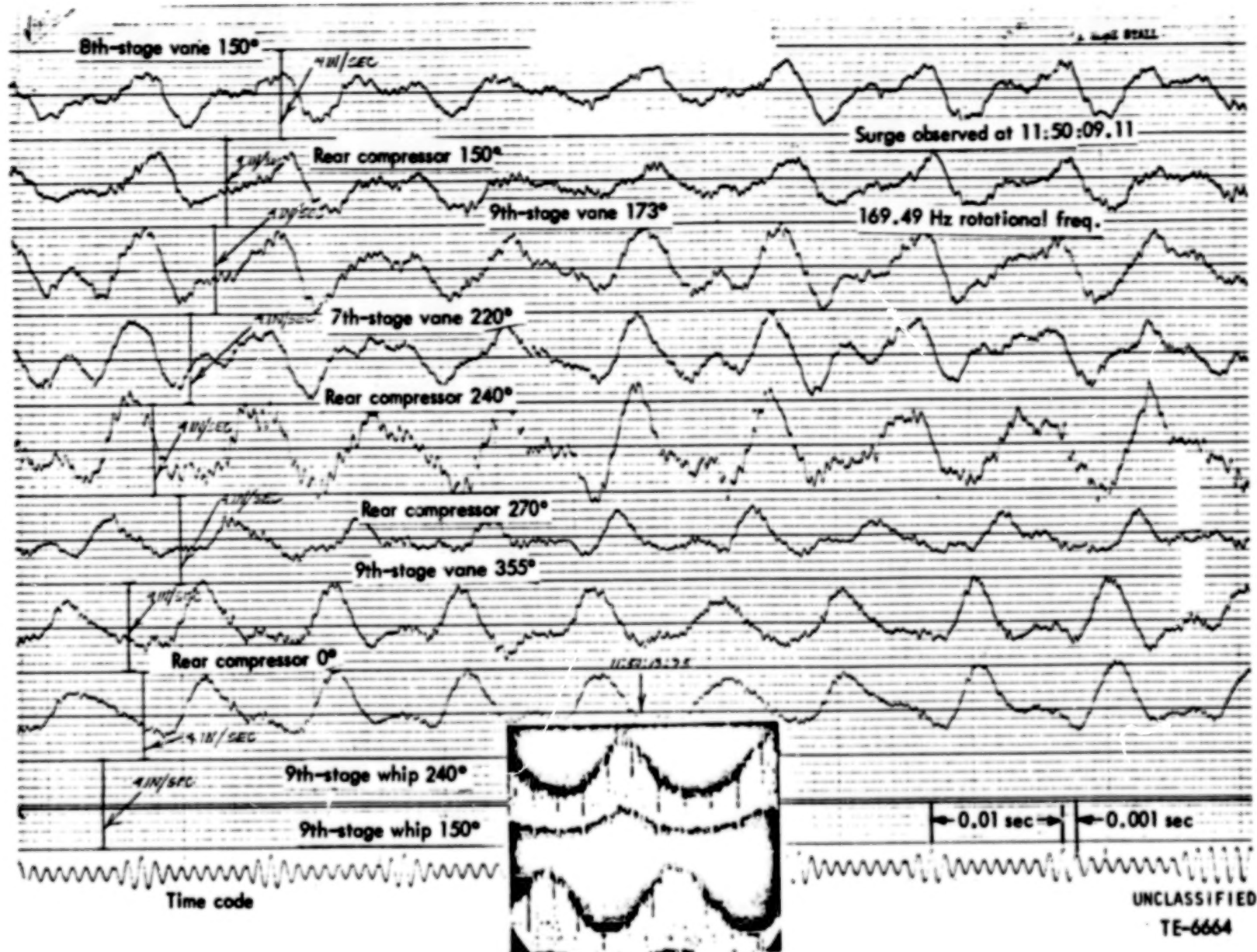
Figure 9. - Vibration induced by single-zone stall.

413

Beam-like behavior
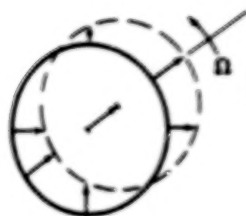
Arrows indicate
induced motion

Egging motion
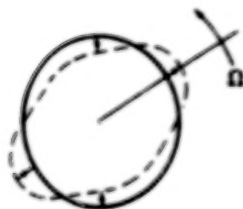
Local distortion
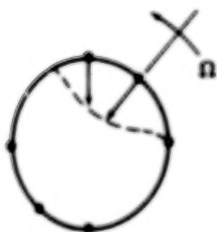
TE-6745

Figure 10. - Case motion descriptions.

INVESTIGATION OF SQUEEZE-FILM DAMPERS

IN FLEXIBLE SUPPORT STRUCTURES

R. Holmes and M. Dogan
University of Sussex
Brighton, England BN1 9QT

SUMMARY

Squeeze-film dampers are a means of curing instabilities in rotating-shaft assemblies. Their efficiency depends very much on the condition of the oil, which in turn depends on inlet and outlet arrangements, on damper geometry and on the flexibility of the rotor and surrounding structure. The work discussed in this paper concerns rig investigations in which structural flexibility is included experimentally and comparisons are made between measured and predicted results.

INTRODUCTION

In two previous papers (refs. 1 and 2), the performance of a squeeze-film damper unassisted by any retainer spring was examined when interposed between a rigid rotor and its rigid bearing pedestals. In many gas turbine applications, however, both rotor and pedestals are flexible, the latter to the extent that the first two rotor-pedestal critical speeds are essentially bounce modes, in which the rotor does not bend to any significant degree. Instead, on increase in speed the rotor often vibrates first in a symmetric and then in an anti-symmetric mode, while the pedestals are the only elements to show any appreciable degree of dynamic deflection. For such systems a squeeze-film damper interposed between one or more of the rolling-element bearings of the rotor and the pedestals can contribute a degree of damping which may enable the passage of the system through such critical speeds without vibration becoming excessive, and inhibit possible rotational instability.

It is not uncommon in gas turbines for the antisymmetric mode of vibration to exhibit a node near one of the rolling-element bearings. With such an application in mind, a test rig (fig.1) was designed and built, which afforded the investigation of the squeeze-film damper 1 at one of its two rolling-element bearings 2, the other bearing 3 being of the self-aligning variety. This constituted a pivot about which an antisymmetric (i.e. conical) mode of vibration would occur, when the rotor 4 was acted upon by a force arising from rotation of the unbalance mass 5 . The test rig was provided with flexible bars 6, which simulated the pedestal flexibility of an actual engine. Alternatively, the housing 7 could be clamped by the special clamps 8 to afford investigation of the squeeze-film damper alone. A heavy foundation block 9 was provided which represented ground and into which the flexible bars were screwed. Oil of 21 cp viscosity was supplied to the damper via three supply holes 10 and a central circumferential groove (fig.2). End plates were attached at the

---
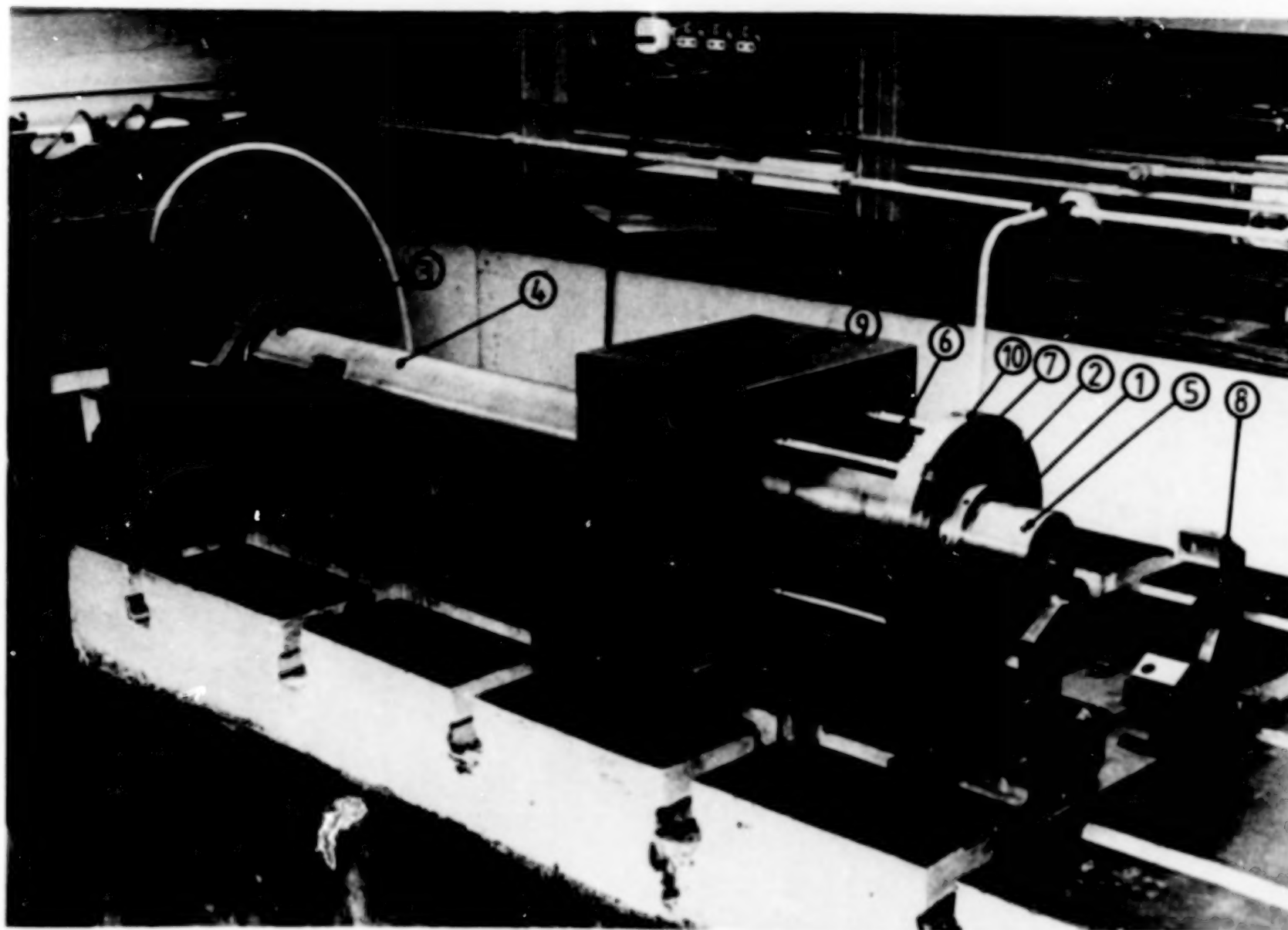
Figure 1. - Damper test rig.
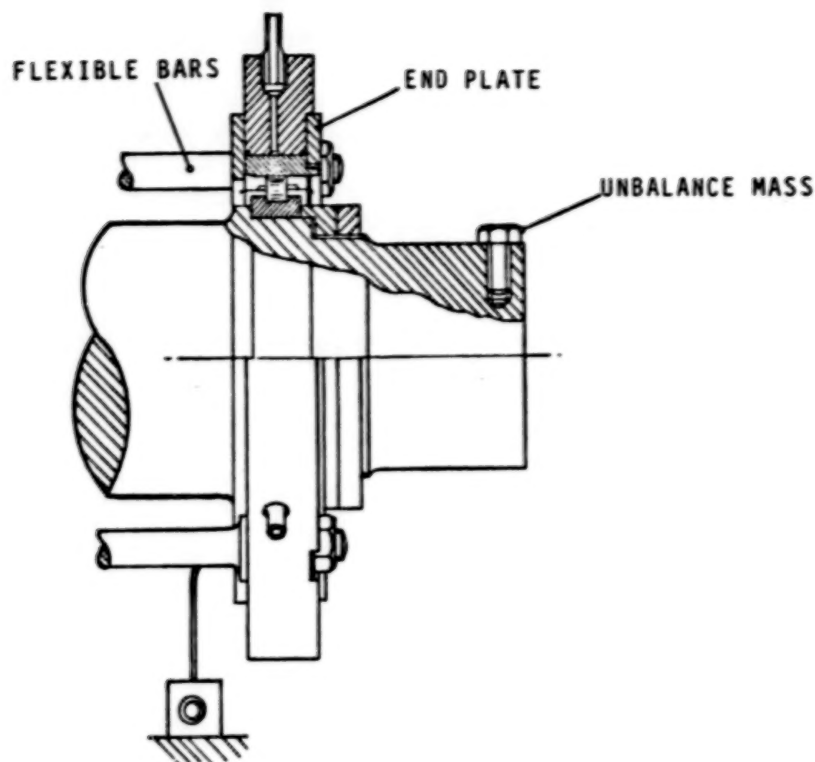
Figure 2. - Detail of damper.

ends of the outer element of the damper to afford some sealing, the extent of which could be varied by the insertion of spacing shims. The squeeze-film dimensions were set by the outer diameter of the rolling bearing (136 mm), the damper land length (9 mm) and its radial clearance (.216 mm).

Proximity vibration pickups were used to measure the vibration of the shaft relative to the pedestal and relative to ground. A pressure transducer was placed at a mid-land position at the base of the squeeze film to measure dynamic pressure in the oil under operating conditions and a thermocouple was also provided there to record oil-film temperature. The presence of the flexible bars allowed convenient recording of transmitted force by the provision of strain gauges.

This paper describes investigations into the performance of the dampers and a comparison of experimental findings with numerical predictions. For the latter, the numerical method developed in reference (2) was used. This was based on the short-bearing approximation applied to the Reynolds equation to describe the pressure field in the squeeze film and required the clearance between the end plates and the inner member of the damper to be wide enough to enable the assumption of atmospheric pressure at the ends of the damper to be used.

In reference (2) it was shown that the independent parameters of the squeeze-film damper could be presented in terms of three non-dimensional groups, namely

$$Q = P/mc\omega^2$$

$$Q_c = P_c/mc\omega^2$$

417

and

$$\beta = \frac{\eta R}{m\omega} \cdot (\frac{\ell}{c})^3 ,$$

in which P is the static load, usually provided by gravity, which for one land of the damper was 147 N, m is the effective mass of the rotor at each land (12.25 kg), c is the radial clearance in the damper (0.216 mm), R is the radius of the inner member of the damper (68 mm), ℓ the damper land length (9 mm) and η the oil viscosity (21 cp). ω is the rotational speed of the shaft carrying the unbalance mass, which provides the required dynamic force, P_c, causing vibration. An essential requirement in the numerical computations is the specification of a cavitation pressure below which the pressure field is curtailed. This pressure was found experimentally.

TESTS WITH CLAMPED HOUSING

Firstly a series of tests was carried out with the housing clamped and details of these are given in Table 1.

TABLE 1. - TESTS WITH HOUSING CLAMPED

Q_c	Rotor speed rev/min		
0.229	4000	4500	5000
0.642	3000	3400	3750

As the value of Q_c was increased the top speed of the rig was successively reduced in order to avoid excessive vibration of the rolling-element bearing in the damper clearance space. The value of speed dictated the corresponding values of the non-dimensional groups Q and β and these are given with the appropriate experimental recordings and numerical predictions shown later. An oil supply pressure of 34.48 KN/m^2 (5 lbf/in^2) was used throughout these tests to avoid excessive outflow from the ends of the damper through the rather wide end-plate clearances of 1.25 mm.

A set of experimental vibration orbits and pressure recordings is given in figure 3a for Q_c = 0.229. Fig. 3b shows the corresponding numerical predictions. Each numerical hydro-dynamic pressure distribution was curtailed at its experimentally-observed negative pressure limit before integration to obtain the squeeze-film forces which acted on the rotor to produce the orbit of vibration. Figures 4a and b show similar comparisons for a higher value of Q_c of 0.642, and are typical of many others.

Some significant general observations can be made from these comparisons. In figure 3a, the general sizes and dispositions of the vibration orbits are well predicted, while both the experimental and numerical recordings show a reversal in position of the sharp 'tail' between 4500 and 5000 rev/min. The pressure waveforms also show good agreement in respect of general shape and height. The orbits of figure 4a are quite well predicted in general shape, size and disposition (even to the extent of showing a sudden increase in size between 3700 and 3750 rev/min). Whilst the experimental pressure waveform at 3000 rev/min is fairly well predicted, the waveform at 3400 rev/min does not show such good agreement in that numerical computations indicate a sharp positive pressure spike, which is not reproduced experimentally. It seems probable that the slightly shallower slopes of the experimental vibration orbits do not give rise to such pressures, which are very sensitive to orbit shape. An inspection of the second experimental pressure peak in a given cycle will, however, indicate a good comparison with the numerical prediction.

4000 rev/min
Q = 0.316
β = 0.02
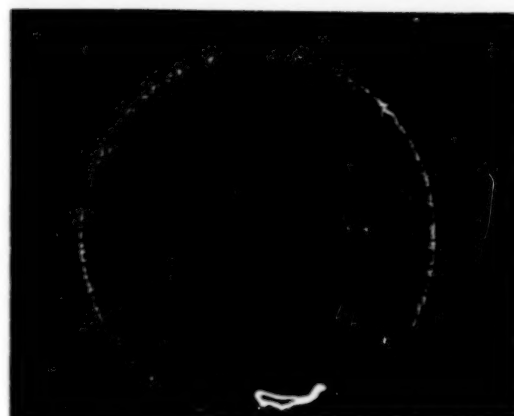
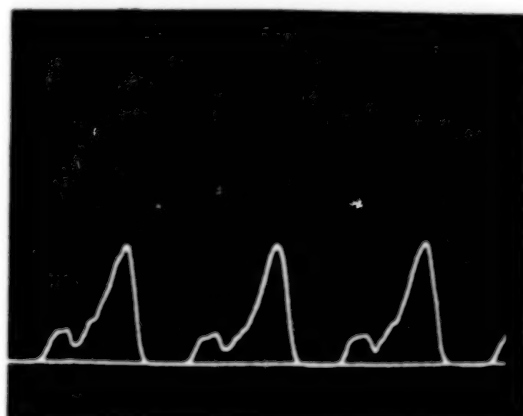4500 rev/min
Q = 0.25
β = 0.018
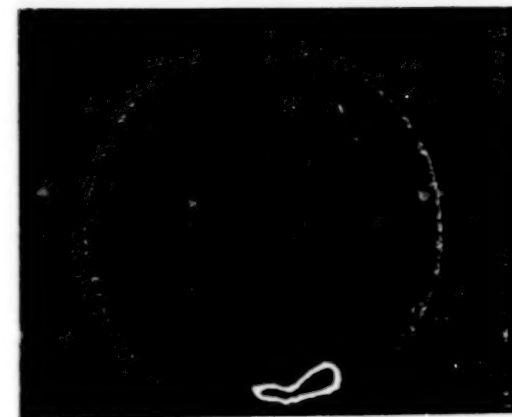
5000 rev/min
Q = 0.2
β = 0.016
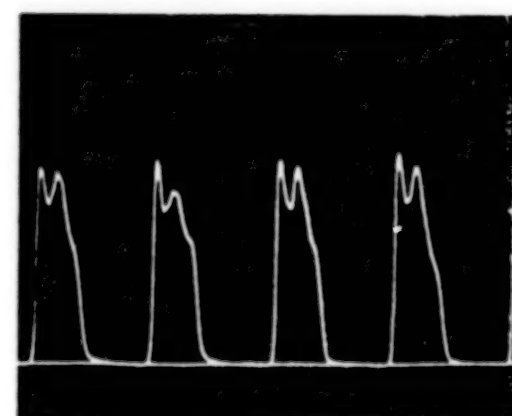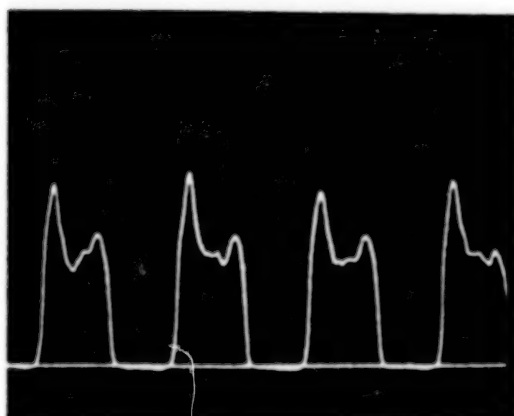
Figure 3(a). - Experimental orbits and pressure recordings (1 cm = 127 psi = 876 kN/m^2). Q_c = 0.229.

419

420

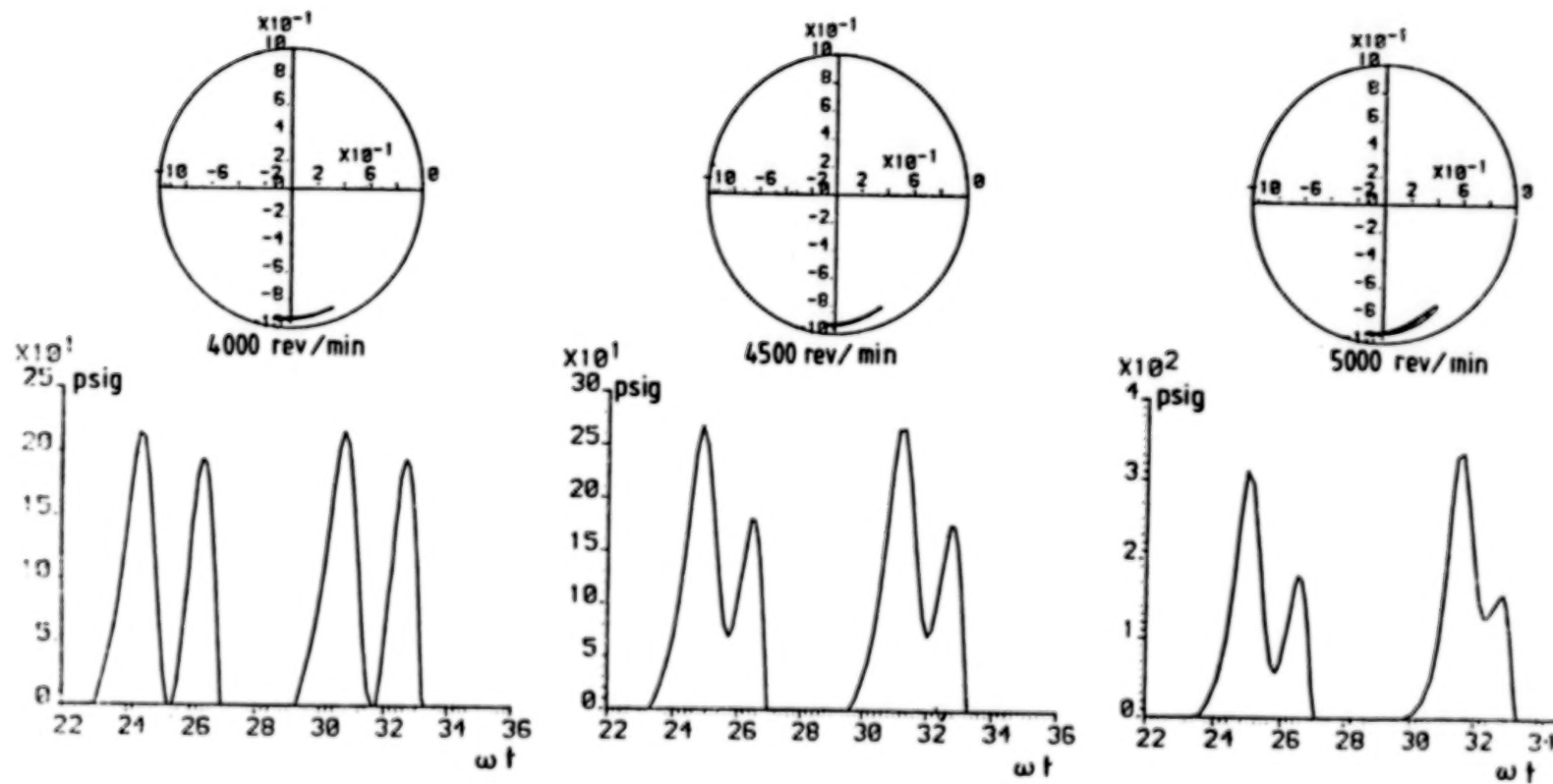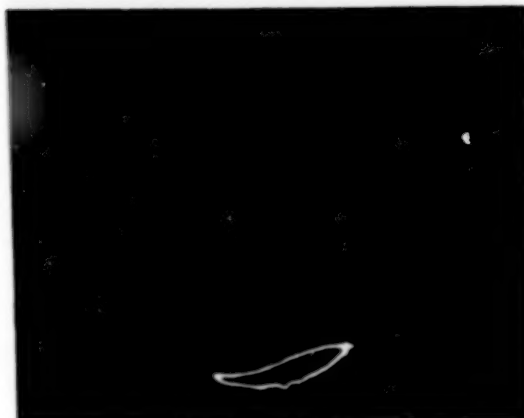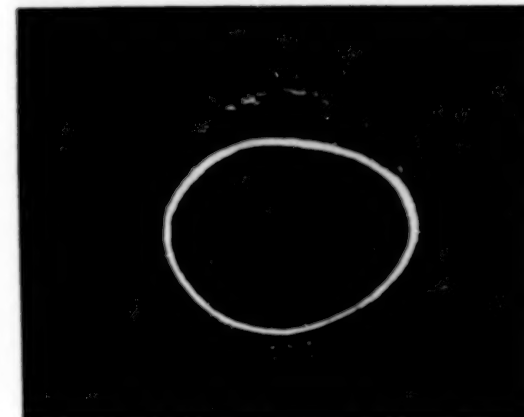Figure 3(b). - Numerical orbits and pressures. $Q_c = 0.229$.

420

3000 rev/min
Q = 0.562
β = 0.027

3400 rev/min
Q = 0.44
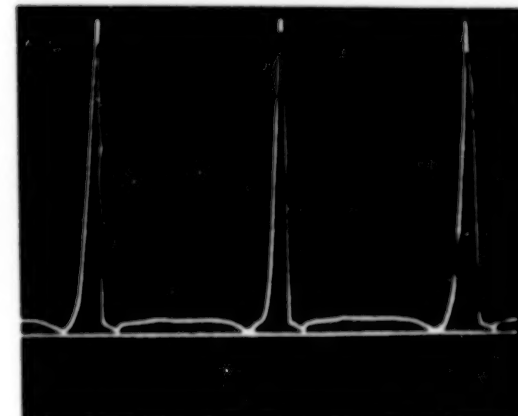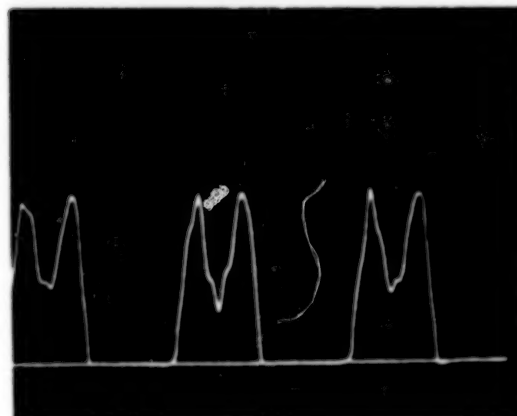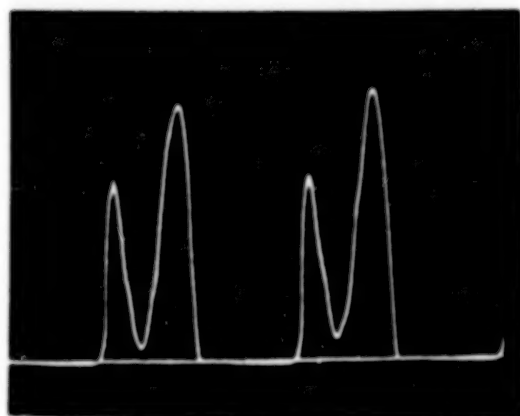β = 0.024

reduced scaling
3750 rev/min
Q = 0.36
β = 0.0215

Figure 4(a). - Experimental orbits and pressure recordings (1 cm = 127 psi = 876 kN/m^2). Q$_c$ = 0.642.

BEST DOCUMENT AVAILABLE

421
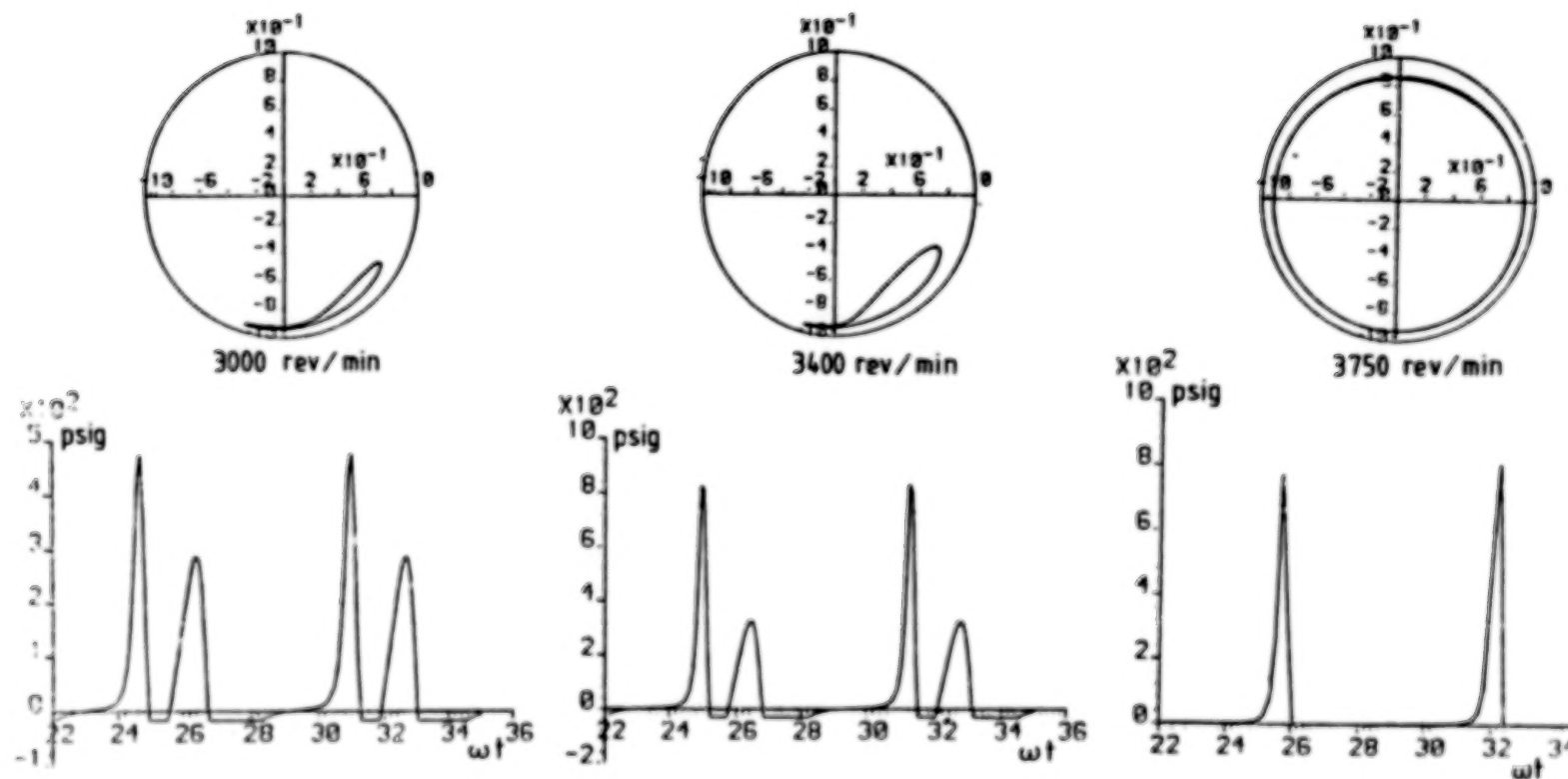
Figure 4(b). - Numerical orbits and pressures. $Q_c = 0.642$.

422

322

3500 rev/min
$Q = 0.413$
$\beta = 0.023$

3800 rev/min
$Q = 0.35$
$\beta = 0.0212$

4200 rev/min
$Q = 0.287$
$\beta = 0.0192$

4500 rev/min
$Q = 0.25$
$\beta = 0.018$

423
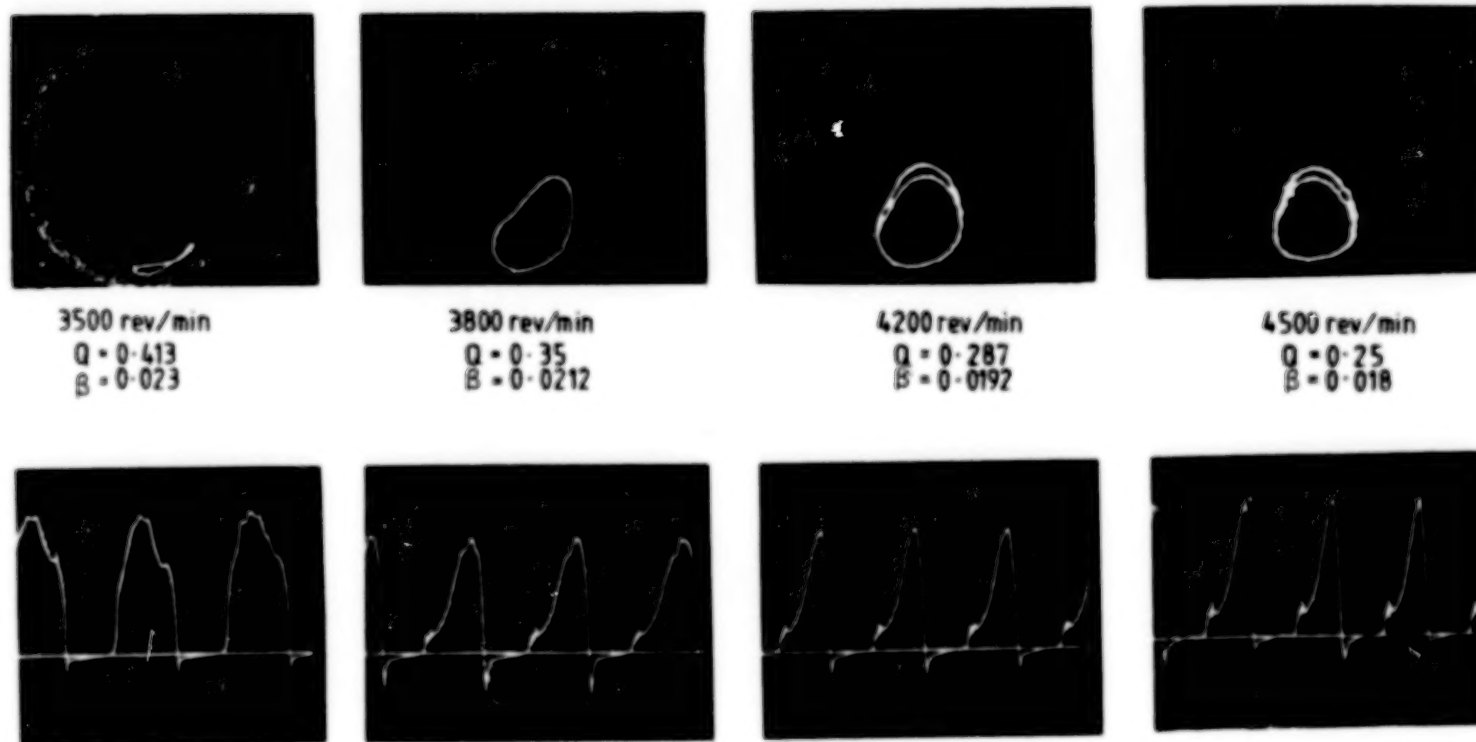
Figure 5(a). - Experimental orbits and pressure recordings (1 cm = 181 psi   1251 kN/m^2). $Q_c = 0.229$.

423
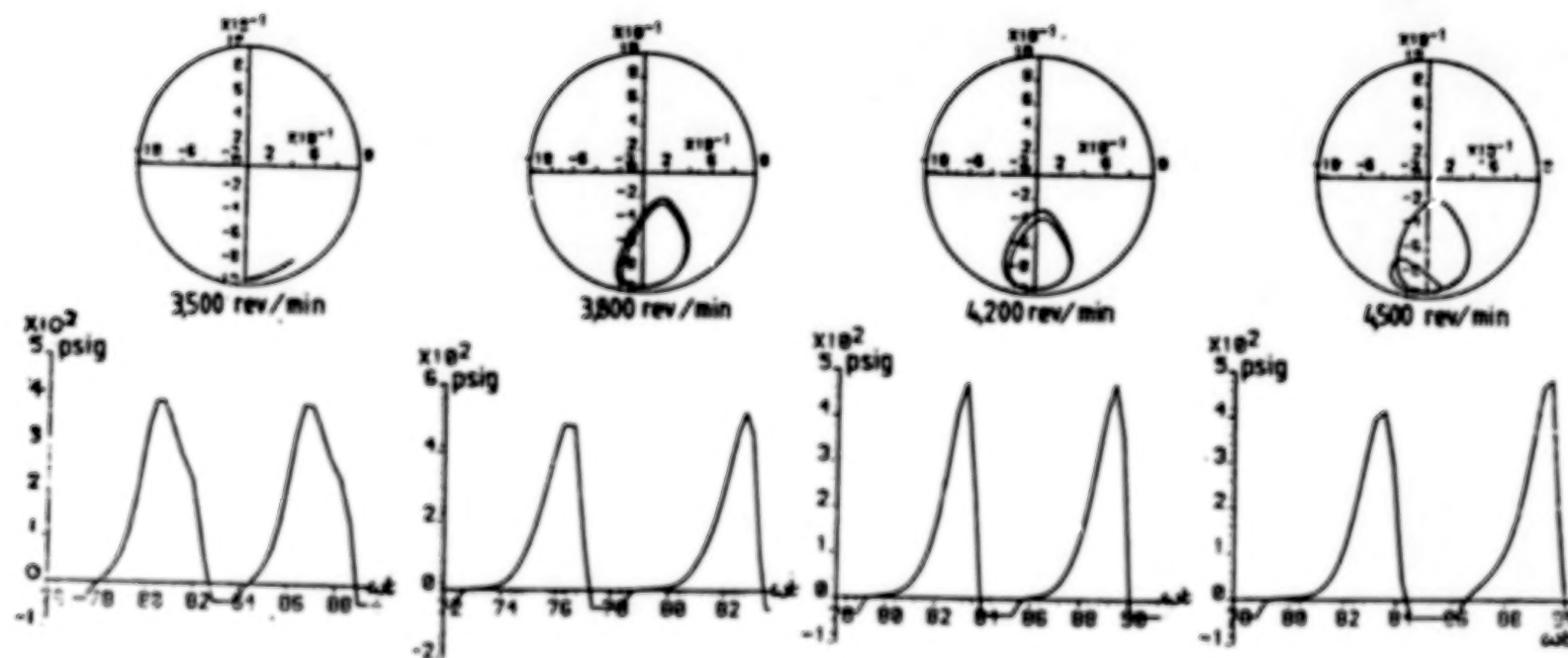
Figure 5(b). - Numerical orbits and pressures. Q_c = 0.229.

425

3500 rev/min   3800 rev/min   orbits   4200 rev/min   4500 rev/min
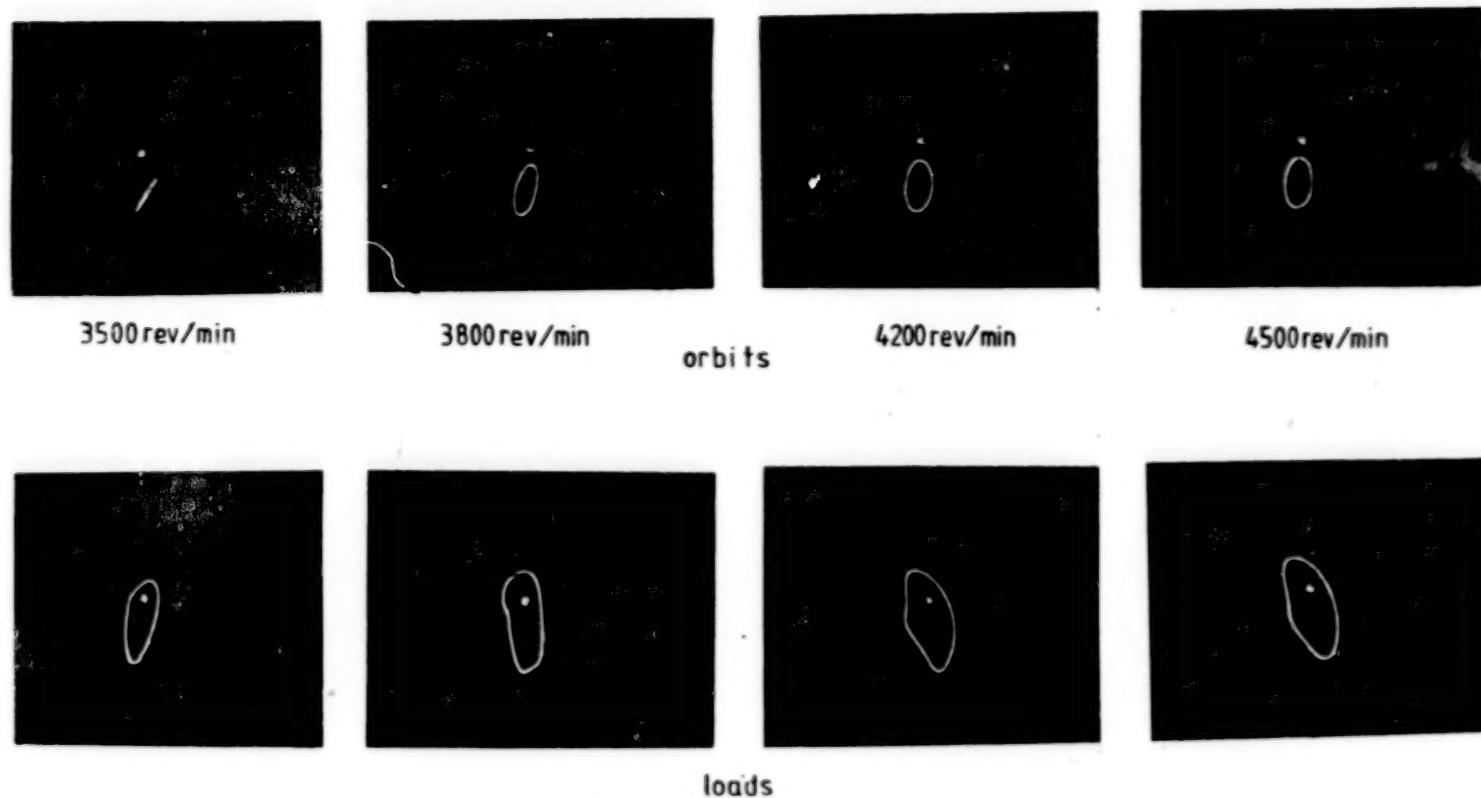
loads

Figure 6(a). - Experimental orbits relative to ground and polar load diagrams. Q_c = 0.229.
(1 cm = 0.5 mm and 1 cm = 1070 N).

425

BEST DOCUMENT AVAILABLE

426
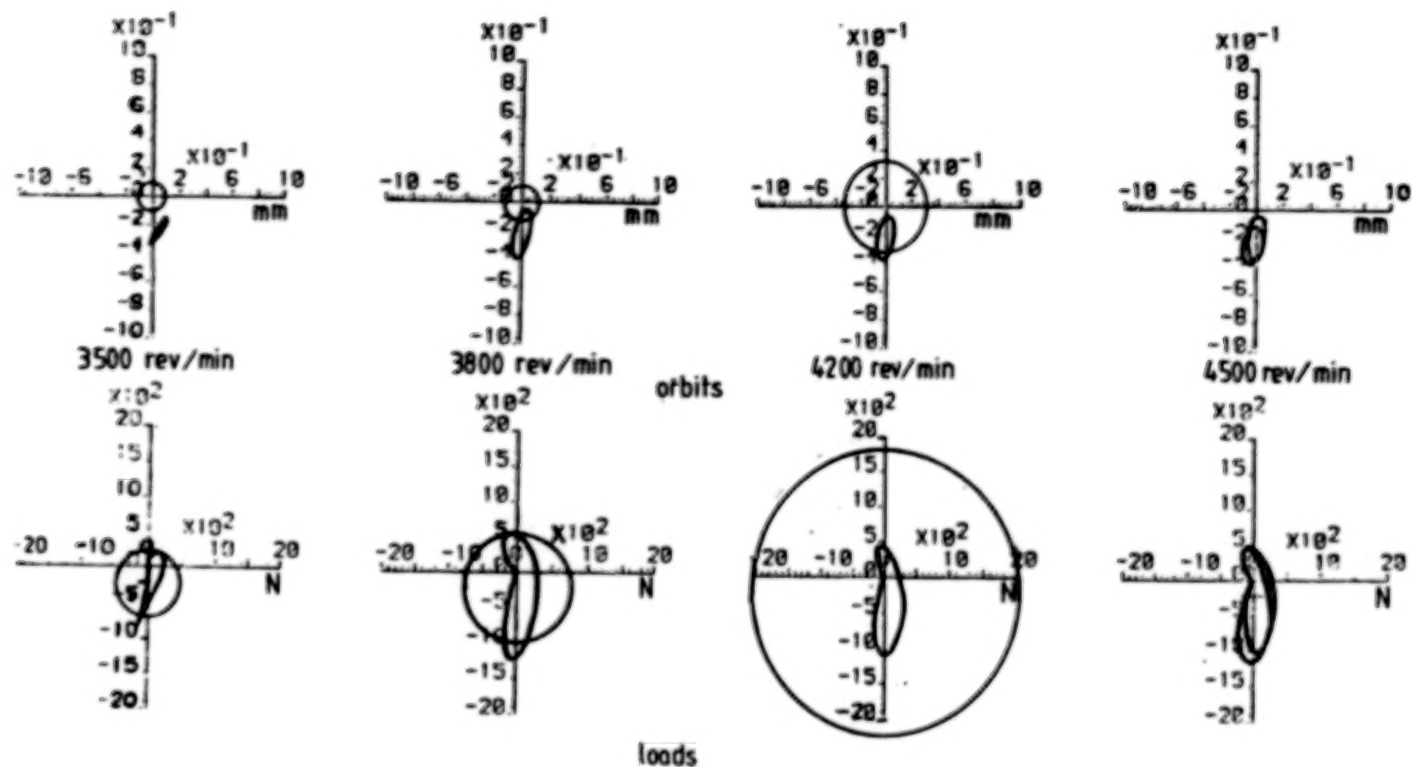
Figure 6(b). - Numerical orbits and loads. $Q_c = 0.229$.

426

TESTS WITH FLEXIBLY MOUNTED HOUSING

The housing was now unclamped, giving an undamped natural frequency of the system of about 4500 c/m. A series of tests was carried out using a Q_c value of 0.229 at speeds of 3500, 3800, 4200 and 4500 rev/min. In addition to obtaining vibration orbits of the rotor relative to the housing, orbits of the rotor relative to ground and polar diagrams of transmitted force were obtained. For such a configuration the mathematical model for the structure included the same damper model as previously, together with the stiffness of the bearing pedestal, but for speed of computation, neglected the relatively small housing mass which was only 14% of the effective rotor mass.

Comparisons of experimental and numerically predicted orbits are shown in figures 5 a,b and indicate good agreement. For the case of 3500 rev/min, a distorted figure of eight pattern is observed in both experimental and numerical recordings. The double loops visible in the other experimental recordings persisted over the entire periods of experimentation and those in the numerical predictions persisted up to a non-dimensional time ωt of 96, that is about 15 revolutions, when the length of computing time became prohibitive. The general sizes, shapes and dispositions show good agreement, and the size at 4200 rev/min is observed to be larger than at the undamped natural frequency of 4500 rev/min. The pressure recordings of figure 5b also show fair agreement in shape and size. Negative 'spikes' are evident in figure 5a, indicating that the oil can temporarily support tensile forces. Such tensile forces have been discussed in reference 2.

Turning now to the vibration orbits of the rotor relative to ground (figs. 6a,b), very good agreement prevails both in size, shape and disposition and a peak vibration between 4200 and 4500 rev/min is again observed. This suggests that the squeeze-film damper has had some effect in reducing the critical speed of the system. The polar diagrams of total dynamic load transmitted from both lands show striking agreement in many respects, such as size, shape and disposition. In particular the kink in each experimental polar diagram for 3800, 4200 and 4500 rev/min is predicted by numerical computation. These latter results give extra confidence in accepting the short bearing model of reference 2 for the squeeze film, albeit with a negative pressure curtailed at an experimentally recorded limit.

Also shown in figure 6b are circles representing total displacements and transmitted forces when no damper is present. The effect of gravity on the flexible bars increased displacements by about 0.04 mm and all forces by about 274 N. It can be seen that, at the lower speeds the damper is not really beneficial. However, at speeds approaching the critical speed, its benefits become apparent, especially at the undamped critical speed of 4500 rev/min where, without the damper the amplitudes of vibration and transmitted force would theoretically be infinite.

CONCLUSIONS

Continuing on from experience gained on test rigs involving open-ended squeeze-film dampers interposed between rigid rotors and rigid bearing pedestals (refs.1,2), this paper has described experimental and numerical work on weakly sealed dampers with flexible pedestals. Good agreement has been observed between experimental observations and numerical predictions over a wide range of operating parameters. These observations included vibration of rotor relative to bearing housing and relative to ground, dynamic pressure in the squeeze-film damper and transmitted force to ground. The work shows that, given the correct interpretation of boundary conditions in the

damper, reliance can be placed on a mathematical model incorporating the short-bearing approximation. The benefits of such a damper can also be readily seen.

This work will shortly be extended to include the effect on the damper of tighter sealing and the use of higher supply pressures and very low oil viscosities, in keeping with present-day operational practice with gas turbines.

REFERENCES

1. Humes,B. and Holmes,R.: The role of sub-atmospheric film pressure in the vibration performance of squeeze-film bearings. Jnl Mech.Eng.Sci., vol.20, no.5, pp.283-289.

2. Holmes,R. and Dede,M.: Dynamic pressure determination in a squeeze-film damper. Proc.I.Mech.E. Paper C260/80. Second International Conference on Vibrations in rotating machinery. Cambridge, Sept. 1980.

Linear theory as a qualitative predictor

Although the squeeze-film bearing is a highly non-linear element, it is worth examining its contribution to the damping of a system against a linear assessment.
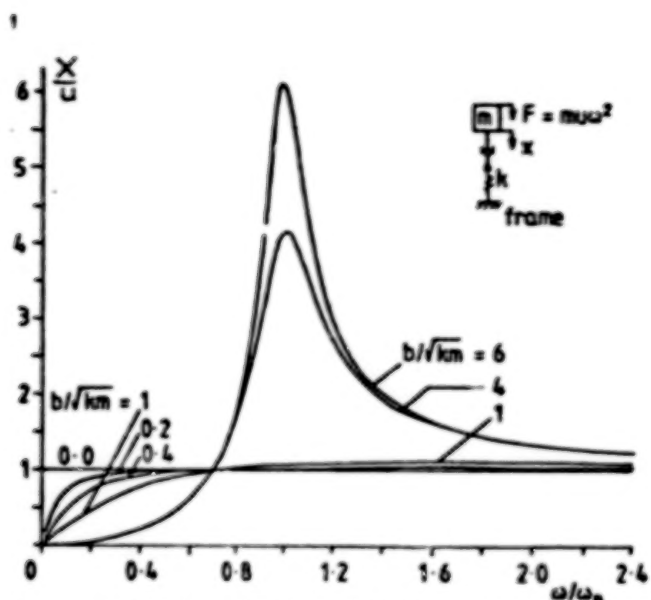
Figure 7(a). - Rotor vibration amplitude relative to the engine frame.
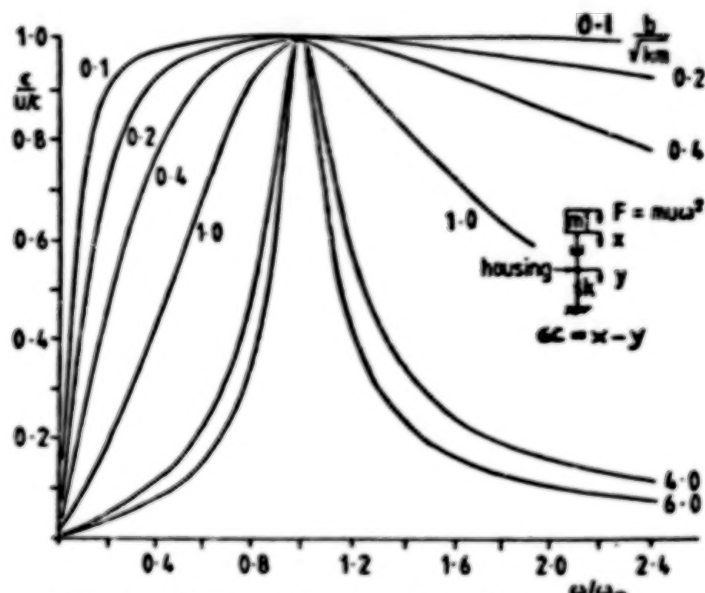
Figure 7(b). - Rotor vibration amplitude relative to the bearing housing.
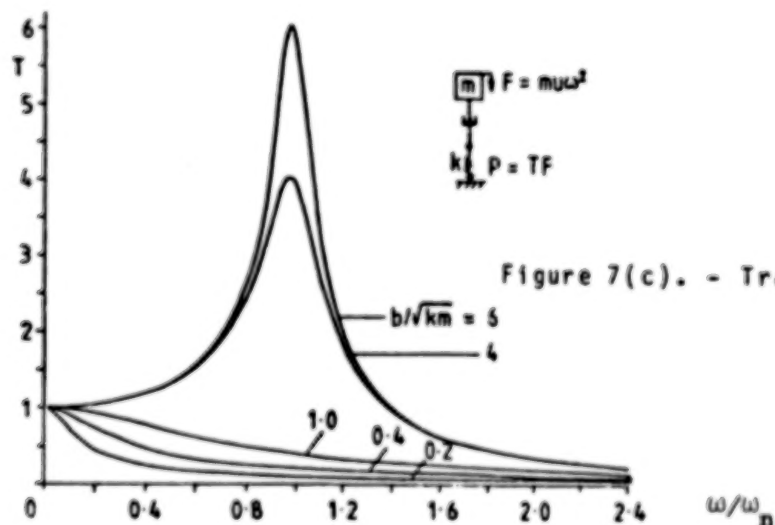
Figure 7(c). - Transmissibility.

If we consider a linear structure consisting of a series combination of mass, damper and spring, the graphs shown in Fig.7 are readily obtained. The most notable features of these graphs are, in Fig. 7a, the cross-over point $(1/\sqrt{2}, 1)$, and the increase in vibration amplitude with damping at a frequency ratio of 1; in Fig.7b, the independence of vibration with damping at $\omega/\omega_n = 1$; in Fig. 7c, the increase in transmissibility with damping at $\omega/\omega_n = 1$.

Figs. 8a, b, c show results obtained from the test rig when running at the critical speed of 4500 rev/min i.e. $\omega/\omega_n = 1$. In these figures, damping is increased in three separate ways:

i) by tightening the end sealing (Fig. 8a)
ii) by increasing the lubricant viscosity from 6 to 21 cp (Fig.8b)
and   iii) by increasing the lubricant supply pressure from 5 to 45 psi (Fig.8c).

In each of these figures the photographs may be identified as follows:

a) Vibration orbit relative to bearing housing
b) Vibration orbit relative to ground
c) Pressure recording
d) Polar load diagram of transmitted force.

It may be seen that in all cases the results support the qualitative conclusion of the linear treatment, namely that at the critical speed an increase in damping by whatever means results in an increase in rotor vibration relative to ground, and an increase in transmissibility, but little change in the rotor vibration relative to the squeeze-film container.
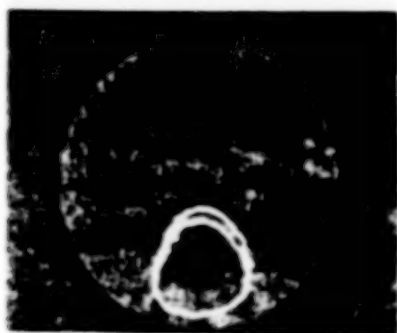
(a)
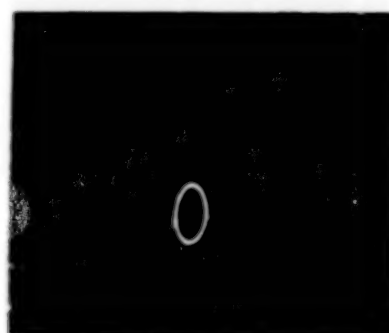
(b)
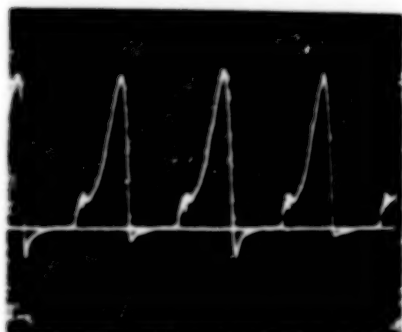
(c)

(d)

(a)

(b)
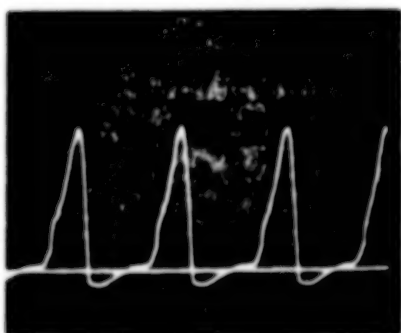
(c)
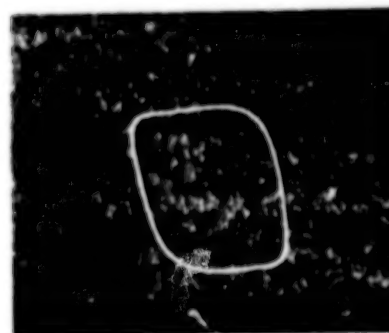
(d)

Figure 8(a). - Effect of sealing.

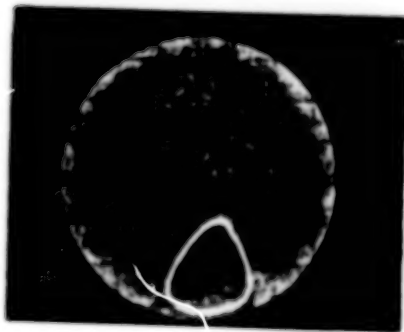Upper four figures loose sealing
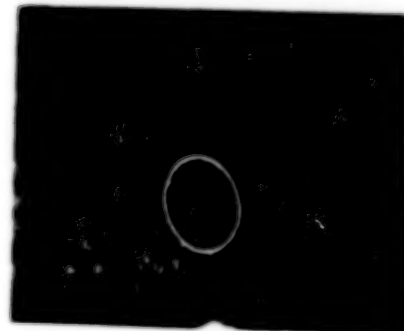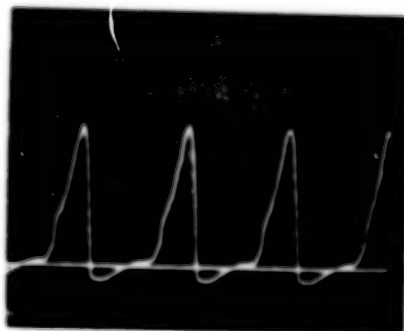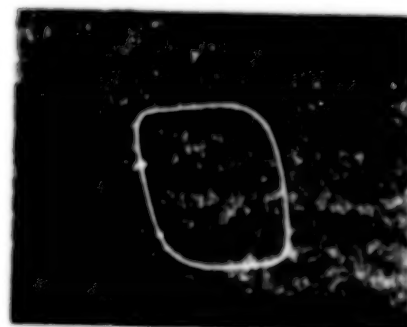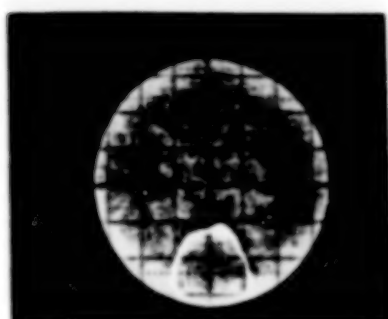Lower four figures tight sealing

431

(a)

(b)

(c)

(d)
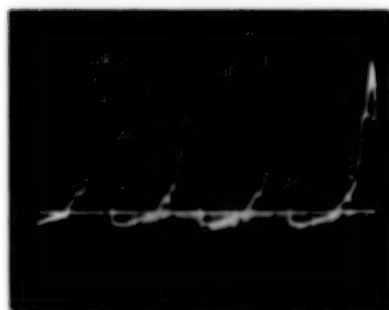
(a)

(b)

(c)

(d)
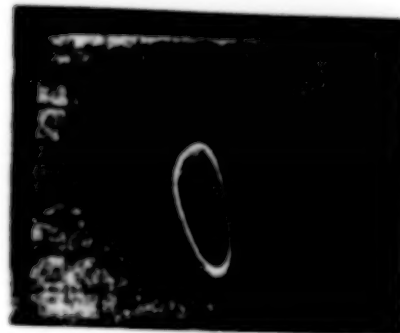
Figure 8(b). - Effect of lubricant viscosity.

Upper four figures 6 cp
Lower four figures 21 cp

432
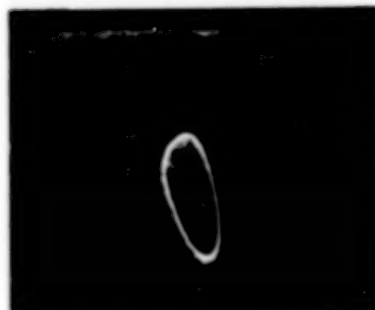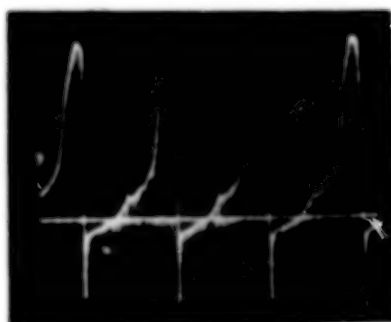
Figure 8(c). - Effect of lubricant supply pressure.

Upper four figures 5 psi
Lower four figures 45 psi

433

VIBRATION LIMITING OF ROTORS BY FEEDBACK CONTROL

David W. Lewis, James W. Moore, Philip L. Bradley, and Paul E. Allaire
Department of Mechanical and Aerospace Engineering
University of Virginia
Charlottesville, Virginia 22901

SUMMARY

This work reports some experimental findings of a three-mass rotor with four channels of feedback control. The channels are independently controllable with force being proportional to the velocity and/or instantaneous displacement from equilibrium of the shaft at the non-contacting probe locations (arranged in the vertical and horizontal attitudes near the support bearings).

The findings suggest that automatic feedback control of rotors is feasible for limiting certain vibration levels. Control of one end of a rotor does afford some predictable vibration limiting of the rotor at the other end. The next step in the work is to move from acoustic drivers to electro-hydraulics so that larger force levels may be experimented with.

INTRODUCTION

High speed turbomachines are subject to lateral vibrations, which may limit their performance level [1,2]. Machines are often required to operate at least 20% away from a rotor critical speed. They must also be designed so that, for machines operating above one critical speed, all clearances in the machine are sufficient to accommodate high amplitudes of vibrations near a critical speed. Lastly, machines are sometimes subject to subsynchronous vibrations, which can lead to machine failures [1]. One type of means for reducing these vibrations is that of active vibration control.

A number of analytical studies of active feedback controls for rotating machinery have been presented in the literature [3-6]. These have been primarily developed by researchers in the automatic controls area and the results are normally presented in terms associated with automatic control theory. A very limited number of experimental works have reported the use of active control for laboratory test rigs [7-9]. With the possible exception of the electromagnetic bearing, there has not been an application of active feedback control to an industrial rotor at this time.

This work considers unbalances in rotating machinery which might be compensated by use of active feedback control circuits. With proper algorithms, such closed loop automatic control devices could permit machinery to be run longer even though the unbalanced forces grew to significant values. Such an approach would have little impact for small and noncritical rotors. However, for very important systems for which an unscheduled shut-down would be costly, an analog or digital closed-loop feedback controlled force actuator(s) could be justified.

434

Also, for some very expensive turbines, pumps, and compressors, active feedback controlled force actuators would allow machinery to pass through the criticals with smaller clearances (because of controlled vibration levels) resulting in more efficient running. With such an application, the proposed devices would be functioning only during runup or rundown of the machinery permitting certain advantages for the designers of the machinery.

Values in the text are given in both SI and U.S. Customary Units. The measurements and calculations were made in U.S. Customary Units.

EXPERIMENTAL UNIT

A small test rotor has been constructed and is generally described by the schematic drawing of Fig. 1. It consists of a 12.7 mm (0.5 inch) diameter shaft supported on ball bearings which are 406 mm (16 inches) apart. For these tests, three masses, uniformly distributed between the bearings were attached to the shaft by simple setscrews. These disks weighed 8.9 N (2.0 lbs), 13.3 N (3.0 lbs), and 8.9 N (2.0 lbs) with the larger one at the center. The bearing carriers with the associated hardware each weighed 4.4 N (1.0 pound). Shaft weight is 4.0 N (0.90 pound).

Each bearing has mechanical springs at 11.7 N/mm (67 pounds per inch) in the vertical and horizontal directions plus loud speaker motors (acoustic drivers) attached to the bearings directed in the vertical and horizontal attitudes. This test rotor is unique in that forces may be applied to the bearings, through acoustic drivers that are independent from one another in the vertical and horizontal directions. These four acoustic drivers provide four independent routes for applying forces to the bearings.

The vertical and horizontal displacements near the bearings were measured relative to the static equilibrium position. A force was generated through an analog feedback loop in the same attitude but of the direction opposing the motion. At the same time, an additional force was generated that was proportional to the instantaneous velocity (and also oppositely directed). These forces were then applied to the shaft, through the ball bearings, by means of the acoustic drivers. These four acoustic drivers are independently operable. The controls for setting the constants for generating the forces, as a function of displacement or velocity or some combination of displacement and velocity, are also independent one from another.

EXPERIMENTAL RESULTS

A number of experimental runs were made. The ones reported here are for runs with the rotor fairly well balanced and with no control, a low level of control, and a high level of control. Control was limited in these cases to the velocity feedback loops so that, effectively, only damping was being controlled. In addition, the system was modelled and theoretical response was obtained on a digital computer.

The results of the first run are shown in Fig. 2. The lines with data points shown represents the experimental results and the continuous line is for theoretical results. There is an excellent match of critical speeds at 700 and 1200 rpm and a reasonable agreement of results for a critical near 6000 rpm. In the midrange ampli-

tudes are not in close agreement. It is noted that the displacement monitoring system
had a limit at about 0.56 mm (22 mils).

For the second run the control loop gains were set to give an effective damping
constant at each bearing of 0.047 N sec/mm (0.27 lb sec/in). This was for all four
control loops. However, just as the run was about to start it was found that the
current amplifier in the free-end vertical control loop was not functioning. The run
was continued with data being taken at the motor end. The results here were very
similar to those of the uncontrolled system except that the critical at 700 rpm is
eliminated. The theoretical response did not agree well except for the location of
the criticals.

A large damping factor was applied in the last experimental and theoretical
runs. The results are shown in Fig. 4. The damping constant was estimated to be
about 0.37 N sec/mm (2.13 lb sec/in), about eight times greater than the previous run.
Results are dramatic over the range of all three criticals.

DISCUSSION AND CONCLUSIONS

This limited set of experiments has shown some of the effects that may be obtained
with the use of feedback control. Here, the analog control signals were applied in
both directions at the motor end and only to the vertical direction at the other end.
For Fig. 4, the motor end resulted in a small circular orbit and simultaneously a very
flat ellipse at the other end. The effects obtained here are through the use of velo-
city feedback only with the velocity gain setting at about one fourth of its full
scale values.

These runs were made using analog control only. The experimental rig has a com-
plete digital control system, also. The full potential for the analog system has yet
to be explored. However, it is known that it would use some adaptive ability, either
speed sensitive or logical, in order to fully develop its potential.

The digital control system is potentially far more flexible. In this experimental
system it can be brought into play by simply turning it on and flipping a switch. The
digital unit in the control loop is an Intel 8086 single board computer. This offers
a sixteen bit manipulator. We can anticipate some very interesting control algorithms
with this system which at the present time has been used for a simple look-up algorithm
only. There will be a possibility of even employing an algorithm that "learns" what
combination of displacement and velocity (when multiplied by appropriate constants)
will produce the minimum response for the system at each speed for that particular
rotor condition. Then as the rotor condition changes (through erosion, accumulation
of dirt onto the disks, etc.) this "learning" algorithm could accommodate the chang-
ing disturbance.

The acoustic drivers are small, yielding forces that are small. Typically, the
output for the drivers is approximately 15 watts maximum but with the proper phasing
does produce significant results. It is felt that electro-hydraulics will be the
preferred means of applying forces in an industrial atmosphere. Preliminary calcu-
lations indicate that electro-hydraulics will be satisfactory directly for speeds up
through 10,000 rpm. For speeds above that, it will be necessary to employ one or
more revolutions of the shaft to make the necessary calculations as part of the
control algorithm. However, this time delay (or more specifically the rotation delay)

will not likely be significant as rotors must go through many cycles before amplitudes change an appreciable level.

REFERENCES

1. Allaire, P. E., "Design of Journal Bearings for High Speed Rotating Machinery," Fundamentals of the Design of Fluid Film Bearings, Fluid Film Bearings Committee of Lubrication Division (ASME, 1979), pp. 45-84.

2. Barrett, L. E., Gunter, E. J., and Allaire, P. E., "Optimum Bearing and Support Damping for Unbalance Response and Stability of Rotating Machinery," Journal of Engineering for Power, Transactions of the ASME, Vol. 100, No. 1 (January 1978), pp. 89-94.

3. Moore, J. W., Lewis, D. W., and Heinzmann, J. D., "Feasibility of Active Feedback Control of Rotor Dynamic Instability," Presented at Workschop on Rotor Dynamic Instability Problems in High Performance Turbomachinery, NASA/ARO Conference, Texas A&M University, May 1980, pp. 1-9.

4. Heinzmann, J. D., "The Implementation of Automatic Vibration Control in a High Speed Rotating Test Facility," M.S. Thesis, University of Virginia, January 1980.

5. Stanway, R. and Burrows, C. R., "Active Vibration Control of a Flexible Rotor on Flexibly-Mounted Journal Bearings," Joint Automatic Controls Conference, Charlottesville, Virginia, June 1981.

6. Allaire, P. E., Lewis, D. W., and Jain, V. K., "Feedback Control of a Single Mass Rotor on Rigid Supports," Journal of the Franklin Institute, Vol. 312, No. 1, pp. 1-11.

7. Nikolajsen, J. L. and Holmes, R., "Investigation of Squeeze-Film Isolators for the Vibration Control of a Flexible Rotor," Journal of Mechanical Engineering Science, Vol. 21, 1979, pp. 247-252.

8. Schweitzer, G. and Lange, R., "Characteristics of a Magnetic Rotor Bearing for Active Vibration Control," Institution of Mechanical Engineers Conference on Vibrations in Rotating Machinery, Cambridge, 1976, paper C239/76.

9. Gondhaleker, V. M., Nikolajsen, J. L., and Holmes, R., "Electromagnetic Control of Flexible Transmission Shaft Vibrations," Proc. IEEE, Vol. 126, 1979, pp. 1008-1010.
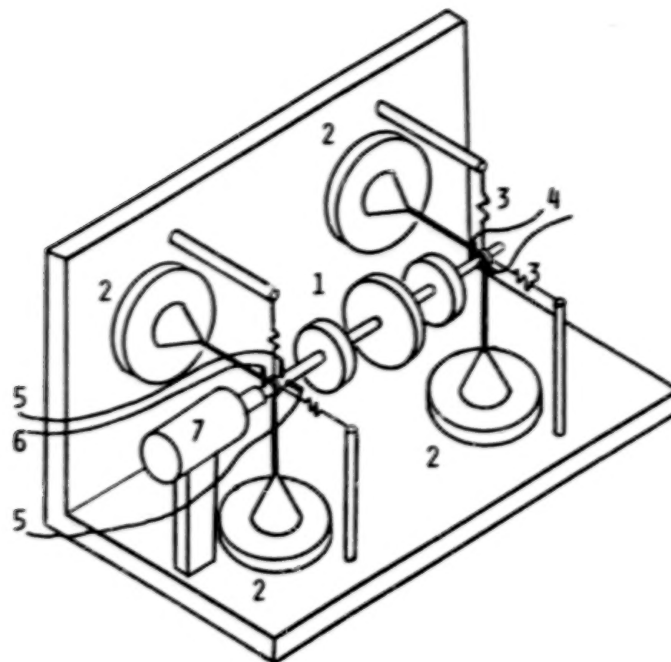
Figure 1. - Schematic diagram showing three-mass rotor 1, loud speaker motors 2, mechanical support springs 3, non-contacting probe signals for measuring the position of the shaft at the outboard bearing 4, similar signals for the motor-end bearing 5, key phasor signal for speed measurement 6, and a variable speed motor 7.
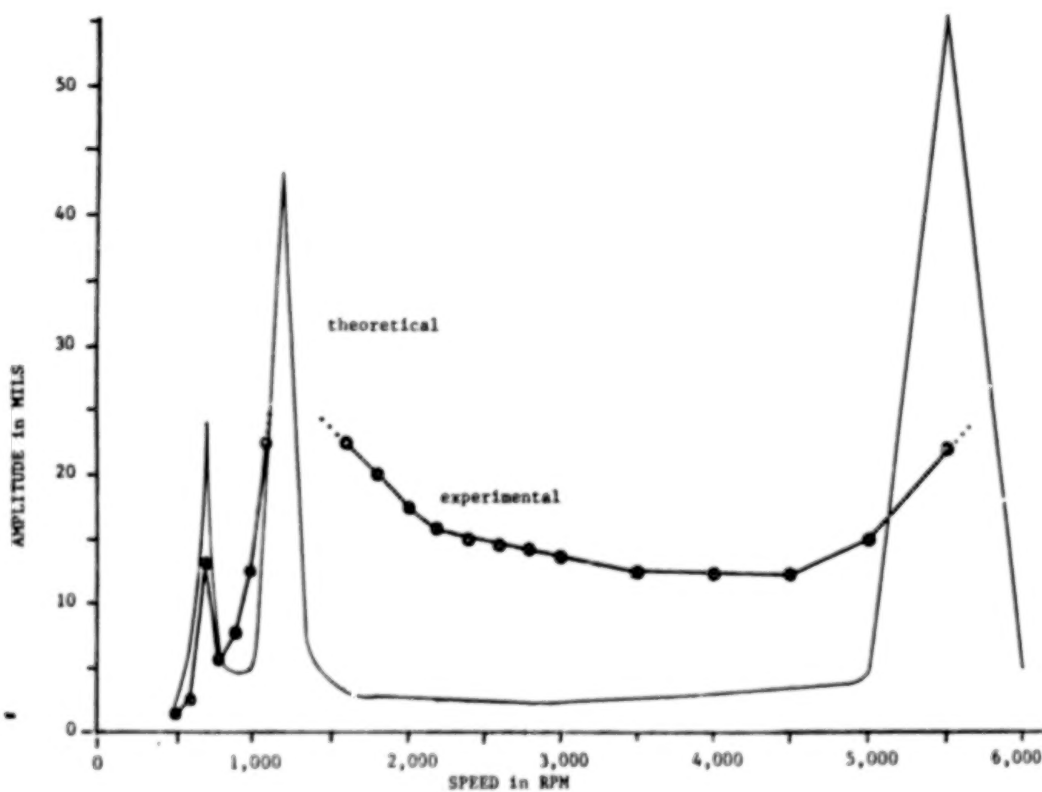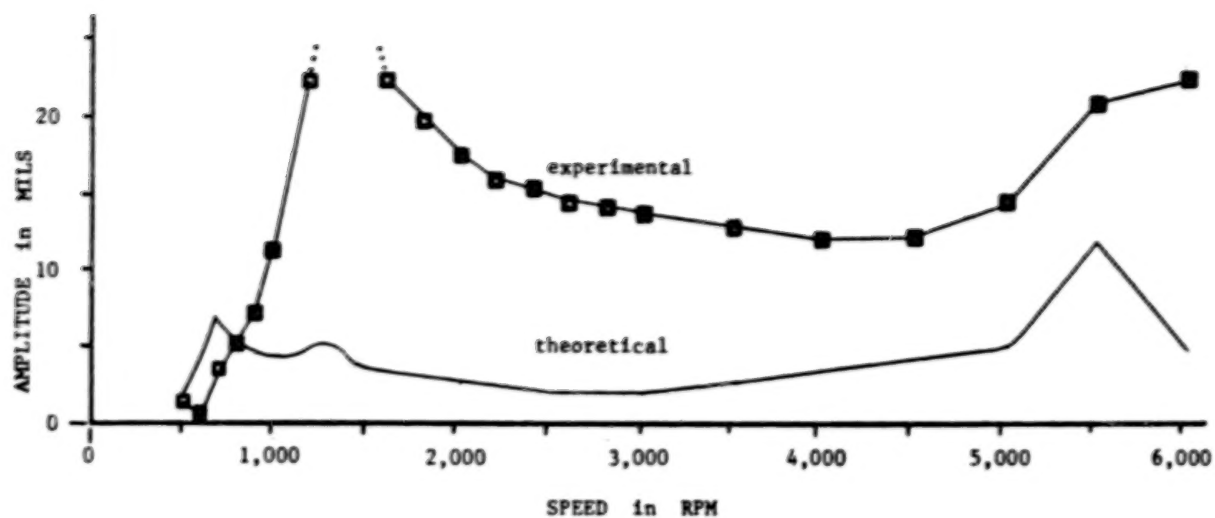

Figure 2. - No feedback control.
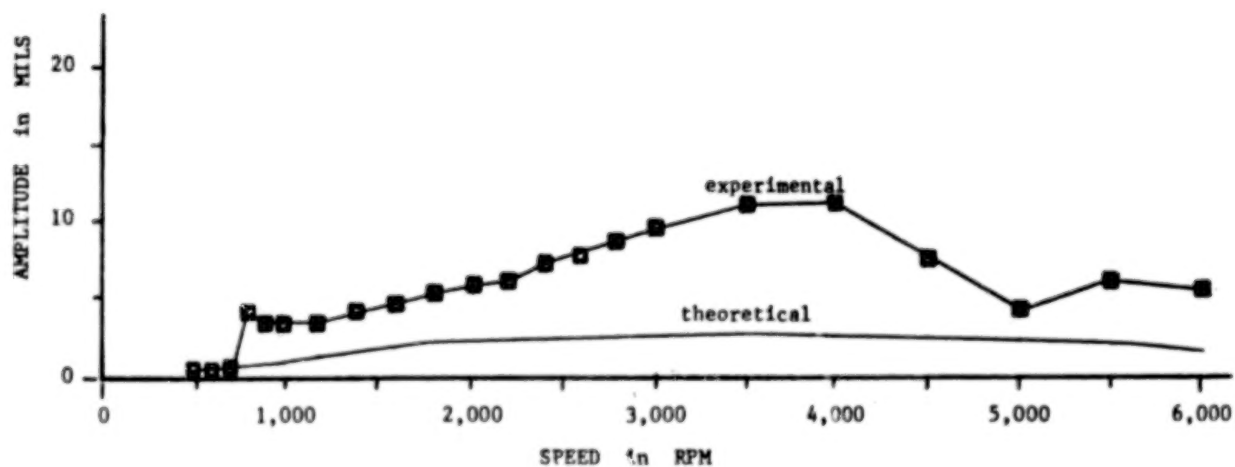
438

Figure 3. - Small velocity feedback control.

Figure 4. - Large velocity feedback control.

439

EVALUATION OF SHEAR MOUNTED ELASTOMERIC DAMPER

E. Zorzi and J. Walton
Mechanical Technology, Inc.
Latham, New York   12110

SUMMARY

The safe and reliable operation of high speed rotating machinery often requires the use of devices that dissipate undesirable rotor vibrations. As an alternative to the more conventional squeeze film bearing damper designs, a Viton-70 elastomeric shear mounted damper was built and tested on a T-55 power turbine spool in the rotor's high speed balancing rig. This application of a shear mounted elastomeric damper demonstrated for the first time, the feasibility of using elastomers as the primary rotor damping source in production turbine engine hardware. The shear damper design was selected because it was compatible with actual gas turbine engine radial space constraints, could accommodate both the radial and axial thrust loads present in gas turbine engines, and was capable of controlled axial preload. The shear damper was interchangeable with the production T-55 power turbine roller bearing support so that a direct comparison between the shear damper and the production support structure could be made. Test results show that the Viton-70 elastomer damper operated successfully and provided excellent control of both synchronous and non-synchronous vibrations through all phases of testing up to the maximum rotor speed of 16,000 rpm. Excellent correlation between the predicted and experienced critical speeds, mode shapes and log decrements for the power turbine rotor and elastomer damper assembly was also achieved.

INTRODUCTION

With the advent of higher power density turbomachinery and the use of long unsupported shaft segments, rotor systems are operating near or above one or more critical speeds and are therefore susceptible to any number of destabilizing mechanisms. To insure the safe and reliable operation of this machinery, considerable effort is often expended in an attempt to control both synchronous and non-synchronous vibrations. Since balancing technology has matured to the point that the control of synchronous vibrations is not a limiting factor, emphasis has been directed at methods of dissipating undesirable vibrations and stabilizing rotor bearing systems. Squeeze film dampers provide one method of control but, close tolerance machining, oil supply requirements, and the associated hydraulic plumbing make these systems expensive and vulnerable. As an alternative to the squeeze film bearing damper a convenient, compact, self sufficient and inexpensive dry damper with a wide range of stiffness and damping characteristics that will provide comparable vibration control is desired. Elastomer dampers have many of the desirable features but, their use has been limited due to the lack of adequate design information and demonstrations of capability. With the research reported on in References 1 thru 5, considerable progress has been made in establishing the design guidelines for elastomer dampers. As a demonstration of elastomer damper

capability in the control of rotor vibration an experimental investigation was performed at MTI. In this test program a Viton-70 shear mounted elastomeric damper was designed specifically to control the vibrations of a T-55 power turbine rotor mounted in a high-speed balancing rig. The high-speed balancing rig used as the test facility in this program was constructed by MTI under a NASA contract (NAS 3-20609) managed by Robert Cunningham for the U.S. Army's Corpus Christi Army Depot (CCAD) and was used with the Army's permission. The CCAD high speed balancing facility incorporates production engine bearings, support structure and is capable of achieving operational speeds. It therefore provided an excellent opportunity to test a production gas turbine engine hardware compatible, elastomer damper design for the first time.

Since many gas turbines are multi-shafted and radial design flexibility is inhibited, the damper was designed to be active in shear. This design configuration (fig. 1) minimizes the required radial envelope and accommodates axial thrust loading which may be required in typical gas turbine applications. Once an analytical model of the production CCAD balancing rig was established and calibrated against typical response characteristics for the rig, damper optimization studies were performed. The results of the optimization studies provided the required ranges of damper stiffness and loss coefficients for this application.

As documented, the shear elastomer damper operated successfully to the maximum operating speed of 16,000 RPM. Orbit control was reliable with no severe or large nonsynchronous components of vibration observed. Thermocouple monitoring showed that the temperature of the elastomer never exceeded 65°C during testing. Further, there was excellent agreement between the analytical predictions and measured data for critical speeds, mode shapes and logarithmic decrement which clearly demonstrated the ability of the T-55 power turbine elastomer damper to predictably control rotor vibration for safe and reliable operation.

ROTOR OPTIMIZATION STUDIES

A typical response profile of the CCAD rig with production hardware and a T-55 power turbine installed is shown in figure 2. This figure is a trace of the synchronous response of a slow acceleration pattern for a 90° pair of probes (vertical and horizontal) at approximately midshaft location. The two dominant features are the peaks at approximately 4,000 and 6,000 RPM. This highly elliptical horizontal orbit occurring at 4,000 RPM, rapidly changing to a dominant vertical ellipse at 6,000 RPM, is typical of characteristics of a retrograde and forward precession encouraged by asymmetric support characteristics. The response of the turbine end at these two speeds is dominant whereas the roller bearing end (cold end) showed little activity, indicating a strong precession of the turbine such as produced by a rigid body conical mode shape. A subsequent set of peaks occurred in the 8,000 to 9,000 RPM speed range, with all probe sets along the shaft indicating motion. The activity at this speed was not predicted analytically, but was generally subordinate to the two main peaks at 4,000 and 6,000 RPM and was most likely due to the structure.

To further assess possible rotor modes and determine the acceptability of the proposed rotordynamic model, a small exciter was attached to the CCAD rig to excite the nonrotating T-55 power turbine. Swept sine-wave excitation indicated three possible structural modes:

- 115 Hz bounce mode of turbine

- 210 Hz bending mode of shaft

- 600 Hz bending mode of shaft

Figure 3 indicates the location of these structural frequencies when compared to a tuned analytical model of the T-55 (whirl speed marked by "X" at zero spin speed axis). This analytic model also predicted a first retrograde (backward) precession turbine conical mode at 4,500 RPM, a first forward mode at 6,000 RPM and a first bending (2nd critical) at 21,000 RPM. The production engine support rigidity needed to calibrate this model was reasonable, with a roller bearing stiffness of 8.75×10^7 N/m (500,000 lb/in.) and a ball bearing (turbine) pedestal stiffness of 1.40×10^7 N/m (80,000 lb/in.).

Further evidence of the models validity was obtained by observing the super-synchronous excitation of the small 2/rev component of motion throughout a normal acceleration pattern to maximum speed. The 2/rev peaked while operating at 7,100 RPM indicating the presence of a mode as shown in figure 3 at the intersection of the 2/rev excitation line and the second critical speed line.

Therefore, from observation of rotor synchronous response, static shaker excitation data and observation of the 2/rev vibration, the rotor-dynamics model was considered acceptable for analytic examination of possible elastomeric-damper designs.

Previous elastomer material testing of shear specimens (ref. 1) was reviewed for candidate elastomer material selection. Viton-70 at 32°C showed the largest measured value of loss coefficient for the entire range of frequencies expected. As the loss coefficient is a measurement of the ratio of material damping to stiffness, a higher value of loss coefficient reflects an increased capacity to dissipate energy. Temperature increases make the selection of material for damping somewhat arbitrary as the loss coefficient for all materials, Buna-N, EPDM, Neoprene and Viton ranges between 0.1 and 0.2 for the entire frequency range at a temperature of 88°C. Therefore the decision to use Viton as the damping material was based upon the following:

- Viton-70 shows superior damping properties compared to the other materials tested for 32°C or 66°C operation (figs. 4 and 5).

- Viton-70's dissipation characteristics are as good as any of the other materials tested for operation at 88°C.

- Viton-70 was previously used as a damper in success-ful testing of high-speed rotor dampers (refs. 1 and 5).

- Unused Viton material was available from MTI elastomer test activity under NASA Programs NAS 3-18546.

Based on data obtained from shear specimen shaker testing of Viton-70 (ref. 5) a range of loss coefficients from 0.15 to 0.75 could conceivably be expected for the 0-16,000 RPM operation of the CCAD balancing rig (fig. 6). Accordingly, the T-55 power-turbine rotor-dynamics model was modified to determine the optimal damper design (figs. 7 and 8). All system damping was assumed to be due to the elastomer damper, consequently no structural damping was modeled for the turbine or gearbox bearing. However, the two disk pack couplings were included as elastic elements which offered a minimum of bending rigidity but offered full shear restraint.

As a result of the rotor damper optimization studies (figs. 7 and 8) a number of facts surfaced regarding the design of the elastomeric damper:

- The first critical speed is a conical precession of the turbine with its nodal point extremely close to the elastomer damper test bearing location. Accordingly, the first critical speed offers little damping and is insensitive to the elastomer damper stiffness or damping characteristics.

- The second and third mode shapes offer significant activity of the elastomeric damper. Consequently, the critical speed location and log decrement of those critical speeds are sensitive to damper selection.

- A best, or optimal, tradeoff between the second and third mode is obtained by a Viton-70 elastomeric damper of between $5.25 \times 10^6 - 7.0 \times 10^6$ N/m (30,000-40,000 lb/in.).

- It is expected with this value of stiffness, the T-55 rotor mounted on the elastomeric damper would traverse the second critical, which is not within the operational range of the roller-bearing mounted production T-55 configuration (fig. 3).

- The range of log decrement expected for the second critical speed is between 0.2 to 1.1 dependent upon the loss coefficient (temperature of operation) for the elastomer damper.

DAMPER DESIGN AND FABRICATION

Past elastomer designs at MTI consisted of button configurations because of the need to have either interchangeability for comparisons of different elastomers or for direct comparisons with squeeze film bearing dampers. T-55 damper design however, offered uniquely challenging problems since this configuration had to be compatible with actual gas turbine design technology and constraints. Most gas turbines do not have the large amounts of radial envelope required by button designs, particularly if they are multishaft turbofan or turboshaft engines such as the T-55. On the other hand, design maneuverability and flexibility are often generally less restricted in the axial direction. Additionally, the design must accommodate

443

possible thrust loading (although the T-55 roller bearing mount does not take thrust) in combination with radial loads and be capable of controlled preload. These requirements were satisfied by the shear damper configuration.

Figure 1 illustrates the concept used for the elastomer damper mount on the T-55 roller-bearing support. Two Viton-70 shear rings mounted along the entire circumference satisfied all requirements. Axial preload was accommodated by controlled machining of the outer flanges which attached to the housing by twelve equally spaced socket head cap screws. An overload protector was installed by using an O-ring with a prescribed clearance of 0.254 mm (0.010 in.) to avoid interference with normal operation of the damper while still providing backup protection should the shear damper or bond fail.

To obtain the required stiffness for the Viton-70 damper previous shear specimen data was used (ref. 5). The resulting design, 6.98 cm (2.75 in.) I.D. and 9.52 cm (3.75 in.) O.D. for a 3.175 mm (0.125 in.) thick Viton-70 specimen, produced a stiffness range in shear of approximately 6.12×10^6 - 7.0×10^6 N/m (35,000 to 40,000 lb/in.) depending upon strain amplitude experienced. These analytically predicted values of stiffness were validated prior to test through static load testing. The static values determined were between 6.12×10^6 and 6.47×10^6 N/m (35,000 to 37,000 lb/in.). Axial compression stiffness was also determined and was found to be approximately 1.26×10^7 N/m (72,000 lb/in.). In all cases the static loads were applied and held constant for up to 5 minutes to determine if any load relaxation would occur. No measurable load relaxation was observed.

TEST RESULTS

The baseline run of a balanced T-55 power turbine supported on the production roller bearing support housing showed the characteristics previously noted in fig. 2 and reconfirmed the existence of the turbine horizontal and vertical rigid body precessional modes at 4,000 and 6,000 RPM respectively. Additionally, the intermediate peaks in the 8,000-9,000 RPM range were again observed though not confirmed analytically (although suspected to be induced by the rigs' structure). The data collected during the initial elastomer damper tests showed that a substantial reduction in synchronous response occurred for both the 6,000 RPM and 8,000 RPM peaks but that the response near 14,000 RPM increased as can be seen in fig. 9. Through an unbalance sensitivity study this new peak was determined to be the second critical speed as was predicted analytically.

A comparison of the analysis performed for the elastomer-damper supported system with the measured data provides good correlation for mode shapes (fig. 10). Table I provides a comparison of critical speeds and logarithmic decrements for the two criticals observed.

There is excellent correlation in whirl speed, but the first critical's log decrement is significantly different in value between test and analysis. This is due to the fact that analysis has indicated a node at the damper for the first critical. Slight changes in rigidity of the shaft or location of roller-bearing support would alter the analytically predicted value of log decrement for the first critical appreciably. Further, consideration of structural damping which occurs at the turbine end bearing (which is heavily participating in the first critical, fig. 10) was not included in the analysis. Therefore, the analysis does not reflect

this form of structural damping which can greatly effect the measured log decrement of the first critical speed.

Typical measured response indicated dominant 1/rev excitation of the rotor through the testing with the elastomer damper active. Figure 11 presents a typical frequency spectrum at 13,000 RPM. As shown, relatively minor subsynchronous and supersynchronous excitations were experienced and the operation of the T-55 power turbine was as predicted throughout the entire test phase.

CONCLUSION

This successful application of elastomer damper technology presents an opportunity to reflect upon the many uses for elastomers as alternatives to the conventional squeeze film dampers. While this work does establish an initial benchmark for elastomers as viable alternatives for damping of high speed rotating machinery, further efforts are required to firmly establish this technology. In particular, these efforts need to address the testing of elastomers in the rather hostile but realistic gas turbine environments. The authors are cognizant of the temperature limitations of elastomers however, newer and greater varieties are being introduced each year that do offer a wide variety of application opportunities particularly in the colder (compressor) section of gas turbines. Therefore, this contribution is offered in the hope that further exploration of "dry damper" technology be encouraged.

REFERENCES

1. Tecza, J. A.; Darlow, M. S.; and Smalley, A. J., "Development of Procedures for Calculating Stiffness and Damping of Elastomers in Engineering Applications - Part V." NAS3-18546, February 1979.

2. Chiang, T.; Tessarzik, J. M.; and Badgley, R. H., "Development of Procedures for Calculating Stiffness and Damping Properties of Elastomers in Engineering Applications - Part I: Verification of Basic Methods." NASA Report CR-120905, March 1972.

3. Gupta, P. K.; Tessarzik, J. M.; and Cziglenyi, L., "Development of Procedures for Calculating Stiffness and Damping Properties of Elastomers in Engineering Applications, Part II: Elastomer Characteristics at Constant Temperature." NASA Report CR-134704, April 1974.

4. Darlow, M. S.; and Smalley, A. J., "Development of Procedures for Calculating Stiffness and Damping Properties of Elastomers in Engineering Application, Part IV: Testing of Elastomers Under a Rotating Load." NASA Report CR-135355, November 1977.

5. Rieger, A.; Burgess, G.; and Zorzi, E., "Development of Procedures for Calculating Stiffness and Damping Properties of Elastomers in Engineering Applications, Part VI." NASA Report CR-159838, April 1980.

TABLE I.

	Analysis		Measured	
	Speed (RPM)	Log Decrement	Speed (RPM)	Log Decrement
First Critical	6,022	0.001	6,007	0.090*
Second Critical	13,535	0.?01	13,666	0.206*

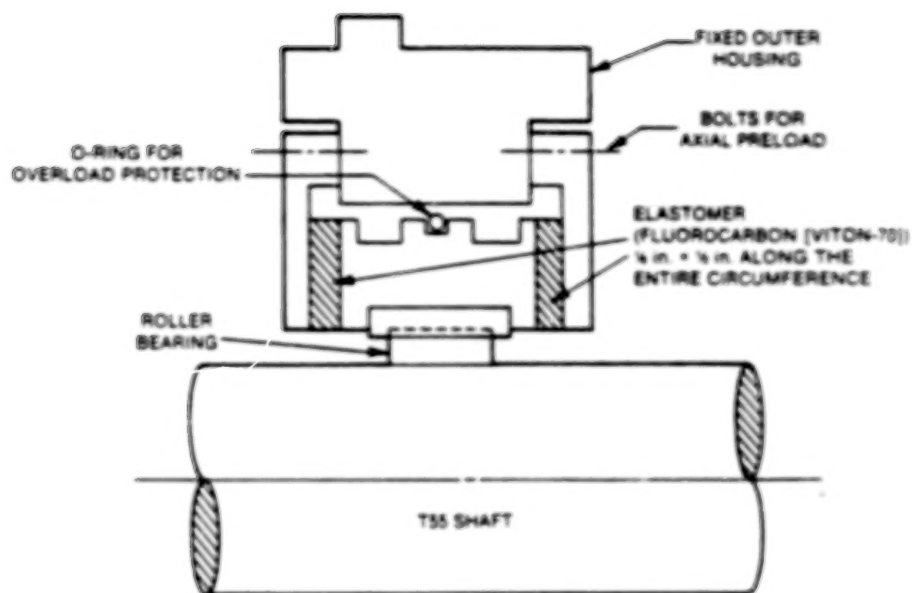* Average value for all data obtained.

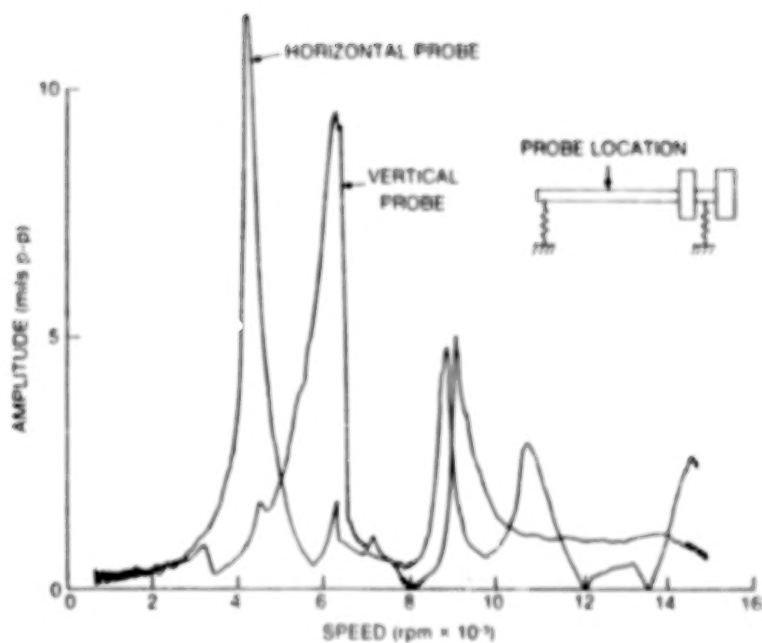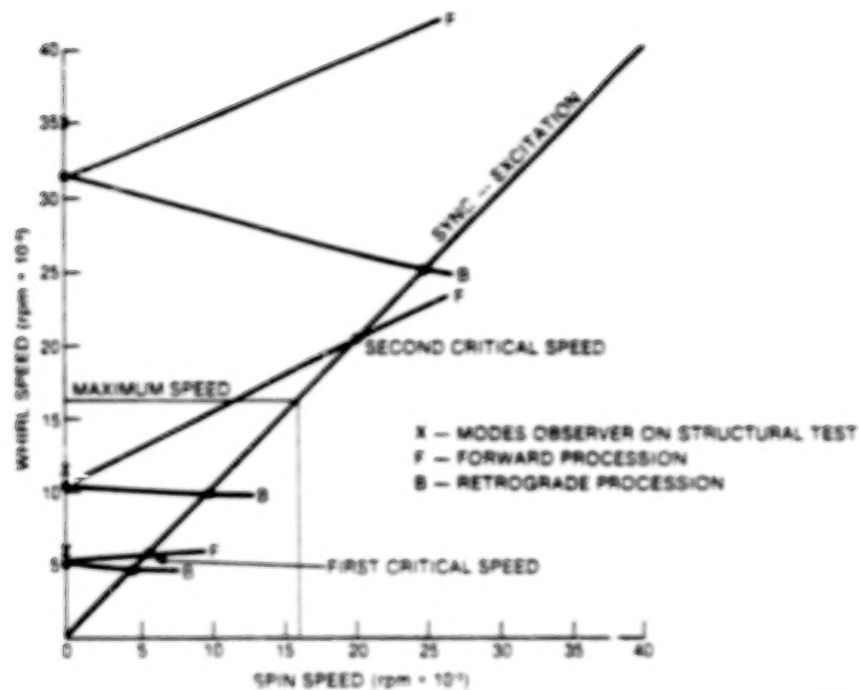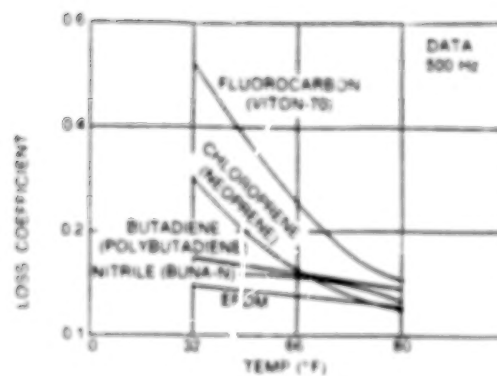Figure 1. - T-55 Elastomer supported roller bearing cartridge.

Figure 2. - Synchronous response of T-55 on CCAD rig.

447

Figure 3. - Whirl speed versus spin speed.

Figure 4. - Temperature variation of elastomer loss coefficient (at 500 Hz) for shear tests.
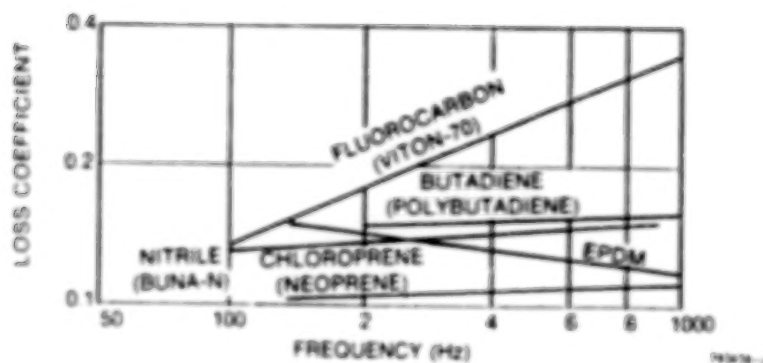
Figure 5. - Shear specimen data at 66°C.
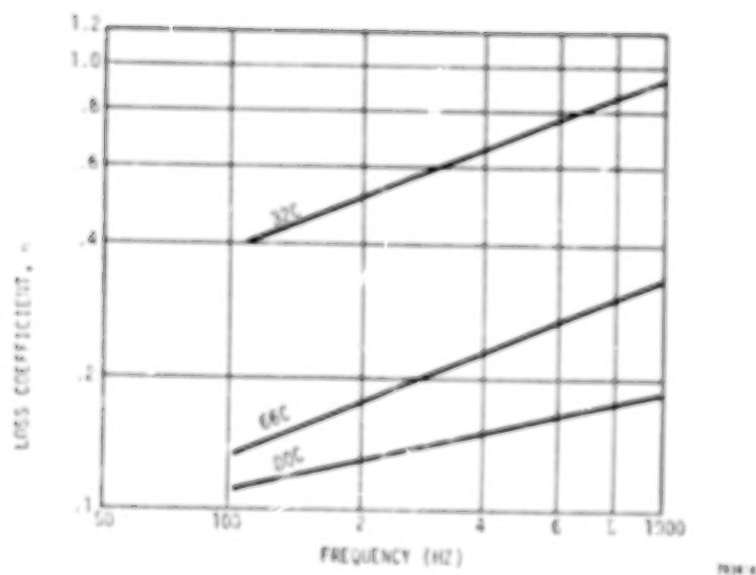
Figure 6. - Fluorocarbon (Viton-70) shear specimen data.

449
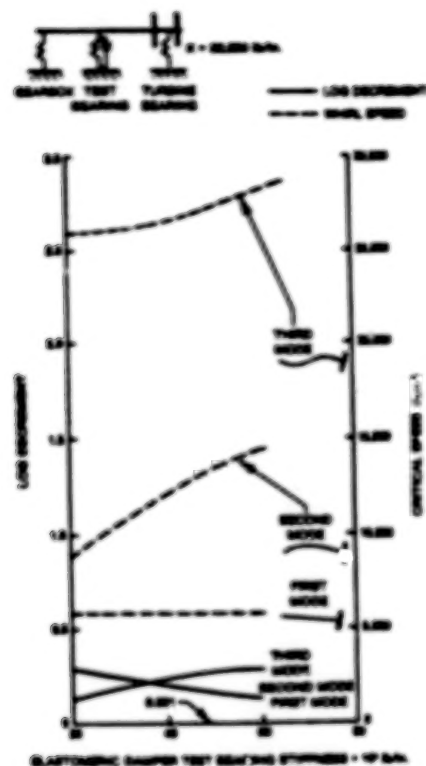
Figure 7. - T-55 power turbine - critical speeds and log decrement vs. bearing stiffness for Viton-70 elastomeric damper (η = 0.15).
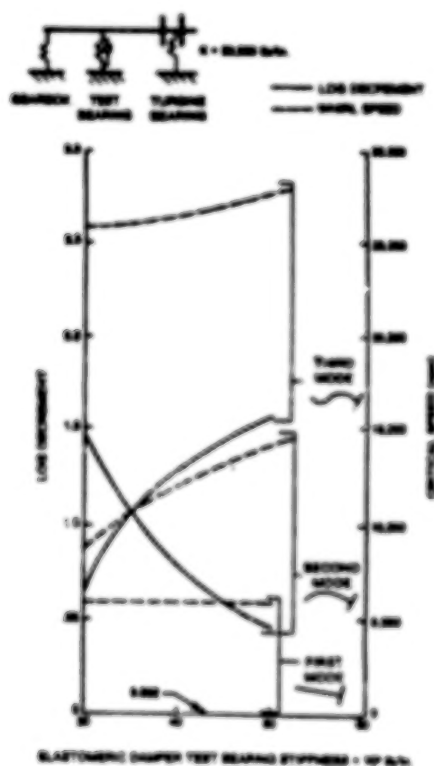
Figure 8. - T-55 power turbine - critical speeds and log decrement vs. bearing stiffness for Viton-70 elastomeric damper (η = 0.75).
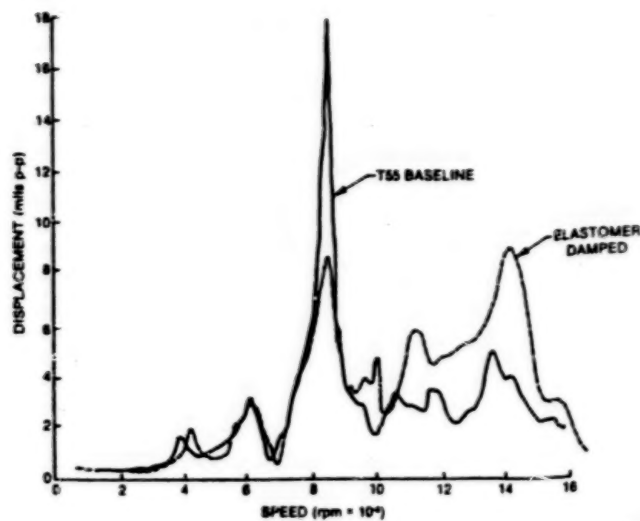
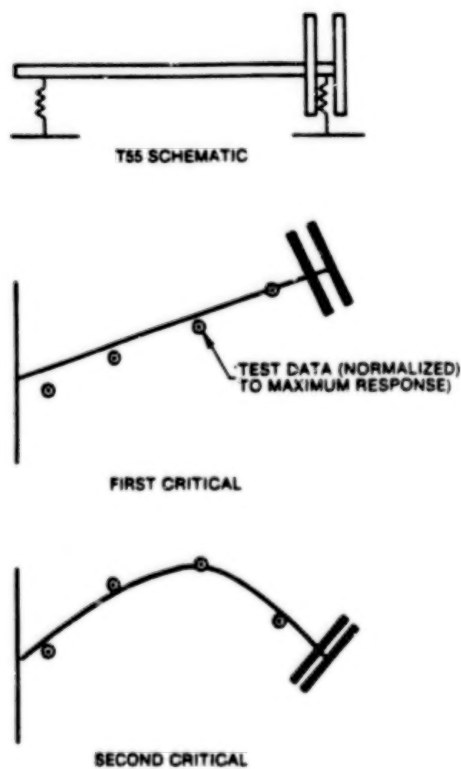Figure 9. - Vibration plot comparing baseline and elastomer mounted rotor response.

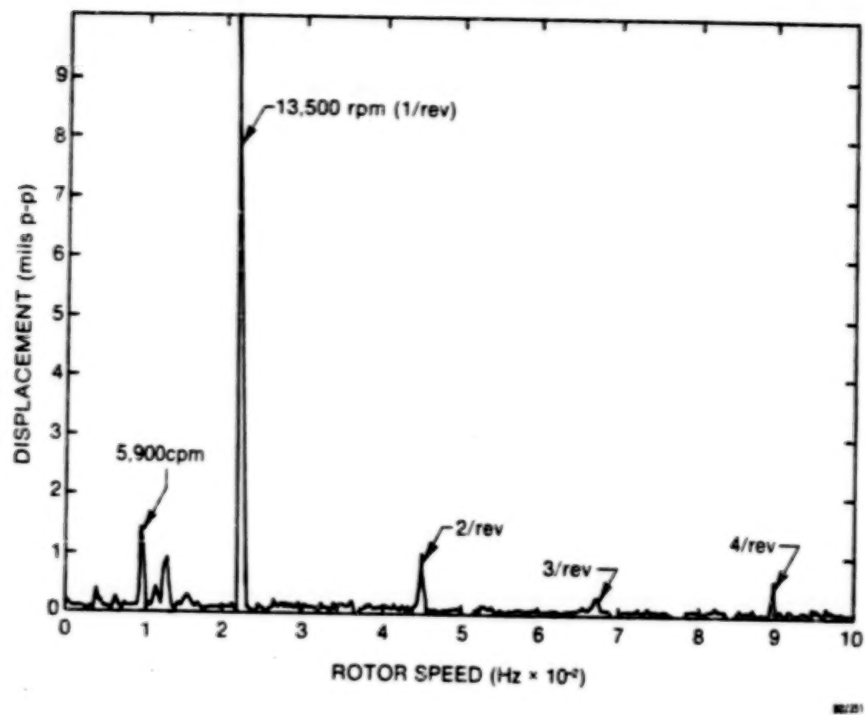Figure 10. - Comparison of test data with analytic predicted modes.

Figure 11. - Spectrum plot on elastomer probe #5; 3 gm @ 300° plane 1.

BEST DOCUMENT AVAILABLE

1. Report No. NASA CP-2250	2. Government Accession No.	3. Recipient's Catalog No.
4. Title and Subtitle ROTORDYNAMIC INSTABILITY PROBLEMS IN HIGH-PERFORMANCE TURBOMACHINERY - 1982		5. Report Date December 1982
		6. Performing Organization Code 505-32-42
7. Author(s)		8. Performing Organization Report No. E-1287
		10. Work Unit No.
9. Performing Organization Name and Address NASA Lewis Research Center Cleveland, OH 44135		
		11. Contract or Grant No.
		13. Type of Report and Period Covered Conference Publication
12. Sponsoring Agency Name and Address National Aeronautics and Space Administration Washington, D.C. 20546		
		14. Sponsoring Agency Code

15. Supplementary Notes

16. Abstract

The first rotordynamics workshop proceedings (NASA CP-2133) emphasized a feeling of uncertainty involved in predicting the stability characteristics of turbomachinery. The present workshop proceedings demonstrates that many of these uncertainties have been substantially reduced. To a considerable extent, papers presented herein report the results of programs that have been established to systematically resolve the problems of predicting stability characteristics of high-performance turbomachinery. The emphasis on experimental validation of the forces that influence rotordynamics is particularly encouraging.

17. Key Words (Suggested by Author(s)) Rotordynamics Turbomachinery Instability	18. Distribution Statement Unclassified - unlimited STAR Category 37	
19. Security Classif. (of this report) Unclassified	20. Security Classif. (of this page) Unclassified	21. No. of Pages 458 22. Price* A20

J+ 53